SOLIDS TRANSPORT IN LAMINAR, OPEN CHANNEL FLOW OF NON-NEWTONIAN SLURRIES

A Thesis Submitted to the College of

Graduate Studies and Research

in Partial Fulfilment of the Requirements

for the Degree of Doctor of Philosophy

in the Department of Chemical Engineering

University of Saskatchewan

Saskatoon, Saskatchewan, Canada

by

Ryan Brent Spelay

PERMISSION TO USE

In presenting this thesis in partial fulfilment of the requirements for a postgraduate degree from the University of Saskatchewan, I agree that the libraries of this University may make it freely available for inspection. I further agree that permission for copying of this thesis in any manner, in whole or in part, for scholarly purposes may be granted by the professor or professors that supervised my thesis work or, in their absence, by the Head of the Department or the Dean of the College in which my thesis work was done. It is understood that any copying or publication or use of this thesis or parts thereof for financial gain shall not be allowed without my written permission. It is also understood that due recognition shall be given to me and to the University of Saskatchewan in any scholarly use which may be made of any material in my thesis.

Requests for permission to copy or make use of material in this thesis in whole or part should be addressed to:

Head of the Department of Chemical Engineering

University of Saskatchewan

Saskatoon, Saskatchewan, Canada S7N 5A9

ABSTRACT

Thickened tailings production and disposal continue to grow in importance in the mining industry. In particular, the transport of oil sands tailings is of interest in this study. These tailings must be in a homogeneous state (non-segregating) during pipeline flow and subsequent discharge. Tailings are often transported in an open channel or flume. Slurries containing both clay and coarse sand particles typically exhibit non-Newtonian rheological behaviour. The prediction of the flow behaviour of these slurries is complicated by the limited research activity in this area. As a result, the underlying mechanisms of solids transport in these slurries are not well understood. To address this deficiency, experimental studies were conducted with kaolin clay slurries containing coarse sand in an open circular channel.

A numerical model has been developed to predict the behaviour of coarse solid particles in laminar, open channel, non-Newtonian flows. The model involves the simultaneous solution of the Navier-Stokes equations and a scalar concentration equation describing the behaviour of coarse particles within the flow. The model uses the theory of shear-induced particle diffusion (Phillips et al., 1992) to provide a number of relationships to describe the diffusive flux of coarse particles within laminar flows. A sedimentation flux has been developed and incorporated into the Phillips et al. (1992) model to account for gravitational flux of particles within the flow. Previous researchers (Gillies et al., 1999) have shown that this is a significant mechanism of particle migration.

The momentum and concentration partial differential equations have been solved numerically by applying the finite volume method. The differential equations are non-linear, stiff and tightly coupled which requires a novel means of analysis. Specific no-flux, no-slip and no-shear boundary conditions have been applied to the channel walls and free surface to produce simulated velocity and concentration distributions. The results show that the model is capable of predicting coarse particle settling in laminar, non-Newtonian, open channel flows. The results of the numerical simulations have been compared to the experimental results obtained in this study, as well as the experimental results of previous studies in the literature.

ACKNOWLEDGEMENTS

I would like to express my deepest gratitude to my supervisor Dr. R.J. Sumner for proofreading this thesis and providing guidance throughout the study. Not only has he taught me the subtleties of what it takes to conduct successful research, but he has also become a close friend. I would also like to express my sincerest appreciation to the late Dr. C.A. Shook for inspiring me to undertake graduate studies and opening my eyes to an amazing field of research. It was truly a privilege to be associated with such a distinguished person.

I will forever be indebted to Dr. R.G. Gillies and the staff at the Saskatchewan Research Council's Pipe Flow Technology Centre (P. Schergevitch, C. Litzenberger, C. Knops, D. Riley, J. Fenez, D. McEwan, R. Sun, A. Holmes, Dr. M.J. McKibben, and D. Soveran). All have made important contributions to this study and without their technical expertise and sound advice this body of work would not have been possible.

I would like to thank Dr. R.S. Sanders and Mr. J. Schaan. Their expertise in the area of slurry flow and the oil sand industry, as well as their willingness to provide guidance to this study, is appreciated. I would also like to acknowledge D. Tomczak, A. May, C. Ash and N. Rolston for providing valuable assistance during the collection of experimental data in this study.

I would like to thank Dr. A.V. Phoenix, Dr. G.A. Hill and Dr. D.J. Bergstrom for being members of my advisory committee. I would also like to thank Dr. K. Nandakumar for being the external examiner. Their valuable input and constructive criticism has helped shape this thesis into a complete and thorough body of work.

The financial support of NSERC (Natural Sciences and Engineering Research Council of Canada), Syncrude Canada Ltd. and the University of Saskatchewan (Department of Chemical Engineering and the College of Graduate Studies and Research) is gratefully acknowledged and appreciated.

Finally, I would like to thank my family and friends. In particular, I would like to express my deepest appreciation to my parents for instilling in me a true desire to learn and pursue my goals. Their love and support have been crucial to many of the successes I have been able to achieve.

DEDICATION

This thesis is dedicated to my wife Tanya. I doubt completing it would have been possible without her persistent encouragement and unconditional love.

TABLE OF CONTENTS

PERMISSION TO USE i
ABSTRACT ii
ACKNOWLEDGEMENTS iii
DEDICATION iv
TABLE OF CONTENTS v
LIST OF TABLES viii
LIST OF FIGURES xi
LIST OF SYMBOLS xviii

1. INTRODUCTION 1
   1.1. Present Study 3

2. LITERATURE REVIEW 5
   2.1. Homogeneous Fluid Models 5
   2.2. Slurry Flow Background 7
   2.3. Open Channel Flow 9
   2.4. Kozicki and Tiu Model 16
   2.5. Single Particle Settling 19
   2.6. Multi-Particle Systems 22
   2.7. Sediment Transport 26
   2.8. Pastes 27
   2.9. Stabilized Flow 28
   2.10. Bingham Fluid Model 33
   2.11. Characterization 35
      2.11.1. Pipeline Viscometry 35
      2.11.2. Couette Viscometry 38
      2.11.3. Vane Viscometry 40
      2.11.4. Slump Test 41
   2.12. Pitot Tubes 42
   2.13. Low Reynolds Number Pitot Tube Effect 43
   2.14. Numerical Models 45
      2.14.1. Two-Layer Model 45
      2.14.2. Microscopic Modeling Background 47
      2.14.3. Dispersive Stress Modeling 48

3. EXPERIMENTAL PROCEDURES AND CONDITIONS 53
   3.1. Experimental Flume Setup 53
   3.2. Pitot Tube 58
   3.3. Low Reynolds Number Pitot Tube Study 60
   3.4. Gamma Ray Densitometer 65
   3.5. Procedure and Operation 67
      3.5.1. Sand-Water Slurries 71
      3.5.2. CT Slurries 73
      3.5.3. Thickened Tailings Slurries 74
      3.5.4. Clay-Water Slurries 74

4. NUMERICAL MODEL 76
   4.1. Governing Equations 76

4.2. Shear-Induced Particle Diffusion Modeling History 80
4.3. Phillips Model Background 84
4.4. The Phillips Model 86
4.4.1. Flux due to spatially varying interaction frequency 87
4.4.2. Flux due to spatially varying viscosity 88
4.4.3. Flux due to particle sedimentation 89
4.5. Adjustable Parameters 92
4.6. Scalar Model Transport Equation 95
4.7. Supplementary Equations 96
4.8. Related Modeling Investigations 101
4.9. Finite Volume Method 104
4.9.1. Navier-Stokes Equation (z-wise) 108
4.9.2. Scalar Concentration Transport Equation 110
4.10. Solution Procedure 114
4.11. Tridiagonal Matrix/Thomas Algorithm (TDMA) 115
4.12. Indirect/Iterative Solvers 117
4.13. Boundary Conditions 119
4.13.1. Velocity 120
4.13.2. Concentration 123
4.14. Error Analysis 128
4.15. Interpolation Schemes 129
4.15.1. Linear 129
4.15.2. Geometric 130
4.16. Shear Rate 131
4.17. Concentration Scaling 133
4.18. Singularities 134

5. EXPERIMENTAL RESULTS AND DISCUSSION 138
5.1. Test matrix 138
5.2. Rheological Characterization 139
5.3. Wall Roughness 141
5.4. Slurry Rheology 144
5.4.1. Clay-Water Slurries 144
5.4.2. Sand-Water Slurries 147
5.4.3. CT Slurries 150
5.4.3.1. CT ‘No Gypsum’ Slurry 151
5.4.3.2. CT ‘Gypsum’ Slurry 152
5.4.4. Thickened Tailings Slurries 153
5.5. Flume Wall Shear Stresses and Friction Factors 154
5.5.1. Water 156
5.5.2. Sand-Water Slurries 158
5.5.3. Clay-Water Slurries 163
5.5.4. Clay-Water Slurries in Rectangular Channels 172
5.5.5. CT Slurries 175
5.5.6. Thickened Tailings Slurries 180
5.6. Sampling 184
5.7. Concentration Profiles 187
5.7.1. Sand-Water Slurries 187
5.7.2. CT Slurries 192
5.7.3. Thickened Tailings Slurries 195
5.8. Velocity Profiles 201

5.8.1. Low Reynolds Number Pitot Tube Effect 201
5.8.2. Flume Velocity Profiles 205
5.8.2.1. Water 206
5.8.2.2. Clay-Water Slurries 207
5.8.2.3. Sand-Water Slurries 209
5.8.2.4. CT Slurries 212
5.8.2.5. Thickened Tailings Slurries 215

6. NUMERICAL RESULTS AND DISCUSSION 218
6.1. Commercial Software 218
6.1.1. CFD2000 219
6.1.2. ADINA 219
6.1.3. WRAFTS 220
6.1.4. CFX and FLUENT 220
6.2. Phillips Model Verification 221
6.3. Grid Refinement 225
6.4. Model Tailings Simulations 226
6.4.1. Thickened Tailings Slurries 226
6.4.2. CT 'Gypsum' Slurries 236
6.5. Simulation Discussions 245
6.6. Reduced Immersed Weight Simulation 252
6.7. Gillies Model Comparison 253

7. CONCLUSIONS 260
7.1. Experimental Conclusions 260
7.2. Numerical Conclusions 261

8. RECOMMENDATIONS 264

9. REFERENCES 265

APPENDIX A: COMPUTER CODE 278
APPENDIX B: MATERIALS 309
APPENDIX C: CALIBRATIONS 313
APPENDIX D: EXPERIMENTAL DATA 343
APPENDIX E: SIMULATION DATA 396
APPENDIX F: PHOTOGRAPHS 409

LIST OF TABLES

3.1:	Dimensions of Pitot-static tubes employed in low Reynolds Pitot tube number study	65
5.1:	Compositions of the mixtures investigated in the 156.7 mm flume experiments	138
5.2:	Test matrix for the 156.7 mm flume experiments	139
5.3:	Rheological properties of the mixtures investigated in the 156.7 mm flume experiments	140
5.4:	Rheological properties of the carrier fluids for the model tailings mixtures investigated in the 156.7 mm flume experiments	141
5.5:	Maximum packing concentrations (v/v) for the Unimin 188 μm (Granusil 5010) sand employed in the 156.7 mm flume tests	148
5.6:	Sampling results for the kaolin clay-water slurry experimental tests	185
5.7:	Sampling results for the Syncrude CT 'no gypsum' experimental tests	186
5.8:	Sampling results for the Syncrude CT 'gypsum' experimental tests	186
5.9:	Sampling results for the Syncrude Thickened Tailings experimental tests	186
5.10:	Coarse to fines ratios as determined by the traversing gamma ray densitometer for the model tailings experiments in the 156.7 mm flume	200
5.11:	Comparison of segregating behaviour of coarse solids with the acceleration and deceleration of the model tailings mixtures in the 156.7 mm flume	201
5.12:	Comparison of unsheared region velocities with free surface velocities for a 22.6% v/v kaolin clay-water slurry with 0.03% TSPP in the 156.7 mm flume	208

Appendices

D.1:	Pressure gradient versus velocity data for Saskatoon tap water to determine the roughness of the 53 mm pipe feed test section during the testing of the model tailings slurries	344
D.2:	Pressure gradient versus velocity data for a 25% v/v sand-water slurry in the 53 mm pipe feed test section	345
D.3:	Pressure gradient versus velocity data for a CT 'no gypsum' model tailings slurry in the 53 mm pipe feed test section	346
D.4:	Pressure gradient versus velocity data for a CT 'gypsum' model tailings slurry in the 53 mm pipe feed test section	346
D.5:	Pressure gradient versus velocity data for a model Thickened Tailings slurry in the 53 mm pipe feed test section	347
D.6:	Pressure gradient versus velocity data for Saskatoon tap water to determine the roughness of the 53 mm pipe feed test section during the testing of the kaolin clay-water slurries before polishing	347
D.7:	Pressure gradient versus velocity data for Saskatoon tap water to determine the roughness of the 53 mm pipe feed test section during the testing of the kaolin clay-water slurries after polishing but before testing	348
D.8:	Pressure gradient versus velocity data for Saskatoon tap water to determine the roughness of the 53 mm pipe feed test section during the testing of the kaolin clay-water slurries after testing	349
D.9:	Pressure gradient versus velocity data for a 22.2% v/v kaolin clay-water slurry in the 53mm test section; ρ=1375 kg/m^3	350
D.10:	Pressure gradient versus velocity data for a 22.6% v/v kaolin clay-water slurry with 0.03% TSPP in the 53mm test section; ρ=1384 kg/m^3	351

D.11: Pressure gradient versus velocity data for a 22.8% v/v kaolin clay-water slurry with 0.10% TSPP in the 53mm test section; ρ=1386 kg/m^3 352
D.12: Frictional loss measurements for Saskatoon tap water in the 156.7 mm flume 353
D.13: Old Inlet frictional loss measurements for a 25% v/v, sand-water slurry in the 156.7 mm flume; ρ=1410 kg/m^3 356
D.14: New Inlet frictional loss measurements for a 25% v/v, sand-water slurry in the 156.7 mm flume; ρ=1410 kg/m^3 357
D.15: Frictional loss measurements for a CT 'no gypsum' model tailings slurry in the 156.7 mm flume; ρ=1598 kg/m^3 358
D.16: Frictional loss measurements for a CT 'gypsum' model tailings slurry in the 156.7 mm flume; ρ=1598 kg/m^3 358
D.17: Frictional loss measurements for a model Thickened Tailings slurry in the 156.7 mm flume; ρ=1510 kg/m^3 358
D.18: Frictional loss measurements for a 22.2% v/v kaolin clay-water slurry in the 156.7 mm flume; ρ=1375 kg/m^3 359
D.19: Frictional loss measurements for a 22.6% v/v kaolin clay-water slurry with 0.03% TSPP in the 156.7 mm flume; ρ=1384 kg/m^3 365
D.20: Frictional loss measurements for a 22.8% v/v kaolin clay-water slurry with 0.10% TSPP in the 156.7 mm flume; ρ=1386 kg/m^3 370
D.21: Solids (sand) concentration profile measurements for a 25% v/v sand-water slurry in the 156.7 mm flume; ρ=1410 kg/m^3 375
D.22: Solids and sand concentration profile measurements for a CT 'no gypsum' model tailings slurry in the 156.7 mm flume; ρ=1598 kg/m^3 376
D.23: Solids and sand concentration profile measurements for a CT 'gypsum' model tailings slurry in the 156.7 mm flume; ρ=1598 kg/m^3 377
D.24: Solids and sand concentration profile measurements for a model Thickened Tailings slurry in the 156.7 mm flume; ρ=1510 kg/m^3 378
D.25: Centerline mixture velocity profile measurements for Saskatoon tap water in the 156.7 mm flume 378
D.26: Centerline mixture velocity profile measurements for a 22.6% v/v kaolin clay-water slurry with 0.03% TSPP in the 156.7 mm flume; ρ=1384 kg/m^3 379
D.27: Centerline mixture velocity profile measurements for a 22.8% v/v kaolin clay-water slurry with 0.10% TSPP in the 156.7 mm flume; ρ=1386 kg/m^3 379
D.28: Flume two-dimensional mixture velocity profile measurement positions in the 156.7 mm flume (see Figure D.1) 380
D.29: Mixture velocity profile measurements for a 25% v/v sand-water slurry in the 156.7 mm flume; ρ=1410 kg/m^3 381
D.30: Mixture velocity profile measurements for a CT 'no gypsum' model tailings slurry in the 156.7 mm flume; ρ=1598 kg/m^3 382
D.31: Mixture velocity profile measurements for a CT 'gypsum' model tailings slurry in the 156.7 mm flume; ρ=1598 kg/m^3 382
D.32: Mixture velocity profile measurements for a model Thickened Tailings slurry in the 156.7 mm flume; ρ=1510 kg/m^3 383
D.33: Pressure gradient versus velocity data for Saskatoon tap water to determine the roughness of the 25 mm up test section for the low Reynolds number Pitot tube experiments 384
D.34: Low Reynolds number Pitot tube data with ethylene glycol using the PSL in the 25 mm vertical pipe circuit 385

D.35: Low Reynolds number Pitot tube data with ethylene glycol using the PSS in the 25 mm vertical pipe circuit 388
E.1: Steady state Phillips model verification simulation results for neutrally buoyant spheres in a rectangular duct of infinite width 397
E.2: Model simulation results at t = 9.5 s for a Thickened Tailings test (5 L/s, 4^{o}) 398
E.3: Transient model simulation results for a Thickened Tailings test (5 L/s, 4 ^{o}) 399
E.4: Model simulation results at t = 48.5 s for a Thickened Tailings test (5 L/s, 4.5 ^{o}) 400
E.5: Model simulation results at t = 8.5 s for a Thickened Tailings test (5 L/s, 5.4 ^{o}) 401
E.6: Model simulation results at t = 500 s for a Thickened Tailings slurry test with a reduced immersed weight (4 ^{o}) 402
E.7: Model simulation results at t = 0.65 s for a CT 'gypsum' test (5 L/s, 2 ^{o}) 403
E.8: Transient model simulation results for a CT 'gypsum' test (5 L/s, 2 ^{o}) 404
E.9: Model simulation results at t = 0.20 s for a CT 'gypsum' test (5 L/s, 2.5 ^{o}) 405
E.10: Model simulation results at t = 3.3 s for a CT 'gypsum' test (2.5 L/s, 3 ^{o}) 406
E.11: Model concentration gradient comparison for the transport of a sand in glycol slurry in laminar pipe flow (Gillies et al., 1999) 407
E.12: Model concentration gradient comparison for the transport of a sand in oil slurry in laminar pipe flow (Gillies et al., 1999) 408

LIST OF FIGURES

2.1: Rheograms of various continuum fluid models (Litzenberger, 2003) 5
2.2: Schematic illustration of non-uniform, axial flow in a flume 11
2.3: Schematic illustration of the cross-sectional view of open channel flow in a circular flume 11
2.4: Schematic illustration of the cross-sectional view of open channel flow in a rectangular flume 17
2.5: Schematic illustration of the force balance for steady, horizontal, fully developed pipe flow 36
2.6: Schematic illustration of a concentric cylinder viscometer 39
2.7: Schematic diagram of (a) the vane, (b) the vane apparatus: (A) vane, (B) motor, (C) torsion head, (D) instrument console, (E) recorder (Nguyen and Boger, 1983) 40
3.1: Saskatchewan Research Council's 156.7 mm flume circuit used in the experimental program 54
3.2: Schematic illustration of the helical chute and stand tank arrangement on the 156.7 mm flume circuit 55
3.3: Water performance curve for the 3x2 Linatex pump on the 156.7 mm flume circuit (Lawjack Equipment Ltd, Montreal, QC) 56
3.4: Schematic illustration of the traversing Pitot-static tube apparatus on the 156.7 mm flume 59
3.5: Saskatchewan Research Council's 25 mm vertical pipe loop 61
3.6: Schematic illustration of the traversing gamma ray densitometer on the 156.7 mm flume 67
3.7: Schematic illustration of the vertical suction system employed in the sand-water tests in the 156.7 mm flume 72
4.1: Schematic diagrams of irreversible two-body collisions with (a) constant viscosity and (b) spatially varying viscosity (Phillips et al., 1992) 87
4.2: Plot of shear stress versus time rate of shear strain for a Bingham fluid 97
4.3: One dimensional yielding response for (a) a modified Herschel-Bulkley fluid; (b) a Bingham fluid, where τ_y is the yield stress, η the viscosity and η_r the "unyielded" viscosity. $\dot{\gamma}_c$ is the critical shear rate in the biviscosity model (Beverly and Tanner, 1992) 98
4.4: Schematic illustration of a Cartesian coordinate system control volume 107
4.5: Schematic illustration of a finite volume method Cartesian grid 107
4.6: Tridiagonal matrix of discrete algebraic equations for an implicit finite volume method formulation 117
4.7: Schematics of the (a) free surface boundary and (b) channel wall boundary fictitious cell volumes 120
5.1: Pressure gradient versus velocity for Saskatoon tap water to determine the pipe roughness of the 53 mm test section for the model tailings slurry tests 142
5.2: Pressure gradient versus velocity for Saskatoon tap water to determine the pipe roughness of the 53 mm test section for the clay-water experiments before the line was polished 143
5.3: Pressure gradient versus velocity for Saskatoon tap water to determine the pipe roughness of the 53 mm test section for the clay-water experiments after polishing but before testing 143

5.4: Pressure gradient versus velocity for Saskatoon tap water to determine the pipe roughness of the 53 mm test section for the clay-water experiments after testing 144
5.5: Pressure gradient versus velocity for a 22.2% v/v kaolin clay-water slurry in the 53 mm test section; ρ=1375 kg/m^3 145
5.6: Pressure gradient versus velocity for a 22.6% v/v kaolin clay-water slurry with 0.03% TSPP in the 53 mm test section; ρ=1384 kg/m^3 146
5.7: Pressure gradient versus velocity for a 22.8% v/v kaolin clay-water slurry with 0.10% TSPP in the 53 mm test section; ρ=1386 kg/m^3 147
5.8: Particle size distribution of the Unimin (Granusil 5010) sand employed in the 156.7 mm flume tests; d_{50} = 188.5 μm 148
5.9: Pressure gradient versus velocity for a 25% v/v sand-water slurry in the 53 mm test section; ρ=1410 kg/m^3 149
5.10: Pressure gradient versus velocity for a model Syncrude CT 'no gypsum' slurry in the 53 mm test section; ρ=1598 kg/m^3 151
5.11: Pressure gradient versus velocity for a model Syncrude CT 'gypsum' slurry in the 53 mm test section; ρ=1598 kg/m^3 153
5.12: Pressure gradient versus velocity for a model Syncrude Thickened Tailings slurry in the 53 mm test section; ρ=1510 kg/m^3 154
5.13: Wall shear stress versus velocity for Saskatoon tap water in the 156.7 mm flume 156
5.14: Fanning friction factor versus Reynolds number for Saskatoon tap water in the 156.7 mm flume 157
5.15: Experimental wall shear stress comparison with turbulent rough prediction for Saskatoon tap water in the 156.7 mm flume 158
5.16: Wall shear stress parity plot comparison for Saskatoon tap water in the 156.7 mm flume 158
5.17: Wall shear stress versus velocity for a 25% v/v, sand-water slurry in the 156.7 mm flume; ρ=1410 kg/m^3 160
5.18: New inlet wall shear stress versus velocity for a 25% v/v sand-water slurry in the 156.7 mm flume at various angles; ρ=1410 kg/m^3 160
5.19: Experimental wall shear stress comparison with equivalent fluid model for a 25% v/v sand-water slurry in the 156.7 mm flume; ρ=1410 kg/m^3 161
5.20: Wall shear stress parity plot comparison for a 25% v/v sand-water slurry in the 156.7 mm flume; ρ=1410 kg/m^3 162
5.21: Fanning friction factor versus Reynolds number for a 25% v/v sand-water slurry in the 156.7 mm flume; ρ=1410 kg/m^3 163
5.22: Wall shear stress versus velocity for a 22.2 % v/v kaolin clay-water slurry in the 156.7 mm flume; ρ=1375 kg/m^3 164
5.23: Fanning friction factor versus Zhang Reynolds number for a 22.2% v/v kaolin clay-water slurry in the 156.7 mm flume; ρ=1375 kg/m^3 165
5.24: Experimental wall shear stress comparison with Kozicki and Tiu prediction for a 22.2 % v/v kaolin clay-water slurry in the 156.7 mm flume; ρ=1375 kg/m^3 166
5.25: Wall shear stress parity plot comparison for a 22.2 % v/v kaolin clay-water slurry in the 156.7 mm flume; ρ=1375 kg/m^3 166
5.26: Wall shear stress versus velocity for a 22.6 % v/v kaolin clay-water slurry with 0.03% TSPP in the 156.7 mm flume; ρ=1384 kg/m^3 167
5.27: Fanning friction factor versus Zhang Reynolds number for a 22.6% v/v kaolin clay-water slurry with 0.03% TSPP in the 156.7 mm flume; ρ=1384 kg/m^3 168

5.28: Experimental wall shear stress comparison with Kozicki and Tiu prediction for a 22.6 % v/v kaolin clay-water slurry with 0.03% TSPP in the 156.7 mm flume; ρ=1384 kg/m^3 169
5.29: Wall shear stress parity plot comparison for a 22.6 % v/v kaolin clay-water slurry with 0.03% TSPP in the 156.7 mm flume; ρ=1384 kg/m^3 169
5.30: Wall shear stress versus velocity for a 22.8 % v/v kaolin clay-water slurry with 0.10% TSPP in the 156.7 mm flume; ρ=1386 kg/m^3 170
5.31: Fanning friction factor versus Reynolds number for a 22.6% v/v kaolin clay-water slurry with 0.10% TSPP in the 156.7 mm flume; ρ=1386 kg/m^3 170
5.32: Experimental wall shear stress comparison with turbulent rough prediction for a 22.6 % v/v kaolin clay-water slurry with 0.10% TSPP in the 156.7 mm flume; ρ=1386 kg/m^3 172
5.33: Wall shear stress parity plot comparison for a 22.6 % v/v kaolin clay-water slurry with 0.10% TSPP in the 156.7 mm flume; ρ=1386 kg/m^3 172
5.34: Fanning friction factor versus Zhang Reynolds number for the kaolin clay-water slurries of Haldenwang (2003) in 75, 150 and 300 mm rectangular channels 173
5.35: Fanning friction factor versus Zhang Reynolds number for the bentonite clay-water slurries of Haldenwang (2003) in 75, 150 and 300 mm rectangular channels 174
5.36: Experimental wall shear stress parity plot comparison with Kozicki and Tiu prediction for the kaolin clay-water slurries of Haldenwang (2003) in 75, 150 and 300 mm rectangular channels 174
5.37: Experimental wall shear stress parity plot comparison with Kozicki and Tiu prediction for the bentonite clay-water slurries of Haldenwang (2003) in 75, 150 and 300 mm rectangular channels 175
5.38: Wall shear stress versus velocity for a model Syncrude CT ‘no gypsum’ slurry in the 156.7 mm flume; ρ=1598 kg/m^3 176
5.39: Wall shear stress versus velocity for a model Syncrude CT ‘gypsum’ slurry in the 156.7 mm flume; ρ=1598 kg/m^3 176
5.40: Fanning friction factor versus Reynolds number for a model Syncrude CT ‘no gypsum’ slurry in the 156.7 mm flume; ρ=1598 kg/m^3 177
5.41: Fanning friction factor versus Zhang Reynolds number for a model Syncrude CT ‘gypsum’ slurry in the 156.7 mm flume; ρ=1598 kg/m^3 178
5.42: Experimental wall shear stress comparison with turbulent rough prediction for a model Syncrude CT ‘no gypsum’ slurry in the 156.7 mm flume; ρ=1598 kg/m^3 179
5.43: Wall shear stress parity plot comparison for a model Syncrude CT ‘no gypsum’ slurry in the 156.7 mm flume; ρ=1598 kg/m^3 179
5.44: Experimental wall shear stress parity plot comparison with Kozicki and Tiu prediction for a model Syncrude CT ‘gypsum’ slurry in the 156.7 mm flume; ρ=1598 kg/m^3 180
5.45: Wall shear stress versus velocity for a model Syncrude Thickened Tailings slurry in the 156.7 mm flume; ρ=1510kg/m^3 181
5.46: Fanning friction factor versus Zhang Reynolds number for a model Syncrude Thickened Tailings slurry in the 156.7 mm flume; ρ=1510 kg/m^3 182
5.47: Experimental wall shear stress parity plot comparison with Kozicki and Tiu prediction for a model Syncrude Thickened Tailings slurry in the 156.7 mm flume; ρ=1510 kg/m^3 183
5.48a: Old inlet solids concentration profiles (y/h) for a 25% v/v sand-water slurry in the 156.7 mm flume; ρ=1410 kg/m^3 189

5.48b: Old inlet solids concentration profiles (y/D) for a 25% v/v sand-water slurry in the 156.7 mm flume; ρ=1410 kg/m^3 189
5.49a: New inlet solids concentration profiles (y/h) at 3.5^o for a 25% v/v sand-water slurry in the 156.7 mm flume; ρ=1410 kg/m^3 190
5.49b: New inlet solids concentration profiles (y/D) at 3.5^o for a 25% v/v sand-water slurry in the 156.7 mm flume; ρ=1410 kg/m^3 190
5.50a: New inlet solids concentration profiles (y/h) at 3^o for a 25% v/v sand-water slurry in the 156.7 mm flume; ρ=1410 kg/m^3 191
5.50b: New inlet solids concentration profiles (y/D) at 3^o for a 25% v/v sand-water slurry in the 156.7 mm flume; ρ=1410 kg/m^3 191
5.51a: Solids concentration profiles (y/h) for a model Syncrude CT 'no gypsum' in the 156.7 mm flume; ρ=1598 kg/m^3 193
5.51b: Solids concentration profiles (y/D) for a model Syncrude CT 'no gypsum' in the 156.7 mm flume; ρ=1598 kg/m^3 193
5.52a: Solids concentration profiles (y/h) for a model Syncrude CT 'gypsum' in the 156.7 mm flume; ρ=1598 kg/m^3 194
5.52b: Solids concentration profiles (y/D) for a model Syncrude CT 'gypsum' in the 156.7 mm flume; ρ=1598 kg/m^3 194
5.53a: Solids concentration profiles (y/h) for a model Syncrude Thickened Tailings slurry in the 156.7 mm flume; ρ=1510 kg/m^3 197
5.53b: Solids concentration profiles (y/D) for a model Syncrude Thickened Tailings slurry in the 156.7 mm flume; ρ=1510 kg/m^3 197
5.54: Correlations and experimental data for low Reynolds number Pitot tube measurements plotted as a function of Re_D 203
5.55: Correlations and experimental data for low Reynolds number Pitot tube measurements plotted as a function of Re_d 204
5.56: Centerline velocity profiles at various angles for water in the 156.7 mm flume with and without a HPLC purge 206
5.57: Centerline velocity profiles at various angles for a 22.6 % v/v kaolin clay-water slurry with 0.03% TSPP in the 156.7 mm flume with a HPLC purge; ρ=1384 kg/m^3 207
5.58: Centerline velocity profiles at various angles for a 22.8 % v/v kaolin clay-water slurry with 0.10% TSPP in the 156.7 mm flume with a HPLC purge; ρ=1386 kg/m^3 209
5.59: Schematic of the two dimensional velocity profiles obtained from the Pitot-static tube measurements in the 156.7 mm flume 210
5.60: Velocity profiles at 3.5 ^{o} for a 25% v/v sand-water slurry in the 156.7 mm flume; ρ=1410 kg/m^3; a) 5 L/s; b) 4.5 L/s; c) 3.9 L/s 211
5.61: Velocity profiles at 3 ^{o} for a 25% v/v sand-water slurry in the 156.7 mm flume; ρ=1410 kg/m^3; a) 6.5 L/s; b) 6 L/s; c) 5.6 L/s 212
5.62: Velocity profiles for a model Syncrude CT 'no gypsum' slurry in the 156.7 mm flume; ρ=1598 kg/m^3; a) 5 L/s & 3^o; b) 5 L/s & 2^o; c) 5 L/s & 1.5^o; d) 2.5 L/s & 3^o 213
5.63: Velocity profiles for a model Syncrude CT 'gypsum' slurry in the 156.7 mm flume; ρ=1598 kg/m^3; a) 5 L/s & 3^o; b) 5 L/s & 2.5^o; c) 5 L/s & 2^o; d) 2.5 L/s & 3^o 215
5.64: Velocity profiles for a model Syncrude Thickened Tailings slurry in the 156.7 mm flume; ρ=1510 kg/m^3; a) 5 L/s & 5.4^o; b) 5 L/s & 4.5^o; c) 5 L/s & 4^o; d) 2.5 L/s & 4.5^o 216
6.1: Phillips model verification concentration profile for 0.475 mm neutrally buoyant spheres in a rectangular duct of infinite width 222
6.2: Phillips model verification mixture velocity profile for 0.475 mm neutrally buoyant spheres in a rectangular duct of infinite width 223

6.3: Phillips model verification concentration profile for 0.188 mm neutrally buoyant spheres in a rectangular duct of infinite width 224
6.4: Numerical and experimental concentration profile comparison for a Thickened Tailings slurry test (5 L/s, 4 ^{o}) at t = 9.5 s 227
6.5: Simulated velocity profile for a Thickened Tailings slurry test (5 L/s, 4 ^{o}) at t = 9.5 s 228
6.6: Simulated concentration profiles in time for a model Thickened Tailings slurry (5 L/s, 4 ^{o}) 229
6.7: Simulated velocity profiles in time for a model Thickened Tailings slurry (5 L/s, 4 ^{o}) 230
6.8: Ratio of the delivered concentration to the in-situ concentration versus simulation time for the transport of a model Thickened Tailings slurry in open channel flow (5 L/s, 4 ^{o}) 232
6.9: Simulated and experimental concentration profile comparison for a Thickened Tailings slurry test (5 L/s, 4.5 ^{o}) at t = 48.5 s 233
6.10: Simulated velocity profile for a Thickened Tailings slurry test (5 L/s, 4.5^{o}) at t = 48.5 s 234
6.11: Simulated and experimental concentration profile comparison for a Thickened Tailings slurry test (5 L/s, 5.4 ^{o}) at t = 8.5 s 235
6.12: Simulated velocity profile for a Thickened Tailings slurry test (5 L/s, 5.4^{o}) at t = 8.5 s 236
6.13: Simulated and experimental concentration profile comparison for a CT ‘gypsum’ slurry test (5 L/s, 2 ^{o}) at t = 0.65 s 237
6.14: Simulated velocity profile for a CT ‘gypsum’ slurry test (5 L/s, 2 ^{o}) at t = 0.65 s 238
6.15: Simulated concentration profiles in time for a model CT ‘gypsum’ slurry (5 L/s, 2^{o}) 239
6.16: Simulated velocity profiles in time for a model CT ‘gypsum’ slurry (5 L/s, 2 ^{o}) 240
6.17: Ratio of the delivered concentration to the in-situ concentration versus simulation time for the transport of a model CT ‘gypsum’ slurry in open channel flow (5 L/s, 2^{o}) 241
6.18: Simulated and experimental concentration profile comparison for a CT ‘gypsum’ slurry test (5 L/s, 2.5 ^{o}) at t = 0.20 s 242
6.19: Simulated velocity profile for a CT ‘gypsum’ slurry test (5 L/s, 2.5 ^{o}) at t = 0.20 s 242
6.20: Simulated and experimental concentration profile comparison for a CT ‘gypsum’ slurry test (2.5 L/s, 3 ^{o}) at t = 3.3 s 243
6.21: Simulated velocity profile for a CT ‘gypsum’ slurry test (2.5 L/s, 3 ^{o}) at t = 3.3 s 244
6.22: Local variation in mixture viscosity at a snapshot in time for a Thickened Tailings slurry simulation (5 L/s, 4 ^{o}) at t = 9.5 s 250
6.23: Simulated concentration profile for a slurry with a reduced particle immersed weight (4 ^{o}) at t = 500 s 252
6.24: Simulated velocity profile for a slurry with a reduced particle immersed weight (4 ^{o}) at t = 500 s 253
6.25: Numerically simulated and experimental concentration profiles for the transport of a sand in glycol slurry in laminar pipe flow (Gillies et al., 1999) 255
6.26: Numerically simulated and experimental velocity profiles for the transport of a sand in glycol slurry in laminar pipe flow (Gillies et al., 1999) 255
6.27: Comparison of model concentration gradients for the transport of a sand in glycol slurry in laminar pipe flow (Gillies et al., 1999) 256
6.28: Numerically simulated and experimental concentration profiles for the transport of a sand in oil slurry in laminar pipe flow (Gillies et al., 1999) 257

6.29: Numerically simulated and experimental velocity profiles for the transport of a sand in oil slurry in laminar pipe flow (Gillies et al., 1999) 258
6.30: Comparison of model concentration gradients for the transport of a sand in oil slurry in laminar pipe flow (Gillies et al., 1999) 259

Appendices

B.1: Photomicrograph of the Unimin round grain sand used in the experimental tests (Granusil 5010, d_{50} = 188 μm) 312
B.2: Photomicrograph of the sand from Syncrude oil sand washed tailings 312
C.1: Sample digital photograph of the flume Pitot-static tube tip (2002) 320
C.2: Sample digital photograph of the flume Pitot-static tube tip (2006) 329
C.3: Sample digital photograph of the PSL Pitot-static tube tip 339
C.4: Sample digital photograph of the PSS Pitot-static tube tip 340
D.1: Flume two-dimensional mixture velocity profile measurement positions in the 156.7 mm flume (see Table D.28) 381
F.1: Rippled free surface of a turbulent water flow in the 156.7 mm flume test section 410
F.2: Deposit in the old 156.7 mm flume inlet with the 25% v/v sand-water tests 410
F.3: Deposit in the 156.7 mm flume test section with the 25% v/v sand-water tests 411
F.4: Deposit in the 156.7 mm flume viewing section with the 25% v/v sand-water tests 411
F.5: View of the 156.7 mm flume circuit from the stand tank catwalk 412
F.6: View of the 156.7 mm flume circuit from inlet to outlet (left to right) 412
F.7: View of the 156.7 mm flume circuit winch and hoisting apparatus 413
F.8: Landscape view of the 156.7 mm flume development length and test section (left to right) 413
F.9: Data acquisition computer workstations used in the 156.7 mm flume experiments 414
F.10: Data acquisition server computer used in the 156.7 mm flume experiments 414
F.11: Linatex 3x2 centrifugal pump on the 53 mm feed pipe used in the 156.7 mm flume experiments 415
F.12: Ronan densitometer on the 53 mm feed pipe used in the 156.7 mm flume experiments 415
F.13: Aircom temperature sensor on the 53 mm feed pipe used in the 156.7 mm flume experiments 416
F.14: Validyne pressure transducer bodies and demodulators used in the 156.7 mm flume experiments 416
F.15: Pump motor variable frequency drive (VFD) pot used in the 156.7 mm flume experiments 417
F.16: Proportional controller for the system temperature on the 53 mm feed pipe used in the 156.7 mm flume experiments 417
F.17: Belimo control valve on the glycol-water fluid heat exchanger line used to control the system temperature in the 53 mm feed pipe used in the 156.7 mm flume experiments 418
F.18: 2 inch Foxboro magnetic flowmeter on the 53 mm feed pipe used in the 156.7 mm flume experiments 418
F.19: New 156.7 mm flume inlet conditions 419
F.20: Depth of flow measurement gauge on the 156.7 mm flume test section 419
F.21: Traversing Pitot-static tube apparatus on the 156.7 mm flume 420
F.22: HPLC purge pump for the Pitot-static tube measurements during the 156.7 mm flume experiments 420
F.23: Ronan traversing gamma ray densitometer on the 156.7 mm flume 421

F.24: Hand pump apparatus used to traverse the Ronan gamma ray densitometer on the 156.7 mm flume 421
F.25: Stand tank for the 156.7 mm flume circuit 422
F.26: Baldor mixer in the 156.7 mm flume circuit stand tank 422

LIST OF SYMBOLS

Nomenclature

a	particle radius (m) Kozicki and Tiu Equation geometric shape parameter, (Section 2.4)
a_i	finite volume method discrete algebraic equation coefficient
A	cross-sectional area of flow (m^2) Churchill Equation parameter, (Equation 2.22b) biviscosity model scaling parameter, (Equation 4.34a) low Reynolds number Pitot tube correlation parameter, (Equation 5.3)
A_{ij}	matrix determinant cofactor, (Equation 4.40d)
$\overline{\overline{A}}$	matrix of discrete algebraic equation coefficients, (Equation 4.64)
b	Kozicki and Tiu Equation geometric shape parameter, (Section 2.4)
b_i	finite volume method discrete algebraic equation coefficient
$\overline{b}$	vector of algebraic coefficients for b_i, (Equation 4.64)
B	Churchill Equation parameter, (Equation 2.22c) low Reynolds number Pitot tube correlation parameter, (Equation 5.3)
C	concentration (v/v or w/w) Chezy Equation constant, (Equation 2.5)
C_D	settling particle drag coefficient, (Equation 2.34)
C_P	pressure coefficient, (Equation 2.63)
C_r	in-situ concentration (v/v or w/w)
C_v	delivered concentration (v/v or w/w)
d	particle diameter (m) Pitot tube opening diameter (m)
d_{50}	median particle diameter (m)
d_{85}	representative coarse particle diameter (m), (Equation 2.48a)
D	pipe diameter (m) Pitot tube outside diameter (m) vane viscometer spindle diameter (m) Brownian diffusivity (m^2/s), (Equation 4.20)
D_h	hydraulic diameter (m), (Equation 2.19)
$\hat{D}$	dimensionless diffusivity, (Equation 4.13)
D_ϕ	scalar transport equation diffusivity (m^2), (Equation 4.22b)
D_μ	scalar transport equation diffusivity (m^2), (Equation 4.22c)
f	fanning friction factor, (Equation 2.17) explicit, semi-implicit, implicit time scheme factor, (Equation 4.43)
$f(\phi)$	hindrance function, (Equation 4.18)
F_g	gravitational driving force (N), (Equation 2.11b)
F_τ	resisting wall shear stress force (N), (Equation 2.11a)
F_k	kinetic force (N), (Equation 2.11c)

F_P	pressure force (N), (Equation 2.11d)
Fr	Froude number, (Equation 2.4)
$F(\phi_{fs})$	Newton-Raphson objective equation, (Equation 4.76)
$F'(\phi_{fs})$	Derivative of Newton-Raphson objective equation, (Equation 4.77)
g	acceleration due to gravity (m/s^2)
h	depth of flow in channel (m)
H	vane viscometer spindle height (m) pump head (m)
i , j , k	iteration counter
$\hat{i}$, $\hat{j}$, $\hat{k}$	Cartesian coordinate unit vectors, (Equation 4.72c)
J_s	scalar transport flux, (Equation 4.22a)
$\lvert J \rvert$	determinant of the Jacobian, (Equation 4.40a)
K	Power-Law, Herschel-Bulkley model consistency index ($Pa\text{-}s^n$) gravitational body force per unit volume (N/m^3), (Equation 4.50h)
K_c	spatially varying interaction frequency coefficient, (Equation 4.14b)
K_s	sedimentation flux coefficient (kg/m^3), (Equation 4.19b)
K_η	spatially varying viscosity coefficient, (Equation 4.15b)
L	length of pipe (m) length of viscometer spindle (m) length (m), (Equation 2.4)
m	exponential decay parameter, (Equation 4.33)
n	Power Law, Herschel-Bulkley model flow behaviour index Richardson and Zaki Equation exponent, (Equation 2.43) Manning Equation constant, (Equation 2.6)
$\vec{n}$	channel wall normal, (Equation 4.72a)
N	measured intensity (counts/s), (Equation 3.3) particle flux in scalar concentration transport equation number of nodes in numerical model simulation domain
N_0	unattenuated intensity (counts/s), (Equation 3.3)
N_b	Phillips model flux due to Brownian motion (m/s), (Equation 4.20)
N_c	flux due to spatially varying interaction frequency (m/s), (Equation 4.14a)
N_s	flux due to particle sedimentation (m/s), (Equation 4.19a)
N_η	flux due to spatially varying viscosity (m/s), (Equation 4.15a)
P	pressure (Pa)
$P_{,i}$	pressure gradient, (Pa/m)
P_∞	static pressure (Pa)
Pe	Peclet Number
Q	volumetric flowrate (m^3/s)
r	radial direction in pipe, cylindrical coordinates (m)
r_i	geometric interpolation ratio, (Equation 4.85)
R	radius of pipe (m)

R_1	concentric cylinder viscometer spindle radius(m)
R_2	concentric cylinder viscometer cup radius (m)
R_h	hydraulic radius (m), (Equation 2.20)
Re	Reynolds number, (Equation 2.21)
Re_d	Pitot tube opening diameter Reynolds number, (Equation 2.64)
Re_P	particle Reynolds number, (Equation 2.36)
Re_{Zhang}	Zhang Reynolds number, (Equation 2.18)
Re_∞	infinite dilution particle Reynolds number, (Equation 2.45)
Re*	Dominguez open channel Reynolds number, (Equation 2.48b)
S	wetted perimeter of flow (m) specific gravity
S_0	slope of uniform channel
S_C	explicit component of source term linearization (1/s), Equation (4.57c)
S_P	implicit component of source term linearization (1/s), Equation (4.57e)
S_ϕ	scalar concentration transport equation source term (1/s), (Equation 4.12)
$\overline{S}_\phi$	average scalar transport equation source term (1/s), (Equation 4.57b)
t	time (s)
T	torque on viscometer spindle (N-m) Temperature (^{o}C)
u	local velocity (m/s)
$u*$	shear velocity (m/s), (Equation 2.58)
v	local velocity (m/s)
v_0	Kozicki and Tiu slip velocity at wall (m/s), (Section 2.4)
v_s	particle settling velocity (m/s), (Equation 2.43)
v_∞	particle settling velocity infinite dilution (m/s), (Equation 2.34)
	local freestream fluid velocity, (Equation 2.63)
V	bulk mixture velocity (m/s) numerical model cell volume (m^3)
V_D	Dominguez critical deposition velocity (m/s), (Equation 2.48a)
V_N	Wilson and Thomas equivalent Newtonian velocity (Equation 2.59c)
w	mass flowrate (kg/s) width of rectangular channel (m)
x	Cartesian coordinate, transverse direction path length through pipe interior (m), (Equation 3.3)
x_w	path length through pipe wall (m), (Equation 3.3)
y	Cartesian coordinate, vertical direction vertical distance above bottom flume wall (m), (Figure 2.3)
$\overline{y}$	centroid of flow (m), (Equation 2.15)
Y	Shields parameter, (Equation 2.46)
z	Cartesian coordinate, axial direction

Greek Symbols

α	Thomas Algorithm solver coefficient, (Equation 4.62a) angle of internal friction of solid particles (^{o}), (Equation 2.66) Wilson and Thomas rheogram shape factor, (Equation 2.59a)
β	Thomas Algorithm solver coefficient, (Equation 4.62b) flume free surface angle (rad), (Equation 2.7) ratio of Pitot tube opening diameter to outside diameter
β_u	diffusive velocity gradient constant, (Equation 4.48)
β_ϕ	diffusive concentration gradient constant, (Equation 4.52)
Δ_{ij}	rate of deformation tensor (m/s), (Equation, 2.50)
Δ_i	cell face to node geometric interpolation distance, (Equation 4.85)
ΔP	pressure differential (Pa)
Δt	numerical model time step (s)
Δx	numerical model cell volume width (m), transverse
Δy	numerical model cell volume height (m), vertical
Δz	numerical model cell volume depth (m), axial
$\Delta : \Delta$	2nd invariant of the rate of deformation tensor, (Equation 4.88)
ε	equivalent pipe roughness (m)
ϕ	concentration of coarse solids (v/v) Kozicki and Tiu rectangular channel parameter, (Equation 2.31)
$\phi_{\max}$	maximum packing concentration of coarse solids (v/v)
$\overline{\phi}$	average volumetric concentration of solids (v/v), (Equation 4.26)
$\overline{\phi_i}$	vector of current values for ϕ_i, (Equation 4.64)
$\dot{\gamma}$	time rate of shear strain, shear rate (1/s)
Γ	scalar concentration transport equation diffusivity (m^2/s), (Equation 4.12)
η	effective mixture viscosity (Pa-s) Wilson and Thomas equivalent Newtonian viscosity (Equation 2.59e)
η_f	fluid apparent viscosity (Pa-s)
η_r	relative viscosity (Pa-s)
η_{shear}	shear effect on mixture viscosity (Pa-s), (Equation 4.35)
η_{conc}	concentration effect on mixture viscosity (Pa-s), (Equation 4.35)
η_s	coefficient of sliding friction, (Equation 2.47)
φ	geometric bed height function, (Equation 2.47)
λ	linear concentration, (Equation 2.41) Kozicki and Tiu rectangular channel aspect ratio, (Equation 2.30)
μ	Newtonian viscosity (Pa-s)
μ_f	absorption coefficients of the carrier fluid (1/m), (Equation 3.3)
μ_d	dispersive viscosity, (Equation 2.65)
μ_c	Casson viscosity (Pa-s), (Equation 2.3d)
μ_P	Bingham plastic viscosity (Pa-s), (Equation 2.3b)

μ_s	absorption coefficients of the solids (1/m), (Equation 3.3)
μ_w	absorption coefficients of the pipe wall (1/m), (Equation 3.3)
θ	angle of flume inclination (^{o}) Cylindrical coordinates, azimuthal direction
ρ	mixture density (kg/m^3)
ρ_f	fluid density (kg/m^3)
ρ_s	solids density (kg/m^3)
τ	shear stress (Pa)
τ_c	Casson yield stress (Pa), (Equation 2.3d)
τ_{ij}	shear stress tensor (Pa), (Equation 2.49a)
τ_w	wall shear stress (Pa)
τ_y	yield stress (Pa)
$\tau : \tau$	2nd invariant of the stress tensor, (Equation 2.49)
ω	angular velocity of viscometer spindle (rad/s) relaxation coefficient, (Equation 4.66)
Ω	Wilson and Thomas parameter, (Equation 2.59b)
ξ	ratio of yield stress to wall shear stress, (Equation 2.57)
∇	gradient operator
$\nabla \cdot$	divergence operator
$\nabla \cdot \nabla$	Laplacian operator (also ∇^2)

Superscripts

0	previous time step (explicit)
1	current time step (implicit)
i , j , k	iteration counter
u	momentum transport equation
ϕ	scalar concentration transport equation
$\cdot$	derivative with respect to time

Subscripts

0	condition at the wall
1	position 1 in flume (Figure 3.1)
2	position 2 in flume (Figure 3.1)
1, 2 , 3	x, y, and z coordinate directions
apparent	apparent viscosity
avg	average
carrier	carrier fluid phase
clay	fines and clay solid phase
cr	critical condition
fs	free surface condition

i	x coordinate index
	iteration number
ij	tensor direction
j	y coordinate index
k	z coordinate index
m	mean
	Mixture
min	minimum condition
max	maximum condition
n , s	north and south faces of elemental cell volume
N	Newtonian fluid
N , S	cells to the north and south of elemental cell volume
P	node location of elemental cell volume
r	relative quantity
	in-situ quantity
	cylindrical coordinate, radial direction
$sand$	coarse solids phase
$solids$	total solids
v	delivered quantity
	volumetric quantity
w	weight quantity
	wall condition
x	Cartesian coordinate, transverse direction
y	Cartesian coordinate, vertical direction
z	Cartesian and cylindrical coordinate, axial direction
θ	cylindrical coordinate, azimuthal direction
∞	freestream, static Pitot tube condition, (Equation 2.63)
	infinite dilution

1. INTRODUCTION

Slurry flows occur in many industrial applications. Specific industrial applications include: oils sands tailings transportation, mining and mineral ore transportation, pulp and paper, concrete, food processing, metal injection molds, ceramics and heavy oil production. There are also many situations arising in nature which involve slurry flow. Some examples include sediment transport in alluvial flows and saturated soils including oceanic and coastal flows (Lalli and Mascio, 1997).

Nearly every chemical processing industry involves the transport or handling of some type of slurry or liquid-particulate mixture. For example pipeline transport is utilized in a variety of ways in the processing of oil sands from the initial transport of oil sands ore to the disposal of the concentrated tailings mixtures. Slurries or pastes often exhibit complex, non-Newtonian behaviour. However, most flow models have been developed for fluids that exhibit Newtonian behaviour. Therefore, research into the flow behaviour of non-Newtonian slurries is required for both a better understanding of the underlying fluid mechanics and for the proper design and optimization of their transport.

The specific motivation for studying the transport of solids in laminar open channel flow in this investigation is associated with the disposal of industrial tailings mixtures. In particular the transport of oil sands tailings is of interest. Tailings pipelines in Fort McMurray are among the largest in the world handling “coarse” or “settling” slurries (Shook et al., 2002). Syncrude Canada Ltd. has been mining oil sand from the Athabasca deposits in Northern Alberta Canada since 1978 (Schaan et al., 2004). Using unique extraction processes, the bitumen is separated from the sand and upgraded through conventional processes. The large scale of the extraction process results in a significant quantity of tailings which create unique challenges. In 2003 the combined operations generated approximately 120,000 tonnes of fine sand and clay per day (Schaan et al., 2004).

Along with the production of large quantities of solids, a significant amount of water is used in the process. Oil sands tailings typically contain both coarse sand and fine clays. Historically, the tailings have been transported by pipeline to a disposal facility where the tailings are discharged. Following discharge, the coarse sand settles while the run-off, consisting of a dilute fine particle slurry, is stored in a tailings pond or settling basin. Since the consolidation process is extremely slow and large volumes of fine tailings are produced, the settling basins are large (Sego et al.,

2002). The goal of the tailings replacement strategy is to minimize land disturbance and reduce the amount of water input into the process. Any improvements, which can reduce the operational costs of this process or improve the efficiency, would not only reduce the environmental impact of the tailings disposal process but it would also represent an economic benefit to the oil sands lease holders (Sanders et al., 2002).

One method which improves water reclamation involves the production of thickened tailings. This approach reduces the amount of water used in the tailings disposal process and has been widely adopted by the mining industry. In general, these slurries have both a higher solids concentration and a larger fraction of fine particles. Because of this they exhibit a greater degree of non-Newtonian fluid behaviour. Due to their high apparent viscosity thickened tailings slurries are typically transported under laminar flow conditions. Only a limited amount of research on solids transport has been performed under these flow conditions.

Regardless of whether consolidated tailings slurries with lower fines contents, thickened tailings slurries, or some intermediate slurry is utilised, one of the key requirements will be that the tailings stream continues to be non-segregating, with a uniform concentration distribution from the point of production to the final, in-situ placement location (Sanders et al., 2002). This will include the intermediate stage of pipeline transport, followed by open channel flow within the deposit.

Typically the clay and water components of the tailings slurry can be modeled as a homogeneous, non-settling carrier fluid phase. The presence of fines often results in a carrier fluid with non-Newtonian properties. If the fines are flocculated the slurry will exhibit a yield stress which increases exponentially in magnitude with fines concentration (Sumner et al., 2000). For yield stresses above a specific limit, the immersed weight of the coarse particle fraction will be supported and the particles will not settle under static conditions (Spelay et al, 2006). However, it has been shown experimentally that when sheared, particles tend to settle despite the presence of a yield stress (Sanders et al., 2002). A high apparent viscosity is associated with slurries which exhibit a high yield stress. As a result these slurries normally flow in the laminar regime.

An upper free surface is associated with all open channel flows. The free surface is not bound by an upper channel wall. This allows the depth of flow to rise or fall depending on the system configuration. Unlike a pipeline system, no pressure gradient exists in an open channel flow.

Rather the driving force behind the flow is the combination of gravity and the angle of the flume inclination. This coupled with the ability of the free surface to vary drastically changes the dynamics of the system.

A significant amount of slurry flow research has been conducted, particularly since the early 1950's. These investigations have been devoted primarily to the flow of slurries in pipes and closed conduits. However, the complex interactions that occur in certain slurry applications, such as open channel flow, are still not well understood and have received scant attention in the literature (Wilson, 1980). Further investigations are required to determine the underlying mechanisms present in the flow.

1.1. Present Study

The focus of this study is directed at the flow of concentrated clay-sand-water slurries in an open channel, or flume. These slurries can be classified as two-phase flows where coarse sand particles exist as one phase while the clay-water carrier fluid represents the second phase. The objective of this study is to develop a numerical model which accurately predicts the behaviour of solids transport in laminar, non-Newtonian, open channels flow. The added complexity of turbulent flow is beyond the scope of this work and will not be considered. As will be described in more detail, the constitutive model developed by Phillips et al. (1992) has been applied to this laminar solids transport application. Novel considerations have been made to the model to account for the non-Newtonian behaviour of the carrier fluid, and the gravitational flux of solids, which were not originally considered by Phillips et al. (1992).

One of the objectives of this study was to use numerical modeling to investigate the force mechanisms which are important in the transport of coarse particles in non-Newtonian, open channel, laminar flows. Another objective of this study involved experimentally investigating the nature of flume flow of coarse particles in clay-water slurries. Overall, the present work is focused on the steady transport of coarse solid particles. The main direction of the work was to investigate the variation of the local flow parameters within the cross-section of the geometry and about the wetted perimeter (wall shear stress, concentration, local velocity). Experimental results were obtained in a 156.7 mm flume for slurries modeled specifically after oil sands tailings. The numerical modeling component of this work is therefore well suited to determine these effects and should provide a basis for comparison with the experimental work.

The shear-induced diffusion model originally proposed by Leighton and Acrivos (1987b), and developed into a phenomenological constitutive model by Phillips et al. (1992) is used to model the coarse particle transport in laminar open channel flows of non-Newtonian slurries in this study. Similar, in form, to the dispersive mixture viscosity models of Hill (1996) and Gillies et al. (1999), the shear-induced model developed in this study incorporates theoretical scaling relationships to describe the transport of particles via flux terms. These fluxes are combined to form an overall scalar transport equation which can be solved to represent the transient behaviour of the concentration distribution.

A literature review outlining the theory and background is presented in Section 2. Section 3 describes the experimental apparatus, instruments, methods and techniques that were employed in the experimental study. The details of the numerical model and the associated finite volume method of analysis are discussed in Section 4. The results of the experimental study are provided in Section 5. The numerical simulation results are presented in Section 6. The conclusions and recommendations of the study are provided in Sections 7 and 8, respectively.

2. LITERATURE REVIEW

2.1. Homogeneous Fluid Models

A fluid is a substance that undergoes continuous displacement as long as shearing forces are applied to it (Shook et al., 2002). Viscosity is a measure of the resistance of a fluid to deform under shear stress. Viscosity describes a fluid's internal resistance to flow (friction) and is a material property relating the shear stress (τ) and the time rate of shear strain ($\dot{\gamma}$) in a moving fluid. Equation 2.1 below shows the relationship for these parameters in a Newtonian fluid.

$$\tau = \mu\dot{\gamma} \tag{2.1}$$

For Newtonian fluids, a constant, scalar parameter, the dynamic viscosity, can be used to relate the shear stress to the applied rate of shear strain. For Newtonian fluids the viscosity is independent of both τ and $\dot{\gamma}$. The shear stress is a linear function of the shear rate, with the slope of the curve being equal to the viscosity. Figure 2.1 shows a graphical representation of the shear stress versus time rate of shear strain behaviour plotted as a rheogram for a number of different continuum fluid models.

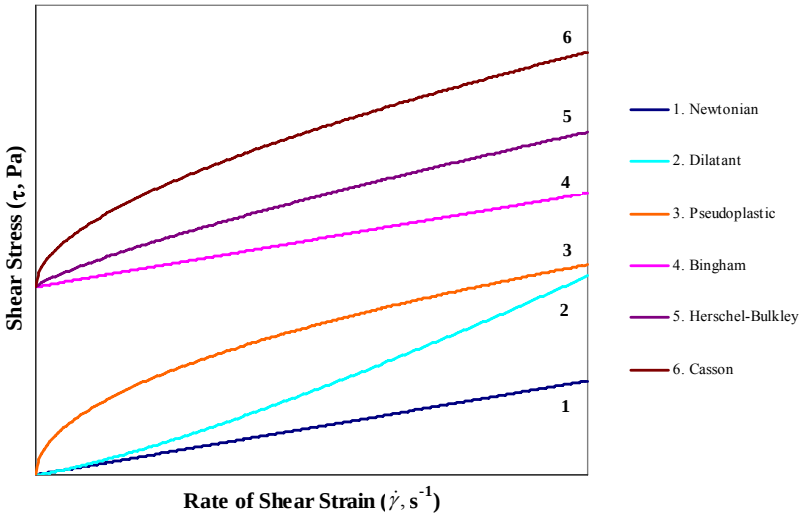

Figure 2.1: Rheograms of various continuum fluid models (Litzenberger, 2003)

Rheology is the study of the deformation of matter. The rheological behaviour of homogeneous fluids can be described by a shear stress versus rate of shear strain relationship:

$$\tau = \eta\dot{\gamma} \tag{2.2}$$

Equation 2.2 represents the basic equation relating the time rate of deformation of a fluid to an applied shear stress. In Equation 2.2, η is the apparent viscosity of the fluid. For Newtonian mixtures, the apparent viscosity is equal to the fluid viscosity ($\eta = \mu$). This is not the case for non-Newtonian fluids where η is a function of multiple rheological parameters as well as τ and $\dot{\gamma}$.

For non-Newtonian fluids, more than a single parameter is required to relate the shear stress to the applied rate of shear strain. The constitutive model equations for selected non-Newtonian fluids are shown below (Bird et al, 1960; Shook and Roco, 1991):

Power-Law	$\tau = K\dot{\gamma}^n$	two parameter	(2.3a)
Bingham	$\tau = \tau_y + \mu_P\dot{\gamma}$	two parameter	(2.3b)
Herschel-Bulkley	$\tau = \tau_y + K\dot{\gamma}^n$	three parameter	(2.3c)
Casson	$\tau^{1/2} = \tau_c^{1/2} + \left(\mu_c\dot{\gamma}\right)^{1/2}$	two parameter	(2.3d)

Of most interest in slurry flow applications are the behaviour of the fluids following the models of Equations 2.3b to 2.3d. All show the inclusion of a yield stress term (τ_y or τ_c). Fine particle suspensions, colloidal mixtures, and drilling muds typically exhibit a yield stress (Litzenberger, 2003; Bennett and Myers, 1982). In order for the fluid to flow, the applied shear stress must exceed the yield stress. Once the applied shear stress exceeds the yield stress, the rate of deformation of the fluid is determined by the difference between the applied stress and the yield stress.

In this study slurries which exhibit a yield stress will be represented with the Bingham rheological model (Equation 2.3b). The Bingham model is the simplest of the rheological models containing a yield stress. Unlike the Casson model (Equation 2.3d, Casson, 1959), and the Herschel-Bulkley model (Equation 2.3c), the Bingham model represents a linear relationship between the shear stress and rate of shear strain. It is described by a yield stress (τ_y) and a

plastic viscosity (μ_P) which correspond to the y-intercept and slope on the Bingham rheogram shown in Figure 2.1, respectively.

Non-Newtonian slurries can also display time dependent behaviour. For slurries exhibiting time dependent behaviour the shear stress is a function of time at a constant shear rate. For a rheopectic fluid the shear stress increases with time at a constant shear rate; for a thixotropic fluid the shear stress decreases with time at a constant shear rate (Bennett and Myers, 1982).

2.2. Slurry Flow Background

Slurries can generally be classified into two categories: homogeneous and heterogeneous. Unfortunately there is no single, all-inclusive definition that distinguishes heterogeneous slurries from homogeneous slurries. Shook et al. (2002) suggests that for flows with a mean particle diameter greater than 50 μm and a low flocculated fines concentration (i.e. carrier fluid has a low viscosity), the slurry will display heterogeneous properties. However, this may not be true for slurries of varying composition, concentration and test conditions.

Fine particles slurries (d_{50} < 50 μm) typically exhibit homogeneous fluid behaviour. Even though the mixture consists of two distinct phases, these mixtures are treated as a continuum possessing the density of the mixture. These types of slurries generally deviate from Newtonian behaviour and exhibit non-Newtonian characteristics. Many continuum models (i.e. Power-Law, Bingham, Casson) have been developed for slurries of this type and their behaviour can be accurately predicted in laminar flow. Models that have been developed more recently have considered turbulent pipe flow of non-Newtonian slurries. Based on the experience of the SRC Pipe Flow Technology Centre (Gillies, 2006), the models of Wilson and Thomas (1985) and Thomas and Wilson (1987) have been found to accurately represent turbulent pipe flow.

Heterogeneous slurries exhibit a more complicated flow behaviour when compared to homogeneous slurries. These slurries are typically a mixture of coarser particles in a homogeneous carrier fluid. Due to the submerged weight and effects of gravity on the coarse particles, sedimentation occurs within the flow. As a result, concentration and velocity profiles across the flow domain are non-uniform and asymmetrical (Shook and Roco, 1991). These slurries also often possess a significant Coulombic or mechanical friction component between the settled particles and the flow domain boundaries.

The behaviour of heterogeneous slurries in Newtonian carrier fluids in turbulent flow has been well studied and numerous models and correlations exist to predict slurry flow behaviour in pipelines (Shook et al., 1986; Gillies et al., 1991; Shook and Roco, 1991; Gillies, 1993; Gillies and Shook, 1994; Matousek, 1997; Gillies et al., 2000; Gillies and Shook, 2000; Shook and Sumner, 2001; Matousek, 2004; Gillies et al. 2004a; Sanders et al., 2004). Studies have investigated the minimum velocity required to suspend all particles in a pipe flow (critical deposition velocity) and other flow features including concentration and velocity profiles, and axial pressure gradient.

Regardless of the type of slurry, flows can be classified into two regimes: laminar and turbulent. Laminar flow is a low Reynolds number phenomenon characterized by smooth, streamline flow which is dominated by momentum diffusive effects as opposed to convection. Turbulence is a state of fluid motion which is characterized by apparently random and chaotic motions. It is a high Reynolds number phenomenon and it is a departure from smooth, organized laminar flow to a chaotic, disorganized flow.

A limited amount of research has been conducted on the study of sand transportation in laminar pipe flow with a Newtonian carrier fluid. Gillies et al. (1999) showed that significant quantities of sand could be transported in laminar flow as long as the axial pressure gradient was above a minimum value (approximately 2 kPa/m). Thomas et al. (2004) have shown that the minimum axial pressure gradient principle also applies to laminar flow of non-Newtonian slurries.

Earlier slurry flows theories suggested that turbulence or inertial effects were required to support particles within heterogeneous flows. However, in recent studies it has been shown that under laminar flow conditions, viscous forces are capable of resuspending settled particles (Leighton and Acrivos, 1987a, 1987b). Although an understanding of laminar transport of coarse solids in a non-Newtonian fluid is of importance to industry, few studies have been performed in this area.

Laminar flows have the added benefits of reduced fluid friction and pipe wear. However, if not operated properly they typically result in the formation of a settled bed of particles. An added concern is associated with the fact that small changes in chemical properties can significantly increase the apparent viscosity of non-Newtonian carrier fluids (Litzenberger and Sumner, 2004).

This could cause a heterogeneous slurry flow, which was initially operating in the turbulent regime, to transition to the laminar flow regime.

2.3. Open Channel Flow

Open channel flow of water and Newtonian fluids is a topic that has been studied extensively (Henderson, 1966; Chaudry, 1993; Chanson, 1999). A significant amount of research has been applied to the study of the transport of sand and sediments in open channel flows (Hunt, 1954; Coleman, 1969; Beal, 1970; Novak and Nalluri, 1974; Yalin, 1977; Nnadi, 1992).

Theoretical studies of non-Newtonian, open channel flows have been performed by Kozicki and Tiu (1967, 1988), Tiu and Kozicki (1969) and Matsuhisa and Bird (1965). As well, numerical studies have also been performed examining the non-Newtonian flow of fluids down inclined planes (Astarita et al., 1964, Liu and Mei, 1989, Coussot, 1994, Coussot and Proust, 1996, Federico, 1999). However, these models are only appropriate for homogeneous fluids and limited experimental research was performed to validate these models.

Recently, experimental studies of non-Newtonian, open channel flow have been conducted by Haldenwang (Haldenwang et al., 2000; Haldenwang et al., 2002; Haldenwang, 2003; Haldenwang et al., 2004). There is no mention of coarse particle transport in laminar or turbulent flow in any of this work. The only work to date considering the effects of a coarse particle phase in non-Newtonian open channel flows is the research performed by Sanders et al. (2002) and the research in conducted in this study.

The flow behaviour associated with open channel or flume flow is unique and quite different from pipe flow. The most obvious difference is that an open channel flow has a free surface such that part of the fluid within the flow is open to the surrounding conditions. In addition, an open channel flow is driven by gravity whereas a pipe flow is driven by a pressure gradient along with gravitational effects. Typically, for a flow with only one velocity component, the free surface can be said to have zero shear (and thus the maximum velocity in the flow generally occurs at the free surface). However, secondary currents can exist and this can cause the maximum velocity to exist somewhere below the free surface (Henderson, 1966). In this study, it is assumed that the free surface is a zero-shear boundary.

A dimensionless parameter which is commonly calculated for open channel flows is the Froude number (Fr), (Henderson, 1966; Yalin, 1977). The value of the Froude number (Equation 2.4) indicates whether the flow is critical, subcritical or supercritical. It is a ratio of inertial forces to gravitational effects in the flow and applies to wave and free surface behaviour. It also has an impact on the stability of the flow as well as the conditions upstream and downstream of the flow.

$$Fr = \frac{V}{\sqrt{gL}} \tag{2.4}$$

In Equation 2.4, V represents the average velocity in the channel while g represents the local acceleration due to gravity. L is the characteristic length of the channel (depth of flow, hydraulic radius). For Froude numbers greater than 1 the flow is said to be supercritical. In open channel flows this means that the flow can be controlled only by an upstream weir or height control device (Balanchandar, 2000). Likewise for Froude numbers less than 1 the flow is said to subcritical. This means that the flow can only be controlled by downstream devices. The Froude number criterion was developed for Newtonian flows and its application to non-Newtonian fluid flows is uncertain.

The existing formulas and theory for pipe flow typically are not applicable to open channel flow. Pipe flow is bounded in all directions by solid walls which fix the velocity based on the local cross-sectional area. However, the velocity is not fixed in an open channel flow as the conditions dictate the depth of flow, which in turn dictates the average velocity. Chezy was the first to propose an equation relating the velocity in the channel to the depth of flow and channel slope (Henderson, 1966). His equation is given below (2.5):

$$V = C\sqrt{R_h S_0} \tag{2.5}$$

where R_h represents the hydraulic radius of the channel while S_0 represents the channel slope or gradient. Originally it was thought that C was a constant, however, it has been shown to vary with channel roughness and channel shape. Manning expanded upon the work of Chezy and developed an equation for fully developed turbulent flow (Henderson, 1966):

$$V = \frac{1}{n} R_h^{2/3} S_0^{1/2} \tag{2.6}$$

where n is a function of the channel roughness and shape. This equation is still in wide use today.

As accurate as these correlations are, they are only valid for the prediction of turbulent flow of Newtonian fluids in open channels. They do not account for non-Newtonian behaviour nor do they account for the presence of solids in the flow. Kuhn (1980) and Blench et al. (1980) provide criteria applying to the design of industrial flumes for transporting solids. However, many of the correlations to date involving solids transport in open channels are highly empirical and based on industrial data (Wood, 1980; Lytle and Reed, 1984; Faddick, 1986).

For flow in an open channel, the wall shear stress is dependent upon the flume slope angle, the mass flowrate of material, and the cross-sectional flow area.

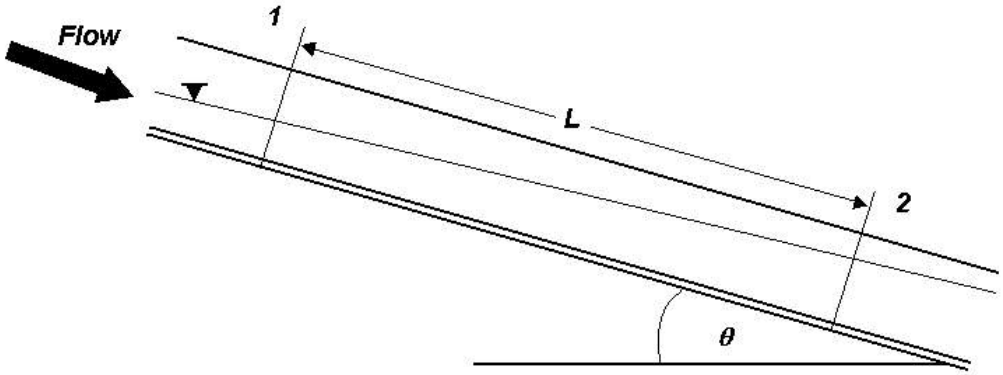

Figure 2.2: Schematic illustration of non-uniform, axial flow in a flume

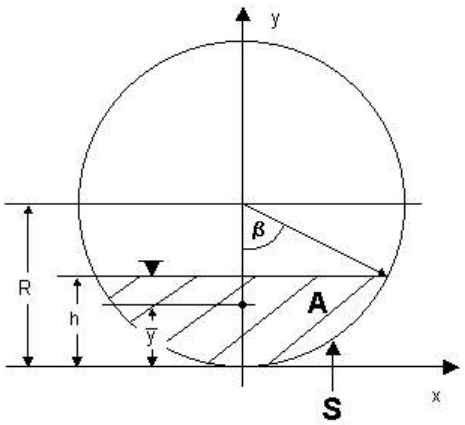

Figure 2.3: Schematic illustration of the cross-sectional view of open channel flow in a circular flume

Equations will be developed for an open-channel flow where the bulk density of the fluid is ρ, flowing at a mass flowrate of w in a flume of circular cross section, as depicted in Figures 2.2 and 2.3. The flume is inclined at an angle θ from the horizontal plane. At plane 1, the wetted perimeter is S_1 and the cross-sectional flow area is A_1. Similarly, at plane 2, the wetted perimeter is S_2 and the flow area is A_2. As Figure 2.2 shows, A_1 and A_2 are not necessarily equivalent. A_1 is greater than A_2 if the flow is accelerating and less than A_2 if the flow is decelerating. The figures also show the location of the centroid of the cross-sectional area of flow ($\overline{y}$), the depth of flow h, and the angle β, which describes the location of the free surface relative to the location of the centre of the pipe. Equation 2.7 details how the parameter β is determined. The variable R represents the inside radius of the circular flume cross-section.

$$\cos\beta = \left(1 - \frac{h}{R}\right) \tag{2.7}$$

Therefore, the cross sectional area (A) of the flow can be calculated as:

$$A = R^2\left(\beta - \sin\beta\cos\beta\right) \tag{2.8}$$

and the wetted perimeter (S) can be calculated as:

$$S = \beta D \tag{2.9}$$

and the bulk velocity at any location in a steady flow can be calculated by:

$$V = \frac{Q}{A} \tag{2.10}$$

The average wall shear stress in the flume can be determined by a force balance on the system. A steady state Eulerian rate of momentum balance (force balance) for the fluid element bounded by planes 1 and 2 is written as:

$$F_\tau + F_g + F_k + F_P = 0 \tag{2.11}$$

where each term can be expressed as:

$$F_\tau = -\tau_w S_m L \tag{2.11a}$$

$$F_g = \rho g\left[A_1\left(L\sin\theta + \bar{y}_1\cos\theta\right) - A_2\bar{y}_2\cos\theta\right] \tag{2.11b}$$

$$F_k = \rho\left(A_1V_1^2 - A_2V_2^2\right) \tag{2.11c}$$

$$F_P = P_1A_1 - P_2A_2 \tag{2.11d}$$

where F_τ represents the force due to the resisting wall shear stress, F_g represents the gravitational driving force, F_k represents a force due to the change in bulk velocity and thus momentum between the two planes and F_P represents a pressure force arising due to the fact that the centroid of the flow cross section at each plane is at a different depth. Therefore the area over which the pressure force is exerted is different. It should be noted that the resisting stress at the free surface has been assumed to be negligible. When simplified this reduces to:

$$\tau_w = \frac{\left[\rho g\left[A_1\left(L\sin\theta + \bar{y}_1\cos\theta\right) - A_2\bar{y}_2\cos\theta\right] + \rho\left(A_1V_1^2 - A_2V_2^2\right) + P_1A_1 - P_2A_2\right]}{LS_m} \tag{2.12}$$

Equation 2.12 reduces to the theoretical relationship for the force balance on a unit volume of fluid in the limit of a fully filled pipe:

$$-\frac{dP}{dz} - \rho g\sin\theta = \frac{4\tau_w}{D} \tag{2.13}$$

For a steady, uniform flow ($h_1 = h_2$), a force balance over a control volume of fluid can be performed to reduce Equation 2.12 to:

$$\tau_W = \frac{A}{S}\rho g\sin\theta = \rho g R_h\sin\theta \tag{2.14}$$

The wall shear stress varies along the wetted perimeter of the flow and the value calculated in Equations 2.12 and 2.14 is the average quantity between planes 1 and 2 in the flume test section. The pressure term of Equation 2.12 refers to the pressure force exerted at planes 1 and 2 and acts not through the centre of the circular cross-section, but through the centroid ($\overline{y}$) of the cross-sectional area of flow at each plane, as shown in Figure 2.2. The centroid of the cross-sectional area of flow in Figure 2.2 can be calculated from the equation:

$$\bar{y} = R + \frac{\frac{2}{3} R \sin\beta\left(\cos^2\beta - 1\right)}{\beta - \sin\beta\cos\beta} \tag{2.15}$$

and the pressure force can be evaluated as (Sanders et al., 2002):

$$PA = \rho g R^3 \left[\sin\beta\cos^2\beta - \beta\cos\beta + \frac{2}{3}\sin^3\beta \right] \tag{2.16}$$

Equation 2.16 can be substituted into Equation 2.12 to obtain the formula for calculating the average wall shear stress. The three terms on the right-hand side of Equation 2.12 can be evaluated once the depth of the slurry flow has been measured at height measurement positions 1 and 2 (Figure 2.2). The Fanning friction factor, f, can then be calculated from the mean wall shear stress, τ_w, according to the definition:

$$f = \frac{2\tau_w}{\rho V^2} \tag{2.17}$$

To determine whether the flow regime was laminar or turbulent, the Reynolds number according to Zhang (Hao and Zhenghai, 1982; Haldenwang et al., 2000) which relates total inertial to total viscous effects, was applied to account for the Bingham rheological properties of the slurries in the flume. The Reynolds number relationship is shown in Equation 2.18:

$$\mathrm{Re}_{Zhang} = \frac{8\rho V^2}{\tau_y + \frac{8V}{D_h}\mu_P} \tag{2.18}$$

where D_h is the hydraulic diameter:

$$D_h = \frac{4A}{S} \tag{2.19}$$

and

$$D_h = 4R_h \tag{2.20}$$

It should be noted that for Newtonian fluids the Zhang Reynolds number simplifies to the standard Reynolds number ($\tau_y = 0$, $\mu_P = \mu$):

$$\mathrm{Re} = \frac{\rho V D_h}{\mu} \tag{2.21}$$

As well, the Fanning friction factor for laminar and turbulent flow can be predicted using the empirical equation for pipeline frictional losses developed by Churchill (1977). This is shown below in Equation 2.22. In the equations A and B are parameters to describe the turbulent behaviour of the fluid while ε is the equivalent roughness of the pipe wall.

$$f = 2\left[\left(\frac{8}{\mathrm{Re}}\right)^{12} + (A+B)^{-3/2}\right]^{1/12} \tag{2.22a}$$

$$A = \left[-2.457 \ln\left(\left(\frac{7}{\mathrm{Re}}\right)^{0.9} + 0.27\frac{\varepsilon}{D_h}\right)\right]^{16} \tag{2.22b}$$

$$B = \left(\frac{37530}{\mathrm{Re}}\right)^{16} \tag{2.22c}$$

In Equation 2.22, as the Reynolds number approaches the laminar flow range (Re < 2000), the parameters A and B become very large. Churchill's equation reduces to equation 2.23 in laminar flow.

$$f = \frac{16}{\mathrm{Re}} \tag{2.23}$$

In the analysis of the experimental data, Equations 2.22 and 2.23 have not been used to predict frictional losses in the flume. Rather the equations are used to aid in determining the flow regime of the experimental tests and to compare the frictional behaviour of what is predicted by theory to what is experimentally measured in the flume for the different mixtures. The roughness term in the turbulent equation for the parameter A has been modified with the hydraulic diameter to be appropriate for open channel flow. A roughness value of 0 denotes a smooth wall. Of course the roughness has no explicit effect on the frictional losses in laminar flow as can be seen in Equation 2.23.

2.4. Kozicki and Tiu Model

Kozicki et al. (1966), Kozicki and Tiu (1967, 1988), Tiu et al. (1968), and Tiu and Kozicki (1969) have proposed an analytical method by which frictional effects resulting from non-Newtonian fluid flow can be predicted in ducts of arbitrary cross-section. The method involves the use of two geometric parameters, a and b, to describe the duct. This was an extension of the research of Matsuhisa and Bird (1965) who solved the laminar flow problem of the non-Newtonian Ellis fluid in various geometries. Additional relevant research included the work of Metzner and Reed (1955) and Straub et al. (1958) who attempted to correlate data and create a method for predicting wall shear stress and turbulent transition for non-Newtonian and Newtonian fluids in ducts of various cross-sections.

Kozicki and Tiu (1971) attempted to create a more accurate analytical model by including more geometric parameters. However, this approach is not as simple or popular as their original two parameter approach. In their 1967 and 1988 papers they showed that the two parameter method can be applied to open channel gravity flows with the following conditions.

- incompressible, time independent, non-Newtonian fluid
- isothermal, steady, one-dimensional, laminar, gravity flow
- no-slip at channel walls
- zero shear free surface
- flow is uniform (free surface height does not change with axial position), with no waves

- channel wall is smooth

In this study, open channel flow in flumes of circular cross-section is of particular interest. However, the work of Haldenwang (2003), which was performed in rectangular channels, was also reviewed so both types of channels have been considered. A schematic of the cross section of a rectangular channel is illustrated in Figure 2.4. Figure 2.3 shows a schematic of the cross section of the circular channel employed in this study.

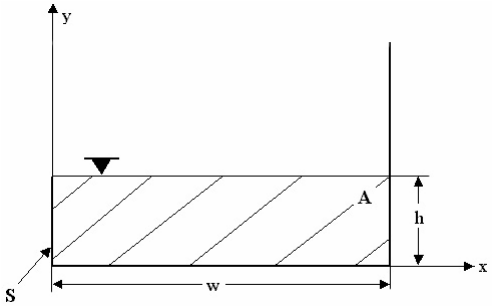

Figure 2.4: Schematic illustration of the cross-sectional view of open channel flow in a rectangular flume

Equations 2.24 and 2.25 can be used to calculate the cross sectional area (A), and wetted perimeter (S) in rectangular channels.

$$A = wh \tag{2.24}$$

$$S = 2h + w \tag{2.25}$$

Integrating the Rabinowitsch-Mooney equation, given in Kozicki and Tiu (1967), yields a formulation that can be applied to any non-Newtonian fluid model of the form presented in Equation 2.2. For Newtonian fluids this equation simplifies to:

$$\frac{2(V - v_0)}{R_h} = \frac{\tau_w}{\mu}\left(\frac{1}{b+a}\right) \tag{2.26}$$

$$\mathrm{Re} = \frac{4R_h(V - v_0)\rho}{\mu}\left(\frac{1}{b+a}\right) \tag{2.27}$$

while for Bingham fluids it reduces to:

$$\frac{2(V-v_0)}{R_h}=\frac{\tau_w}{\mu_P}\left[\frac{1}{b+a}-\frac{1}{b}\left(\frac{\tau_y}{\tau_w}\right)+\frac{a}{b(b+a)}\left(\frac{\tau_y}{\tau_w}\right)^{b/a+1}\right] \tag{2.28}$$

$$\mathrm{Re}=\frac{4R_h(V-v_0)\rho}{\mu_P}\left[\frac{1}{b+a}-\frac{1}{b}\left(\frac{\tau_y}{\tau_w}\right)+\frac{a}{b(b+a)}\left(\frac{\tau_y}{\tau_w}\right)^{b/a+1}\right] \tag{2.29}$$

One can see from the relationships for a Bingham fluid flow that the wall shear stress versus velocity equation is non-linear (Equation 2.28). To solve for the theoretical wall shear stress, a Newton-Raphson iterative approach was employed (Rao, 2002).

Kozicki and Tiu determined the values of a and b to be 0.25 and 0.75 for open circular channels. Sestak (1974) showed, using bipolar coordinates, that an assumption made in Kozicki and Tiu's original determination of a and b was inappropriate. This assumption stated that for circular channels, as the ratio of the depth of the flow to the channel diameter approaches zero, the flow approaches that of an infinitely wide flow down an inclined plane. Sestak proved, using bipolar integration, and the equations developed by Chaudhury (1964) and Buffham (1968), that the system actually converges to a point flow at this condition. However, this is only important at extremely low depths of flow and it does not have a significant effect on the calculated wall shear stress obtained from Kozicki and Tiu for the larger depths of flow that were observed in the experiments of Sanders et al. (2002). For more information see the work of Sestak (1974) and Kozicki and Tiu (1988). Thus, the values for a and b used in the analysis of 0.25 and 0.75, respectively, were acceptable.

For rectangular channels the relationships for determining a and b are:

$$\lambda=\frac{w}{2h} \tag{2.30}$$

$$\phi=\frac{1-\frac{32}{\pi^3}\sum_0^\infty\frac{(-1)^n}{(2n+1)^3}\frac{1}{\cosh\left[\frac{(2n+1)}{2}\pi\lambda\right]}}{1-\frac{192}{\lambda\pi^5}\sum_0^\infty\frac{1}{(2n+1)^5}\tanh\left[\frac{(2n+1)}{2}\pi\lambda\right]} \tag{2.31}$$

$$a = \frac{1}{2}\left(\frac{\lambda}{\lambda+1}\right)^2\left[1 - \frac{32}{\pi^3}\sum_0^\infty \frac{(-1)^n}{(2n+1)^3}\frac{1}{\cosh\left[\frac{(2n+1)}{2}\pi\lambda\right]}\right]^{-1} \tag{2.32}$$

$$b = a(3\phi - 1) \tag{2.33}$$

It should be noted that a misprint in the original paper of Kozicki and Tiu (1967) neglected to include the parameter λ in the denominator of Equation 2.31. Based on the results presented in Kozicki et al. (1966), it was clear that the correct equations were used in their earlier derivation. Therefore the correction to the equation has been made with this work.

It should be stressed that these equations are for homogeneous flow. The frictional behaviour that occurs in coarse particle transport may not obey these equations. Other modeling techniques must be used to address the complexities that arise from the addition of a settling coarse particle phase.

2.5. Single Particle Settling

A thorough review of particle settling behaviour is given in Wallis (1969). Depending on the forces acting on a particle, it can either be at rest, accelerating, decelerating or settling at the terminal settling velocity. Equations have been derived which relate the velocity of the particle to the physical properties of the particle and the fluid in which it is submersed (Hill, 1996; Shook and Roco, 1991). The equation for the terminal settling velocity (v_∞) is shown below:

$$v_\infty = \sqrt{\frac{4gd(\rho_s - \rho_f)}{3\rho_f C_D}} \tag{2.34}$$

where

d = particle diameter

g = local acceleration due to gravity

ρ_s = solids density

ρ_f = fluid density

C_D = drag coefficient

The drag coefficient, C_D, is a function of the Reynolds number of the particle. For smooth spherical particles the relationship between the drag coefficient and the Reynolds number is shown below in Equation 2.35 (Wallis, 1969; Hill, 1996):

$$C_D = \frac{24}{\mathrm{Re}_P} \quad ; \mathrm{Re}_P < 0.2 \quad \text{Stokes} \quad (2.35a)$$

$$C_D = \frac{24}{\mathrm{Re}_P}\left(1 + 0.15\,\mathrm{Re}_P^{0.687}\right) \quad ; 0.2 < \mathrm{Re}_P < 1000 \quad \text{Intermediate} \quad (2.35b)$$

$$C_D = 0.44 \quad ; 1000 < \mathrm{Re}_P < 3x10^5 \quad \text{Newton's} \quad (2.35c)$$

and

$$\mathrm{Re}_P = \frac{\rho_f v_\infty d}{\eta_f} \quad (2.36)$$

where

η_f = fluid viscosity

From the relations shown in Equation 2.35, it is possible to determine the terminal settling velocity of the particle solely as a function of the physical properties of the fluid and the particle. For many applications, particles are found to settle in the Stokes' law region. The equation for terminal settling velocity of a particle in the Stokes' law region is:

$$v_\infty = \frac{gd^2\left(\rho_s - \rho_f\right)}{18\eta_f} = \frac{2ga^2\left(\rho_s - \rho_f\right)}{9\eta_f} \quad (2.37)$$

where

a = particle radius

However, there are added complications that can limit the use of these equations:

1. Particle or the solids concentration is significant (system is not dilute)
2. The fluid is not quiescent (stagnant)
3. Particles are non-spherical
4. Ratio of the diameter of the particle to the diameter of the vessel is significant
5. The fluid is non-Newtonian

The simple Stokes' law relation in Equation 2.37 typically does not apply if any of the above complications exist. Non-spherical shape is typically addressed by the use of sphericity factors and equivalent diameters. Effects resulting from high solids concentration are addressed by incorporating hindered settling relationships. This will be discussed in more detail in Sections 2.6.

Until recently, particle diameter was considered to be the most important parameter for slurry flows in a pipeline. However, Schaan et al. (2000) has shown that the angularity and shape of a particle, along with size, has a strong affect on frictional losses. If the size of the particles is comparable to the size of the vessel then added complications arise due to wall effects. This is an important consideration since all of the energy losses will occur in the near wall region.

If a significant fraction of fine particles exist in a mixture, the slurry will typically exhibit non-Newtonian behavior. If the fines are at a sufficiently high concentration and are flocculated, the slurry will exhibit a yield stress. This yield stress can act to keep coarse particles in suspension, preventing them from settling under static conditions (Hill, 1996; Shook and Roco, 1991; Song and Chiew, 1997). The minimum yield stress required to support a spherical particle under static conditions, $\tau_{y,\min}$, has been derived by Shook and Roco (1991) and is given in Equation 2.38.

$$\tau_{y,\min} = \frac{(\rho_s - \rho_f) g d}{1.5\pi} \tag{2.38}$$

Wilson and Horsley (2004) determined the settling velocities of particles in non-Newtonian fluids. Their approach uses the shape factor (α) from the rheogram of the non-Newtonian fluid, which is the ratio of the areas under the curves of the non-Newtonian and Newtonian rheograms at the same conditions, to provide a generalized settling velocity calculation method. The approach also provides a method to address the added effect of local shear rate on the settling of particles. However, the method has not been verified against any experimental data.

Dedegil (1986) and Atapattu et al. (1988) attempted to develop correlations to predict settling velocities for solid particles in unsheared Bingham fluids. Chhabra (2002) also attempted to provide a method by which prediction of settling rates in non-Newtonian fluids can be approached. The paper provides techniques to predict the effects for both spherical and non-spherical particles. Thomas et al. (2004) briefly considered particle settling in laminar flows. He proposed that particles settle more slowly in non-Newtonian fluids because of increased viscous resistance. However, he also noted that the local shear rate must be considered when determining the particle fall velocity in a sheared fluid. Although no method of settling velocity prediction is given, he does suggest using an equivalent viscosity approach to show that particles settle faster in regions of higher shear rate. Techniques from each of these papers will be employed in this study. However, no definitive correlations, which have been verified against experimental data, result from either of the studies.

2.6. Multi-Particle Systems

Infinite dilution is a condition such that the effect of neighbouring particles on a settling particle is negligible. The assumption of infinite dilution is not applicable when the solids concentration in a mixture is above 5 to 10% by volume. The particles no longer settle as a single particle in an infinitely dilute fluid but rather interact with each other in the sedimentation process.

Einstein proposed a theoretical relative viscosity (η_r) equation to predict the increase in mixture viscosity due to the effect of particles on the streamlines within the flow (Shook and Roco, 1991):

$$\eta_r = 1 + 2.5\phi \tag{2.39}$$

where ϕ is the volumetric concentration of solids. Einstein's equation accounts for the distortion of the shear field due to the presence of particles, but neglects the more complex behaviour that occurs at higher concentrations. In the dilute region, particle-particle interaction effects are negligible. Equation 2.39 is therefore applicable to suspensions with solids concentrations less than 10% by volume.

Particle-particle interactions, which occur in more concentrated suspensions, are accounted for with additional terms in the relative viscosity equation. The relative viscosity is simply the ratio of the mixture viscosity to the viscosity of the pure fluid without any particles. Frankel and Acrivos (1967), and Jeffrey and Acrivos (1976) proposed empirical equations to account for interparticle interactions in concentrated systems. Some common relative viscosity equations are shown below:

$$\eta_r = \left(1 - \frac{\phi}{\phi_{\max}}\right)^{-1.82} \qquad \text{Krieger (1972)} \qquad (2.40a)$$

$$\eta_r = 1 + 2.5\phi + 10.05\phi^2 + 0.00273e^{16.6\phi} \qquad \text{Thomas (1965)} \qquad (2.40b)$$

$$\eta_r = 1 + 2.5\phi + 10\phi^2 + 0.0019e^{20\phi} \qquad \text{Gillies et al. (1999)} \qquad (2.40c)$$

$$\eta_r = 1 + 2.5\phi + 0.16\lambda^2 \qquad \text{Schaan (2001)} \qquad (2.40d)$$

where λ is the linear concentration as proposed by Bagnold (1954). It can be considered to be the ratio of the distance between the centers of adjacent particles to the shortest distance between their surfaces (Schaan, 2001). Equation 2.41 expresses the relationship between the linear concentration and the maximum packing factor.

$$\lambda = \left[\left(\frac{\phi_{\max}}{\phi}\right)^{1/3} - 1\right]^{-1} \qquad (2.41)$$

From equations 2.39, 2.40 and 2.41, it can be seen that the relative viscosity is independent of particle size. It is only appropriate for uniformly distributed, fine particle suspensions (Shook et al., 2002). Equation 2.40d is a function of the maximum packing concentration of the particles ($\phi_{\max}$). The maximum packing concentration is independent of particle size and is only a function of the particle shape and the particle size distribution (Schaan, 2001).

The equation given by Schaan (2001) includes an additional $0.16\lambda^2$ term to account for interparticle interactions. However, this term is included in the evaluation of the relative viscosity for both dilute and concentrated suspensions. In the dilute region a small error in the relative viscosity is introduced. Gillies (2006) proposed an equation to account for this deviation:

$$\eta_r = 1 + 0.21\lambda^2 \qquad \text{Gillies (2006)} \qquad (2.40e)$$

This equation eliminates the errors associated with Schaan's equation at low concentrations. It reduces to a function that is similar to Einstein's equation at low concentrations while still accounting for interparticle interactions in concentrated systems. However, to be consistent with previous studies in the area, Equation 2.40d will be employed in this study.

Nir and Acrivos (1973) suggested that a bias exists in experimental techniques used to determine relative viscosity. These researchers used a heat transfer approach which they believed was independent of the experimental geometry. However, they failed to develop a conclusive relative viscosity relationship with this type of setup.

The relative viscosity equations presented above accurately represent the effects of particles on the viscosity of a Newtonian carrier fluid. However, special considerations must be made to account for the effect of particles on the rheology of non-Newtonian fluids.

Gillies (2006) has also provided scaling arguments for the effect of a particle phase on the yield stress and plastic viscosity of a Bingham fluid. The relationships are given below in Equations 2.41a and 2.41b. However, the correlations have not been tested thoroughly against experimental data.

$$\left(\tau_y\right)_r = \frac{\tau_y}{\left(\tau_y\right)_f} = 1 + 0.016\lambda^{2.5} \qquad (2.41a)$$

$$\left(\mu_P\right)_r = \frac{\mu_P}{\left(\mu_P\right)_f} = 1 + 0.21\lambda^2 \qquad (2.41b)$$

Non-Newtonian fluids are characterized by two or more parameters to describe the rheological behaviour or shear stress versus shear rate relationship. An apparent viscosity can be calculated from the ratio between the shear stress and rate of shear strain:

$$\eta_{apparent} = \frac{\tau}{\dot{\gamma}} \qquad (2.42)$$

The apparent viscosity for a slurry under a specific shear rate can therefore be represented using a single viscosity parameter. This viscosity can be scaled by the relative viscosity equations, presented above, to determine the mixture effective viscosity.

Interparticle interactions result in a hindrance or reduction in the settling velocity for a given particle. Hindered settling effects begin to dominate at higher concentrations. For most cases of concentrated particle systems, the Richardson and Zaki (1954) approach can be used to predict the deviations in settling characteristics of particles due to concentration effects (Wallis, 1969; Gillies and Shook, 1994; Shook and Roco, 1991). Gillies et al. (2004b) suggested using the Richardson and Zaki (1954) hindered settling approach of the form shown in Equation 2.43 in their turbulent dispersive diffusivity model:

$$v_s = v_\infty (1-\phi)^n \tag{2.43}$$

where

v_s = hindered settling velocity

v_∞ = settling velocity in infinite dilution

ϕ = volumetric concentration of solids

An empirical relationship has been developed for the parameter n of Equation 2.43 (Wallis, 1969):

$$n = 4.7 \frac{\left(1 + 0.15\,\mathrm{Re}_\infty^{0.687}\right)}{\left(1 + 0.253\,\mathrm{Re}_\infty^{0.687}\right)} \tag{2.44}$$

where Re_∞ is calculated by:

$$\mathrm{Re}_\infty = \frac{\rho_f v_\infty d}{\eta_f} = \frac{2\rho_f v_\infty a}{\eta_f} \tag{2.45}$$

and a is the radius of the settling particle.

2.7. Sediment Transport

A thorough review of the mechanisms of sediment transport is given in Yalin (1977). However, most of the models are empirical and only applicable to dilute systems. A good review of the hyperconcentrated flow of solids in the Yellow River in China is given by Wan and Wang (1994). Some numerical work on hyperconcentrated, non-Newtonian pastes in open channels was performed by Liu and Mei (1989), Coussot (1994), Federico (1999) and Astarita et al. (1964). This research has produced some interesting results but the work was for flow in simple flume geometries and did not consider the effects of a coarse particle phase. No theoretical correlations exist to accurately describe the mechanisms associated with the transport of coarse solids to date.

The Shields parameter is one of the most frequently used conditions to relate the suspended sediment to the dynamic parameters of a flowing slurry (Yalin, 1977). This parameter addresses the critical stage of a mobile bed and the initiation of grain motion en masse, not the detachment of an individual grain.

$$Y = \frac{\tau}{g\left(\rho_s - \rho_f\right)d} \tag{2.46}$$

The Shields parameter can be calculated without iteration if the properties of the fluid and the sediment being transported are known as shown in Equation 2.46. For turbulent flow the dimensionless shear stress (Y_{cr}) at the inception of sediment transport is approximately 0.05 (Nnadi, 1992).

In a related study, Fan and Masliyah (1990) have applied the Shields parameter theory to investigate beach profiles in tailings disposal using a Meyer-Peter and Muller sediment transport relationship (Yalin, 1977). However, it is important to note that their theory only applies to dilute sediment slurries, a classification which cannot be applied to most industrial tailings mixtures. As well, the research is focused on the prediction of bed load, saltation and incipient motion of single particles. This is not equivalent to the critical deposition velocity condition described in pipelines for more concentrated systems. This model is not appropriate for non-Newtonian flows where concentrated slurries are being transported.

Van Rhee (2002a, 2002b, 2004) successfully applied a parameter resembling the Shields parameter to numerically model solids transport in turbulent trailing suction hopper dredges. He coupled the Shields parameter to a $k-\varepsilon$ turbulent modeling technique to produce two-dimensional results which accurately represented his experimental data.

Schaflinger et al. (1995) also attempted to use a factor which resembled the Shields parameter to study viscous resuspension of settled particles in laminar shear flows. Tremblay et al. (1998) attempted to correlate sand production and wormhole development in heavy oils to a critical shear condition. However, both of these methods are applicable to viscous Newtonian carrier fluids only.

2.8. Pastes

Prior to the use of hydraulic transport, highly concentrated materials were transported by mechanical methods. Some of these methods include conveyor belts, transportation by truck, and transportation by sea. Although these methods are simple to design and operate, the costs associated with these forms of transportation are high. The relative costs associated with hydraulically transporting a material are typically much less than mechanically transporting the material, although the capital costs might be more for some systems (i.e. positive displacement pumps). Material transported using a pipeline can be moved long distances by employing only pumps and a piping system. As well, it has been shown that there are added advantages to moving a material via a pipeline for some industrial mixtures. This is true in the oil sand industry. Moving the oil sand hydraulically not only decreases operating costs but it also preconditions the material for processing by allowing for enhanced mixing (Sanders et al., 2000).

A paste is a high density mixture of predominately fine particles and water (10 to 25% w/w). The mixture may "bleed" water when left motionless, but this water can be easily redispersed (Brackebusch, 1994). The tailings of a milling or ore processing operation represent the most common sources of the solid material for a paste. The majority of paste mixtures exhibit non-Newtonian behaviour (Brackebusch, 1994). This is primarily due to the fine solid particles that are usually in great abundances in the processes generating tailings and their tendency to flocculate which produces a yield stress.

One of the problems with the emerging paste technology is the relative lack of knowledge associated with the transport of the highly viscous non-Newtonian fluids. In addition to non-Newtonian behaviour they may also exhibit time dependent behaviour, which calls for additional modeling requirements. The rheology of pastes is material specific in that these properties can vary significantly from one generation site to the next. A paste can also cause appreciable erosion on pipeline equipment due to their high solids concentration (Shook et al., 1990). The life of the equipment and the efficiency associated with their operation will be reduced as a result of the erosion effects (Shook and Roco, 1991).

2.9. Stabilized Flow

A common misconception in industry is that solids can only be transported in turbulent flow in pipes and open channels. It has been shown that solids transport can occur under laminar flow conditions even though the turbulent support mechanisms (i.e. dispersive forces and eddies) do not exist (Thomas et al., 2004). With the increasing interest in transporting more concentrated slurries, the possibility of operating in the laminar regime is being considered. Laminar transport in fluids which exhibit a yield stress is often referred to as stabilized flow. This is because under static conditions the yield stress of the carrier fluid is large enough to support the submerged weight of the coarse particles (Equation 2.38).

Thomas (1979) described stabilized flow or "stab-flo" as transport of a slurry with a yield stress where particles are supported under static conditions. He believed that the flocculated vehicle (the carrier fluid) traps particles and prevents them from settling. It was believed that if the carrier matrix could suspend the coarse phase then the slurry would be non-settling and could be transported under laminar flow conditions. The advantages of this are less wear on the pipe and fittings as well as the ability to transport more concentrated suspensions. However, once sheared, the yield stress of the mixture was no longer able to suspend the particles and much of the coarse phase was transported as a sliding or saltating layer on the bottom pipe wall (Thomas, 1979). This was disadvantageous since it resulted in a much higher operational pressure gradient.

Settled particles are transported by the pressure gradient (gravity in open channels). The forces acting on the system result in a balance between the pressure gradient and the frictional resistance of the solid particles on the wall (Coulombic friction). However, the Coulombic friction term (i.e. the minimum pressure gradient required to transport particles) is both velocity independent

and pipe size independent. At incipient motion (stationary bed of particles) the pressure gradient ($-dP/dz$) required for motion is (Thomas, 1979):

$$-\frac{dP}{dz} = 2\eta_s \phi_{\max} g\left(\rho_s - \rho_f\right)\varphi \tag{2.47}$$

where

$\eta_s =$ coefficient of sliding friction between the bed and pipe wall

$\phi_{\max} =$ maximum packing concentration by volume of the settled bed

$\varphi =$ geometric function which depends on the height of the sliding bed

As one can see, this pressure gradient is independent of pipe diameter. Transport in larger diameter pipes is increasingly uneconomical. As well, settled beds in long distance pipelines can present difficulties in startup and shutdown. Thomas (1979) also observed that slurry behaviour was qualitatively similar for both Newtonian and non-Newtonian carrier fluids.

Tests and results from recirculating pipeloops must be examined carefully as the length of the experimental circuit is an important factor. The equilibrium length, associated with laminar transport of particles, required to obtain fully developed velocity and concentration distributions (settled/sliding beds) can be significant in some cases (Thomas, 1979). The key conclusions resulting from Thomas' study were:

1. Just because laminar flow without deposition was possible in a small pipe doesn't mean that the same slurry can flow in laminar flow without a deposit in a larger pipe.
2. Obtaining laminar flow without a deposit in a short pipe length does not mean that no deposit will exist in the same diameter pipe of longer length.
3. If fully developed flow exists, the pressure gradient required to transport particles in laminar flow and prevent deposition is nearly constant for all pipe sizes.
4. Flow in larger diameter pipes also should take longer to develop since particles have to settle further.
5. There is not much advantage in using more viscous fluids to transport solids.

It should be noted that Thomas (1979) performed tests with fluids which exhibited yield stresses just high enough to exceed the support criteria of the submerged particles. Even the slightest degree of shear will cause particles to settle under these conditions. It is recommended that fluids should exhibit larger yield stresses which greatly exceed the minimum criteria given by Shook and Roco (1991).

Elliot and Glidden (1970) obtained laminar transport results in a variety of pipelines without a deposit. Their results seem to contradict the work of Thomas (1979). They observed that non-Newtonian settled beds were less compacted than the Newtonian beds. They believed that this effect could be attributed to coarse particles being separated by compressible carrier fluid flocs. This results in more compaction in smaller pipes and that a less compacted sliding bed will be observed at the bottom of the pipe with larger pipes. This suggests that the critical pressure gradient decreases with increasing pipe size. This relationship is a function of the particle size and the yield stress of the carrier fluid (floc strength/structure). This effect can be so significant as to cause the critical pressure gradient to vary inversely with pipe diameter. They suggested that the deposition condition in non-Newtonian carriers varies with wall shear stress rather than a pressure gradient.

Paterson et al. (2004) studied gravity driven copper concentrate transport in canals and pipelines from high elevations in Peruvian mines. The operation was found to operate more efficiently at high solids concentrations. This is because thickening downstream and recycling water back to the mine is not economically feasible. In their tests they observed that once a particle settles in laminar flow it is not possible to resuspend it. The particles settle on the bottom of the flow and effectively reduce the flow area available for transport. Pressure gradients of 1 to 2 kPa/m are generally required, as a rule of thumb, to force the bed to move along the bottom of the pipe. They also observed that flow in open channels (as opposed to flow in closed pipes) required steeper gradients to prevent settling.

An in depth review of laminar flow settling was performed by Cooke (2002). In the past, slurries would be thickened for laminar flow transportation. Process specifications now require slurries to be transported in laminar flow. He too showed that no effective mechanism exists to resuspend particles in laminar flow. However, despite the undesired condition of settling, industry is moving towards laminar transport due to the requirements of low water usage and environmental concerns.

Laminar solids transport literature has shown that ensuring a slurry is stable when static is no guarantee that it will be stable under sheared conditions (Thomas, 1978). Yield stress does not play a role in suspending particles in the sheared annulus of pipe flow (Thomas, 1978). Fluid shear acts to break down the floc structure of the annulus allowing particle settling to occur. Particles in the sheared region can be assumed to be settling in a fluid with a viscosity equal to that of the plastic viscosity of the Bingham carrier (Thomas, 1978). The high concentration of particles on the bottom of the pipe results in a significant difference between delivered and in-situ concentration. However, settling is low in laminar flow meaning that for short pipelines solids can be transported without significant settling (Cooke, 2002; Wasp, 1999).

Graham et al. (2002) performed non-intrusive measurements on laminar flow transport of solids with MRI (magnetic resonance imaging) and ERT (electrical resistance tomography) instruments. Three important observations were made from the measured profiles:

1. The settled bed moved en-bloc although some tests have shown that shearing occurs across the bed.
2. The solids were confined to the pipe invert (bottom of the pipe) for all of the tests. Deposition and bed formation only seemed to be occurring in the vertical direction (y). The transverse gradients (x-wise), dC/dx, were not significant.
3. The yield stress has an effect on the bed formation. The bed is not sheared at the pipe wall for fluids which have a sufficiently high yield stress.

Since the Coulombic friction term (Shook and Roco, 1991) is velocity and pipe size independent, open channel flow becomes a more increasingly economical means of moving the coarse solid phase as the scale of the transportation problem becomes larger. Solids have been transported by flumes, launders, and open channels for many years. Wilson (1980) states that solids were conveyed by open channels in industry since the gold rush. Early references from the Hydrotransport proceedings provide several examples of open channel transport of solids suggesting that this method is common in the mining industry (Kuhn, 1980; Blench and Galay, 1980). The transport of concentrated, coarse solids mixtures is of particular interest in these applications.

A thorough review of solids transport in open channels is given by Wilson (1980). Although no quantitative results are presented, the paper presents a thorough review of the existing technology and methods to date. Past research demonstrated that transport of solids by flumes was not only achievable, but it was also economically feasible. Wood (1980) investigated the important parameters governing slurry flows in flumes. Faddick (1986) performed a preliminary qualitative investigation into the critical deposition condition in flumes and related the critical velocity to a minimum velocity gradient.

Lytle and Reed (1984) suggested that conveyance of run-of-mine coal by open channel flow would permit Western Canadian producers to stay competitive in global markets. Finally, Novak and Nalluri (1974) attempted to correlate a deposition velocity condition with the critical incipient motion condition for turbulent flows. However, they suggested that further research needs to be performed on the transport of solids by contact load (settled particles in bed) as opposed to the more thoroughly researched area of transport by suspended load (particles in suspension).

Only one critical deposition study could be found for the open channel geometry in the literature. Dominguez et al. (1996) developed an empirical equation to predict deposition velocity in open channel flows. Experiments were performed over a wide range of conditions but little experimental control existed with respect to fluid properties since industrial mixtures were used in the analysis. The correlation is applicable for Newtonian carrier fluids and channel shape is accounted for by the use of the hydraulic radius.

$$V_D = 1.833\left[8gR_h\frac{\rho_s-\rho_m}{\rho_m}\right]^{0.5}\left[\frac{d_{85}}{R_h}\right]^{0.158}1.2^{\left(\frac{3100}{\mathrm{Re}^*}\right)^3} \tag{2.48a}$$

$$\mathrm{Re}^* = \frac{\rho_m R_h\left(gR_h\right)^{0.5}}{\mu} \tag{2.48b}$$

Equation 2.48 is empirical. Since the equation was developed using Newtonian carrier fluids, it is inappropriate for use with non-Newtonian slurries. It is also worth noting that the correlation is dependent on the particle size distribution as the d_{85} (the particle diameter in which 85% of the distribution is finer than) is required to represent the coarse phase of the solids particles.

However, the most troubling aspect of the correlation is that no apparent link is given between the inclination of the channel (driving force) and the critical deposition velocity.

An analytical correlation to predict the critical deposition condition of coarse solids in open channel, laminar non-Newtonian flow does not exist at this time. This is due to the complexity of the flow and the large number of correlating parameters. Limited empirical correlations exist but they are specific to the geometry and the conditions under which the experimental data was gathered (Dominguez et al., 1996).

2.10. Bingham Fluid Model

As stated earlier the Bingham model is the simplest of the rheological models containing a yield stress. The model represents a linear relationship between the shear stress and rate of shear strain. Unlike for the three parameter Herschel-Bulkley model (Equation 2.3c), most often changes in the concentration, chemical addition, temperature or pH can be directly correlated to the two parameters of the Bingham model. Although the three parameters of the Herschel-Bulkley model may provide a better fit to the specific experimental data collected, it may not always be the most appropriate choice or provide the most meaningful rheological parameters or results. It is important to remember that experimental data will always be better fit by the inclusion of an additional parameter. Because of the risk of interpolation and extrapolation errors, the three parameter Herschel-Bulkley model should only be used when an extensive experimental program is used to justify the use of the additional parameter, n, and allow for its value to be accurately determined.

In the studies performed at the Saskatchewan Research Council, concentrated kaolin clay-water slurries are often most accurately represented by the Bingham model (Shook et al., 2002). The electrostatic forces in clays are of importance because these particles are generally very small in size and can often be considered to be colloids (Van Olphen, 1977). Many particles have surface charges associated with them. The combination of a high degree of surface charge associated with the significant surface area, combined with a small particle size and mass results in high charge to mass ratios leading to the important effects observed with clays.

Surface chemistry is an important area in aqueous clay mixtures. Most clay particles have a plate like particle shape with specific charges on the faces and edges of the particle. When they are

placed in aqueous solution they tend to form agglomerates in a face to edge manner which increases the mechanical strength of the agglomerate and thus the yield stress of the mixture (Tadros, 1988). Certain chemical additions (i.e. flocculants or coagulants) can cause ion exchange to occur between the solution and the particles, which further increases the strength of these "card-house" structures (Litzenberger, 2003). This can increase the yield stress and plastic viscosity of the mixture. However, dispersant additions can eliminate the electrostatic forces between the clay particles, which has been shown to reduce both the plastic viscosity and yield stress of the mixture (Litzenberger and Sumner, 2004).

The shear stress versus shear rate relationship for a Bingham fluid is given in Equation 2.3b. The equation can also be expressed in multiple dimensions (Bird et al., 1960):

$$\tau_{ij} = -\left[\mu_P + \frac{\tau_y}{\left|\sqrt{\frac{1}{2}(\Delta:\Delta)}\right|}\right]\Delta_{ij} \quad ; \qquad \tfrac{1}{2}(\tau:\tau) > \tau_y^2 \tag{2.49a}$$

$$\Delta_{ij} = 0 \qquad ; \qquad \tfrac{1}{2}(\tau:\tau) \le \tau_y^2 \tag{2.49b}$$

$$\Delta_{ij} = \frac{\partial u_i}{\partial x_j} + \frac{\partial u_j}{\partial x_i} \tag{2.50}$$

$$\dot{\gamma} = \sqrt{\tfrac{1}{2}(\Delta:\Delta)} \tag{2.51}$$

where

$\Delta_{ij} =$ rate of deformation tensor

$\Delta:\Delta =$ second invariant of the rate of deformation tensor

This equation can be rearranged to express an apparent viscosity in terms of the rheological parameters and the shear rate:

$$\eta = \mu_P + \frac{\tau_y}{\left|\sqrt{\frac{1}{2}(\Delta:\Delta)}\right|} \tag{2.52}$$

or, for a one dimensional problem:

$$\eta = \frac{\tau_y}{\dot{\gamma}} + \mu_P \tag{2.53}$$

Both the yield stress and the plastic viscosity have been shown to be functions of the volumetric concentration of fine particles (Litzenberger, 2003). Sumner et al. (2000) have shown that for kaolin clay slurries this dependency is exponential. They also showed that the rheological parameters are strong functions of pH and chemical additive concentration. Thomas (1963) showed that for a given mineral, yield stresses are known to be strong functions of particle diameter and solids concentration. He showed that the addition of clay or sand will cause a nearly cubic increase in yield stress with concentration.

2.11. Characterization

Bingham fluids can be characterized through a variety of experimental techniques. Currently the most common methods being used are: pipeline viscometry, Couette viscometry, vane viscometry and the slump test.

2.11.1. Pipeline Viscometry

Pipeline viscometry is often used to characterize fluids exhibiting a yield stress. In this method a measured volumetric flowrate of slurry is transported through a straight length of pipe of known diameter. If adequate development length has been allowed, the pressure loss measured over a known length of pipe will provide the pressure gradient for fully developed flow. If the flow is homogeneous, the wall shear stress will be uniform about the wetted perimeter of the pipe. The measured pressure gradient can be related to a wall shear stress using the equation for horizontal pipe flow, obtained from simplifying Equation 2.13 ($\sin\theta = 0$):

$$-\frac{dP}{dz} = \frac{4\tau_w}{D} \tag{2.54}$$

A schematic of the force balance on a unit volume of fluid in fully developed pipe flow is shown in Figure 2.5.

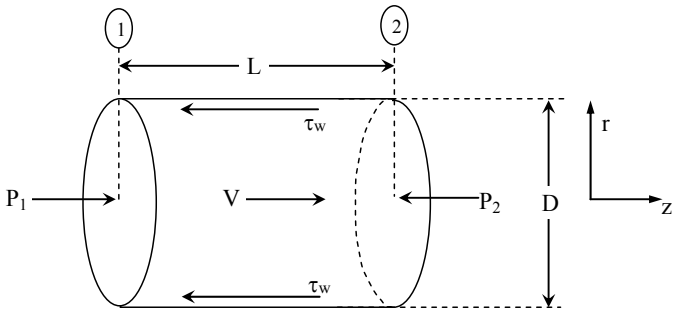

Figure 2.5: Schematic illustration of the force balance for steady, horizontal, fully developed pipe flow

A law in fluid mechanics, which holds for the steady, fully developed, horizontal pipe flow of any fluid or homogeneous slurry, is the shear stress decay law:

$$\frac{\tau_{rz}}{\tau_w} = \frac{r}{R} \tag{2.55}$$

Equation 2.55 predicts a linear stress profile over the pipe diameter. It can also be seen that at $r = 0$, or the center of the pipe, the shear stress is zero. For a Bingham fluid, if the shear stress is less than the yield stress in a given region, the fluid will not be sheared. Therefore, for flow of a Bingham fluid to occur the wall shear stress must be greater than the yield stress. However, due to the decay of the shear stress towards the center of the pipe, for a finite yield stress there will be a position in the pipe where the shear stress equals the yield stress. This results in a plug flow or flat velocity profile in the core region of the pipe cross-section.

Using the shear stress decay law condition, the Navier Stokes equations can be integrated to yield the Buckingham equation (Wilkinson, 1960) for steady, laminar pipe flow of a fully developed Bingham fluid. The Buckingham equation is provided in Equation 2.56:

$$\frac{8V}{D} = \frac{\tau_w}{\mu_p}\left(1 - \frac{4}{3}\xi + \frac{1}{3}\xi^4\right) \tag{2.56}$$

where

$$\xi = \frac{\tau_y}{\tau_w} \tag{2.57}$$

To model the turbulent behaviour of non-Newtonian fluids in fully developed, steady pipe flow Wilson and Thomas (1985) and Thomas and Wilson (1987) developed an analytical model to determine the frictional effects. To account for the non-Newtonian behaviour, a term was added to account for thickening of the viscous sublayer. As well, the shape factor of the rheogram (α) has also been included to account for the non-Newtonian behaviour of the fluid. The Wilson and Thomas model equations are given below:

$$V = V_N + u_*\left[11.6(\alpha - 1) - 2.5\ln\alpha - \Omega\right] \tag{2.58}$$

where

α = ratio of area under the non-Newtonian rheogram to the Newtonian rheogram

V_N = equivalent velocity of a Newtonian fluid at the same wall shear stress

u_* = shear or friction velocity = $\left(\frac{\tau_w}{\rho}\right)^{1/2}$

η = equivalent Newtonian viscosity at the same wall shear stress = $\frac{\tau_w}{\dot{\gamma}_w}$

ε = equivalent pipe roughness

For a Bingham fluid, the parameters shown in Equation 2.58 can be simplified to:

$$\alpha = \int_0^{\dot{\gamma}_w} \frac{2\tau}{\tau_w \dot{\gamma}_w} d\dot{\gamma} = 1 + \xi \tag{2.59a}$$

$$\Omega = -2.5\ln(1-\xi) - 2.5\xi\left(1 + \frac{\xi}{2}\right) \tag{2.59b}$$

$$V_N = \left(\frac{2\tau_w}{f_N \rho}\right)^{1/2} \tag{2.59c}$$

$$\mathrm{Re} = \frac{\rho D V_N}{\eta} \tag{2.59d}$$

$$\eta = \frac{\mu_p}{1-\xi} \tag{2.59e}$$

Equation 2.22 proposed by Churchill (1977) can be used to determine the equivalent turbulent Newtonian Fanning friction factors.

Pullum (2002) noted that scaleup of fine particle suspensions can lead to significant errors in predicted pressure gradient. Fine particle suspensions are not always colloidal (i.e. fine sediment) so settling can occur. One would expect that the particles would be resuspended with the onset of turbulent flow. However, in laminar flow, where the mixture is characterized, resuspension mechanisms may not be large enough to suspend particles resulting in fine particle settling. Scaleup of heterogeneous laminar data can lead to significant errors in predicted turbulent frictional losses.

The transition point from laminar to turbulent flow for Bingham fluids is a topic that has been well researched. However, to date, a definitive correlation does not exist that could be used to accurately predict the transition point. The model of Wilson and Thomas (1987) has been used to predict the crossover between turbulent flow results and the laminar Buckingham equation (Litzenberger, 2003). However, the model has been shown to overpredict turbulent data in specific cases (Xu et al., 1993).

Slatter and Wasp (2004) have attempted to rigorously determine the transition point by use of an all inclusive Reynolds number. Despite attempts with the use of the Herschel-Bulkley model it was not able to predict the transition in every situation. El-Nahhas et al. (2004) successfully used measured pressure fluctuations as an online method to predict transition through an observed spike in the CPV (Coefficient of Pressure Variation). However, no corresponding correlation has been developed to support the experimental results.

Identification of turbulent data points is critical if tube viscometry data is to be accurately interpreted. The Buckingham equation can only be applied to laminar data and including turbulent data in the regression will result in inaccurate model parameters.

2.11.2. Couette Viscometry

Couette viscometry represents another common method used to rheologically characterize homogeneous slurries. The most common setup used to produce a Couette flow is a concentric cylinder viscometer with a stationary cup and a rotating spindle. In this geometry, a cylindrical

cup is filled with the fluid of interest and is immersed in a constant temperature bath to maintain isothermal conditions in the system. The spindle rotates in the cup at a known angular velocity. The viscous resistance of the fluid produces a torque on the rotating spindle which is measured by the instrument. The resulting equation for a Bingham fluid is given in Shook and Roco (1991):

$$\omega = \frac{T}{4\pi\mu_P L}\left[\frac{1}{R_1^2} - \frac{1}{R_2^2}\right] - \frac{\tau_y}{\mu_P}\ln\left(\frac{R_2}{R_1}\right) \tag{2.60}$$

The yield stress and plastic viscosity can be determined directly when the angular velocity (ω) is plotted against the measured torque (T). A schematic of a typical concentric cylinder viscometer setup is shown in Figure 2.6.

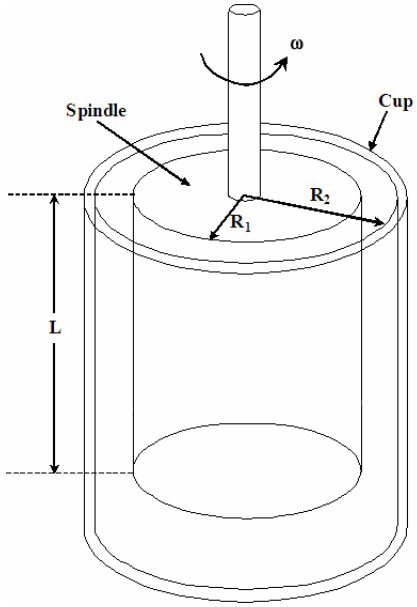

Figure 2.6: Schematic illustration of a concentric cylinder viscometer

Care must be taken to ensure that data is not gathered under conditions of laminar or turbulent Taylor vortices (Schlichting, 1978; Shook and Roco, 1991). As well, for a given measurement, the shear stress (τ) must be greater than the yield stress (τ_y). The lowest value of the shear stress occurs at the surface of the cup. Equation 2.61 provides this condition:

$$\frac{T}{2\pi R_2^2 L} > \tau_y \tag{2.61}$$

Litzenberger (2003), Litzenberger and Sumner (2004), Sumner et al. (2000) and Nguyen and Boger (1987) have all successfully used Couette viscometry to accurately classify non-Newtonian fluids with yield stresses. In general, if slurries are carefully prepared the results are often quite similar to those observed in pipelines. However, Xu et al. (1993) observed a significant difference in plastic viscosities between Couette measurements and the pipeline results for the same slurry. Care must be taken if the viscometer results are to be scaled to larger pipelines.

2.11.3. Vane Viscometry

Typically the most important rheological parameter for slurries from a design perspective is the yield stress. An experimental method that is commonly used to classify the yield stress of the slurry is vane viscometry. The most thorough work with respect to vane viscometry has been performed by Nguyen and Boger (1983, 1985). This device works on the principle that the slurry remains a pseudosolid until the cohesive or flocculated bonds contributing to the yield stress are broken. A bladed mixing shaft as shown in Figure 2.7 is inserted into the slurry and rotated until the slurry shears. The viscometer is operated at very low angular velocities (less than 1 rpm). During the test the internal system of the viscometer continues to turn loading up the torque exerted on the vane shaft. However, the actual vane and fluid remain stationary until a maximum torque corresponding to the yield stress of the fluid is exerted resulting in the cohesive bonds of the slurry being broken and the fluid yielding. It is only then that the vane turns and the fluid has sheared.

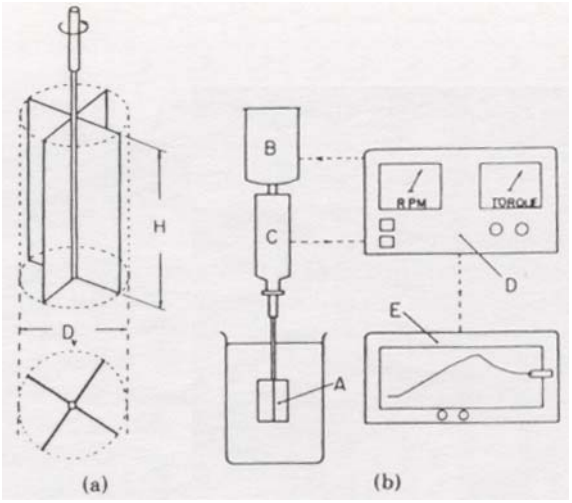

Figure 2.7: Schematic diagram of (a) the vane, (b) the vane apparatus: (A) vane, (B) motor, (C) torsion head, (D) instrument console, (E) recorder (Nguyen and Boger, 1983)

The applied torque versus time curve generated for the process will provide a maximum value related to the torque exerted on the vane when the fluid begins to shear. The slurry will shear along the surface area of a cylinder with the height and diameter of the vane blades. Assuming a constant stress is applied along the sheared cylindrical surface, the yield stress can be determined from the measured maximum torque using the following equation:

$$T_{\max} = \frac{\pi D^3}{2}\left(\frac{H}{D} + \frac{1}{3}\right)\tau_y \tag{2.62}$$

where

H = height of the vane

D = diameter of the vane

Although the assumption that the shear stress is constant along the cylindrical surface is not exactly true, the error associated with the calculated yield stress using Equation 2.62 is not excessive (Nguyen and Boger, 1983).

The yield stress value determined from the vane instrument is often not in perfect agreement with the rheological yield stresses obtained from viscometer and pipeline systems. It is the author's belief that the yield stress obtained from the vane is the true yield stress of the slurry at extremely low shear rates. The yield stress obtained from the Bingham fluid model fit to Couette and pipeline data is determined from extrapolation from higher shear rates. Although it is not a true characteristic property of the slurry, it does provide an accurate prediction of the slurry flow behaviour at higher shear rates. Since most industrial processes, including pipelines and mixers, operate under conditions of higher shear rates, the Couette and pipeline results are often the most accurate to apply under normal operating conditions.

2.11.4. Slump Test

Another method also exists for determining the yield stress of highly flocculated concentrated slurries. The slump test as provided by Pashias et al. (1996) describes a method to determine the yield stress based on the degree of slump, or change in height, experienced by a cylinder of slurry collapsing due to the stresses generated by its own weight. Although commonly used in the testing of concrete (Schowalter and Christensen, 1998), correlations exist that can be used to

predict the rheological properties of industrial tailings slurries (Pashias et al, 1996; Ferraris and de Larrard, 1998). These correlations do not provide the same accuracy in the rheological parameters that can be obtained with the methods discussed above. However, the slump test provides a quick and easy way of measuring the yield stress without the need for sophisticated electronic equipment (Pashias et al, 1996).

2.12. Pitot Tubes

Pitot tube usage as a means to measure local fluid velocity (via pressure) is common in both industry and academia. Their low cost relative to other velocity measurement techniques and their simplicity in both operation and installation make Pitot tubes popular within the scientific community.

Of particular importance to this study is the low Reynolds flow of concentrated clay-sand-water slurries. Besides exhibiting highly non-Newtonian behaviour, these slurries are viscous and extremely abrasive. Their erosive nature can be damaging to sophisticated and expensive, but fragile, velocity measurement equipment (i.e. hot film and hot wire anemometers). Therefore only a limited number of experimental methods are available to measure the local velocity of a flowing slurry. The Pitot tube represents one of these methods since its robust construction makes it resistant to damage.

A Pitot tube is a differential pressure flowmeter that allows for the measurement of a single localised velocity component, when it is aligned streamwise to the flowing fluid. It operates on the conversion of fluid kinetic energy into pressure energy upon stagnation of fluid at the Pitot tube tip. The fluid pressure can be easily related to the local velocity by Bernoulli's equation (2.63):

$$C_p = \frac{P - P_\infty}{\frac{1}{2}\rho v_\infty^2} = 1 \tag{2.63}$$

where

$C_p =$ pressure coefficient

$P =$ stagnation pressure

P_∞ = static pressure

v_∞ = local fluid velocity

ρ = density of the fluid

Although Pitot tubes can be used to measure the local velocity of flowing fluids, literature has indicated limitations at extreme (high and low) Reynolds numbers. Pitot tubes are an intrusive velocity measurement instrument (Albertson et al., 1960), such that errors can result from calculating the velocity based on Bernoulli's equation (2.63). This is true at low Reynolds numbers where viscous effects, not considered in Bernoulli's equation, are important.

2.13. Low Reynolds Number Pitot Tube Effect

A study was undertaken to determine the low Reynolds number effect on Pitot tube measurements to allow for more accurate velocity measurements in this study. Velocity measurements were made with a Pitot tube on viscous slurries in the experimental flume (see Sections 3.2, 3.3 and 5.8.1). Due to the high apparent viscosity of these mixtures many of the velocity measurements were obtained in the low Reynolds number regime. The use of Bernoulli's equation (2.63) to calculate the local mixture velocity is not appropriate under these conditions. At this time no correlation exists to account for the effect of yield stress on low Reynolds number Pitot tube measurements of non-Newtonian slurries.

Experimental tests using ethylene glycol over a range of temperatures were conducted at the Saskatchewan Research Council's Pipe Flow Technology Centre with two sizes of Pitot tubes in a 25 mm internal diameter vertical pipe loop. The use of ethylene glycol reproduced measurements at Reynolds numbers that would be comparable to those obtained with the viscous slurries tested in this study. The use of ethylene glycol, with its higher Newtonian viscosity allowed for greater experimental control.

Barker (1922) conducted pioneering research with Pitot tubes at low Reynolds numbers. She performed experimental testing with water using a bench top apparatus and a single Pitot tube. Her findings showed that a Stokes' law analogy (Schlichting, 1978) could be used to describe the phenomenon occurring at the tip of the Pitot tube at low Reynolds numbers. However, results of

more recent studies, including this investigation, have shown that this analogy is not appropriate over the entire low Reynolds number regime.

A thorough review of the Pitot tube was performed by Folsom (1956). Only a small section of the paper was devoted to the low Reynolds number effect. Much of the focus of this section was given to the theoretical work of Homann (1931) and Chambre (1948). They developed theoretical corrections for Pitot tube measurements at low Reynolds numbers. However, their results along with those presented by Folsom (1956) and Perry (1997), were correlated using the outside diameter of the Pitot tube. As well, their focus was for Pitot tubes of varying tip shapes but limited literature was available for the hemispherical tipped Pitot tubes used in this study.

Two important references are those of MacMillan (1954a) and MacMillan (1954b). In his research he has shown that the internal diameter of the Pitot tube appears be the more appropriate scaling parameter as it reduced the variation in Pitot tube results of previous researchers. Mikhailova and Repik (1976) and Mikhailova and Repik (1979) performed research on Pitot tubes with varying inside to outside diameter ratios. They showed that both the choice of length scale and the ratio of the inside to outside diameters of the Pitot tube are important for Pitot tube calculations. For thin walled Pitot tubes they found no difference in results when either the inside or the outside diameter was used as a length scale. However, as the ratio between the two diameters becomes significant (thick walled Pitot tubes, Pitot-static tubes, hemispherical tubes), the inside diameter becomes the important scaling parameter. Equation 2.64 provides the relationship for determining the Reynolds number based on the inside diameter of the Pitot tube:

$$\mathrm{Re}_d = \frac{\rho d v}{\mu} \tag{2.64}$$

where

$d =$ opening diameter of the Pitot tube

Hurd et al. (1953) performed experiments with blunt nose impact tubes in a tow tank with viscous incompressible liquids. No correlation resulted from the study but he showed that for high d/D ratios the value of C_p can drop below 1 at intermediate Re numbers. As well, Hurd et al. (1953) also showed that at very low Reynolds numbers the data asymptotically converges to a Stokes'

law like curve. They also point out that the correlations developed by Homann (1931) and Chambre (1948) do not converge with Stokes' law at very low Reynolds numbers.

From the dates of the references identified, most of the research in the area of low Reynolds number Pitot tube effects occurred in the 1950's. The most recent research performed by Chebbi and Tavoularis (1991) used laser Doppler anemometry to experimentally verify Pitot tube measurements at very low Reynolds numbers (Re << 1). However, due to the complexity of the experimental technique, only a limited number of measurements were performed. Although this is significant and recent work, much of it is not applicable to the flow of most fluids under standard operating conditions. However, the results obtained by Chebbi and Tavoularis (1991) at very low Reynolds numbers are in good agreement with those predicted by the correlation developed in this study.

The low Reynolds number Pitot tube results of this study are presented in Section 5.8.1 of the thesis.

2.14. Numerical Models

There are two approaches to numerically model fluid flow: macroscopically or microscopically. Microscopic modeling is common in fluid mechanics and it is the basis of CFD (Computational Fluid Mechanics). The mechanistic two-layer model originally developed by Wilson (1976) and expanded upon by the Saskatchewan Research Council, (Shook and Roco, 1991; Shook et al., 2002), is a great example of a macroscopic model that was developed by the application of both theory and experimental data.

2.14.1. Two-Layer Model

In the two-layer model the pipe cross-section is partitioned into two macroscopic control volumes, each of uniform concentration and velocity. Due to the heterogeneous nature of settling slurries the top layer is less concentrated and moving at a faster velocity than the more concentrated, slower moving bottom layer. The model considers the frictional losses associated with both a fluid-like component and a Coulombic friction component. The conservation laws of mass and momentum (force balance) are applied to each control volume and the resulting set of equations are solved iteratively until the correct pressure gradient and deposition velocity are

found. The top layer is commonly referred to as suspended load since the particles in this layer are suspended in the carrier fluid and contribute to viscous frictional losses. The more concentrated bottom layer is referred to as bed load because of its contribution to contact load and Coulombic friction with the pipe wall.

The two-layer model accurately predicts frictional loss behaviour and deposition velocities of heterogeneous slurry flows. However, currently the model is only applicable for Newtonian carrier fluids in turbulent flow. The limited empirical equations within the model are based on specific experimental data over a range of parameters. Use of the model outside of this range may lead to significant prediction errors.

Ghosh (1989) and Ghosh and Shook (1989) used a two-layer model approach to examine the results of coarse particles in power-law fluids. Although the two-layer model approach was found to be useful for low velocity conditions it was found to predict negative velocities in the lower layer suggesting an incorrect interfacial friction factor.

Hill (1996) and Hill and Shook (1998) applied the two-layer model to determine the behaviour of coarse solids transport in Bingham carrier fluids in laminar and turbulent flow. They found that the two-layer model approach worked reasonably well in laminar flow. Pressure gradients were underpredicted indicating additional frictional losses beyond simple fluid and Coulombic friction. The model produced satisfactory results in turbulent flow for slurries with Bingham carrier fluids. The non-Newtonian nature of the slurry was considered when determining the fluid friction and Coulombic friction, and contact load was found using existing correlations. However, the contact load and lower layer concentrations components of the model in laminar flow are still incomplete.

Pullum et al. (2004) proposed a simplified two-layer model for non-Newtonian carrier fluids in pipe flow. The model accounts for interfacial and Coulombic friction and correctly predicts the transport of solids as bed load. However, the model has not been verified against a full range of experimental data. As well, the model has been developed with the use of the Herschel-Bulkley constitutive equation, and assumes that all solids are confined to the bed and is only applicable to pipe flow. Laminar transport of sand in a non-Newtonian carrier fluid has also been investigated by Sun et al. (2001).

2.14.2. Microscopic Modeling Background

Microscopic modeling requires the solution of the governing differential equations describing the fluid flow problem. Typically three methods are available to solve numerical problems: the finite difference method, the finite element method and the finite volume method. Finite difference methods are the simplest means by which to solve numerical problems. Numerical derivatives are used to approximate derivatives in the differential equations at the mesh nodes. A finite set of algebraic equations results and the values at nodes are determined (Rao, 2002).

Finite element methods became popular in the late 1970's and early 1980's. The governing equations are integrated as a residual with interpolation functions. The residual is minimized to zero (Galerkin's method) allowing the conserved variable to be determined at specific nodes using the resulting algebraic equations (Stasa, 1985; Segerlind, 1984; Reddy, 1984).

In the finite volume method partial differential equations are integrated in space and time over the control volumes of a mesh to yield a set of algebraic equations (Patankar, 1980). The value of the variable in the cell is solved directly and the values at the cell faces are determined by an interpolation scheme. Finite difference formulas are used to approximate derivatives in the differential equations.

The governing differential equations can be implemented in either Lagrangian or Eulerian reference frames. In a Lagrangian reference frame, the control volume moves with the flow at and in the direction of the local velocity. This reference frame is often used when individual particles are being modeled in a two-phase flow since it eliminates the convective terms from the governing equations. In the Lagrangian reference frame the exact trajectories and particle interactions are determined based on physical laws. However, for high concentration systems, the number of particles to be tracked is extremely large and therefore the overhead of the calculation and the time required to solve the problem is significant.

In the Eulerian frame, the control volume of fluid is fixed in three-dimensional space while parcels of fluid pass through it. The fluid is modeled as a continuous phase while solids are modeled as a secondary dispersed phase. The effects of the solid particles are accounted for by the use of a diffusional or dispersive stress. In this reference frame, the convective terms remain in the governing partial differential equations and must be modeled accordingly. A thorough

review of the Lagrangian and Eulerian techniques is given in Gouesbet and Berlemont (1999). Caffery (2002) also provides a good review of the key differences between the two different approaches in his Ph.D. thesis.

2.14.3. Dispersive Stress Modeling

Daniel (1965) attempted to model solids transport in a rectangular channel in his Ph.D. thesis. A dispersive stress model for turbulent flow was developed using the Bagnold (1954) model for dispersive stress. Particles are typically supported by turbulent or inertial forces, however when coarse particles can no longer be suspended by turbulence, these particles are supported by the action of a dispersive stress. In his thesis, Daniel suggests that most of the existing open channel work in the literature is concerned with the transportation of fine sediment for dilute concentrations. He makes an analogy between the eddy diffusivity and the momentum diffusivity for the modeling of the solids transport coefficients. In the model, the dispersive stress model accounts for the particles transported by "bed load" whereas the turbulent stress model accounts for the particles in the "suspended load". Coleman (1969) and Hunt (1954) also performed work with mass transfer coefficients applying an analogy between the eddy diffusivity and the momentum diffusivity. However, the model was only appropriate for turbulent flow and dilute slurry systems.

Shook (1980) used a finite element method, a mixture viscosity approach, and a segmented two-layer model approach to predict pressure gradients in laminar pipe flows. The predicted pressure gradients were compared to experimental sand in ethylene glycol slurry data. The results showed that the contact load model applies for both laminar and turbulent flow. However, Maciejewski et al. (1993) transported large rocks in clay suspensions with yield stresses. The presence of a yield stress was significant enough for the flow to become laminar making the contact load and interfacial friction quite different from what one would expect with turbulent flow.

A homogeneous fluid model approach is only accurate when fine particles are uniformly distributed. However, if particle dispersion occurs with coarse particles, the homogeneous approach will not be accurate. Frankiewicz (1991) showed that in laminar flow solids have a tendency to congregate near the bottom half of the flow, which is different from the uniform particle flow associated with turbulent flow. This distribution of particles can lead to inaccurate

scale up to larger pipes as the Coulombic friction, resulting from particle settling, is independent of pipe diameter.

It is uncertain whether a dispersive type modeling approach or a shear-induced self-diffusion of particles model as proposed by Phillips et al. (1992) and Leighton and Acrivos (1987b) can be applied to laminar flow. Under laminar flow conditions, turbulent forces disappear so that they are not available to suspend particles. If particle dispersion and resuspension is to occur, it must be caused by another mechanism. Wilson and Sellgren (2002) and Whitlock et al. (2004) spoke about near wall particle lift and the difference between a laminar Saffman type lift force (Saffman, 1968) and an inertial lift force experienced in the near-wall region of turbulent flows. Similarities in the scaling of the force can be seen with the Saffman lift force and the flux relationships of Leighton and Acrivos (1987b).

Hill (1996) performed pioneering work for solids (sand) transport in non-Newtonian (Bingham) pipeline flows where he has provided detailed numerical and experimental analysis. Hill (1996) and Hill et al. (1997) proposed a model using the concept of Bagnold's (1954) dispersive stress. Bagnold attempted to relate the repulsive stress between particles to the total axial shear stress. Hill used a finite element method of analysis to numerically simulate the settling of particles in pipe flows of slurries with yield stresses. The model is based on a balance between the dispersive force arising from interparticle interactions and the immersed weight of the suspended particles.

The model of Hill (1996) is based on contact forces between particles as well as between particles and the pipe wall. He assumed that the lift forces proposed by Leighton and Acrivos (1987b) were negligible. For his specific flow, the support force could be related to an interparticle normal stress which increases with bed depth (Roco and Shook, 1983). At elevated concentrations the particle-particle interactions contribute more than just to an increased resistance to flow. They also lead to particle dispersion and migration of particles within the flow leading to non-uniform distributions. This effect has been modeled with a dispersive stress relationship. The interparticle normal stress has been assumed to be negligible in the lateral, x-wise direction (Jobson and Sayre, 1970). Hill further relates the interparticle stress to a dispersive viscosity effect, where the dispersive viscosity includes only the higher order interparticle interaction terms in the relative viscosity equation. From Equation 2.40d the dispersive viscosity (μ_d) can be expressed as:

$$\mu_d = 0.16\lambda^2 \tag{2.65}$$

Equation 2.66 shows the concentration distribution equation. In the equation, α is the angle of internal friction of the coarse particles as described by Bagnold (1954). In the study, Hill (1996) has assumed ($\tan\alpha = 1$).

$$\frac{d\phi}{dy} = -\frac{\phi(\rho_s - \rho_f)g_y \tan\alpha}{\eta_f \dot{\gamma}_{yz} \frac{d\mu_d}{d\phi}} \tag{2.66}$$

The model in Equation 2.66 is dependent on experimental data for initial conditions, boundary conditions and convergence. For the kaolin and bentonite slurry simulations, Hill (1996) showed that the velocity profile is not a strong function of the local solids concentration. The shape of velocity distribution is insensitive to variations in local concentration. Hill also stated that it was too complicated to solve velocity and concentration distributions independently and simultaneously. Hill et al. (1997) stated in their conclusions that "an additional mechanism comes into play near the pipe wall, where the continuum model for the slurry ceases to be a reasonable approximation". This seems to suggest that the model should be extended to address the near wall regions of the flow.

Gillies et al. (1999) also used a dispersive stress approach to model the transport of solids (sand) in laminar pipe flows of viscous Newtonian fluids (oil and glycol). The model, which will be subsequently referred to as the 'Gillies model', involves a force balance between the repulsive dispersive stress and the immersed weight of the settling particles to generate an ordinary differential equation to describe the distribution of coarse solids. The concentration distribution model is solved simultaneously with the Navier-Stokes equation for the mixture. Both density and viscosity were varied based on the local solids concentration to determine the velocity and concentration distributions for pipe flow of coarse solids in viscous Newtonian fluids.

Gillies et al. (1999) showed numerically and experimentally that the variation in solids concentration is predicted in terms of a particle-particle interaction mechanism which opposes the effect of gravity. Experimental results show that an axial pressure gradient of at least 2 kPa/m is required to transport significant quantities of sand in laminar pipe flow. However, the pressure gradient required to initiate sand transport was significantly lower for the high density carrier

fluid tests. This may suggest that the driving force for solids transport is more closely related to the immersed density difference between the solid and fluid phase rather than individual densities.

The Gillies model equation presented in Equation 2.67 is identical to the model equation used by Hill (1996) (Equation 2.66).

$$\frac{\partial \phi}{\partial y} = -\frac{\phi(\rho_s - \rho_f) g_y}{\mu_f \left(\frac{\partial v}{\partial y}\right)\left(\frac{\partial \mu_d}{\partial \phi}\right)} \tag{2.67}$$

This equation applies everywhere in the flow except at the fluid boundaries. At the lower pipe wall, lubrication and repulsion forces oppose the effect of gravity. Local variation of concentration in the lateral direction has also been neglected (Graham et al., 2002). A no-slip boundary condition has also been used in the solution of the model. Addie et al. (2004) and Heywood and Alderman (2004) have shown that, under some flow circumstances, the effect of slip can be significant. However, this is typically important only under high shear conditions. Slip is generally insignificant in the laminar, creeping flows modeled in this study.

Gillies et al. (1999) made comparisons of simulations with this model with experimental sand in glycol and sand in oil slurry data were performed. With sand in glycol slurries, the shape and magnitudes of the velocity and concentration distributions were similar. The model underpredicted the required pressure gradient by approximately 25%. However, for the more viscous and laminar sand in oil slurries not only was the model able to predict the behaviour of the distributions but it also yielded more accurate pressure gradient predictions (actually overpredicting the experimentally measured values).

In the models described above, coarse particles and fluid are treated as a mixture. The models are not capable of predicting slip between the phases or the possibility of a sliding bed. This is a limitation since the mixture is being modeled as a Newtonian fluid. The dilation phenomenon, where a shear flow cannot occur if the material is closely packed, is not obeyed with the relative mixture viscosity approach. Shear of the solids phase in a slurry cannot occur unless the particles can slide past each other. The model is appropriate for predictions above the dilation concentration but breaks down once a settled bed of particles forms. For perfect spheres the

theoretical concentration for dilation to occur is $\pi/6$ (0.524). For conditions where a settled bed of particles exists a two-layer model approach as performed by Hill and Shook (1998) would be more appropriate since it can represent Coulombic frictional effects.

3. EXPERIMENTAL PROCEDURES AND CONDITIONS

3.1. Experimental Flume Setup

Figure 3.1 presents the 156.7 mm internal diameter circular flume which was used in the collection of experimental data. The instruments that were used to collect data during the operation of the flume are listed below:

- Differential pressure transducers (Validyne, Engineering, Northridge, CA)
  - 1 – 20 psi for 53 mm pressure drop test section
  - 1 – 5 psi for Pitot-static tube
- Densitometer (Ronan Engineering Ltd., Toronto, ON)
- Temperature sensor (RTD – Resistance Temperature Device) (Aircom, Edmonton, AB)
- 2 inch Foxboro (The Foxboro Co. Ltd., La Salle, QC) and 2 inch Brooks (Brooks Instrument Div, Emerson Electric Co., Statesboro, GA) magnetic-flux flowmeters
- Vernier height measurements (planes 1 and 2), (Mitutoyo Corporation, Tokyo, Japan)
- Traversing Pitot-static tube (United Sensor Corp., Amherst, NH) with a constant HPLC (High Pressure Liquid Chromatography) pump purge (Waters Corp., Model 510, Milford, MA)
- Traversing Ronan gamma ray densitometer (Ronan Engineering Ltd., Toronto, ON)

The flume circuit consists of a flat-bottom mixing tank, a centrifugal pump (Linatex Anti Abrasion 3x2, Lawjack Equipment Ltd, Montreal, QC), and a 53.1 mm internal diameter length of carbon steel pipe which is connected by a flexible rubber hose to the 156.7 mm internal diameter section of pipe which represents the open-channel (flume). Slurry is discharged from the flume section into the mixing tank via a helical chute such that the circuit is operated in a closed recirculating mode. A sketch of the chute and tank is shown in Figure 3.2.

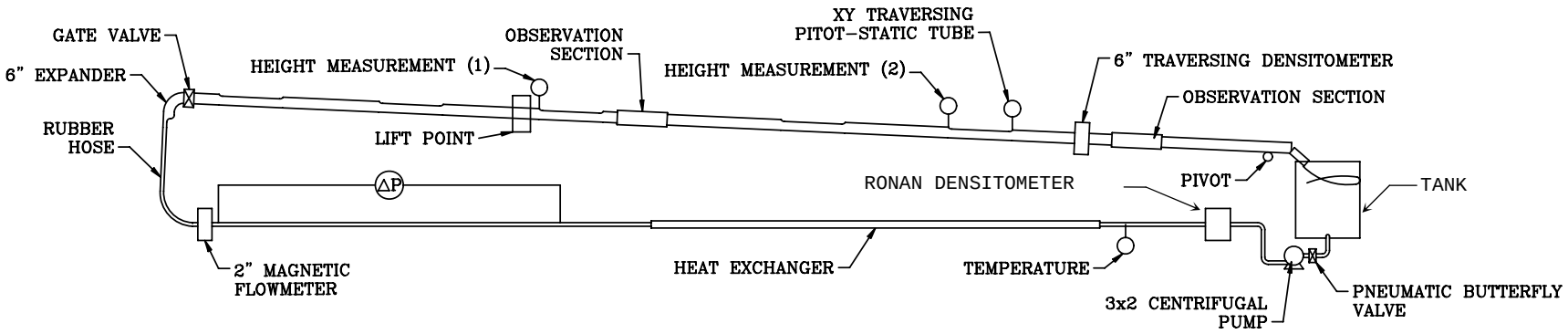

Figure 3.1: Saskatchewan Research Council's 156.7 mm flume circuit used in the experimental program

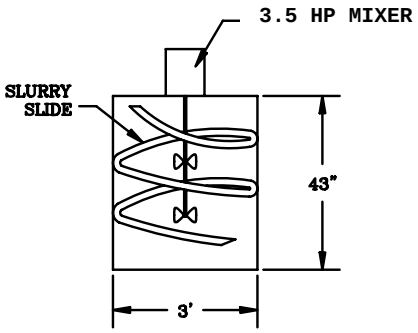

Figure 3.2: Schematic illustration of the helical chute and stand tank arrangement on the 156.7 mm flume circuit

The mixing tank, shown in Figure 3.2, is 0.91 m in diameter and 1.09 m in height and has a total volume of 650 L. It is equipped with mixing baffles and a high-speed (3.5 hp) mixer (Model No: XJC-174, Lightnin Mixers & Aerators, Toronto, ON), which is driven by a 7.5 hp motor (Baldor, Fort Smith, AR) and a variable frequency drive. The mixer shaft is equipped with two impellers. A four-blade radial flow impeller is positioned at the bottom of the shaft and a four blade axial flow impeller is positioned just below the mixture free surface level in the tank. This mixer arrangement is designed to produce homogeneous slurries for the flume flow tests.

The tank is also equipped with a helical chute, shown in Figure 3.2, which was used to transport slurry from the flume outlet into the tank. In earlier work (Sanders et al., 2002) entrained air was observed in slurries during recirculation back to the tank and subsequent discharge to the feed line. This affected both pump performance and the delivered flowrate to the circuit. To minimize these effects a chute was constructed to permit the air bubbles to escape. As well, for the sand-water tests, the outlet of the tank was equipped with a vertical suction pipe. It was constructed from a straight length of pipe 0.38 m in length and 78 mm in diameter. Its purpose was to allow the recirculation of supernatant water for the sand-water slurry tests during start-up and shut-down of the flume circuit. The supernatant water was circulated in the loop to erode particle deposits in the 53 mm feed line or test section of the flume without introducing any additional sand to the system.

The slurry is circulated in the test loop using a 3x2 Linatex centrifugal pump (Lawjack Equipment Ltd, Montreal, QC). The pump is driven by a 22.4 kW (30 hp) motor (Elektrim, Type: Sf, Warsaw, Poland) and a variable frequency drive. The slurry is fed to the pump through a feed line at the base of the flat bottom tank. A pneumatic butterfly valve (Keystone, Tyco Flow Control, Calgary, AB) was installed between the tank and the pump to ensure that no solids could

settle into the pump during shutdown. The water performance curve for the centrifugal pump employed in this study is shown below in Figure 3.3.

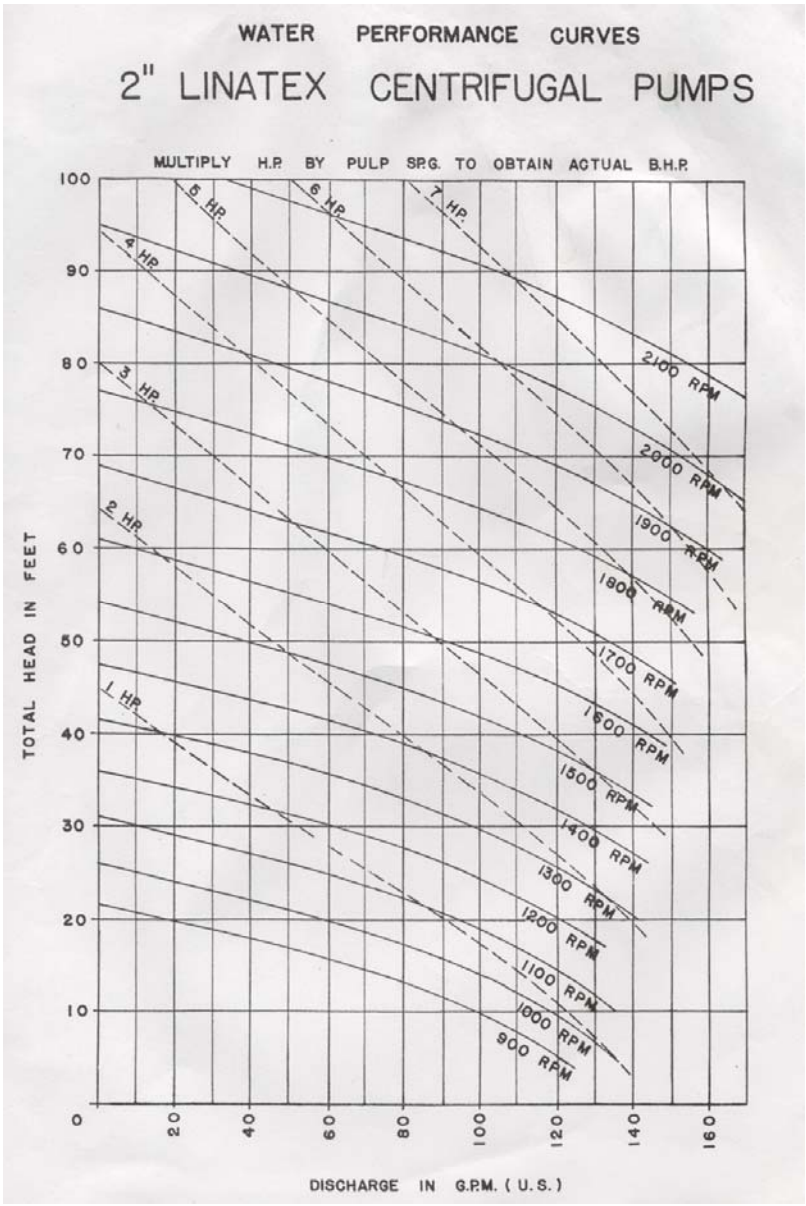

Figure 3.3: Water performance curve for the 3x2 Linatex pump on the 156.7 mm flume circuit (Lawjack Equipment Ltd, Montreal, QC)

The 53.1 mm diameter section of the test loop consists of a straight, horizontal run that is 14.4 m in length. It contains the following instrumentation: electromagnetic-flux flow meter (The Foxboro Co. Ltd., La Salle, QC and Brooks Instrument Div., Mag 3570 Series, Emerson Electric Co., Statesboro, GA), temperature probe (Aircom, Edmonton, AB), and a differential pressure transducer (Validyne Engineering, Northridge, CA) to measure the drop in pressure across a 4.9 m test section.

Bulk mixture velocities were determined with a 2 inch Foxboro magnetic-flux flowmeter (The Foxboro Co. Ltd., La Salle, QC) for the model tailings tests. A 2 inch Brooks magnetic flowmeter (Brooks Instrument Div., Mag 3570 Series, Emerson Electric Co., Statesboro, GA) was employed for the testing of the clay-water slurries in the flume. The meter works on the principles of Faraday's law. Sensor electrodes in the meter detect a small voltage generated by the flow of the conductive fluid through the magnetic field produced by the flowtube (Hill, 1996). The internal electronics of the meter convert the signal into a direct current voltage which is proportional to the mean velocity over the pipeline (Shercliff, 1962). The meter was calibrated by collecting a series of timed and weighed discharge samples for steady state flows with Saskatoon tap water. The result was a calibration curve of volumetric flowrate versus voltage for the meter in the 53 mm test section. Calibration curves for all instruments employed in the study are presented in Appendix C.

An RTD (Resistance Temperature Device), (Aircom, Edmonton, AB), was used to measure the temperature of the fluid in the 53 mm pipe test section. The instrument was calibrated from 10 to 60 ^{o}C using Saskatoon tap water and a liquid in glass mercury thermometer. The result was a linear calibration of temperature versus voltage.

The differential pressure measurement over the 4.9 m test section in the 53 mm pipe was obtained using 20 and 50 psi differential pressure transducers (Validyne Engineering, Northridge, CA). A 50 psi transducer was calibrated using a Double Area Gage Tester (Dead Weight Tester, The Ashton Valve Co., Boston, MA) for the model tailings tests. A 20 psi transducer was calibrated using a Merium fluid (S = 2.95) manometer for the testing of the clay-water slurries in the flume. The result was a linear calibration of differential pressure versus voltage as shown in the calibration curves presented in Appendix C.

A 6.4 m pipe-over-pipe heat exchanger was employed to maintain isothermal conditions in the flume circuit. This was accomplished by employing a temperature control system consisting of a temperature sensor (Aircom, Edmonton, AB), a proportional controller (Johnson Controls, Milwaukee, WI) and a control valve (Belimo, Mississauga, ON) on the heat exchange fluid supply line. The heat transfer fluid consisted of a mixture of water and ethylene glycol.

The return leg of the test loop is an elevated flume constructed from a section of 156.7 mm carbon steel pipe. The total length of the flume section is 18.5 m. The pipe is open to atmosphere through sections cut out of the top portion of the pipe. The cut-away areas are 0.1 m wide by 0.9 m long and spaced 2.3 m apart. Two clear acrylic observation sections (each 0.7 m long) have been built into the flume. The observation sections were positioned 7.6 and 15.6 m from the flume inlet respectively. The sections allowed for observation of the flow at the bottom of the flume so that the formation of a stationary deposit could be noted.

The flume is fitted with two depth gauges located 7.5 and 13.3 m from the flume inlet, which are used to measure the depth of the slurry flow at these locations. The depth gauges are described as "height measurement" points 1 and 2 in Figure 3.1. The distance between the two measurement points is 5.84 m.

The depth of slurry flow was determined by aligning the height measurement gauges with the free surface of the flow at position at points 1 and 2 in the flume. The resulting height was measured with digital calipers (Mitutoyo Corporation, Tokyo, Japan). The depth of flow was calculated by subtracting the measured values with the respective zero positions, which corresponded to the position of the depth gauges aligned with the bottom wall of the flume. The error in a given depth of flow measurement was a function of whether the flow was laminar or turbulent. It was difficult to measure the depth of flow for rippled or wavy surfaces. However, on average, the error in a given measurement was approximately 1 mm. For the conditions investigated in this study, the error in the depth of flow translated into approximately a 10% error in the calculated experimental wall shear stress and a 4 % error in the measured mixture bulk velocity.

The flume is mounted on a steel I-beam. The angle of inclination of the flume was varied using a manually operated 1.5 ton winch (Model No: L-80, Jet, Elgin, IL) attached to the I-beam supported near the top end of the flume (noted as the lift point in Figure 3.1). Angles from 0 to 7.5^{o} could be investigated with this apparatus. A distance of 10.64 m separates the lift point and pivot point of the flume.

3.2. Pitot tube

A hemispherical tipped Pitot-static tube (United Sensor Corporation, Amherst, NH) is located 14.1 m from the flume inlet. The tube had an inside opening diameter of 1.83 mm and an outside

tube diameter of 4.71 mm. The outside diameter of the Pitot tube was measured with digital vernier calipers (Mitutoyo Corporation, Tokyo, Japan). The opening diameter of the Pitot tube was determined by the method described in Section 3.3. The results of the opening diameter calibration are shown in Appendix C. Pictures of the Pitot tube employed in the 156.7 mm flume study can be seen in Appendix C, Figures C.1 and C.2.

The Pitot tube is inserted into the flowing mixture and provides a measure of the local (point) velocity at different positions in the cross-sectional area of the flow. A schematic of the Pitot-static tube assembly is shown in Figure 3.4.

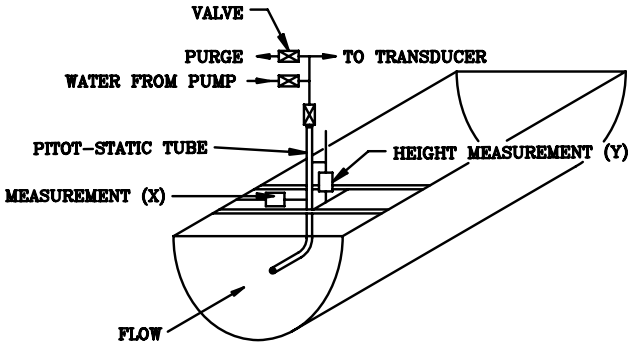

Figure 3.4: Schematic illustration of the traversing Pitot-static tube apparatus on the 156.7 mm flume

A continuous water purge at a flowrate of 9.0 mL/min was provided by a HPLC pump (Model No: 510, Waters Corporation, Milford, MA) to prevent solids from plugging the Pitot tube opening. The actual flowrate delivered by the HPLC pump was determined by the calibration curve generated over a range of flowrates presented in Appendix C. The additional pressure at the tip of the Pitot tube, caused by the flow of purge water, can be accurately determined and subtracted from the measured Pitot tube pressures to obtain the pressure caused by the local velocity only. The resulting pressure can used to calculate the local velocity by applying Bernoulli's equation (Equation 2.63). A low Reynolds number correction, which was developed in this study (Section 5.8.1), was used to correct for data points which exhibited a low Reynolds number Pitot tube effect due to the extremely viscous rheological behaviour of the slurries.

A Validyne differential pressure transducer (Validyne Engineering, Northridge, CA) was used to measure the differential pressure between the stagnation pressure seen at the Pitot tube tip and the static pressure of the flow. The pressure transducer was calibrated over a 5 psi span with a

Merium fluid (S = 1.75) manometer. The result was a linear calibration of differential pressure versus voltage as shown in Appendix C.

The Pitot tube position in the cross-section of the flume flow was recorded in both the x and y directions. A positioning apparatus was designed and constructed so that all positions in the circular half-cross-section of the pipe could be measured. Digital vernier calipers (Mitutoyo Corporation, Tokyo, Japan) were used to measure the position of the Pitot tube from the bottom of the pipe (y) and the centerline of the flow (x). The Pitot tube could be positioned to an accuracy of 0.05 mm. A table of the measurement positions employed is provided in Appendix D, Figure D.1 and Table D.28.

3.3. Low Reynolds Number Pitot Tube Study

A separate experimental investigation was performed to determine the low Reynolds numbers effect on Pitot tube measurements. Tests were conducted at the Saskatchewan Research Council's Pipe Flow Technology Centre with two sizes of hemispherical tipped Pitot-static tubes (United Sensor Corp., Amherst, NH). Experiments were performed in a 25 mm internal diameter vertical pipe loop employing ethylene glycol over a wide range of flow conditions. A significant quantity of low Reynolds number data was generated which produced a correlation that accurately predicts the low Reynolds number behaviour for hemispherical tipped Pitot tubes. A schematic of the SRC's 25 mm (1 inch) internal diameter vertical pipe loop is shown in Figure 3.5. The results of the low Reynolds number Pitot tube experiments are presented in Section 5.8.1. More details regarding the low Reynolds number study can be found in Spelay and Sumner (2007).

The key instruments employed in the low Reynolds number Pitot tube experiments were:

- Differential pressure transducers (Validyne, Engineering, Northridge, CA)
    - 2 - 5 psi for Pitot tube (Pitot-static and wall)
    - 1 - 20 psi for upward flow test section
- Temperature sensor (RTD – Resistance Temperature Device) (Aircom, Edmonton, AB)
- 1 inch Foxboro magnetic-flux flowmeter (The Foxboro Co. Ltd., La Salle, QC)
- Pitot-static tubes – 2 sizes (PSL and PSS) (United Sensor Corp., Amherst, NH)

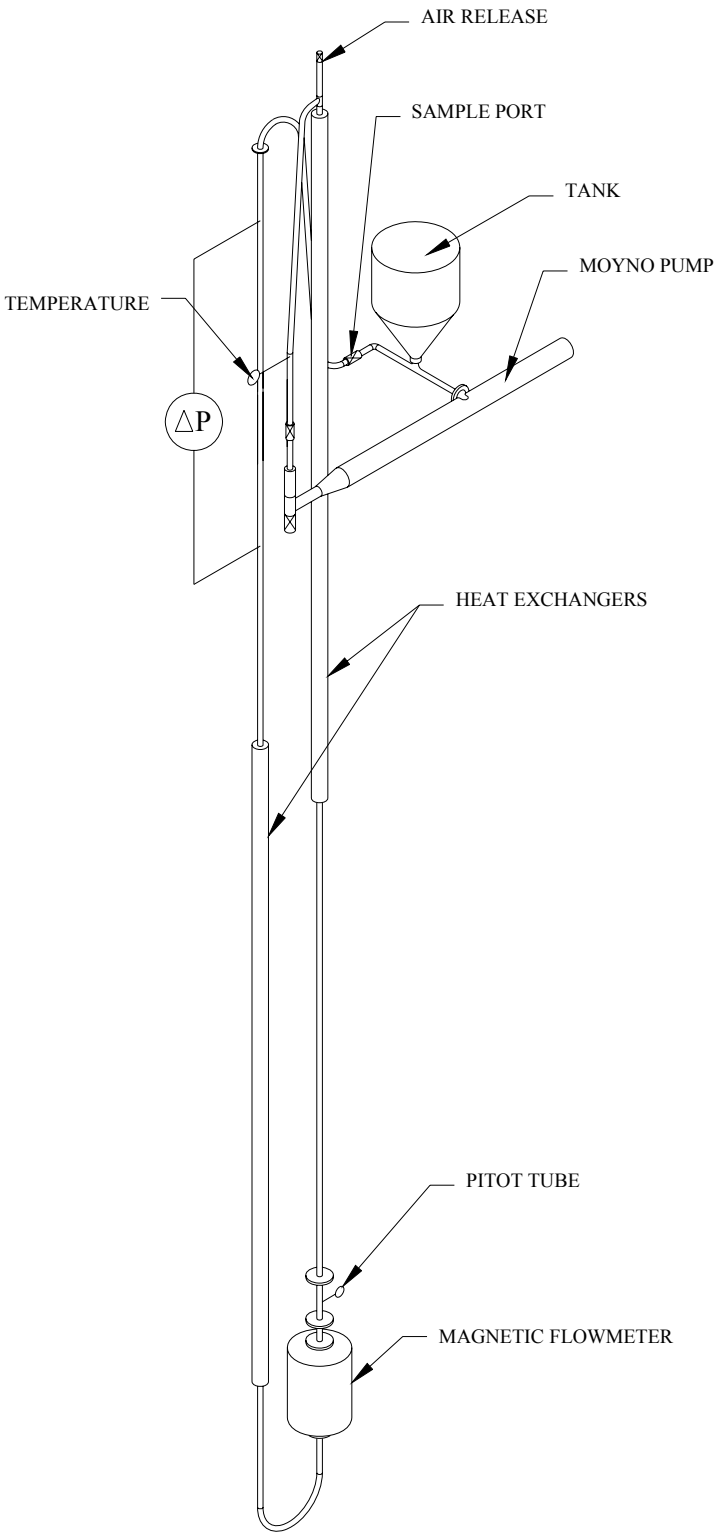

Figure 3.5: Saskatchewan Research Council's 25 mm vertical pipe loop

The controlled (independent) variables during the course of the experimental testing were:

- Experimental fluid composition (ethylene glycol)
- System Temperature (viscosity and density)
- Volumetric Flowrate
- Pitot tube diameter and shape

The measured (dependent) variables were:

- $\Delta P/L$ in the upward flow test section
- Pitot tube differential pressures
    - Stagnation versus pipe wall static pressure
    - Stagnation versus Pitot-static tube static pressure

The pipeloop circuit consisted of a conical-bottom stand tank, a progressive cavity pump, a vertical run of 27.67 mm internal diameter carbon steel pipe on the downflow side and a 25.80 mm internal diameter vertical run of stainless steel pipe on the upflow side. In total, the apparatus spanned a height of 8.68 m and could hold 17.53 L of fluid (not including the stand tank). A progressive cavity pump (Model No: 316L CDQ, Moyno Progressive Cavity Pumps, Springfield, OH) was use to generate flow within the pipe system. A 15 kW (20 hp) motor (Model No: 3A256C4002, Teco Elec. and Mach. Co. Ltd., Edmonton, AB) was used to drive the pump. The rotational speed of the motor (and thus the pump shaft) was controlled by a variable frequency drive (VFD) and recorded with a Pulser Disc magnetic disc counter (Electro-Sensors, Model No. 255, Minnetonka, MN).

The temperature of the fluid in the circuit was measured with a Resistance Temperature Device (Aircom, Edmonton, AB) located directly after the pump outlet. Isothermal conditions were maintained in the circuit with co-current (3.75 m) and counter-current heat exchangers (3.90 m) on the downflow and upflow test sections, respectively. The heat exchange fluid was an ethylene glycol-water mixture.

The Pitot tube assembly was located nearly 241 pipe diameters downstream from the temperature sensors. This entrance length represents sufficient straight length of pipe to allow for fully developed laminar flow at the Pitot tube (Incropera and DeWitt, 1981). The Pitot tube was

mounted directly into the pipe through a tap in the wall, positioned at the center of the pipe and locked into position with a brace and a set screw. The pressure difference between the stagnation and static pressure seen by the Pitot tube was measured with a differential pressure transducer with a 5 psi diaphragm (Validyne Engineering, Northridge, CA), which was calibrated with a Merium fluid (S = 2.95) manometer.

Tests were performed at low Reynolds numbers under steady, fully developed, laminar flow conditions. Under these conditions it is known that the velocity of a Newtonian fluid at the centerline of the pipe is equal to twice the bulk velocity (Equation 3.1):

$$v(r) = 2V\left(1 - \frac{r^2}{R^2}\right) \tag{3.1}$$

where

v = local velocity at radial position r
V = bulk velocity of fluid
R = inside radius of pipe

A 1 inch Foxboro magnetic-flux flowmeter (The Foxboro Co. Ltd., La Salle, QC) was located directly below the Pitot assembly and was used as the primary means to measure the volumetric flowrate within the loop. The average velocity of the ethylene glycol in the loop was calculated from Equation 2.10.

In the upflow section, following the counter-current heat exchanger, was a 1.68 m section of straight pipe followed by a 1.83 m pressure drop test section. This test section was used to determine the Newtonian viscosity (μ) of the ethylene glycol in laminar flow. Equation 3.2 presents Poisseuille's Law which was used to calculate the glycol viscosity at different system temperatures.

$$\mu = \frac{\left(-\frac{\Delta P}{L}\right)D^2}{32V} \tag{3.2}$$

The pressure drop (ΔP) was measured using a differential pressure transducer with a 20 psi diaphragm (Validyne Engineering, Northridge, CA), which was calibrated against a Merium fluid (S = 2.95) manometer. The test section was located approximately 216 pipe diameters from the 180^o elbow which ensured fully developed flow in the test section (Incropera and DeWitt, 1981). The density of the ethylene glycol was determined from pycnometry tests performed over a range of temperatures. A linear calibration curve for the density of the ethylene glycol, over the range of temperatures investigated in the experimental tests, is presented in Appendix C.

To reduce the time required for data collection, all of the instruments were connected to a data acquisition system. Each of the instruments produced either a 0 to 5 volt or a 4 to 20 mA electronic signal. The instruments were calibrated over the desired ranges so that they produced measurements with the optimum resolution. The electronic signals produced by the instruments were conditioned and collected via a server on a personal desktop computer. Linear calibration curves for all instruments employed in the low Reynolds number Pitot tube study can be found in Appendix C.

Two hemispherical tipped Pitot-static tubes (United Sensor Corporation, Amherst, NH) were employed in the study. The larger Pitot tube was referred to as PSL (Pitot-Static Large, Instrument No: PCC-8-KL UEC 9117), while the smaller Pitot tube was referred to as PSS (Pitot-Static Small, Instrument No: PDA-8-F-6-KL).

The outside diameters of the Pitot tubes, D, were measured using Digital vernier calipers (Mitutoyo Corporation, Tokyo, Japan). The accuracy of the calipers was on the order of 0.01 mm. The outside diameter of each Pitot tube was determined from the average of 5 measurements. The inside diameter of the Pitot tube opening, d, was determined with a digital camera (Nikon Coolpix 990, Mississauga, ON). Four digital photographs for each Pitot tube were analyzed to determine the inside diameter of the opening. The resulting dimensions are presented in Table 3.1. The analysis of the results is shown in Appendix C.

Table 3.1: Dimensions of Pitot-static tubes employed in low Reynolds number Pitot tube study

Dimension (mm)	PSL		PSS	
	Mean	Std Dev	Mean	Std Dev
D	3.06	0.01	1.62	0.01
d	1.13	0.02	0.52	0.03
β (d/D)	0.37	0.01	0.32	0.02

3.4. Gamma Ray Densitometer

A traversing gamma ray densitometer is located before the second acrylic viewing section and is 14.8 m from the flume inlet. It is used to measure the horizontal chord-averaged concentrations across the vertical diameter of the pipe (Gillies, 1993). The unit consists of a source, source housing and shutter (Ronan Engineering Ltd., Toronto, ON) and is mounted to a frame attached to a hydraulic jack. The traversing system (Saskatchewan Research Council, Saskatoon, SK) consists of a hand pump which is used to pressurize a hydraulic ram which acts to raise and lower the traversing unit. A needle valve on the connecting line between the pump and the ram was used to hold the unit at specific height locations. The height of the unit could be measured to within 0.1 mm with digital vernier calipers (Mitutoyo Corporation, Tokyo, Japan). Measurements were performed at y/D intervals of 0.05. The calibration and measurement positions for the traversing gamma ray unit mounted on the flume apparatus are presented in Appendix C.

A low energy (3.7 GBq) Cesium-137 source was used to supply the gamma ray radiation. A Cesium 137 source was chosen because the coefficient of absorption of its gamma rays is proportional to the density of the absorbing material. Concentration measurements can be calculated from the measured radiation based on Lambert's law (Shook and Roco, 1991). Equation 3.3 shows Lambert's law for a two phase mixture in a pipe flow.

$$\frac{N}{N_0} = -\exp\left[\mu_w x_w + \mu_f x(1-\phi) + \mu_s x\phi\right] \tag{3.3}$$

where

N = measured intensity

N_0 = unattenuated intensity

μ_w, μ_f, μ_s = absorption coefficients of the pipe wall, fluid and solids

x_w = path length of the beam through the pipe wall

x = path length of the beam through the pipe interior

ϕ = volumetric chord averaged, solids concentration

Before testing, absorption measurements were performed for various thicknesses of steel between the source and detector. A linear relation ship between measured intensity and thickness is presented in Appendix C. The absorption coefficient determined for steel from these tests was found to be in excellent agreement with the prediction from the equation used by the Saskatchewan Research Council shown in Equation 3.4.

$$\mu\left(\text{cm}^{-1}\right) = 6.9676\text{x}10^{-5}\,\rho(\text{kg/m}^3) + 1.5457\text{x}10^{-2} \tag{3.4}$$

The absorption coefficients for water, sand and clay for the density measurements of the model tailings slurries were determined from Equation 3.4. A traverse over the height of an empty pipe at the recording positions was performed to determine the pipe wall thickness (x_w). The inside and outside, top and bottom walls of the flume were also located in this way. Path lengths (x) at each recording positions were determined by performing a traverse over the height of a pipe full of water at a known temperature (density). Before each test, the shutter to the source was closed and a 100 mm (4 inch) lead block was placed in front of the source to determine the background radiation. All concentration measurements were corrected for background radiation.

A scintillation tube and detection system (EG & G Ortec, Oak Ridge, TN) were used to determine the degree of attenuation of the radiation. For each concentration measurement radiation counts seen by the scintillation tube were taken over 60 seconds. The resulting energy signal is examined to only accept counts which are inside the range associated with the gamma rays of interest. A 2 mm slit was used to collimate the gamma ray beam vertically. A schematic of the traversing gamma ray apparatus is shown in Figure 3.6.

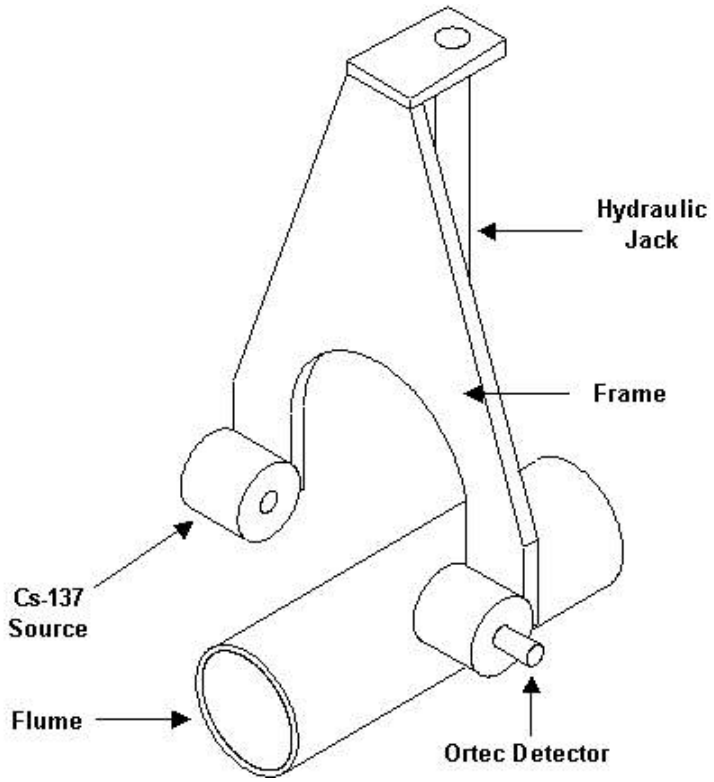

Figure 3.6: Schematic illustration of the traversing gamma ray densitometer on the 156.7 mm flume

3.5. Procedure and Operation

The controlled variables during the course of the 156.7 mm flume experiments were:

- Type of clay particles
- Type of sand particles
- Solids concentration
- Additive concentration (TSPP)
- Volumetric flowrate
- Flume slope angle

For the experiments involving coarse sand particles the effects of three additional controlled variables were also investigated:

- Sand to clay (coarse to fines) ratio
- Additive concentration (Ca^{2+}, TSPP)

For each of the runs the following data were collected

- the slurry depth was measured at planes 1 and 2 (indicated as "height measurement" locations in Figure 3.1) in the flume test section
- Pitot tube traverses were conducted to determine the variation of local velocity with position in the flow cross-sectional area
- the variation of chord-averaged solids concentration with slurry depth in the flume was measured with the traversing gamma ray densitometer
- temperature, volumetric flowrate, pressure drop and bulk density of the slurry were measured in the 53 mm feed line
- sampling of slurry with a wide-mouth syringe from the top and bottom of the flume at height measurement position 2 (Figure 3.1) was performed for selected runs to verify the carrier fluid concentration
    - sand was separated from the clay fraction by wet sieving (200 mesh = 75μm) to verify the sand to clay ratio and the fines concentration in the carrier fluid
    - gravimetric analysis was performed to determine weight fractions of solids in the sampled slurry

As well for the tests involving only clay and water slurries, two additional measurements were made:

- free surface velocity was determined by timing a drop of dye over a known distance of flume length (note that these tests were only applicable in laminar flow where the droplet did not bifurcate/disperse significantly)
- slurry samples were taken from the flume outlet to determine the weight fraction of clay (density of mixture) by gravimetric analysis

A complete set of water tests (Saskatoon tap water) were performed in the flume to commission the instruments in the loop. The water tests were completed over a number of flume angles at a range of flowrates. The flume angle inclinations studied included 0.5, 1, 1.5, 2, 2.5, 3, 3.5, 4, 4.5 and 5^{o} while the flowrates delivered to the system varied from 0.25 to 8 L/s. Most of the data from these tests were in the fully turbulent flow region. Since the diameter of the feed pipe and the physical properties of the water at the system temperature were known, the measured pressure drop could be used to determine the feed pipe wall roughness.

For the clay-water slurry experiments, particle deposition was not a concern since coarse particles were not present. This meant that a wider range of volumetric flowrates and flume angles could be studied. Initially a 43% by weight Kaolin Clay (KT Kaolin Clay, Kentucky-Tennessee Clay Company, Mayfield, KY) was prepared in the flume. Saskatoon tap water was used and no additives were included in the initial preparation for these experiments. A representative analysis of the mineral composition and ionic constituents of Saskatoon tap water are given in Litzenberger (2003).

The total volume of the slurry that was required for an experiment was 650 L. The slurry was prepared by first adding a known mass of water to the tank which corresponded to a final mixture volume of 650 L. A calculated mass of kaolin clay was then added to the water to produce a 43% w/w slurry. The mixer was turned on, system valves were opened and the pump was operated to recirculate the slurry in the loop. Recirculation and mixing was performed for a significant amount of time to ensure that the slurry was well sheared. The rheological properties of the clay slurry were determined to be stabilized, based on the constant pressure gradient observed in the pipe section for a set flowrate. The slurry was also left to sit overnight before any actual testing was performed. The resulting tests showed that this slurry had a yield stress of 32.9 Pa and a plastic viscosity of 0.0368 Pa-s. These properties were similar to the properties of the thickened tailings slurries investigated in this study.

A number of flume angles (6, 5.5, 5, 4.5, 4, 3.5, 3 and 2.5^{o}) were also investigated for this slurry. Tests were performed with this slurry at flowrates varying from 0.25 L/s to 6 L/s at each flume angle. However, the lowest angle that could be achieved in the flume was 2.5^{o}. Below this inclination, the gravitational driving force was not sufficient to overcome the yield stress of the slurry resulting in the flume overflowing.

Once the tests for the high yield stress slurry were complete, an addition of TSPP (tetrasodium pyrophosphate, Sigma-Aldrich Company, St. Louis, MO) was made to the mixture at a dosage of 0.03% w TSPP/w clay. This decreased the yield stress of the slurry such that it had similar properties to the CT (Consolidated Tailings) slurries studied. The resulting Bingham rheological parameters were 6.4 Pa and 0.0160 Pa-s. Before testing, the slurry was again well mixed and recirculated for a significant period of time to ensure that it was well sheared. The differential pressure in the 53 mm test section was monitored during this process and was seen to be relatively constant. This was an indication that the rheological properties of the slurry had

stabilized. Tests for this slurry were performed over a range of flowrates (0.25 to 5 L/s) and flume angles (1, 2, 3, 4, 5 and 6^o). No noticeable lower limit in the allowable flume inclination angle was evident during the test performed with this slurry.

A final addition of TSPP was added to the slurry which increased the TSPP concentration from 0.03% to 0.10 % w TSPP (w TSPP/w clay) and eliminated the yield stress of the slurry. The resulting Newtonian suspension had a viscosity of 0.0067 Pa-s. The slurry was once again recirculated and sheared for a significant period of time (2 hours) to ensure homogeneous distribution of the chemical addition. The rheological properties were observed to have stabilized when the pressure gradient in the 53 mm test section was constant with time for a fixed flowrate. Tests were performed over a range of flowrates (0.5 to 6 L/s) and flume angles (1, 2, 3, 4, 5 and 6^o). Since the slurry was Newtonian there were no operational limitations noted over the range of properties studied.

After the testing of the original high yield stress slurry, samples were withdrawn from the flume and tested in the laboratory with varying TSPP addition. The correct additive dosage was determined by successive doping of the samples and subsequent vane viscometry to determine the yield stress of the slurry. The doping concentrations of TSPP (0.03% and 0.1%) which provided the desired yield stress were determined in this way.

Coarse particle slurries were also investigated as the study of their flow behaviour was the primary objective of the study. A number of sand-water, and clay-sand-water slurries were tested in the 156.7 mm flume.

For the sand-water tests, six volumetric flowrates at two different angles were investigated (three flowrates at each angle). Each flowrate provided a velocity that was high enough to prevent a stationary deposit from being formed. For each angle the test with the lowest flowrate corresponded to a velocity, which was just above the velocity which would cause deposition in the flume. However, for the model tailings slurry tests, a different strategy was followed. For each of the mixtures three runs at 5 L/s and one run at 2.5 L/s were investigated. The angle for each of the tests was chosen based on the results of the previous test. If a deposit formed or was near forming during a given test a higher angle was chosen for the next test. However, if there was no evidence of a deposit, a lower angle was chosen for the next test.

At each stage of the preparation and testing of the mixtures, samples were withdrawn from the flume and vane viscometry was performed to track the yield stress of the slurry. As well, pressure drop versus velocity data were collected from the feed line test section at each stage so that the slurry rheology could be determined. After each addition of either solid material or chemical agent, the slurry was sheared in the stand tank with a high-speed mixer to ensure that it was well mixed and homogeneous. It has been shown that the rheological behaviour of some clay-water slurries, including those containing calcium ions and TSPP, may be sensitive to the duration of applied shear (Litzenberger, 2003). The rheology of a slurry can often be stabilized by subjecting it to a long period of shear. For this reason, the slurries of this study were sheared for a significant period of time until the rheology of the slurries was determined to be relatively constant for a given test. Separate samples were also withdrawn from the flume and analysed to confirm the slurry density.

Throughout the course of the experimental testing many different mixtures were prepared and tested in the 156.7 mm flume. Concentrated sand-water slurries, idealised Thickened Tailings, and model CT (Consolidated Tailings) slurries were all tested. Each mixture required its own unique method of preparation and operation. The procedure that was followed for the preparation and operation of each of the slurries is provided in the following sections.

3.5.1. Sand-Water Slurries

Granusil 5010 (d_{50} = 188 μm) sand was used in all the experiments (Unimin Silica Sand, Le Sueur, MN). The sand diameter represents a typical size for the coarse solids fraction in oil sand tailings. This sand was also chosen because of its round grain characteristics which are also similar to the coarse particles in oil sand. A photomicrograph of the Unimin sand employed in the tests can be found in Appendix B, Figure B.1.

For the sand-water slurries a sand concentration of 25% v/v (47% w/w) was chosen as the operating in-situ concentration. The volume of the tank was initially determined by filling it with a known volume of water. The maximum volume of the tank was determined to be 650 L. The tank was then drained and the line was dried so that slurry could be prepared in the tank. The valve between the tank and the pump was closed and a calculated mass of water (to provide a final volume of 650 L of 25% v/v sand-water slurry) was weighed in a barrel on an industrial scale (Model No: 2081, Toledo Scale Company, Windsor, ON) and added to the tank. Next, the

high-speed (3.5 hp) mixer (Model No: XJC-174, Lightnin Mixers and Aerators, Toronto, ON) was turned on and a predetermined mass of sand was added to the stand tank. When the slurry was thoroughly mixed, the valve to the pump was opened and the slurry was allowed to recirculate in the loop.

The tank design and operating procedures were modified to permit a constant sand concentration to be delivered to the flume loop regardless of the amount of slurry volume in the flume loop and stand tank. The details of the tank design were provided earlier and the operating procedure will now be provided.

The sand particles were found to settle out rapidly to the bottom of the stand tank once the pump and mixer were shut down. For this reason a special procedure was required to collect data on this mixture. Between sets of flume tests, the sand associated with the slurry is stored in the stand tank. A vertical suction system is placed in the stand tank to prevent plugging in the pump inlet and feed line during start-up when the sand is introduced to the flume circuit. The mixer is stopped at the end of a test and the supernatant fluid continues to circulate in the flume while the sand accumulates in the stand tank. At the start of the next test, once the water has been allowed to circulate at steady state through the pipe/flume circuit, the mixer is turned on and sand is reintroduced into the flume loop. The vertical suction pipe remained in the stand tank for the duration of the sand-water tests. A schematic of the vertical suction system is shown in Figure 3.7.

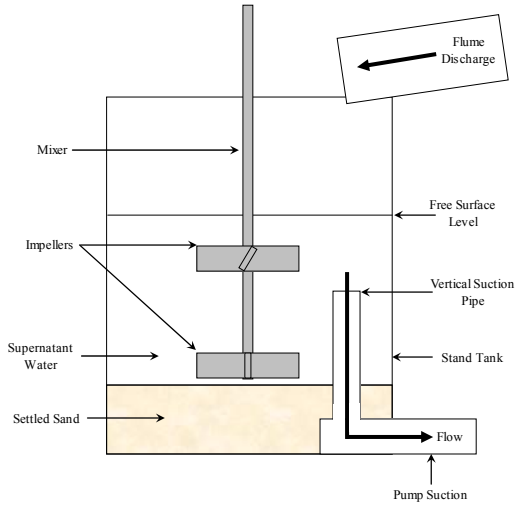

Figure 3.7: Schematic illustration of the vertical suction system employed in the sand-water tests in the 156.7 mm flume

Only a specific range of volumetric flowrates could be applied for a given mixture. The lowest acceptable flowrate was set by the condition that no stationary deposit could occur in either the pipe or the flume sections. The experimental system was particularly sensitive to the formation of a deposit in the flume section since it was found to continually increase in depth until the slurry spilled over the edge of the flume. Photographs of a sand deposit in the flume are presented in Appendix F. With respect to the pipe section, the SRC's Two-Layer Model (Shook et al., 2002) predicted that the deposition velocity for a 25% v/v 0.188 mm sand-water slurry was 1.3 m/s in a 53.1 mm pipe. If the operating pipe velocity was below this value, a stationary deposit would form in the pipe section. This would cause the delivered concentration in the system to change and thus make the flowing slurry concentration uncertain. Additionally, continuous operation below this velocity could have plugged the feed line.

3.5.2. CT Slurries

The coarse and fine solid components for these idealised slurries were chosen to represent Syncrude's consolidated tailings (CT) (FTFC, 1995). An idealised mixture was tested so that the components of the mixture could be controlled.

The idealised CT slurries were prepared using Granusil 5010 sand (Unimin, Silica Sand, Le Sueur, MN) to represent the coarse fraction and kaolin clay (Pioneer Kaolin, Dry Branch Kaolin Clay, Dry Branch, GA) to represent the fine fraction. A 3.5 to 1 coarse to fine (sand to clay) concentration ratio was chosen for these mixtures. Preliminary lab work with the vane viscometer showed that a concentration of 28:8:64 [=] (sand:clay:water v/v) with no chemical additions produced a non-settling pseudo-homogeneous slurry with a vane yield stress of 12 Pa. As well, this slurry had a bulk density of 1598 kg/m^3, which is similar to the density of actual oil sands CT. It should be noted that the kaolin clay, as received, contained calcium and therefore no additional gypsum was required to produce CT-like mixtures.

The original model slurry referred to as 'no gypsum' was prepared by first adding a known mass of water to the tank which corresponded to 650 L of model CT slurry. A calculated mass of kaolin was then added to the water, and the mixer was turned on. This mixture represented the carrier fluid. Finally, a measured mass of sand was added to the carrier fluid to produce 650 L of model CT slurry with the composition expressed above. To eliminate the yield stress, the chemical agent TSPP (tetrasodium pyrophosphate, Sigma Chemical Company, St. Louis, MO)

was added at 0.1% w TSPP/w clay in two stages. The resulting slurry was referred to as CT 'no gypsum' since its properties were similar to those of a CT blend prior to gypsum addition.

Once the tests for the CT 'no gypsum' slurries were complete, a calcium addition (calcium chloride dihydrate, BHD Inc, Toronto, ON) was made to the flume to increase the yield stress of the slurry to 6-8 Pa, which was the desired range for the CT 'gypsum' slurries. A dosage of 0.005% w Ca^{2+}/ w clay was initially added to the flume. After the slurry was well mixed, a vane viscometer measurement showed that the yield stress was above the target value. To correct for this, another addition of TSPP (0.0125% w/w clay) was made to further reduce the yield stress to within the desired range. This slurry was referred to as CT 'gypsum'.

3.5.3. Thickened Tailings Slurries

The Thickened Tailings slurries were prepared using a method similar to the procedure used to prepare the CT slurries. No flocculants were added to the Thickened Tailings slurries. The only difference between the Thickened Tailings and the CT slurries is that a coarse to fine ratio of 1:1 was used and the composition of the slurry was 15.4:15.1:69.5 [=] (sand:clay:water v/v). This produced a slurry with a bulk density of 1510 kg/m^3. Like the CT tests, vane viscometer tests and pipeline pressure drop versus velocity tests were performed to characterise the rheology of the slurry. Due to their high clay concentration, these slurries had yield stresses between 30 and 50 Pa. A similar operating procedure to that used for the CT slurries was employed in the Thickened Tailings tests. The only exception was that the high yield stresses of the Thickened Tailings slurries resulted in higher operating depths of flow in the flume. Care had to be taken to ensure that the flume did not overflow.

3.5.4. Clay-Water Slurries

Modifications were made to the experimental flume circuit prior to conducting the clay-water slurry tests. Using the results of the model tailings tests, modifications were made to the apparatus to allow for a more controlled flow in the flume line. In the clay-water experimental tests the transport of coarse particles was not studied. Only the behaviour of Bingham clay-water carrier fluids was investigated. Frictional loss characteristics for a single concentration of clay-water slurry at three different Bingham rheologies were investigated.

Since sand was not being employed in the testing, the deposition condition or deposition characteristics of the flow did not have to be considered. Gamma ray densitometer scans were not performed during this phase of the testing since the clay-water slurry is known to exhibit homogeneous behaviour under the experimental conditions investigated. As well, a Ronan densitometer was also not required at the pump outlet since density values could be obtained from gravimetric analysis of slurry sampled at the flume outlet.

The slurry was introduced to the flume inlet through an expansion elbow, a 1 m length of 150 mm (6 inch) pipe, and a knife gate valve (NewCon Co., Hibbing, MN). The purpose of these modifications was to dissipate as much of the kinetic energy at the inlet as possible. This drastically reduces waves and instabilities in the flow and allows for a much more rapid development of a uniform flow within the 156.7 mm (6 inch) flume line.

Sluice gates and weirs were incorporated into the flume entrance and exit. The purpose of these flow restrictions upstream and downstream was to control the depth of flowing slurry within the flume for supercritical and subcritical flows, respectively. Accumulation of coarse particles behind these obstacles did not have to be considered since a fine particle slurry was being investigated.

A single clay concentration was used for the slurry employed in these tests. A 43.5% w/w (22.2% v/v) clay-water slurry was prepared to provide a Bingham fluid with an approximate yield stress of 32.9 Pa and a plastic viscosity of 0.0368 Pa-s, similar to the thickened tailings slurry investigated in this study. With appropriate chemical additions, the slurry characteristics could be modified to provide two additional slurries with different rheological properties. Tetrasodium Pyrophosphate (TSPP) was added at 0.03% w TSPP/w clay which produced a slurry with a yield stress of 6.4 Pa and a plastic viscosity of 0.0160 Pa-s. This slurry resembled the CT ‘gypsum’ model tailings slurries. A total addition of 0.10% w TSPP/w clay was added to the mixture which produced a slurry with an equivalent Newtonian viscosity of 0.0067 Pa-s. This Newtonian slurry had a similar composition to the ‘no gypsum’ CT slurries.

4. NUMERICAL MODEL

4.1. Governing Equations

A numerical model has been developed to simulate the transport of coarse particles in a non-Newtonian carrier fluid in a laminar, unidirectional, open channel flow. Cartesian coordinates, which fit the geometry best, will be employed.

The flow can be represented by the Navier-Stokes equations, which are provided in terms of the Continuity Equation (Conservation of Mass, Equation 4.1), and the Momentum Equations (Conservation of Momentum) which is expressed in terms of shear stresses below in Equation 4.2 (Bird et al., 1960):

$$\dot{\rho} + \left(\rho u_i\right)_{,i} = 0 \tag{4.1}$$

$$\rho \dot{u}_i + \rho u_j u_{i,j} = -P_{,i} + \rho g_i - \left(\tau_{ji}\right)_{,j} \tag{4.2}$$

where

ρ = density

u = velocity

P = pressure

g = gravity

τ = shear stress

i , j = coordinate direction indices

The Continuity Equation can be simplified for an incompressible fluid to:

$$u_{i,i} = 0 \tag{4.3}$$

In terms of a Newtonian equivalent viscosity, the momentum balance can be expressed as:

$$\tau_{ji} = -\eta u_{i,j} \tag{4.4}$$

$$\rho \dot{u}_i + \rho u_j u_{i,j} = -P_{,i} + \rho g_i + \left(\eta u_{i,j}\right)_{,j} \tag{4.5}$$

where

η = apparent viscosity

In full form the Continuity Equation (4.6) and momentum partial differential Equations 4.7a, 4.7b and 4.7c are shown below in Cartesian coordinates:

$$\frac{\partial u_x}{\partial x}+\frac{\partial u_y}{\partial y}+\frac{\partial u_z}{\partial z}=0 \tag{4.6}$$

$$\rho\frac{\partial u_x}{\partial t}+\rho u_x\frac{\partial u_x}{\partial x}+\rho u_y\frac{\partial u_x}{\partial y}+\rho u_z\frac{\partial u_x}{\partial z}=-\frac{\partial P}{\partial x}+\rho g_x+\left[\frac{\partial}{\partial x}\left(\eta\frac{\partial u_x}{\partial x}\right)+\frac{\partial}{\partial y}\left(\eta\frac{\partial u_x}{\partial y}\right)+\frac{\partial}{\partial z}\left(\eta\frac{\partial u_x}{\partial z}\right)\right] \tag{4.7a}$$

$$\rho\frac{\partial u_y}{\partial t}+\rho u_x\frac{\partial u_y}{\partial x}+\rho u_y\frac{\partial u_y}{\partial y}+\rho u_z\frac{\partial u_y}{\partial z}=-\frac{\partial P}{\partial y}+\rho g_y+\left[\frac{\partial}{\partial x}\left(\eta\frac{\partial u_y}{\partial x}\right)+\frac{\partial}{\partial y}\left(\eta\frac{\partial u_y}{\partial y}\right)+\frac{\partial}{\partial z}\left(\eta\frac{\partial u_y}{\partial z}\right)\right] \tag{4.7b}$$

$$\rho\frac{\partial u_z}{\partial t}+\rho u_x\frac{\partial u_z}{\partial x}+\rho u_y\frac{\partial u_z}{\partial y}+\rho u_z\frac{\partial u_z}{\partial z}=-\frac{\partial P}{\partial z}+\rho g_z+\left[\frac{\partial}{\partial x}\left(\eta\frac{\partial u_z}{\partial x}\right)+\frac{\partial}{\partial y}\left(\eta\frac{\partial u_z}{\partial y}\right)+\frac{\partial}{\partial z}\left(\eta\frac{\partial u_z}{\partial z}\right)\right] \tag{4.7c}$$

For the one dimensional, unidirectional, fully developed flow problem of interest, the Navier-Stokes equations can be further simplified to a single partial differential equation. The flow is assumed to occur in the z-wise (axial) direction. The lateral (x) and vertical (y) velocity components and all of the convective terms can be eliminated for fully developed one-dimensional flow. Based on these conditions, the momentum Equations 4.7a, 4.7b, and 4.7c can be represented by a single equation:

$$\rho\frac{\partial u_z}{\partial t}=-\frac{\partial P}{\partial z}+\rho g_z+\frac{\partial}{\partial y}\left(\eta\frac{\partial u_z}{\partial y}\right) \tag{4.8}$$

Since a non-Newtonian carrier fluid is being studied, the viscosity term has been left inside the partial derivative on the right hand side. As well, since open channel flows are driven by gravity and the mixture in the open channel is in equilibrium with the ambient pressure, the axial pressure gradient term can be omitted. The momentum equation can therefore be further simplified to:

$$\rho\frac{\partial u_z}{\partial t}=\rho g_z+\frac{\partial}{\partial y}\left(\eta\frac{\partial u_z}{\partial y}\right) \tag{4.9}$$

A number of models are available for determining the transport of solids in suspensions. The applicability of a given model is dependent not only on the flow regime (laminar or turbulent) but also the geometry of the problem and the ranges and values of the flow parameters (physical properties, concentrations). Since this problem considers laminar flow of concentrated tailing mixtures in open channels, the number of appropriate models is greatly reduced.

The general form of the scalar concentration model equation is shown below in tensor notation (Equation 4.10).

$$\dot{\phi} + u_i \phi_{,i} = \left(\Gamma \phi_{,i}\right)_{,i} + S_\phi \tag{4.10}$$

Expanding this equation in Cartesian coordinates yields:

$$\frac{\partial \phi}{\partial t} + u_x \frac{\partial \phi}{\partial x} + u_y \frac{\partial \phi}{\partial y} + u_z \frac{\partial \phi}{\partial z} = \left[\frac{\partial}{\partial x}\left(\Gamma \frac{\partial \phi}{\partial x} \right) + \frac{\partial}{\partial y}\left(\Gamma \frac{\partial \phi}{\partial y} \right) + \frac{\partial}{\partial z}\left(\Gamma \frac{\partial \phi}{\partial z} \right) \right] + S_\phi \tag{4.11}$$

A simplified geometry has been chosen to model the laminar solids transport problem of this study. A rectangular channel of infinite width has been used to represent the open channel flow in the flume since longitudinal concentration gradients have been shown to be of the order of 1% of the vertical gradients (Jobson and Sayre, 1970). Concentration variations in the lateral direction have been assumed to be small and therefore the x-wise (horizontal and normal to the flow) dependence of concentration and velocity has been neglected (Shook et al., 1979; Hill, 1996; Graham et al., 2002). This simplifies the one-dimensional, fully developed transport equation to:

$$\frac{\partial \phi}{\partial t} = \frac{\partial}{\partial y}\left(\Gamma \frac{\partial \phi}{\partial y} \right) + S_\phi \tag{4.12}$$

The terms Γ and S_ϕ represent the diffusivity and the source term of the scalar transport equation. Their relationship to the flow parameters is presented in Section 4.9, Equations 4.41 and 4.42. The model developed by Phillips et al. (1992) will be referred to subsequently in this thesis as the 'Phillips model'.

In Equation 4.12, Γ and S_ϕ are functions of concentration (ϕ) and the shear rate ($\dot{\gamma}$). The mixture velocity, mixture density, coarse particle concentration and viscosity can vary over the depth of flow in the channel. Equations 4.9 and 4.12 can be solved simultaneously to produce steady state velocity and concentration distributions.

The finite volume method has been used to numerically solve the partial differential equations. Although it is typically applied to numerical heat transfer problems, it has been shown that the technique proposed by Patankar (1980) can be applied to numerical fluid flows successfully. It is a model that incorporates aspects from both the finite element method as well as the finite difference method. In the method, the flow geometry is subdivided into elemental cells. The partial differential equations are integrated in both space and time (term-by-term) over each elemental cell with finite difference approximations being substituted for differentials. This produces a set of algebraic equations which can be solved with a variety of numerical techniques.

A uniform, cell centered grid composed of 50 interior nodes has been used in the simulations. No-shear (symmetry) and no-slip boundary conditions have been specified for the velocity at the flume free surface and channel wall respectively to solve the Navier-Stokes momentum equation (4.9). Dirichlet and a mixed Robbins (Rao, 2002) no-flux conditions have been specified for the concentration at the free surface and channel wall respectively to solve the scalar concentration equation (4.12). The no-flux specifications ensure that the mass of coarse particles is conserved in the system during the transient simulation. Special considerations have also been made in the model to deal with the interior singularity which occurs at the interface between the sheared and unsheared regions of the flow.

By employing the specified boundary conditions, the discrete algebraic equations can be transformed into a tridiagonal matrix which can be solved using the Thomas Algorithm (Rao, 2002) at each time step. To increase the stability of the solution, the transient terms in the partial differential equations are included and the simulation is solved using time to relax and stabilize the solution (Patankar, 1980). The addition of a sedimentation flux in the Phillips model results in a stiff scalar concentration equation. To solve the concentration and velocity equations simultaneously, a very small time step is required. To further stabilize the solution and allow for simulations at slightly larger time steps, a linearized source term solution method has been

employed. A geometric interpolation scheme has also been adopted in this model to ensure conservation of flux across internal boundaries.

Four basic rules can be followed to ensure the finite volume method is being implemented properly (Patankar, 1980, p. 64):

1. *Consistency at control volume faces* – flux in and out of a control volume is conserved due to the finite volume discretization and integration of the partial differential equations.
2. *Positive Coefficients* – for all nodes in the domain the discrete algebraic equation coefficients must be positive. An increase in the conserved quantity at one node should lead to an increase in the quantity at the neighbouring nodes.
3. *Negative Slope Linearization of source term* – can be used to increase the stability of the solution. Most physical processes allow for this to occur.
4. *Sum of all neighbour coefficients* – ensures stability of the solution through the Scarborough condition.

The details of these rules, and their application to the numerical model in this study, will be discussed in further detail in the finite volume method model development.

4.2. Shear-Induced Particle Diffusion Modeling History

A number of researchers have attempted to experimentally measure the effects of shear-induced self-diffusion. Much of the work has been performed in Couette devices in order to determine a self-diffusion transport equation and the corresponding diffusion coefficient which can be used to model the flow.

Eckstein et al. (1977) developed a scaling argument for the diffusion coefficient by reducing the dimensionless arguments governing particle-particle interactions. They reasoned that fluid-mechanical interactions among neighbouring particles produce irregular motions leading to lateral migrations from the instantaneous average trajectories resulting in particle dispersion. Self diffusion resembles the molecular collisions that give rise to ordinary diffusion. They determined that the self-diffusion coefficient was proportional to the square of the particle radius and the local shear rate with tests in an experimental concentric cylinder Couette apparatus. The coefficient was found to be nearly linear with concentration up to concentrations of 20% and constant beyond that.

Gadala-Maria and Acrivos (1980) noticed that the effective viscosity of a concentrated system of neutrally buoyant spheres in a concentric cylinder Couette device exhibited abnormal behaviour. During their tests the effective viscosity decreased slowly with shear until it reached a time independent value. However, the magnitude of the viscosity change was quite significant and was seen to be a strong function of concentration. However, the researchers could not determine a reasonable explanation for the phenomenon.

Leighton and Acrivos (1987a) made significant progress in determining the scaling factors for shear-induced self-diffusion. Repeating the original experiments of Gadala-Maria and Acrivos (1980), they showed that particle migrations in the concentric cylinder apparatus were due to irreversible interparticle interactions. This leads to effective diffusivities both normal to the plane of shear and normal to the direction of fluid motion. They used a statistical determination approach and found the diffusion coefficient to be a function of shear rate and the square of the particle radius. They also observed the coefficient to be an increasing function of concentration in the dilute limit as was observed by Eckstein et al. (1977).

Leighton and Acrivos (1987b) observed diffusion normal to the plane of shear in their experimental concentric cylinder Couette apparatus with neutrally buoyant particles. The diffusion mechanism occurred parallel to the velocity gradient due to a slight variation in local concentration. Their proposed mechanisms predict particle migration from regions of high shear stress to regions of low shear stress.

Nadim (1988) also performed measurements in a concentric cylinder Couette device with neutrally buoyant particles. He likened the particle collisions to a bulk diffusive motion as a result of many-body- hydrodynamic interactions. He distinguished it from Brownian motion noting that it only occurs at high Peclet numbers (Pe), and concluded that particle size (a), shear rate ($\dot{\gamma}$) and concentration (ϕ) were the three key parameters governing the diffusion of particles.

Biemfohr et al. (1993) performed measurements on shear-induced self-diffusion coefficients in dilute suspensions. They described the self-diffusion of particles as a displacement of particles away from their original streamlines or a random walk under creeping flow conditions. They determined that it takes three interacting particles to undergo a net displacement, which is

proportional to the square of the concentration, for the case of spherical particles. However, if the particles are not spherical, a two-particle interaction can result in a net displacement proportional to the concentration. They also determined scaling relationships from experimental measurements in a concentric cylinder Couette device, and commented that anisotropy of the particles may play a role in the dispersion behaviour.

Zarraga and Leighton (2002) obtained an unexpectedly large shear-induced self-diffusivity from their measurements in a concentric cylinder Couette apparatus. Their results showed that for two-particle irreversible interactions, the diffusivity scaled proportionately with concentration. However, the asymmetry of three-particle interactions caused the diffusivity to scale with the square of the concentration. These results validate the work of Biemfohr et al. (1993), where they measured experimental diffusivities that were much larger than expected by theory.

Chow et al. (1994) studied shear-induced diffusion effects using nuclear magnetic resonance (NMR) measurement techniques. The experiments were performed in concentric cylinder and parallel plate flow devices. The results showed that the Phillips model is only appropriate for planar shear flows, and to appropriately describe the shear-induced behaviour in curvilinear coordinates, a more generalized formulation is required. The Phillips model constitutive equation predicts an inward radial particle migration for parallel plate flow when in fact, experimentally no particle migration exists in this geometry. For the neutrally buoyant particles investigated, they found that the rate of migration was proportional to the shear rate and the square of the particle radius.

Other researchers like Schaflinger et al. (1995) and Chapman and Leighton (1991) studied viscous resuspension of negatively buoyant particles in a fully developed Hagen-Poiseuille flow. Resuspension occurs when a settled negatively buoyant sphere is lifted into the bulk fluid flow due to the presence of shear. The shear-induced effective diffusivity (gradient diffusivity) is different than shear-induced coefficient of self-diffusion. The latter occurs due to the random motion of the particles in a uniform concentration field. The former is typically more significant and is due to particle flux resulting from the magnitude of the concentration gradient. Both studies showed that the shear induced effective diffusivity is proportional to the Shields parameter (Equation 2.46).

Schaflinger et al. (1990) studied the viscous resuspension of sediment particles within a laminar stratified flow under the action of shear for an initially settled bed of particles. To account for particle settling they employed a Stokes' law formulation and used a hindrance function to account for the interference resulting from particle-particle interactions. Their results showed that negatively buoyant particles could be resuspended at low Reynolds numbers.

Acrivos et al. (1993) performed measurements for shear-induced resuspension in a narrow gap concentric cylinder Couette device. In their work they attempted to model viscous resuspension of a settled bed of particles under laminar flow conditions using an approach that was similar to Leighton and Acrivos (1987). Resuspension was considered possible and was attributed to a balance between the downward flux of particles due to gravity and an upward flux due to the gradients in the particle concentration and shear rate. They also observed that there was no difference between the diffusivity coefficient normal and parallel to the plane of shear. As well, it was found that the height of a settled bed of particles is completely independent of particle size. However, they concluded that the time to reach steady state is dependent on the particle size. The relation for the dimensionless diffusivity used in this study was:

$$\hat{D} = \tfrac{1}{3}\phi^2\left(1 + \tfrac{1}{2}e^{8.8\phi}\right) \tag{4.13}$$

Acrivos (1998) showed that particles subjected to shear in a Newtonian fluid execute a random walk and migrate from regions of high concentration to low concentration and from regions of high shear to low shear. The interactions among neighbouring particles create irregular motions which produce an overall dispersive effect. The variation of shear rate occurs due to a variation in the shear stress. However, since the stress force acting over a sphere is not symmetric, a concentration gradient is generated. The Phillips model relation does not distinguish between transverse and normal fluxes. This suggests that the relations used for flow in a tube should be the same as those for flow in an open channel when the velocity is only in the axial direction.

Experimental studies have been performed to verify the mechanisms of shear-induced particle self-diffusion and viscous resuspension. Tirumkudulu et al. (1999) qualitatively observed the effects of shear-induced diffusion in a horizontally rotating cylinder. Although they could not mathematically formulate a model to predict the behaviour, the resulting particle distributions were attributed to shear-induced particle diffusion. Altobelli et al. (1991) measured velocity and concentration distributions of suspensions of negatively buoyant particles in tube flow by nuclear

magnetic resonance imaging. No numerical model was developed to substantiate their findings. However, their results were in qualitative agreement with viscous resuspension theory. The non-uniform profiles were a result of irreversible interactions among neighbouring particles and the flow-confining boundaries. The segregation in the concentration distribution also increased with decreased velocity (throughput) and increased solids loading as would be expected.

4.3. Phillips Model Background

In the present study, the Phillips model has been chosen to represent the behaviour of the coarse solids transport in laminar non-Newtonian flows. The Phillips model is an extension of the shear-induced particle diffusion model originally proposed by Leighton and Acrivos (1987b). It is only applicable to laminar flow (Couette and Poisseuille) where inertial effects can be ignored.

The model is phenomenological and derived by generalizing the simple scaling arguments based on the shear-induced self-diffusion theory of Leighton and Acrivos (1987b). The model accounts for the fact that particles in a shear flow will not remain stationary, but will migrate to different regions of the flow depending on the variation in local shear rate, concentration and viscosity (Annamalai and Cole, 1986; Nadim, 1988). This resulting model equation accounts for all of the self-diffusion effects discovered by previous researchers combined into a single, scalar transport equation.

The Phillips model is a constitutive model. It does not account for all mechanisms of particle transport. Rather, it only considers those that occur in concentrated suspensions from particle-particle interactions. In concentrated systems there are a variety of interparticle interactions including hydrodynamic and electrostatic (Phillips et al., 1992). However, a rigorous calculation incorporating all possible interparticle interactions in a concentrated system would be computationally expensive. Therefore, one would expect that only low particle populations in the simplest of flow geometries could be resolved in a reasonable amount of time. This is why the Phillips model has been chosen. The critical characteristics of the flow are represented while less important effects are neglected or accounted for in other manners.

Some of the important requirements of the Phillips model are:

1. Hard, rigid, smooth, monomodal spheres. Particle roughness is only important at high concentrations.
2. Newtonian carrier fluid. In this study it was assumed that the Phillips model could be applied to non-Newtonian carrier fluids if an effective/apparent mixture viscosity approach is implemented.
3. Particle motion occurs due to diffusion only.
4. Peclet numbers (Pe), a dimensionless ratio relating the effects of particle transport by shear forces to transport by diffusional mechanisms, are very large.
5. The flow of the solid-liquid mixture is laminar.
6. For this study the size of the coarse particles are large enough that the effects of Brownian motion are negligible.

Neither the Phillips model nor the previous work of Leighton and Acrivos (1987b) account for the sedimentation of negatively buoyant particles. This may not be a concern for systems of smaller or neutrally buoyant particles, but for systems with larger particles with relatively high densities, it is a significant mechanism in solids transportation. This is why a sedimentation flux has been added to the Phillips model in this study.

In close-packed and concentrated systems, hindered settling effects become important. Under these conditions, particles no longer settle as a single particle in infinite dilution but rather the effects of the surrounding particles, fluid and domain boundaries become important. In this study a constitutive hindered settling model similar to that of Richardson and Zaki (1954) will be used to obtain an expression for the sedimentation flux.

The Phillips model can only account for a single particle size (a narrow distribution). Others have attempted to apply the shear-induced self-diffusion models to describe more complex situations. Krishnan and Leighton (1995) and Zarraga and Leighton (2001a) attempted to model dilute bidisperse suspensions. However, these models were greatly simplified and no significant results were achieved. Based on the most recent investigations reviewed, a significant research effort is required to account for multiple particle sizes (bimodal, multimodal) and broad particle size distributions.

The Phillips model only considers two-body or two-particle interactions. Any three-body interactions are not accounted for in the expressions for the particle fluxes. This is because

Leighton and Acrivos (1987) have shown that the resulting fluxes from three-body interactions are an order of magnitude smaller than those of two-body interactions. Thus whenever the term interaction or interparticle is used it simply means "the influence that one particle has on a neighbouring particle" as a result of a two-body irreversible interaction (Phillips et al., 1992).

Two important aspects of interparticle interactions are the differences between reversible and irreversible interactions. A reversible interaction is one in which a particle returns to its original streamline. Acrivos (1998) theorised that under creeping flow conditions the trajectory of a particle should be completely reversible. Originally it was believed that that shear-induced dispersion was due to surface roughness. However, Acrivos (1998) concluded that it is caused by the random chaotic velocity components of a particle which are influenced by the presence of neighbouring particles. If this were the case, a transient concentration distribution would never occur. If a net migration of particles is to occur across a shear gradient, particles must undergo irreversible interactions.

Eckstein et al. (1977) suggest that particle migration normal to the direction of the flow is caused by three mechanisms:

1. Mutually induced velocity fields during shear flow
2. Lift forces
3. Body forces (gravity)

Eckstein et al. (1977) also stated that in simple shear flows, particles rotate with an angular velocity which is approximately half of the shear rate of the fluid (Jeffrey, 1922). The circulatory fluid motion induced by the particle rotation creates a velocity field that exerts drag on neighbouring particles. This results in dispersive behavior which can be expressed in a similar form to Fick's law (Bennett and Myers, 1982) with the coefficient of self-diffusion. Therefore, Eckstein et al. (1977) suggest that the dispersive behaviour associated with self-diffusion resembles the molecular collisions that give rise to ordinary molecular diffusion.

4.4. The Phillips Model

Phillips et al. (1992) have reduced the significant driving forces governing particle transport into two mechanisms. These mechanisms have been reformulated to appear as diffusive terms in the

governing partial differential equation. A third sedimentation mechanism, developed in this study, has been included to account for particle settling. The resulting equation is a second order, non-linear differential equation with respect to the particle volume fraction. The differential equation can be used to represent the behaviour of coarse particles within a laminar flow. The three particle migration mechanisms are described below.

4.4.1. Flux due to spatially varying interaction frequency

Particles move from regions of high shear rate to regions of low shear rate

$$N_c = -K_c a^2 \phi \nabla(\phi\dot{\gamma}) = -K_c a^2 \left(\phi^2 \nabla\dot{\gamma} + \phi\dot{\gamma}\nabla\phi\right) \tag{4.14a}$$

$$K_c = 0.4 \tag{4.14b}$$

Shear flow is an assemblage of shearing surfaces sliding relative to one another. A particle-particle collision occurs when two particles in adjacent shearing surfaces move past one another. This is shown in Figure 4.1a, where the collision occurs at $t = 0$.

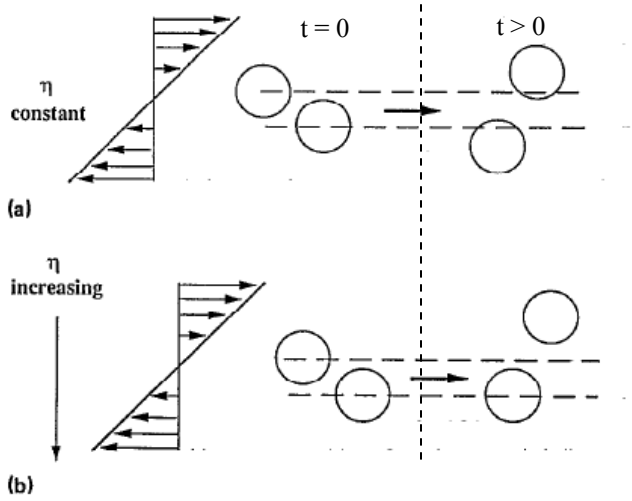

Figure 4.1: Schematic diagrams of irreversible two-body collisions with (a) constant viscosity and (b) spatially varying viscosity (Phillips et al., 1992)

The particles experiencing a higher frequency of collisions from one direction will migrate normal to the shearing surface in the direction of lower collision frequency. Spatially varying interaction frequency flux only occurs with irreversible two-body collisions and can only occur in a shear flow, where a velocity gradient exists.

For a field of equally distributed particles, a particle will experience a greater number of collisions in a location of higher shear rate. This is because particles in regions of higher shear rate are moving at a greater relative velocity to each other and are able to interact more frequently. Phillips et al. (1992) proposed that the number of collisions experienced by a given particle in a concentrated system is proportional to $\phi\dot{\gamma}$ (where $\dot{\gamma}$ is the local shear rate and ϕ is the local concentration of particles). Therefore, a high shear rate or high concentration of particles results in a larger frequency of collisions. According to Phillips K_c is a proportionality constant of order unity. Its value will be discussed in Section 4.5.

The flux of particles is equivalent to a particle migration velocity. A Fickian equivalent relationship for particle transport by diffusion is also included based on density variations in the suspension. Therefore particles also move normal to the concentration gradient from regions of high concentration to regions of low concentration.

The flux due to the variation in shear rate and that due to a concentration gradient generally oppose one another. The shear rate tends to be higher in lower concentration regions moving particles to regions of higher concentration. The second term opposes this migration and tends to transport particles back to regions of lower concentration making the spatially varying interaction frequency flux self-balancing.

4.4.2. Flux due to spatially varying viscosity

Particle concentration affects the local effective viscosity and the migration of particles in a varying viscosity field

$$N_\eta = -K_\eta a^2 \dot{\gamma}\phi^2 \frac{\nabla\eta}{\eta} = -K_\eta a^2 \dot{\gamma}\phi^2 \frac{1}{\eta}\frac{d\eta}{d\phi}\nabla\phi \tag{4.15a}$$

$$K_\eta = 0.6 \tag{4.15b}$$

Local effective viscosity is a function of the local concentration of particles. A concentration gradient produces a spatially varying effective viscosity. This is even more complex for non-Newtonian fluids where the effective viscosity is a function of the local shear rate as well as the local concentration of particles. The spatial variation in viscosity causes the resistance to motion on one side of the particle to be higher than on the other side. This results in particles being

displaced in the direction of decreasing viscosity as shown in Figure 4.1b. Once again the flux is equivalent to a drift velocity that is normal to the plane of shear and proportional to the apparent viscosity gradient. The flux is independent of the local value of the viscosity but depends on the relative spatial variation of viscosity. K_η is a proportionality constant of order unity that will be discussed in Section 4.5.

It should be pointed out that in order to obtain a steady state concentration distribution with neutrally buoyant particles, the fluxes expressed in Equations 4.14a and 4.15a must oppose each other. Based on Newton's law, for the same wall shear stress, a higher viscosity fluid will have a lower velocity gradient. For the fluxes, which have been discussed, one can see that particles move in the direction of decreasing concentration and viscosity. However the movement away from regions of high concentrations is countered by the fact that low concentration areas will have higher velocity gradients due to their lower viscosity. This acts to drive the particles back to higher concentration regions. At steady state there is a balance between these opposing particle fluxes resulting in a distribution of particles that accounts for particle concentration, and the physical properties of the fluid and the flow field.

4.4.3. Flux due to particle sedimentation

Driving force for sedimentation is gravity

$$N_s = \phi\, f(\phi) v_\infty \tag{4.16a}$$

The driving force for sedimentation is the submerged weight of the particles in the carrier fluid. It has been shown that a particle flux is equivalent to a drift velocity. Therefore the particle settling flux can be related to a sedimentation velocity (v_∞). Stokes' Law (Wallis, 1969; Davis and Acrivos, 1985) for particles settling in an infinite dilution can be applied for low concentration suspensions. However, when particle concentrations become significant, Stokes' Law is no longer appropriate. To incorporate particle-particle interactions into the sedimentation flux a hindered settling approach is used.

Inserting the expression for the Stokes' infinite dilution settling velocity, and accounting for hindered settling with the hindrance function, produces the following relation for the sedimentation flux:

$$N_s = \frac{2}{9}\phi\, f(\phi)\frac{a^2 \vec{g}\left(\rho_s - \rho_f\right)}{\eta_f} \tag{4.16b}$$

$$K_s = \frac{2\left(\rho_s - \rho_f\right)}{9\eta_f} \tag{4.16c}$$

In this model the sedimentation flux no longer becomes valid as a settled bed forms. The hindered settling effects assumed in the formulation are only valid for concentrations less than the maximum packing factor of a settled bed (Kawase and Ulbrecht, 1981). The form of the hindrance function, $f(\phi)$, chosen in this study is shown in Equation 4.17. It is a strong function of concentration and the effects of the presence of shear on the hindrance function have not been measured. The exponent n from Equations 2.43 and 2.44 has been assumed to be unity.

$$f(\phi) = \frac{1-\phi}{\eta_r} \tag{4.17}$$

A simpler hindrance function is employed in this study. Schaflinger et al. (1990) stated that their model was insensitive to the choice of hindrance function as long as it was monotonically decreasing with increasing concentration. The hindrance function used in this study, Equation 4.18, is similar in form to that employed by Acrivos et al. (1993).

$$f(\phi) = \frac{(1-\phi)}{\eta} \tag{4.18}$$

The hindrance function in Equation 4.18 incorporates both a viscosity and a concentration effect. It also decreases with increasing concentration, thus reducing the settling flux of the particles in more concentrated regions. Since non-Newtonian fluids are of interest in this study, the mixture effective viscosity has been included in the denominator. Combining Equations 4.16b and 4.18 yields the following relationship for the sedimentation flux:

$$N_s = K_s a^2 \phi\, f(\phi)\vec{g} \tag{4.19a}$$

where

$$K_s = \frac{2}{9}\left(\rho_s - \rho_f\right) \tag{4.19b}$$

It can be seen that K_s is positive for negatively buoyant particles (sinking), zero for neutrally buoyant particles and negative for positively buoyant particles (floating). Note that the sign of the local acceleration due to gravity (g) determines the direction of particle flux in a given coordinate direction.

The Phillips model also accounts for the flux of particles due to Brownian motion (N_b). According to Phillips et al. (1992), Brownian motion can generally be disregarded when the particle Peclet Number (Pe) is much greater than 1.

$$N_b = -D\nabla\phi \tag{4.20}$$

$$Pe = \frac{\dot{\gamma}a^2}{D} \tag{4.21}$$

Brownian motion is only significant for very small particles (typically 10^{-6} m). Although the clay particles employed in this study are of this size, Brownian motion is not of interest with these particles as they are considered part of the continuous, homogeneous carrier fluid. The sand particles represent the particulate phase of interest in the Phillips model. Since these particles have diameters of the order of 10^{-4} m, they are too large for Brownian motion effects to be significant. Therefore, the particle flux due to Brownian motion is not considered in this study.

The Phillips model has been used in a variety of flow situations to successfully model the behaviour of solid particles in slurry flows. The beauty of the model is its simplicity. By combining the solid and carrier fluid phases, the flow can be modeled as a mixture. In this way only momentum equations for the mixture need to be solved (rather than solving the carrier fluid and solid phase momentum equations separately). As well, since the model results in a scalar equation, it only requires the solution of a single additional transport equation.

However, there still exist some complications that require special attention with regards to the Phillips model formulation.

1. For pipe flow, the concentration approaches the maximum packing factor at the pipe center because any counteracting flux vanishes due to the shear rate approaching zero (symmetry condition and neutrally buoyant particles).
2. Some modification needs to be made to account for the fact that particles do in fact undergo collisions at the pipe center despite the shear rate going to zero.
3. The model can not be applied or extended to arbitrarily complex geometries by simply substituting some scalar measure of the shear rate ($\dot{\gamma}$). Instead any migration model must account for both the frequency of collisions and the direction that the particles are displaced during those collisions by the identification of shearing surfaces both normal and parallel to the plane of shear (Seifu et al., 1994).

The third point needs to be considered if a developing flow, in multiple dimensions and in an arbitrary geometry, is to be solved with the Phillips model. Identification of the shearing surfaces is critical to predicting the correct direction of particle migration.

4.5. Adjustable Parameters

Two parameters, K_c and K_η, presented in Equations 4.14a and 4.15a, exist to account for the pseudo-diffusive nature of the Phillips model. They are proportionality constants and are parameters determined from fitting model simulations to experimental results. These parameters represent different material properties, particle shape, size distribution and surface roughness, as they play an important role in irreversible particle collisions. They are of order unity and should be independent of particle size and volume fraction.

Phillips et al. (1992) found from a comparison with their experimental results that a ratio of K_c/K_η of 0.66 provided a best fit to the experimental data under a number of flow geometries. Values for K_c of approximately 0.43 and K_η of 0.65 provided an excellent fit to their experimental concentration profiles in concentrated Couette flow. As well, it was reasoned that the ratio of K_c to K_η can never exceed 1. This ensures particles always migrate down a shear rate gradient. Increasing the ratio has the effect of dramatically increasing the steady concentration gradient across the domain. Leighton and Acrivos (1987a) also proposed values for

similar coefficients by comparison with experimental results in their paper. The results are similar to those obtained by Phillips et al. (1992).

Ideally both parameters would be independent of a, ϕ and $\dot{\gamma}$. However, they should also be independent of the flow geometry and particle density. Other researchers (Tetlow et al., 1998, Rao et al., 2002, Lam et al., 2004) have shown that they are not completely independent of the particle volume fraction. Phillips et al. (1992) admit that due to the sensitivity of the results to the ratio of K_c to K_η that the parameters may in fact be weak functions of local concentration.

Rao et al. (2002) investigated the effects of neutrally buoyant particles in a slow flowing, shear thinning (Carreau model) fluid. Particle migration was due to gradients in shear rate, concentration and viscosity, and they suggested a normal stress correction for non-Newtonian fluids when using the Phillips model because of the anisotropy of non-Newtonian flows. Their results led them to conclude that the Phillips model without normal stress corrections may be fundamentally inadequate for simulating flow in non-Newtonian fluids. Their total flux equation and the proposed values for the self diffusivity coefficients are detailed below:

$$J_s = -\left(\phi D_\phi \nabla\left(\dot{\gamma}\phi\right) + \phi^2 \dot{\gamma} D_\mu \nabla \ln \mu\right) \tag{4.22a}$$

$$D_\phi = 1.4\phi D_\mu \tag{4.22b}$$

$$D_\mu = 0.62a^2 \tag{4.22c}$$

Lam et al. (2004) investigated particle migration in Poiseuille flow of nickel powder injection moldings. They also investigated the effects of a shear thinning carrier fluid which they fit with the non-Newtonian Cross model. They employed the Krieger relative viscosity equation (Equation 2.40a). Their resulting best fit values for the Phillips model adjustable parameters are shown in Equations 4.23 through 4.25.

Power Law Model:

$$K_c = 0.32 \tag{4.23a}$$

$$K_\eta = 0.65 \tag{4.23b}$$

$$K_c / K_\eta = 0.49 \tag{4.23c}$$

Cross Model:

$$K_c = 0.33 \tag{4.24a}$$

$$K_\eta = 0.65 \tag{4.24b}$$

$$K_c / K_\eta = 0.51 \tag{4.24c}$$

Newtonian Model: $$K_c / K_\eta = 0.66 \tag{4.25}$$

All of the above coefficients are in close agreement with what Phillips et al. (1992) determined from their experimental study. Their simulations produced concentration profiles for pressure-driven flows, where solids migration was from the pipe walls to the pipe center. They found that the non-Newtonian, shear thinning behaviour enhanced particle migration from regions of high shear rate to regions of low shear rate

Tetlow et al. (1998) performed experiments and modeling on particle migration in Newtonian fluids for creeping flows in the annular space of a wide gap Couette, concentric cylinder apparatus. They found that the diffusivity should scale with a^3 and not a^2 as shown by Phillips model. They also determined the optimum tuning coefficients for their numerical model based on experimental data. They found that the coefficients K_c and K_η should not be constant but rather slight functions of concentration. Their best-fit ratio of the tunable parameters is shown in Equation 4.26.

$$\frac{K_c}{K_\eta} = 0.01042\bar{\phi} + 0.1142 \tag{4.26}$$

The coefficient $\bar{\phi}$ represents the average global volumetric concentration of solids. Tetlow et al. (1998) also noted that the nature of the migration phenomenon suggest that the steady state concentration profiles develop more quickly for larger particles and that particle radius has little influence on the steady state concentration profile. Experimentally, they observed a small drop in concentration near the outer cylinder wall followed by a sharp increase that is not predicted by the Phillips model. This is likely due to the limitation of how close a particle center can be to the wall which is not accounted for in the Phillips model. Tests performed with larger particles indicated noticeable concentration oscillation near the outer cylinder wall.

The concentration dependence of the adjustable parameters shown by Tetlow et al. (1998) in Equation 4.26 is determined by a best fit comparison of simulation results with their experimental

data. In order to limit the number of empirical dependencies included in the numerical model of this study, values of 0.4 and 0.6 for K_c and K_η, respectively, have been used in the simulations. These values are the best fit parameters of the original Phillips model.

4.6. Scalar Model Transport Equation

The Phillips model with a sedimentation flux is expressed below in both the Lagrangian (Equation 4.27) and Eulerian (Equation 4.28) reference frames. In this study the Eulerian reference frame will be employed. The effective flux resulting from Brownian motion has not been included.

Lagrangian: $$\frac{\partial \phi}{\partial t} = -\nabla \cdot \left(N_c + N_\eta + N_s \right) \tag{4.27}$$

Eulerian: $$\frac{D\phi}{Dt} = -\nabla \cdot \left(N_c + N_\eta + N_s \right) \tag{4.28a}$$

$$\frac{\partial \phi}{\partial t} + v \cdot \nabla \phi = -\nabla \cdot \left(N_c + N_\eta + N_s \right) \tag{4.28b}$$

$$\frac{\partial \phi}{\partial t} + u_x \frac{\partial \phi}{\partial x} + u_y \frac{\partial \phi}{\partial y} + u_z \frac{\partial \phi}{\partial z} = -\nabla \cdot \left(N_c + N_\eta + N_s \right) \tag{4.28c}$$

This model is only valid for predicting particle migration normal to the shearing surface in shear flows. The elimination of the possibility of particles overlapping is accounted for by the inclusion of a maximum packing concentration in the relative viscosity equation (Equation 2.40d and Equation 2.41). Substitution of the fluxes from Equations 4.14a, 4.15a and 4.19a produces the complete scalar transport equation shown in Equation 4.29a.

$$\frac{\partial \phi}{\partial t} + u_x \frac{\partial \phi}{\partial x} + u_y \frac{\partial \phi}{\partial y} + u_z \frac{\partial \phi}{\partial z} = -\nabla \cdot \left[-K_c a^2 \left(\phi^2 \nabla \dot{\gamma} + \phi \dot{\gamma} \nabla \phi \right) - K_\eta a^2 \dot{\gamma} \phi^2 \frac{1}{\eta} \frac{d\eta}{d\phi} \nabla \phi + K_s a^2 \phi \; f(\phi) \vec{g} \right] \tag{4.29a}$$

A complete expansion of the shorthand equation above in Cartesian coordinates is shown in Equation 4.29b.

$$\frac{\partial \phi}{\partial t} + u_x \frac{\partial \phi}{\partial x} + u_y \frac{\partial \phi}{\partial y} + u_z \frac{\partial \phi}{\partial z} = K_c a^2 \left[\frac{\partial}{\partial x} \left(\phi^2 \frac{\partial \dot{\gamma}}{\partial x} + \phi \dot{\gamma} \frac{\partial \phi}{\partial x} \right) + \frac{\partial}{\partial y} \left(\phi^2 \frac{\partial \dot{\gamma}}{\partial y} + \phi \dot{\gamma} \frac{\partial \phi}{\partial y} \right) + \frac{\partial}{\partial z} \left(\phi^2 \frac{\partial \dot{\gamma}}{\partial z} + \phi \dot{\gamma} \frac{\partial \phi}{\partial z} \right) \right]$$

$$+ K_\eta a^2 \left[\frac{\partial}{\partial x}\left(\dot{\gamma}\phi^2 \frac{1}{\eta}\frac{d\eta}{d\phi}\frac{\partial \phi}{\partial x}\right) + \frac{\partial}{\partial y}\left(\dot{\gamma}\phi^2 \frac{1}{\eta}\frac{d\eta}{d\phi}\frac{\partial \phi}{\partial y}\right) + \frac{\partial}{\partial z}\left(\dot{\gamma}\phi^2 \frac{1}{\eta}\frac{d\eta}{d\phi}\frac{\partial \phi}{\partial z}\right)\right]$$

$$- K_s a^2 \left[\frac{\partial}{\partial x}\left(\phi\, f(\phi) g_x\right) + \frac{\partial}{\partial y}\left(\phi\, f(\phi) g_y\right) + \frac{\partial}{\partial z}\left(\phi\, f(\phi) g_z\right)\right] \qquad (4.29b)$$

However, it was noted earlier that the flow is assumed to be fully developed in this study. Therefore, the convective terms can be dropped from the formulation and the scalar transport equation can be expressed as:

$$\frac{\partial \phi}{\partial t} = -\nabla \cdot \left[-K_c a^2 \left(\phi^2 \nabla \dot{\gamma} + \phi \dot{\gamma} \nabla \phi \right) - K_\eta a^2 \dot{\gamma}\phi^2 \frac{1}{\eta}\frac{d\eta}{d\phi}\nabla \phi + K_s a^2 \phi\, f(\phi)\vec{g}\right] \qquad (4.29c)$$

The scalar transport model equation can be reduced to represent variation in one dimension (y-wise), since longitudinal concentration gradients are of the order of 1% of the vertical gradients (Jobson and Sayre, 1970). In addition, the coarse particles are assumed to be monomodal spheres which permits the particle radius term, a^2, to be taken outside of the partial derivative terms. The final form of the scalar transport equation employed in this study is shown in Equation 4.30.

$$\frac{\partial \phi}{\partial t} = K_c a^2 \frac{\partial}{\partial y}\left(\phi^2 \frac{\partial \dot{\gamma}}{\partial y} + \phi \dot{\gamma}\frac{\partial \phi}{\partial y}\right) + K_\eta a^2 \frac{\partial}{\partial y}\left(\dot{\gamma}\phi^2 \frac{1}{\eta}\frac{d\eta}{d\phi}\frac{\partial \phi}{\partial y}\right) - K_s a^2 \frac{\partial}{\partial y}\left(\phi\, f(\phi) g_y\right) \qquad (4.30)$$

4.7. Supplementary Equations

Fluids which exhibit Bingham behaviour are rheologically modeled by two parameters, a yield stress (τ_y) and a plastic viscosity (μ_P). The two parameters together can be used to generate a relationship for the apparent viscosity of the fluid presented in Equation 2.53. The apparent viscosity is not constant over the domain but rather is a function of the local shear rate. A plot of the shear stress versus rate of shear strain relationship for a Bingham fluid is shown below in Figure 4.2.

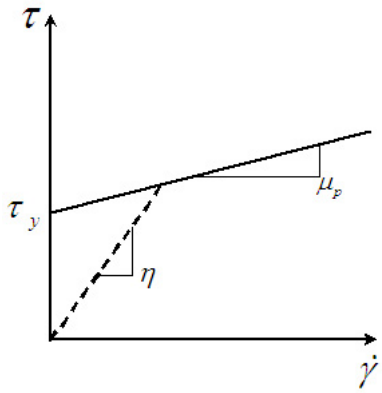

Figure 4.2: Plot of shear stress versus time rate of shear strain for a Bingham fluid

One can see that the plastic viscosity is the tangent slope of the shear stress versus rate of shear strain curve, while the apparent viscosity is a secant slope. If one considers the rheogram of a Bingham fluid shown in Figure 4.2, two important relations arise in the limits when the rate of shear strain approaches zero and infinity.

$$\lim_{\dot{\gamma}\to\infty} \eta = \mu_P \qquad \text{(high shear rates)} \qquad (4.31a)$$

$$\lim_{\dot{\gamma}\to 0} \eta = \infty \qquad \text{(low shear rates)} \qquad (4.31b)$$

The first limit is not physically significant since the flow will become turbulent before $\dot{\gamma}$ approaches infinity. A method for modeling this case can be found in Bartosik et al. (1997). However, the second limit is of significance in this study. As can be seen in Figure 4.2, as the shear rate approaches zero the value of the apparent viscosity approaches infinity. Therefore the Bingham fluid model becomes discontinuous at low shear rates. To account for this discontinuous behaviour, the biviscosity approach proposed by Beverly and Tanner (1992) will be implemented to model the behaviour of Bingham fluids numerically. This method divides the discontinuous Bingham model into two continuous functions as shown in Figure 4.3.

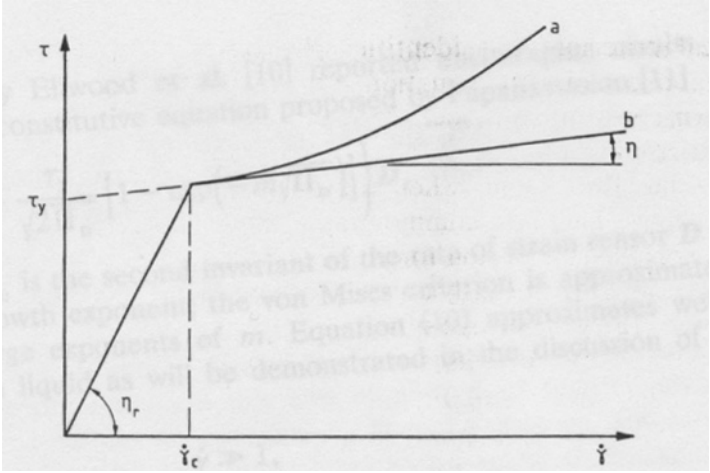

Figure 4.3: One dimensional yielding response for (a) a modified Herschel-Bulkley fluid; (b) a Bingham fluid, where τ_y is the yield stress, η the plastic viscosity and η_r the "unyielded" viscosity. $\dot{\gamma}_c$ is the critical shear rate in the biviscosity model (Beverly and Tanner, 1992)

The biviscosity model of Beverly and Tanner (1992) can be used to numerically analyze the three-dimensional behaviour of Bingham plastic flow. Bingham fluids possess a yield stress which must be exceeded before deformation can occur. The time rate of deformation is proportional to the amount that the shear stress exceeds the yield stress. According to von Mises criterion (Beverly and Tanner, 1992) shown in Equation 4.32, a material flows and deforms significantly only when the second invariant of the stress tensor exceeds the yield stress, otherwise the material behaves like a strained solid.

$$\tau_{ij}\tau_{ij} > 2\tau_y^2 \tag{4.32}$$

The basis of the biviscosity model (Beverly and Tanner, 1992) is that at low shear rates, the rheology of the Bingham fluid is assumed to behave as a viscous Newtonian fluid with a viscosity which is orders of magnitude larger than the plastic viscosity (i.e. 1000 to 10000). However, at higher shear rates the apparent or effective viscosity of the fluid is a function of shear rate and is determined based on the constitutive rheological equation of the Bingham fluid (Equations 2.52 and 2.53). This is the essence of the biviscosity model developed by the combined efforts of Milthorpe and Tanner (1983), O'Donovan and Tanner (1984) and Beverly and Tanner (1989). In this way, the biviscosity model provides a smooth and continuous Bingham flow curve.

An alternative model to the biviscosity model has been proposed by Papanastasiou (1987) where an exponential decay parameter, m, is used to relax the viscosity at low shear rates producing a smooth transition from a state of infinite viscosity to a yielding viscosity. Although the equation does not reduce exactly to the Bingham model, it has been found to provide accurate approximations above the critical shear rate criterion. This is shown in Equation 4.33:

$$\eta = \mu_P + \frac{\tau_y}{\left|\sqrt{\frac{1}{2}(\Delta:\Delta)}\right|}\left[1-\exp\left(-m\left|\sqrt{\tfrac{1}{4}(\Delta:\Delta)}\right|\right)\right] \tag{4.33}$$

Since the biviscosity model is simpler, and a convenient and reliable method of numerically predicting the behaviour of materials with yield stresses, providing one chooses an appropriate value for the reference viscosity, it has been chosen for this investigation. Applying the biviscosity model of Beverly and Tanner (1992) at low shear rates, where in fact no-shear should occur, the apparent viscosity for a one-dimensional problem can be calculated by using the following relation:

$$\eta = \text{minimum}\left(\frac{\tau_y}{\dot{\gamma}}, A\mu_P\right) + \mu_P \tag{4.34a}$$

where

$$\dot{\gamma} = \left|\frac{\partial u}{\partial y}\right| = \text{shear rate} \tag{4.34b}$$

and

A = low shear rate region biviscosity model multiplier

When coarse solids are added to the mixture, the calculation of a total effective viscosity becomes more difficult. Hill (1996) reasoned that the coarse particle concentration would similarly affect the plastic viscosity as it would a Newtonian fluid viscosity, since both terms are associated with the viscous nature of the flow. However, he reasoned that no physical justification exists for scaling the yield stress by the coarse particle concentration since it is due to fine particle flocculation. Recent communication, (Gillies, 2006) has shown that the coarse particle concentration can have an important effect which results in an increase in both the Bingham plastic viscosity and yield stress values of the final mixture in pipeline flows. However, no

relationship exists in the literature yet to quantify this effect. It is for this reason, the effect of concentration on the yield stress will be assumed to be negligible in this study.

Instead of directly scaling the Bingham apparent viscosity with the relative viscosity equation, the Bingham apparent viscosity will be split into a shear effect and a concentration effect in this study. The shear effect incorporates the Bingham yield stress of the carrier fluid. This follows the approach used by Hill (1996) where only the Bingham plastic viscosity of the carrier fluid was scaled by the concentration dependent relative viscosity when calculating the effective mixture viscosity. The yield stress was assumed to be unaffected by the presence of coarse particles (Lalli and Mascio, 1997). Therefore the mixture viscosity can be expressed by the following equation:

$$\eta = \eta_{shear} + \eta_{conc} \tag{4.35a}$$

The apparent viscosity equation, including the effect of solids concentration on the plastic viscosity, is presented in Equation 4.35b.

$$\eta = \text{minimum}\left(\frac{\tau_y}{\dot{\gamma}}, A\mu_P\right) + \mu_P \eta_r(\phi) \tag{4.35b}$$

Thus one can see that a true biviscosity approach is not employed. Only the shear effect of the viscosity is limited by the biviscosity model. However, one can see that the shear effect is often the dominating factor in the equation. The concentration effect is small for dilute systems and only becomes of the same order of magnitude as the shear effect when the local concentration approaches the maximum packing concentration.

The relative viscosity equation according to Schaan (2001) (Equation 2.40d) is considered in this study. Both the relative viscosity and hindrance function are explicit functions of the local particle concentration. The derivatives of both the hindrance function and the relative viscosity equation with respect to coarse solids concentration are detailed below:

$$\frac{d\eta_r}{d\phi} = 2.5 + 2 \cdot 0.16\lambda \frac{d\lambda}{d\phi} \tag{4.36}$$

where

$$\frac{d\eta}{d\phi} = \frac{d}{d\phi}\left(\eta_{shear} + \eta_{conc}\right) \tag{4.37a}$$

$$\frac{d\eta}{d\phi} = \mu_P \frac{d\eta_r}{d\phi} \tag{4.37b}$$

$$\frac{d\lambda}{d\phi} = \frac{\lambda^2}{3\phi}\left(\frac{\phi_{\max}}{\phi}\right)^{1/3} \tag{4.37c}$$

4.8. Related Modeling Investigations

Seifu et al. (1994) applied the Phillips model to calculate the viscous dissipation rate for four different unidirectional flows of concentrated suspensions of neutrally buoyant spheres. The four different flows were:

1. Couette flow between concentric cylinders
2. Pressure-driven Poiseuille flow in a cylindrical tube
3. Couette flow between concentric cylinders with a narrow gap that varies with the cylinder height
4. Flow in the space between rotating and stationary parallel discs in close proximity

Seifu (1994) determined that shear-induced diffusion occurs parallel to the velocity gradient in flows (1) and (2). These are the flows of interest in this study. However, in flows (3) and (4) particles migrate normal to the dominant component of the velocity gradient showing a limitation of the Phillips model. In all cases the steady state dissipation rate was lower than the initial uniform concentration dissipation rate. Particles migrate from regions of high shear, where viscous dissipation occurs, to regions of low shear.

Hampton et al. (1997) studied the migration of neutrally buoyant spheres in slow pressure driven flows in circular conduits. Using a non-intrusive NMR (Nuclear Magnetic Resonance) measurement technique they produced high quality concentration distribution results. Their results showed that steady state profiles are independent of particle size (a/R) but also saw that the Phillips model performed poorly at low concentrations and that shear-induced migration models produced poor results at the pipe walls. However, the Phillips model did provide accurate

estimates in the core of the flow at three bulk concentrations and two particle sizes. They also observed that smaller particles resulted in a much slower profile development but recommended a particle radius to pipe radius ratio of $a/R > 0.02$ to satisfy the continuum assumption. They also noted that continuum models are not able to predict particle-level phenomena such as the formation of particle structures or phase lags (slip between solids and fluid) which is a deficiency in the modeling technique.

Hampton et al. (1997) also noticed that particles migrated to the center of the flow which results in a blunting of the velocity profile. They showed that the velocity profile developed more quickly than the concentration distribution and was not sensitive to small changes in concentration. They recommended concentration dependence effects on the model parameters as well as three body (or more) particle collision effects be investigated. As well, particle shape and non-Newtonian behaviour should be the focus of future work.

More recently, researchers have been interested in the effects of normal stress on particle migration in laminar flows. Morris and Boulay (1999) investigated the role of the normal stress in curvilinear flows. In their study, the total overall effective viscosity is split into a shear viscosity and a normal stress viscosity. For Newtonian carrier fluids, they observed that the normal stress viscosity vanished as the concentration approached zero. They felt that the anisotropy of the normal stress in non-Newtonian flows is associated with the presence of particles. The normal stress is responsible for the cross-stream flux of particles since particles migrate due to a normal stress on the particle. They concluded that the inclusion of a normal stress term in a rheological model could help to properly address particle migration in curvilinear flows.

Buyevich (1996) attempted to develop an all inclusive model which incorporated the shear-induced diffusion effects of previous researchers. He also expanded and incorporated mechanisms which are not accounted for in the Phillips model. He investigated particle distributions of suspensions in shear flows and attempted to develop a model that accounts for all normal stresses that originate from random particle fluctuations. In addition, he also included the joint effect of thermal and shear-induced fluctuations. The model also incorporates a dispersed phase and a continuous phase momentum equation. However, in order to account for all of the interactions, much more empirical modeling was required to close the resulting set of equations. His model is much more complicated than the Phillips model, and although it may be more

appropriate in more complex geometries, it produced similar results in a concentric cylinder Couette flow (Buyevich, 1996).

Zarraga and Leighton (2001b) presented an exhaustive set of normal stresses for dilute suspensions of hard spheres. In their paper they stated:

> In a suspension of rigid spheres undergoing low Reynolds number shear, stresses are produced within the fluid as a result of the inability of the rigid particles to deform with the flow. If the particles are perfectly smooth and Brownian motion and non-hydrodynamic forces are negligible, the particle interactions are symmetric and reversible so that no net normal stresses are generated within the fluid. However, when particle interact repulsively…the interactions are no longer symmetric and a net nonisotropic stress field within the suspension results.

This approach is much more complex than that employed in the Phillips model, but it accounts for the anisotropy of the flow. Zarraga and Leighton (2001b) only derived expressions applicable to dilute systems and found that, to a first order approximation, the extra stresses induced are only dependent on the gradient in the plane of shear. Although their results seem to overpredict those of the Phillips model, they propose that this type of modeling would perform better in concentrated systems.

Recently, Lalli and Mascio (1997), Lalli et al. (2005) and Lalli et al. (2006) have attempted to develop an equation which incorporates shear-induced diffusion effects to model sediment transport in coastal and river engineering problems. The limited literature in the area is evident from their statement "Transport of particles in a flowing current is one of the most important and least understood problems in fluid dynamics". Their model accounts for the slurry mixture as both a Newtonian fluid and a Bingham fluid in dilute and concentrated regions of the suspension respectively. The mixture is modeled as a Bingham fluid in concentrated regions to account for the effect of a packed bed and the fact that shear flow cannot occur if the material is closely packed (i.e. volumetric dilatancy, Reynolds, 1885). Closure of the problem is based on sedimentation and shear-induced self-diffusion effects. However, no model simulation results are presented in the papers. This raises doubts on the validity of the two fluid approach of their model.

The Phillips model with the inclusion of a sedimentation flux is only applicable for flows above the settled stationary bed condition. It is not applicable for situations in which particles are being

transported at the maximum packing concentration. The model is not capable of predicting a sliding bed condition. Even though the model converges to a solution near the maximum packing condition, once it reaches this state the model and method are no longer applicable as it only applies to fluid conditions. At the settled bed condition, the mixture has an infinite viscosity resulting in no flow of the mixture in this region.

The model is also not capable of predicting Coulombic friction effects which makes it inappropriate for use with significant bed loads. However, it can be used to predict when the onset of deposition will occur, which is of interest since it is inefficient to operate below the critical deposition condition. Industry is not interested in transporting slurries with significant bed loads due to the large energy costs associated with this condition as well as the wear that occurs on the transport equipment.

4.9. Finite Volume Method

The flow problem considered in this investigation was modeled using the Finite Volume Method (FVM). A detailed description of the method is given in Patankar (1980). The related computer code developed in this study is presented in Appendix A. The finite volume method involves integrating the governing partial differential equations with respect to time and space over a specific control volume (cell). Integrating the differential equations, rather than applying finite differences approximations, helps to ensure that a physically realistic solution is obtained. Numerical truncation errors are also reduced through the use of this approach. Numerical methods that involve integration rather than differentiation are likely to be more accurate. An example of the integration that is performed in the finite volume methodology is shown below in Equation 4.38.

$$\int_t^{t+\Delta t}\int_V \phi dV dt = \int_t^{t+\Delta t}\int_z^{z+\Delta z}\int_y^{y+\Delta y}\int_x^{x+\Delta x} \phi dx dy dz dt \tag{4.38}$$

The above integration has been performed using Cartesian coordinates. However, the finite volume method is not limited to a rectangular coordinate system. It can also be performed in curvilinear coordinates by using the Jacobian. The Jacobian is a matrix of partial derivatives relating each Cartesian coordinate to the transformed coordinate. A Jacobian transformation from

the (x_1, x_2, x_3) rectangular coordinates to (y_1, y_2, y_3) coordinates is shown below (Spiegel, 1968):

$$\int_V \phi dV = \int_{x_3}^{x_3+\Delta x_3} \int_{x_2}^{x_2+\Delta x_2} \int_{x_1}^{x_1+\Delta x_1} \phi dx_1 dx_2 dx_3 = \int_{y_3}^{y_3+\Delta y_3} \int_{y_2}^{y_2+\Delta y_2} \int_{y_1}^{y_1+\Delta y_1} \phi |J| dy_1 dy_2 dy_3 \tag{4.39}$$

where $|J|$ is the determinant of the Jacobian:

$$|J| = \left| \frac{\partial x_i}{\partial y_j} \right| = \left| \frac{\partial (x_1, x_2, x_3)}{\partial (y_1, y_2, y_3)} \right| \tag{4.40a}$$

and

$i = 1,\ 2,\ 3$ row

$j = 1,\ 2,\ 3$ column

$$|J| = \begin{vmatrix} \frac{\partial x_1}{\partial y_1} & \frac{\partial x_1}{\partial y_2} & \frac{\partial x_1}{\partial y_3} \\ \frac{\partial x_2}{\partial y_1} & \frac{\partial x_2}{\partial y_2} & \frac{\partial x_2}{\partial y_3} \\ \frac{\partial x_3}{\partial y_1} & \frac{\partial x_3}{\partial y_2} & \frac{\partial x_3}{\partial y_3} \end{vmatrix} \tag{4.40b}$$

The determinant is calculated by:

$$|J| = (\mathrm{i} = 1, 2, \ldots \mathrm{n}) \sum_{\mathrm{j}=1}^{\mathrm{m}} a_{ij} A_{ij} = (\mathrm{j} = 1, 2, \ldots \mathrm{m}) \sum_{\mathrm{i}=1}^{\mathrm{n}} a_{ij} A_{ij} \tag{4.40c}$$

where

$$A_{ij} = (-1)^{i+j} \left| a_{ij} - row_i - col_j \right|_{(n-1)x(m-1)} \tag{4.40d}$$

However, since Cartesian coordinates have been employed in this study, the determinant of the Jacobian is equal to unity and no transformation is required.

One can now perform a term-by-term integration on the conservation of momentum equation (Equation 4.9) as well as the scalar solids transport equation (Equation 4.30). Fitting the Phillips model scalar transport equation to the general form of the scalar transport equation presented in Equation 4.12 yields the following relationships for the diffusivity and source term:

$$\Gamma = K_c a^2 \phi\dot{\gamma} + K_\eta a^2 \dot{\gamma}\phi^2 \frac{1}{\eta}\frac{d\eta}{d\phi} = a^2\phi\dot{\gamma}\left(K_c + K_\eta \phi \frac{1}{\eta}\frac{d\eta}{d\phi}\right) \tag{4.41}$$

$$S_\phi = K_c a^2 \frac{\partial}{\partial y}\left(\phi^2 \frac{\partial \dot{\gamma}}{\partial y}\right) - K_s a^2 \frac{\partial}{\partial y}\left(\phi\ f(\phi) g_y\right) \tag{4.42}$$

The governing partial differential equations for this transport problem are both non-linear (in velocity and concentration) and parabolic (in time). The momentum equation is non-linear in velocity since the effective viscosity of the mixture is a function of both concentration and the shear rate (velocity gradient). The scalar solids transport equation is non-linear in concentration. This is shown explicitly in the terms containing ϕ, ϕ^2 and the gradient of the concentration ($\nabla\phi$) as well as the terms containing effective viscosity (η) which is also a function of local solids concentration.

The geometry in which the problem is being solved is a one-dimensional open channel. Since the flow has been assumed to be uniform as well as fully developed, only a single coordinate direction needs to be considered with respect to the velocity and concentration distributions (y-wise). Uniform, cell centered grids composed of 50 nodes were defined once the depth of flow was specified. The grids were examined to determine the potential distributions of a variety of fluid flow parameters relevant to the coarse solids transport in non-Newtonian carrier fluids.

The term-by-term integration generates N algebraic equations for the velocity and N algebraic equations for the concentration, where N is the number of nodes in the grid. There are N interior nodes (one at the center of each cell) for the solution mesh. A cell-centered approach (node is located between the cell faces at the center point of the control volume) has been used with both techniques. Schematics of the control volumes and the solution grid are shown in Figures 4.4 and 4.5 respectively. The diagrams represent the implementation of a uniform grid. Note that fictitious nodes have been included at the domain boundaries. Their purpose will be described later on in Section 4.13.

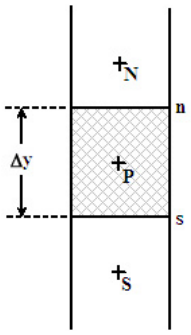

Figure 4.4: Schematic illustration of a Cartesian coordinate system control volume

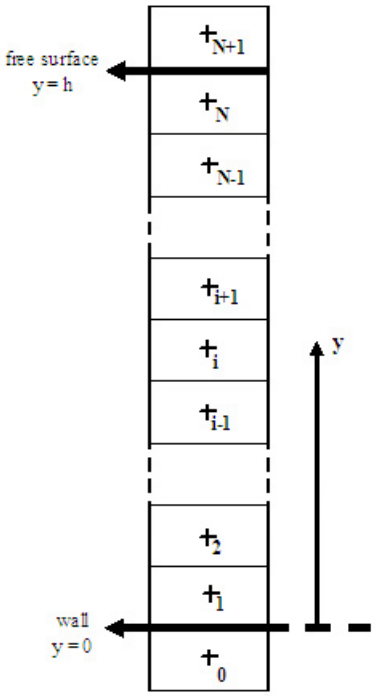

Figure 4.5: Schematic illustration of a finite volume method Cartesian grid

In this study, the dynamic solution of the unsteady parabolic problem is not of interest. The transient terms were retained in the formulation to relax or accelerate the numerical technique to assist in obtaining the final steady state solution. Since the parabolic transient terms are included in the solution, a time interpolation scheme must be implemented. A fully implicit approach was utilized. This approach has been shown to be the most stable of all of the methods (Patankar, 1980). The implicit time scheme is shown in more detail below:

$$\int_0^1 \phi dt \approx \left[\phi^0 + f\left(\phi^1 - \phi^0\right)\right]\Delta t \tag{4.43}$$

where

$f = 0$	explicit	(4.44a)
$0 < f < 1$	semi-implicit	(4.44b)
$f = 1$	implicit	(4.44c)

In Equation 4.43, the superscripts 0 and 1 denote the value of ϕ at the previous and current time steps respectively. A fully implicit assumption ($f = 1$), produces the following formulation:

$$\int_{t}^{t+\Delta t} \phi_P dt = \int_{0}^{1} \phi_P dt \approx \phi_p^1 \Delta t \tag{4.45}$$

4.9.1. Navier Stokes Equation (z-wise)

The effective mixture viscosity has been retained within the partial derivative of Equation 4.9 since a non-Newtonian fluid is being considered. The viscosity is not a constant value but rather is a function of the current velocity and concentration distribution. The dependence of the viscosity on the local shear rate results in a non-linear equation which requires an iterative solution.

The substitution, $u_z = u$, is made to simplify the derivation since the flow is one-dimensional. In order to apply the finite volume method to the equation, it must be integrated in space and time on a term-by-term basis. Referring to Figure 4.4, each cell volume can be integrated from the north face to the south face in the y-wise direction.

Since no longitudinal (transverse) or axial variations of the velocity are being considered in this study, the values of Δx and Δz can be assumed to be unity. The subscript ' n ' denotes the north face of the cell while ' s ' denotes the south face of the cell. The subscript ' P ' denotes the specific cell being considered. The subscript ' N ' denotes the cell to the north of the cell being considered. The subscript ' S ' denotes the cell to the south. The values of u and ρ are assumed to be constant within a given cell volume.

Applying the integration scheme presented in Equation 4.46 to each term of Equation 4.9:

$$\int_y^{y+\Delta y} \phi dy = \int_s^n \phi dy \tag{4.46}$$

Transient Term: $\int_0^1 \int_z^{z+\Delta z} \int_s^n \int_x^{x+\Delta x} \rho \frac{\partial u}{\partial t} dxdydzdt = \rho \Delta x \Delta y \Delta z \left(u_P^1 - u_P^0 \right)$ (4.47a)

Gravitational Term: $\int_0^1 \int_z^{z+\Delta z} \int_s^n \int_x^{x+\Delta x} \rho g_z dxdydzdt = \rho g_z \Delta x \Delta y \Delta z \Delta t = K \Delta x \Delta y \Delta z \Delta t$ (4.47b)

Diffusive Term: $\int_0^1 \int_z^{z+\Delta z} \int_s^n \int_x^{x+\Delta x} \frac{\partial}{\partial y} \left(\eta \frac{\partial u}{\partial y} \right) dxdydzdt = \left[\left(\eta \frac{\partial u}{\partial y} \right)_n - \left(\eta \frac{\partial u}{\partial y} \right)_s \right] \Delta x \Delta z \Delta t$ (4.47c)

A finite difference approximation will be used for the diffusive velocity gradient terms at the faces of the control volume:

$$\left. \frac{\partial u}{\partial y} \right|_n \approx \beta_u \left(\frac{u_N - u_P}{y_N - y_P} \right) \tag{4.48a}$$

$$\left. \frac{\partial u}{\partial y} \right|_s \approx \beta_u \left(\frac{u_P - u_S}{y_P - y_S} \right) \tag{4.48b}$$

The diffusive gradient constant β_u is assumed to be unity for most diffusive problems. However, it has been retained in the formulation in this study for the sake of completeness. The viscous term can be further simplified to:

$$\left[\left(\eta \frac{\partial u}{\partial y} \right)_n - \left(\eta \frac{\partial u}{\partial y} \right)_s \right] \Delta x \Delta z \Delta t \approx \left[\beta_u \eta_n \left(\frac{u_N^1 - u_P^1}{y_N - y_P} \right) - \beta_u \eta_s \left(\frac{u_P^1 - u_S^1}{y_P - y_S} \right) - \right] \Delta x \Delta z \Delta t \tag{4.49}$$

Combining all of the integrated terms, dividing all terms by $\Delta x \Delta z \Delta t$, and rearranging yields:

$$a_P^u u_P^1 = a_N^u u_N^1 + a_S^u u_S^1 + b^u \tag{4.50a}$$

where

$$a_P^{u0} = \frac{\rho \Delta y}{\Delta t} \tag{4.50b}$$

$$a_N^u = \frac{\beta_u \eta_n}{y_N - y_P} \tag{4.50c}$$

$$a_S^u = \frac{\beta_u \eta_s}{y_P - y_S} \tag{4.50d}$$

$$a_P^u = a_P^{u0} + a_N^u + a_S^u \tag{4.50e}$$

$$b^u = a_P^{u0} u_P^0 + K\Delta y \tag{4.50f}$$

$$\Delta y = y_n - y_s \tag{4.50g}$$

$$K = \rho g_z \tag{4.50h}$$

Equation 4.50 is the general form of the discrete algebraic equation obtained from applying the finite volume method to the momentum equation. When combined for all of the cells in the domain these equations form a tridiagonal matrix of equations. A number of numerical solution techniques are available for solving this matrix of equations (Rao, 2002; Patankar, 1980). Since the equation is non-linear, a direct solution is not possible. An iterative solution technique, the Thomas Algorithm, is implemented in this study. Iterations are performed with the algorithm to solve the velocity distribution until the velocity field converges.

4.9.2. Scalar Concentration Transport Equation

Equations 4.12, 4.30, 4.41 and 4.42 represent the scalar concentration equation. Following a similar approach to that taken with the z-wise momentum equation, the following equations are obtained from a term-by-term integration over an elemental cell volume:

Transient Term: $$\int_0^1 \int_z^{z+\Delta z} \int_s^n \int_x^{x+\Delta x} \frac{\partial \phi}{\partial t} dxdydzdt = \Delta x \Delta y \Delta z \left(\phi_P^1 - \phi_P^0 \right) \tag{4.51a}$$

Diffusive Term: $$\int_0^1 \int_z^{z+\Delta z} \int_s^n \int_x^{x+\Delta x} \frac{\partial}{\partial y} \left(\Gamma \frac{\partial \phi}{\partial y} \right) dxdydzdt = \left[\left(\Gamma \frac{\partial \phi}{\partial y} \right)_n - \left(\Gamma \frac{\partial \phi}{\partial y} \right)_s \right] \Delta x \Delta z \Delta t \tag{4.51b}$$

Source Term: $$\int_0^1 \int_z^{z+\Delta z} \int_s^n \int_x^{x+\Delta x} S_\phi dxdydzdt = S_\phi \Delta x \Delta y \Delta z \Delta t \tag{4.51c}$$

In the development of Equations 4.51, the value of the source term is assumed constant over the entire cell volume. A finite difference approximation will be used for the diffusive concentration

gradient terms at the faces of the control volume, which is similar in form to the velocity gradient used in the solution of the momentum partial differential equation:

$$\left.\frac{\partial\phi}{\partial y}\right|_n \approx \beta_\phi\left(\frac{\phi_N-\phi_P}{y_N-y_P}\right) \tag{4.52a}$$

$$\left.\frac{\partial\phi}{\partial y}\right|_s \approx \beta_\phi\left(\frac{\phi_P-\phi_S}{y_P-y_S}\right) \tag{4.52b}$$

Once again the diffusive gradient constant β_ϕ has been kept in the formulation for the sake of completeness. The diffusive term can be further simplified to:

$$\left[\left(\Gamma\frac{\partial\phi}{\partial y}\right)_n-\left(\Gamma\frac{\partial\phi}{\partial y}\right)_s\right]\Delta x\Delta z\Delta t \approx \left[\beta_\phi\Gamma_n\left(\frac{\phi_N^1-\phi_P^1}{y_N-y_P}\right)-\beta_\phi\Gamma_s\left(\frac{\phi_P^1-\phi_S^1}{y_P-y_S}\right)-\right]\Delta x\Delta z\Delta t \tag{4.53}$$

Once again combining all of the terms and dividing by $\Delta x\Delta z\Delta t$ yields:

$$a_P^\phi\phi_P^1 = a_N^\phi\phi_N^1 + a_S^\phi\phi_S^1 + b^\phi \tag{4.54a}$$

where

$$a_P^{\phi 0} = \frac{\Delta y}{\Delta t} \tag{4.54b}$$

$$a_N^\phi = \frac{\beta_\phi\Gamma_n}{y_N-y_P} \tag{4.54c}$$

$$a_S^\phi = \frac{\beta_\phi\Gamma_s}{y_P-y_S} \tag{4.54d}$$

$$a_P^\phi = a_P^{\phi 0} + a_N^\phi + a_S^\phi \tag{4.54e}$$

$$b^\phi = a_P^{\phi 0}\phi_P^0 + S_\phi\Delta y \tag{4.54f}$$

$$\Delta y = y_n - y_s \tag{4.54g}$$

Substitution of the values of Γ and S_ϕ into Equations 4.54c to 4.54f yields:

$$a_P^{\phi 0} = \frac{\Delta y}{\Delta t} \tag{4.55a}$$

$$a_N^{\phi} = \frac{\beta_\phi a^2 \phi_n \dot{\gamma}_n}{y_N - y_P}\left(K_c + K_\eta \frac{\phi_n}{\eta_n}\frac{d\eta}{d\phi}\bigg|_n \right) \tag{4.55b}$$

$$a_S^{\phi} = \frac{\beta_\phi a^2 \phi_s \dot{\gamma}_s}{y_P - y_S}\left(K_c + K_\eta \frac{\phi_s}{\eta_s}\frac{d\eta}{d\phi}\bigg|_s \right) \tag{4.55c}$$

$$a_P^{\phi} = a_P^{\phi 0} + a_N^{\phi} + a_S^{\phi} \tag{4.55d}$$

$$b^{\phi} = a_P^{\phi 0}\phi_P^0 + \left[K_c a^2 \frac{\partial}{\partial y}\left(\phi^2 \frac{\partial \dot{\gamma}}{\partial y} \right)_P - K_s a^2 g_y \frac{\partial}{\partial y}\left(\phi\ f(\phi) \right)_P \right] \Delta y \tag{4.55e}$$

$$\Delta y = y_n - y_s \tag{4.55f}$$

Applying a finite difference approximation over the cell from the north face to south face provides a more amenable equation:

$$b^{\phi} = a_P^{\phi 0}\phi_P^0 + \frac{1}{\Delta y}\left[K_c a^2 \left(\phi_n^2 \frac{\partial \dot{\gamma}}{\partial y}\bigg|_n - \phi_s^2 \frac{\partial \dot{\gamma}}{\partial y}\bigg|_s \right) - K_s a^2 g_y \left(\phi_n\ f(\phi_n) - \phi_s\ f(\phi_s) \right) \right] \Delta y \tag{4.56}$$

Preliminary tests indicated that the scalar concentration partial differential equation was stiff. In fact, a small time step was required to obtain a stable, non-oscillatory solution. Since the velocity and concentration equations are solved simultaneously, and are tightly coupled, they must be solved with the same time step. This resulted in a long simulation time.

In order to increase the stability of the scalar concentration solution and decrease the stiffness of the discrete algebraic equations, the source term of the scalar concentration equation was reconfigured. According to Patankar (1980) one advantage of the finite volume method is its ability to implement negative source term linearization. This can be performed when the source term is an explicit function of the conserved variable which is being solved for.

The source term for the scalar concentration equation is highly non-linear. Since the linearization for this problem is not straight-forward, the source term must first be rearranged. There are a number of different methods that can be used to implement a source term linearization (Patankar,

1980). A Taylor Series truncation approximation was employed in this study. For this scalar transport equation, the negative source term slope can be found by applying the chain rule to the original source term (Equation 4.42).

$$S_\phi = S_C + S_P\phi \tag{4.57a}$$

$$\overline{S}_\phi = S_\phi^0 + \left(\frac{\partial S_\phi}{\partial \phi}\right)^0 \left(\phi_P^1 - \phi_P^0\right) = \left[S_\phi^0 - \left(\frac{\partial S_\phi}{\partial \phi}\right)^0 \phi_P^0\right] + \left(\frac{\partial S_\phi}{\partial \phi}\right)^0 \phi_P^1 \tag{4.57b}$$

Therefore, the linearized source term is composed of an explicit component (S_C) and an implicit component (S_P).

$$S_C = S_\phi^0 - S_P\phi_P^0 \tag{4.57c}$$

$$S_P = \left(\frac{\partial S_\phi}{\partial \phi}\right)^0 = K_c a^2 \frac{\partial}{\partial y}\left(2\phi^0 \frac{\partial \dot{\gamma}}{\partial y}\right) - K_s a^2 g_y \frac{\partial}{\partial y}\left(f(\phi^0) + \phi^0 \frac{\partial f(\phi)}{\partial \phi}\bigg|^0\right) \tag{4.57d}$$

Applying a finite difference approximation to the gradients over the cell from the north face to south face results in:

$$S_P = \frac{1}{\Delta y}\left[K_c a^2\left(2\phi_n^0 \frac{\partial \dot{\gamma}}{\partial y}\bigg|_n - 2\phi_s^0 \frac{\partial \dot{\gamma}}{\partial y}\bigg|_s\right) - K_s a^2 g_y\left(f(\phi_n^0) + \phi_n^0 \frac{\partial f(\phi)}{\partial \phi}\bigg|_n^0 - f(\phi_s^0) - \phi_s^0 \frac{\partial f(\phi)}{\partial \phi}\bigg|_s^0\right)\right] \tag{4.57e}$$

Although this method changes the form of the source term, it does not affect the final steady state solution. The concentration values converge at the node of each cell volume under steady state conditions. Therefore, at steady state, $\phi^1 = \phi^0$ for all of the nodes in the domain and the value of the source term and algebraic equation coefficients revert to their original formulation as shown in Equations 4.54, 4.55 and 4.56. The linearization changes the path the solution takes from the initial conditions to the final converged steady state solution. The change in path results in a more stable solution and allows the simulation to be performed at larger time steps, thus reducing the required simulation time.

Applying this new source term manipulation to the discrete equation development presented earlier results in changes to the following coefficients:

$$a_P^{\phi} = a_N^{\phi} + a_S^{\phi} + a_P^{\phi 0} - S_P \Delta y \tag{4.58a}$$

$$b^{\phi} = a_P^{\phi 0} \phi_P^0 + S_C \Delta y \tag{4.58b}$$

The negative slope increases the stability of the solution since it increases the value of the a_P coefficient. The Scarborough stability criteria (Patankar, 1980) requires that the sum of the neighbouring coefficients be less than or equal to the value of the coefficient a_P. This will be discussed in Section 4.12. This approach results in an increase in the value of a_P since the negative slope is subtracted in the equation at each discrete node. The increase in a_P results in a wider band of stability.

4.10. Solution Procedure

The approach used to represent the flow situation considered in this study results in the formulation of two non-linear parabolic, partial differential equations. The equations are linked through the concentration dependence of the mixture viscosity and density. Since the equations are non-linear, an iterative solution technique is required to solve the equations.

As described in the previous sections, the equations can be reduced to a one-dimensional set of discrete algebraic equations for each of the velocity and concentration differential equations. A number of different solution methods, both direct and indirect, are available to solve this set of equations (Rao, 2002; Patankar, 1980). A direct technique is efficient in that it typically only needs to be executed once. Although an indirect or iterative technique may not be as efficient, they are often the only method available to solve complex problems. Due to the non-linear and coupled nature of the equations in this study, a combination of techniques will be applied to solve the equations.

The Thomas Algorithm is an example of a direct technique used to solve tridiagonal matrices (Rao, 2002). The Thomas Algorithm is a line solver. It is particularly useful for cell based systems since it solves the entire line or one-dimensional domain simultaneously in a single step.

It also has the advantage of transmitting boundary condition information across the domain within a given step where an indirect technique can only pass the boundary condition information a maximum of one node per iteration (Patankar, 1980). Because of the advantages of the direct approach, it has been chosen to solve the partial differential equations in this study. It is of the order N in both computation time and storage compared to N^2 and N^3 for the common indirect techniques (Patankar, 1980).

4.11. Tridiagonal Matrix/Thomas Algorithm (TDMA)

Direct line solving techniques can be applied to implicit and semi-implicit problems. They are not required with explicit problems since the terms, which are to be evaluated, are known from the previous time step. Therefore, the direct approach performs only a single set of calculations of the solution domain (for one-dimensional problems) to solve the simultaneous equations. This differs from an iterative technique (Gauss-Seidel or Jacobi iteration) which requires the simultaneous equations to be solved iteratively until convergence is obtained.

Equations 4.59a and 4.59b are the postulated relations for the Thomas Algorithm used in this study (Rao, 2002; Patankar, 1980). In the equations, the subscript '$i+1$' refers to the point north of 'i', and '$i-1$' refers to the point south of 'i'. The variable ϕ refers to the parameter being solved in the equation (velocity (u) or concentration (ϕ)) at the current time step. To keep the equations general, the superscripts associated with the coefficients are not shown.

$$\phi_i = \alpha_i \phi_{i+1} + \beta_i \tag{4.59a}$$

Also expressing the term ϕ_{i-1} in the form of the postulated relation gives:

$$\phi_{i-1} = \alpha_{i-1} \phi_i + \beta_{i-1} \tag{4.59b}$$

Expressing the general algebraic equation in terms of i gives:

$$a_p \phi_i = a_N \phi_{i+1} + a_S \phi_{i-1} + b \tag{4.60}$$

Substituting into the general algebraic equation, rearranging and simplifying results in:

$$\phi_i = \frac{a_N}{a_P - a_S\alpha_{i-1}}\phi_{i+1} + \frac{a_S\beta_{i-1} + b}{a_P - a_S\alpha_{i-1}} \tag{4.61}$$

from which the following relations for α and β are found:

$$\alpha_i = \frac{a_N}{a_P - a_S\alpha_{i-1}} \tag{4.62a}$$

$$\beta_i = \frac{a_S\beta_{i-1} + b}{a_P - a_S\alpha_{i-1}} \tag{4.62b}$$

In this problem the grid consists of $N+2$ control volumes. Of those cells, N are interior and exist within the domain while the outer two nodes are fictitious and exist in order to implement the boundary conditions. The boundary conditions will be detailed in Section 4.13. During the assignment of values for α and β, α_0 and β_0 are determined based on the values of the discrete algebraic equation coefficients at the fictitious node beneath the wall boundary ($i = 0$). Since a_S is equal to zero for both the concentration and velocity boundary conditions at the bottom wall (where $i = 0$), the evaluation of α_{-1} and β_{-1} is not required.

When calculations are being conducted at the top of the domain ($i = N+1$) and the postulated relation (Equation 4.61) is used to calculate velocity or concentration from $i = N+1$ to 0, the value of ϕ_{i+1} (at the fictitious node above the free surface) is required to start the calculation of the variables. When calculations are being performed at $i+1$ the value of ϕ_{i+2} does not exist and therefore the relation for the velocity or concentration at the fictitious node must be calculated using Equation 4.63. At this point, back calculations through all of the nodes can now be completed which results in the solution of the velocity and concentration fields.

$$\phi_{i+1} = \beta_{i+1} \tag{4.63}$$

A total of $N+2$ unknowns exist in the computational grid employed in this study. However, N (number of cells) + 2 (boundary conditions) independent equations are available. Therefore the system is specified and the tridiagonal matrix of algebraic equations results in an $(N+2)$ x $(N+2)$ matrix of coefficients. The matrix relations for the tridiagonal matrix of equations are shown in Equations 4.64a and 4.64b. A schematic of the matrix that exists for both the concentration and velocity equations is provided in Figure 4.6.

$$a_P\phi_P^1 - a_N\phi_N - a_S\phi_S = b \tag{4.64a}$$

$$\overline{\overline{A}}\,\overline{\phi_i} = \overline{b} \tag{4.64b}$$

$$\begin{bmatrix} a_{P,0} & -a_{N,0} & 0 & \dots & \dots & \dots & 0 \\ -a_{S,1} & a_{P,1} & -a_{N,1} & 0 & \dots & \dots & 0 \\ 0 & -a_{S,2} & a_{P,2} & -a_{N,2} & 0 & \dots & 0 \\ \dots & \dots & \dots & \dots & \dots & \dots & \dots \\ 0 & 0 & -a_{S,i} & a_{P,i} & -a_{N,i} & 0 & 0 \\ \dots & \dots & \dots & \dots & \dots & \dots & \dots \\ 0 & \dots & 0 & -a_{S,N-1} & a_{P,N-1} & -a_{N,N-1} & 0 \\ 0 & \dots & \dots & 0 & -a_{S,N} & a_{P,N} & -a_{N,N} \\ 0 & \dots & \dots & \dots & 0 & -a_{S,N+1} & a_{P,N+1} \end{bmatrix} \begin{bmatrix} \phi_{P,0} \\ \phi_{P,1} \\ \phi_{P,2} \\ \dots \\ \phi_{P,i} \\ \dots \\ \phi_{P,N-1} \\ \phi_{P,N} \\ \phi_{P,N+1} \end{bmatrix} = \begin{bmatrix} b_0 \\ b_1 \\ b_2 \\ \dots \\ b_i \\ \dots \\ b_{N-1} \\ b_N \\ b_{N+1} \end{bmatrix}$$

Figure 4.6: Tridiagonal matrix of discrete algebraic equations for an implicit finite volume method formulation

One can see that $\phi_{P,i-1} = \phi_{S,i}$ and that $\phi_{P,i+1} = \phi_{N,i}$. Therefore only a single velocity and concentration array needs be stored for each of the velocity and concentration solvers. The same is true for the other variables and coefficients since a banded matrix is being investigated. A banded matrix is one that consists of non-zero diagonal elements while the remaining elements in the matrix are zero. The reduced storage requirement is one reason why the TDMA algorithm is such an efficient solver.

4.12. Indirect/Iterative Solvers

Indirect and cell based iterative solution techniques, like Gauss-Seidel and Jacobi update, are not as efficient as a direct techniques for banded matrices. Gauss-Seidel is often the method used most frequently since it enforces that updated values are used within an iterative scan of the

domain where Jacobi update uses the values from the previous time iteration. The Gauss-Seidel method requires fewer iterations to meet the same convergence criteria compared to the Jacobi update method (Rao, 2002).

When the matrices are no longer banded an iterative technique becomes more efficient than a direct technique. As well, these methods are only required to solve matrices that arise from implicit and semi-implicit formulations. Unlike a direct technique, which only requires a single sweep of the computational domain to determine the solution field for a given set of coefficients, an iterative or indirect technique requires a number of iterations to determine the solution fields.

An advantage of an iterative solution method over a direct method is the ease at which it can be implemented. The direct technique requires the discrete equations to be reformulated whereas an iterative technique uses the formulation of the discrete algebraic equation resulting from the finite volume analysis. However, indirect techniques are more susceptible to instability. This is a major weakness associated with iterative techniques. The general form of the Scarborough condition (Patankar, 1980) as shown in Equation 4.65a, can be used to determine if a stable solution will be obtained for a given set of discrete equation coefficients. The Scarborough condition applying to the one-dimensional problem investigated in this study is shown in Equation 4.65b.

$$\left|a_P\right| \geq \sum_{neighbours} \left|a_{i,nb}\right| \tag{4.65a}$$

$$\frac{\left|a_N\right| + \left|a_S\right|}{\left|a_P\right|} \leq 1 \tag{4.65b}$$

To determine whether a set of equations can be solved iteratively, one can calculate eigenvalues of the coefficient matrix. This approach is quite involved. An alternative method to determine if a matrix or system of linear equations can be solved is to ensure that the matrix of coefficients is diagonally dominant. This can be determined by ensuring that the Scarborough condition is satisfied at each node. If the condition is not satisfied, an unstable solution will likely result.

To reduce the calculation time required by the iterative solver or improve stability, a technique known as relaxation can be used. With this method, the difference between what a solution predicts for a variable and the value at the previous iteration is scaled and added to the previous

iteration to obtain an updated value. Equation 4.66 details the method that is used to update the variable at each node:

$$\phi_P^{k+1} = \phi_P^k + \omega\left(\phi_P^{k+1/2} - \phi_P^k\right) \tag{4.66}$$

In Equation 4.66, $k+1$ represents the new variable value while k and $k+1/2$ represent the variable value from the previous iteration and the predicted value from the simulation, respectively. Over-relaxation ($1 < \omega < 2$) can be used to greatly reduce the time it takes for a simulation to reach convergence. However, it is possible that stability issues will occur with the use of over-relaxation. Under-relaxation ($0 < \omega < 1$) can be used to slow down a solution and increase stability. If no relaxation is used ($\omega = 1$) a Gauss-Seidel iterative scheme results. For a given problem, the value of ω can be varied to optimize the speed and efficiency at which the solution converges. It has been shown that for values of ω greater than or equal to 2 the solution can become unstable. As well, if ω is set equal to zero, the solution field will remain at the old values and the solution will not advance between iterations.

In this study a direct technique is employed to solve for the velocity and concentration field. However, since the equations are non-linear, a Gauss-Seidel iterative technique is used ($\omega = 1$) to obtain convergence in time with each velocity and concentration field. Once convergence is reached the velocity and concentration arrays are updated and the process is repeated until a steady state solution is obtained.

4.13. Boundary Conditions

In this study the grid has been constructed so that the south and north faces of the top and bottom control volumes lie on the free surface and wall boundary respectively (i.e. imaginary node formulation on domain boundaries). Schematics of the free surface and the wall boundary nodes are shown in Figure 4.7a and 4.7b respectively.

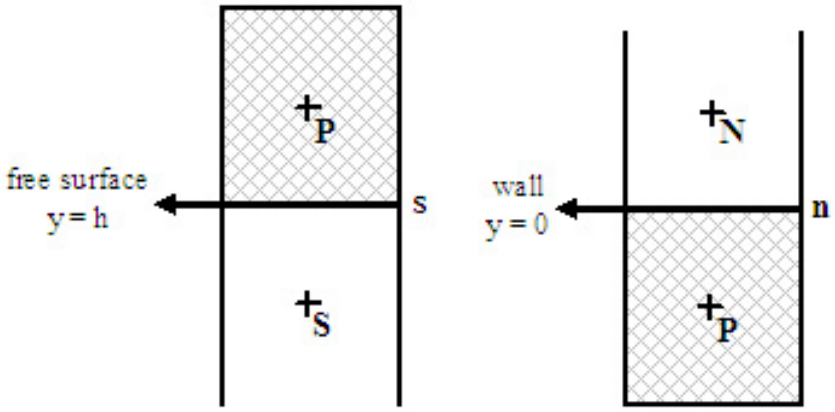

(a) (b)

Figure 4.7: Schematics of the (a) free surface boundary and (b) channel wall boundary fictitious cell volumes

The boundary conditions for the momentum and scalar concentration equations at the free surface and the wall are detailed below.

4.13.1. Velocity

a) No-Shear at Free Surface (y = h)

The free surface is assumed to be unaffected by the viscosity of the ambient air and surface tension acting on the flowing slurry. Therefore, a zero shear stress condition will be employed at the free surface. The condition of a zero shear stress implies that a zero velocity gradient will exist at the same position. Therefore the free surface represents a point of symmetry in the velocity profile.

Since an imaginary node formulation has been chosen, the location of the boundary relative to the imaginary node is on the south face. Node P is a fictitious node located at one control volume above the free surface (the south face of P is at $y = h$) (Figure 4.7a).

$$\left(\frac{\partial u}{\partial y}\right)_{y=h} = 0 \tag{4.67a}$$

$$\frac{u_P - u_S}{y_P - y_S} \approx 0 \tag{4.67b}$$

$$u_P = u_S \tag{4.67c}$$

Applying Equation 4.67c at the free surface boundary node, and relating it to Equation 4.50 produces the momentum equation coefficients for node $N+1$:

$$a_P^u u_P = a_N^u u_N + a_S^u u_S + b^u \tag{4.68a}$$

where

$$a_P^u = 1 \tag{4.68b}$$

$$a_N^u = 0 \tag{4.68c}$$

$$a_S^u = 1 \tag{4.68d}$$

$$b^u = 0 \tag{4.68e}$$

b) No-Slip at Wall (y = 0)

For the lower boundary condition at the wall of the domain ($y = 0$), the no-slip assumption was applied to the axial velocity component. Yilmazer and Kalyon (1989) and Addie et al. (2004) noticed significant slip between the fluid and particle phases in their experimental slurry measurements. However, this could be attributed to the high mixture velocities encountered in their studies. In this study low Reynolds number flows are being investigated. The difference between the velocities of the solid particles and carrier fluid phases is not expected to be significant under these conditions.

In the model it is assumed that the coarse particle phase and the carrier fluid move at the same velocity (i.e. there is not slip between the phases). Because of this only a single momentum equation for the bulk mixture is solved (coarse particle and carrier fluid combined). Other methods exist to solve for each phase separately (i.e. particle tracking) but are much more robust, complicated and involved. In this method the links between the phases are the mixture viscosity and density. No distinction is made between the fluid and the particle velocity, only a mixture velocity is determined.

Since the north face of the imaginary cell volume lies at $y = 0$ (Figure 4.7b), the face velocity must be set equal to zero to ensure no-slip. At this boundary, P is a fictitious node one control volume below the wall (the north face of P is at $y = 0$). In this case, a linear approximation is

made between the fictitious node, P, outside the domain, and the real node, N, which is just above the fictitious node inside the domain. Since the grid is determined prior to the simulation, the geometric positions of the nodes are known and can be used to determine the appropriate coefficients for the algebraic equation.

Using linear interpolation (not geometric as that would result in a non-linear boundary condition) the no-slip equation is shown in Equation 4.69.

$$u_{y=0} = 0 = u_P + \frac{y_w - y_P}{y_N - y_P}\left(u_N - u_P\right) \tag{4.69a}$$

$$0 = u_P + \frac{0 - y_P}{y_N - y_P}\left(u_N - u_P\right) \tag{4.69b}$$

$$u_P = \frac{y_P}{y_N} u_N \tag{4.69c}$$

Note that y_P is less than zero as it lies outside the domain. This will lead to a negative coefficient for a_N. However, this does not violate the finite volume rules discussed in Section 4.1 stating that coefficients cannot be negative, since it occurs at a fictitious node. This is permitted since it is not in the actual physical domain of the solution. Only nodes within the domain are required to possess positive coefficients. Therefore applying the general algebraic equation to the above equation at the wall node yields:

$$a_P^u u_P = a_N^u u_N + a_S^u u_S + b^u \tag{4.70a}$$

where

$$a_P^u = 1 \tag{4.70b}$$

$$a_N^u = \frac{y_P}{y_N} = \frac{y_0}{y_1} \tag{4.70c}$$

$$a_S^u = 0 \tag{4.70d}$$

$$b^u = 0 \tag{4.70e}$$

The coefficients at this node are constants for the duration of the simulation, as long as the grid remains unchanged. The evaluation of the α and β coefficients is dependent on the coefficients at the lower boundary where the loading phase begins in the Thomas Algorithm presented in Section 4.11. In order to initiate the solver, the values of α_0 and β_0 need to be calculated. The relationships used to calculate α_0 and β_0 at the lower boundary are presented in Equations 4.71a and 4.71b.

$$\alpha_0^u = \frac{a_{N,0}^u}{a_{P,0}^u - a_{S,0}^u \alpha_{-1}^u} = \frac{y_0}{y_1} \tag{4.71a}$$

$$\beta_0^u = \frac{a_{S,0}^u \beta_{-1}^u + b_0^u}{a_{P,0}^u - a_{S,0}^u \alpha_{-1}^u} = 0 \tag{4.71b}$$

4.13.2. Concentration

a) No-Flux at Wall (y = 0)

In order to ensure that the model does not permit particles to leave the domain, no-flux boundary conditions must be used at the physical boundaries of the domain (i.e. the free surface and the flume wall) for the scalar concentration equation. Initially, zero gradient conditions were considered for the concentration. However, these conditions do not conserve mass in the flow domain and thus required physically unrealistic scaling of the solution fields. For extremely stiff problems this could lead to solution instabilities making the Phillips model approach inappropriate.

The no-flux condition has been shown to be most appropriate at the bottom wall. The solution to the problem will not occur in a physically realistic manner if a flux of particles is allowed to occur through this boundary. In order to implement a no-flux condition at the wall, the scalar transport equation has to be considered at steady state. For the one-dimensional problem of this study the no-flux equation development is presented in Equation 4.72.

$$\left(N_c + N_\eta + N_s\right) \cdot \vec{n} = 0 \tag{4.72a}$$

In this problem the wall normal ($\vec{n}$) acts in the positive y direction so it is equal to the $\hat{j}$ direction vector. Equation 4.72b shows each flux expressed in its gradient components.

$$\left[-K_c a^2\left(\phi^2\nabla\dot{\gamma}+\phi\dot{\gamma}\nabla\phi\right)-K_\eta a^2\dot{\gamma}\phi^2\frac{1}{\eta}\frac{d\eta}{d\phi}\nabla\phi+K_s a^2\phi\, f(\phi)\vec{g}\right]\cdot\vec{n}=0 \tag{4.72b}$$

Regrouping and noting that the steady boundary condition is independent of particle size, as well as simplifying and expanding the gradients to their vector components (considering only y-wise for the one-dimensional flow problem) give:

$$\left[\left(\phi\dot{\gamma}\left(K_c+\phi\frac{K_\eta}{\eta}\frac{d\eta}{d\phi}\right)\frac{d\phi}{dy}\right)\hat{j}+\left(K_c\phi^2\frac{d\dot{\gamma}}{dy}\right)\hat{j}-\left(K_s\phi f(\phi)g_y\right)\hat{j}\right]\cdot\hat{j}=0 \tag{4.72c}$$

Performing a dot product, the boundary equation simplifies to:

$$\phi\dot{\gamma}\left(K_c+\phi\frac{K_\eta}{\eta}\frac{d\eta}{d\phi}\right)\frac{d\phi}{dy}+K_c\phi^2\frac{d\dot{\gamma}}{dy}-K_s\phi f(\phi)g_y=0 \tag{4.73a}$$

Rearranging and formulating the equation at the wall results in a mixed Robbins type boundary condition (Rao, 2002) for the concentration gradient which ensures no particle flux occurs at the wall.

$$\left.\frac{d\phi}{dy}\right|_w=\frac{K_s\phi_w f(\phi_w)g_y-K_c\phi_w{}^2\left.\frac{d\dot{\gamma}}{dy}\right|_w}{\phi_w\dot{\gamma}_w\left(K_c+\phi_w\frac{K_\eta}{\eta_w}\left.\frac{d\eta}{d\phi}\right|_w\right)} \tag{4.73b}$$

Applying finite difference formulas for the gradients yields:

$$\left.\frac{\phi_N - \phi_P}{y_N - y_P}\right|_w = \frac{K_s \phi_w f(\phi_w) g_y - K_c \phi_w{}^2 \left.\frac{d\dot{\gamma}}{dy}\right|_w}{\phi_w \dot{\gamma}_w \left(K_c + \phi_w \frac{K_\eta}{\eta_w} \left.\frac{d\eta}{d\phi}\right|_w \right)} \tag{4.73c}$$

which in turn gives:

$$\phi_P = \phi_N - (y_N - y_P) \frac{K_s \phi_w f(\phi_w) g_y - K_c \phi_w{}^2 \left.\frac{d\dot{\gamma}}{dy}\right|_w}{\phi_w \dot{\gamma}_w \left(K_c + \phi_w \frac{K_\eta}{\eta_w} \left.\frac{d\eta}{d\phi}\right|_w \right)} \tag{4.73d}$$

The equation above can be rearranged to fit the form of the discrete algebraic equation:

$$a_P^\phi \phi_P = a_S^\phi \phi_S + a_N^\phi \phi_N + b^\phi \tag{4.74a}$$

where

$$a_P^\phi = 1 \tag{4.74b}$$

$$a_S^\phi = 0 \tag{4.74c}$$

$$a_N^\phi = 1 \tag{4.74d}$$

$$b^\phi = -(y_N - y_P) \frac{K_s \phi_w f(\phi_w) g_y - K_c \phi_w{}^2 \left.\frac{d\dot{\gamma}}{dy}\right|_w}{\phi_w \dot{\gamma}_w \left(K_c + \phi_w \frac{K_\eta}{\eta_w} \left.\frac{d\eta}{d\phi}\right|_w \right)} \tag{4.74e}$$

Here the values of the term b^ϕ are calculated explicitly and are dependent on the values determined in the previous time step. When possible, the most current variables are used to help stabilize the solution. However, the boundary condition is explicit in that it is dependent on the values of the concentration at the previous time step. As the solution converges toward a steady state this is no longer a concern.

The relationships used to calculate α_0 and β_0 at the lower boundary are presented in Equations 4.75a and 4.75b.

$$\alpha_0^{\phi} = \frac{a_{N,0}^{\phi}}{a_{P,0}^{\phi} - a_{S,0}^{\phi}\alpha_{-1}^{\phi}} = 1 \tag{4.75a}$$

$$\beta_0^{\phi} = \frac{a_{S,0}^{\phi}\beta_{-1}^{\phi} + b_0^{\phi}}{a_{P,0}^{\phi} - a_{S,0}^{\phi}\alpha_{-1}^{\phi}} = b_0^{\phi} \tag{4.75b}$$

b) No-Flux at Free Surface (y = h)

Similar to the condition at the wall, a no-flux condition at the free surface is also employed to ensure that mass cannot be transported through this boundary. Even if a symmetry condition in the concentration profile is employed, in the absence of a concentration gradient the flux due to a spatially varying interaction frequency results in a flux of particles out of the domain through the free surface due to a local variation in the shear rate. However, due to the steady state formulation of the derivative of the concentration (Equation 4.73b), and the momentum equation boundary condition of symmetry at the free surface, a different approach must be taken to ensure that no-flux of particles occurs at the free surface.

The wall no-flux condition is a mixed Robbins expression and is dependent on the shear rate in the denominator of Equation 4.73b. However, because of the symmetry velocity condition, the velocity gradient (shear rate) at the free surface is zero and the concentration gradient goes to infinity. Since and infinite gradient cannot be implemented in a numerical scheme, a unique approach has been taken which incorporates the no-flux condition in a different manner. A fictitious node approach was again used on the free-surface boundary.

Equation 4.76 details the resulting relation at the free surface due to the symmetry of the velocity profile.

$$F(\phi_{fs}) = K_s \phi_{fs} f(\phi_{fs}) g_y - K_c \phi_{fs}^2 \left.\frac{d\dot{\gamma}}{dy}\right|_{fs} = 0 \tag{4.76}$$

Likewise the derivative of this equation with respect to the concentration at the free surface can be expressed as:

$$F'(\phi_{fs}) = K_s g_y \left(f(\phi_{fs}) + \phi_{fs} \left. \frac{df(\phi)}{d\phi} \right|_{fs} \right) - 2K_c \left. \frac{d\dot{\gamma}}{dy} \right|_{fs} \phi_{fs} \tag{4.77}$$

These equations are highly non-linear functions of concentration. At the free surface boundary the concentration can be determined using a Newton-Raphson numerical technique (Rao, 2002; Spiegel, 1968):

$$\phi_{fs}^{i+1} = \phi_{fs}^{i} - \frac{F(\phi_{fs}^{i})}{F'(\phi_{fs}^{i})} \tag{4.78}$$

Equation 4.78 can be solved iteratively with the requirement that $F(\phi)$ reduces to some acceptable limit and ceases to change with further iteration. Once the value of the concentration values are known at the free surface boundary, the values at the neighbouring nodes, specifically the fictitious node outside the domain, can be determined so that the coefficients at the fictitious node can be calculated. Although a geometric interpolation scheme is used at the interior cell faces in this study, a linear interpolation scheme is employed at the free surface boundary. Using the more accurate geometric scheme at the free surface will result in a non-linear equation where there is a requirement for a linear set of equations. The linear interpolation of the free surface concentration to the neighbouring fictitious node is shown in Equation 4.79.

$$\phi_{fs} = \phi_S + (\phi_P - \phi_S) \frac{(y_{fs} - y_S)}{(y_P - y_S)} \tag{4.79a}$$

$$(y_{fs} - y_S)\phi_P = (y_{fs} - y_P)\phi_S + (y_P - y_S)\phi_{fs} \tag{4.79b}$$

Rearranging Equation 4.79b to fit the algebraic system of equations results in Equation 4.80, which represents the no-flux free surface boundary condition:

$$a_P^{\phi}\phi_P = a_S^{\phi}\phi_S + a_N^{\phi}\phi_N + b^{\phi} \tag{4.80a}$$

where

$$a_P^{\phi} = y_{fs} - y_S \tag{4.80b}$$

$$a_S^{\phi} = y_{fs} - y_P \tag{4.80c}$$

$$a_N^{\phi} = 0 \tag{4.80d}$$

$$b^{\phi} = \left(y_P - y_S\right)\phi_{fs} \tag{4.80e}$$

The value for the free surface concentration is explicit and satisfies the no-flux condition based on the solution from the previous time step. The no-flux requirement becomes less of a concern when the solution approaches convergence.

4.14. Error Analysis

In order to determine the quality of the solution there are three conditions that must be checked.

1. Did the solution converge?
2. Does the solution satisfy the discrete equations?
3. Is the solution physically realistic?

These questions can be answered by calculating a number of different quantities, which define both the quality, and accuracy of the numerical solution.

Since a non-linear problem is being solved, an iterative method is required. This means that the Thomas Algorithm must be repeated until the velocity and concentration fields stop changing within a specified range. An absolute convergence criteria can be used which is acceptable for variables with a large magnitude but will not be sufficient for variables that are small in magnitude. To make the code and the convergence criteria applicable to all magnitudes of the variables of interest, a relative convergence criteria will be used. The relative error is summed over all interior nodes using Equation 4.81. Only non-zero nodal values are considered in this formulation.

$$\text{convergence error} = \frac{1}{N}\sum_{i=1}^{N}\left|\frac{\phi_{i,new} - \phi_{i,old}}{\phi_{i,new}}\right| \tag{4.81}$$

When the result of this equation is less than the specified convergence criteria the variables have stopped changing and the solution has converged. This is applied to the solution of the concentration and velocity distributions after each result of the direct solution technique.

Besides the convergence of the solution, the actual precision of the numerical technique must also be evaluated. This involves calculation of residuals. The residual is simply the difference between the left hand side and the right hand side of the discrete algebraic equations (Equations 4.50, 4.54 and 4.58). In this problem, it is possible to calculate an average residual since a system with N interior nodes was investigated. The average residual is calculated using Equation 4.82. It can be applied to both the discrete concentration and the velocity equations and should approach zero as the solution fields converge.

$$\text{Residual} = \frac{1}{N}\sum_{i=1}^{N}\left|a_P\phi_P - a_N\phi_N - a_S\phi_S - b\right| \tag{4.82}$$

4.15. Interpolation Schemes

In the simulation calculations, the cell volume is assumed to have constant properties. However, these property values change from cell-to-cell and need to be interpolated to the faces of the cell in order to evaluate the discrete equation coefficients. Two different types of spatial interpolation schemes were considered in this study: arithmetic average (linear interpolation) and harmonic average (geometric interpolation) (Patankar, 1980). Details of the two schemes are shown below.

4.15.1. Linear

$$\phi_f = \phi_{\mathrm{i}} + \left(\phi_{\mathrm{i+1}} - \phi_{\mathrm{i}}\right)\frac{\left(y_f - y_{\mathrm{i}}\right)}{\left(y_{\mathrm{i+1}} - y_{\mathrm{i}}\right)} \tag{4.83}$$

Here f represents the face being interpolated to (n or s) while 'i' is the node below the face and '$i+1$' is the node above the face. For a uniform, cell centered grid, this equation reduces to an arithmetic mean between neighbouring cells:

$$\phi_f = \frac{\phi_{\mathrm{i+1}} - \phi_{\mathrm{i}}}{2} \tag{4.84}$$

4.15.2. Geometric

Patankar (1980) suggests that a harmonic mean or geometric interpolation scheme be used for finite volume method calculations. This is especially true for non-uniform grids as well as for simulations which have regions of high gradients. Using the following geometric interpolation scheme also ensures conservation of flux across internal boundaries:

$$\phi_f = \frac{\phi_i \, \phi_{i+1}}{r_i \phi_{i+1} + r_{i+1} \phi_i} \tag{4.85a}$$

where

$$r_i = \frac{\Delta_i}{\Delta_i + \Delta_{i+1}} \tag{4.85b}$$

$$r_{i+1} = \frac{\Delta_{i+1}}{\Delta_i + \Delta_{i+1}} \tag{4.85c}$$

$$\Delta_i = y_f - y_i \tag{4.85d}$$

$$\Delta_{i+1} = y_{i+1} - y_f \tag{4.85e}$$

Likewise for a uniform cell centered grid:

$$\phi_f = \frac{2\phi_i \, \phi_{i+1}}{\phi_i + \phi_{i+1}} \tag{4.86}$$

Patankar (1980) has shown that if the asymptotic performance of the two methods is considered for the one-dimensional scalar transport equation, the geometric mean results in a conservation of flux while the arithmetic mean becomes singular. For this reason, the geometric interpolation scheme was chosen to interpolate values associated with the cell faces in this study. This is especially important since many variables exhibit steep spatial gradients throughout the solution domain.

4.16. Shear Rate

The shear rate, or time rate of shear strain, of the fluid is a scalar quantity representing all velocity gradients acting on the fluid. The expression for the shear rate in three dimensions is shown below (Bird et al., 1960):

$$\dot{\gamma} = \sqrt{½(\Delta : \Delta)} \tag{4.87a}$$

where:

$$\Delta_{ij} = \frac{\partial u_i}{\partial x_j} + \frac{\partial u_j}{\partial x_i} \tag{4.87b}$$

The quantity Δ_{ij} is the symmetrical rate of the deformation tensor. $\Delta : \Delta$ is the second invariant of the strain rate tensor (Bird et al., 1960). The invariant is the summation of the deformation tensors over all components and can be calculated by the following relation:

$$\Delta : \Delta = \sum_{i=1}^{3} \sum_{j=1}^{3} \Delta_{ij} \Delta_{ji} \tag{4.88}$$

For a three dimensional problem, this results in a complicated summation of nine rate of deformation tensors. However, since only a single dimension is being investigated in this study, the evaluation of the second invariant is quite simple. If $x = 1$, $y = 2$, and $z = 3$, then only a single velocity component exists in the z-direction (3), and it only varies in the y-wise direction (2). Therefore evaluating the shear rate gives:

$$\dot{\gamma} = \sqrt{½(\Delta : \Delta)} = \left[½\left(\Delta_{11}^2 + \Delta_{12}\Delta_{21} + \Delta_{13}\Delta_{31} + \Delta_{21}\Delta_{12} + \Delta_{22}^2 + \Delta_{23}\Delta_{32} + \Delta_{31}\Delta_{13} + \Delta_{32}\Delta_{23} + \Delta_{33}^2\right)\right]^{1/2} \tag{4.89a}$$

$$\dot{\gamma} = \sqrt{½(\Delta : \Delta)} = \left[½\left(\Delta_{23}\Delta_{32} + \Delta_{32}\Delta_{23}\right)\right]^{1/2} = \left[\Delta_{23}\Delta_{32}\right]^{1/2} \tag{4.89b}$$

where

$$\Delta_{23} = \Delta_{32} = \frac{\partial u_3}{\partial x_2} = \frac{\partial u_z}{\partial y} \tag{4.89c}$$

Since Δ_{23} is equal to Δ_{32} the shear rate is equal to the y-wise velocity gradient:

$$\dot{\gamma} = \left| \frac{\partial u_z}{\partial y} \right| \tag{4.90}$$

The shear rate must be equal to a positive scalar value. Defining the shear rate as a positive scalar quantity ensures that particles will migrate from regions of high shear to low shear. Expressions for the shear rate at the north and south faces of a cell are shown below. Finite difference approximations are shown in Equations 4.91a and 4.91b.

$$\dot{\gamma}_n = \left| \frac{u_N - u_P}{y_N - y_P} \right| \tag{4.91a}$$

$$\dot{\gamma}_s = \left| \frac{u_P - u_S}{y_P - y_S} \right| \tag{4.91b}$$

The flux due to a spatially varying interaction frequency also includes the gradient of the shear rate, which must be evaluated at the cell faces in the source term. Equations 4.93a and 4.93b detail the finite difference approximations used to calculate the shear rate gradient at the north and south faces respectively. In order to calculate the shear rate gradient at a cell face, the shear rate must be determined at the cell centers. This is done by first interpolating velocities to the cell faces. The shear rate is then calculated at the cell center. With the shear rate at each cell center known, a finite difference approximation can be used to calculate the gradient of the shear rate at the north and south faces of each cell:

$$\dot{\gamma}_P = \left| \frac{u_n - u_s}{y_n - y_s} \right| \tag{4.92}$$

Therefore,

$$\left. \frac{\partial \dot{\gamma}}{\partial y} \right|_n = \frac{\dot{\gamma}_N - \dot{\gamma}_P}{y_N - y_P} \tag{4.93a}$$

$$\left.\frac{\partial \dot{\gamma}}{\partial y}\right|_s = \frac{\dot{\gamma}_P - \dot{\gamma}_S}{y_P - y_S} \tag{4.93b}$$

4.17. Concentration Scaling

Physical laws prevent the local concentration at any node from being either negative or greater than the maximum packing concentration. Therefore, the value of the concentration solved in the scalar transport equation must be within the range of 0 to $\phi_{\max}$ at all interior nodes within the domain (fictitious nodes can possess physically unrealistic values).

Two different average concentrations within the flow can also be calculated. The expressions used to evaluate the in-situ and the delivered concentrations are shown below in Equations 4.94 and 4.95.

In-Situ: $$C_r = \frac{1}{A}\int_A \phi \, dA \tag{4.94}$$

Delivered: $$C_v = \frac{1}{VA}\int_A \phi \, \mathrm{v} dA \tag{4.95}$$

The in-situ concentration is a measure of the local concentration within a cross-section of the pipe. It is area averaged over the flow cross-section. The delivered concentration is a measure of the solids concentration being transported within the system. It is area averaged but also weighted by the local carrier fluid and coarse particle flow velocities (mixture velocity in this study).

The delivered concentration and the in-situ concentration are equal when a slurry flow is homogeneous or the particles are evenly distributed throughout the cross-section of the flow and there is no difference between the fluid and solids velocities. However, for stratified heterogeneous flows where there is a significant segregation of solids, or flows where there is a difference between the fluid and solids velocities, the delivered concentration is less than the in-situ concentration (Shook et al., 2002).

The delivered concentration is of interest to the design engineer because it expresses what is actually moving in the flow and being "delivered" by the system. The in-situ concentration is of

interest to the research engineer since it is useful when defining mechanisms occurring within the flow. A change in the in-situ concentration can be related to the presence of a stationary or sliding bed. In a horizontal recirculating loop, the in-situ concentration is the same regardless of whether there is a bed present (for steady flow). In a vertical recirculating loop the delivered concentration is equal to the in-situ concentration.

In the model, local concentration can also be scaled within the iterative solution. If mass is not being conserved (due to the explicit nature of the boundary conditions), the overall solids concentration can decrease with solution time. If this loss of solids is significant, physically unrealistic results will be obtained. To address this issue, the simulation results can be scaled at each iteration step.

A measure of the average volumetric solids concentration is input into the model initially (in-situ concentration). For the remainder of the calculation, where there is no stationary bed present, the total in-situ concentration of solids should remain equal to this value. Therefore, after each iteration, the average concentration in the domain is calculated and compared to the initial value input. If the two values differ, the local concentration at each node in the domain is scaled linearly to force the in-situ concentration values to be the same. As well, the condition that the concentration cannot be negative or greater than the maximum packing factor at interior nodes is also enforced to ensure physically realistic concentrations for the next iteration.

If a small enough time step is employed in the solution, the no-flux boundary conditions at the wall and free surface result in a negligible loss of solids. The time steps used in this study were small enough such that the concentration scaling technique was not required and was therefore not employed in the code used in this investigation. Concentration scaling was only required when a zero concentration gradient boundary condition was applied to the channel wall. All of the results presented in this thesis were obtained using no-flux concentration boundary conditions.

4.18. Singularities

Ames (1977) showed that finite difference approximations fail near singular points (discontinuities) at both the external boundaries of the system as well as at interior points of the domain (i.e. corners of a rectangular system). Discontinuities in value, as well as derivative, can

cause instabilities in the local region surrounding the singularity. If the methods used are stable, the instabilities caused by the singularity typically decay, but may still cause errors in the final simulation results. As a result, finite difference approaches are typically inappropriate in the region near the discontinuity.

Interior singularities occur when the coefficients of the partial differential equations become singular. One accepted technique to address the singularity is to eliminate it by subtracting out the singularity where possible. Although the resulting equations are stable, this generates a new problem with new boundary conditions. This technique works well for linear problems but is more difficult to implement for non-linear problems. Other techniques proposed by Ames (1977) include a transformation of variables or mesh refinement.

With mesh refinement, the singularity is ignored and its effect is diminished by refining the mesh in the localized region. This results in the addition of more nodes to the domain in the region of the singularity. By doing this, the area affected by the singularity is minimized, and even though eliminating the singularity is preferable to refining the mesh, mesh refinement is much easier to implement.

Finer meshes typically increase the accuracy of the finite difference approximations. However, a reduction in the time step is associated with grid refinement for stability resulting in an increase in the overall simulation time. The grid refinement technique was determined to be the most appropriate method for reducing the effects of singularities in this study.

The singularity encountered in this study is an internal discontinuity commonly referred to as a shock discontinuity, which occurs at boundaries separating media of different physical properties. The Bingham biviscosity solution causes a shock interface at the point where the flow changes from a region of sheared fluid to an unsheared pseudo-solid.

The coefficients of the partial differential equation for the scalar concentration transport equation are singular at the interface between the unsheared plug and the sheared fluid region in the flow. In the unsheared region the apparent viscosity approaches infinity. This cannot be numerically implemented. The biviscosity model approximates this condition by assigning a high viscosity in the unsheared region, which is orders of magnitude greater than the plastic viscosity of the

mixture. The significant difference between the properties in the unsheared region compared to those in the sheared region is that the coefficients become singular in the unsheared region.

The singularity causes a large oscillation or an overshoot in the concentration value just below the interface in the sheared region. This is not physically realistic behaviour and must be addressed. If the oscillations are large they can lead to unrealistic solids transport simulation results.

The critical shear rate is used to determine whether the slurry is sheared or unsheared. In the determination of the coefficients for the momentum and scalar transport equations, the shear rate is calculated at both the north and south faces of each node. With respect to the domain, the interface will exist within one node. The north face of the cell will be in the unsheared region while the south face will be in the sheared region. As a result, a large gradient in viscosity exits over this cell. As well, the shear rate also varies dramatically from a finite value at the south face to a small value (approaching zero) at the north face. This variation in viscosity virtually eliminates the flux of particles due to spatially varying viscosity while the dramatic drop in shear rate creates a large pseudo-flux of particles due to the spatially varying interaction frequency. This results in an oscillation of the concentration distribution in the interface region resulting in physically unrealistic results.

The oscillation effect of the singularity is addressed in four ways.

1. Harmonic means (geometric interpolations) have been used to interpolate the values of the variables (concentration and velocity) at the faces of the cells from the neighbouring nodes. This ensures that the flux of particles is conserved throughout the domain. As well, it also allows for more accurate interpolation of parameters in regions of large gradients.
2. The grid has been refined. Originally a mesh consisting of 25 internal nodes was considered. However, upon further inspection, the number of nodes was doubled to 50 to reduce the steepness of the gradients in the region near the interface. This reduces the level of overshoot resulting from the discontinuity in the viscosity. The number of nodes was further increased to 100 with no noticeable difference in simulation results. A discussion on the number of nodes chosen for the simulations is given in Section 6.3.
3. The viscosity and shear rate at the face, which resides in the unsheared region have been manipulated. A geometric mean between the north and south face viscosities is assigned

to the north face to reduce the dramatic variation across the cell. This does not affect the momentum solution since new values are calculated prior to the next iteration.

4. An interface routine has been included to find the exact location of the sheared and unsheared transition. If the node exists in the unsheared region (i.e. the shear rate is less than minimum critical shear rate) then the concentration assigned to that cell is given the average value between the prior north and south face concentrations. As well, the average concentration from the north and south faces is assigned to the cell associated with the interface. This node has been found to be challenging to contend with and represents the origin of the oscillatory behaviour. Manipulating the concentration at the transition has been found to significantly reduce the oscillation and the overshoot effects occurring near the interface. It has also been found to have only a minimal effect on the overall development of the momentum or concentration profiles.

5. EXPERIMENTAL RESULTS AND DISCUSSION

5.1. Test Matrix

A detailed description of the composition of the slurries that were investigated in the experimental program of this study is presented in Table 5.1.

Table 5.1: Compositions of the mixtures investigated in the 156.7 mm flume experiments

Mixture	Name	Density (kg/m^3)	Concentration %						Coarse: Fines	Additives (w/w clay)	
			v/v			w/w					
			Sand	Clay	Water	Sand	Clay	Water		TSPP	Ca^{2+}
1	Saskatoon Tap Water	1000	0	0	100	0	0	100	n/a	n/a	n/a
3	Kaolin-Water	1375	0	22.2	77.8	0	43.5	56.5	0	0	0
4	Kaolin-Water-TSPP 1	1384	0	22.6	77.4	0	44.1	55.9	0	0.03%	0
5	Kaolin-Water-TSPP 2	1386	0	22.8	77.2	0	44.4	55.6	0	0.10%	0
2	Sand-Water Slurry	1410	25	0	75	47	0	53	n/a	n/a	n/a
6	CT-No Gypsum	1598	28	8	64	46.5	13.5	40	3.5:1	0.10%	0
7	CT-Gypsum	1598	28	8	64	46.5	13.5	40	3.5:1	0.1125%	0.005%
8	Thickened Tailings	1510	15.4	15.1	69.5	27	27	46	1:1	0	0

Table 5.2 provides information on the test matrix that was employed in the experimental program. The flowrate, angle of flume inclination and testing date are provided in the table. Details of the water runs performed to commission the equipment are not included in this table.

Traversing gamma ray density scans were performed in the experiments involving slurries containing coarse particles. Pitot-static tube velocity measurements were performed in all of the tests. For runs 7 and 11 through 18, samples were collected from the top and bottom of the flume as described in Section 3.5. The results were used to determine the uniformity of clay particles in the clay-water carrier fluid. For all of the runs, samples were collected from the outlet of the flume to verify the solids concentration of the flowing mixture.

Table 5.2: Test matrix for the 156.7 mm flume experiments

Run	Material	Date	Flowrate (L/s)	θ (deg)
1	Sand-Water	7/30/2002	5	3.5
2	Sand-Water	7/30/2002	4.5	3.5
3	Sand-Water	7/30/2002	3.9	3.5
4	Sand-Water	7/30/2002	6	3
5	Sand-Water	7/30/2002	5.6	3
6	Sand-Water	7/31/2002	6.5	3
7	CT-No Gypsum	8/8/2002	5	3
8	CT-No Gypsum	8/8/2002	5	2
9	CT-No Gypsum	8/8/2002	5	1.5
10	CT-No Gypsum	8/9/2002	2.5	3
11	CT-Gypsum	8/13/2002	5	3
12	CT-Gypsum	8/13/2002	5	2
13	CT-Gypsum	8/13/2002	5	2.5
14	CT-Gypsum	8/14/2002	2.5	3
15	Thickened Tailings	8/20/2003	5	4
16	Thickened Tailings	8/20/2003	5	4.5
17	Thickened Tailings	8/21/2003	5	5.4
18	Thickened Tailings	8/21/2003	2.5	4.5
21	Kaolin-Water	4/4/2006	0.33-6.4	5.5
22	Kaolin-Water	4/5/2006	0.25-6.1	6.0
23	Kaolin-Water	4/5/2006	0.26-6.1	5.0
24	Kaolin-Water	4/6/2006	0.24-6.0	4.0
25	Kaolin-Water	4/6/2006	0.29-3.5	3.0
26	Kaolin-Water	4/6/2006	0.28-0.73	2.5
27	Kaolin-Water	4/6/2006	0.26-6.0	3.5
28	Kaolin-Water	4/7/2006	0.25-6.0	4.5
29	Kaolin-Water-TSPP 1	4/10/2006	0.30-3.8	5.0
30	Kaolin-Water-TSPP 1	4/10/2006	0.25-4.9	4.0
31	Kaolin-Water-TSPP 1	4/10/2006	0.28-4.9	3.0
32	Kaolin-Water-TSPP 1	4/10/2006	0.24-5.0	2.0
33	Kaolin-Water-TSPP 1	4/11/2006	0.25-5.0	1.0
34	Kaolin-Water-TSPP 1	4/11/2006	0.28-4.5	6.0
35	Kaolin-Water-TSPP 2	4/12/2006	0.56-4.9	6.0
36	Kaolin-Water-TSPP 2	4/12/2006	0.46-5.0	5.0
37	Kaolin-Water-TSPP 2	4/12/2006	0.50-5.1	4.0
38	Kaolin-Water-TSPP 2	4/12/2006	0.50-6.0	3.0
39	Kaolin-Water-TSPP 2	4/12/2006	0.45-6.1	2.0
40	Kaolin-Water-TSPP 2	4/13/2006	0.31-6.2	1.0

5.2. Rheological Characterization

Rheological parameters for the mixtures presented in Table 5.2 were determined from the relationship between pressure gradient and bulk velocity in the 53 mm pipe test section. Table 5.3 presents the calculated rheological parameters. The experimental data from the 53 mm pipe test section for all of the mixtures tested is presented in Appendix D.

Table 5.3: Rheological properties of the mixtures investigated in the 156.7 mm flume experiments

Material	Density (kg/m^3)	Temp (^oC)	τ_y (Pa)	μ_P (Pa-s)
Sand-Water	1410	n/a	n/a	n/a
CT-No Gypsum	1598	25.4	0	0.0074
CT-Gypsum	1598	20.3	10.2	0.0104
CT-Gypsum	1598	24.6	14.4	0.0104
Thickened Tailings	1510	19.6	35.9	0.0410
Thickened Tailings	1510	23.2	48.6	0.0389
Thickened Tailings	1510	23.8	50.6	0.0357
Thickened Tailings	1510	24.7	55.9	0.0377
Kaolin-Water	1373	24.6	36.4	0.0282
Kaolin-Water	1373	21.5	33.5	0.0320
Kaolin-Water	1373	21.2	33.4	0.0327
Kaolin-Water	1375	20.3	34.1	0.0305
Kaolin-Water	1375	20.0	32.4	0.0393
Kaolin-Water	1375	20.3	28.9	0.0818
Kaolin-Water	1375	20.5	34.2	0.0306
Kaolin-Water	1377	19.8	34.3	0.0319
Kaolin-Water-TSPP 1	1384	20.8	7.0	0.0125
Kaolin-Water-TSPP 1	1384	19.4	6.1	0.0159
Kaolin-Water-TSPP 1	1384	19.3	6.5	0.0133
Kaolin-Water-TSPP 1	1384	19.7	6.4	0.0144
Kaolin-Water-TSPP 1	1384	21.0	6.8	0.0144
Kaolin-Water-TSPP 1	1384	20.3	6.8	0.0138
Kaolin-Water-TSPP 2	1386	19.2	0	0.0071
Kaolin-Water-TSPP 2	1386	18.9	0	0.0072
Kaolin-Water-TSPP 2	1386	19.6	0	0.0067
Kaolin-Water-TSPP 2	1386	19.7	0	0.0067
Kaolin-Water-TSPP 2	1386	19.9	0	0.0065
Kaolin-Water-TSPP 2	1387	19.7	0	0.0066

Note that the rheological parameters given for the CT 'no gypsum', CT 'gypsum' and Thickened Tailings slurries in Table 5.3 were obtained with the carrier fluid and coarse sand mixture. Rheological parameters for each slurry, which have been determined for the clay-water carrier fluids without coarse solids from Equations 2.41a and 2.41b, are presented in Table 5.4.

Table 5.4: Rheological properties of the carrier fluids for the model tailings mixtures investigated in the 156.7 mm flume experiments

Material	Density (kg/m^3)	Temp (^oC)	τ_y (Pa)	μ_P (Pa-s)
CT-No Gypsum	1188	25.4	0	0.0020
CT-Gypsum	1188	20.3	7.3	0.0028
CT-Gypsum	1188	24.6	10.3	0.0028
Thickened Tailings	1303	19.6	33.6	0.0245
Thickened Tailings	1303	23.2	45.4	0.0233
Thickened Tailings	1303	23.8	47.3	0.0214
Thickened Tailings	1303	24.7	52.3	0.0226

5.3. Wall Roughness

As stated in Section 3.1, the circuit consisted of both a feed test section and a flume test section. Tests conducted with water were performed to determine the equivalent roughness of the 53 mm pipe test section. Saskatoon tap water was used as the water source. To ensure that the tap water had properties as close as possible to those available in the literature, it was first heated to 50 ^oC to remove any dissolved air. Following this, it was cooled to operating temperatures between 20 ^oC and 25 ^oC and a series of pressure drop versus flowrate measurements were taken. Only fully developed turbulent points could be used in the analysis since laminar pipe flow is independent of pipe roughness.

Figure 5.1 shows the results of a pipe roughness test analysis. The experimental data set is a combination of three separate roughness tests. A pipe roughness of 24.7 μm agrees well with the experimental data. The density of water was obtained from the physical properties of water charts presented in Perry (1997). Equation 5.1 was used to determine the viscosity of water at different system temperatures (Bennett and Myers 1982).

$$\mu_{water}(\mathrm{Pa}\cdot\mathrm{s}) = \frac{1}{10}\left[2.1482\left[\left(T(^{o}\mathrm{C})-8.435\right)+\sqrt{8078.4+\left(T(^{o}\mathrm{C})-8.435\right)^{2}}\right]-120\right]^{-1} \qquad (5.1)$$

The roughness determined from evaluation of the data presented in Figure 5.1 applies to the tests performed for the ideal model tailings slurries. The CT 'no gypsum', CT 'gypsum', Thickened Tailings and sand-water slurries were all delivered to the flume in a 53 mm feed test section with a roughness of approximately 24.7 μm.

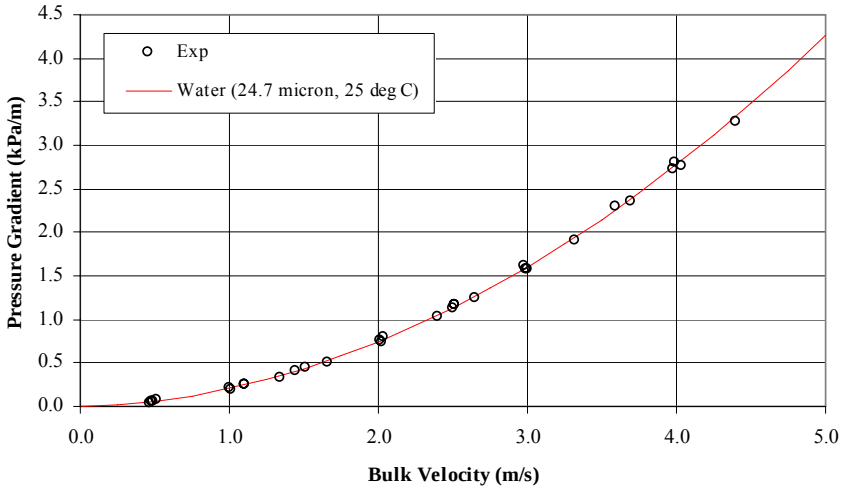

Figure 5.1: Pressure gradient versus velocity for Saskatoon tap water to determine the pipe roughness of the 53 mm test section for the model tailings slurry tests

Wall roughness tests were also performed during the second phase of experiments where the kaolin clay-water slurries were studied. These slurries contained no coarse sand. Water tests were again performed to determine the equivalent roughness of the 53 mm feed test section. Roughness tests were performed before and after the study to see if any significant change occurred during the experimental testing.

Figure 5.2 shows the pressure gradient versus velocity data for water in the 53 mm feed test section before it was polished. Before testing began the flume apparatus was inactive for approximately 45 months. The equivalent roughness of the 53 mm feed test section was determined to be 95.7 μm based on a single test performed at 14 ^{o}C. This level of roughness was deemed to be too high for the experimental requirements of this study. In order to reduce the roughness, the line was polished with a highly angular Torpedo sand (Inland Aggregates Limited, Saskatoon, SK).

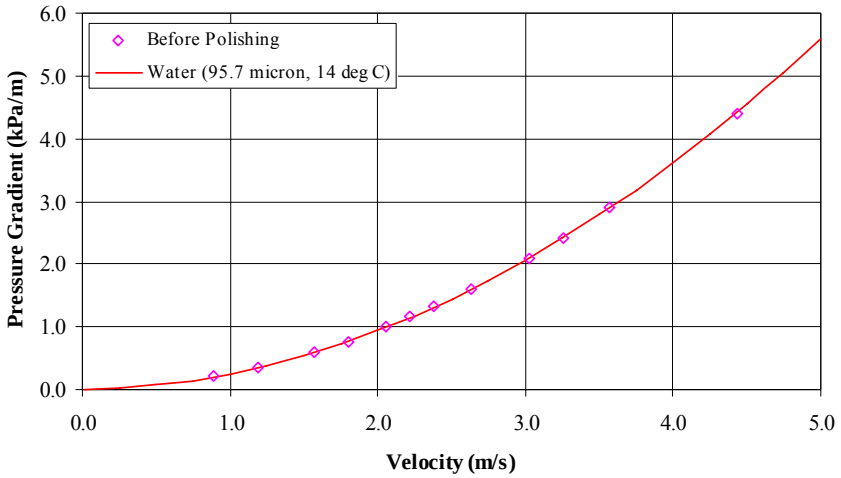

Figure 5.2: Pressure gradient versus velocity for Saskatoon tap water to determine the pipe roughness of the 53 mm test section for the clay-water experiments before the line was polished

A 5% v/v (approximate) slurry composed of a highly angular Torpedo sand was circulated through the experimental loop to polish the pipe surface. Figure 5.3 presents the results of the roughness tests performed after polishing but prior to testing. The experimental data presented in Figure 5.3 is a combination of six different roughness tests ranging in temperature from 21 to 32 ^{o}C. The polishing reduced the roughness from 95.7 to 60.7 µm. The experimental data set is denoted as 'Exp Before Testing'.

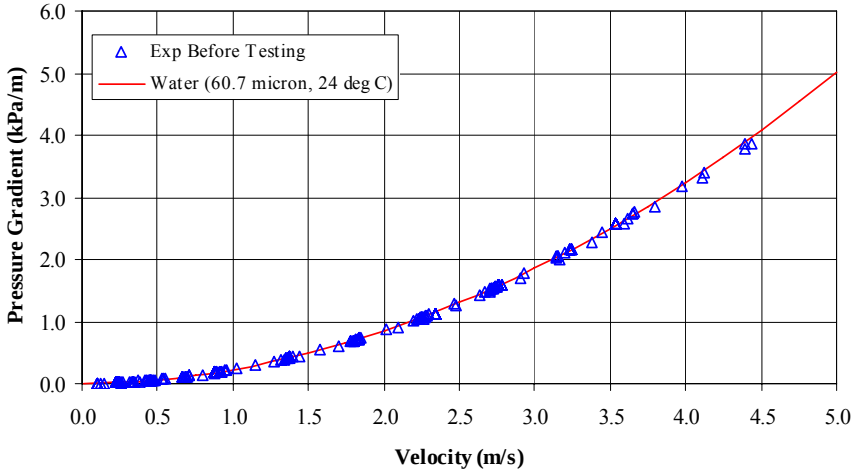

Figure 5.3: Pressure gradient versus velocity for Saskatoon tap water to determine the pipe roughness of the 53 mm test section for the clay-water experiments after polishing but before testing

The results presented in Figure 5.4 correspond to roughness tests performed after the experimental testing of the slurries was completed. Figure 5.4 shows a plot of the pressure gradient versus velocity in the 53 mm feed test section for three separate roughness tests. An equivalent roughness of 60.2 μm was determined to best represent the experimental data at 20 ^{o}C. Comparing this value to the 60.7 μm roughness determined prior to the experiments, it can be seen that no significant roughness change occurred over the course of the experimental testing.

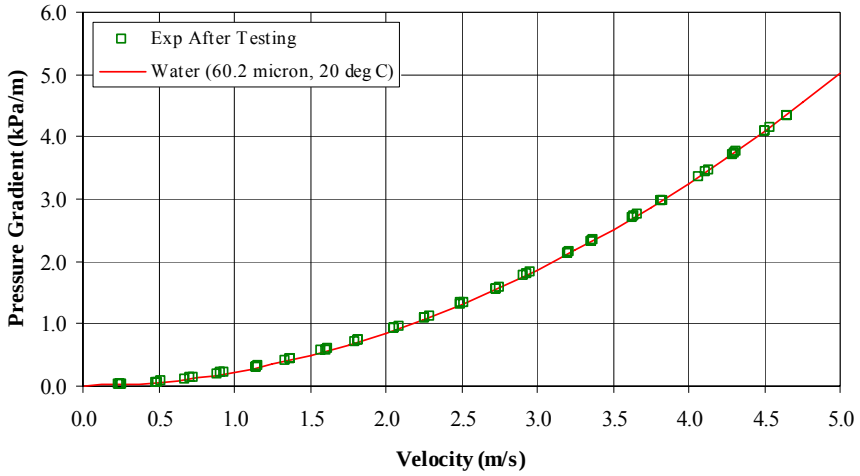

Figure 5.4: Pressure gradient versus velocity for Saskatoon tap water to determine the pipe roughness of the 53 mm test section for the clay-water experiments after testing

5.4. Slurry Rheology

5.4.1. Clay-Water Slurries

Pressure gradient versus velocity plots for the clay-water slurries tested in the 53 mm feed line are shown below in Figures 5.5 to 5.7. A series of pressure gradient and velocity measurements were obtained from the differential pressure transducer and the magnetic flux flowmeter. The resulting data was collected under fully developed, steady pipe flow conditions and correlated against the theoretical pipe flow equations for Bingham and Newtonian fluids to determine the best fit rheological parameters. The Buckingham equation (Equation 2.56) was used to determine the Bingham rheological parameters under laminar flow conditions for slurries exhibiting Bingham properties. Equation 2.22 (Churchill, 1977) was used to determine the viscosity for slurries exhibiting Newtonian properties. Experimental data for all of the clay-water test runs can be found in Appendix D.

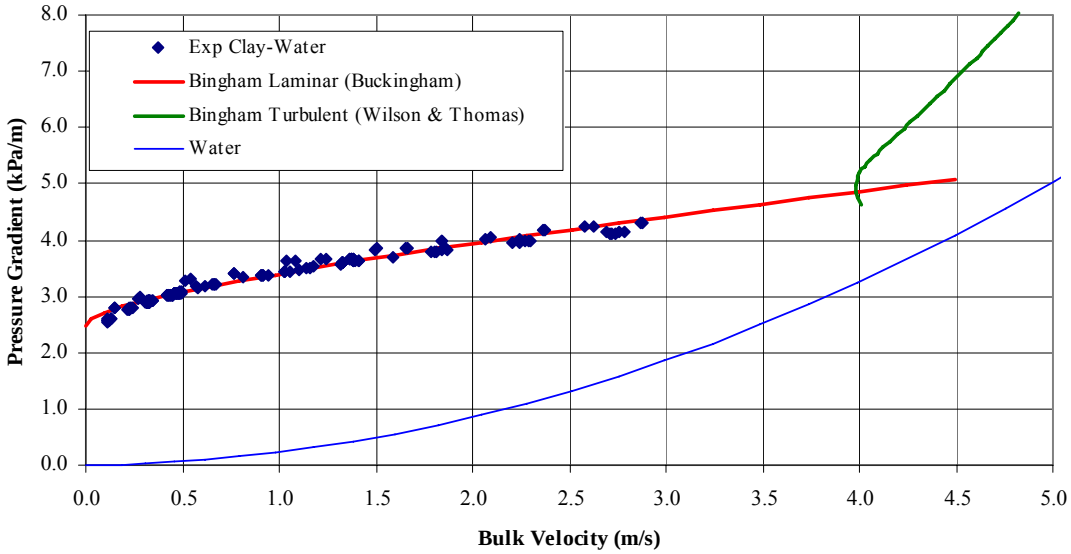

Figure 5.5: Pressure gradient versus velocity for a 22.2% v/v kaolin clay-water slurry in the 53 mm test section; ρ=1375 kg/m^3

Figure 5.5 shows the pressure gradient versus velocity relationship for the 22.2% v/v kaolin clay-water slurry in the 53 mm feed test section with no chemical additions. The density of this slurry was 1375 kg/m^3. The plot combines all of the experimental data obtained in eight different tests. The data was accurately represented by the Buckingham equation (Equation 2.56) using a yield stress of 32.9 Pa and a plastic viscosity of 0.0368 Pa-s. The fit of the Wilson and Thomas turbulent prediction (Equation 2.58) and a water curve at the same system conditions are also shown on the plot.

One can see that the bulk velocities measured were well below the values associated with the turbulent curve predicted by the Wilson and Thomas model. Therefore, the measurements obtain in this test were all in the laminar regime. This is likely due to the large yield stress of the slurry. The rheological parameter results for each of the eight different tests can be found in Table 5.3.

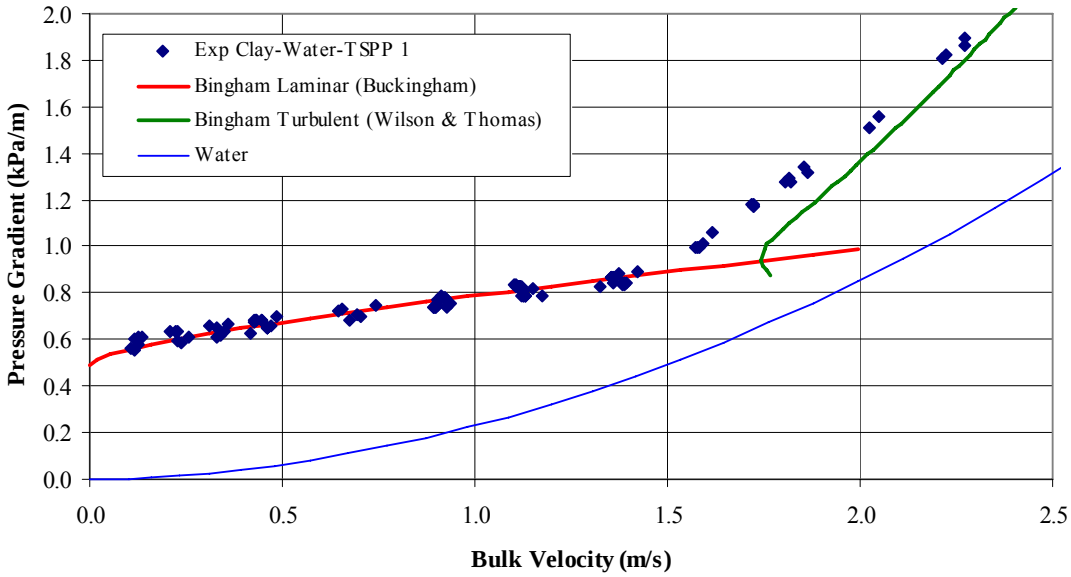

Figure 5.6: Pressure gradient versus velocity for a 22.6% v/v kaolin clay-water slurry with 0.03% TSPP in the 53 mm test section; ρ=1384 kg/m^3

Figure 5.6 shows the pressure gradient versus velocity data obtained with a kaolin clay-water slurry with a 0.03% TSPP (tetra-sodium pyrophosphate, Appendix B) addition. The data presented in this figure was obtained from six different tests. Due to evaporation effects over the course of the experimental tests, the concentration of this slurry increased to 22.6% v/v from 22.2% v/v and the density rose to 1384 kg/m^3 from 1375 kg/m^3. From a least squares analysis with the Buckingham equation (Equation 2.56), the Bingham yield stress and plastic viscosity were determined to be 6.4 Pa and 0.0160 Pa-s respectively. Therefore, the addition of the TSPP to the clay-water slurry significantly reduced the yield stress and plastic viscosity of the slurry.

The Wilson and Thomas turbulent prediction and a water curve at the system conditions are also included in the plot. The turbulent model prediction shows that this slurry was in turbulent flow in the 53 mm test section when the bulk velocities exceeded 1.5 m/s. The Wilson and Thomas turbulent flow curve predicts this to occur at a velocity of 1.75 m/s. Despite this discrepancy, the Wilson and Thomas equation does an adequate job of predicting the turbulent flow behaviour of this slurry in the 53 mm test section.

Figure 5.7 shows the pressure gradient versus velocity relationship in the 53 mm feed test section for the kaolin clay-water slurry with a 0.10% TSPP addition. The experimental results shown in

the figure were a combination of six different tests. Once again, due to evaporation effects, the concentration increased slightly to 22.8% v/v from 22.6% v/v and the density rose to 1386 kg/m^3 from 1384 kg/m^3. As can be seen in Figure 5.7, the increased TSPP concentration completely eliminated the yield stress of the slurry, resulting in a Newtonian slurry.

All of the data points presented in Figure 5.7 were in turbulent flow. The Newtonian viscosity which best fit the experimental data was 0.0067 Pa-s, assuming a roughness of 60.7 μm in the 53 mm feed test section, which was determined from the water test results in Figure 5.3.

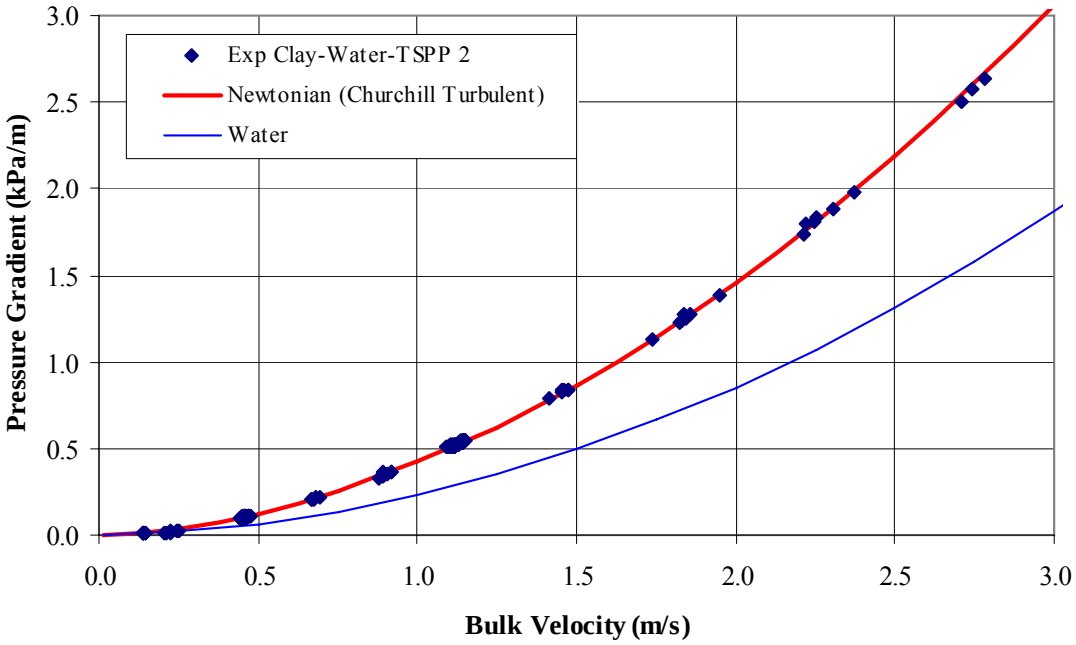

Figure 5.7: Pressure gradient versus velocity for a 22.8% v/v kaolin clay-water slurry with 0.10% TSPP in the 53 mm test section; ρ=1386 kg/m^3

5.4.2. Sand-Water Slurries

Prior to the experimental testing of the sand-water slurries in the flume, tests were performed to determine the maximum packing factor of the sand (Granusil 5010, Unimin Silica Sand, Le Sueur, MN). Schaan (2001) has shown that the maximum packing factor is independent of particle size, and is a function of particle size distribution and particle shape only. A particle size distribution for the sand is shown below in Figure 5.8. The particle size distribution was determined from a dry sieve analysis using a representative sample of the solids by the technical

staff at the SRC Pipe Flow Technology Centre in Saskatoon, SK. The distribution is presented as a logarithmic plot of cumulative % retained versus the particle size in μm (microns).

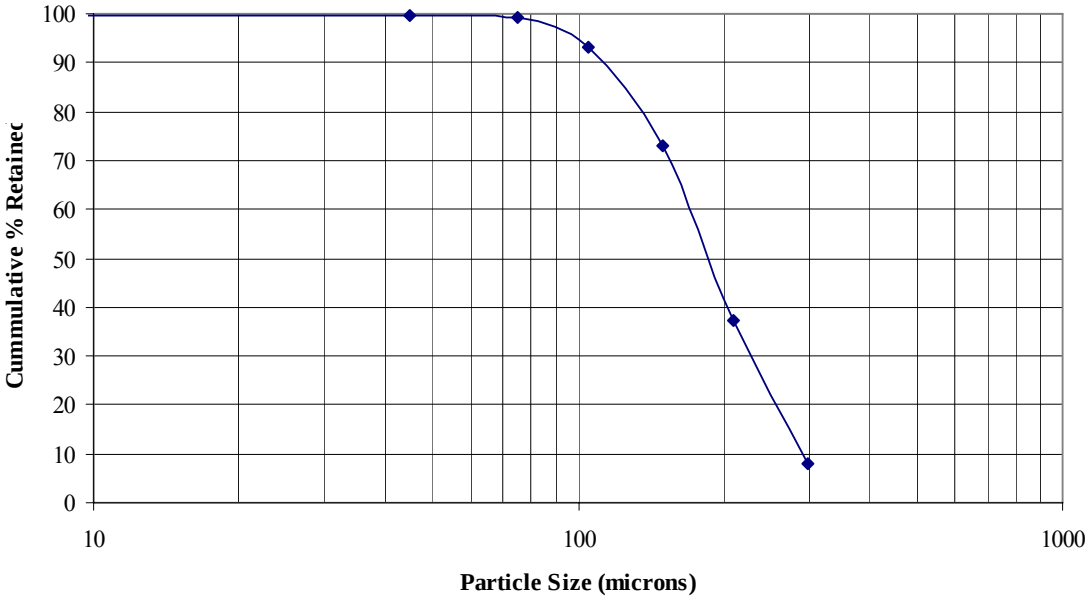

Figure 5.8: Particle size distribution of the Unimin (Granusil 5010) sand employed in the 156.7 mm flume tests; d_{50} = 188.5 μm

Table 5.5 shows the experimental maximum packing concentrations of the sand. Five different controlled sedimentation experiments were conducted in 1000 mL graduated cylinders to determine the maximum packing concentration (freely settled bed). The average packing concentration from the tests was 0.582 v/v. The Unimin sand had a round grain particle shape (Appendix B, Figure B.1) and a rather narrow particle size distribution. The value obtained for the maximum packing concentration is typical of sands with similar characteristics (Schaan, 2001).

Table 5.5: Maximum packing concentrations (v/v) for the Unimin 188 μm (Granusil 5010) sand employed in the 156.7 mm flume tests

Trial	ϕ_{max}
1	0.587
2	0.584
3	0.570
4	0.564
5	0.605
AVG	**0.582**

A sand-water slurry with a concentration of 25% v/v was tested in the experimental apparatus. The in-situ density of this slurry was 1410 kg/m^3, which is similar in magnitude to conventional oil sands tailings. A plot of pressure gradient versus velocity for the 25% v/v sand-water slurry in the 53 mm feed test section is presented in Figure 5.9. All of the data was gathered in the turbulent regime. A theoretical curve for water at the same conditions is also shown. One can see that the frictional losses for water are much less than those for the sand-water mixture.

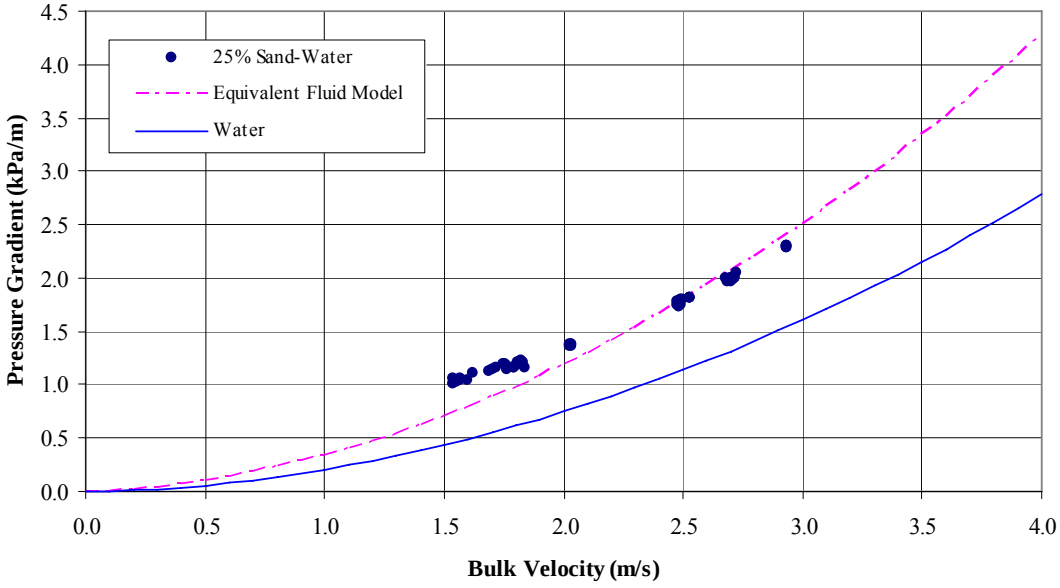

Figure 5.9: Pressure gradient versus velocity for a 25% v/v sand-water slurry in the 53 mm test section; ρ=1410 kg/m^3

Table 5.3 does not provide an estimate for the rheological properties of the sand-water slurry. This is because the slurry is classified as a heterogeneous, settling slurry. In horizontal pipe flow segregation of solids towards the bottom of the pipe occurs below a critical flowrate (deposition velocity). A portion of the segregated solids contribute to the contact load and contribute to Coulombic mechanical friction (Shook et al., 2002). Frictional losses are therefore greater than what would be predicted by viscous fluid friction mechanisms alone. Under these conditions, the slurry cannot be fit with an equivalent viscosity since the solids concentration is not uniform (homogeneous).

For all of the sand-water experiments, the circuit was operated above the critical deposition velocity associated with the feed line. The SRC's Two-Layer Model (Shook et al., 2002)

predicted this to occur at 1.3 m/s based on the operating conditions. The experimental data in Figure 5.9 shows that the critical value seems to occur somewhere below 1.5 m/s.

An equivalent fluid model curve is also shown in Figure 5.9. This curve represents the frictional losses of the sand-water slurry if it were assumed to behave as a homogeneous slurry with a viscosity equal to 0.0029 Pa-s. The viscosity value was determined by scaling the viscosity of water at the temperature of the system with the relative viscosity of the mixture (Equation 2.40d). A best fit comparison of the experimental data above velocities of 2.0 m/s with an equivalent fluid model also yields a slurry viscosity of 0.0029 Pa-s. However, it should be pointed out that the relative viscosity approach is only appropriate for fine particle slurries (Schaan, 2001). There is no particle size dependence in equation 2.40d. For coarse solids, the particle behaviour at the wall is complex and should be addressed with a particle friction factor (f_s) (Shook et al., 2002). At lower velocities, near the critical deposition velocity, the use of an equivalent fluid model is not appropriate.

Comparing the equivalent fluid model curve with the experimental data shows that it provides an adequate prediction at high velocities where turbulent suspension is significant enough to suspend the particles uniformly throughout the pipe cross-section. This is evident in the pipe flow experimental data above velocities of 2.0 m/s. However, the equivalent fluid model fails as the critical deposition velocity is approached. Coulombic friction is likely significant under these conditions. This results in the equivalent fluid model drastically underpredicting the frictional losses of the slurry, verifying that homogeneous fluid models are not appropriate for predicting frictional losses under conditions with significant particle segregation.

5.4.3. CT Slurries

As outlined in Section 3.5.2, a clay, sand and water slurry was prepared to model Syncrude CT (Consolidated Tailings) (FTFC, Fine Tailings Fundamentals Consortium, 1995). The resulting pressure gradient versus velocity curves acquired for these mixtures are shown in Figures 5.10 and 5.11.

The experimental data show that the slurry exhibits non-Newtonian behaviour and must be fit with a multi-parameter model rather than a single-parameter Newtonian model. Past experience has shown that the Bingham model is appropriate for slurries of this kind (Sanders et al., 2002).

The Buckingham equation (Equation 2.56) was used to obtain the Bingham model parameters using the laminar experimental data for each of the test runs. The resulting rheological parameters for the carrier fluid and the coarse particle mixture are provided in Tables 5.4 and 5.3, respectively.

5.4.3.1. CT 'No Gypsum' Slurry

The experimental pressure gradient data for the original makeup of CT slurry, with no additives, is shown in Figure 5.10. The data indicates that the slurry has a significant yield stress. The slurry was composed of 3.5:1 sand to clay ratio (by mass), with a total solids concentration of 36% v/v and a bulk density of 1598 kg/m^3. As well, a laminar to turbulent transition also exists at approximately 2.50 m/s in the 53 mm pipe test section.

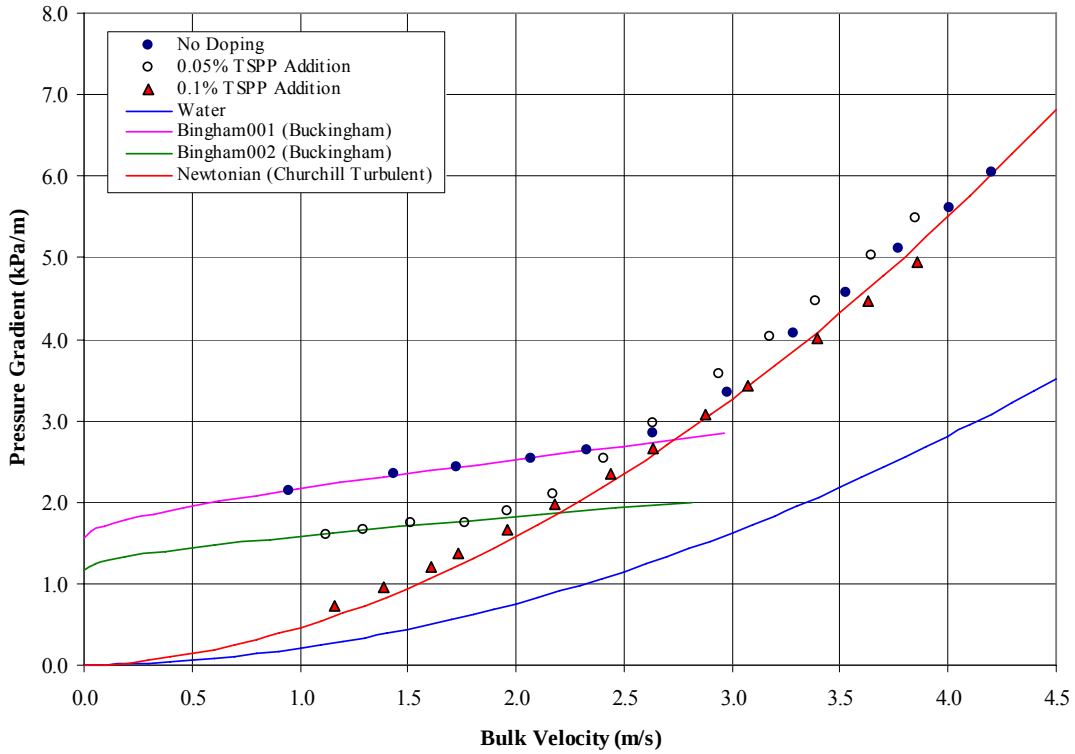

Figure 5.10: Pressure gradient versus velocity for a model Syncrude CT 'no gypsum' slurry in the 53 mm test section; ρ=1598 kg/m^3

Figure 5.10 also shows the experimental data for slurries with varying TSPP addition amounts. One can see that the yield stress of the slurry is reduced with each addition of TSPP. The final dosage of TSPP (0.10% w TSPP/w clay) corresponds to the slurry that was used to represent the CT 'no gypsum' slurry. The rheological data in Figure 5.10 shows that the final slurry has no

yield stress and that all of the data points are in turbulent flow. Treating the CT 'no gypsum' slurry as a Newtonian fluid and fitting the pipe flow data to Equation 2.22 resulted in an equivalent fluid viscosity of 0.0074 Pa-s.

5.4.3.2. CT 'Gypsum' Slurry

A new slurry was not prepared to model the CT 'gypsum' slurry. Calcium chloride dihydrate (Ca^{2+}, Appendix B) was added to the 'no gypsum' slurry, in the previous section, to model CT slurry with a yield stress (i.e. a gypsum addition in industry). Figure 5.11 shows the data for the resulting CT 'gypsum' slurries.

Comparing Figure 5.10 to 5.11 and noting the CT rheological parameters in Table 5.3, one can see that the addition of calcium ion increases the plastic viscosity and the yield stress of the slurry. However, at this concentration the slurry rheology shows some time dependent behaviour similar to the behaviour observed by Litzenberger (2003). To determine the extent of the variation, the rheological behaviour was tracked over the two days of experimental testing. The data also shows that the turbulent pressure drop versus velocity relationship is independent of the additive concentration (i.e. yield stress of the slurry) for the range of concentrations considered in this study.

Based on equipment limitations, a limited number of measurements were performed in the laminar regime with the CT 'Gypsum Day 1' slurry. This limited data set made it difficult to fit the Buckingham equation (Equation 2.56) to the experimental data. It also appears that deposition effects are important in the 53 mm feed test section near the laminar to turbulent transition at 1.4 m/s for this slurry. A slight increase in the measured pressure gradient was observed with a decrease in the bulk velocity of the slurry at the lowest velocities employed. Further operation below this velocity was not attempted as it may have resulted in a settled bed in the feed line to the flume.

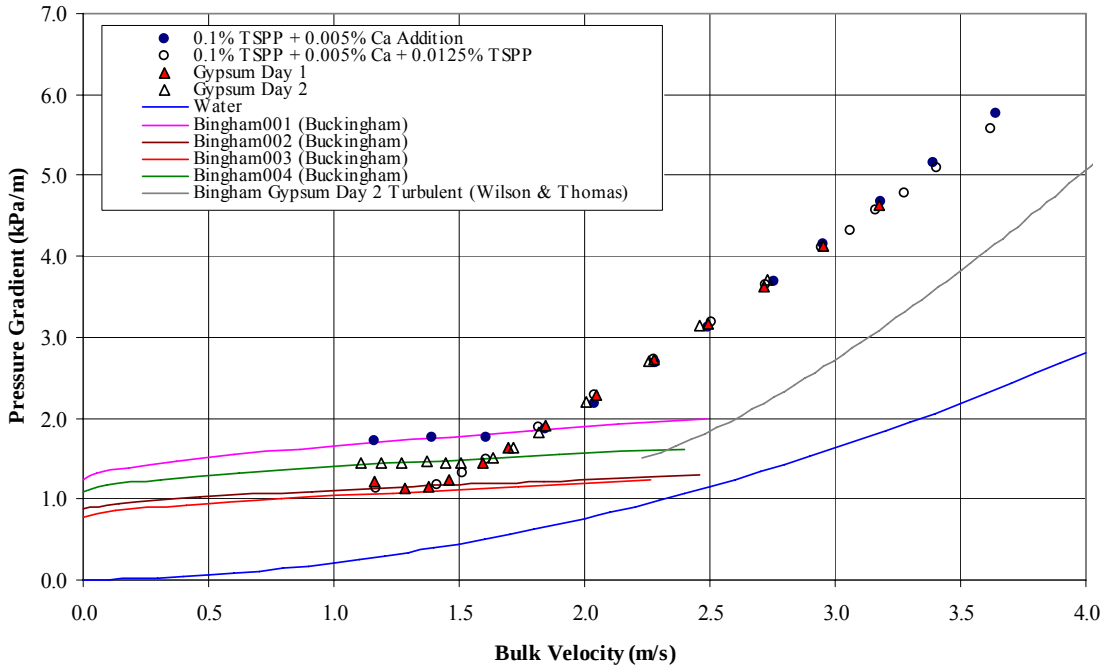

Figure 5.11: Pressure gradient versus velocity for a model Syncrude CT 'gypsum' slurry in the 53 mm test section; ρ=1598 kg/m^3

5.4.4. Thickened Tailings Slurries

The model Thickened Tailings slurries that were investigated in this study consisted of a 1:1 sand to clay ratio (by mass) and a bulk density of 1510 kg/m^3. Considering the pressure drop versus velocity data in Figure 5.12, it can be seen that this highly viscous slurry remains in the laminar regime over a wide range of operating velocities in the 53 mm test section, and transitions to turbulent flow only at the highest velocities attainable in the experimental circuit.

As was observed with the CT 'gypsum' slurries, the Thickened Tailings slurries also exhibited time dependent behaviour. The rheological properties were tracked during the experimental testing to monitor the extent of this behaviour. Table 5.3 indicates that the plastic viscosity and the yield stress for the Thickened Tailings slurries were quite high, and were on average approximately 0.040 Pa-s and 40 Pa respectively. The best fit curves obtained with the Buckingham equation (Equation 2.56) for the Thickened Tailings slurries are shown in Figure 5.12.

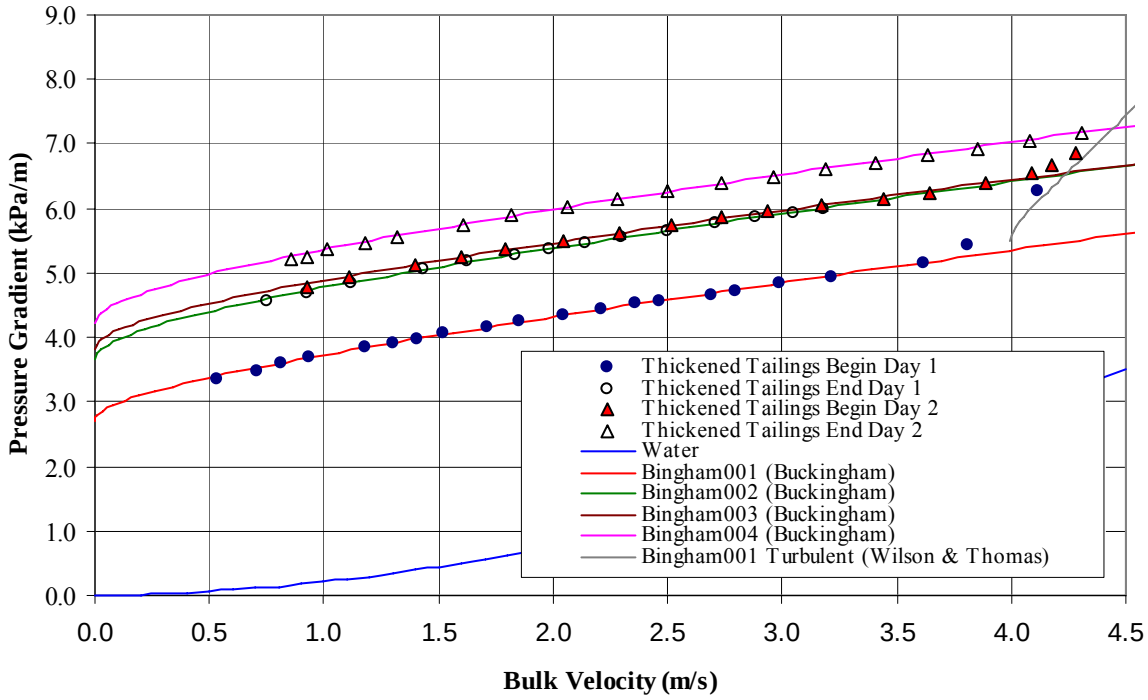

Figure 5.12: Pressure gradient versus velocity for a model Syncrude Thickened Tailings slurry in the 53 mm test section; ρ=1510 kg/m^3

5.5. Flume Wall Shear Stresses and Friction Factors

The wall shear stress and friction factor for a given test were calculated using Equations 2.12 and 2.17 respectively. It should be noted that the calculated wall shear is an averaged quantity. It represents the average wall shear stress in the flume test section. It is the mean wall shear stress about the wetted perimeter of the flume and the average wall shear stress between height measurement positions 1 and 2 in the flume test section. Since the average wall shear stress is used to calculate the Fanning friction factor, the friction factor also represents an averaged quantity in the flume test section. The experimental data for all of the mixtures tested in the flume circuit is presented in Appendix D.

The friction factor results for the mixtures are compared to the laminar and turbulent friction factor curves. For slurries with yield stresses, these curves are obtained using the Zhang Reynolds number (Equation 2.18). For Newtonian slurries the curves are obtained using the standard Reynolds number (Equation 2.21). For open channel flows, the hydraulic diameter associated with the cross section area of the flume flow (Equation 2.19) has been used in place of

the pipe diameter. Churchill's (1977) equation (Equation 2.22) has been used to predict friction factors for the open channel flows.

For slurries exhibiting a yield stress, predictions of the average wall shear stress in laminar flow were made using the approach suggested by Kozicki and Tiu (1967) (Equation 2.28). The approach requires one to specify the Bingham yield stress and plastic viscosity of the slurry, along with slurry density, hydraulic radius and the average velocity of the flow. Parity plots have been generated to illustrate the level of agreement between the experimentally measured wall shear stress and the wall shear stress predicted by the Kozicki and Tiu (1967) model.

Unlike pipe or closed conduit flow, the average fluid velocity in an open channel cannot be determined prior to testing because the depth of flow is unknown. Unless a weir or some type of height control device is installed within the flow (i.e. weir, upstream control for supercritical flows, downstream control for subcritical flows, Henderson, 1966) an *a priori* estimate of the depth of flow is not possible.

When performing slurry flow calculations in systems where the cross-sectional geometry is not circular, the hydraulic diameter is a common parameter used to model the flow. Equation 2.19 is used to calculate hydraulic diameter. It reduces to the actual pipe diameter for flow in a closed circular conduit. In turbulent flow, much of the frictional loss occurs near the wall and the solid boundaries. For flows of this kind, the hydraulic diameter accurately addresses the frictional loss behaviour. As well, at a short distance from the wall, the variation in velocity in the flow is nearly uniform with a value that approaches the mean velocity. This makes the hydraulic diameter a suitable choice since the entire cross-section is nearly under the same flow conditions.

In laminar flows, velocity profiles are typically parabolic. The local velocity is not uniform and different behaviour occurs in different regions throughout the flow cross-section. Typically this type of flow behaviour is not accurately addressed using the hydraulic diameter since a single velocity can not be used to represent the majority of the flow domain. Attention and caution should be used when applying a hydraulic diameter to laminar flows. Often an equivalent diameter term which accounts for the geometry of the flow should be applied. Kozicki and Tiu (1967) used an equivalent diameter approach by employing geometric parameters a and b.

In open channel flows, the wall shear stress distribution about the wetted perimeter is not uniform. The hydraulic diameter (in laminar flow) may not be the best choice as an appropriate length scale. However, it has been used in this study, since slurries with yield stresses have an unsheared plug where a fairly uniform velocity profile exists over a large fraction of the cross section of the flow.

5.5.1. Water

Tests with water were conducted in the flume before any investigations were performed with slurries. Figure 5.13 shows a plot of the average wall shear stress versus the mean velocity in the flume for a series of Saskatoon tap water tests. These tests were performed over a range of flume inclinations between 0.5 and 5 ^{o} as discussed previously in Section 3.5. A concave up wall shear stress versus velocity relationship is observed for the flows in the flume which is similar to what is observed with pipe flow. All of the data was gathered in the turbulent regime. As well, at higher velocities there is a large degree of scatter in the experimental data. This is due to the difficulty in measuring the depth of flow for turbulent fluids in the experimental flume. This led to errors in both the calculated wall shear stress and average velocity of the order of 10% and 4%, respectively.

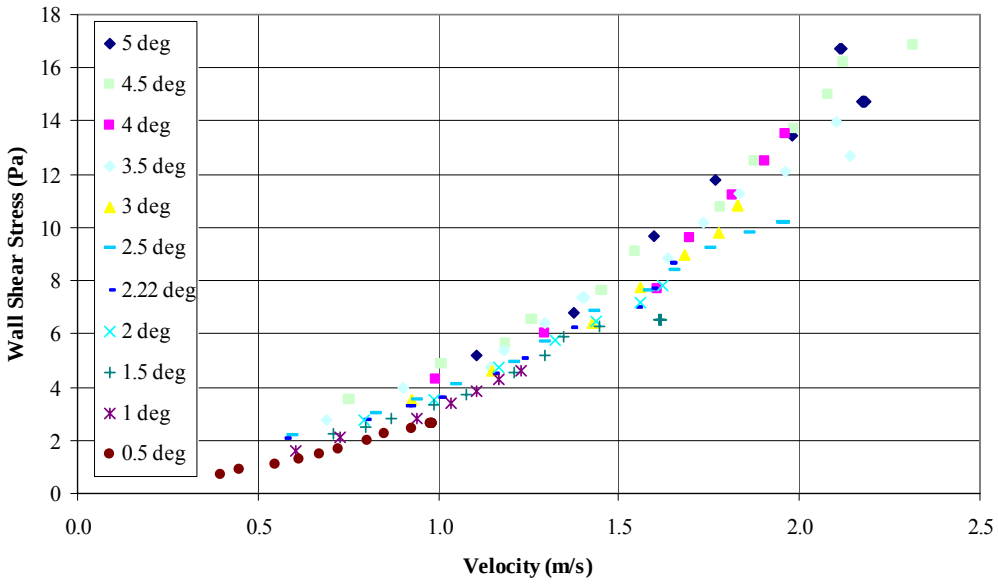

Figure 5.13: Wall shear stress versus velocity for Saskatoon tap water in the 156.7 mm flume

Figure 5.14 presents a plot of Fanning friction factor versus Reynolds number for the water tests shown in Figure 5.13. Theoretical curves representing smooth and rough turbulent flow in the

flume test section for water according to the empirical frictional correlation proposed by Churchill (1977) are also included. The experimental water data was used to determine an equivalent pipe roughness in the flume. A least squares correlation with Equation 2.22 for fully turbulent points (Re > 10000) produced a dimensionless roughness, ε/D_h, of 0.00296 in the flume test section. Based on this result, a roughness of 193 μm in the flume test section was determined to best fit the data using the depths of flow measured for these tests and the calculated hydraulic diameters. However, it should be noted that this roughness does not affect the frictional loss behaviour of the more viscous slurries exhibiting yield stresses in laminar flow since laminar flow is independent of pipe roughness. Despite the difficulty in measuring the depth of flow with the turbulent water slurries, the agreement between the experimental data and Churchill's (1977) curve is quite good.

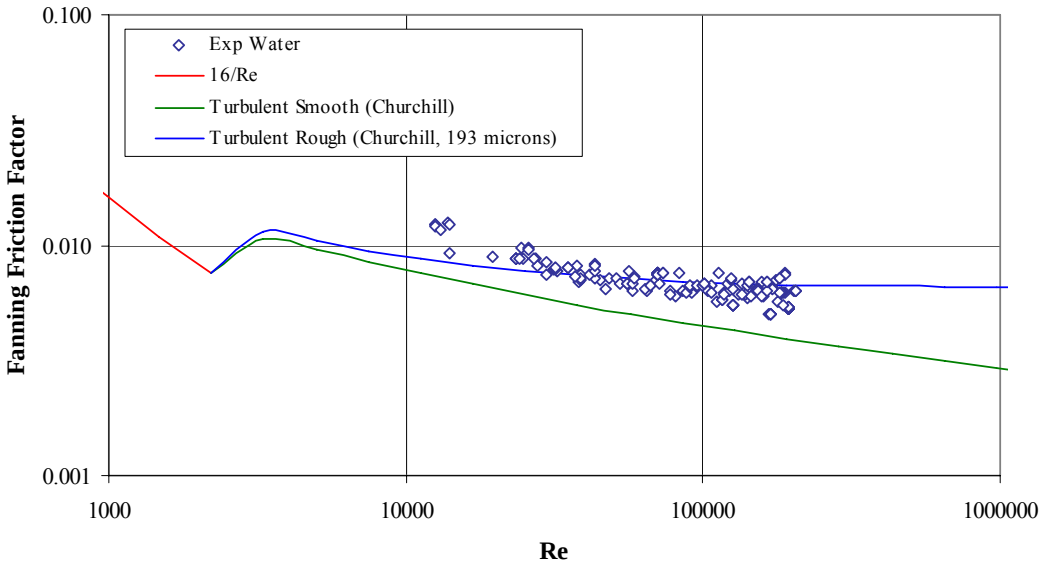

Figure 5.14: Fanning friction factor versus Reynolds number for Saskatoon tap water in the 156.7 mm flume

Figure 5.15 presents a plot of the experimental wall shear stress data for Saskatoon tap water compared to the an experimental prediction from Equation 2.22, which includes the effects of roughness determined from the least squares analysis of the data in Figure 5.14. The agreement is quite good except at high velocities where there is a significant scatter in the experimental data. This is most likely due to error associated in measuring the depth of flow at high flow rates. Figure 5.16 shows the same data plotted on a parity plot. Once again the agreement between the experimental predictions and theory is acceptable only deviating at the highest wall shear stresses (average velocities).

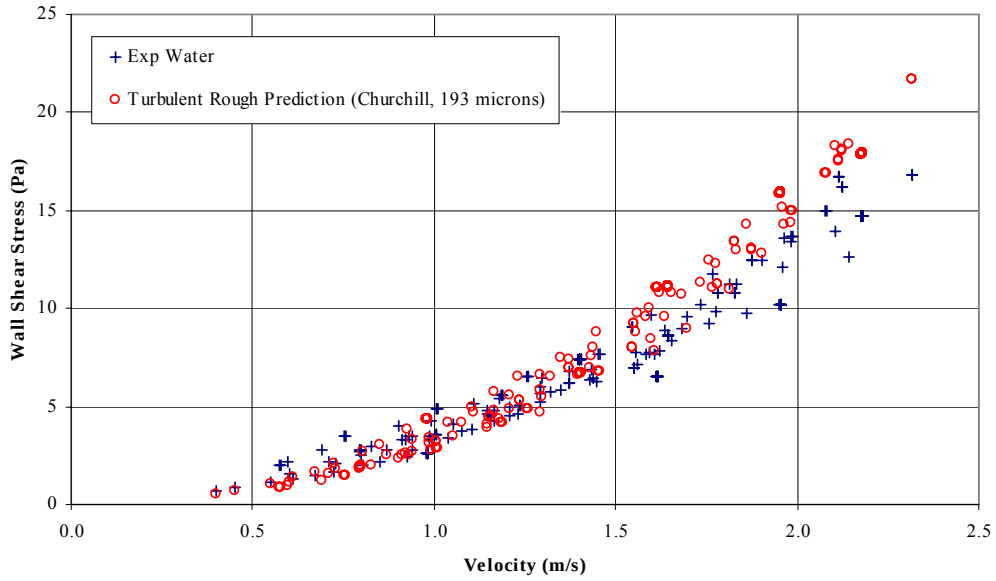

Figure 5.15: Experimental wall shear stress comparison with turbulent rough prediction for Saskatoon tap water in the 156.7 mm flume

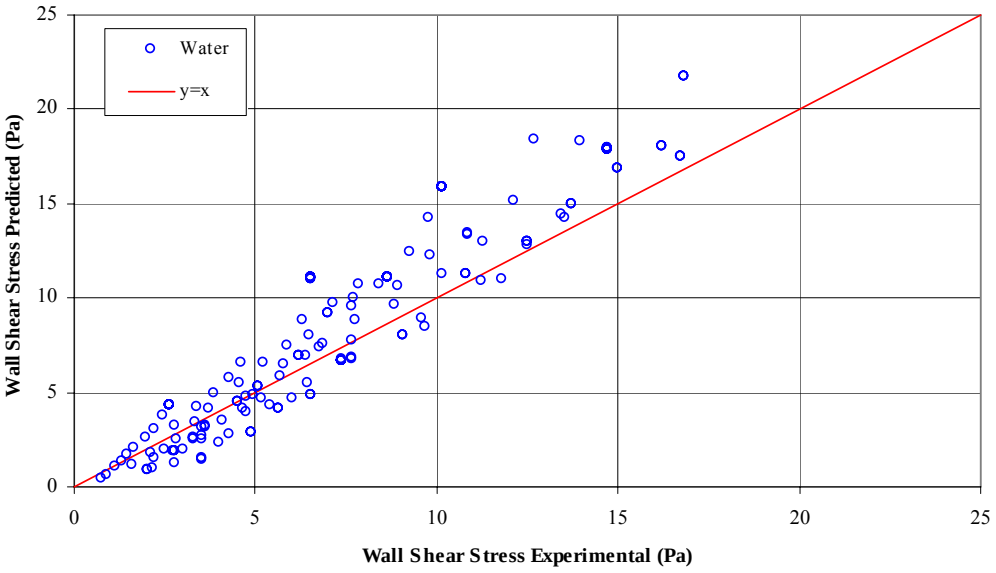

Figure 5.16: Wall shear stress parity plot comparison for Saskatoon tap water in the 156.7 mm flume

5.5.2. Sand-Water Slurries

The average wall shear stress versus velocity behaviour for the 25% v/v sand-water slurries in the flume test section is shown in Figures 5.17 to 5.19. Figure 5.20 presents a parity plot of the experimental and predicted wall shear stresses in the flume. Figure 5.21 presents the Fanning

friction factor versus Reynolds number results for the 25% v/v sand-water tests. As can be observed in the wall shear stress versus velocity plots, there seems to be a significant amount of scatter in the data. There are a number of possible explanations to account for this experimental error. Variation in inlet conditions with the sand-water tests, the error in the height measurement at planes 1 and 2, and the apparent relationship between wall shear stress and flume slope angle are all possible explanations.

Two different inlet conditions were employed in the sand-water tests. The original inlet condition (Old Inlet) corresponded to one where the slurry was transferred from the feed line to the flume through a flexible rubber hose which was orientated parallel to the flume. With this setup, the sand deposited at the inlet of the flume. This produced a stationary bed which made flow measurements impossible. Dominguez et al. (1996) also noted this difficulty. They showed that when velocities fall below the critical deposit velocity, there is a serious risk of blocking the channel system.

The inlet condition was improved so that the slurry was transferred from the feed line to the flume through a flexible rubber hose which was orientated perpendicular to the flume (New Inlet). A photograph of the new inlet condition is presented in Appendix F. This increased the kinetic energy of the slurry at the entrance of the flume which delayed sand deposition until the flume outlet, when there was a potential for it to occur under a given set of test conditions. The experimental data presented in Figure 5.17 shows that the wall shear stresses obtained with the original inlet condition are much higher than the shear stresses obtained with the revised inlet. This may be explained by the increased segregation of sand in the flume test section observed with the original inlet condition.

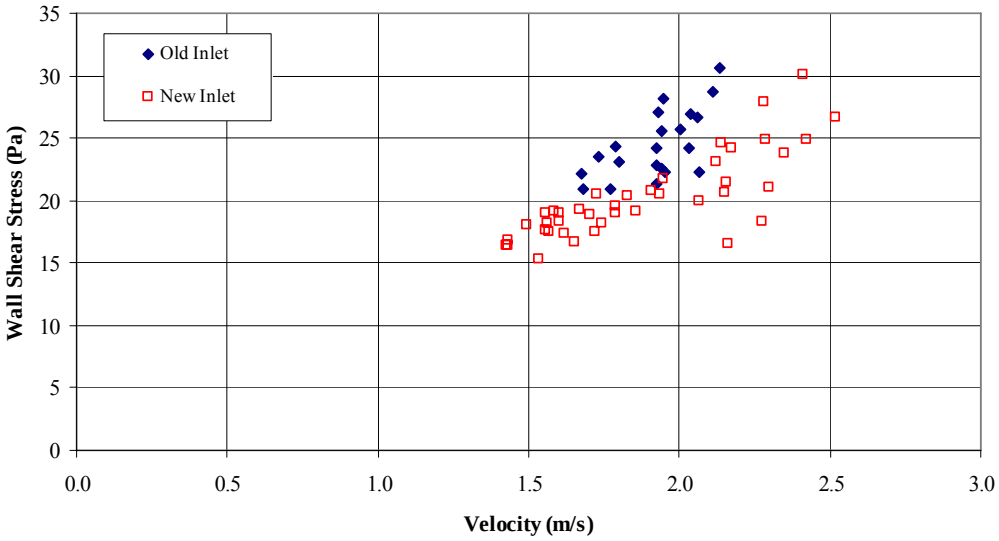

Figure 5.17: Wall shear stress versus velocity for a 25% v/v sand-water slurry in the 156.7 mm flume; ρ=1410 kg/m^3

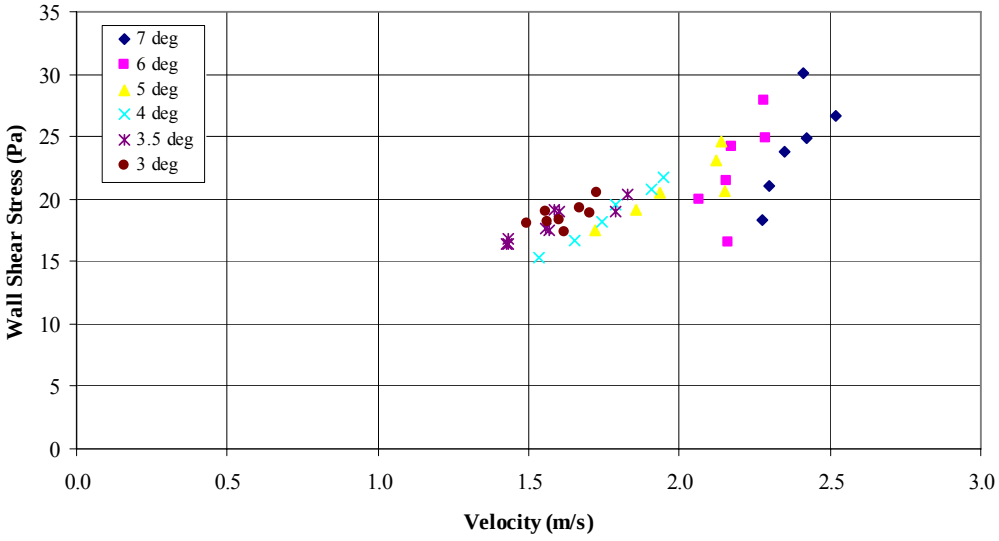

Figure 5.18: New inlet wall shear stress versus velocity for a 25% v/v sand-water slurry in the 156.7 mm flume at various angles; ρ=1410 kg/m^3

A plot of wall shear stress versus average velocity is presented in Figure 5.18 for the 25% v/v sand-water slurry. This plot presents data as a function of flume slope angle. One can see that if the velocity is held constant, a definite increase in wall shear stress with decreasing flume slope angle occurs. This behaviour was not observed with the water slurries in the flume and is believed to be associated with particle segregation. Particle segregation would be expected to be

more prominent at lower flume angles. If the bulk velocity were held constant, a larger wall shear stress should exist at a lower flume angle since a larger frictional (Coulombic) contribution from the solid particles would be anticipated at this condition. This is the most likely reason for the high degree of scatter in the data. Since steady state operation with a stationary deposit could not be achieved with the sand-water slurry, the data does not reach a point where the shear stress increases with decreasing velocity.

Figure 5.19 provides a comparison of the experimental wall shear stress results with the shear stress values predicted by the equivalent fluid model (EFM) with a viscosity of 0.0029 Pa-s. The EFM predictions of the slurry wall shear stress in an open channel are reasonably accurate. A roughness value of 193 μm was used in the EFM model and Equation 2.22. The data presented in this plot is scattered but the theoretical prediction appears to represent the general trend. The equivalent fluid model provides an acceptable means of predicting the experimental wall shear stress at higher velocities. However, at the lower velocities the experimental wall shear stress is much larger than the equivalent fluid model prediction. The viscous dissipation mechanism of the EFM does not consider the Coulombic friction effect which would be expected to be more significant at lower velocities. A parity plot comparing experimentally measured wall shear stress with those predicted from the EFM is given in Figure 5.20.

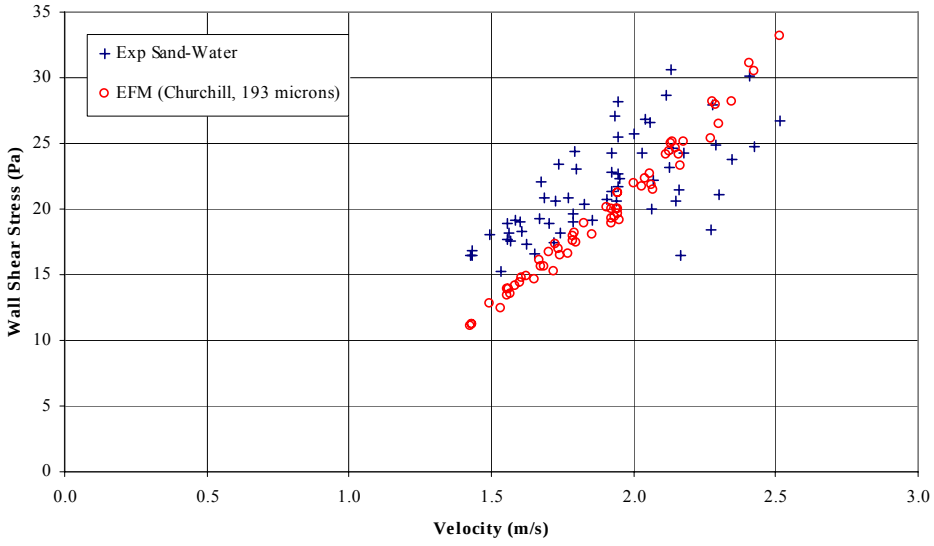

Figure 5.19: Experimental wall shear stress comparison with equivalent fluid model for a 25% v/v sand-water slurry in the 156.7 mm flume; ρ=1410 kg/m^3

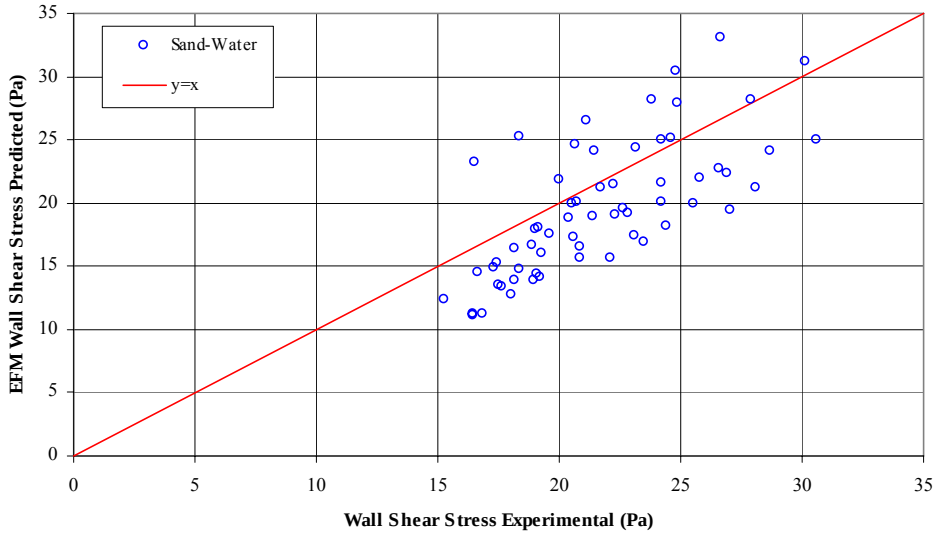

Figure 5.20: Wall shear stress parity plot comparison for a 25% v/v sand-water slurry in the 156.7 mm flume; ρ=1410 kg/m^3

It is important to note that the equivalent fluid model is only valid when the suspension is homogenous. Any particle segregation would result in a Coulombic friction term which generates additional frictional losses that are not included in the EFM model. This applies to both pipe flow and open channel flow. Wilson (1980) describes how the Coulombic friction mechanism acts similarly in the two distinct flow geometries. At high flume angles and high velocities, the EFM should be expected to yield accurate predictions. This is not the case at lower angles and lower velocities when operating near the critical deposition velocity.

Figure 5.21 presents a plot of Fanning friction factor versus Reynolds number for the sand-water tests in the flume. The equivalent fluid viscosity (0.0029 Pa-s) and density of the mixture (1410 kg/m^3) have been used in the Reynolds number calculation. For the most part, the resulting friction factors were higher than what would be predicted by theory for a rough wall turbulent flume flow (Equation 2.22). Particle segregation may represent the most plausible explanation for this effect. Particle segregation was observed for most of the sand-water tests conducted at lower velocities and flume angles (Figures 5.48, 5.49, 5.50). The added Coulombic friction effect associated with particle segregation would result in higher friction factors than the homogenous equation would predict.

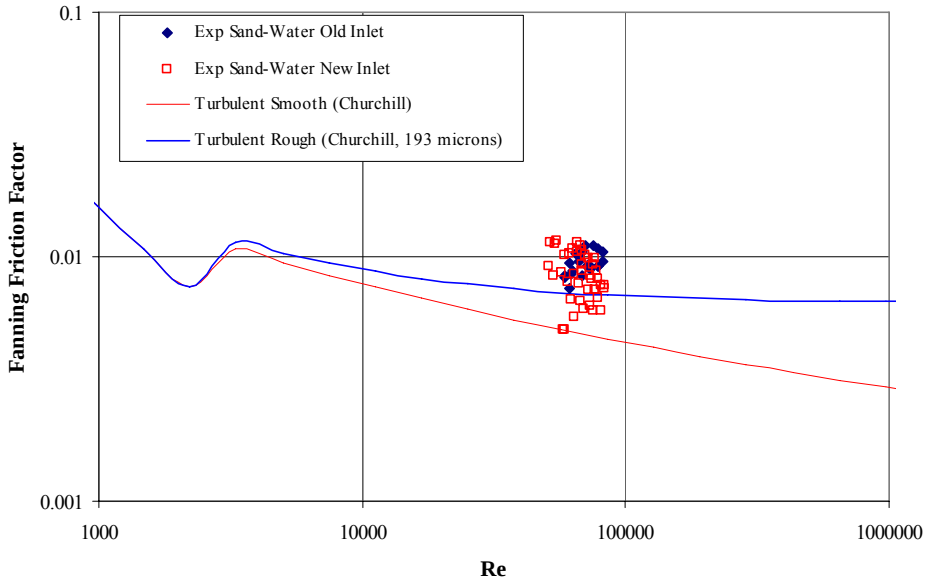

Figure 5.21: Fanning friction factor versus Reynolds number for a 25% v/v sand-water slurry in the 156.7 mm flume; ρ=1410 kg/m^3

5.5.3. Clay-Water Slurries

Figures 5.22 to 5.33 show the frictional loss behaviour of the kaolin clay and water slurries in the flume. Figure 5.22 presents an average wall shear stress versus velocity plot for the original makeup of a 22.2 % v/v kaolin clay and Saskatoon tap water slurry at a number of different angles in the flume. The density of the slurry was 1375 kg/m^3.

Based on the experimental data presented in Figure 5.22 the flume angle does not appear to affect the average wall shear stress over the range of velocities considered in this study. All of the data exhibits a trend similar to that measured with the slurry presented in Figure 5.5 under laminar pipe flow conditions. The scatter in the data presented in Figure 5.22 is most likely due to the inability to accurately measure the depth of flow of the slurry. The depth of flow error was discussed earlier and was shown to produce errors in wall shear stress and average velocity of the order of 10 and 4%, respectively. Some additional variation in the experimental data may be caused by variation in the rheological properties of the kaolin-water slurries. The degree of variation in these parameters is presented in Table 5.3.

It is interesting to note that some of the average wall shear stress values presented in Figure 5.22 fall below the value of the Bingham yield stress (32.9 Pa) evaluated using the 53 mm pipe

section. One would expect that no flow would be possible if the driving force for the flow is less than the yield stress. However, flow is possible because the wall shear stress is not uniform about the wetted perimeter of the flume cross section. The maximum wall shear stress occurs at the bottom of the pipe and is greater than the yield stress in this region where flow occurs. Therefore, even when the average wall shear stress is less than the yield stress, the local wall shear stress can be greater than the yield stress in specific locations about the perimeter allowing the slurry to flow in the flume.

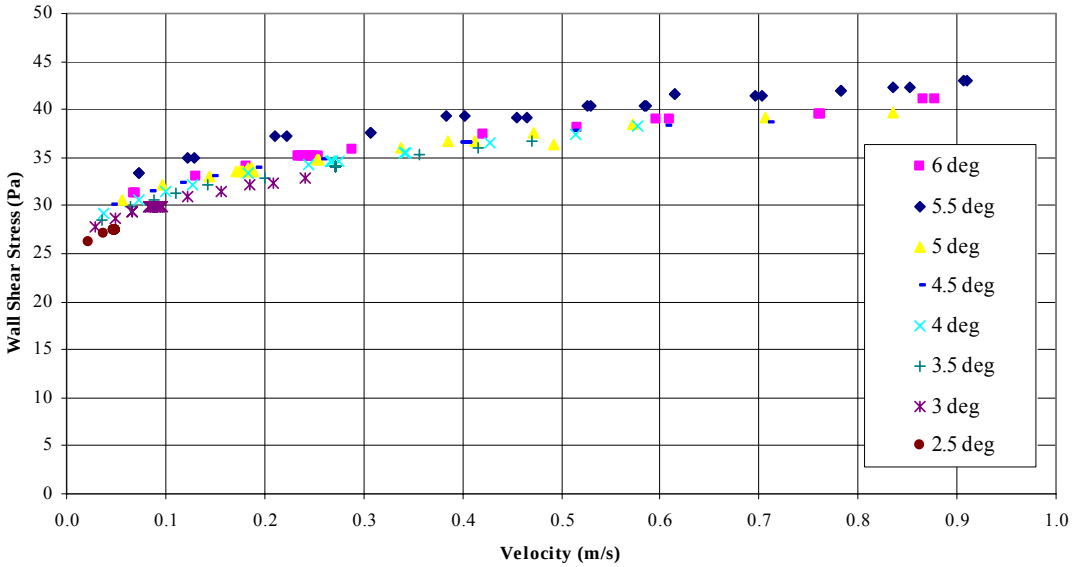

Figure 5.22: Wall shear stress versus velocity for a 22.2 % v/v kaolin clay-water slurry in the 156.7 mm flume; ρ=1375 kg/m^3

Figure 5.23 presents the experimental clay-water slurry data as a plot of Fanning friction factor versus the Zhang Reynolds number. The results provided in the figure indicate that all of the experimental data is in the laminar regime since the data closely follows the line associated with the function $16/\mathrm{Re}$. Equation 2.22 reduces to $16/\mathrm{Re}$ for Reynolds numbers less than 2000. The agreement with the theoretical laminar curve also suggests that the Zhang Reynolds number (Equation 2.18) and use of the hydraulic diameter (Equation 2.19) provide an accurate method to predict the frictional losses of homogeneous slurries in open channel flows.

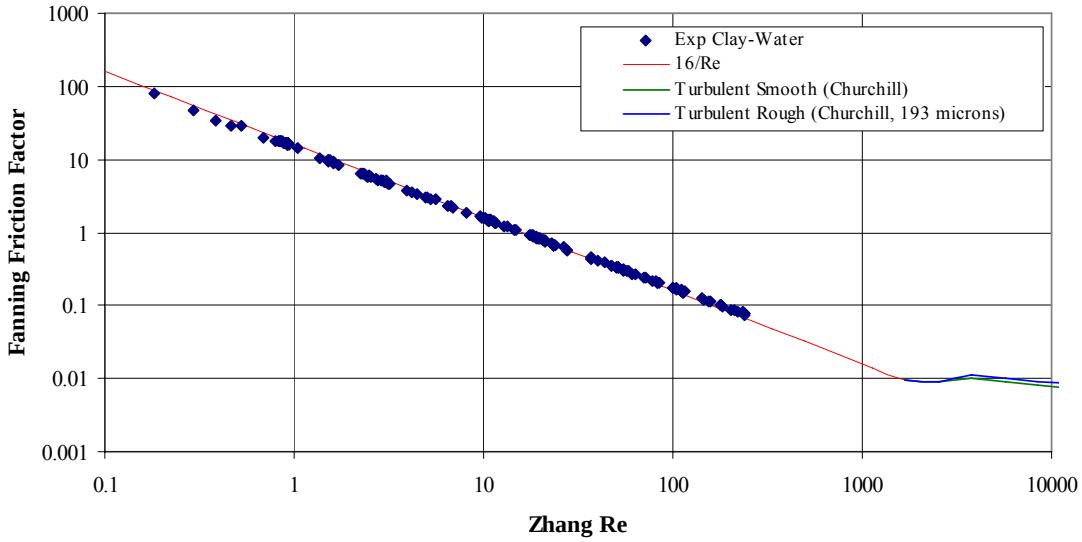

Figure 5.23: Fanning friction factor versus Zhang Reynolds number for a 22.2% v/v kaolin clay-water slurry in the 156.7 mm flume; ρ=1375 kg/m^3

Figures 5.24 and 5.25 present a comparison between the experimentally determined wall shear stresses for the kaolin clay-water slurry, and the wall shear stress predicted by Equation 2.28 (Kozicki and Tiu, 1967). For this slurry, there is poor agreement between the predicted and experimentally determined wall shear stresses at low and high velocities. However, the agreement is acceptable at intermediate velocities. Experimental average wall shear stress values, which were less than the Bingham yield stress, have not been included in the comparison since evaluation of the Kozicki and Tiu model is not possible under these conditions. Even though the localised predictions of Kozicki and Tiu are inaccurate in some cases, the parity plot presented in Figure 5.25 suggests that overall the predicted wall shear stresses are in agreement with the experimental values. For homogeneous slurries with high yield stresses, the Kozicki and Tiu (1967) model is capable of providing reasonable wall shear stress predictions.

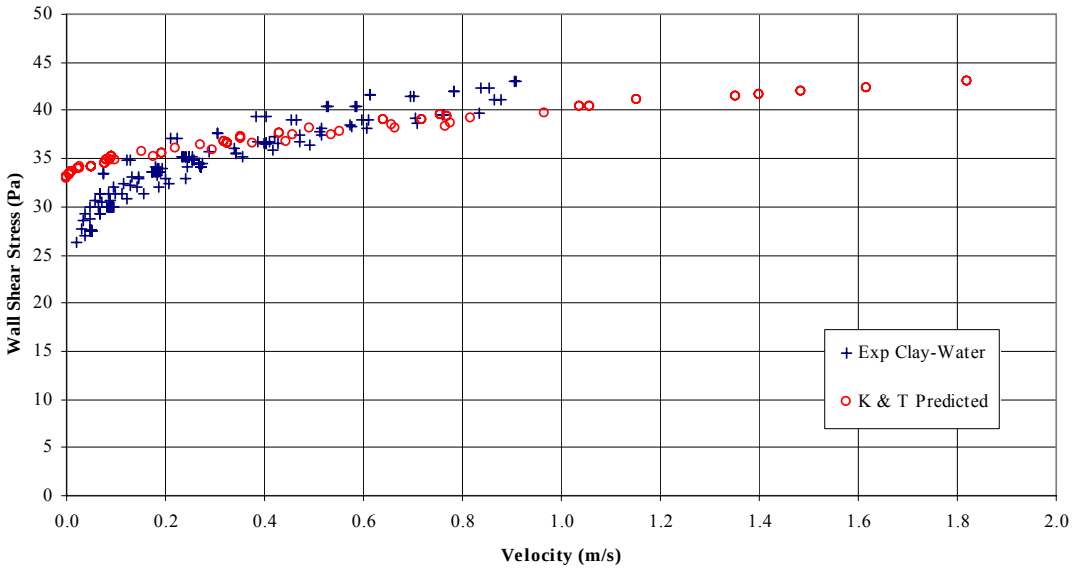

Figure 5.24: Experimental wall shear stress comparison with Kozicki and Tiu prediction for a 22.2 % v/v kaolin clay-water slurry in the 156.7 mm flume; ρ=1375 kg/m^3

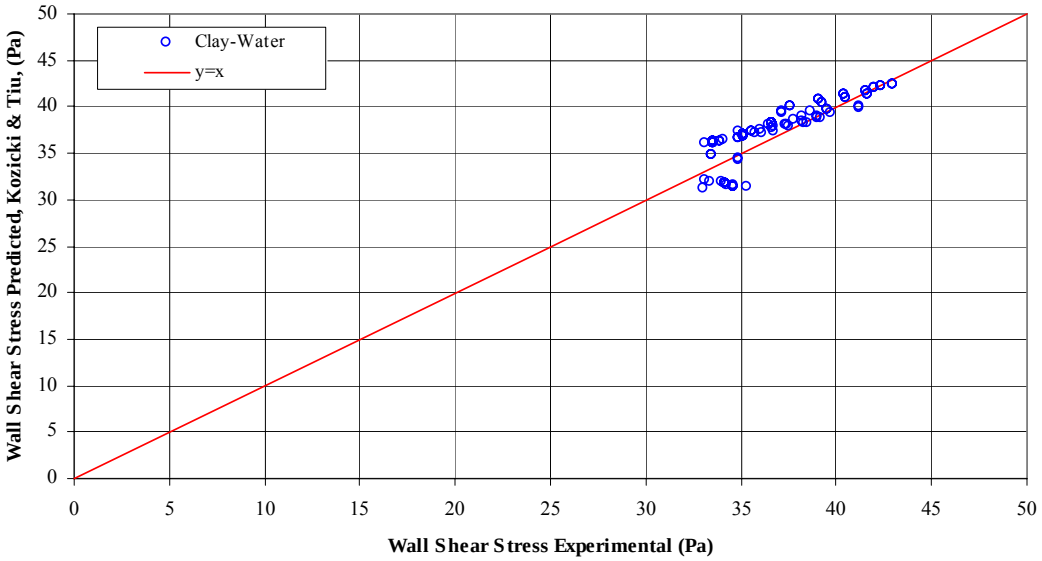

Figure 5.25: Wall shear stress parity plot comparison for a 22.2 % v/v kaolin clay-water slurry in the 156.7 mm flume; ρ=1375 kg/m^3

Figure 5.26 presents the flume wall shear stress versus velocity data obtained with the kaolin clay-water slurry containing 0.03% TSPP. This slurry had a solids concentration of 22.6% v/v and a density of 1384 kg/m^3. The Bingham yield stress was 6.4 Pa and the plastic viscosity was 0.0160 Pa-s. As was seen earlier with the clay-water slurries with no TSPP addition, the average wall shear stress does not appear to be a function of the flume angle over the range of bulk

velocities considered. At low velocities and flume angles, the slurry was in laminar flow. However, at higher flume angles the slurry appears to be transitioning to turbulent flow in the flume.

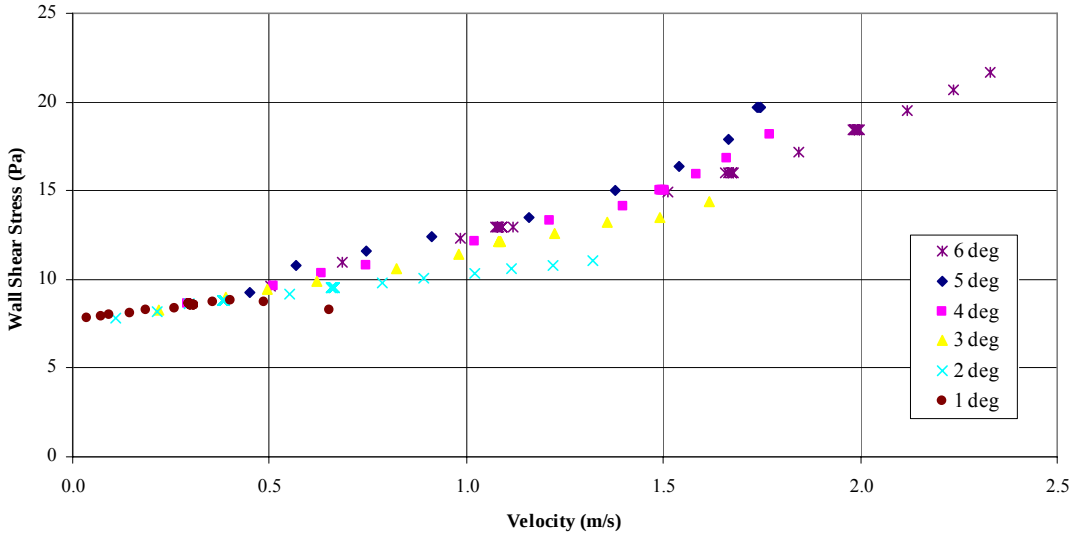

Figure 5.26: Wall shear stress versus velocity for a 22.6 % v/v kaolin clay-water slurry with 0.03% TSPP in the 156.7 mm flume; ρ=1384 kg/m^3

The data presented in Figure 5.27 appears to have been collected under laminar flow conditions although the flow may be transitioning to a turbulent state at the highest flowrates and flume angles. The data is in close agreement with the curve associated with Churchill's equation (1977). However, in the Reynolds number region near the transition to turbulent flow, the laminar flow curve underpredicts the experimental Fanning friction factors.

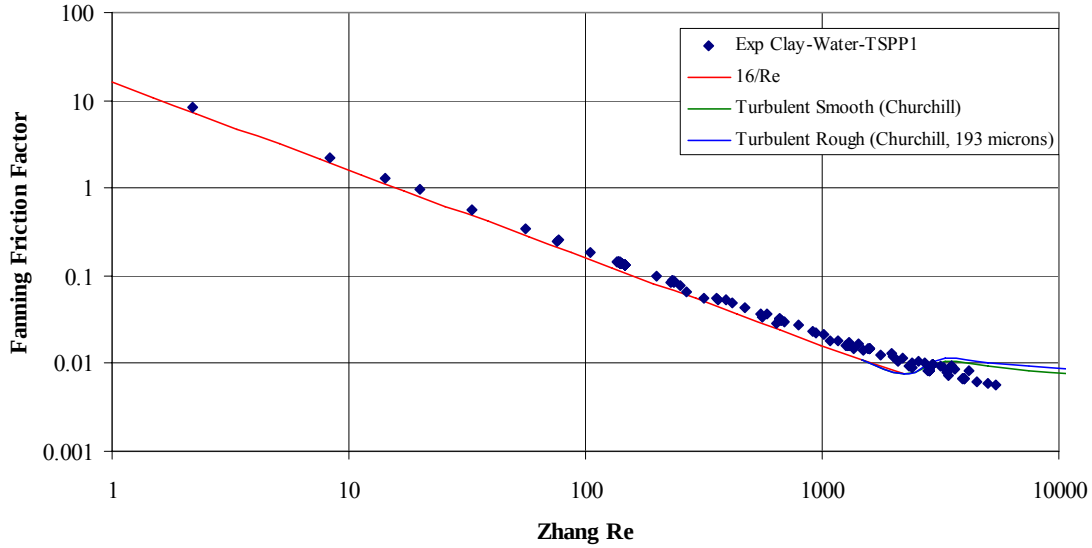

Figure 5.27: Fanning friction factor versus Zhang Reynolds number for a 22.6% v/v kaolin clay-water slurry with 0.03% TSPP in the 156.7 mm flume; ρ=1384 kg/m^3

Figures 5.28 and 5.29 present the experimental results obtained with the clay-water slurries with a 0.03% TSPP addition and the predictions obtained with the Kozicki and Tiu (1967) model. The results presented in Figure 5.28 suggest that the Kozicki and Tiu model provides an adequate prediction of the average wall shear stress at different velocities in the flume. Only laminar flow points are considered in the analysis since Equation 2.28 is not applicable to turbulent flow. As well, average wall shear stress values which fall below the Bingham yield stress have been excluded.

Figure 5.29 provides a parity plot comparison between the experimentally determined wall shear stress and the wall shear stress predicted by Kozicki and Tiu (1967). Considering the error associated with measuring the depth of flow, the agreement between the Kozicki and Tiu prediction and the experimentally determined wall shear stress is quite good. The level of agreement is similar to what was observed with the kaolin clay-water slurries without any chemical additions. Therefore, it appears that the Kozicki and Tiu model is capable of providing reasonably accurate wall shear stress predictions for homogeneous slurries with low yield stresses.

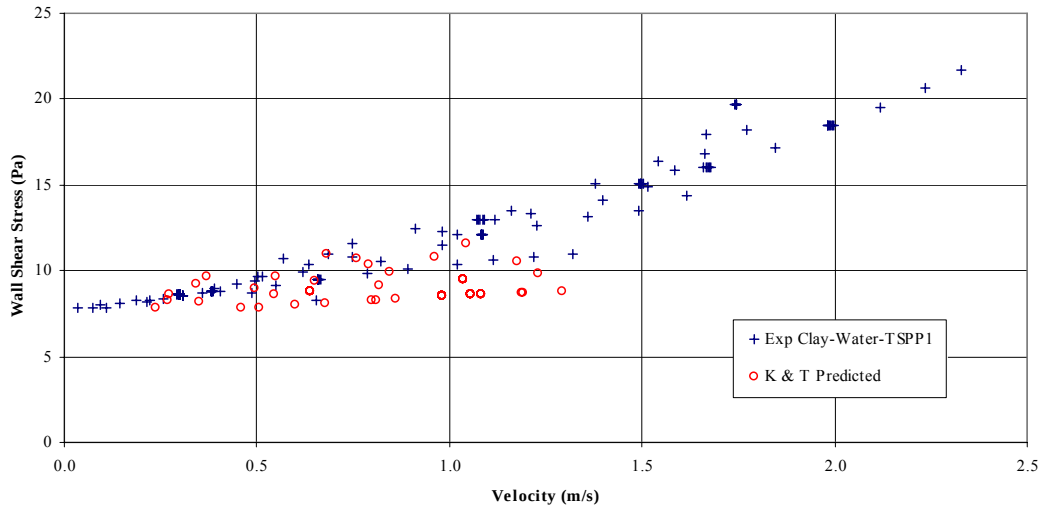

Figure 5.28: Experimental wall shear stress comparison with Kozicki and Tiu prediction for a 22.6 % v/v kaolin clay-water slurry with 0.03% TSPP in the 156.7 mm flume; ρ=1384 kg/m^3

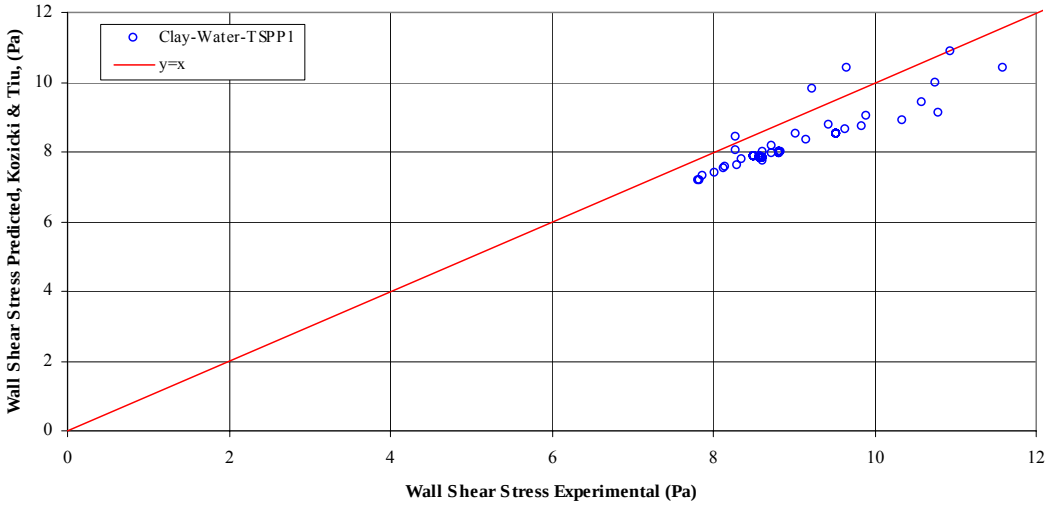

Figure 5.29: Wall shear stress parity plot comparison for a 22.6 % v/v kaolin clay-water slurry with 0.03% TSPP in the 156.7 mm flume; ρ=1384 kg/m^3

The existence of a yield stress was completely eliminated by adding 0.10% TSPP to the kaolin-clay water slurry. The resulting mixture became a homogeneous Newtonian slurry. The slurry viscosity of the 22.8% v/v slurry was 0.0067 Pa-s based on rheological analysis in the 53 mm feed pipe. The density of this slurry was 1386 kg/m^3. Figure 5.30 presents the average wall shear stress versus velocity data for this slurry in the flume. As has been observed with the other clay slurries, the flume angle does not appear to affect the average wall shear stress over the range of

velocities considered. As can also be seen, judging from the trend of the data, the slurry is flowing in turbulent regime in the flume.

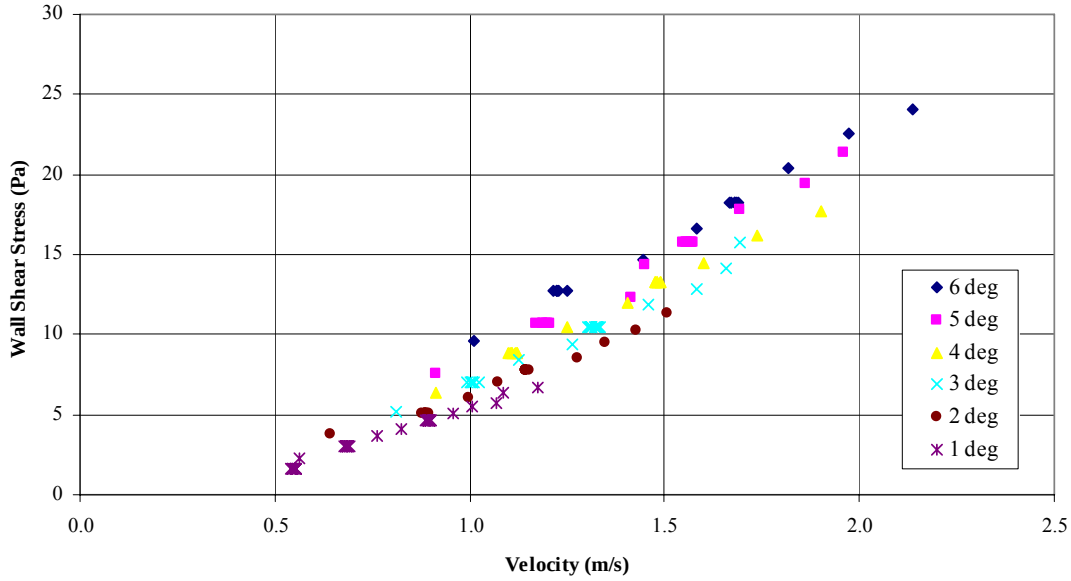

Figure 5.30: Wall shear stress versus velocity for a 22.8 % v/v kaolin clay-water slurry with 0.10% TSPP in the 156.7 mm flume; ρ=1386 kg/m^3

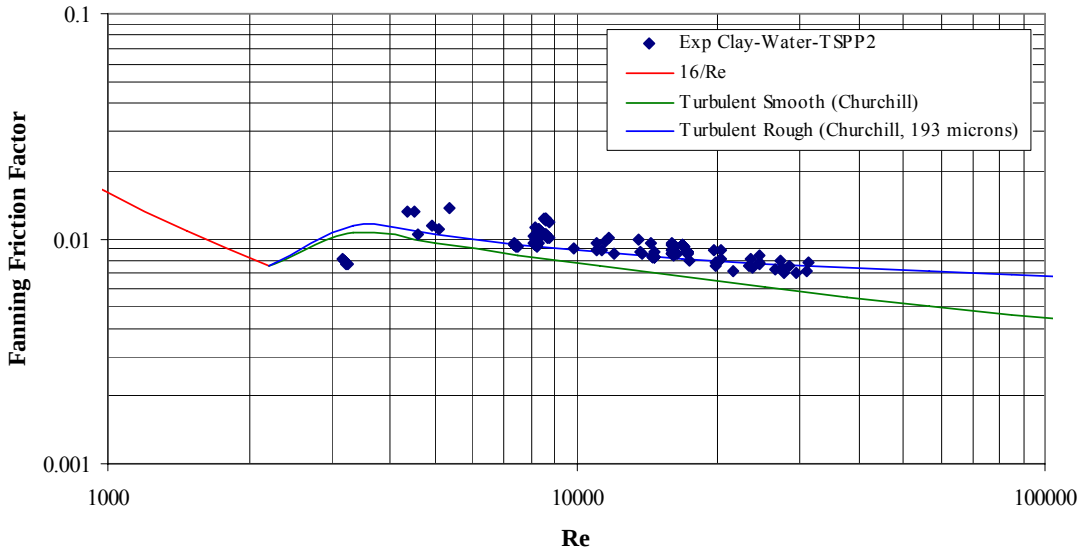

Figure 5.31: Fanning friction factor versus Reynolds number for a 22.6% v/v kaolin clay-water slurry with 0.10% TSPP in the 156.7 mm flume; ρ=1386 kg/m^3

In Figure 5.31, slurry frictional losses in the flume have been converted to Fanning friction factors and have been plotted against the Reynolds number for the clay-water slurry containing

0.10% TSPP. The Churchill (1977) turbulent flow curves determined from Equation 2.22 suggest that all of the data were collected under turbulent flow conditions. The curve predicted by Equation 2.22 with a roughness value of 193 μm in the flume test section, provides an accurate prediction of the friction factor in the flume. This is the same roughness value obtained from the analysis of the water data in the flume from Figure 5.14.

Figures 5.32 and 5.33 present a comparison between the experimental wall shear stresses and the wall shear stress determined by Equation 2.22. The Kozicki and Tiu, (1967) model was not appropriate for this set of measurements since the slurry was Newtonian and turbulent. The agreement between the experimental data and predictions obtained with Churchill's equation is evident as is shown in Figure 5.32. The scatter in the experimental data can be attributed to the difficulty in obtaining accurate measurements for the depth of flow under turbulent conditions in the flume leading to errors in the wall shear stress and average velocity.

Figure 5.33 presents a parity plot comparing the experimental wall shear stresses and the wall shear stress predicted with Equation 2.22. The data is randomly distributed about the $y = x$ curve. Therefore, it would appear that the hydraulic diameter can be used with Equation 2.22 to provide accurate predictions for the frictional loss behaviour of Newtonian slurries in turbulent flow in flumes. de Nevers (2005) showed that the standard pipe flow equations work quite well when the hydraulic diameter is applied to non-circular cross sections. However, he cautioned that the equations do not work well for shapes that depart radically from a circular cross section.

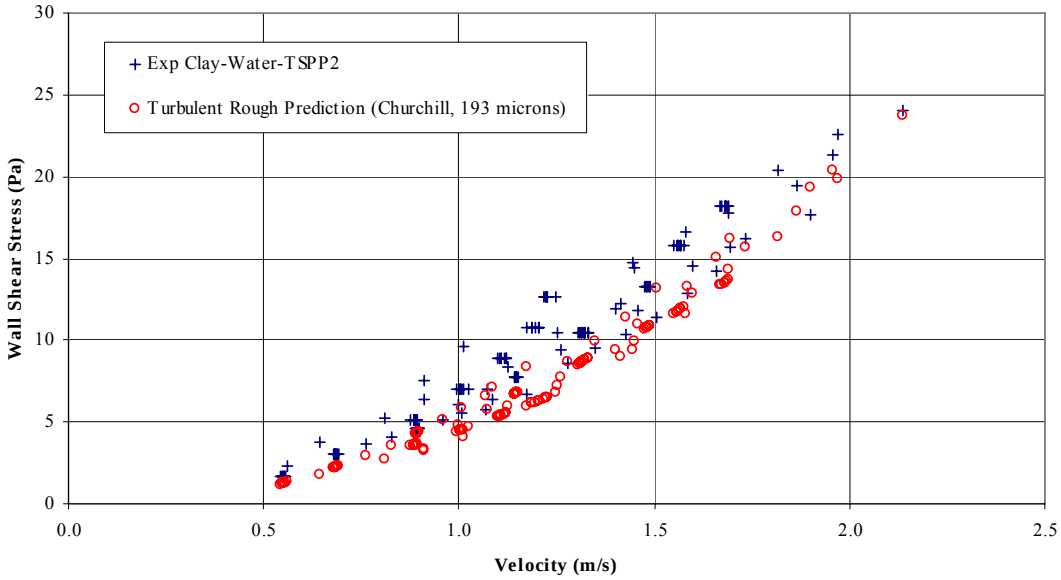

Figure 5.32: Experimental wall shear stress comparison with turbulent rough prediction for a 22.6 % v/v kaolin clay-water slurry with 0.10% TSPP in the 156.7 mm flume; ρ=1386 kg/m^3

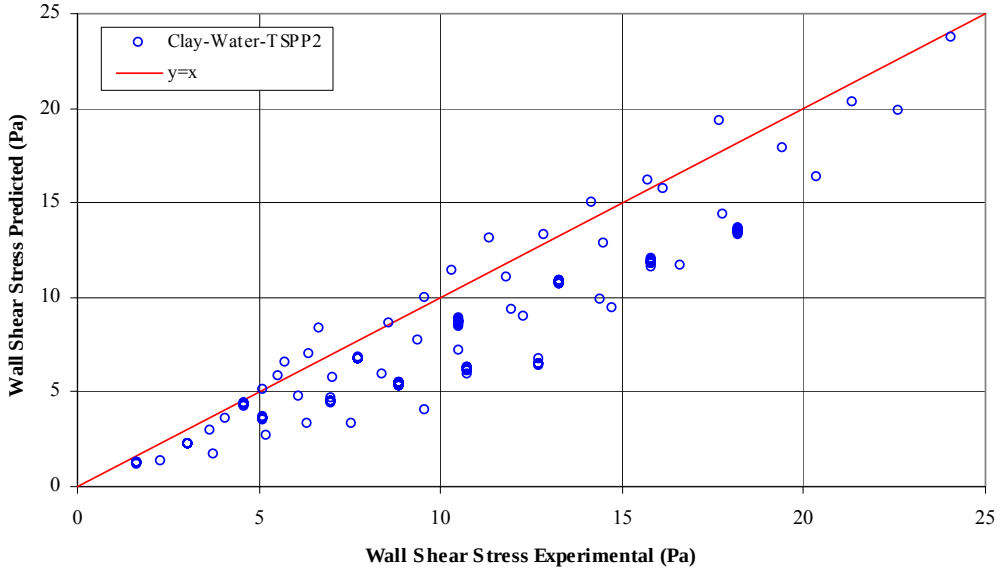

Figure 5.33: Wall shear stress parity plot comparison for a 22.6 % v/v kaolin clay-water slurry with 0.10% TSPP in the 156.7 mm flume; ρ=1386 kg/m^3

5.5.4. Clay-Water Slurries in Rectangular Channels

The data collected in this experimental study were obtained in a single flume apparatus. This study only considered a flume with a circular cross-section. In addition, only a single internal

diameter, 156.7 mm, was considered. Flume flow results from other studies in the literature were considered in order to determine if the Zhang Reynolds number correlation (Equation 2.18) and the Kozicki and Tiu model (Equation 2.28) are appropriate for Bingham slurries in flumes of different geometries and sizes.

Haldenwang (2003) performed tests on kaolin and bentonite clay-water slurries in three different rectangular flume widths (75, 150, 300 mm) over a range of solids concentrations (slurry densities from 1014 to 1165 kg/m^3) and a range of flume inclinations (1 to 5^o). The rheological data of Haldenwang (2003) has been fit with the Bingham model so that it could be used in this investigation and applied to the models presented in Sections 2.3 and 2.4. The goodness of fit of the Bingham model to the rheological data of Haldenwang (2003) was determined to be acceptable and as good as the Herschel-Bulkley fit applied by Haldenwang in his analysis.

Figures 5.34 and 5.35 present the experimental results of Haldenwang (2003) plotted as Fanning friction factor versus Zhang Reynolds number. The friction factors values show good agreement with the laminar curve (16/Re), with the use of the Zhang Reynolds number using the Bingham model parameters, for both the kaolin and bentonite slurry data. As well, both slurries transition to turbulence at approximately the same Zhang Reynolds number as was observed in the flume tests conducted in this study.

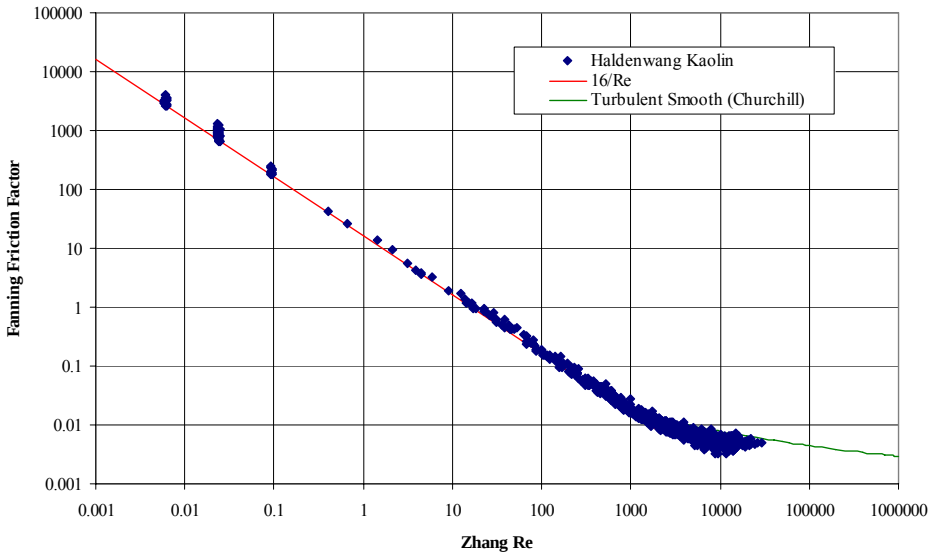

Figure 5.34: Fanning friction factor versus Zhang Reynolds number for the kaolin clay-water slurries of Haldenwang (2003) in 75, 150 and 300 mm rectangular channels

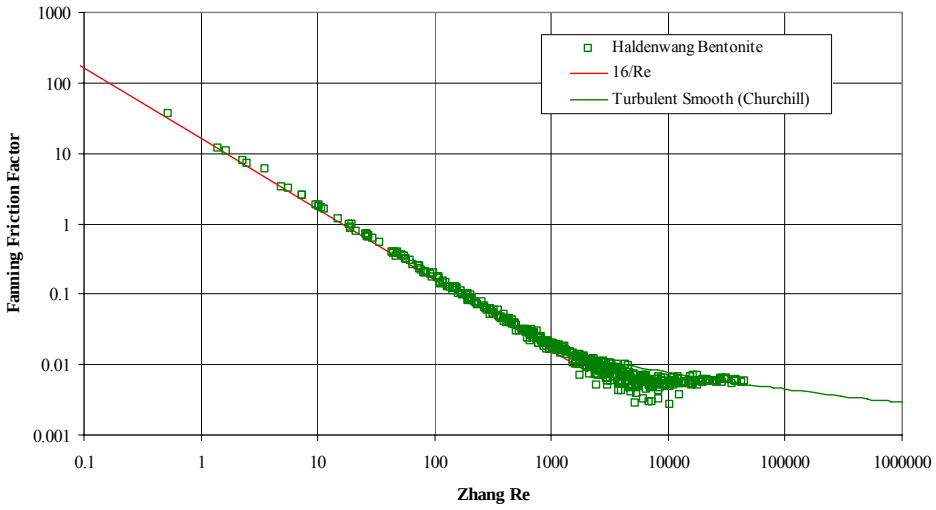

Figure 5.35: Fanning friction factor versus Zhang Reynolds number for the bentonite clay-water slurries of Haldenwang (2003) in 75, 150 and 300 mm rectangular channels

Figures 5.36 and 5.37 provide a comparison of the experimentally determined wall shear stress of Haldenwang (2003) with the prediction of Kozicki and Tiu (1967) for tests performed in rectangular open channels. The experimental results are in agreement with the Kozicki and Tiu prediction for both the kaolin (Figure 5.36) and bentonite (Figure 5.37) slurries.

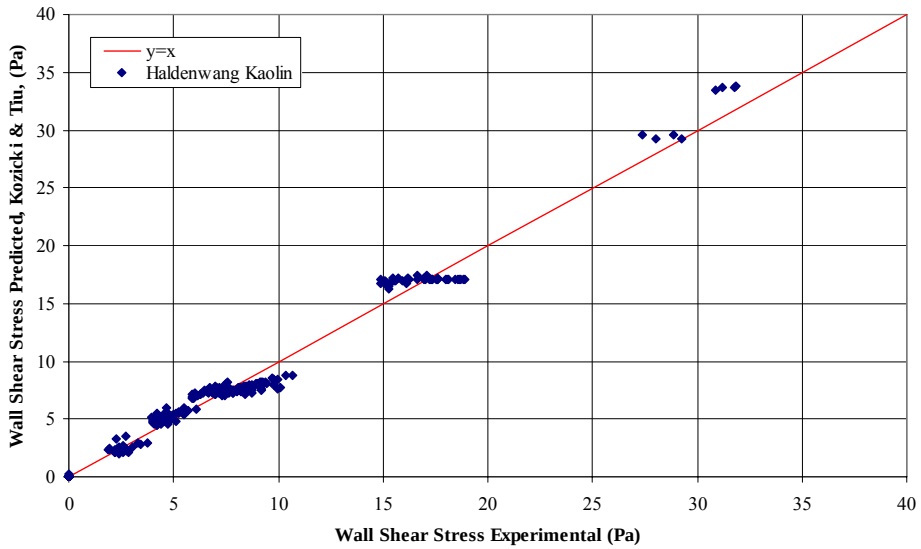

Figure 5.36: Experimental wall shear stress parity plot comparison with Kozicki and Tiu prediction for the kaolin clay-water slurries of Haldenwang (2003) in 75, 150 and 300 mm rectangular channels

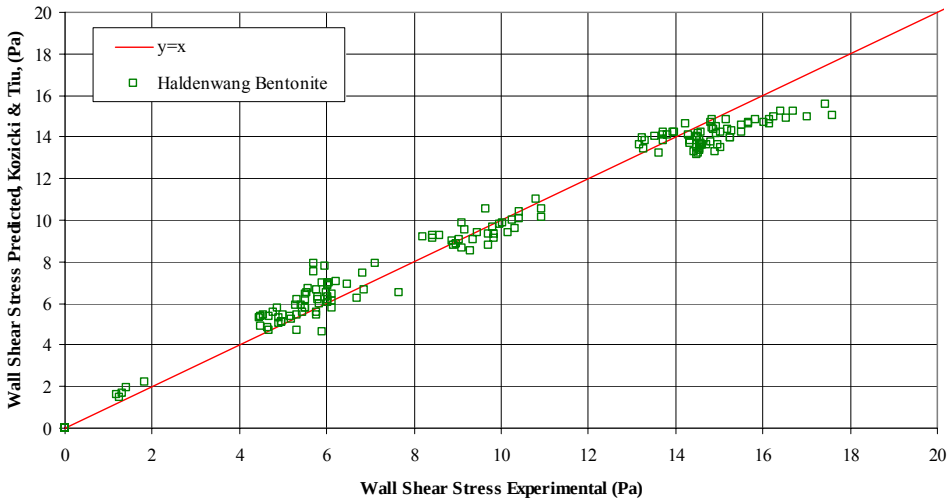

Figure 5.37: Experimental wall shear stress parity plot comparison with Kozicki and Tiu prediction for the bentonite clay-water slurries of Haldenwang (2003) in 75, 150 and 300 mm rectangular channels

The results presented in Section 5.5.3 and 5.5.4 suggest that the flow of homogeneous slurries in open channels is accurately modeled by using the modified Zhang Reynolds number with the hydraulic diameter of the flow, and employing the existing single phase Newtonian pipe flow frictional relationships. In laminar flow, the theoretical curve of $16/\mathrm{Re}$ accurately predicts the experimental results for the homogeneous slurries investigated in this study. In turbulent flow, the empirical correlation developed by Churchill (1977) can be used to determine turbulent frictional losses in the flume.

5.5.5. CT Slurries

Figures 5.38 and 5.39 show the experimentally determined wall shear stress versus velocity data for the model Syncrude CT slurries ('no gypsum' and 'gypsum' respectively). With both slurries, wall shear stress increases with bulk velocity when the velocity is above approximately 1 m/s. However, the wall shear stress increased with decreasing velocity for measurements performed below 1 m/s. This behaviour can be explained by considering the concentration profiles presented in Figures 5.51 and 5.52. For both slurries, a significant degree of coarse particle segregation occurred with the 2.5 L/s tests compared to the 5 L/s tests. The increased solids concentration near the bottom of the pipe caused an increase in the contact load of solids on the

pipe wall and an increase in the Coulombic friction component. This explains the larger wall shear stresses at lower velocities with the 2.5 L/s tests.

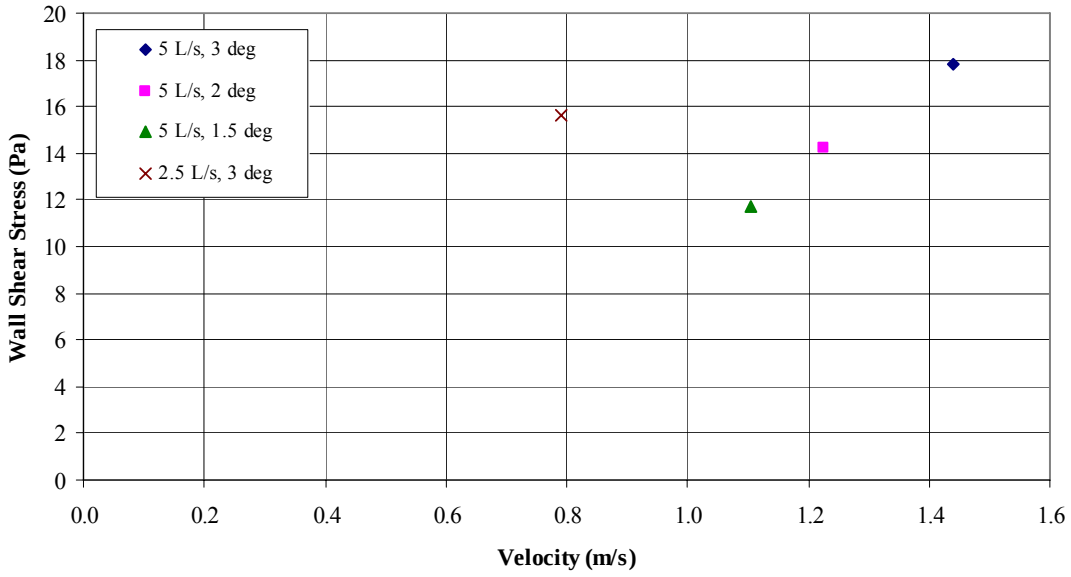

Figure 5.38: Wall shear stress versus velocity for a model Syncrude CT 'no gypsum' slurry in the 156.7 mm flume; ρ=1598 kg/m^3

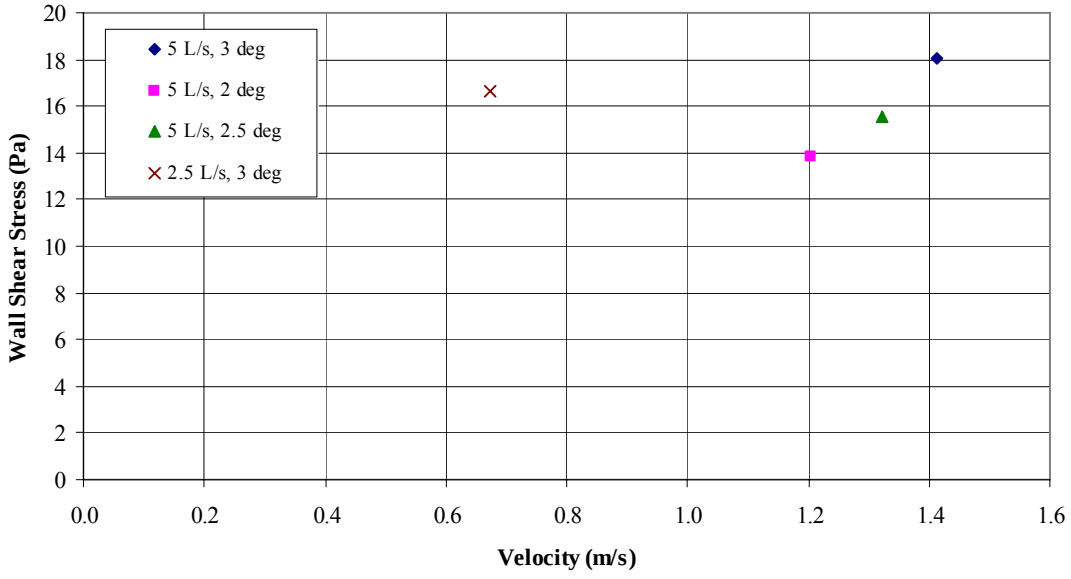

Figure 5.39: Wall shear stress versus velocity for a model Syncrude CT 'gypsum' slurry in the 156.7 mm flume; ρ=1598 kg/m^3

Similar wall shear stress behaviour was measured with the CT 'gypsum' slurry even though this slurry has a higher yield stress compared to the CT 'no gypsum' slurry. The most likely explanation for the similar behaviour is the nearly uniform concentration profiles noted at the higher velocities with both types of slurries. The Coulombic friction term would be expected to be significant only at lower velocities where the concentration profiles are not uniform. Figures 5.40 and 5.41 present the Fanning friction factor versus Zhang Reynolds behaviour for the CT 'no gypsum' and 'gypsum' slurries respectively, at the same conditions presented in Figures 5.38 and 5.39.

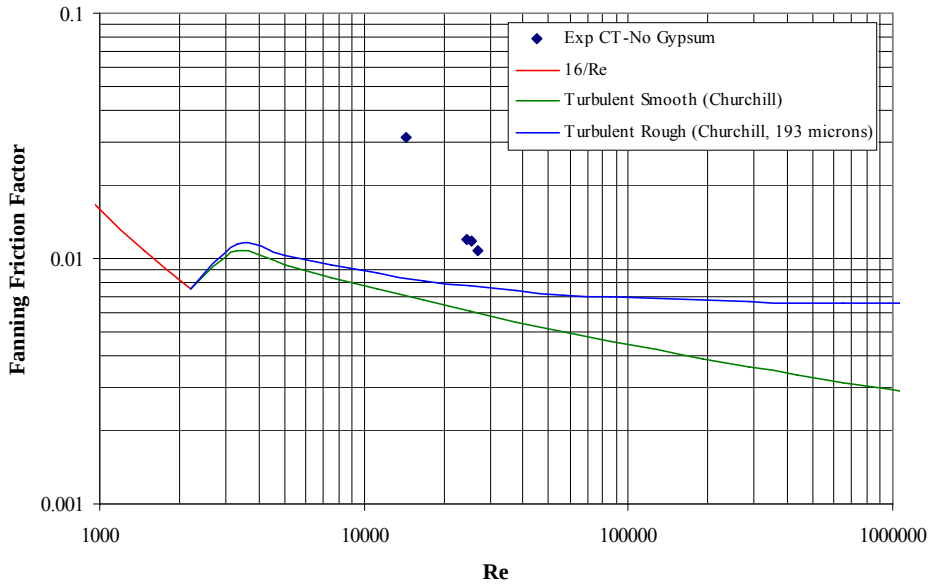

Figure 5.40: Fanning friction factor versus Reynolds number for a model Syncrude CT 'no gypsum' slurry in the 156.7 mm flume; ρ=1598 kg/m^3

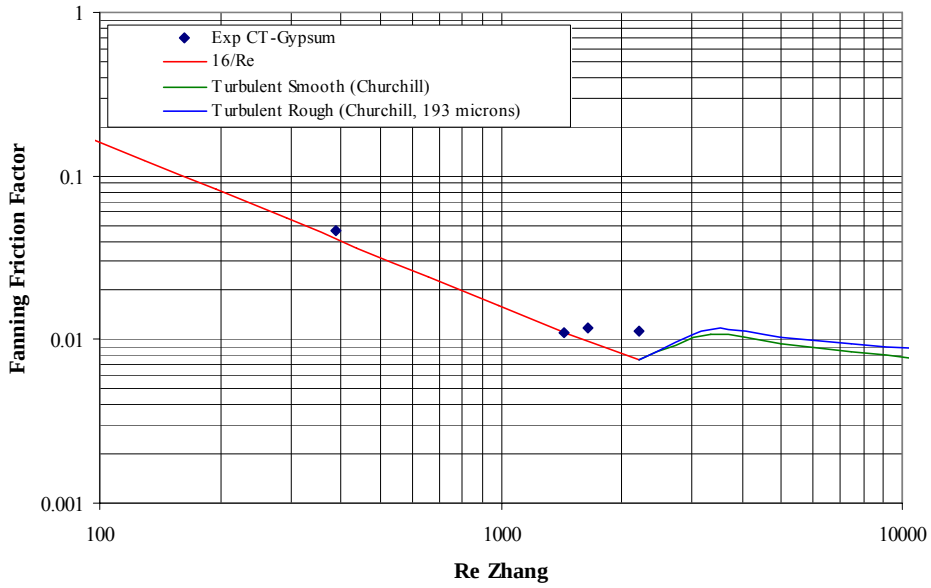

Figure 5.41: Fanning friction factor versus Zhang Reynolds number for a model Syncrude CT 'gypsum' slurry in the 156.7 mm flume; ρ=1598 kg/m^3

The rheological parameters determined for the CT 'no gypsum' slurries included the effect of the coarse sand fraction in the 53 mm feed pipe. In Figure 5.40, a significant discrepancy is observed between the experimental results and the homogeneous model prediction. The experimentally measured friction factors for the tests with high degrees of segregation were much greater than what the theoretical turbulent equation predicts. This is true even when the roughness of the flume is considered. This effect is consistent with what one would anticipate if the Coulombic friction component were significant.

For the 2.5 L/s tests, a large degree of segregation occurred within the flow for both the CT 'gypsum' and CT 'no gypsum' slurries. The homogeneous model assumes a uniform concentration profile, which is not true for highly segregated flows, and it is therefore not appropriate for predicting frictional losses in flows where segregation is significant. The increased solids concentration near the bottom of the pipe increases the Coulombic component of the wall shear stress. Coulombic friction is not accounted for in homogeneous models. As can be seen in Figure 5.41, the effect of the yield stress on the rheology of the CT 'gypsum' slurries caused the flow in the flume to be nearly laminar while the tests for the CT 'no gypsum' slurries, without a yield stress, were in the turbulent flow regime.

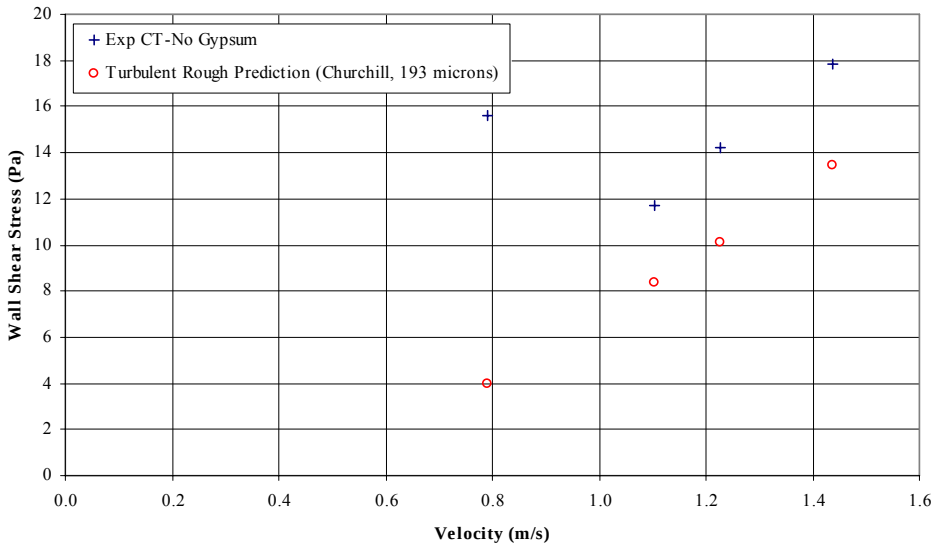

Figure 5.42: Experimental wall shear stress comparison with turbulent rough prediction for a model Syncrude CT 'no gypsum' slurry in the 156.7 mm flume; ρ=1598 kg/m^3

As can be seen for all of the test data presented in Figure 5.42, the homogeneous model underpredicts the wall shear stress of the 'no gypsum' slurries. This can also be seen in the parity plot presented in Figure 5.43 where the agreement between the experimental wall shear stress and the theoretical prediction is quite poor.

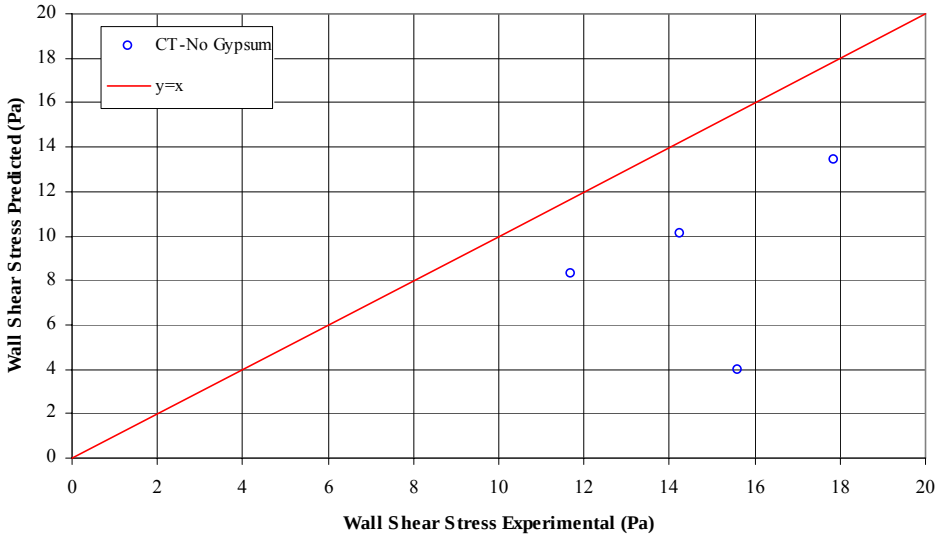

Figure 5.43: Wall shear stress parity plot comparison for a model Syncrude CT 'no gypsum' slurry in the 156.7 mm flume; ρ=1598 kg/m^3

Figure 5.44 shows a parity plot comparison of the experimentally measured wall shear stress with the Kozicki and Tiu (1967) prediction for the CT 'gypsum' slurries. The experimentally determined wall shear stresses were larger than the predicted wall shear stress for all but one of the tests. This is believed to be caused by a significant Coulombic friction term resulting from the high degree of segregation of coarse particles within the flow. As well the Kozicki and Tiu model is not appropriate to predict the wall shear stress for three of the four tests on the CT 'gypsum' slurries. It is only applicable in laminar flow and from Figure 5.41 one can see that the majority of the experimental data points are near the transition to turbulent flow.

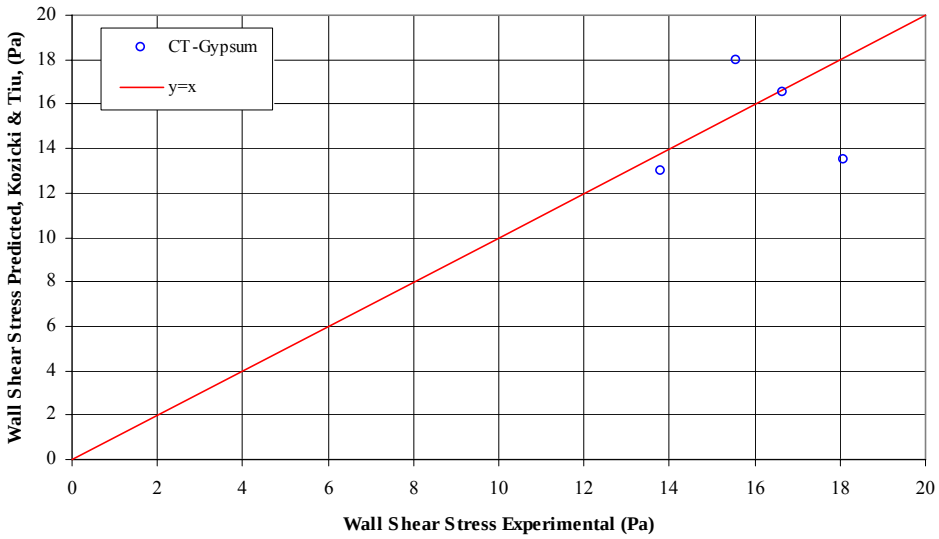

Figure 5.44: Experimental wall shear stress parity plot comparison with Kozicki and Tiu prediction for a model Syncrude CT 'gypsum' slurry in the 156.7 mm flume; ρ=1598 kg/m^3

5.5.6. Thickened Tailings Slurries

Figure 5.45 presents a plot of the average wall shear stress versus velocity for the Thickened Tailings tests in the flume. The same behaviour that was observed with the CT slurries was also observed with the Thickened Tailings. A decrease in velocity resulted in an increase in the wall shear stress for the low velocity (2.5 L/s) experiment. This effect can be explained by the variation in rheological properties of the slurry which was measured during the two days of testing. During this period the yield stress gradually increased. Therefore, the results presented in Figure 5.45 were all obtained with the same slurry composition but the yield stress was higher for the 2.5 L/s test. As well, at 2.5 L/s, a small degree of segregation occurred which would also increase the wall shear stress. However, the segregation effect could not have been too

significant as the calculated friction factors agreed closely with the theoretical prediction. Therefore the homogeneous model can accurately predict friction factors for the conditions considered in these tests.

As was seen earlier with the CT 'gypsum' slurries, the Thickened Tailings mixture flowed in the laminar regime as a result of the high yield stress measured with this slurry. The Zhang Reynolds number was used to calculate an equivalent Reynolds number in the flume flow. There is excellent agreement between the experimental friction factors and the theoretical frictional loss predictions as can be seen in Figure 5.46.

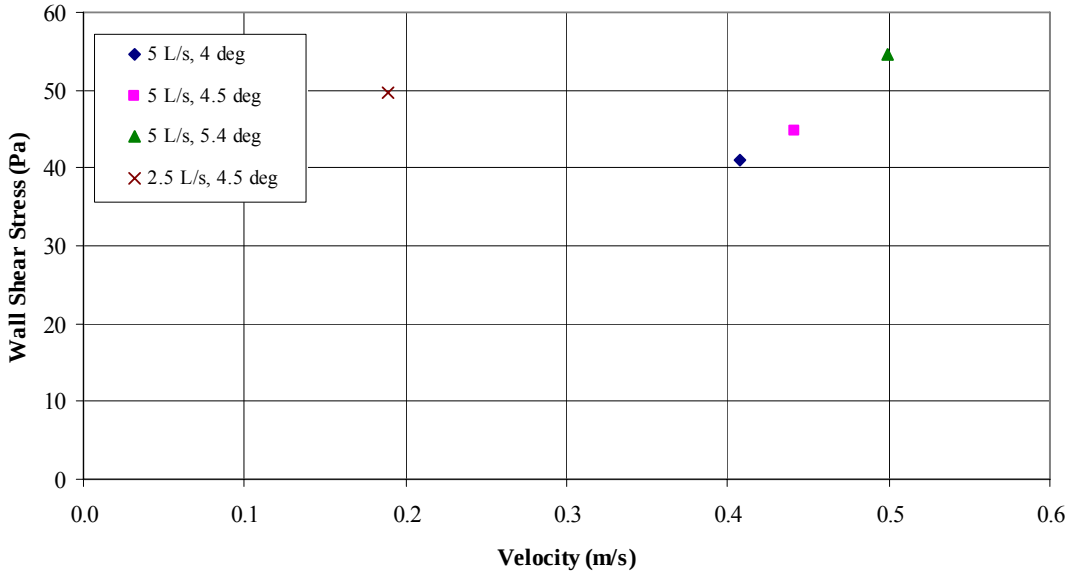

Figure 5.45: Wall shear stress versus velocity for a model Syncrude Thickened Tailings slurry in the 156.7 mm flume; ρ=1510kg/m^3

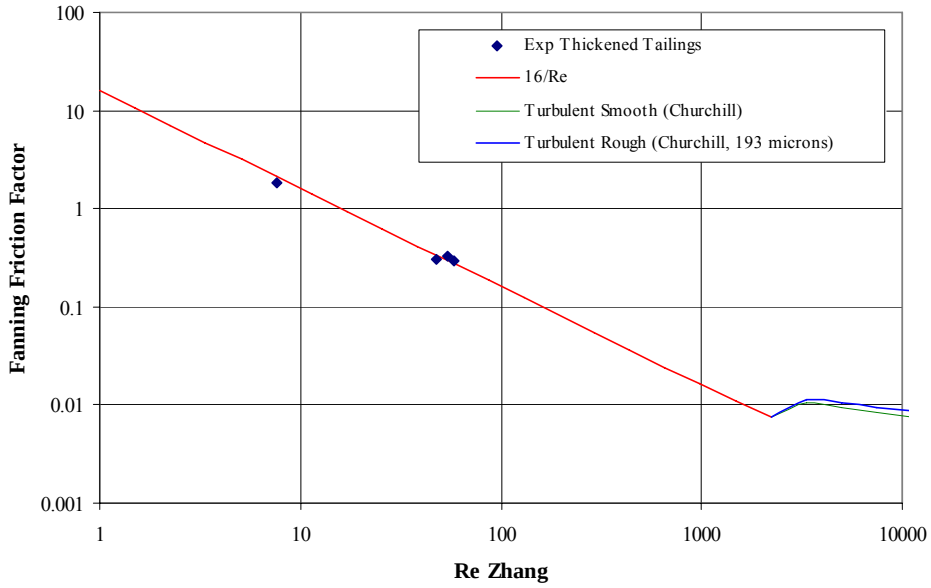

Figure 5.46: Fanning friction factor versus Zhang Reynolds number for a model Syncrude Thickened Tailings slurry in the 156.7 mm flume; ρ=1510 kg/m^3

Figure 5.47 presents a parity plot which compares the experimentally determined wall shear stresses and wall shear stresses predicted by the Kozicki and Tiu (1967) model. The Kozicki and Tiu model slightly overpredicts the experimentally measured wall shear stresses for most of the tests. With the CT slurries, the opposite effect was observed where the Kozicki and Tiu model underestimated the experimental wall shear stress. This can be explained by the fact that the CT slurry data was obtained near the transition to turbulent flow in the flume. The Kozicki and Tiu model prediction is only applicable to laminar flows which is the reason for the underprediction.

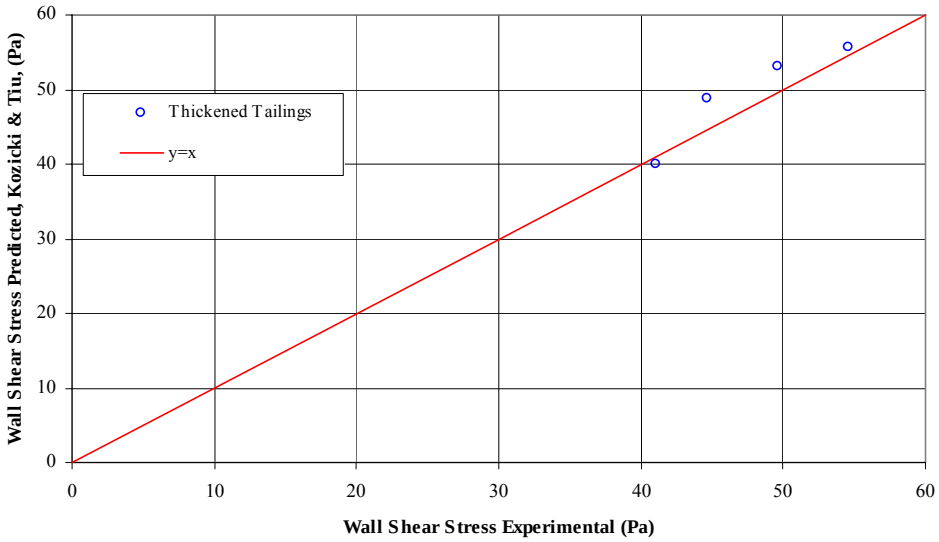

Figure 5.47: Experimental wall shear stress parity plot comparison with Kozicki and Tiu prediction for a model Syncrude Thickened Tailings slurry in the 156.7 mm flume; ρ=1510 kg/m^3

The success of the homogeneous model with the Thickened Tailings is most likely due to the smaller coarse particle concentration (15% v/v compared to 28% v/v for the CT tests) and larger fines fraction (15% v/v compared to 8% v/v) associated with this slurry. The effect of particle segregation on the average wall shear stress does not appear to be significant for the high yield stress, laminar flow, Thickened Tailings tests. Therefore, a significant Coulombic friction term did not exist for these slurries. As well, for the same conditions in the flume, the higher yield stress of the Thickened Tailings slurries translated into a higher apparent viscosity and a reduced settling rate of the segregating coarse particle phase. It is important to note that the homogenous fluid model could not be used with the CT slurries where segregation of coarse particles was significant.

Although the Coulombic friction contribution does not appear to be significant for the Thickened Tailings tests, a greater contribution would be expected if higher coarse solids fractions, lower slurry yield stresses, lower volumetric flowrates or lower flume angles were investigated. If the Coulombic friction term were substantial, the Kozicki and Tiu (1967) model should significantly underpredict the wall shear stress. However, for the conditions tested in this study, the Kozicki and Tiu (1967) model is capable of providing reasonably accurate wall shear stress predictions despite the heterogeneous behaviour of the slurries.

Overall, the results are somewhat surprising. When segregation of coarse particles occurs (presented in the concentration profiles of Section 5.7) a significant Coulombic friction term would be anticipated (Shook et al., 2002), which would cause the measured wall shear stress to exceed the predicted viscous friction term. The Coulombic term was evident in the CT 'no gypsum' slurries where the use of a homogenous model did not provide an accurate means to predict the wall shear stress. This effect could also be seen at low velocities with the 25% v/v sand-water slurries.

For the CT 'gypsum' slurries, the flows were laminar and in some cases, near the transition to turbulence. The high fraction of coarse sand led to significant segregation in the flow in the flume. A slight Coulombic friction term existed, but the use of the Kozicki and Tiu (1967) homogenous fluid model still provided a reasonably accurate prediction of the wall shear stress. For the Thickened Tailings slurries the concentration of coarse sand was reduced and the fines content was increased. The significant yield stress associated with this slurry caused it to be non-settling under static conditions. The high yield stress caused the slurry to flow under laminar conditions and also reduced the effect of the particle segregation. As a result, the Kozicki and Tiu homogeneous fluid model provided accurate predictions for the wall shear stress under all conditions considered for the Thickened Tailings slurries in this study.

5.6. Sampling

The coarse to fines ratio of the slurry can be used to show the extent to which coarse particles have settled in the flow. Equation 5.2 details how this ratio is obtained.

$$\frac{coarse}{fines} = \frac{C_{sand}}{C_{clay}} = \frac{C_{solids}\left(1 - C_{carrier}\right)}{C_{carrier}\left(1 - C_{solids}\right)} - 1 \qquad (5.2)$$

In Equation 5.2, $C_{carrier}$ is the concentration of clay (fines) in the carrier fluid and C_{solids} is the total concentration of solids (coarse and fines) in the slurry. A 74 μm sieve (200 mesh) was used to separate the coarse sand from the fine clays in the analysis. The particle size distribution for the sand used in this study is shown in Figure 5.8. From the size distribution only trace amounts of sand were found to be less than 74 μm.

Variation in coarse solids concentrations with depth of flow in the flume was measured in some experiments. In order to confirm that the variation in concentration was due to the settling of coarse particles only, an extensive sampling campaign was undertaken in conjunction with the main experimental program. Tables 5.6 to 5.9 present the results of the slurry sampling with each of the idealised model slurries. The sampling procedure employed in this study was discussed earlier in Section 3.5.

Initially, samples were obtained with slurries containing only kaolin clay and water, with no coarse sand, to provide a measure of the overall solids concentration of the slurry. The results of these tests are provided in Table 5.6. The solids concentration was determined from gravimetric analysis. For each test, three samples were taken from the outlet of the flume and averaged to obtain a total solids (clay) concentration.

Table 5.6: Sampling results for the kaolin clay-water slurry experimental tests

Test	**Makeup**	**Cv (v/v)**	**Cw (w/w)**	**Density (kg/m^3)**
ClayWater001	Clay-Water	0.222	0.434	1376
ClayWater002	Clay-Water	0.221	0.434	1375
ClayWater003	Clay-Water	0.221	0.434	1375
ClayWater004	Clay-Water	0.222	0.435	1377
ClayWater005	Clay-Water	0.222	0.435	1377
ClayWater006	Clay-Water	0.222	0.435	1377
ClayWater007	Clay-Water	0.222	0.435	1377
ClayWater008	Clay-Water	0.223	0.437	1379
ClayWater009	Clay-Water-TSPP 1	0.226	0.441	1384
ClayWater010	Clay-Water-TSPP 1	0.226	0.441	1384
ClayWater011	Clay-Water-TSPP 1	0.226	0.441	1384
ClayWater012	Clay-Water-TSPP 1	0.226	0.441	1384
ClayWater013	Clay-Water-TSPP 1	0.226	0.441	1384
ClayWater014	Clay-Water-TSPP 1	0.226	0.441	1384
ClayWater015	Clay-Water-TSPP 2	0.227	0.443	1386
ClayWater016	Clay-Water-TSPP 2	0.227	0.443	1386
ClayWater017	Clay-Water-TSPP 2	0.227	0.443	1386
ClayWater018	Clay-Water-TSPP 2	0.227	0.443	1386
ClayWater019	Clay-Water-TSPP 2	0.227	0.443	1386
ClayWater020	Clay-Water-TSPP 2	0.228	0.444	1387

Following tests with the clay-water slurries, slurries containing both clay and coarse sand were tested. The results of these tests, which are presented in Tables 5.7 to 5.9, show that the change in solids concentration throughout the cross-section of the flume can be attributed to the settling of coarse particles only. The fines:water ratio did not vary between the top and bottom samples for

all of the tests performed. As well, the experimental fines:water ratio determined from sampling is in good agreement with the fines:water ratio based on the initial composition of the slurry. Any discrepancy between these concentration values can be attributed to the fact that the tests were run over a period time and evaporation of water from the test circuit would have occurred which would cause the sampled clay concentration to increase slightly.

Table 5.7: Sampling results for the Syncrude CT 'no gypsum' experimental tests

Material	Q (L/s)	θ (^{o})	Position	Concentration (w/w) Sand	Clay	Water	Coarse:Fines (v/v)	Fines:Water (v/v)	Density (kg/m^3)	Carrier Concentration (w/w) Clay	Water
CT-No Gypsum	5	3	top	45.5	14.3	40.2	3.2	0.133	1596	26.3	73.7
CT-No Gypsum	5	3	bottom	52.0	12.7	35.4	4.2	0.133	1676	26.4	73.6
									AVG	26.3	
									STD DEV	0.041	
									Actual	25.8	

Table 5.8: Sampling results for the Syncrude CT 'gypsum' experimental tests

Material	Q (L/s)	θ (^{o})	Position	Concentration (w/w) Sand	Clay	Water	Coarse:Fines (v/v)	Fines:Water (v/v)	Density (kg/m^3)	Carrier Concentration (w/w) Clay	Water
CT-Gypsum	5	3	top	47.8	13.9	38.3	3.5	0.135	1627	26.7	73.3
CT-Gypsum	5	3	bottom	48.1	13.9	38.1	3.5	0.135	1630	26.7	73.3
CT-Gypsum	5	2.5	top	46.4	14.3	39.3	3.3	0.135	1610	26.7	73.3
CT-Gypsum	5	2.5	bottom	52.4	12.8	34.9	4.2	0.136	1685	26.8	73.2
CT-Gypsum	5	2	top	43.1	15.2	41.6	2.9	0.136	1573	26.8	73.2
CT-Gypsum	5	2	bottom	51.0	13.1	35.9	4.0	0.135	1667	26.7	73.3
CT-Gypsum	2.5	3	top	43.0	15.4	41.5	2.8	0.138	1575	27.1	72.9
CT-Gypsum	2.5	3	bottom	68.4	8.5	23.0	8.2	0.137	1922	27.0	73.0
CT-Gypsum	7.4	2	total	45.6	14.6	39.8	3.2	0.136	1602	26.8	73.2
									AVG	26.8	
									STD DEV	0.138	
									Actual	25.8	

Table 5.9: Sampling results for the Syncrude Thickened Tailings experimental tests

Material	Q (L/s)	θ (^{o})	Position	Concentration (w/w) Sand	Clay	Water	Coarse:Fines (v/v)	Fines:Water (v/v)	Density (kg/m^3)	Carrier Concentration (w/w) Clay	Water
Thickened Tailings	5	5.4	top	26.9	26.9	46.1	1.0	0.217	1509	36.9	63.1
Thickened Tailings	5	5.4	bottom	44.5	20.5	35.0	2.2	0.217	1684	36.9	63.1
Thickened Tailings	5	4.5	top	26.6	26.9	46.4	1.0	0.215	1504	36.7	63.3
Thickened Tailings	5	4.5	bottom	38.3	22.6	39.0	1.7	0.215	1616	36.7	63.3
Thickened Tailings	5	4	top	26.8	26.8	46.3	1.0	0.215	1506	36.7	63.3
Thickened Tailings	5	4	bottom	42.6	21.1	36.4	2.1	0.215	1660	36.7	63.3
Thickened Tailings	2.5	4.5	top	27.7	26.7	45.6	1.1	0.217	1516	36.9	63.1
Thickened Tailings	2.5	4.5	bottom	44.3	20.6	35.2	2.2	0.217	1681	36.9	63.1
Thickened Tailings	4	4.5	total	26.5	27.0	46.5	1.0	0.216	1504	36.8	63.2
Thickened Tailings	2.5	4.5	total	26.0	27.3	46.7	1.0	0.217	1501	36.9	63.1
									AVG	36.8	
									STD DEV	0.111	
									Actual	37.0	

The results of the sampling verifies that the fine particles are not responsible for the variation in solids concentration which occurred between the top and bottom samples. The dispersive forces acting on the clay particles during the flow in flume are large enough to keep the clay concentration uniform (homogeneous). If the dispersive forces are not capable of supporting the coarser particle fraction, segregation will occur and, if the gravitational forces are sufficiently significant, deposits will form. If segregation occurs, the bulk concentration and the solids

concentration of the upper and lower samples will be different. Therefore, if coarse solids segregation were significant, the upper sample should have a lower ratio of coarse to fine particles compared to the original slurry and the lower sample should have a higher ratio. This is in fact the case for some of the samples collected in this study as can be seen in results presented in Tables 5.7 to 5.9. In other cases the ratio at the top of the flume is the same as the ratio at the bottom of the flume and the bulk slurry concentration indicating that the flow is homogeneous. These results were verified with the gamma ray concentration measurements which are presented in Section 5.7.

5.7. Concentration Profiles

Concentration profile measurements were obtained with slurries composed of either sand and water or sand, clay and water. Experimental data for these tests is provided in Appendix D. The method used to determine the solids concentration with the traversing gamma ray densitometer is presented in Section 3.4. The traversing gamma ray densitometer calibrations, specific to the 156.7 mm flume apparatus, are presented in Appendix C.

The solids concentration is plotted in two ways. The first involves plotting concentration against a normalised fluid height (y/h) so that data can be compared regardless of the depth of slurry flow. In this way tests with different depths of flow can be compared on the same graph. Since the height of the free surface could not be directly measured using the traversing gamma ray unit, an alternate method of extrapolating the height at the gamma ray unit in the flume was determined by using the two other height measurements at 1 and 2 (Figure 3.1). The concentration is also plotted against y/D, where D is the internal diameter of the flume. This allows the different depths of flow to be compared for a given mixture in conjunction with the concentration profile. This type of comparison is also important since the flume is circular in cross section and segregation is occurring on a curved surface which makes the absolute concentration measurement position important.

5.7.1. Sand-Water Slurries

Figures 5.48a and 5.48b present the concentration profiles (y/h and y/D) for the 25% v/v sand-water tests at high flume angles (5 to 7^o). As can be seen from the figures, the depth of the

flowing slurry increased with decreasing flume angle. This caused the bulk velocity of the slurry to decrease. The concentration profiles presented in these figures indicate that the concentration at the bottom of the pipe increased with decreasing flume angle. The reduction in bulk velocity may explain the observed segregation and verifies the behaviour observed in Figure 5.18 where at the same bulk velocity larger wall shear stresses were found at smaller flume angles. It is interesting to note that all of the sand-water tests were turbulent. Therefore, it appears that segregation can occur in the flume in turbulent flow based on the gamma ray concentration measurements.

The concentration of solids at the bottom of the pipe (y/D = 0.05) at the higher angles (5, 6, 7^o) was approximately 0.3. Considering Figures 5.49 and 5.50, the lowest flowrate tested at both 3 and 3.5^o was the minimum flowrate that could be maintained in the flume under the operating conditions without the presence of a deposit. All of the tests were conducted for conditions above the critical deposition velocity in the flume. For the lower angles of 3.5 and 3^o where segregation could occur, the concentration of solids at the bottom of the pipe was 0.35 and 0.4 respectively. The figures show that as the flume angle was decreased the flowrate slightly above where a deposit forms increased. This explains why higher flowrates were required to maintain flow without a deposit at lower angles and why the degree of segregation at lower angles was so much greater. This also explains why the equivalent fluid model did not provide an accurate prediction of the wall shear stress at the lower angles and velocities. The particle segregation resulted in an additional Coulombic friction which resulted in higher wall shear stresses near the deposition condition.

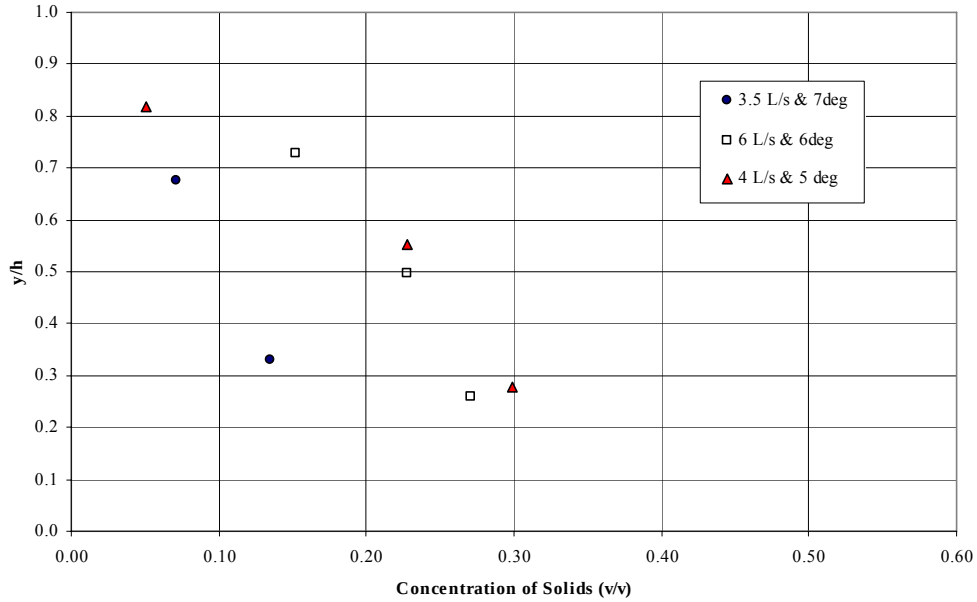

Figure 5.48a: Old inlet solids concentration profiles (y/h) for a 25% v/v sand-water slurry in the 156.7 mm flume; ρ=1410 kg/m^3

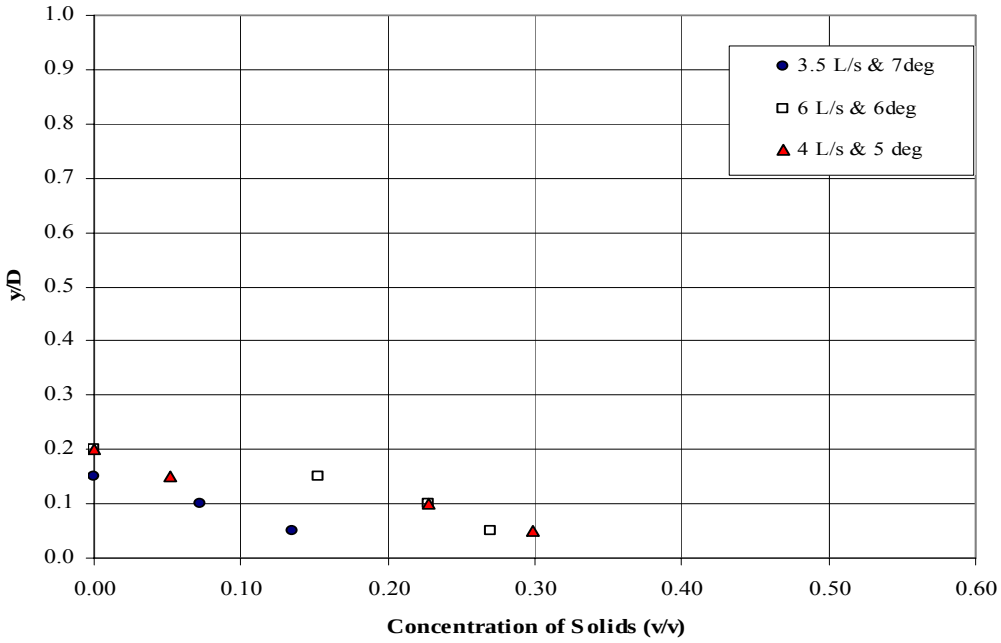

Figure 5.48b: Old inlet solids concentration profiles (y/D) for a 25% v/v sand-water slurry in the 156.7 mm flume; ρ=1410 kg/m^3

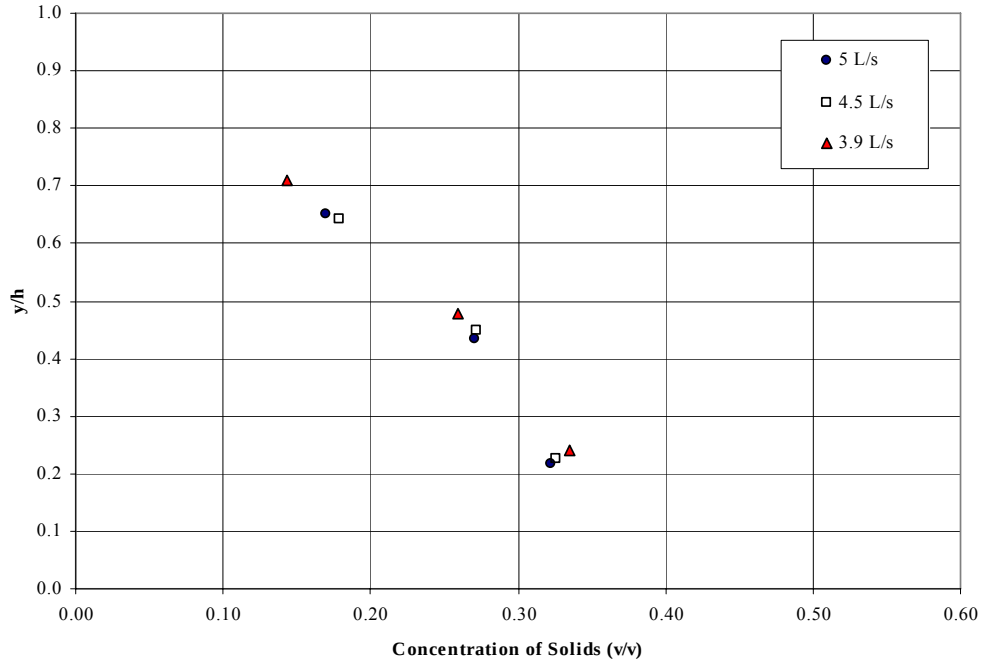

Figure 5.49a: New inlet solids concentration profiles (y/h) at 3.5^{o} for a 25% v/v sand-water slurry in the 156.7 mm flume; ρ=1410 kg/m^{3}

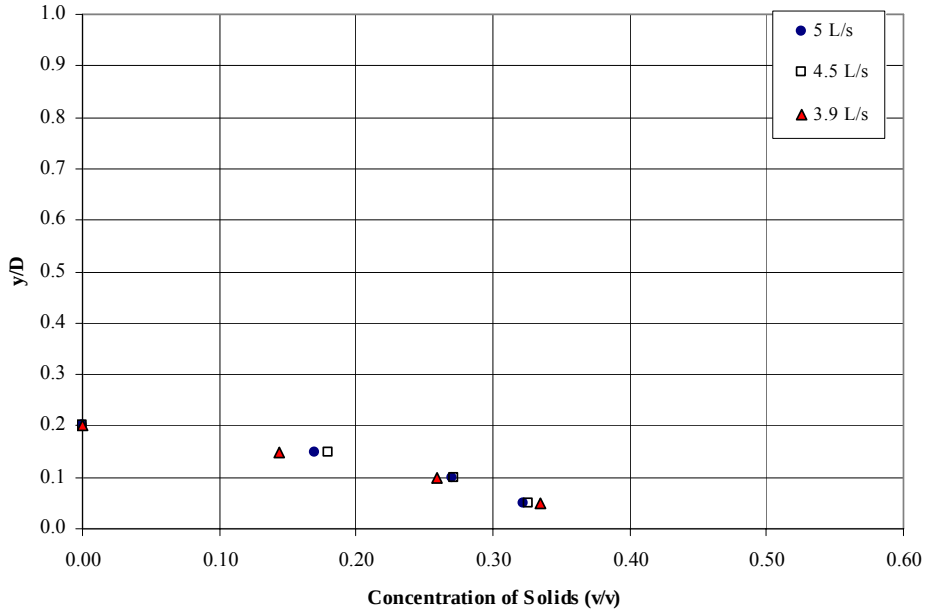

Figure 5.49b: New inlet solids concentration profiles (y/D) at 3.5^{o} for a 25% v/v sand-water slurry in the 156.7 mm flume; ρ=1410 kg/m^{3}

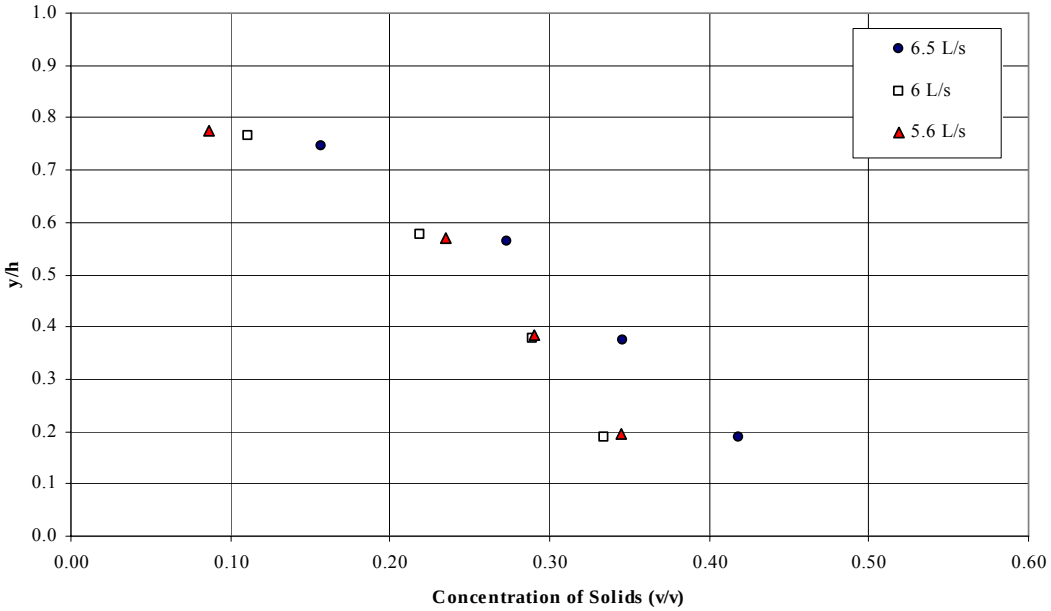

Figure 5.50a: New inlet solids concentration profiles (y/h) at 3° for a 25% v/v sand-water slurry in the 156.7 mm flume; ρ=1410 kg/m^3

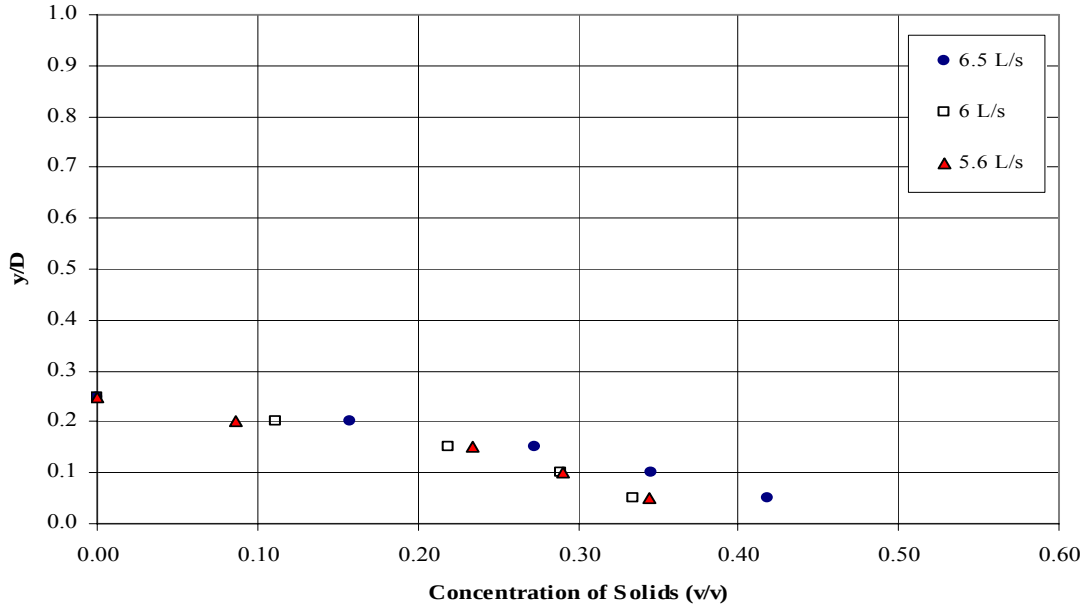

Figure 5.50b: New inlet solids concentration profiles (y/D) at 3° for a 25% v/v sand-water slurry in the 156.7 mm flume; ρ=1410 kg/m^3

5.7.2. CT Slurries

Figure 5.51 presents the concentration profiles measured with the CT 'no gypsum' slurries in the flume. These tests, like the sand-water tests, were turbulent. The CT 'no gypsum' slurry had a higher density carrier fluid (1188 kg/m^3) which reduced the immersed weight of the sand particles. In addition, the carrier fluid associated with this slurry had a higher viscosity due to the presence of clay. The overall viscosity of the mixture was 0.0074 Pa-s based on measurements with the 53 mm feed test section.

The concentration profile presented in Figure 5.51a, which was obtained at a high flowrate (5 L/s) and flume angle (3^o), is fairly uniform which would indicate that the slurry flow was homogeneous. Segregation of solid particles was not occurring at this condition since the turbulent forces were probably high enough to support the solid particles in the flow. The bulk solids concentration of the slurry, based on the slurry preparation and on the concentration profile, was in close agreement and was approximately 0.36 v/v. As the flume slope angle was reduced from 3^o to 1.5^o, the bulk velocity of the mixture decreased. This is shown by the increase in the depths of flow in Figure 5.51b. The concentration of solids near the bottom of the pipe increased under these conditions.

A different type of behaviour was observed with the low flowrate test (2.5 L/s) where the concentration profile is similar to the concentration profiles measured in the sand-water tests. With this flowrate the flow was heterogeneous and segregation was evident. The concentration at the bottom of the flume ($y/D = 0.05$) changed from 0.36 v/v for the 5 L/s tests to 0.60 v/v for the 2.5 L/s tests. This is near the maximum packing concentration associated with the coarse sand particles, which suggests that the concentration was approaching that of a stationary deposit. This is most likely the reason for the disagreement between the experimental wall shear stress results and the homogenous flow prediction. The increased solids concentration near the pipe wall resulted in a significant Coulombic friction term.

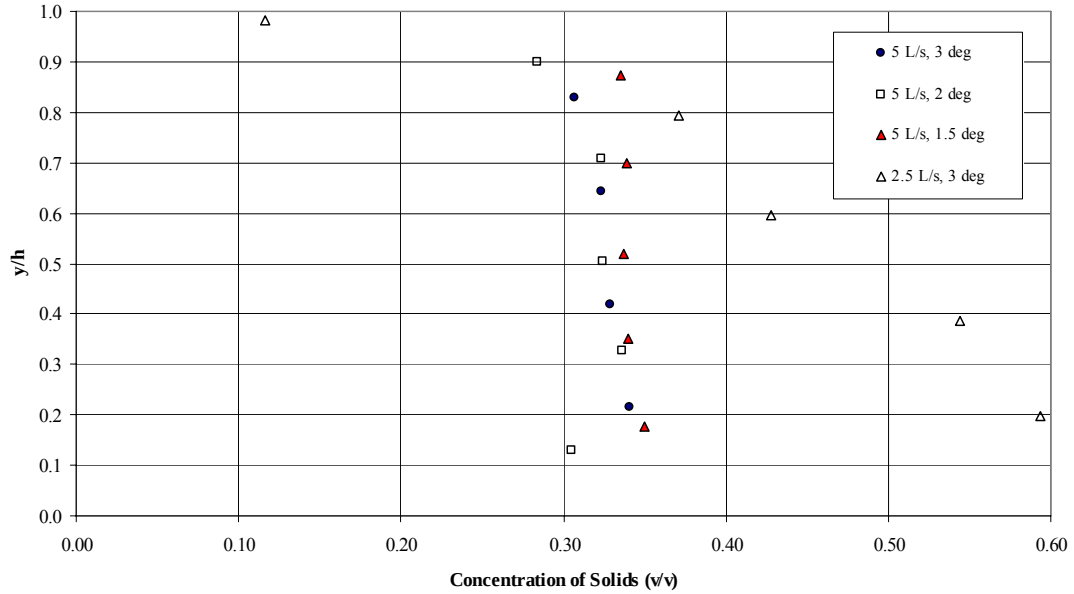

Figure 5.51a: Solids concentration profiles (y/h) for a model Syncrude CT 'no gypsum' in the 156.7 mm flume; ρ=1598 kg/m^3

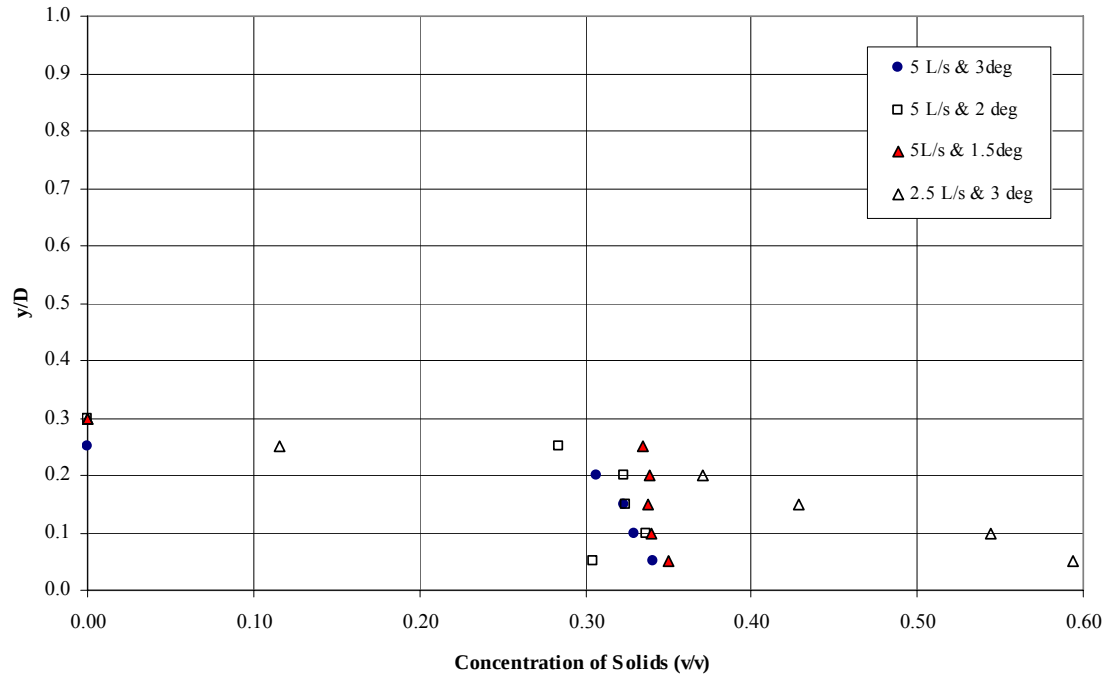

Figure 5.51b: Solids concentration profiles (y/D) for a model Syncrude CT 'no gypsum' in the 156.7 mm flume; ρ=1598 kg/m^3

Figure 5.52 presents the concentration profiles for the CT 'gypsum' tests in the flume. For these tests, both the laminar and turbulent regimes were obtained. As mentioned earlier, the only difference between the 'no gypsum' slurry and the 'gypsum' slurry was that calcium was added

to ‘gypsum’ slurry, which increased its yield stress to 10.2 Pa. This yield stress was large enough to suspend the sand particles when the slurry was static. With the ‘no gypsum’ slurry, which had a negligible yield stress, the sand settled immediately when the mixture was stationary.

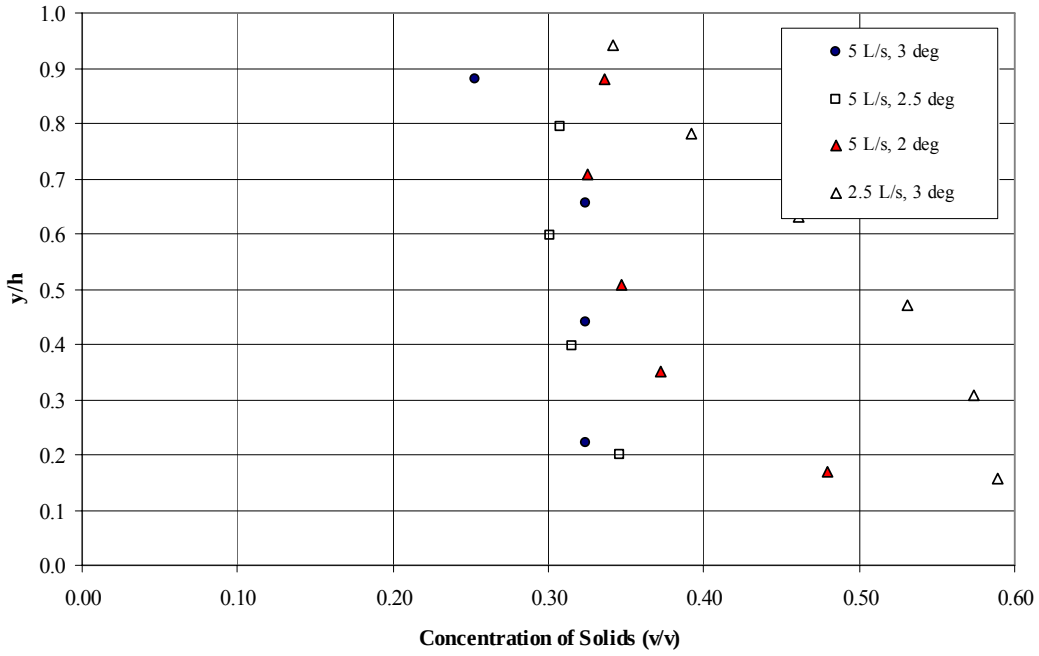

Figure 5.52a: Solids concentration profiles (y/h) for a model Syncrude CT ‘gypsum’ in the 156.7 mm flume; ρ=1598 kg/m^3

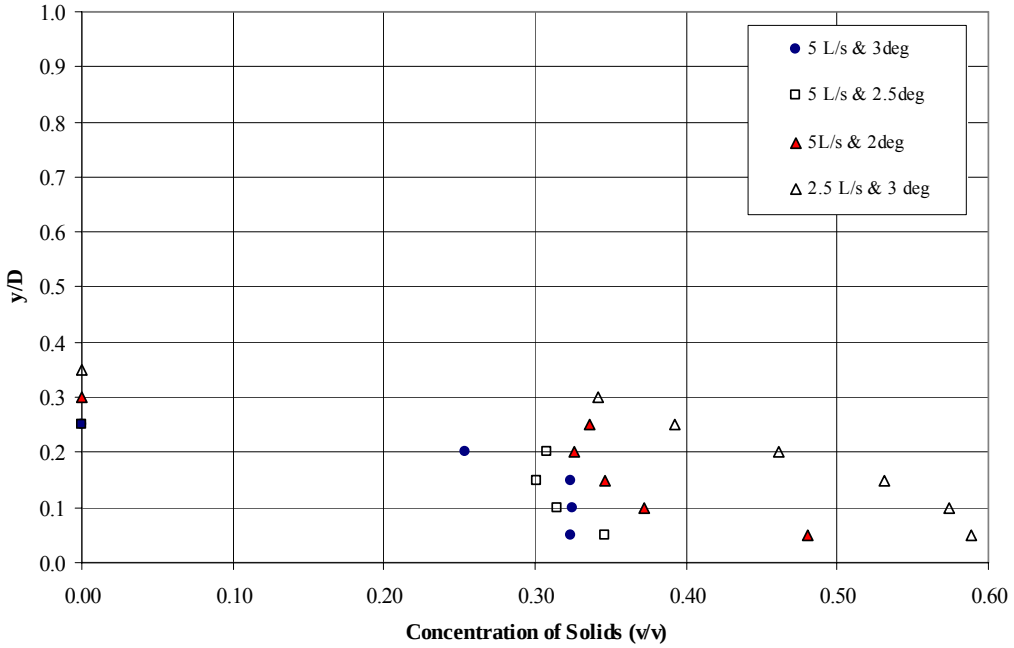

Figure 5.52b: Solids concentration profiles (y/D) for a model Syncrude CT ‘gypsum’ in the 156.7 mm flume; ρ=1598 kg/m^3

The concentration profiles measured with the CT 'gypsum' slurry at high flowrates (5 L/s) and higher flume angles (2.5 and 3°) were nearly uniform based on the results presented in Figure 5.52a. However, in contrast to the 'no gypsum' results, segregation was observed at the bottom of the pipe at the highest flowrate and lowest angle (5 L/s and 2°) where the solids concentration at $y/D = 0.05$ was nearly 0.50 v/v. This may be explained by the fact that the flow was nearly laminar and thus the turbulent dispersive forces were not significant enough to keep the solids in suspension. The equivalent concentration value for the 'no gypsum' slurry was 0.35 v/v.

The yield stress of the 'gypsum' slurry caused the depth of flow in the flume to be higher than the depth of flow in the flume with 'no gypsum' slurry under similar flow conditions. This is likely due to the larger frictional losses associated with the higher apparent viscosity of the 'gypsum' slurry. An increase in the depth of the flow will reduce the bulk velocity of the slurry which should cause an increase in the amount of segregation.

Segregation was observed at the lowest flowrate studied with the 'gypsum' slurry. As was discussed earlier, similar behaviour was seen at the lower flowrates with the 'no gypsum' and sand water slurries. For both the 'gypsum' and 'no gypsum' slurries, the solids concentration at the bottom of the pipe ($y/D = 0.05$) was 0.60 v/v when the flowrate was 2.5 L/s. This resulted in a highly non-uniform concentration distribution and likely a significant Coulombic friction term. This may explain the discrepancy between the experimentally measured wall shear stress and the prediction of the Kozicki and Tiu (1967) homogeneous slurry model.

5.7.3. Thickened Tailings Slurries

The concentration profiles for the Thickened Tailings results presented in Figure 5.53 are quite different from the profiles measured with the sand-water and CT slurries. Laminar flow occurred with all of the Thickened Tailings tests. Segregation also occurred in all of the tests. The concentration of solids in the bulk slurry was roughly 0.30 v/v based on gravimetric measurements. The concentration in the uniform portion of the flow was also approximately 0.30 v/v for all of the tests. The concentration near the bottom of the pipe varied between 0.35 to 0.40 v/v.

Of the slurries considered in this program, the Thickened Tailings slurries had the highest apparent viscosity where the yield stress of this slurry was approximately 40 Pa and the plastic viscosity was approximately 0.040 Pa-s. As anticipated, the increase in flow resistance associated with the higher rheological parameters of the Thickened Tailings slurry caused an increase in the depth of the flume flow. Laminar flow behaviour would be expected with a slurry having such a high apparent viscosity for the range of conditions considered in this study.

For laminar flows of Bingham fluids, the flow cross-sectional area can be divided into two regions: sheared and unsheared. The sheared region represents the flow region where the shear stress is greater than the yield stress. The unsheared region corresponds to the region where velocity gradients do not exist and the shear stress is less than the yield stress.

The sheared region of the flume occurs near the pipe wall since the highest shear stresses occur in this region. Considering Figure 5.53a, one can see that segregation occurred in this region. As can also be seen in Figure 5.53a, near the centre of the flow, where the shear stresses were less than the yield stress, an unsheared region exists. The yield stress of the Thickened Tailings slurry was high enough to support the solid particles when the slurry was stationary. Since the fluid is essentially stationary in the unsheared region, one would not expect segregation or particle settling to occur. In the sheared region the velocity gradient was greater than zero and therefore segregation occurred. This suggests that segregation only occurs in the sheared region for laminar flows of fluids with yield stresses for the experimental conditions considered in this study.

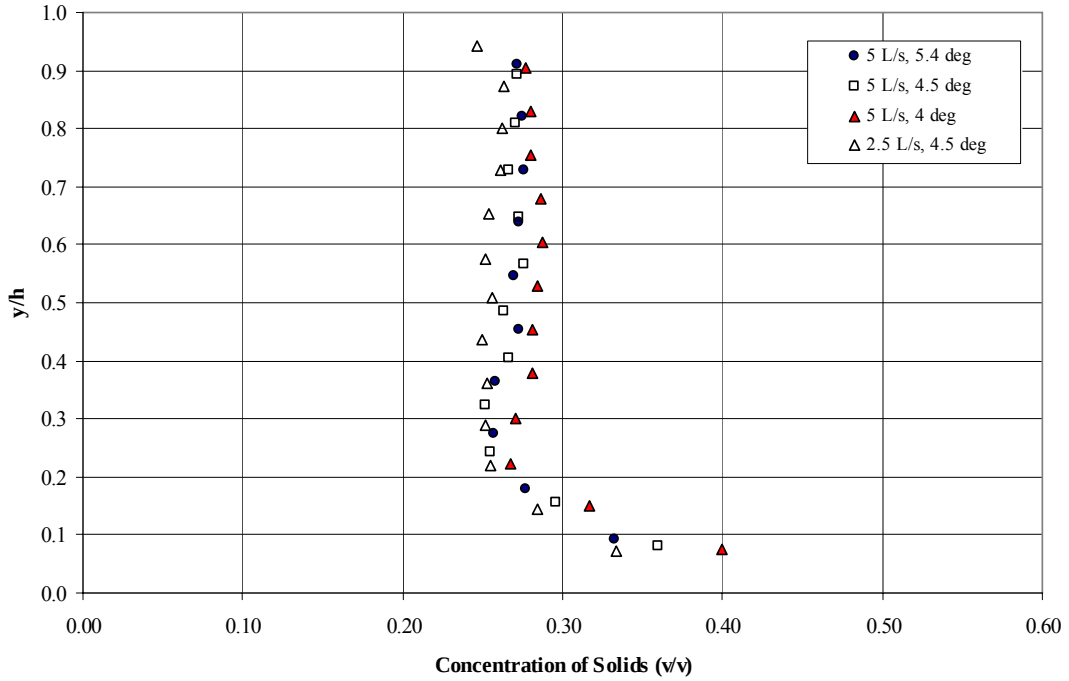

Figure 5.53a: Solids concentration profiles (y/h) for a model Syncrude Thickened Tailings slurry in the 156.7 mm flume; ρ=1510 kg/m^3

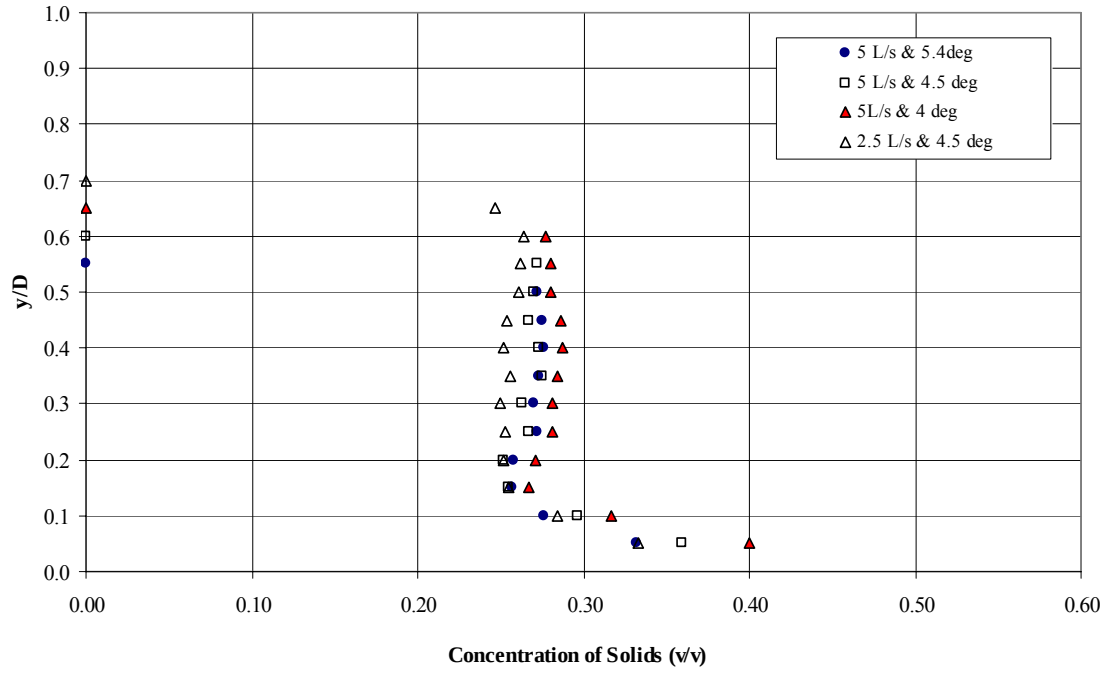

Figure 5.53b: Solids concentration profiles (y/D) for a model Syncrude Thickened Tailings slurry in the 156.7 mm flume; ρ=1510 kg/m^3

Equation 2.38 can be used to determine the minimum yield stress required to support a single solid particle under infinite dilution conditions in a stationary Bingham fluid (Shook and Roco,

1991). Based on this equation, the Thickened Tailings slurry would have to have a yield stress of 0.52 Pa to support the sand used in this study (d_{50}=188μm). A yield stress of 0.57 Pa would be required to suspend particles in the CT 'gypsum' slurry. Therefore, the 40 Pa yield stress of the Thickened Tailings and the 10 Pa yield stress of the CT 'gypsum' slurry were sufficient to suspend the particles. Visual observation of the slurry when stationary also verified the non-settling behaviour of the coarse particles.

It is important to note that the horizontally orientated gamma ray measurement device provides the chord average solids concentration associated with a horizontal line through the flume at a specific axial and vertical position. This applies to the concentration measurements presented in all of the concentration profile figures. This may explain why the unsheared region is not exactly uniform. The sheared regions associated with the side walls of the pipe, where some degree of particle segregation and migration would occur, would make some contribution to the horizontally averaged solids concentration.

The uniform concentration in the unsheared region was slightly less than the total solids concentration of the bulk slurry (0.30 v/v based on the composition of the prepared slurry) for all of the tests. One can also see that for a decrease in flume angle, and the resulting decrease in velocity, the degree of segregation was greater. As well, for the lower flowrate test (2.5 L/s), and corresponding lower wall shear stresses, the unsheared region was larger. This would be anticipated since a smaller region of the flow will have a shear stress that exceeds the yield stress.

Based on the results presented in Figure 5.53, measurements just below the uniform concentration region indicate a slight reduction in solids concentration. The concentration then increases as the lower flume wall is approached as would be expected with particle settling. Fluid shearing occurs in the lower region of the flume cross-section where the shear stress exceeds the yield stress. The high concentration measured near the lower flume wall may be explained if one assumes that coarse particles will settle when shearing occurs in this region even if the yield stress is high enough to prevent settling in the unsheared region. The reduction in coarse sand concentration, which occurred just below the unsheared region, may be the result of a depletion of particles in this zone due to particle settling. The numerical simulations presented in Section 6.4.1 are consistent with the concentration measurements.

The amount of segregation observed with the Thickened Tailings was quite small for the conditions investigated in this study. Only a 10% change in solids concentration occurred between the sheared and unsheared regions. This may explain why the Coulombic friction term was small enough such that the homogeneous fluid model prediction of the Kozicki and Tiu (1967) model provided accurate estimates of the average wall shear stress. The relatively uniform solids concentration in the unsheared region results in reasonably homogenous slurry properties over the flume cross-section.

A stationary deposit did not occur with any of the tests results presented. If a stationary deposit was generated during a test, the flow depth grew until the slurry spilled over the sides of the flume. Sanders et al. (2002) suggested that the length required to reach steady state conditions (entrance length) should be better understood. The appropriate entrance length required for the conditions of this study is unknown. Velocity measurements obtained with clay-water slurries indicated that the length of flume was sufficient to provide uniform flow and fully developed velocity profiles which would be anticipated with a homogeneous slurry. However, it is not clear how the presence of coarse particles in slurries affects the required entrance length. For this reason, one cannot be certain that the gamma ray concentration device was located at an axial position corresponding to fully developed flow. A greater entrance length may in fact be required to reach an equilibrium when coarser particles are present since the particle distribution may still be developing.

Table 5.10 presents the coarse to fines ratios calculated from the traversing gamma ray concentration measurements. Equation 5.2 was used to calculate the coarse to fines ratio at a given position since the uniformity of the clay-water ratio over the flume cross-section was established in Section 5.6.

Table 5.10: Coarse to fines ratios as determined by the traversing gamma ray densitometer for the model tailings experiments in the 156.7 mm flume

Material	Run	Q (L/s)	θ (°)	Coarse : Fines (v/v) top y/D bottom 0.65	0.60	0.55	0.50	0.45	0.40	0.35	0.30	0.25	0.20	0.15	0.10	0.05
CT	1	5	3	--	--	--	--	--	--	--	--	--	2.5	2.8	2.9	3.1
No Gypsum	2	5	2	--	--	--	--	--	--	--	--	2.2	2.8	2.8	3.1	2.5
	3	5	1.5	--	--	--	--	--	--	--	--	3.0	3.1	3.1	3.1	3.3
	4	2.5	3	--	--	--	--	--	--	--	--	0.1	3.7	5.0	8.5	10.7
	total	--	--	3.5												
CT	1	5	3	--	--	--	--	--	--	--	--	--	1.7	2.8	2.8	2.8
Gypsum	2	5	2.5	--	--	--	--	--	--	--	--	--	2.6	2.4	2.7	3.2
	3	5	2	--	--	--	--	--	--	--	--	3.1	2.9	3.2	3.8	6.4
	4	2.5	3	--	--	--	--	--	--	--	3.2	4.2	5.8	8.0	9.8	10.5
	total	--	--	3.5												
Thickened	1	5	5.4	--	--	--	0.7	0.7	0.8	0.7	0.7	0.7	0.6	0.6	0.8	1.3
Tailings	2	5	4.5	--	--	0.7	0.7	0.7	0.7	0.8	0.6	0.7	0.6	0.6	0.9	1.6
	3	5	4	--	0.8	0.8	0.8	0.9	0.9	0.8	0.8	0.8	0.7	0.7	1.1	2.1
	4	2.5	4.5	0.5	0.6	0.6	0.6	0.6	0.5	0.6	0.5	0.6	0.6	0.6	0.8	1.3
	total	--	--	1.0												

As can be seen in Table 5.10, the coarse to fines ratio for a given mixture changed with depth of flow for all of the tests. These results are in agreement with the coarse to fines ratios determined from the sampling. The average coarse to fines ratio of the bulk slurry is also shown for each test in Table 5.10. For the 2.5 L/s tests, the coarse to fines ratio at the bottom of the pipe was very high for both CT slurries. A coarse to fine ratio of 10 was measured at the bottom of the flume while the average slurry ratio was only 3.5. The results in the table also indicate that the coarse to fines ratios for the 'gypsum' slurry tests were slightly higher than the ratios for the 'no gypsum' slurry tests for roughly the same flow conditions. This suggests that there was a greater degree of segregation in the 'gypsum' slurries.

For the Thickened Tailings tests, the coarse to fines ratios in the unsheared region were approximately constant. Therefore, no segregation of coarse particles occurred in this region. However, in the sheared region near the bottom of the pipe, the ratios were greater than unity. This supports the belief that particle settling occurs in the sheared region since the coarse to fines ratio in the lower part of this region would be expected to be greater than that of the original bulk slurry.

Table 5.11 presents a qualitative comparison for all of the model tailings tests results. For each model tailings mixture, the volumetric flowrate, the flume inclination, and the flow regime are presented for each test performed with the slurry. Also shown is whether the slurry was accelerating or decelerating between height measurement points 1 and 2 in the flume, and whether there was significant segregation of coarse solids. One can see for the CT tests at higher

flowrates (turbulent and transitional), and higher flume angles, no segregation occurred in the flow which corresponds to the slurry flowing uniformly or accelerating axially. However, for the CT tests at the lower flowrates and flume angles, as well as for all of the Thickened Tailings tests (laminar), segregation of coarse solids occurred within the flow. This corresponds to a deceleration of the slurry in the flume. The deceleration results in an increase in the depth of flow, which is caused by the increased solids concentration at the bottom of the flow.

Table 5.11: Comparison of segregating behaviour of coarse solids with the acceleration and deceleration of the model tailings mixtures in the 156.7 mm flume

CT 'No Gypsum'				
Q (m^3/s)	0.00497	0.00504	0.00499	0.00259
θ (^{o})	3.00	2.00	1.50	3.00
Regime	turbulent	turbulent	turbulent	turbulent
Accelerating/Decelerating	A	A	D slight	D
Segregation	no	no	no	yes
CT 'Gypsum'				
Q (m^3/s)	0.00497	0.00504	0.00498	0.00255
θ (^{o})	3.00	1.92	2.47	3.00
Regime	transitional	transitional	transitional	laminar
Accelerating/Decelerating	A	D	A	D
Segregation	no	slight	no	yes
Thickened Tailings				
Q (m^3/s)	0.00497	0.00498	0.00510	0.00253
θ (^{o})	4.00	4.50	5.41	4.50
Regime	laminar	laminar	laminar	laminar
Accelerating/Decelerating	D	D	D	D
Segregation	yes	yes	yes	yes

5.8. Velocity Profiles

Velocity profiles were measured using a Pitot-static tube. Details of the procedures used to obtain measurements are provided in Section 3.2.

5.8.1. Low Reynolds Number Pitot Tube Effect

A Reynolds number correction was developed in this study which was used to correct for Pitot tube measurements at low Reynolds numbers. An additional viscous term, which is not accounted for in Bernoulli's equation (2.63), is incorporated into the relationship for C_p, the pressure coefficient. The correlation corrects for non-ideal behaviour associated with the very

high apparent viscosity of the slurries considered in this investigation. Details of this study can be found in Sections 2.13 and 3.3, and in Spelay and Sumner (2007).

A total of 728 measurements were conducted in the low Reynolds number Pitot tube study where the Pitot tube Reynolds number (Equation 2.64), based on the opening diameter of the Pitot tube, was varied between 3 and 120. The transition Reynolds number was found to be 36. Bernoulli's equation is no longer appropriate for Pitot tube Reynolds numbers below the transition value. An analysis of the low Reynolds number results was performed with measurements conducted below the transition value.

The form of the equation selected for the correlation (Equation 5.3a) is similar to the equations used by Homann (1936) and Chambre (1948).

$$C_p = 1 + \frac{6}{\mathrm{Re}_d + A\,\mathrm{Re}_d^B} \tag{5.3a}$$

Values of correlation parameters, A and B, were obtained by applying the Levenberg-Marquardt minimization method to the data collected below the transition Reynolds number (Press et al., 1992). The parameter in the numerator was set to 6 so that the equation reduces to Stokes' law at very low Reynolds numbers (Re < 10). The results in the literature, presented by Folsom (1956), suggest that the parameters A and B are related to the shape and specific geometry of the Pitot tube tip. As a result, the correlation is appropriate for hemispherical tipped Pitot tubes, as were used in this investigation. In addition, it should be used to predict the low Reynolds number effect where the diameter of the Pitot tube opening is used as the length scale parameter. Photographs of the Pitot-static tubes employed in the low Reynolds number Pitot tube study are shown in Appendix C, Figures C.3 and C.4. The best fit parameters for the low Reynolds number correlation based on the experimental data of this study are presented in Equation 5.3b.

$$C_p = 1 + \frac{6}{\mathrm{Re}_d + 0.00217\,\mathrm{Re}_d^{3.12}} \tag{5.3b}$$

The data of the previous researchers in the literature along with the data obtained in this study are presented in Figures 5.54 and 5.55. Figure 5.54 presents the experimental pressure coefficient

data plotted against the Reynolds number based on the outside diameter of the Pitot tube. The correlations developed by Barker (1922), Homann (1936) and Mikhailova and Repik (1976) are also provided on the figure. Figure 5.55 presents a plot of all of the experimental data gathered in the study as well as the experimental data of other researchers in the literature plotted against the Reynolds number based on the opening diameter of the Pitot tube. Barker's (1922) correlation (Stokes' Law) is also provided in this figure.

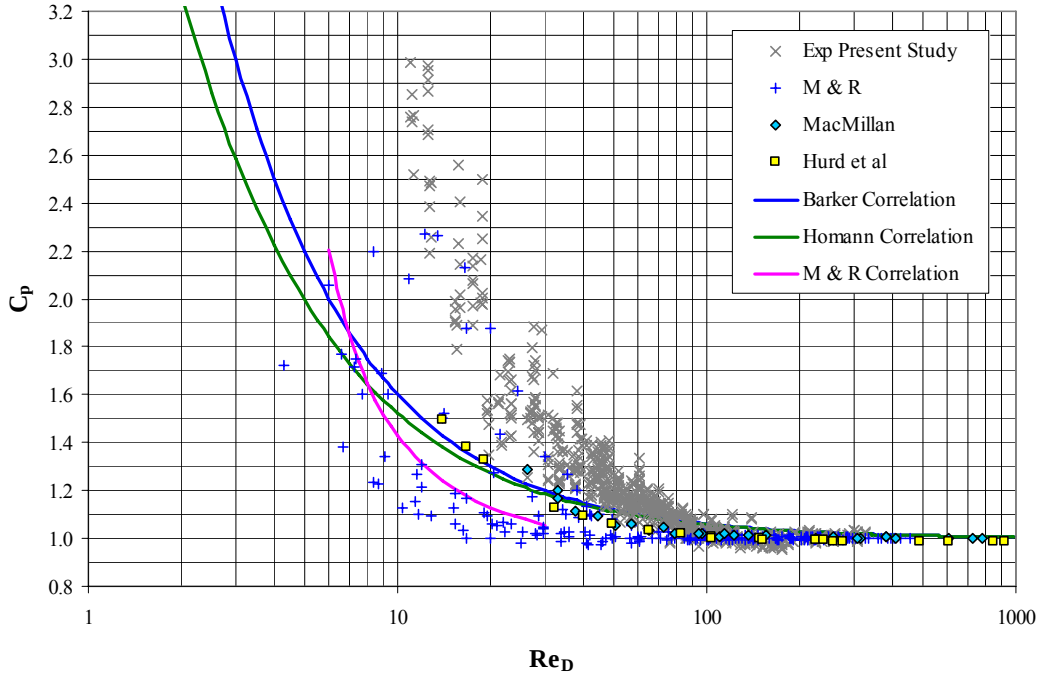

Figure 5.54: Correlations and experimental data for low Reynolds number Pitot tube measurements plotted as a function of Re_D

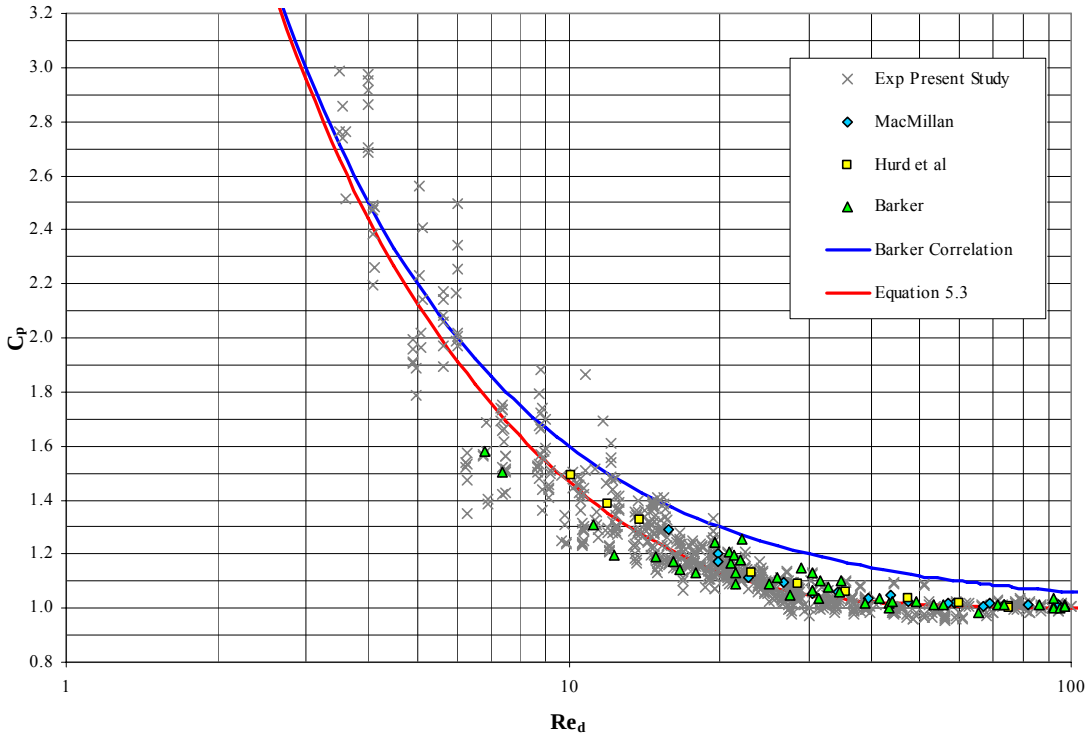

Figure 5.55: Correlations and experimental data for low Reynolds number Pitot tube measurements plotted as a function of Re_d

As can be seen in Figure 5.54 and 5.55, all of the results correlate more closely to the data plotted as a function of the internal diameter rather than the outside diameter. The experimental data produced and the correlation developed in this study, (Equation 5.3), closely follow the experimental results of Barker (1922), Hurd et al. (1953) and MacMillan (1954a).

It is important to note that there are differences between the experiments performed by the other researchers. Most important is the shape of the Pitot tube tip. Barker (1922), Hurd et al. (1953) and MacMillan (1954a) all used blunt tipped Pitot tubes while hemispherical tipped Pitot tubes were employed in this study. In spite of this difference, the correlation provides an accurate prediction of the low Reynolds number phenomenon for all of the cases considered. This suggests that using the appropriate diameter in the correlation, the opening diameter, is more important than correcting for Pitot tube tip shape.

Figure 5.54 and 5.55 suggests that the correction developed in this study provides a more accurate prediction of the low Reynolds number phenomenon compared to the other correlations identified in the literature, including the Barker (1922) correction. As can be seen in Figure 5.55, the correlation developed in this study (Equation 5.3) is also asymptotically appropriate because:

1. It converges with Stokes' Law at Re < 10, ($6/\mathrm{Re}$).
2. It diminishes to $C_p = 1$ near the transition Reynolds number of 40.

The correlation maintains the theoretical aspect of the Barker correction at the very low Reynolds number creeping flows. It also significantly reduces the step function behaviour previously observed with Barker's correction near the transition Reynolds number. It is important to note that the Barker correction is still used extensively in Pitot tube calculations at low Reynolds numbers.

The correlation developed in this investigation also provides a more accurate means to predict Pitot velocities over the entire low Reynolds number range. This includes the intermediate Reynolds number range proposed by Pai (1956), where inertial effects make Stokes' law invalid. It also verifies that the inside diameter is the appropriate length scale parameter for hemispherical tipped Pitot tubes with thick walls.

The low Reynolds number correlation applies to hemispherical tipped Pitot tubes with circular openings in Newtonian fluids. Based on the discussion of Mikhailova and Repik (1976), the correlation developed in this study is only appropriate for smaller ratios of Pitot tube opening to outside diameter where, throughout the entire Reynolds number range, the value of pressure coefficient (C_p) does not fall below 1.

No literature could be identified which considered the use of a Pitot tube for measurements in non-Newtonian flows containing solids. Therefore, the use of Pitot tubes to obtain accurate local velocity measurements in this application is uncertain. Based on the results of this study, it is recommended that a correlation be developed for non-Newtonian slurry flows with significant solids concentrations since low Reynolds number measurements of these flows are industrially relevant.

5.8.2. Flume Velocity Profiles

Water tests were performed in the flume to commission the instruments before slurries were tested. Pitot tube measurements were conducted for water with and without the HPLC pump

purge to ensure accurate operation of the Pitot tube under both conditions. Figure 5.56 shows three sets of Pitot tube velocity measurements generated with water flowing in the flume. The normalized local velocity (v/V) is plotted on the abscissa while the dimensionless flow depth (y/h) is plotted on the ordinate.

5.8.2.1. Water

Traverses were orientated so that velocity measurements were performed along the channel centerline of the flume. The results presented in Figure 5.56 show that similar velocity profiles are obtained for water when a constant HPLC purge is being used and when no purge is provided. As well, nearly identical profiles were obtained in the flume at three different flume angles and flowrates. The profiles show a gradual change in velocity over the bulk of the cross-section while a sharp velocity gradient exists near the flume wall ($y/h = 0$). The observed variation in local velocity was anticipated since the flow was turbulent. The local velocity is nearly uniform near the free surface ($y/h = 1$) and equal to 1.35 times the bulk velocity.

The local Pitot tube Reynolds numbers were approximately 3000 and higher based on the opening diameter of the Pitot tube. Since only measurements with Pitot tube Reynolds number less than approximately 40 are considered to be in the low Reynolds number range, a low Reynolds number correction was not required for the water tests.

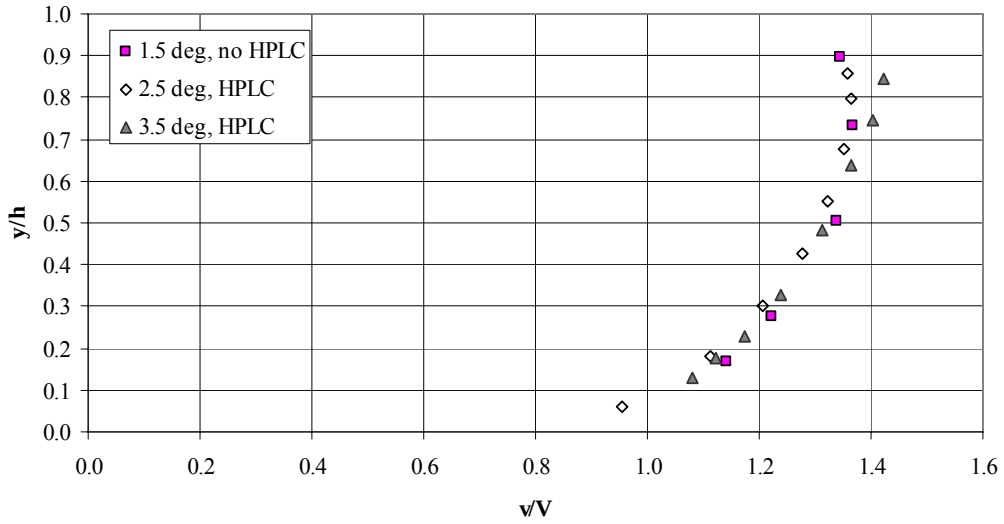

Figure 5.56: Centerline velocity profiles at various angles for water in the 156.7 mm flume with and without a HPLC purge

5.8.2.2. Clay-Water Slurries

Pitot tube measurements were also conducted with the clay-water slurries. To ensure that accurate measurements were obtained, they were conducted using purge water from the HPLC pump to prevent the tip of the tube from being plugged by clay particles.

The 22.2% v/v kaolin clay-water slurry was too viscous to obtain accurate velocity measurements with a Pitot tube. The low operational velocities in the flume and high apparent viscosity of the slurry resulted in very low Pitot tube Reynolds numbers. Unfortunately, no correction method is available to address the Pitot tube flow effects associated with a Bingham slurry with a high yield stress. As a result, unrealistic local velocities (v/V values of 5 and greater) were measured. These results have been omitted from the thesis for this reason.

Velocity measurements were made with the Pitot tube for the clay-water slurries with a 0.03% TSPP addition in the flume. This slurry was in laminar flow for most of the tests. It had a much smaller yield stress (6.4 Pa). The plastic viscosity of the mixture (0.0160 Pa-s) was used to calculate the Pitot tube Reynolds number, which were of the order 200 and greater. Therefore, no correction factor needed to be applied since none of the measurements were in the low Reynolds number region. The results, which are presented in Figure 5.57, appear to be realistic.

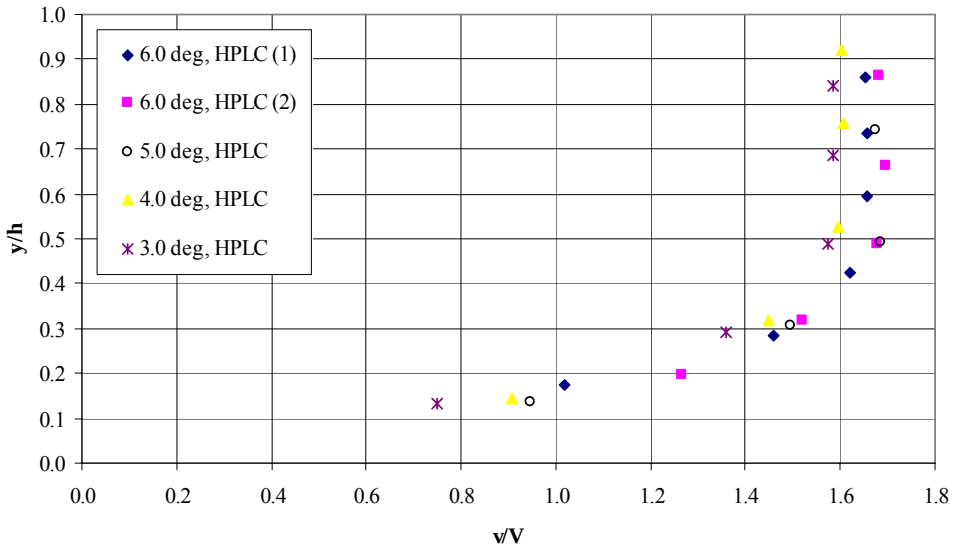

Figure 5.57: Centerline velocity profiles at various angles for a 22.6 % v/v kaolin clay-water slurry with 0.03% TSPP in the 156.7 mm flume with a HPLC purge; ρ=1384 kg/m^3

The velocity profiles presented in Figure 5.57, which were measured at different flume angles and flowrates, appear to be very similar. These profiles were all obtained along the flume centerline. The nearly uniform velocity profile near the free surface ($y/h=1$) supports the earlier suggestion that an unsheared region exists near the free surface. Below the unsheared region, the velocity decreases as the flume wall is approached ($y/h=0$). This is in agreement with the Bingham profiles discussed in the literature. The measured Pitot velocities near the free surface were also in close agreement with the free surface velocity measured using the dye technique. A comparison of the results between the velocity in the unsheared region and the free surface velocity is presented in Table 5.12.

Table 5.12: Comparison of unsheared region velocities with free surface velocities for a 22.6% v/v kaolin clay-water slurry with 0.03% TSPP in the 156.7 mm flume

Test	Free Surface Velocity		% Difference
	Pitot (m/s)	Dye (m/s)	
ClayWater009	3.41	3.33	2.4
ClayWater010	2.68	2.62	2.5
ClayWater011	1.89	1.95	-2.9
ClayWater012	0.58	0.64	-9.1
ClayWater013	0.40	0.43	-7.8
ClayWater014	3.50	3.04	15.2
ClayWater014	2.91	2.77	5.1

The Pitot tube velocity profiles for the clay-water slurry with a 0.10 % TSPP addition are presented in Figure 5.58. Sufficient TSPP was added to this slurry to completely eliminate the yield stress. As a result, the slurry had a Newtonian viscosity of 0.0067 Pa-s. All of the tests presented in Figure 5.58 were performed with a water purge and all of the flume flows investigated with this slurry were turbulent. The velocity profiles, which were obtained at the centerline of the flume, were performed over a number of different flowrates and flume angles. The velocity profile recorded at 1^{o} was conducted with a flow that was near the transition between the turbulent and laminar regimes.

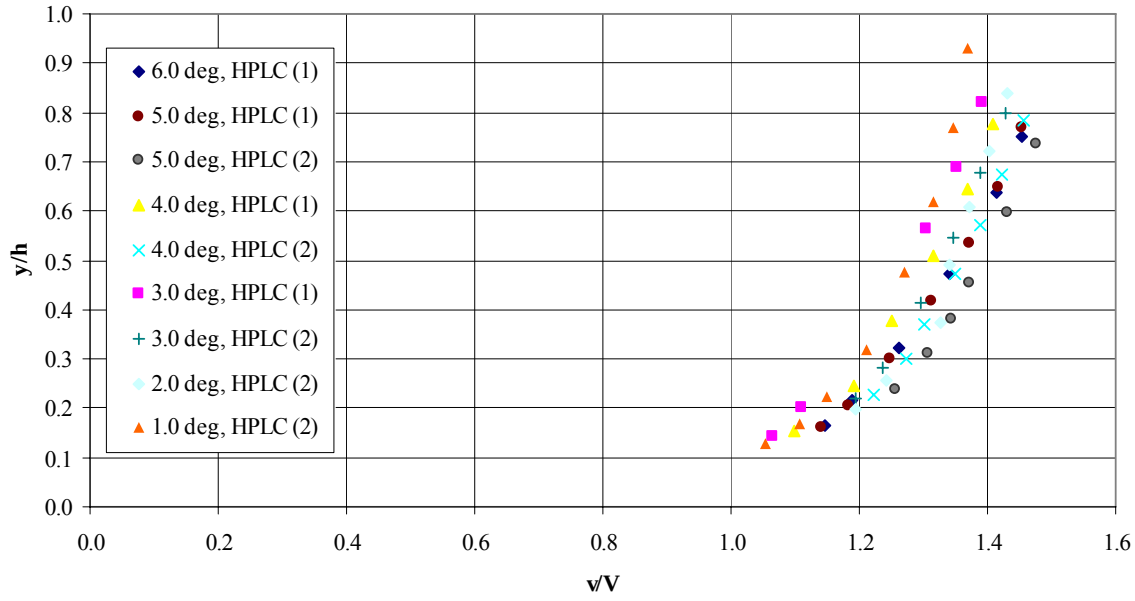

Figure 5.58: Centerline velocity profiles at various angles for a 22.8 % v/v kaolin clay-water slurry with 0.10% TSPP in the 156.7 mm flume with a HPLC purge; ρ=1386 kg/m^3

The shape of the velocity profiles of these slurries is similar to that of the water slurries. Near the free surface ($y/h=1$) the velocity is approximately 1.4 times the bulk velocity. The velocity gradually reduces to zero as the wall is approached. This compares quite closely with the value of 1.35 observed in the water measurements. The Pitot tube Reynolds numbers calculated with these tests were much lower (500 and greater) than those measured with water. However, they were still not low enough to apply the low Reynolds number Pitot tube correction.

5.8.2.3. Sand-Water Slurries

Two-dimensional velocity scans were performed with selected slurry flow conditions in the flume since a significant amount of time was required to obtain measurements at a single operating condition. Some of the velocities values associated with these measurements were so low that the low Reynolds number correction (Equation 5.3) was required. The correction factor was developed using Newtonian fluids. In this study, the plastic viscosity of the Bingham fluid was substituted for the Newtonian viscosity in the calculation of the Pitot tube Reynolds number (Equation 2.64). No experimental tests have been performed to validate whether this substitution appropriately captures the low Reynolds number behaviour for Pitot tubes in Bingham fluids. However, the relative velocity values within a profile should be meaningful.

The two-dimensional mixture velocity profiles are presented in Figures 5.60 to 5.64 and the results are provided in Appendix D. In these figures, dimensionless velocity, v/V, is plotted against x/R and y/R which represent the dimensionless coordinates within the cross-section of the flume. A schematic is provided in Figure 5.59 to assist in the interpretation of the two-dimensional velocity plots. The schematic represents half of the flume cross-section. The exact location in the cross section can be determined from the transverse (x) and vertical (y) coordinate directions. The velocity component, v/V, shown on the schematic is in the axial direction. The bottom of the flume is located at $y/R = 0$ while the top of the flume is located at $y/R = 2$. The channel centerline is located at $x/R = 0$. An example of a free surface position of the flow and the pipe wall position are also shown in Figure 5.59.

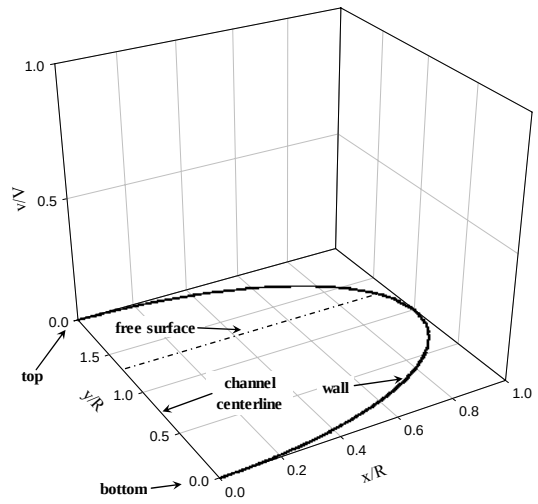

Figure 5.59: Schematic of the two dimensional velocity profiles obtained from the Pitot-static tube measurements in the 156.7 mm flume

The velocity profiles for the sand-water tests at 3.5 ^{o} and 3 ^{o} are shown in Figures 5.60 and 5.61. As can been seen from the profiles, the depths of flow for the sand-water runs were not very high. Therefore, only a limited number of local velocities could be measured for a given test.

The same trend is observed for both the 3.5 ^{o} tests in Figure 5.60 as well as the 3^{o} tests in Figure 5.61. The local velocity seems to decrease along the perimeter of the pipe wall as one travels from the free surface to the bottom of the pipe. One possible explanation for this behaviour is that the wall shear stress varies with position along the cross-sectional perimeter. This would result in different velocity gradients and thus different local velocities at different positions away from the wall around the perimeter. Another explanation involves sand segregation in the high

shear regions of the flow. The concentration profiles obtained with the sand-water slurries indicated that segregation of sand occurred as the bottom wall is approached. This segregation caused regions at lower depths to travel slower since the concentration of solids in the region and the associated resistance to flow was higher. Therefore the velocity gradient variation along the perimeter of the pipe was not constant since the solids concentration also varies along the perimeter.

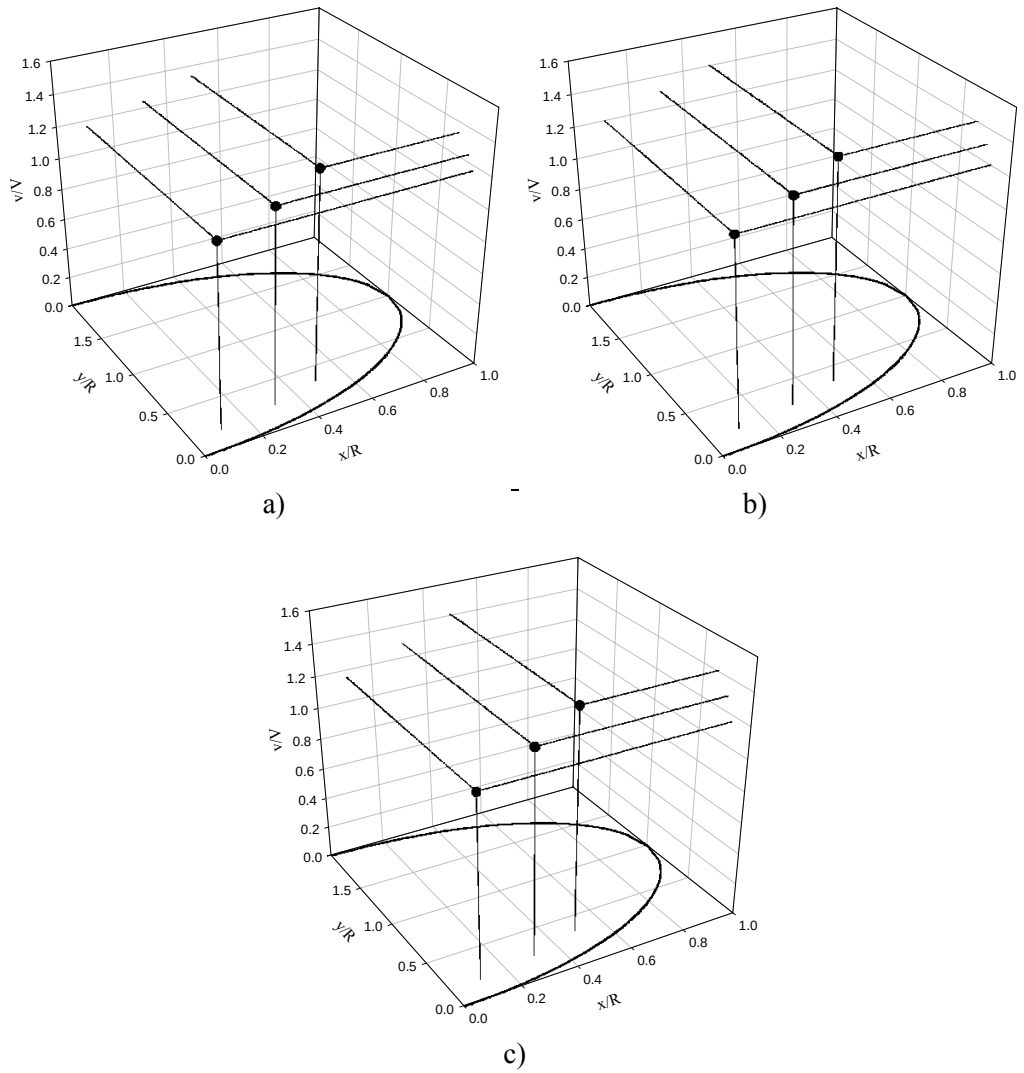

Figure 5.60: Velocity profiles at 3.5 ^{o} for a 25% v/v sand-water slurry in the 156.7 mm flume; ρ=1410 kg/m^3; a) 5 L/s; b) 4.5 L/s; c) 3.9 L/s

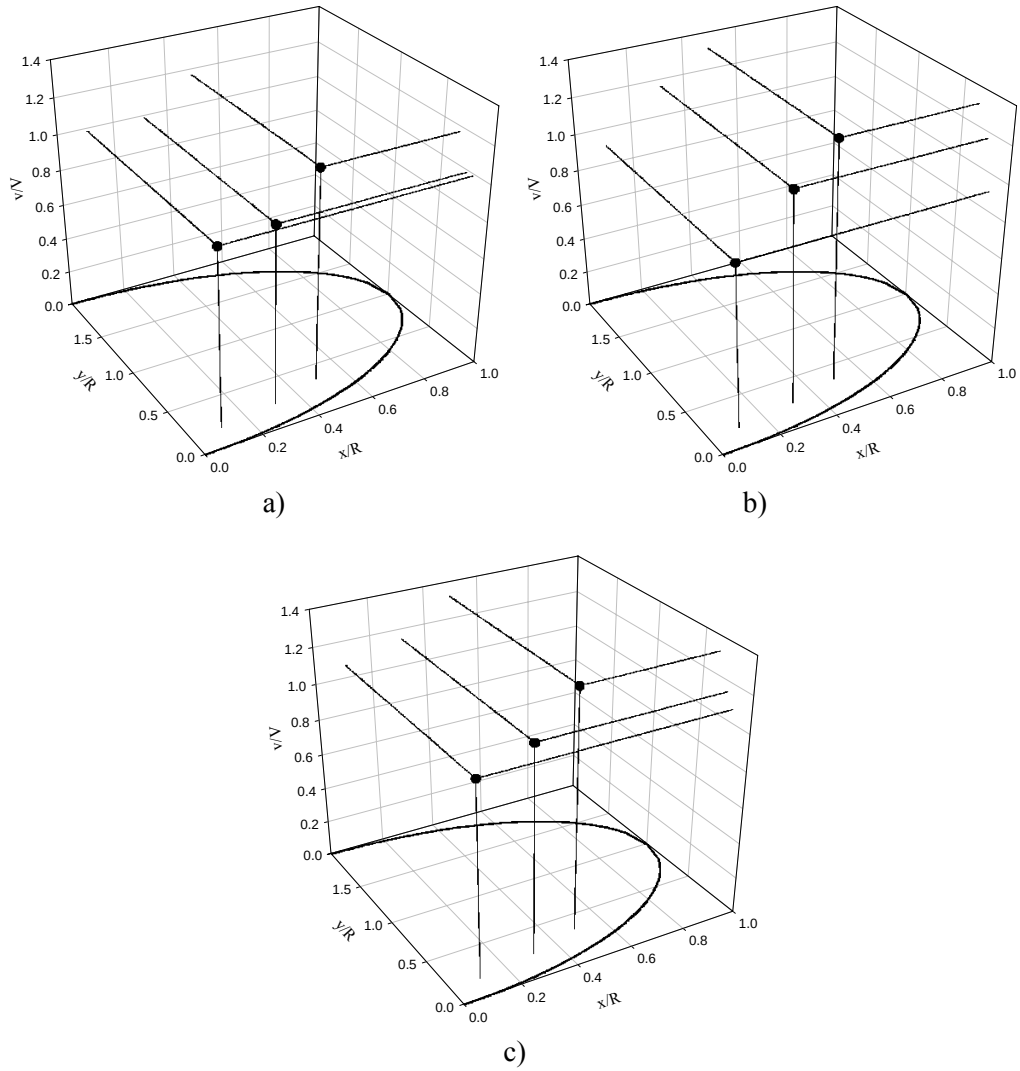

Figure 5.61: Velocity profiles at 3 ^{o} for a 25% v/v sand-water slurry in the 156.7 mm flume; ρ=1410 kg/m^3; a) 6.5 L/s; b) 6 L/s; c) 5.6 L/s

5.8.2.4. CT Slurries

Velocity profiles for the CT 'no gypsum' slurries are shown in Figure 5.62. The 'no gypsum' slurries did not have very large depths of flow as was seen earlier with the sand-water tests. A similar velocity gradient reduction along the perimeter of the pipe wall was also observed for the 'no gypsum' slurries. However, for the high flowrate tests conducted with the 'no gypsum' slurries, a homogeneous, uniform concentration profile was observed. Therefore, with this slurry, the change in velocity along the wall could only be attributed to a variation in wall shear stress along the perimeter. The depth of flow and the magnitude of the change in velocity along the

perimeter increased as the flume slope angle was decreased. This is apparent from the progression of the velocity profiles from Figure 5.62a to 5.62d.

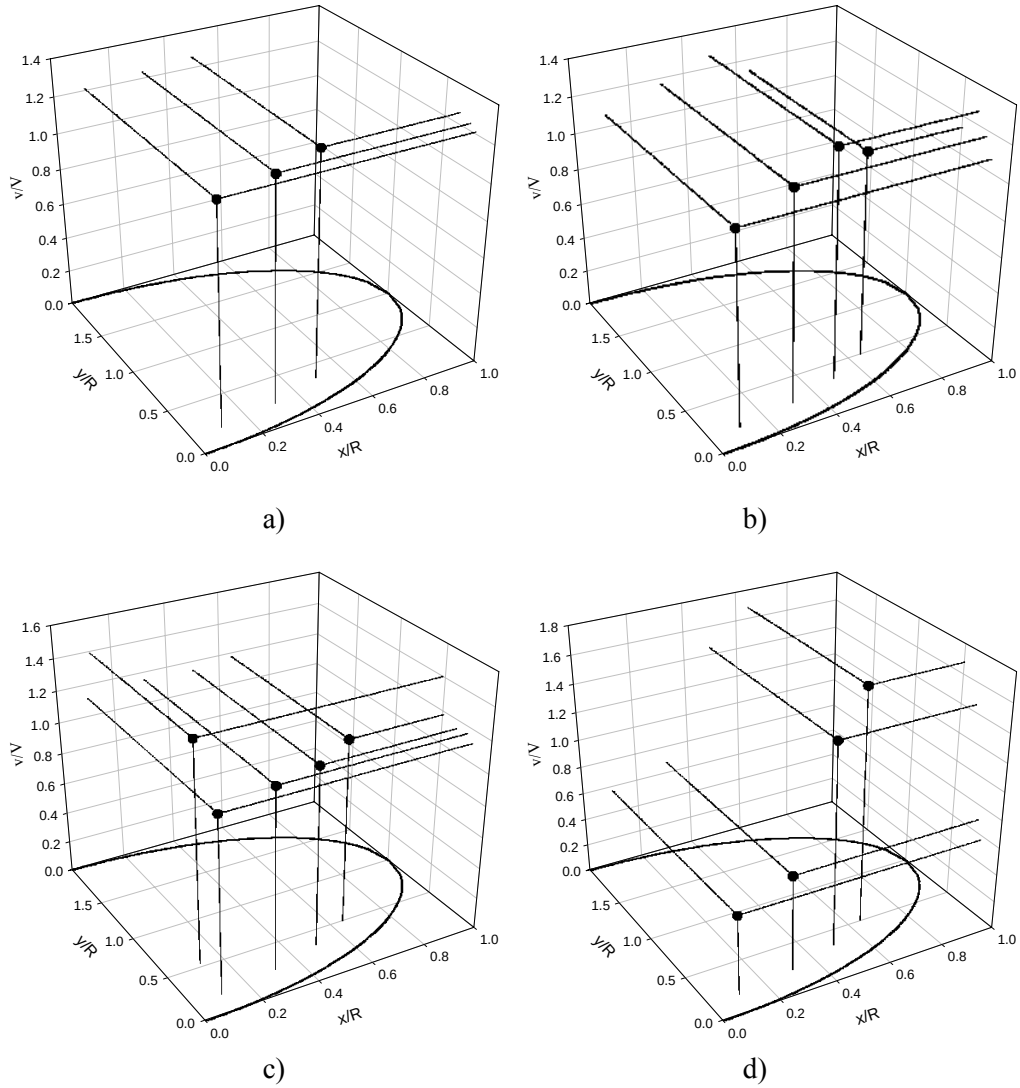

Figure 5.62: Velocity profiles for a model Syncrude CT 'no gypsum' slurry in the 156.7 mm flume; ρ=1598 kg/m^3; a) 5 L/s & 3^o; b) 5 L/s & 2^o; c) 5 L/s & 1.5^o; d) 2.5 L/s & 3^o

Based on the results presented in Figure 5.62d, particle segregation appears to have a significant effect on local velocity when the volumetric flowrate is 2.5 L/s and the flume angle is 3 ^{o}. The small mixture velocity at the base of the pipe is caused by particle segregation. This is consistent with the earlier concentration measurements where a high solids concentration (0.60 v/v) was measured near the base of the pipe (coarse:fines = 10.7). The absolute value of the velocity for this profile is very small since the effective mixture viscosity is very high in regions of high solids concentration (Shook et al., 2002). With regard to the Pitot tube measurements, the low

Reynolds number correction was applied for measurements obtained in regions of high particle segregation. The large decrease in velocity near the bottom of the flume would be anticipated with the higher coarse particle concentration in this region.

Velocity profiles for the CT 'gypsum' slurries are shown in Figure 5.63. Significant depths of flow were observed at high flowrates with the CT 'gypsum' slurries. As well, for the uniform concentration profiles presented in Figure 5.52, the same decrease in the velocity gradient associated with wall shear stress observed with the 'no gypsum' slurries was observed around the perimeter of the flume in Figures 5.63a and 5.63b. The CT 'gypsum' slurries exhibit a significant yield stress and high local apparent viscosity. The concentration profiles for the CT 'gypsum' slurries indicated that segregation was taking place. The significant change in velocity noted near the bottom of the flume in Figures 5.63c and 5.63d can be attributed to the increase in local effective viscosity associated with the higher solids concentration due to particle segregation.

The results indicate issues associated with the application of the low Reynolds number Pitot tube correction where the solids concentration in a region is significantly different from the bulk concentration. As a result of segregation, high local solids concentrations occur near the flume perimeter. High apparent viscosities would be anticipated as a result of the elevated concentration. This creates a difficulty in applying the low Reynolds number Pitot tube correction since the plastic viscosity of the slurry, scaled by the relative viscosity of the mixture, is used in Equation 2.64 and Equation 5.3. As a result, physically unrealistic v/V values of 2 or greater are noted in Figures 5.63c and 5.63d. The higher concentrations values which exist near the flume wall with the 'gypsum' slurries are shown in Figure 5.52. Overall, the trend of decreasing velocities along the pipe perimeter and the shape of the velocity profile suggest segregation and settling of sand particles and is consistent with an accumulation of coarse particles at the bottom of the flume.

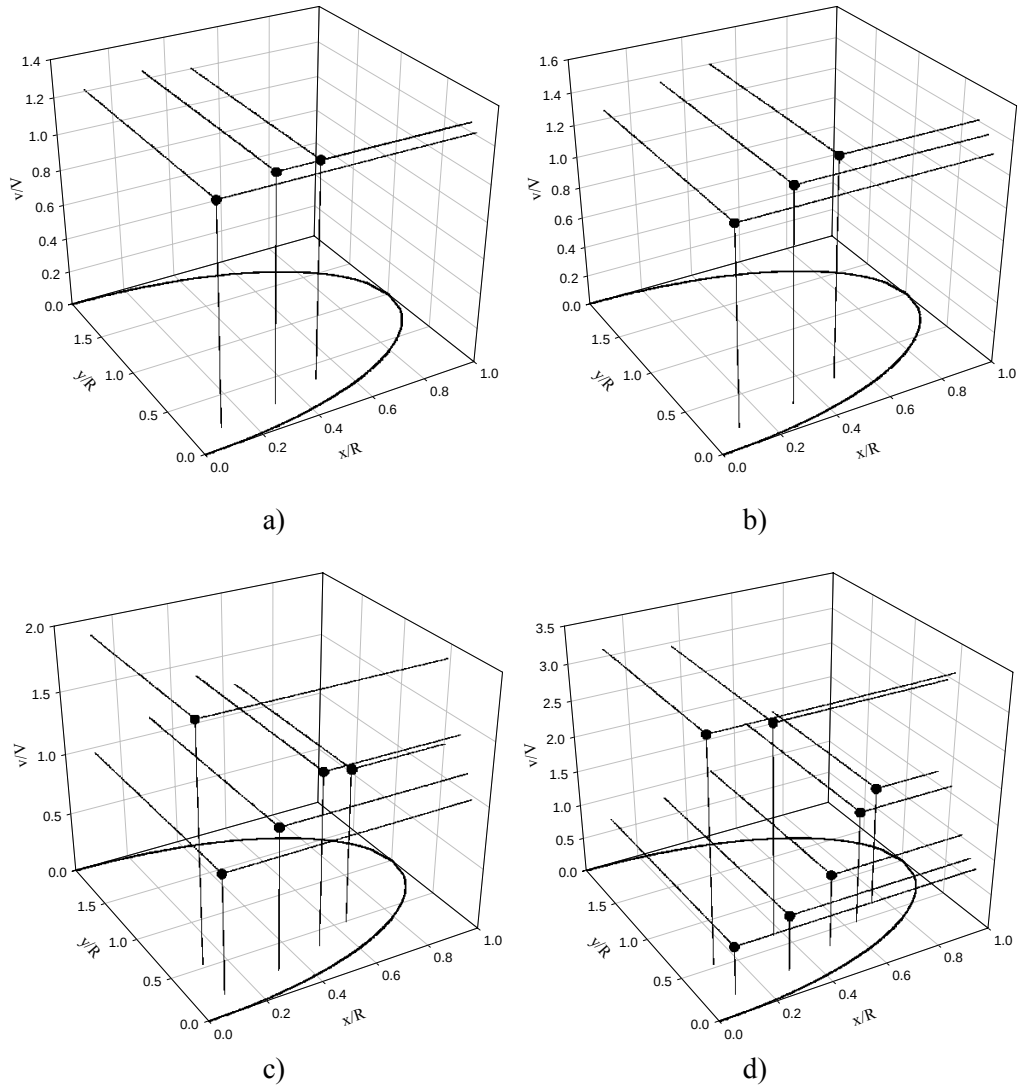

Figure 5.63: Velocity profiles for a model Syncrude CT 'gypsum' slurry in the 156.7 mm flume; ρ=1598 kg/m^3; a) 5 L/s & 3^o; b) 5 L/s & 2.5^o; c) 5 L/s & 2^o; d) 2.5 L/s & 3^o

5.8.2.5. Thickened Tailings Slurries

Velocity profiles for the Thickened Tailings tests are shown in Figure 5.64. Since the slurry investigated was viscous, the depths of flow for these tests were large. This meant that a large number of local velocities could be measured for a given test. All the Thickened Tailings tests were laminar due to the viscous nature of the slurries. As a result, the values of the local velocity inferred from the Pitot tube measurements were not physically realistic for the same reasons discussed with the previous slurries. In some cases v/V was greater than 3.

The shapes of the Thickened Tailings slurry velocity profiles, presented in Figure 5.64a to 5.64d, show some interesting trends. The velocity gradient approaches zero in the central region of the flow. This suggests the existence of an unsheared region which would be anticipated with a mixture which exhibits a significant yield stress. The existence of an unsheared region is further supported by the concentration profiles in Figure 5.53 where the concentration was uniform in this region. The trend of a decreasing velocities along the pipe perimeter at the bottom of the flume and the shape of the velocity profile suggest migration and settling of sand particles toward the bottom of the flow in the sheared region.

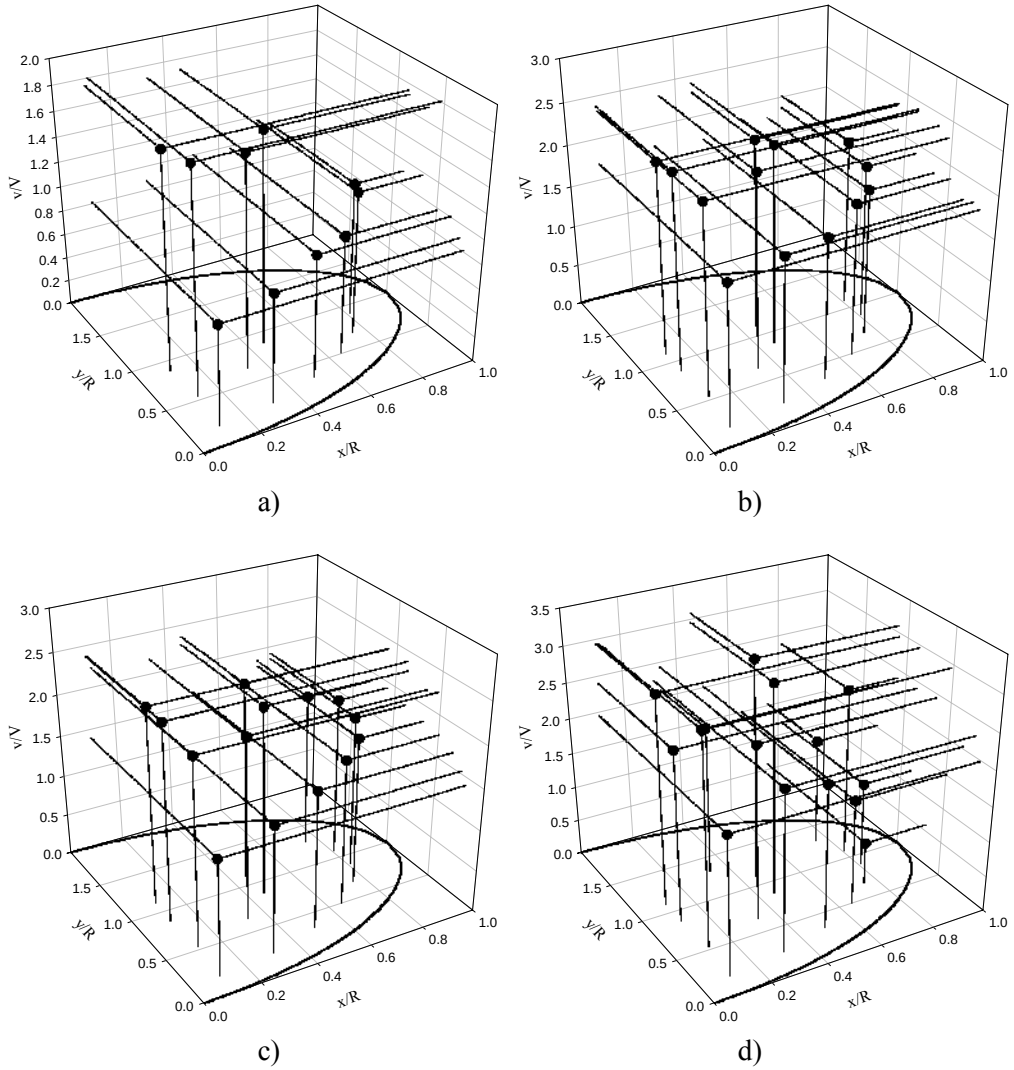

Figure 5.64: Velocity profiles for a model Syncrude Thickened Tailings slurry in the 156.7 mm flume; ρ=1510 kg/m^3; a) 5 L/s & 5.4^o; b) 5 L/s & 4.5^o; c) 5 L/s & 4^o; d) 2.5 L/s & 4.5^o

Comparing the results for all of the mixtures, it is evident that segregation occurs in both laminar and turbulent flow. As well, the flow is likely to be laminar and have high depths of flow when the slurry has a significant yield stress. If the flow is laminar and the slurry has a yield stress, the flow cross section will have an unsheared region where segregation does not occur and a sheared region where segregation can occur. Segregation of coarse particles is more likely to occur at low velocities and low flume angles resulting in a high concentration zone near the bottom flume wall. Under these conditions, care should be taken to ensure that the velocity does not fall below the critical deposition velocity, which would result in the formation of a stationary deposit and the contents of the flume overflowing.

6. NUMERICAL RESULTS AND DISCUSSION

6.1 Commercial Software

One of the original goals of this study was to develop a complete Navier-Stokes solver. However, as the literature in the area of non-Newtonian, open channel flow was reviewed, it was determined that this would not be feasible. The solution of the full three-dimensional Navier-Stokes equations in a complex three-dimensional flume geometry was determined to be too large of an undertaking. In addition, when the additional complexities of the three- dimensional solution of the Phillips model combined with gravitational sedimentation effects, was examined it was clear that the scope of the undertaking was beyond this study. Therefore, the use of a commercial software package to aid in solving the solids transport problem was investigated.

Currently the most common means to solve a two-phase flow problem is through a Lagrangian particle tracking method (Gouesbet and Berlemont, 1999). This method uses a statistical approach to represent the effects of individual particles interactions to solve the governing conservation equations. However, for high concentration systems, the number of particles to be tracked is significant and thus the calculation overhead and the time required to solve the problem is significant.

If an Eulerian frame of reference is employed, then the individual phase momentum differential equations must be solved (Gouesbet and Berlemont, 1999). The number of momentum equations which must be solved is dependent on the number of coordinate dimensions and the number of phases. A full three-dimensional solution of a two phase problem requires the solution of six momentum equations. The simultaneous solutions of this many equations is both complex and time consuming. As well, the concentrated solid phase and the fluid phase interaction relationships are not always well understood.

The two phases can be combined together to solve the momentum equations which provides an elegant method to solve solids transport problems. If the carrier fluid is non-Newtonian, an apparent viscosity approach can be employed to model the effective viscosity of the slurry mixture. The non-Newtonian effective viscosity is a function of both local concentration and shear rate. A scalar concentration differential equation is used to account for the interaction between the solid and the fluid phases. This results in a coupled solution between the momentum

and solids concentration equations. Using this approach, only a single momentum equation needs to be solved (for each velocity component) and the slurry can be considered to be a mixture with variable density according to the concentration of the coarse solids phase.

A number of commercial CFD (Computational Fluid Dynamics) software packages have been considered for this solids transport problem. The packages that were considered in this study included CFD2000, ADINA, WRAFTS, CFX, and FLUENT.

6.1.1. CFD2000

CFD2000 is a basic and introductory commercial software package (Adaptive Research, Alhambra, CA). It is based on the finite volume method and is easily accessible since our research group owns a perpetual license. It was found to be easy to learn but its functionality and user specifications are quite limited. It works well for Newtonian flow problems and simple geometries. The Lagrangian particle tracking method is employed for solving two phase flow problems. Although it has non-Newtonian fluid capabilities, it is unable to represent an additional coarse particle phase within the non-Newtonian carrier fluid. Therefore, the solution of an independent scalar equation, which would be required for the solution of the Phillips model, is not possible. As well, the source code of the software was not available for manipulation. This meant that the scalar transport equation could not be solved simultaneously with the Navier-Stokes equations.

6.1.2. ADINA

The next software package considered was the ADINA (Automatic Dynamic Incremental Nonlinear Analysis) finite element package (ADINA R&D, Inc., Watertown, MA). This software package was available on a general license to the University of Saskatchewan, College of Engineering computer labs. Even though the software is best known for its application to solid body mechanics, it also has a CFD solver via the ADINA-F module. The software was not capable of solving the problem of interest in this study. It did not have the capabilities to solve highly viscous, non-Newtonian fluids that exhibit a yield stress. As well, the source code was not available for manipulation, making implementation of the scalar concentration solver impossible.

6.1.3. WRAFTS

The next software package investigated was WRAFTS (Weighted Residual Analysis of Flow TransientS) (Capcast, EKK, Inc., Walled Lake, MI). This is a three-dimensional, transient, finite element code that was recommended by Backer (2004). It is the most comprehensive casting filling simulation module. In the code, Backer (2004) has incorporated the Phillips model to create a commercial software package capable of solving problems similar to the kind considered in this study. However, a complete academic software license was beyond the means of our funding. As well, the code would not have been open source and it was unclear whether the effect of gravitational sedimentation could be incorporated into the code.

6.1.4. CFX and FLUENT

The final two commercial software packages considered were CFX (Ansys, Inc., Canonsburg, PA) and Fluent (Fluent Inc., Lebanon, NH). Both codes use a finite volume method approach. Academic licenses are available for these codes through the University of Saskatchewan. These two programs are the most popular commercial packages available today. CFX allows user input through Fortran subroutines while Fluent permits user input through C subroutines. A number of other user accessible options are available for modifying the source code. For example, the method that the code used to represent viscosity could be modified to permit a non-Newtonian viscosity to be used for the carrier fluid. After researching the problem, it was determined that either code was capable of solving a scalar concentration equation involving the Phillips model. On the basis of availability, Fluent was chosen for further investigation.

Fluent has been used to successfully solve fluid-particle flow problems (Caffery, 1996). The flow of particle-fluid systems can be solved by the implementation of either a Lagrangian or an Eulerian approach. In this study an Eulerian approach will be employed and the effect of particles on the system will be determined by the solution of a single scalar transport equation. The implementation of the Phillips model will be incorporated into Fluent via the diffusivity and source term variables in its internal scalar transport equation. Fluent's UDFs (User Defined Functions) or subroutines will be used to access and modify flow parameters during the solution.

Initially, one-dimensional simulations were performed using the Phillips model for the case of the flow of neutrally buoyant particles in an open channel. The results showed that a Neumann

boundary condition (Rao, 2002), which sets the concentration gradient to zero at the channel wall and free surface, led to unrealistic concentration distributions. These results did not agree with those presented by Phillips et al. (1992) for the same conditions. In addition, the fraction of coarse particles within the system was not being conserved in the simulation due to unrealistic boundary conditions. Flux of solids particles was occurring through the domain boundaries. A scaling procedure had to be developed to ensure that no loss or gain of particles occurred within a given simulation.

By setting no-flux boundary conditions at the domain boundaries, for the scalar concentration equation (Section 4.13.2), more realistic results were obtained which were in agreement with the simulations of Phillips et al. (1992). Additional work indicated that no-flux boundary conditions were necessary for solving the Phillips model equations with sedimentation. However, since they are not constant value Neumann or Dirichlet conditions, they cannot be easily inserted into the numerical subroutines of Fluent. In fact, when the sedimentation term is included, the no-flux boundary condition at the wall is a complicated non-linear Robbins boundary conditions (Rao, 2002). It is difficult to implement this type of boundary condition within Fluent. Only constant values or single value gradients could be used as boundary conditions.

A method to incorporate non-linear boundary conditions into Fluent could not be identified. It may have been possible to create a subroutine that could be used to patch the required no-flux conditions at the domain boundaries. However, after careful consideration it was determined that due to the difficulty in implementing these boundary conditions, and the uncertain success of this approach, another method of solving the problem should be considered. It is for this reason that a stand-alone, one-dimensional solver was pursued. The code for the numerical model developed in this study is presented in Appendix A. The results of the one-dimensional simulations should provide the same general velocity and concentration trends as would be illustrated by a more complicated three-dimensional solution.

6.2. Phillips Model Verification

The numerical model developed in this study is based on the constitutive Phillips model. Simulations were performed to both verify the correct operation of the numerical solver code and test the validity of the Phillips model. Phillips et al. (1992) tested and calibrated their model using experimental results obtained with flow in a pipe and Couette flow in a wide-gap,

concentric cylinder apparatus. Figure 6.1 shows the simulated concentration profile based on a 40% v/v suspension of neutrally buoyant 0.475 mm spheres in a Newtonian carrier fluid. The fluid has a density of 870 kg/m^3 and a viscosity of 0.20 Pa-s. The simulation is performed in a rectangular duct of infinite width with a half-height of 0.05 m. The coarse particles have a maximum packing concentration of 0.58 v/v.

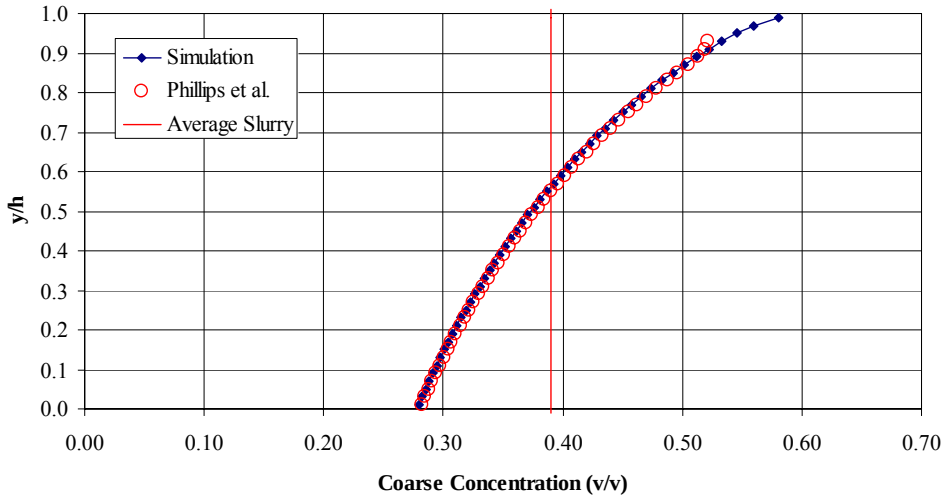

Figure 6.1: Phillips model verification concentration profile for 0.475 mm neutrally buoyant spheres in a rectangular duct of infinite width

Figure 6.1 also presents the concentration results obtained from the analytical expression developed by Phillips et al. (1992) (Equation 6.1) developed for flows under similar conditions. In this equation the subscript 'w' denotes values at the duct wall. In order to evaluate the analytical expression values for the shear rate and concentration at the wall were required. The values used to evaluate the analytical expression were obtained from the numerical simulation shown in Figure 6.1 and Figure 6.2. From the plots in Figure 6.1, there is excellent agreement between the analytical expression developed by Phillips et al. (1992) for the steady, fully developed flow of neutrally buoyant spheres and the simulated results for the same set of test conditions. Although this evaluation does not indicate whether the approach is physically reasonable, the agreement between the results shows that the model and solver used to simulate the problem were functioning correctly.

$$\frac{\phi}{\phi_w} = \frac{\dot{\gamma}_w}{\dot{\gamma}} \left(\frac{\eta_{r_w}}{\eta_r} \right)^{K_\eta / K_c} \tag{6.1}$$

As can be seen in the simulated concentration distribution presented in Figure 6.1, there is a flux of particles away from the duct wall towards the centre of the flow. If one considers a mixture consisting of negatively buoyant particles in laminar flow, a resuspension force exists to counteract the effects of gravity on a settling particle. For the case considered with neutrally buoyant particles, the resuspension force was so significant that the concentration near the centre of the flow approached the maximum packing concentration of the particles.

The velocity profile associated with the neutrally buoyant particle simulation is presented in Figure 6.2. The migration of particles to the centre of the flow leads to a plug like, or blunting of the mixture velocity profile due to the increase in the effective mixture viscosity in this region.

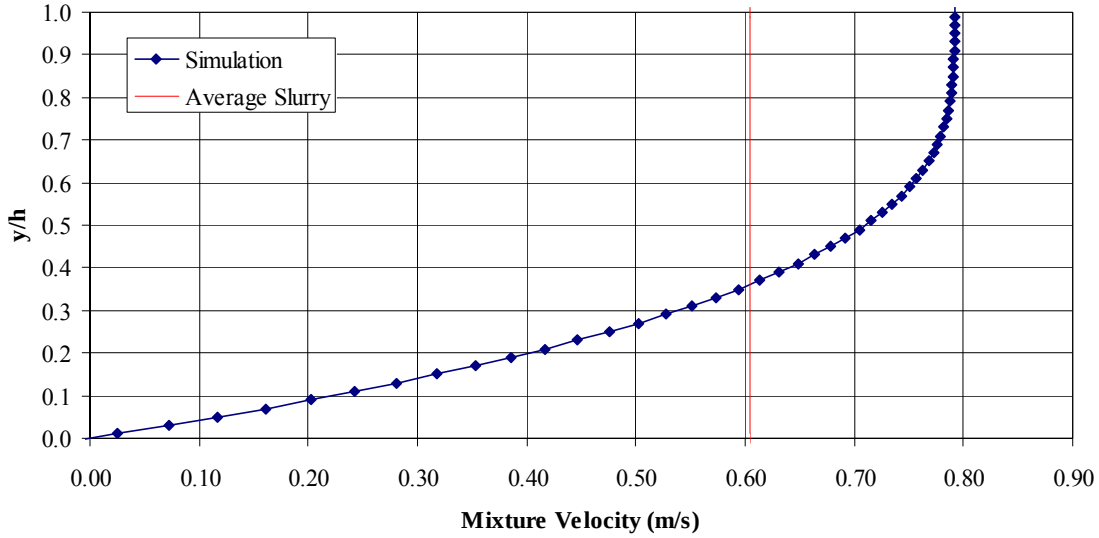

Figure 6.2: Phillips model verification mixture velocity profile for 0.475 mm neutrally buoyant spheres in a rectangular duct of infinite width

Figure 6.3 shows the simulated concentration profile for the same conditions as those performed with the simulation results presented in Figures 6.1 and 6.2, except that the diameter of the spherical particles is 0.188 mm instead of 0.475 mm. As before, the simulated concentration profile is similar to the results of the analytical relationship developed by Phillips et al. (1992) (Equation 6.1).

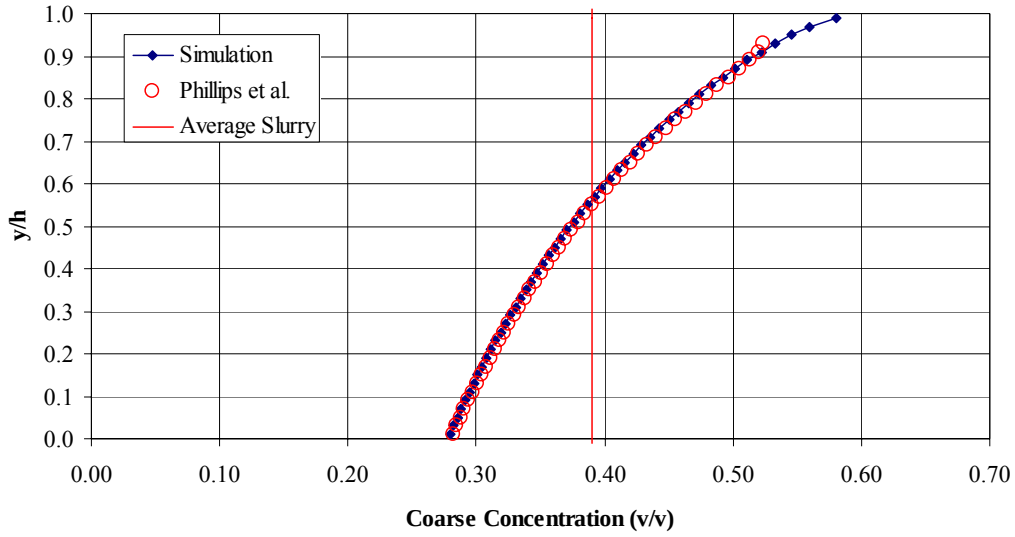

Figure 6.3: Phillips model verification concentration profile for 0.188 mm neutrally buoyant spheres in a rectangular duct of infinite width

If one compares Figure 6.1 and 6.3 for the 0.475 mm and 0.188 mm particles (simulation results are presented in Appendix E), the final steady state concentration profiles are the same. Equation 6.1 for neutrally buoyant particles shows that the concentration distribution has no dependence on particle size (particle radius, a). The final steady state concentration distribution is independent of particle size.

It is interesting to note that Gillies et al. (1999) experimentally determined that particle size did not significantly influence the steady state distribution of the negatively buoyant solids in their pipe flow experiments, but rather only influenced the time required to reach a steady operating state. Since the concentration distributions for the two different particle sizes in the simulations of this study are the same, the resulting mixture velocity profile for the 0.188 mm spheres is also identical to the velocity profile simulated for the 0.475 mm spheres shown in Figure 6.2. The close agreement between the results obtained with the simulations and analytical solutions with the two different particle diameters provides further verification of the solver and code developed in this study. As well, the results are in qualitative agreement with the experimental concentration profile measurements of Phillips et al. (1992).

Using a time step of 100 s, the 0.475 mm particles simulation required 181 iterations to reach a steady state. However, the simulation for the 0.188 mm particles under the same test conditions required 1003 iterations. Therefore, based on two simulations, it appears that the time required to

reach steady state is approximately inversely proportional to the square of the particle size. A similar proportionality was noted with other simulations performed in this study. Similar steady state time proportionality with particle size has been noted in other studies (Hampton et al., 1997; Acrivos et al., 1993; Tetlow et al., 1998).

6.3. Grid Refinement

The simulation time step (Δt) and grid cell size (Δy) were parameters that were considered carefully in the study. The time step can be used to stabilize the simulation. The transient term can be used to assist in the solution of the highly non-linear and stiff transport equations. By adjusting the time step, the solution can advance in time without significant instabilities or oscillations. The momentum and scalar transport equations are solved simultaneously with the same time step. Simulations were attempted with time steps greater than 2 s. Significant instabilities occurred in the solution of the concentration and mixture velocities with this time step. When the time step was reduced to 0.25 s, the simulation was stabilized for the conditions investigated in this study. No advantage or significant differences in the results were observed when the time step decreased below 0.25 s. It is interesting to note that for neutrally buoyant particle simulations in Figures 6.1 to 6.3, solutions were possible with time steps as high as 100 s. Therefore, it is the sedimentation flux that increases the stiffness of the scalar transport equation requiring small time steps.

A cell-centered, uniform grid was employed to make implementation of the boundary conditions and interpolations to the cell faces simpler. The grid cell size (Δy) and number of nodes (N) are related to each other through the depth of flow in the domain (h). A larger number of nodes (finer grid) will lead to a more accurate solution due to more accurate finite difference approximations associated with the numerical derivatives. However, the accumulated round off error and simulation time becomes more significant with smaller time steps since both increase with an increase in the number of nodes. This becomes even more significant when the simulation time step must be small to address the stiff differential equations, as is the case in this study.

To determine the effect of varying the grid cell size, simulations were performed with grids of 25, 50 and 100 nodes. An increase in the accuracy of the simulation results was observed for the 50 node simulations compared to the 25 node simulations. However, no significant difference in

results occurred when the number of nodes was increased from 50 to 100 nodes. As well, it was observed that the 50 node simulation led to a dramatic reduction in the oscillatory behaviour due to the singularity at the sheared-unsheared interface compared to the 25 node simulation. Based on these results, a 50 node mesh has been employed in the numerical simulations presented in this study.

6.4. Model Tailings Simulations

Along with including the Phillips shear-induced diffusion model, the model developed in this study included the effect of a non-Newtonian carrier fluid and the effect of gravitational settling which were not considered by Phillips et al. (1992). This further complicates model development. The model equations are so complicated that the development of an analytical expression for the concentration distribution, like the one presented in Equation 6.1, is no longer possible. The governing differential equation must, therefore, be solved using numerical methods. Details of the numerical model and the technique employed in this study were presented in Sections 4.4 and 4.9.

Experiments were performed in an open circular flume as outlined in Section 3.1. The flume was an 18.5 m length of 156.7 mm internal diameter pipe with sections cut from the top to create an open channel flow. Chord averaged concentration profiles, which were measured near the flume outlet with a traversing gamma ray densitometer, are presented in Section 5.7. From the perspective of the modeling efforts, the results of the tailings slurries composed of a coarse sand phase, kaolin clay and water are of particular interest. Since the numerical model developed in this study is only applicable to laminar flow, the numerical simulations will only be compared with the results of the Thickened Tailings and CT 'gypsum' tests.

6.4.1. Thickened Tailings Slurries

Figure 6.4 presents an example of a simulated concentration profile for a Thickened Tailings slurry. The results from the experimental study cannot be directly compared to the model simulations since the one-dimensional simulation is based on a rectangular open channel of infinite width (flow down an inclined plane of infinite width) while the experimental results were obtained in a flume of circular cross-section. However, the simulations are performed under the same test conditions and with the same hydraulic radius as the experimental tests, which should

allow the general features of the profiles to be compared. For rectangular channels of infinite width, the hydraulic radius is equivalent to the depth of flow. Despite the differences in geometry, the physical mechanisms driving the settling of particles should be accurately represented by the model. Although the simulation geometry is highly simplified, it represents a useful starting point for studying solids transport in laminar open channel flows.

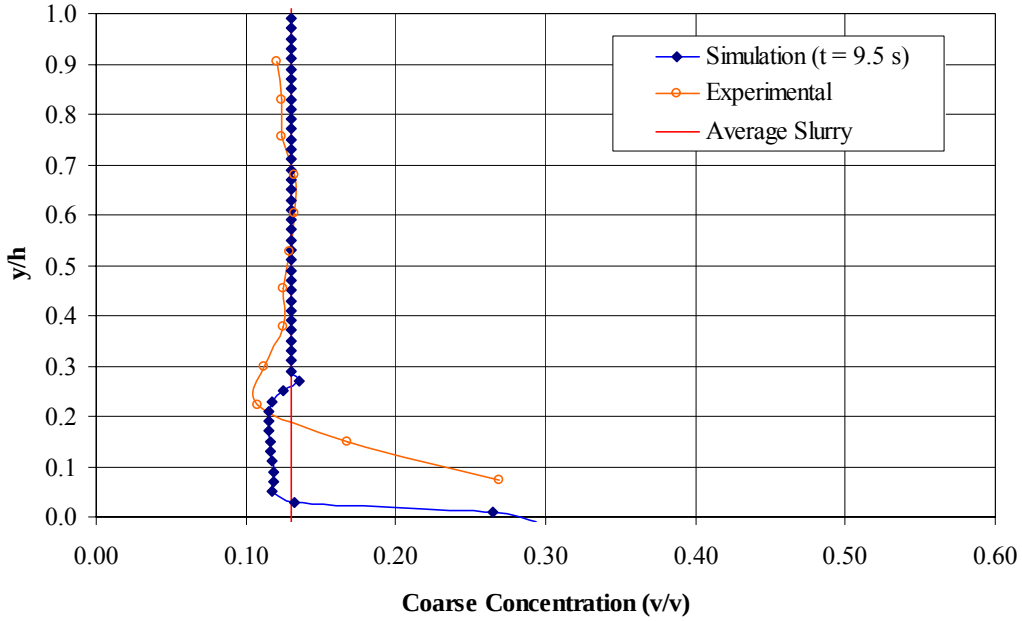

Figure 6.4: Numerical and experimental concentration profile comparison for a Thickened Tailings slurry test (5 L/s, 4 ^{o}) at t = 9.5 s

Figure 6.4 represents a snapshot in time of a concentration profile for the test performed at volumetric flow rate of 5 L/s and flume angle of 4^{o}. For both the experimental test and the simulation, the hydraulic radius was 0.0455 m, and the mean particle diameter and density were 0.188 mm and 2650 kg/m^3 respectively. The clay-water carrier fluid had a density of 1303 kg/m^3, a yield stress of 33.6 Pa and a plastic viscosity of 0.0245 Pa-s. The bulk concentration of coarse particles in the slurry was 13.1% v/v and the particles had a maximum packing concentration of 58.2% v/v.

In Figure 6.4, the simulation was stopped before it had reached steady state. A steady state balance between the particle fluxes had not yet been achieved. Despite the differences in flow geometries, there are similarities between the experimental concentration distribution and the simulated profile. In both profiles the concentration is uniform in the unsheared region. The

concentration in the unsheared region is also equal to the average slurry concentration in both cases. There is also an initial decrease, or particle depletion, directly below the unsheared region followed by an increase in particle concentration near the wall, which would be caused by particles settling in the sheared region. Therefore, the general features of both distributions are similar.

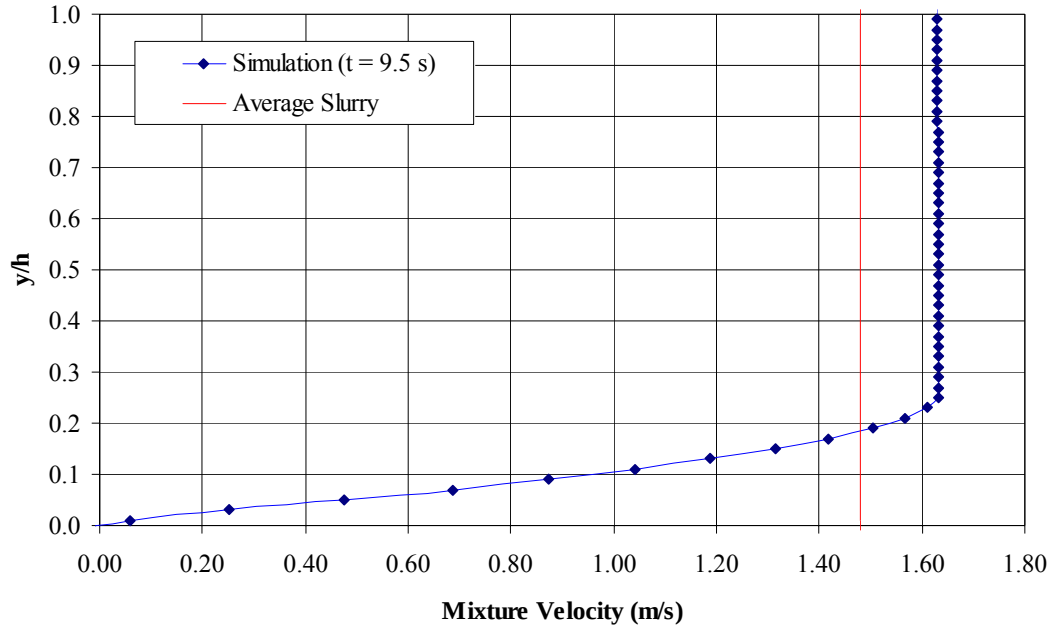

Figure 6.5: Simulated velocity profile for a Thickened Tailings slurry test (5 L/s, 4 ^{o}) at t = 9.5 s

Figure 6.5 shows the simulated mixture velocity profile for the concentration profile presented in Figure 6.4. Despite the segregation near the bottom wall observed in the simulated concentration profile, one can see that the mixture velocity profile does not vary significantly from the velocity profile of a homogeneous Bingham fluid (Figure 5.57). This may be the reason that the theoretical homogeneous models, which only account for viscous frictional losses, provided a reasonable prediction for the experimental wall shear stress in the flume (Figure 5.46).

The simulation profiles shown in Figures 6.4 and 6.5 correspond to a simulation duration of 9.5 s. The bulk mixture velocity was 1.48 m/s in the simulation. Using a pseudo steady state assumption, 9.5 seconds of simulation time is approximately equivalent to a flume length of 14.1 m. This is similar to the flume entrance length associated with densitometer (14.8 m) which was used to obtain concentration profile measurements in this study. The simulation length is only an approximation since the dynamic components of the flow were not exactly represented.

Nevertheless, the basic shape of the simulated concentration profile should be representative of that obtained with a dynamic simulation. For this reason, the fact that the experimental and simulation profile shapes are similar would suggest that the dispersion and gravitational forces are correctly represented by the simulation.

When the simulation illustrated in Figure 6.4 is allowed to progress, one can see that particles continue to settle with further simulation time. Figure 6.6 provides a series of concentration profiles arranged according to increasing simulation time. The corresponding velocity profiles are shown in Figure 6.7. If the simulation is allowed to continue for a sufficient period of time, the sheared region of the flow becomes completely depleted of particles and a settled bed of particles forms along the bottom wall. At the same time, particles continue to be transported in the unsheared region and do not settle. Therefore, the only particles that deposit at the bottom of the channel are those from the sheared region. The series of concentration profiles suggest that for the simulations, the flow in the channel never reaches a steady state as particles will continue to settle until the sheared region becomes completely depleted of particles.

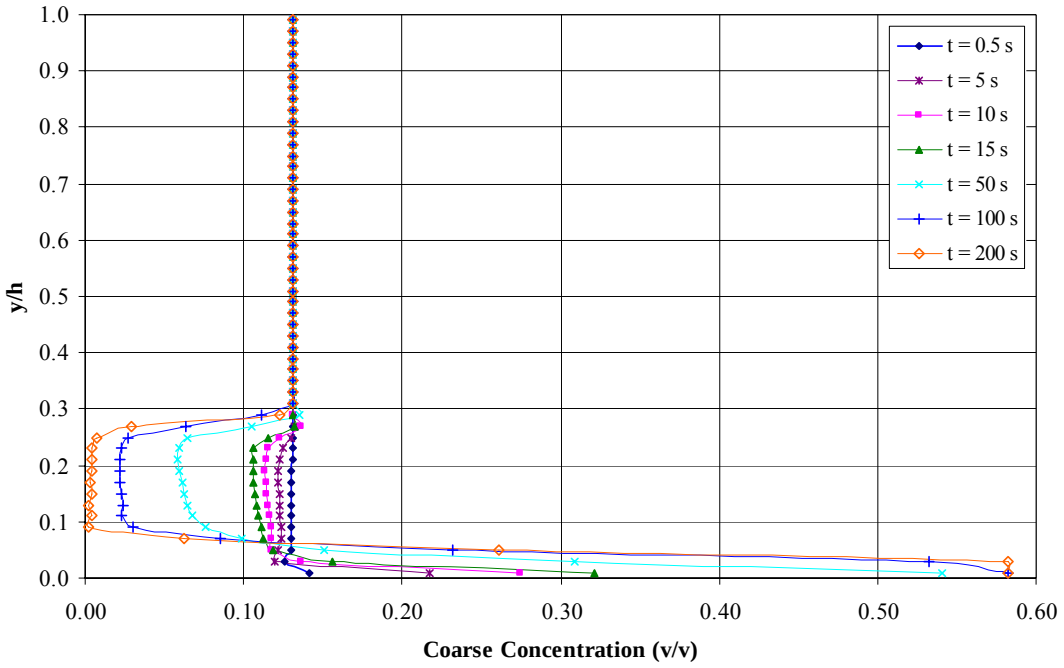

Figure 6.6: Simulated concentration profiles in time for a model Thickened Tailings slurry (5 L/s, 4 ^{o})

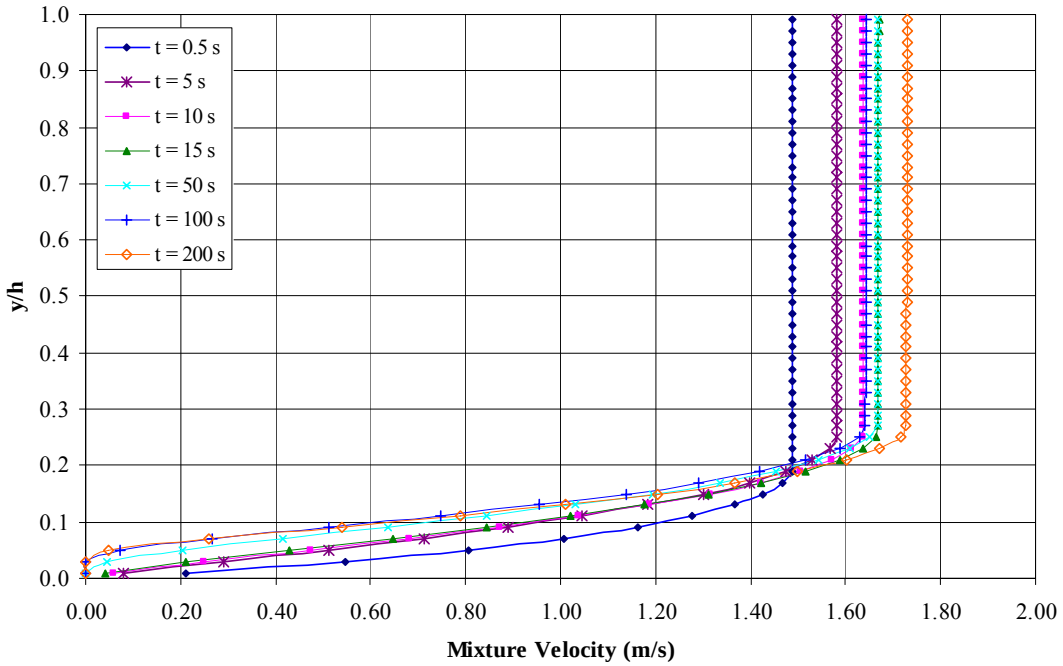

Figure 6.7: Simulated velocity profiles in time for a model Thickened Tailings slurry (5 L/s, 4 ^{o})

Figure 6.7 shows that the mixture velocity profile, particularly in the sheared region, is fairly insensitive to the degree of coarse particle segregation for the range of velocities considered in this study. The insensitivity of the mixture velocity may be a property of the both the existence of a yield stress and the high apparent viscosity of the Bingham carrier fluids used in this study. The velocity profiles do not distort or develop a significant asymmetry until a settled bed of particles forms at the bottom of the channel ($t > 100$ s). This may be why the homogeneous friction models provide accurate predictions even when there was significant particle segregation. The effects of Coulombic friction are not significant until a bed forms and therefore do not generate significant changes in the mixture velocity profile.

The velocity profile presented in Figure 6.2 suggests that this is not the case for Newtonian carrier fluids transporting neutrally buoyant particles. In this case, the increase in coarse particle concentration near the centre of the flow results in a more blunt mixture velocity profile near the channel centreline.

It is interesting to note that the average mixture velocity in the channel increases with time and the related increase in the degree of coarse particle segregation. This is a limitation of the fully

developed, uniform flow assumptions made in the model developed in this study. The depth of flow is assumed to remain constant throughout the simulation. In reality, the formation of a settled bed of particles would result in an increase in the depth of flow. Therefore, the mixture velocity above the bed would not increase since the depth of flow would rise with an increase in bed depth. It is for this reason that a steady state simulation is not achievable for the Thickened Tailings slurry tests.

Based on the model simulation, a settled bed of particles did not occur until 100 s of simulation time had elapsed. The average mixture velocity of the simulation in Figure 6.7 was 1.44 m/s. Using the pseudo steady state assumption presented earlier, 100 s of simulation time roughly equates to approximately 150 m of flume length. The flume used in the experiments was 18.5 m. Therefore, based on the rough estimate of the required entrance length, the axial length of the experimental flume may not have been long enough to allow for the measurement of a fully developed coarse particle concentration distribution. A much longer flume would have been required to experimentally observe the segregation observed in the simulations after an extended period of time.

For the test conditions investigated in this study, solids could be transported in the flume, primarily in the unsheared region. However, if the solids had to be transported longer distances in laminar flow, it is possible that a settled bed of particles would form. Based on observations during the experiments, the formation of a settled bed would cause the depth of the overall flowing fluid to increase until the slurry spilled over the sides of the flume. The model was not capable of simulating this situation. It is important to note that this condition would be detrimental to any open channel transport system.

Figure 6.8 provides the ratio of the delivered concentration to the in-situ concentration that occurred during the simulation. In the simulation, the in-situ concentration remained nearly constant with time at approximately 13% v/v. This is due to the no-flux boundary conditions at the wall and free surface of the channel. However, due to the settling of coarse particles, and the development of a settled bed near the bottom of the channel, the delivered concentration dropped from an initial value of 13% to 10.9% v/v after 200 seconds of simulation time. Despite the presence of a settled bed, solids are still transported within the unsheared region. This is demonstrated in Figure 6.8 by the fact that the delivered concentration approaches a constant value with increasing simulation time.

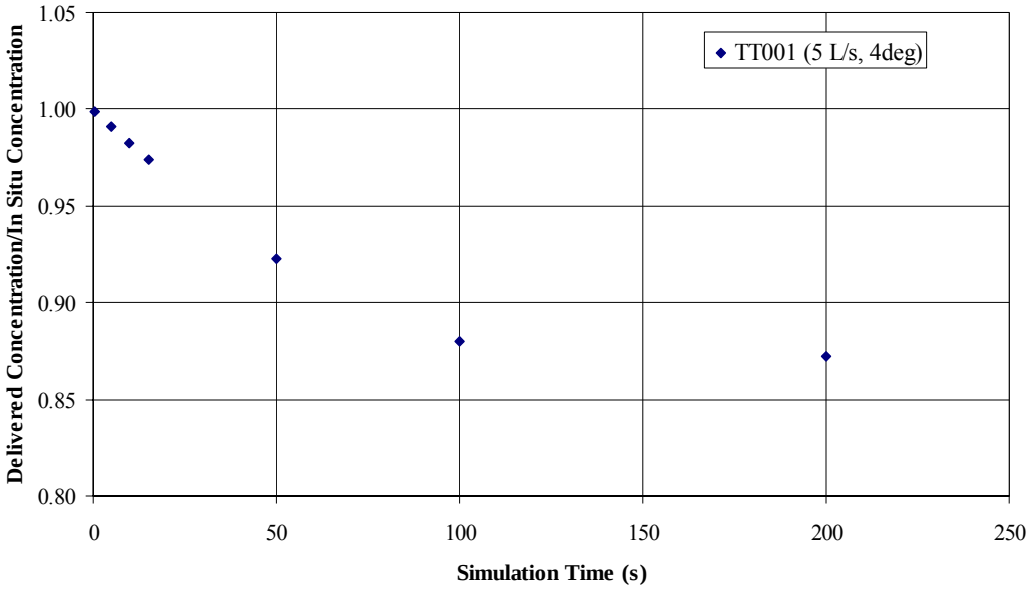

Figure 6.8: Ratio of the delivered concentration to the in-situ concentration versus simulation time for the transport of a model Thickened Tailings slurry in open channel flow (5 L/s, 4 ^{o})

Simulations were also performed with other conditions corresponding to the experimental Thickened Tailings tests and compared with the experimental results. Figures 6.9 and 6.10 show the simulated concentration and velocity profiles for the Thickened Tailings test performed at 5 L/s and 4.5^{o}. The hydraulic radius for the simulation was 0.0441 m. The simulation employed the same experimental coarse particle size, carrier fluid density, sand density and maximum packing factor as the previous simulation. However, the yield stress and plastic viscosity of the clay-water carrier fluid were 45.4 Pa and 0.0233 Pa-s, respectively. The average concentration of coarse particles was 11.3 % v/v. The input parameters and results for all of the simulations performed can be found in Appendix E.

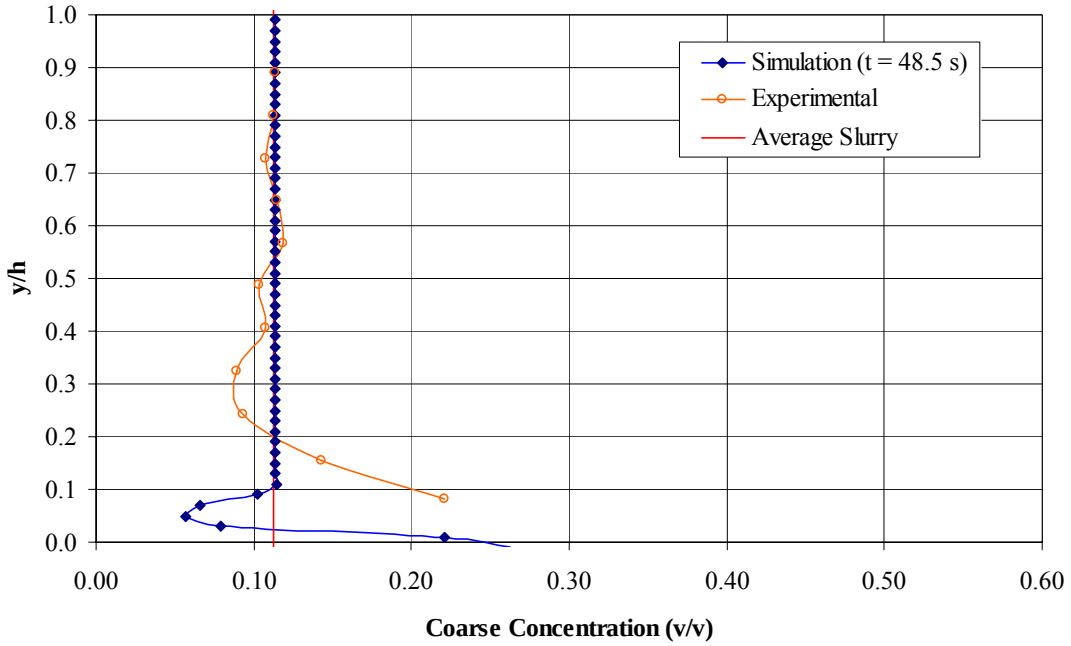

Figure 6.9: Simulated and experimental concentration profile comparison for a Thickened Tailings slurry test (5 L/s, 4.5 ^{o}) at t = 48.5 s

The concentration profile presented in Figure 6.9 was obtained after 48.5 s of simulation time. The average mixture velocity in the simulation was 0.18 m/s, which equates to an approximate flume length of 8.5 m. The general shape of the simulated concentration profile is similar to the profiles obtained with the previous simulations. As can be seen in Figure 6.9, the particle concentration near the bottom wall of the channel is increasing with simulation time, while particle depletion is occurring in the upper portion of the sheared region. The concentration in the unsheared region is equal to the average slurry concentration in the channel. Once again, despite the differences in the experimental and simulation flume geometries, the general trends of both the experimental and simulated profiles are similar.

The mixture velocity profile presented in Figure 6.10 corresponds to the simulated concentration profile shown in Figure 6.9. Despite the coarse particle segregation in the sheared region, the mixture velocity profile is fairly insensitive to the variation in the coarse particle concentration. As mentioned earlier, this may explain why the homogeneous fluid model was capable of providing accurate predictions for the frictional losses in the flume.

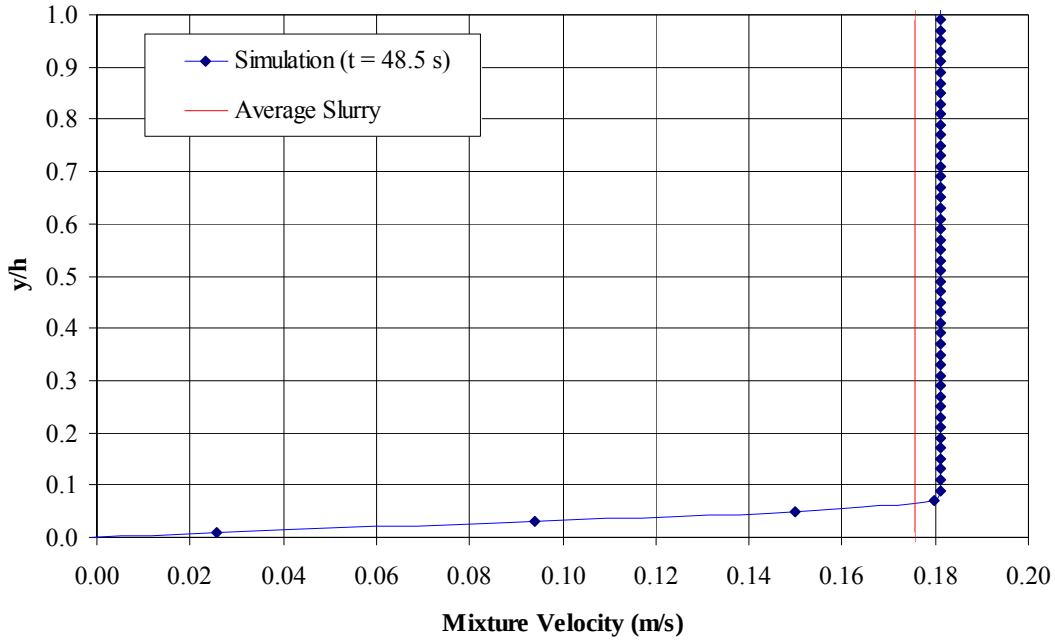

Figure 6.10: Simulated velocity profile for a Thickened Tailings slurry test (5 L/s, 4.5°) at t = 48.5 s

The remaining simulation results for the Thickened Tailings tests are shown in Figures 6.11 and 6.12. The simulated concentration profile for the test performed at 5 L/s and 5.4° is shown in Figure 6.11. The conditions of this simulation were the same as the previous simulations, with the following exceptions: the hydraulic radius was 0.0415 m, the yield stress was 47.3 Pa, the plastic viscosity was 0.0214 Pa-s and the average coarse solids concentration was 11.5% v/v. The main observations associated with the profiles presented in these figures are similar to the observations made with other simulated profiles presented in this section. Coarse particle settling occurred almost immediately in the sheared region. A slight reduction in concentration is observed just below the interface between the unsheared and sheared regions. The average coarse particle concentration remained uniform in the unsheared region. As well, the trends of the simulated and experimental concentration profiles are similar.

Figure 6.12 presents the mixture velocity profile obtained from the simulation at conditions of 5 L/s and 5.4°. As was observed earlier, the homogeneous model would be expected to provide an accurate prediction of the frictional losses of the flow since the degree of segregation did not have a significant effect on the shape of the overall velocity profile. However, it is important to remember that the velocity profiles shown in Figure 6.7 represents a simulation time before the system has reached steady state. If the simulation were allowed to continue, particle settling

would persist and a significant quantity of solids would accumulate at the bottom of the channel. Under these conditions, as is shown in Figure 6.7, the change in the concentration profile would significantly impact the mixture velocity profile. The homogeneous model would not be appropriate for predicting frictional loss behaviour under these conditions.

The results presented in Figures 6.11 and 6.12 were obtained with a simulation time of 8.5 s. The average mixture velocity associated with this simulation time was 0.64 m/s. Using the method provided earlier, a simulation time of 8.5 s corresponds to an approximate flume length of 5.4 m which is comparable to the length of the flume employed in the experimental program.

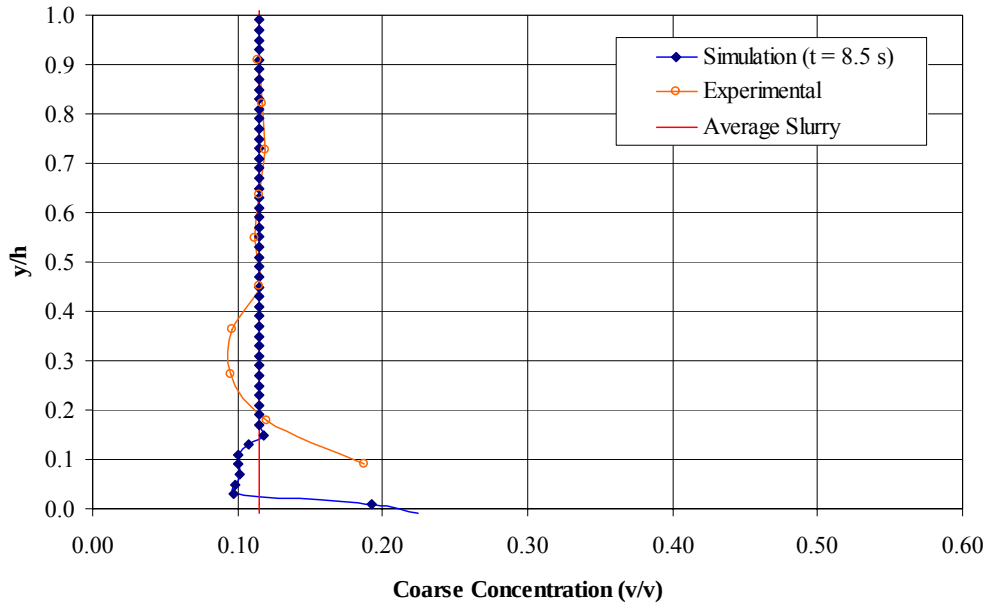

Figure 6.11: Simulated and experimental concentration profile comparison for a Thickened Tailings slurry test (5 L/s, 5.4 ^{o}) at t = 8.5 s

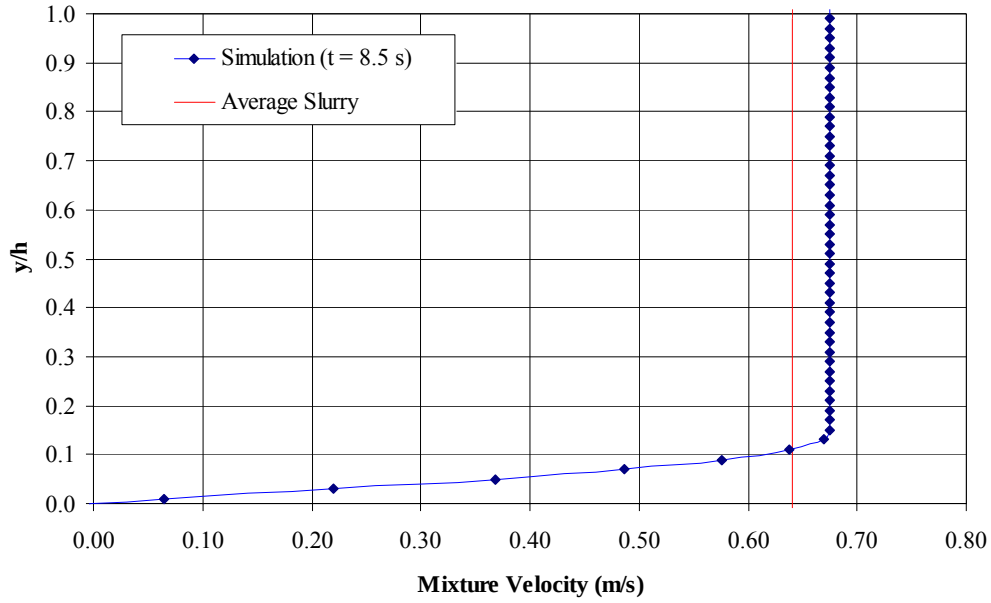

Figure 6.12: Simulated velocity profile for a Thickened Tailings slurry test (5 L/s, 5.4^{o}) at t = 8.5 s

An attempt was made to compare the model to the results obtained with the Thickened Tailings test which was conducted at a volumetric flowrate of 2.5 L/s and a 4.5 ^{o} flume angle. In the actual experiment, the hydraulic radius was found to be 0.046 m which results in an initial wall shear stress (under homogeneous conditions) in the simulation of 50.9 Pa. Since the carrier fluid yield stress (52.3 Pa) was greater than the wall shear stress, the model predicted that no flow could occur. As was noted earlier, it is possible for flow to occur in the experimental flume under these conditions if the local wall shear stress exceeds the yield stress of the slurry.

6.4.2. CT 'Gypsum' Slurries

Simulations were performed for the CT (Consolidated Tailings) slurries (Sanders et al., 2002) under the test conditions investigated in this study. However, the only tests that could be simulated were those performed with a calcium (Ca^{2+}) or 'gypsum' addition. It was not possible to model the 'no gypsum' results since these slurries produced turbulent flow.

Figure 6.13 presents the simulated and experimental concentration profiles associated with the CT 'gypsum' test performed at 5 L/s and 2 ^{o}. The predicted profile presented in Figure 6.13 represents a snapshot in time of a simulation concentration profile. The hydraulic radius was 0.0256 m and the coarse sand had a mean particle size of 0.188 mm and a density of 2650 kg/m^3.

The clay-water carrier fluid had a density of 1188 kg/m^3, a yield stress of 7.3 Pa and a plastic viscosity of 0.0028 Pa-s. The concentration of coarse particles was 27.5% v/v. These particles had a maximum packing concentration of 58.2% v/v.

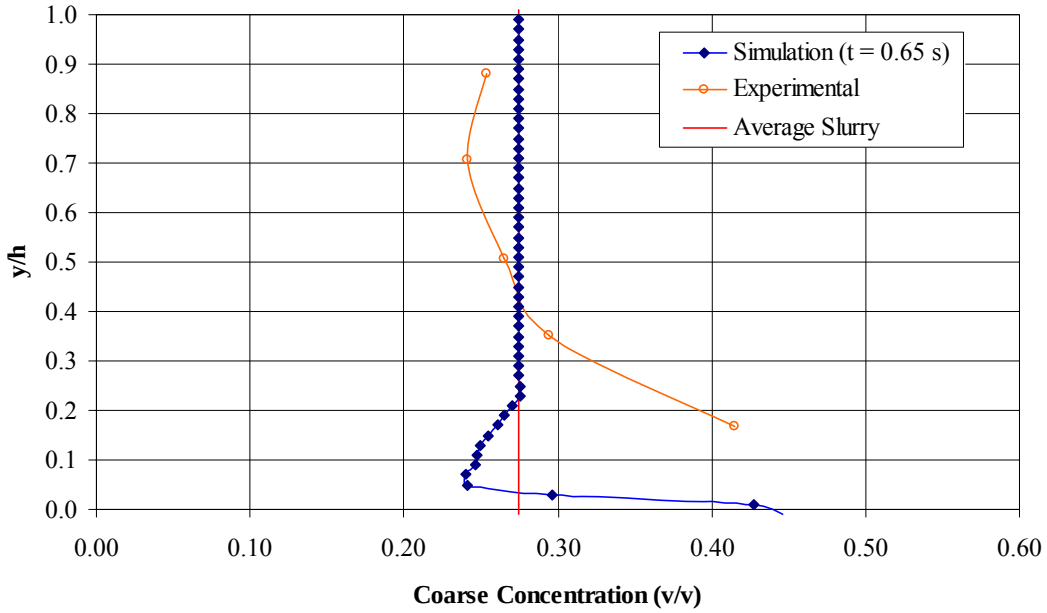

Figure 6.13: Simulated and experimental concentration profile comparison for a CT 'gypsum' slurry test (5 L/s, 2 °) at t = 0.65 s

The snapshot shown in Figure 6.13 was taken 0.65 s into the simulation. Compared to the Thickened Tailings tests, segregation of particles occurs almost immediately as the average mixture velocity was only 1.24 m/s equating to an axial length of approximately 0.8 m. More rapid particle settling would be anticipated with the CT 'gypsum' tests since the carrier fluid has a lower density and lower apparent viscosity compared to the Thickened Tailings slurries of this study. These two factors would cause the particle to have a higher immersed weight in the slurry and a lower drag force when settling. Despite, the differences in the carrier fluid composition and the higher coarse particle concentration (28% v/v) associated with the CT 'gypsum' simulation, the general shape of the concentration profiles is similar to the profiles generated in the Thickened Tailings simulations.

The mixture velocity profile shown in Figure 6.14 resembles that of a homogeneous Bingham fluid velocity profile as was seen earlier with the Thickened Tailings tests. Considering the degree of coarse particle segregation that has occurred, it is surprising that the velocity profile is not significantly affected.

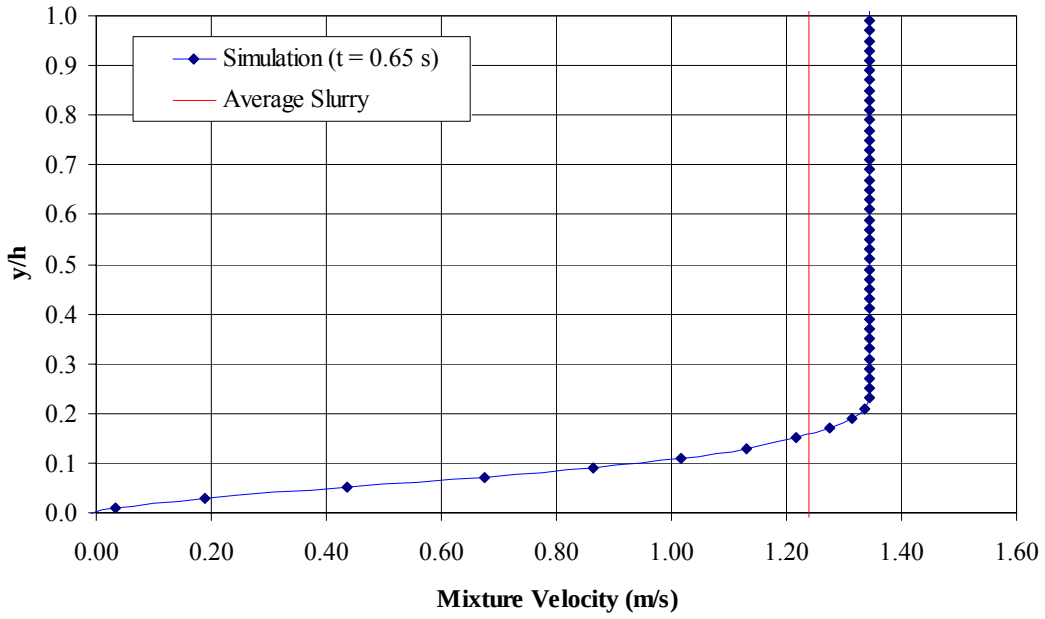

Figure 6.14: Simulated velocity profile for a CT 'gypsum' slurry test (5 L/s, 2 ^{o}) at t = 0.65 s

The simulated concentration profile presented in Figure 6.13 had not yet reached steady state. Figure 6.15 shows the development of the concentration profile relative to simulation time. One can see that particles continue to settle with further simulation time as was seen earlier with the Thickened Tailings slurries. However, the particle settling time scale with the CT 'gypsum' slurries is much smaller than was noted with the more viscous Thickened Tailings slurries.

A settled bed occurs after nearly 5 seconds of simulation time. With greater simulation time, the bed continues to grow as particle depletion occurs in the sheared region. As well, the height of the settled bed is much more significant than what was found in the Thickened Tailings simulations because of the higher coarse particle concentration associated with the CT 'gypsum' slurries. Even though settling in the sheared region is significant, particles are still transported and do not settle in the unsheared region.

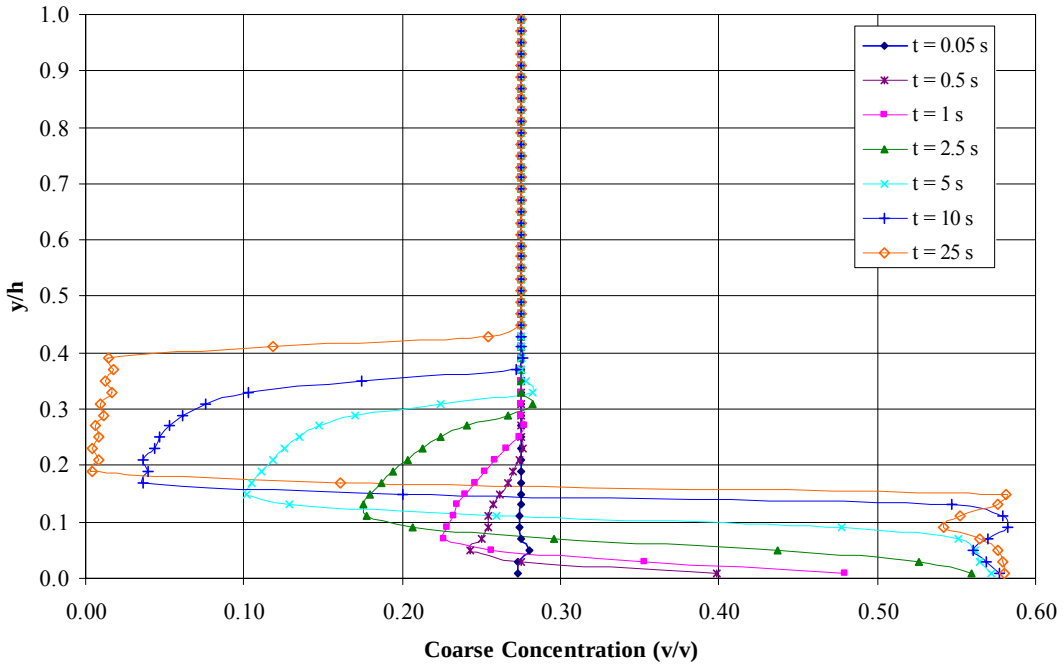

Figure 6.15: Simulated concentration profiles in time for a model CT 'gypsum' slurry (5 L/s, 2 ^{o})

Figure 6.16 presents the velocity profiles which correspond with the simulated concentration profiles shown in Figure 6.15. The effect of segregation on the mixture velocity profile is not significant early in the simulation. However, as the simulation progresses the degree of segregation becomes significant and the mixture velocity above the settled bed begins to increase. This is due, in part, to the reduced solids concentration in the sheared region and thus a reduction in the local mixture viscosity occurs. However, the increase in velocity is caused to some degree by a limitation of the model.

The mixture velocity would only increase with the formation of a settled bed of particles in a pipe or closed conduit. In open channel flow, an increase in the depth of the flow would occur with the formation of a bed. The numerical model assumes that the flow is uniform (constant depth of flow) and fully developed throughout the simulation. Since the model cannot represent an increase in the depth of flow, an artificial reduction in available cross-sectional area occurs with the bed formation causing the mixture velocity to increase. Therefore, the mixture velocity profiles presented after the formation of a settled bed ($t > 5$ s) are not physically realistic and the numerical model is not appropriate for conditions where a settled bed has developed.

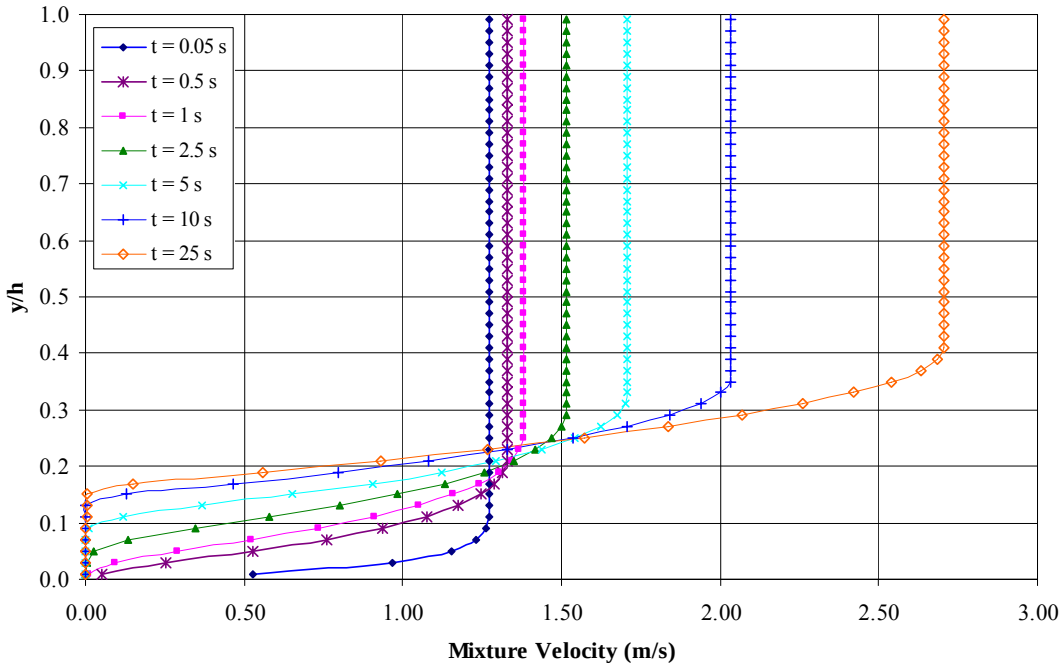

Figure 6.16: Simulated velocity profiles in time for a model CT 'gypsum' slurry (5 L/s, 2^{o})

Figure 6.17 presents the simulated ratio of the delivered concentration to the in-situ concentration for the transient simulation CT 'gypsum' slurry at 5 L/s and 2^{o}. Once again for the test conditions investigated in this study, solids could be transported in the flume, primarily in the unsheared region for the CT 'gypsum' slurries. However, these solids could not be transported over significant distances due to the early formation of a settled bed of particles. The concentration within the unsheared region remained nearly constant at 27.5% v/v throughout the simulation. However, due to the rapid settling of the coarse particles, the delivered concentration dropped from 27.5% initially to 21.6% v/v after 25 seconds of simulation time.

Simulations with the CT 'gypsum' slurries produced a much lower delivered to in-situ concentration ratio than the ratio determined in the Thickened Tailings simulations. This is likely due to the higher degree of segregation observed with the CT 'gypsum' simulation. Since all of the solids within the sheared region formed a deposit at the bottom of the flume, there was no solids transport from this region. As well, since the CT 'gypsum' slurry exhibited a lower yield stress compared to the Thickened Tailings slurry, the unsheared region was also smaller. Since solids are primarily transported in the unsheared region, this would further reduce the delivered concentration value.

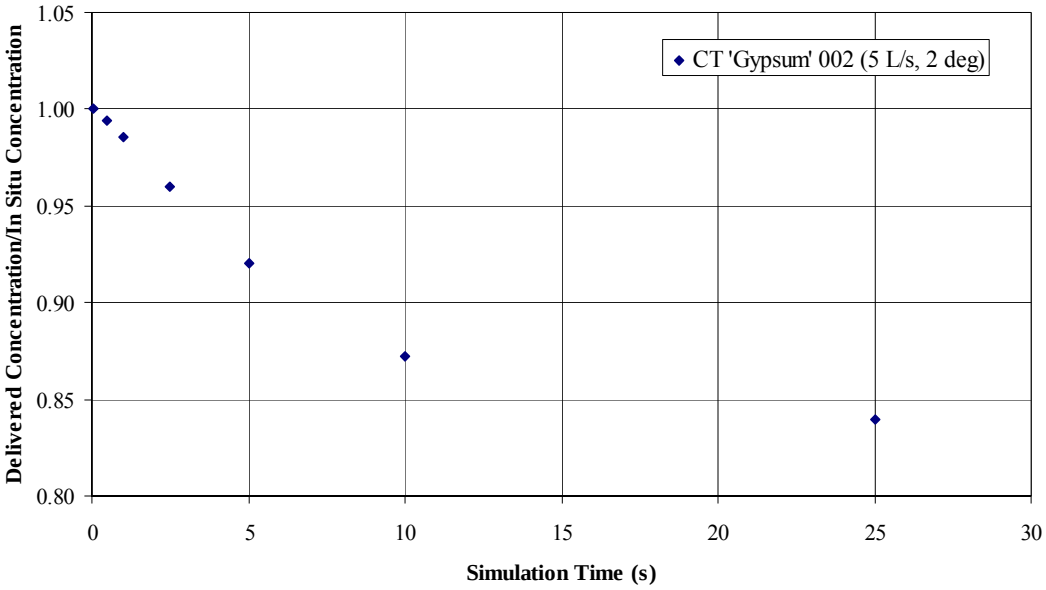

Figure 6.17: Ratio of the delivered concentration to the in-situ concentration versus simulation time for the transport of a model CT 'gypsum' slurry in open channel flow (5 L/s, 2 ^{o})

Simulations were conducted for the remaining CT 'gypsum' test conditions. Figures 6.18 and 6.19 show the simulated concentration and velocity profile for the CT 'gypsum' test performed at 5 L/s and 2.5 ^{o}. A hydraulic radius of 0.0231 m was used in the simulation. The coarse particle size, carrier fluid density, sand density, and maximum packing factor were not changed from the previous simulation. However, the yield stress and plastic viscosity of the clay-water carrier fluid was changed to 10.3 Pa and 0.0028 Pa-s, respectively. The average coarse particle concentration was set to 22.7 % v/v.

Figure 6.18 presents both the experimentally measured concentration profile and simulated concentration profile obtained after 0.20 s of simulation time. This duration of simulation time approximately represents 0.15 m of flume length. As can be seen from the Figure 6.18, the particle settling and segregation occurred almost immediately. However, comparing the results of Figure 6.18 (2.5 ^{o} flume angle) and Figure 6.13 (2.0 ^{o} flume angle), it appears that increasing the flume angle results in a reduction in the segregation rate. This is evident in both the experimental and simulation results. The mixture velocity profile simulation results presented in Figure 6.19 are similar to the results observed with earlier simulations.

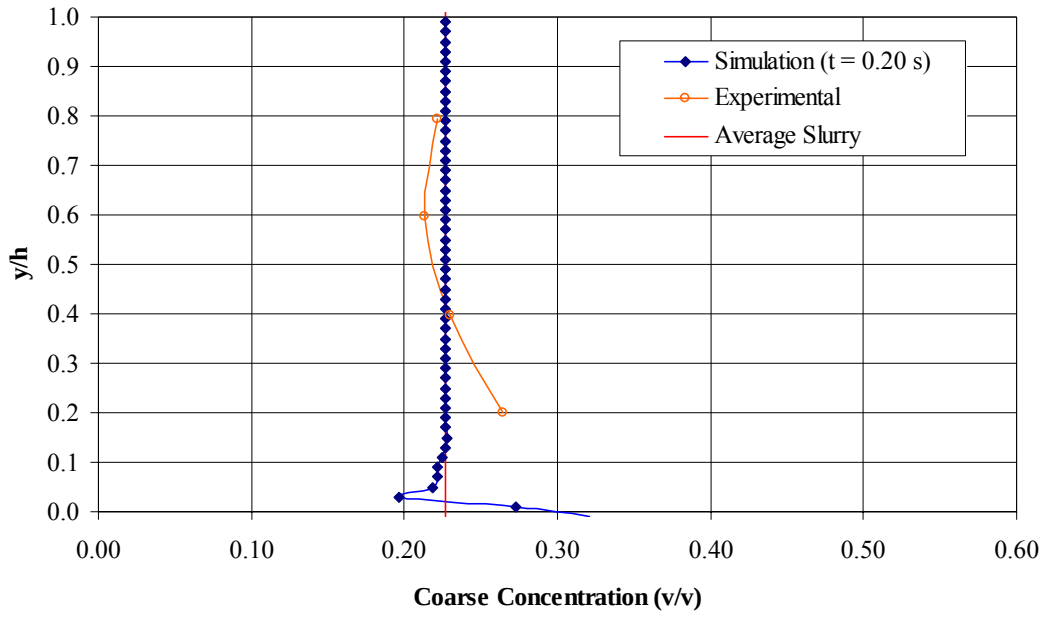

Figure 6.18: Simulated and experimental concentration profile comparison for a CT 'gypsum' slurry test (5 L/s, 2.5 ^{o}) at t = 0.20 s

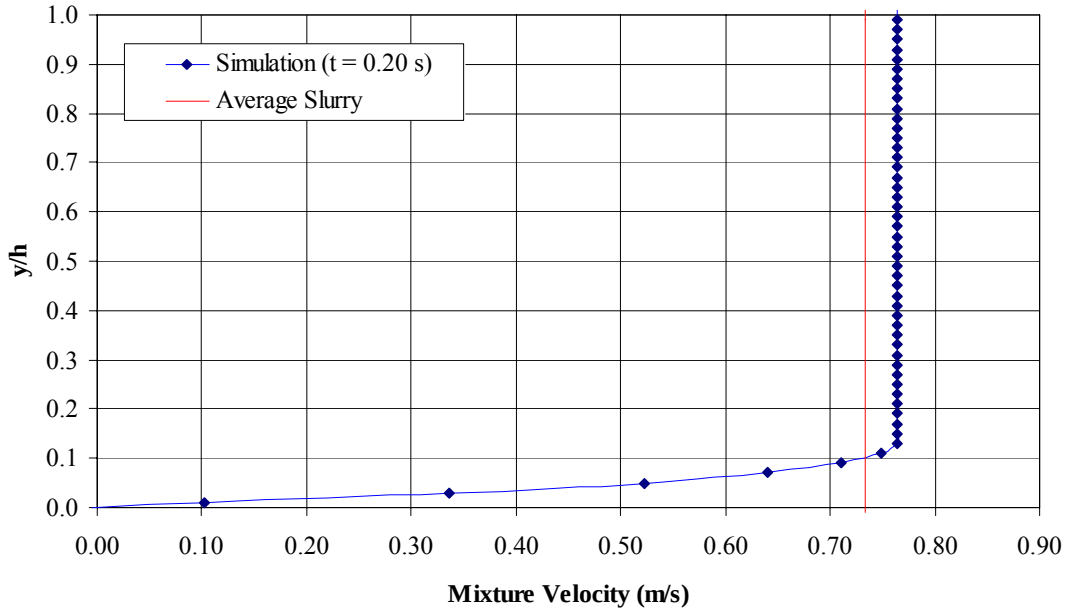

Figure 6.19: Simulated velocity profile for a CT 'gypsum' slurry test (5 L/s, 2.5 ^{o}) at t = 0.20 s

Figures 6.20 and 6.21 present the simulated concentration and velocity profiles based on a CT 'gypsum' test which was conducted at a volumetric flowrate of 2.5 L/s and a flume and of 3 ^{o}. The remaining test conditions used in the simulation were identical to the test conditions at 5 L/s

and 2.5 ^{o} except that the hydraulic radius of the flow was 0.0281 m and average slurry concentration was 28% v/v. The simulation profiles presented in these figures were obtained by stopping the simulation after 3.3 s of operation. This corresponds to a flume axial length of 12.0 m, based on the predicted average mixture velocity of 3.63 m/s. The shape of the experimental and simulated concentration profiles presented in Figure 6.20 are quite different. The experimental profile increases gradually near the bottom of the flume. There is no evidence of an unsheared region in the experimental measurements. The simulation concentration results illustrate roughly the same profile in the unsheared and sheared regions as was seen in earlier simulations. With both the experimental and simulation profiles, the concentration approaches that of maximum packing, 0.582 v/v near the channel wall ($y/h = 0$). Therefore, the experimental and simulation results both suggest that a settled bed could form near the bottom of the channel under these conditions. This test was performed at a lower flowrate resulting in a lower Reynolds number in the laminar flow region. This is likely the reason for the better agreement in terms of axial development distance than the results of the previous CT 'gypsum' slurries.

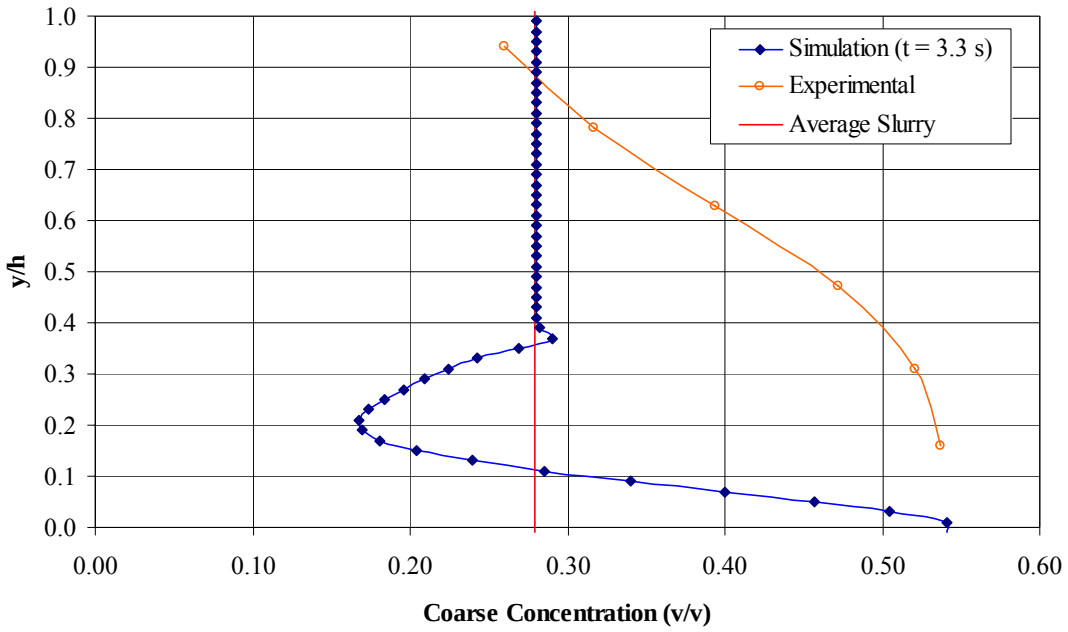

Figure 6.20: Simulated and experimental concentration profile comparison for a CT 'gypsum' slurry test (2.5 L/s, 3 ^{o}) at t = 3.3 s

The experimental and simulated concentration profiles presented in Figure 6.20 are not in good agreement. The experimental profile does not possess a distinct unsheared region, with a uniform

concentration, like the profiles observed from the previous experimental tests and simulations. This may be due to the differences in geometry between the experiments and the simulations. However, the difference is more likely due to the smaller apparent viscosity and increased immersed weight of the CT 'gypsum' slurries. From Figure 5.41, the CT 'gypsum' tests were conducted near the transition to turbulent flow in the flume. The Phillips model may not be appropriate for modeling the transport of particles in these types of slurries for the conditions investigated in this study.

A settled bed of particles has nearly formed in the channel for the simulation results presented in Figure 6.20. The effect of the segregation of coarse particles can be seen in the mixture velocity profile shown in Figure 6.21. An unsheared region still exists near the free surface. However, as the bottom wall is approached the mixture is moving at a lower velocity due to the high coarse particle concentration in this region. Solids are not being transported near the flume wall which results in a reduced delivered concentration. This may also explain the slightly higher experimentally measured friction factor for this test compared to that predicted by the laminar Zhang Reynolds prediction which considers viscous effects only. When the solids concentration is high near the bottom of the flume, the Coulombic friction component would be expected to be significant.

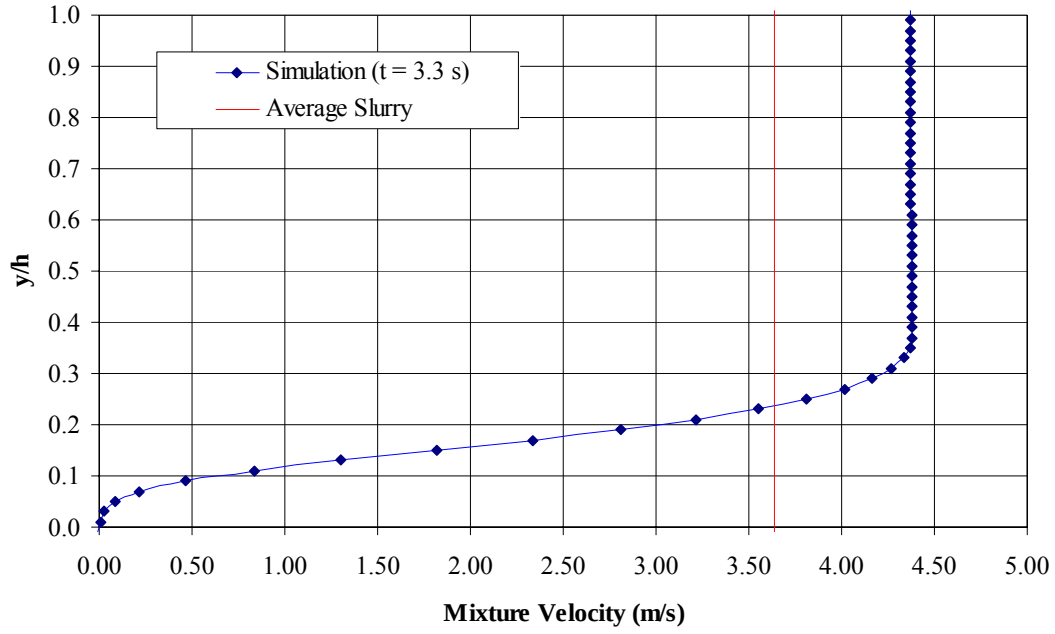

Figure 6.21: Simulated velocity profile for a CT 'gypsum' slurry test (2.5 L/s, 3 ^{o}) at t = 3.3 s

For the most part, the CT 'gypsum' simulation results tests do not predict the experimental results. It is important to note that the tests conducted in the experimental flume at 5 L/s were performed near the transition to turbulent flow while the Phillips model is only appropriate for laminar flow. This may explain some of the distinct differences between the experimentally measured concentration profiles and the numerical simulation results. Any inertial or turbulent effects that may have existed with the experiments performed near the laminar-turbulent transition would produce concentration profiles which would be quite different from those predicted with the laminar solids transport model.

6.5. Simulation Discussions

As discussed in Section 6.2, one of the interesting features noted during the development of the laminar model presented in Equations 4.30 and 6.1 is that the steady state concentration profiles are not a function of particle size. Gillies et al. (1999) observed this in the laminar pipe flows of slurries with varying particle size. Phillips et al. (1992), in their work with neutrally buoyant particles in laminar flow between concentric cylinders, which was presented in Figures 6.1, 6.2 and 6.3, showed that the particle size only affects the transient development of the profile and not the steady state solution. With respect to transient behaviour, larger particles migrate faster and reach a steady state solution sooner than smaller particles.

Several mechanisms exist which would explain the effect of the total solids concentration on the steady state concentration profile. The slurry mixture density, which is determined by the slurry concentration, directly affects the magnitude of the wall shear stress. The magnitude of the flux terms in the scalar concentration model are also directly related to the local concentration. Increasing the coarse particle concentration decreases the particle settling velocity through the hindered settling correction. In addition, increasing particle concentration increases the local apparent slurry viscosity, which also decreases the particle settling velocity.

For the conditions considered in this study, the simulation results show that all of the particles in the sheared region will eventually settle. The fraction of the cross-sectional area associated with the sheared region depends on the yield stress of the carrier fluid. The size of this region determines the quantity of particles available to settle. Since simulation results are only appropriate prior to the formation of a settled bed, it is not possible to see the effect of particle deposition on an unsheared region which changes in size. Once deposition occurs, the depth of

flow is likely to increase changing the dynamics of the system. The model developed in this study is incapable of dealing with this type of behaviour. Conclusions can not be made for simulation results which occur after the formation of a settled bed.

The shear stress distribution in experimental open circular flume is quite different from the distribution predicted by the one-dimensional simulation. The one-dimensional simulation has a uniform wall shear stress along the bottom wall. In the experimental flume, the maximum wall shear stress is located at the bottom of the flume. The value of this wall shear stress is much larger than the average value observed along the wetted perimeter. This may explain why differences sometimes exist between the sizes of the sheared and unsheared flow regions between the experimental tests and the model simulations. However, the general shapes of the experimental and predicted concentration and velocity distributions were similar for most of the test conditions considered.

As was demonstrated in the earlier figures, the concentration profiles approaching a steady state do not resemble the experimentally measured results. The predicted profiles presented in Section 6.4 are simply snapshots in time of the simulated results during the transient solution. During the simulated concentration profile development, a specific intermediate profile was typically found to be reasonably similar to the experimentally measured profile. Uniform profiles were initially input into the solution for both velocity and concentration as a starting point for the code. The final steady state distributions show a nearly settled bed of particles. This behaviour was not observed experimentally for the same experimental conditions.

It should be noted that simulations assumed fully developed, uniform flow. It should also be pointed out that the simulation results do not exactly represent the axially development of the concentration profile since the model does not consider the convective terms in the governing differential equations. For this reason, the migration of the coarse particles is not exactly represented. Nevertheless, for all of the experimental tests considered, simulations indicate that a settled bed is the eventual result. The experimental axial flume length was not long enough to physically observe this behaviour. Therefore, particle transport can only occur in the unsheared region which is reflected in the gradual reduction in delivered concentration which occurs with elapsed simulation time.

The difference between the simulated profiles and measured profiles, along with the fact that an intermediate simulation profile is similar to the measured profiles, has led the author to the conclusion that the experimentally measured profiles were not fully developed (with respect to the coarse particle phase). It is important to note that the experimental flows occurred under steady conditions with respect to time. Since the intermediate simulated profiles are not at steady state equilibrium, the axial length of the experimental flume was not long enough to achieve a balance in the model particle fluxes. Although the experimental flume was capable of transporting coarse particles, it is uncertain whether solids could be transported under the same test conditions in a flume with a significantly longer axial length.

The predicted development of the velocity profile is quite different from the predicted development of the concentration profile. The mixture velocity distribution develops rather quickly and is insensitive to changes in the concentration distribution even though a significant degree of particle segregation occurs in the concentration profiles. For the test conditions observed in the experimental study for Bingham carrier fluids, changes in concentration do not have a significant effect on the velocity distribution as long as a settled bed is not present. For local concentration conditions, which approach the maximum packing concentration, the shear rate and mixture velocity approaches zero.

There are similarities in the flow features between pipe and open channel flows. For both cases, similar equations can be developed to represent particle segregation, fluid friction, and Coulombic friction mechanisms. However, pipe flow is driven by a pressure gradient while open channel flows are driven by gravity (slope of the channel). As well, in open channel flow, gravity does not act in the direction normal to the bottom wall. This reduces the submerged weight of the coarse particles, the normal force and the resulting Coulombic friction. Even though the Coulombic friction force may be reduced compared to pipe flow, the forces which support flow in the flume are generally smaller than the forces associated with the pressure gradient in pipe flow. As a result, it is more likely that a settled bed will form in an open channel flow than in a pipe flow with the same mixture properties and flow rate.

Another flow feature that is similar for pipes and flumes has to do with the variation of the velocity components during flow development. Along with the axial velocity component, velocity components exist in the radial and azimuthal directions while the flow is developing.

When the pipe or flume flow is fully developed, the magnitudes of these components approach zero.

One of the important differences between pipes and open channels is the existence of the free surface in an open channel flow. The free surface is not confined. As a result, when flow is developing in a flume, the depth of flow is free to vary. This has important implications for the transport of solids in open channel Bingham flows.

Consider the simulation results obtained for particles in fluids with a yield stress. In the sheared region, particles settle almost immediately while in the unsheared region the particles are supported so that no settling occurs. The unsheared region that exists downstream in the fully developed region is not necessarily the same as that which exists upstream where the flow is developing. If the depth of flow is greater downstream, then the size of the unsheared region will also be larger compared with the upstream unsheared region. Particles, which have migrated out of the unsheared region, are not able to re-enter the larger downstream region. Therefore the migration of particles associated with the upstream flow will influence the concentration distribution in the fully developed region.

The convective terms in the momentum and scalar concentration transport model equation are not considered in the one-dimensional numerical model developed in this study. Therefore, simulation results do not exist for a true axial development in the flow. A much more involved model is required to completely model the three-dimensional axial development of the solids transport problem in an open channel flow. This will involve the transient solution of all three Navier-Stokes velocity component equations in three dimensions in addition to the three-dimensional scalar transport equation (Phillips model with sedimentation). Additional boundary conditions accounting for the free surface position, and depth of flow with time and axial position would also need to be considered (Nichols and Hirt, 1971; Hirt and Nichols, 1981).

In order for the flow to become fully developed or fully established an equilibrium must be reached between all of the fluxes acting on the particles. As well, in the case of laminar flow, all of the non-axial velocity components must disappear. This means that the sum of the Phillips model fluxes (N_c and N_η) and the sedimentation flux (N_s) must sum to zero at every point in the domain.

For particle transport in laminar flows with Newtonian carrier fluids, the carrier fluid viscosity is constant and not a function of the shear rate. The only parameter affecting the effective mixture viscosity is the local concentration. As particles settle and become more concentrated near the bottom of the flow:

1. Mixture viscosity increases resulting in hindrance effects becoming more significant. These two factors decrease the sedimentation flux (N_s) which acts downward in the vertical direction since the coarse particles are more dense than the surrounding medium.
2. The flux due to particle interaction frequency (N_c) depends on two factors: the motion of particles from regions of higher shear into regions of lower shear with significant variation in shear rate (collision frequency), and particle motion in the direction of decreasing concentration. This flux is typically self-balancing. However, for high particle concentrations the shear effects dominate and there is a net downward flux toward the high concentration region at the bottom of the flow. With respect to the shear rate, the increase in the mixture viscosity in the high concentration regions at the bottom of the flow reduces the magnitude of the shear rate. The shear rate is quite high where a significant change from a low concentration region to a high concentration region occurs.
3. The flux due to spatially varying viscosity (N_η) causes particles to move in the direction of least flow resistance (i.e. from regions of high viscosity to regions of low viscosity). Therefore, as particle concentrations and the effective mixture viscosity increase near the wall, particles move to regions of lower concentration resulting in an upward flux.

The overall effect of the fluxes near the bottom of the flume can now be considered. In this region, the increase in concentration causes the viscosity flux term to initially dominate. Eventually, the effects of shear dampening and hindered settling become more important. Although these fluxes should balance as the maximum packing concentration is approached, the particles form a settled bed before an equilibrium state can be achieved.

When the carrier fluid exhibits a yield stress, the fluxes acting on the particles are different from those observed with Newtonian fluids due to the effect of the yield stress on the effective viscosity of the mixture. As stated earlier, the apparent viscosity of the fluid in the unsheared region is infinite. In this region, the fluid acts as a pseudo solid mixture. As mentioned earlier,

coarse particles will be supported in the unsheared region if the carrier fluid yield stress is larger than the minimum required yield stress based on Equation 2.38 (Shook and Roco, 1991).

The effective slurry viscosity is a function of both the shear rate and the local concentration. However, in this study, only the plastic viscosity is modified by the particle concentration while the yield stress remains constant. Therefore, the yield stress only modifies the value of the effective viscosity through its effect on the shear rate of the mixture.

Overall, the particle migration observed with a carrier fluid exhibiting a yield stress is quite different from the migration observed with a Newtonian fluid. With the Bingham carrier fluid, the concentration remains constant in the unsheared region since no settling occurs. Particle settling immediately occurs in the sheared region of the pipe. As a result, there is a decrease in particle concentration near the top of the sheared region and an increase in concentration at the bottom of the flow near the wall. The value of the mixture viscosity is highest just below the unsheared region since the shear rate is low in this region. However, near the bottom wall, shear rate, coarse particle concentration and mixture viscosity are all high. The effect of these parameters can be clearly seen in Figure 6.22 which illustrates the variation in the simulated apparent mixture viscosity with flume position. The simulation, corresponding to Figures 6.4 and 6.5, had run for 9.5 s and had not reached steady state.

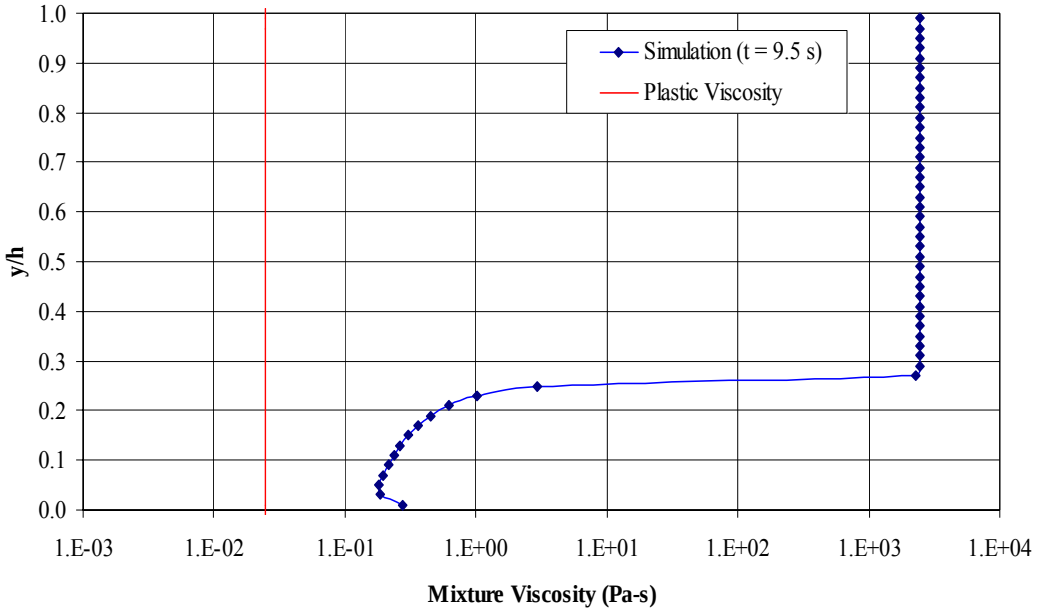

Figure 6.22: Local variation in mixture viscosity at a snapshot in time for a Thickened Tailings slurry simulation (5 L/s, 4 ^{o}) at t = 9.5 s

Therefore, as particles settle within the sheared region and become more concentrated in the lower region of the flume, the response of the flux terms is as follows:

1. The sedimentation flux acts downward. The higher concentration value causes the hindrance effects to increase and the magnitude of the downward sedimentation flux (N_s) decreases. The sedimentation process does not significantly affect the velocity profile even though there is a large degree of variation in the apparent mixture viscosity.
2. Particle concentration is noticeably affected by shear rate through the spatially varying interaction frequency flux (N_c). This flux term causes particles to move in the direction of decreasing shear rate (upward flux) as well as the direction of decreasing concentration (upward flux).
3. The mixture viscosity goes through an absolute minimum in the sheared region as can be seen in Figure 6.22. In the upper half of the sheared region, where particle depletion has taken place, the spatially varying viscosity flux (N_η) acts downward. However, near the bottom wall, which has a higher particle concentration, the flux acts upward since this direction represents a decreasing apparent viscosity gradient.

There are several points that can be made concerning the net effect of the fluxes. In the bottom region near the wall, both the interaction frequency flux (N_c) and the viscosity flux (N_η) act upward. However, the sedimentation flux (N_s), which acts downward, is still dominant. Therefore, the net effect of the fluxes is to cause particles to settle. The upward flux mechanisms (both N_c and N_η) which occur with a Bingham carrier fluid act to reduce the rate of sedimentation when compared to the results obtained with a Newtonian carrier fluid. For this reason, coarse particles can be transported significant distances with a Bingham fluid before a settled bed forms. This was observed both experimentally and numerically with the Thickened Tailings slurries, which had a significant yield stress, compared to the CT 'gypsum' slurries which had a much smaller yield stress. However, for all of the conditions investigated, a settled bed of particles forms at the bottom wall of the flow after a significant simulation time.

6.6. Reduced Immersed Weight Simulation

To better understand the effect of coarse particle buoyancy on the process, a carrier fluid with a higher density and coarse particle with reduced density were modeled using the simulation code. No experimental tests were performed with the modeled slurry although some of the conditions considered were similar to the Thickened tailings slurries. For the simulation, the slurry was composed of a 15% v/v mixture of 0.188 mm particles, which had a maximum packing factor of 0.582 v/v and a density of 2000 kg/m^3. The carrier fluid had a density of 1600 kg/m^3, a yield stress of 50 Pa and a plastic viscosity of 0.050 Pa-s. The flume had an inclination angle of 4 ^{o} and a hydraulic radius was set to 0.05 m.

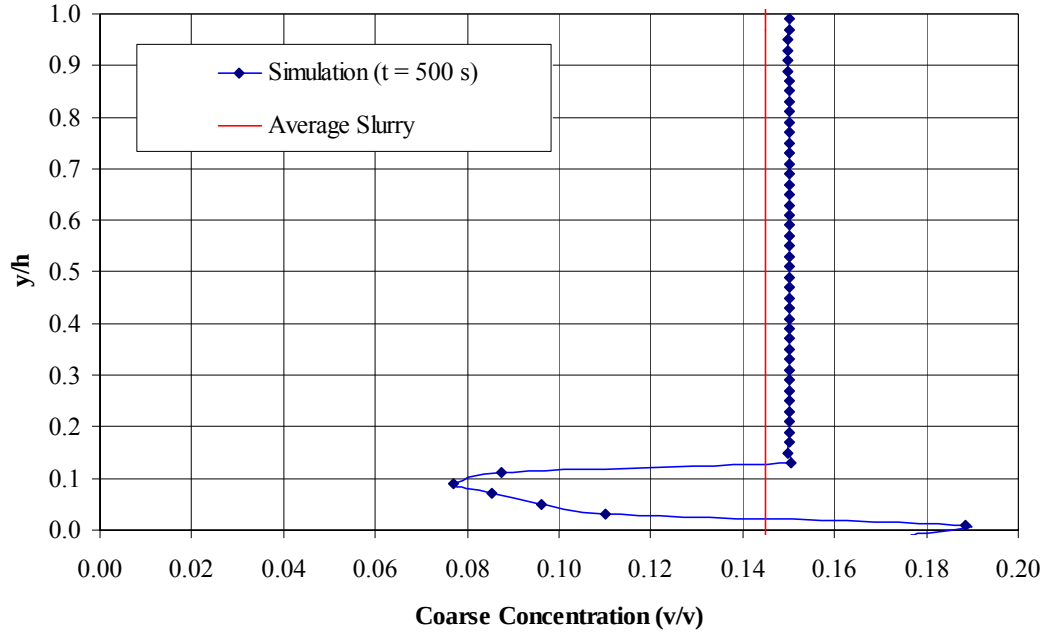

Figure 6.23: Simulated concentration profile for a slurry with a reduced particle immersed weight (4 ^{o}) at t = 500 s

The results of the simulation are presented in Figure 6.23. The model was stopped after 500 s of simulation time. As can be seen from the plot, particles do not settle in the unsheared region while particle segregation occurs in the sheared region. However, due to the reduced immersed weight of the coarse particles, a settled bed has not formed after a significant amount of simulation time. In this case, a balance between the Phillips model and sedimentation fluxes has been achieved.

With the Thickened Tailings simulations, a settled bed formed after approximately 100 seconds of simulation time. With the CT 'gypsum' tests, a settled bed occurred after only 5 seconds of simulation time. With the simulation results presented in Figure 6.23, the concentration at the bottom of the channel after 500 s of simulation time is approximately 19% v/v which is well below the maximum packing concentration (58.2% v/v). Therefore, solids transport in the open channel geometry and resuspension of particles is possible under the conditions considered in the simulation.

The mixture velocity profile obtained in the reduced immersed weight simulation is shown in Figure 6.24. The results are similar to previous simulations where coarse particle segregation does not have a noticeable effect on the mixture velocity profile.

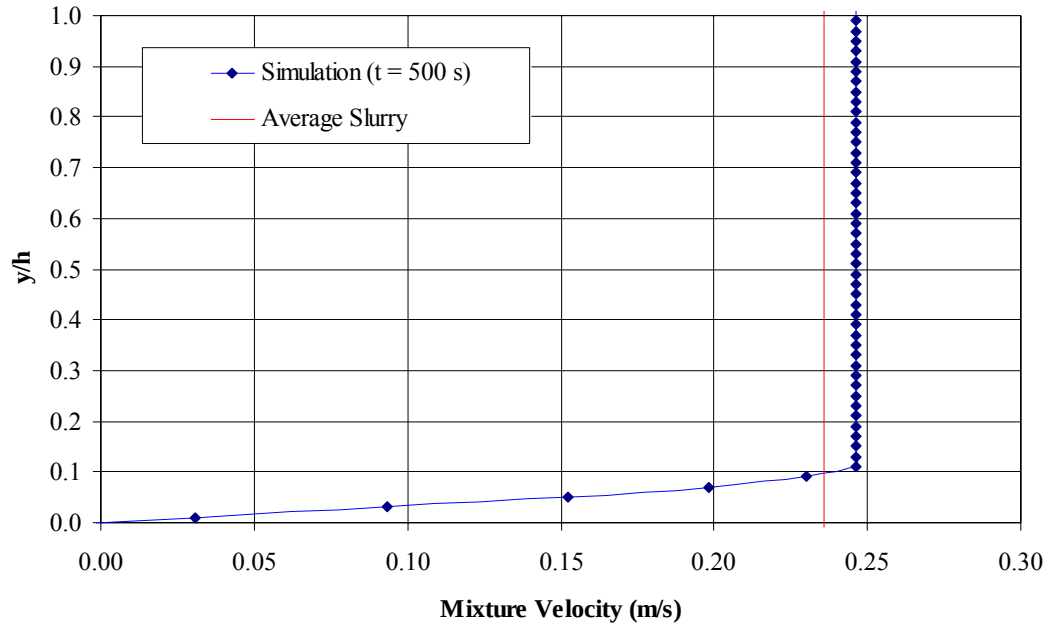

Figure 6.24: Simulated velocity profile for a slurry with a reduced particle immersed weight (4^o) at t = 500 s

6.7. Gillies Model Comparison

Several simulations were conducted to allow a comparison between the model developed for laminar solids transport in this study and the model developed by Gillies et al. (1999). In this section, the 'Gillies model' refers to the model presented in Gillies et al. (1999) (Equation 2.67). Gillies et al. (1999) investigated the transport of coarse sand with viscous Newtonian carrier fluids in laminar, horizontal pipe flow conditions. Two experimental data sets will be considered

from this work. Both tests employed 20 % v/v slurries composed of 0.43 mm sand. The main difference between the two tests is that one used a glycol for the carrier fluid phase while the other test used a viscous oil.

The Gillies model was developed to predict the coarse particle concentration distribution and is similar, in form, to the model of Hill (1996) (Equation 2.66). In this section, the experimental and numerical results obtained by Gillies et al. (1999) are compared with the results predicted by the model developed in this study. It is important to note that the experimental measurements were performed in a pipe of circular geometry while the model developed in this study was based on a one-dimensional rectangular duct of infinite width. For this reason, the results of the experimentally measured profiles and the simulation results are not directly comparable. However, the general trends associated with the experimental and predicted results should be comparable. Adjustments were made to the model developed in this study so that it could simulate duct flow conditions. No-slip and no-flux boundary conditions were applied to the model to change the free surface into a wall boundary condition.

Figure 6.25 shows the concentration distribution result for a 20% v/v, 0.43 mm sand in glycol slurry in a 52 mm pipe with a pressure gradient of 2.05 kPa/m. The viscosity of the glycol was 0.046 Pa-s and the density was 1132 kg/m^3. The corresponding simulated velocity profile is shown in Figure 6.26. The asymmetric nature of both the concentration and velocity distribution is evident. As can be seen in Figure 6.25, the general trends of the experimentally measured concentration profile and the simulated result are similar. However, the experimental measurements showed that solids were being transported in the upper half of the pipe while the simulation predicts no solids transport in this region. The model accurately predicts the formation of a settled bed near the bottom of the pipe since the concentration approaches the theoretical maximum packing condition (0.64 v/v). This effect is reflected in the value of the delivered concentration where the simulation predicts a delivered concentration of 1.1% v/v as opposed to an in-situ concentration of 19.5%. For practical purposes, no solids are being transported in the pipe under these conditions.

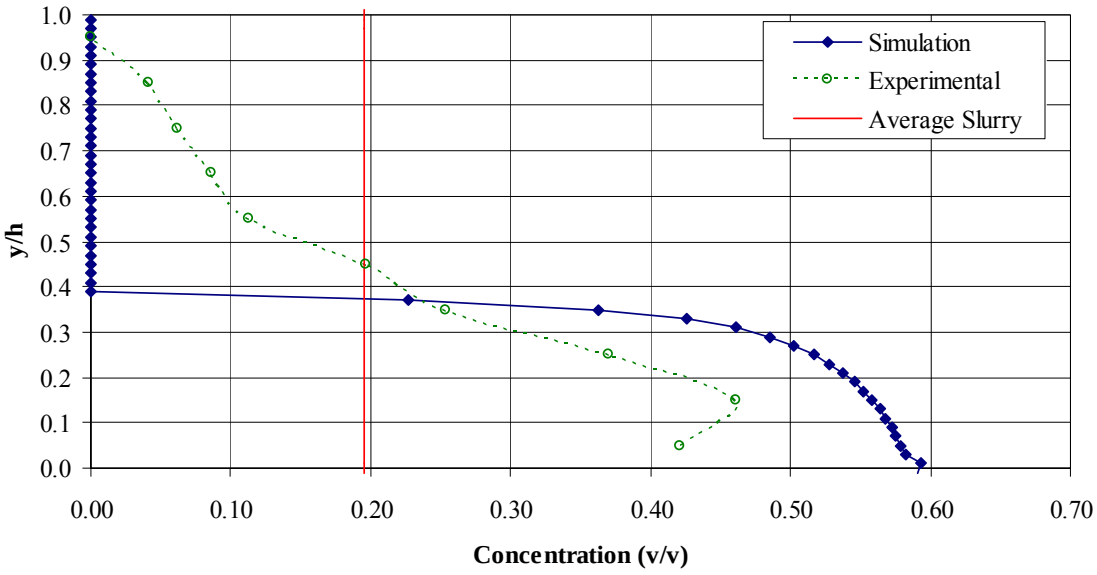

Figure 6.25: Numerically simulated and experimental concentration profiles for the transport of a sand in glycol slurry in laminar pipe flow (Gillies et al., 1999)

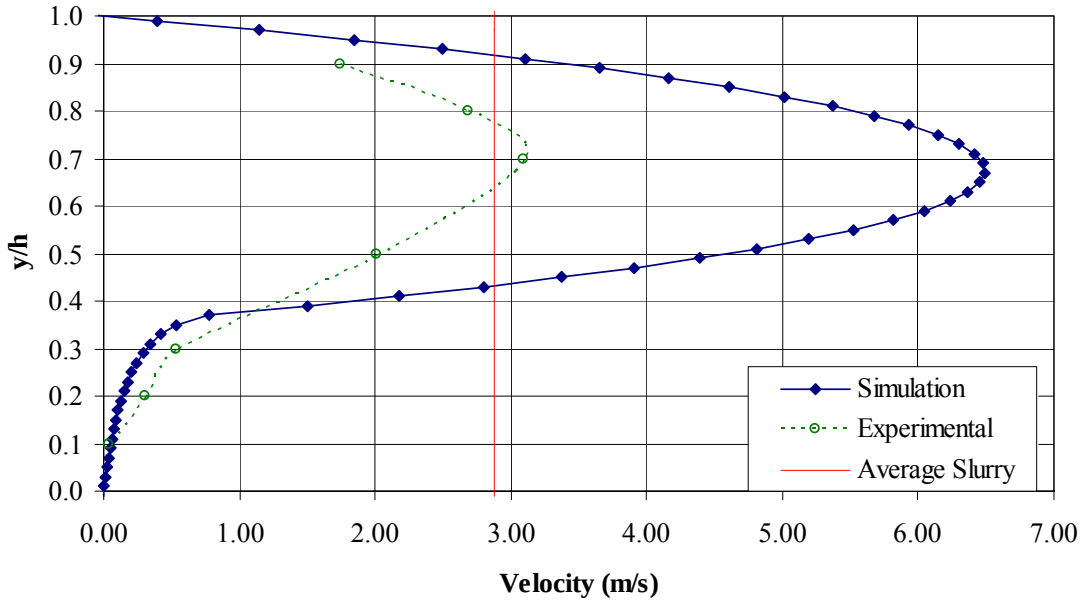

Figure 6.26: Numerically simulated and experimental velocity profiles for the transport of a sand in glycol slurry in laminar pipe flow (Gillies et al., 1999)

Figure 6.26 provides a comparison between the experimentally measured and predicted velocity profiles. The general shape of the profiles, and the asymmetry observed in both profiles suggest that the mixture is moving at a low velocity near the bottom of the pipe where the majority of the solids exist. The discrepancy in the absolute values may be explained by the difference in the

simulation geometries. As well, the experimental measurements indicated that solids were present in the upper half of the pipe which was not predicted by the model. The presence of solids would increase the mixture viscosity and reduce the mixture velocity as was experimentally measured.

Figure 6.27 shows a comparison of the concentration gradients predicted by both the model developed in this study and the Gillies model for the simulation results in Figures 6.25 and 6.26. Both models predict similar concentration gradient trends. However, as the upper region, which does not contain solids, is approached, it is evident that the model used in this study predicts much steeper concentration gradients. As the bottom of the duct is approached, the concentration gradients predicted by the model developed in this study are similar to the gradients predicted by the Gillies model.

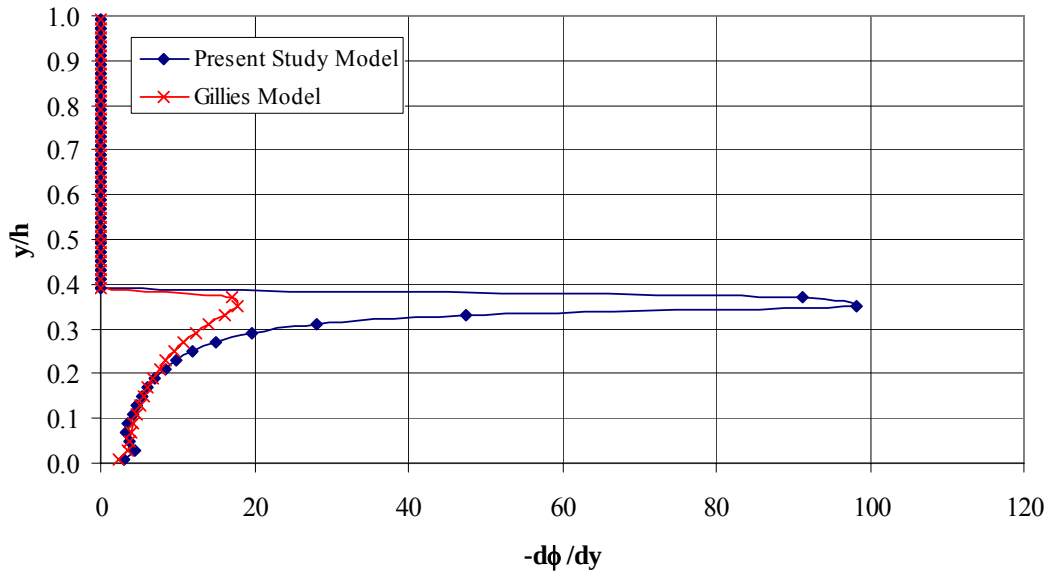

Figure 6.27: Comparison of model concentration gradients for the transport of a sand in glycol slurry in laminar pipe flow (Gillies et al., 1999)

Figures 6.28 and 6.29 present the experimental and simulation results for a 0.43 mm diameter sand in viscous oil slurry in a 105 mm circular pipe which is modeled as a rectangular duct of infinite width. The simulation was performed at the same test conditions of the experiments: h = 0.1047 m, ϕ_{max} = 0.64, ρ_s = 2650 kg/m^3, ρ_f = 870 kg/m^3, μ_f = 0.714 Pa-s, $-dp/dz$ = 1.65 kPa/m. Once again, it should be noted that the experimental measurements were made in a circular pipe while the simulation was performed in a rectangular duct of infinite width.

The predicted concentration results, presented in Figure 6.28, agree closely with the experimental measurements made by Gillies et al. (1999). The agreement between the experimental data and the simulation results suggest that the model developed in this study accurately predicts the behaviour of the coarse solid particles in the flow.

As mentioned earlier, the main difference between the two experimental tests was the viscosity of the carrier fluid. The carrier fluid used in the first test was glycol (μ_f = 0.046 Pa-s; ρ_f = 1132 kg/m^3). The second test used oil (μ_f = 0.714 Pa-s; ρ_f = 870 kg/m^3). This means that in the second test, the driving force for sedimentation has been increased because of the increase in immersed weight of the solids, but the viscous resistance to settling has also been increased. Both the simulated concentration and velocity profiles for the sand in oil slurry are similar in shape to the sand in glycol simulations. However, the resulting bulk velocity for the sand in oil slurry was only 0.62 m/s. As well, nearly all of the solids settled to the bottom of the pipe which resulted in a delivered concentration of less than 1%. It is interesting to note that the simulation results were similar even with the differences in fluid and flow properties of the sand in glycol and sand in oil slurries. The fact that the results were similar would suggest that the absolute value of the carrier fluid viscosity does not play a major role in the transport of solids in laminar flow for the viscosity range considered by Gillies et al. (1999).

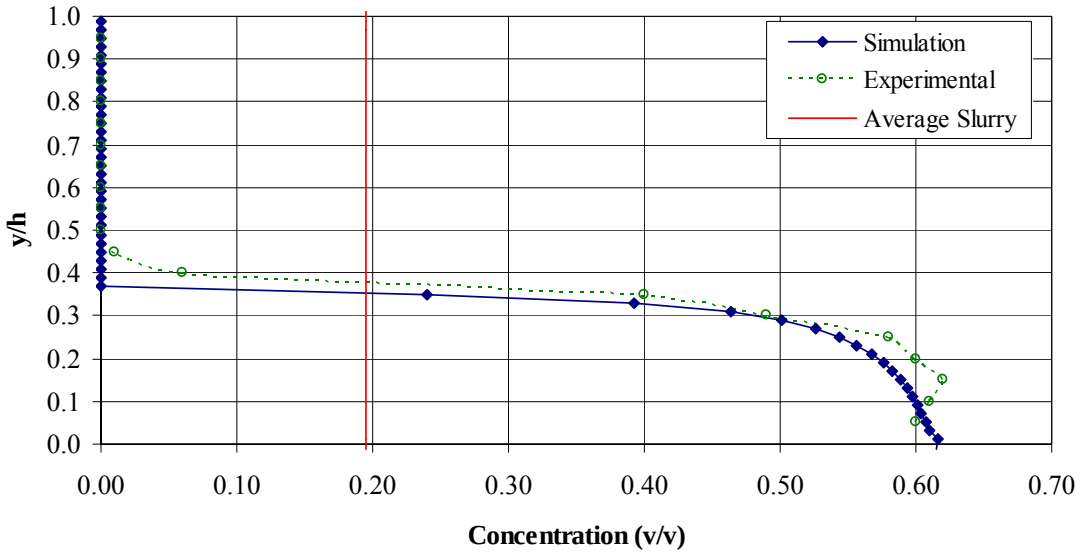

Figure 6.28: Numerically simulated and experimental concentration profiles for the transport of a sand in oil slurry in laminar pipe flow (Gillies et al., 1999)

In their study, Gillies et al. (1999) did not perform local mixture velocity measurements for the sand in oil experiments. However, based on review of previous simulation results, the trend and asymmetry of the simulated velocity profile in Figure 6.29 is consistent with the simulated concentration distribution shown in Figure 6.28. Figure 6.28 shows that the solids are confined to the lower part of the pipe, representing roughly 40 % of the flow cross section. Figure 6.29 shows that the mixture velocity approaches zero in this region. Gillies et al. (1999) determined that an axial pressure gradient greater than 2 kPa/m must be applied for particles to be transported in laminar pipe flow. This is the driving force required to overcome Coulombic friction and push the settled bed of particles along the pipe invert (Equation 2.47). The experimental pressure gradients of the two experimental data sets considered in this section were near or less than 2 kPa/m. This may explain why the delivered concentration approaches zero and the transport of solids practically ceases under these conditions.

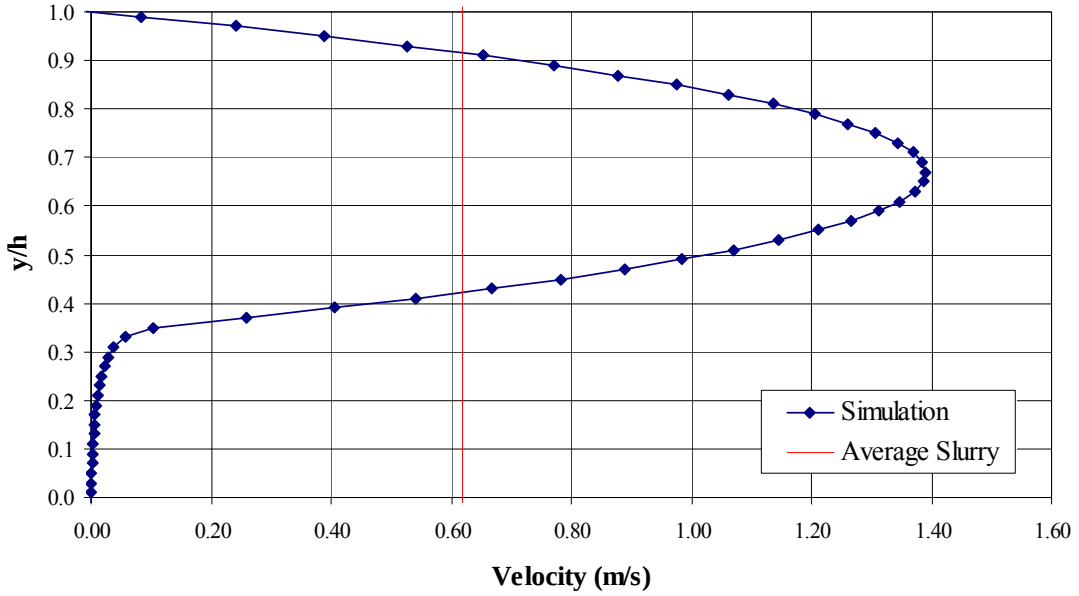

Figure 6.29: Numerically simulated and experimental velocity profiles for the transport of a sand in oil slurry in laminar pipe flow (Gillies et al., 1999)

Figure 6.30 shows a comparison of the concentration gradients predicted by the model developed in this study and the Gillies model for the simulation results in Figure 6.28 and 6.29. Both models predict similar trends in the concentration gradient. Once again, near the interface between the solids and pure carrier fluid in the upper region of the flow, it is evident that the

model used in this study predicts much steeper concentration gradients. However, similar behaviour and concentration gradient values occur as the bottom wall is approached.

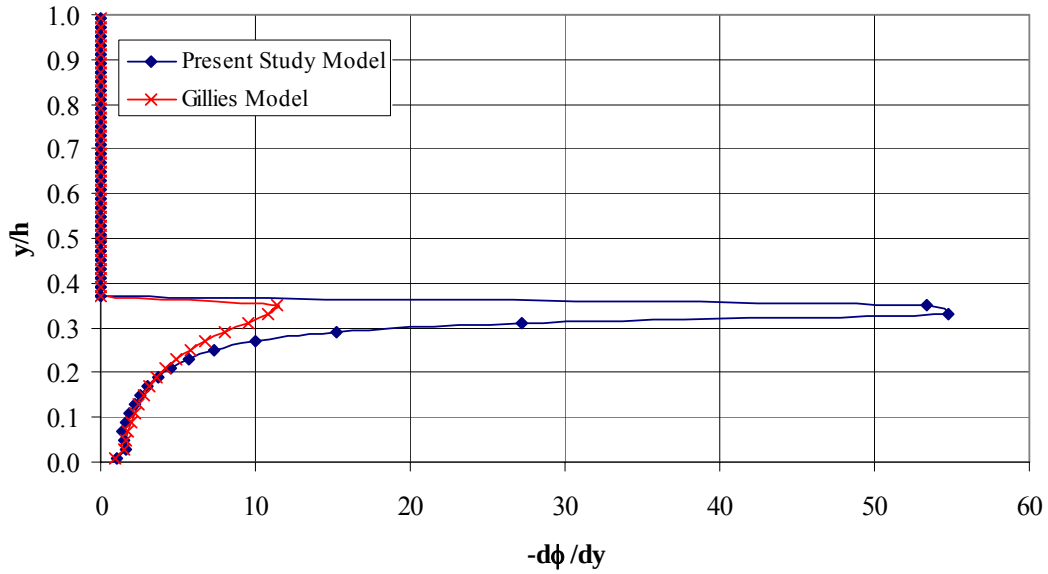

Figure 6.30: Comparison of model concentration gradients for the transport of a sand in oil slurry in laminar pipe flow (Gillies et al., 1999)

The predicted concentration gradients obtained with the Gillies model and the Phillips model developed in this study were in much closer agreement with the oil-sand slurry. This may be explained by the smaller inertial effects associated with the sand in oil slurries since the higher viscosity of the oil ensures that the flow is truly laminar.

The performance of the Gillies model with non-Newtonian carriers was not tested. There are several important distinctions between the Gillies model and the model developed in this study which would present difficulties if the Gillies model were to be applied to situations where the carrier fluid exhibited a yield stress. With the Gillies model, (Equation 2.67), only a dispersive viscosity effect is considered in the equation for the concentration gradient. Therefore, the yield stress and the plastic viscosity of the carrier fluid cannot be accounted for in this concentration prediction model. The importance of these rheological parameters has been demonstrated to be significant in this study. The shear rate term in the denominator has also been shown to be important since in the unsheared region the shear rate is zero. A different modeling technique would need to be applied to the unsheared region if Equation 2.67 were to be applied to laminar flows of fluids with yield stresses.

7. CONCLUSIONS

7.1. Experimental Conclusions

Physical measurements were made using a flume of circular cross-sectional area. The following conclusions are based on subsequent analysis of the measurements:

1. If a slurry has a significant yield stress, flows are likely to be laminar. In laminar flow, an unsheared region will exist in regions where the shear stress is less than the yield stress. The remaining flow area is a sheared region where the shear stress is greater than the yield stress.
2. Under specific flow conditions, a significant vertical concentration gradient was measured. The variation in concentration with height above the bottom of the flume was caused by coarse solids settling.
3. Local solids concentrations did not vary significantly in the upper region of the flume cross-section. For slurries with a yield stress, this indicates an unsheared region where the yield stress exceeds the available shear stress, such that particle sedimentation does not occur.
4. For slurries with significant yield stresses, migration of coarse particles only occurs in the sheared region of the flow.
5. If a stationary deposit was present, continuous operation of the flume flow circuit was not possible. Operation of the flume below the critical deposition velocity results in a continually growing deposited layer until the contents of the flume spill over its edges.
6. For the flume considered in this study, transport of coarse particles under laminar flow conditions was possible with slurries which exhibit a yield stress. However, it is not certain whether coarse particle transport would be possible if a longer flume were employed.
7. Friction factors were calculated based on the clay-water slurry flow data obtained in the circular flume. The slurries were modeled as Bingham fluids. The results closely followed the laminar friction factor curve ($16/\mathrm{Re}$) expressed in terms of the Zhang Reynolds Number and hydraulic diameter.
8. The analytical wall shear stress predictions of Kozicki and Tiu (1967) for homogeneous fluids were found to be in agreement with data of this study and that reported in the literature (Haldenwang, 2003) for flumes of different sizes and geometries.
9. For flow of slurries in flumes, homogeneous fluid models are inappropriate for predicting the frictional losses of slurries when a high degree of particle segregation is present. However, using the bulk rheological parameters (coarse phase and carrier fluid) did provide a close

approximation of the frictional effects for most of the test conditions investigated in this study.

10. Based on the results obtained with hemispherical tipped Pitot tubes with low d/D ratios, Pitot tube velocities could not be accurately predicted by Bernoulli's equation when the Pitot tube Reynolds numbers (based on the diameter of the Pitot tube opening) was less than approximately 40.
11. An empirical correlation has been developed for hemispherical tipped Pitot tubes with low d/D ratios based on the diameter of the Pitot tube opening. Compared to other correlations available in the literature, it more accurately predicts the low Reynolds number effect for the results of this study along with the results of previous researchers in the literature. The correlation reduces to Stokes' law at very low Reynolds numbers and Bernoulli's equation near the transition Reynolds number.

7.2. Numerical Conclusions

A one-dimensional numerical model was found to be useful for representing the flume flows of this study. The conclusions from the numerical model apply to a slurry containing negatively buoyant particles within a Bingham carrier fluid flowing in an open channel of infinite width and uniform depth.

1. Laminar flow of Bingham fluids transporting coarse particles in open channels results in three flow regions:
    i. an unsheared region which suspends particles
    ii. a particle depleted sheared region where particles settle
    iii. a particle rich zone near the bottom wall
2. If the yield stress is sufficiently high, particles will not settle in the unsheared region. As well, in the unsheared region, the Phillips model fluxes are negligible so there is no particle migration caused by gradients in shear rate, concentration or viscosity. This was verified both experimentally and numerically.
3. The concentration of coarse particles in the unsheared region matches the average concentration of coarse particles at the flume inlet. Particles cannot leave or re-enter unsheared regions of the flow. Therefore particle transport is possible in the unsheared region of laminar, open channel flows in slurries with yield stresses.

4. In laminar flow, the steady state distribution of particles is independent of particle size. The particle size only affects the time required to reach a steady state solution. Steady state is reached more rapidly with increasing particle size.
5. Based on model developed in this study, the flume considered in the experimental study was not long enough to permit the concentration distribution of coarse particles in the flume to become fully developed. The simulation results show that if the flume exceeds a specific length, particles are depleted from the sheared region of the flow and form a packed bed near the bottom wall. This was not observed experimentally.
6. For the conditions investigated in this study, the simulation predicts that a settled bed of particles forms near the bottom wall before a balance in the particle fluxes can be achieved. This would suggest that, for the slurries tested, solids will not be transported in the sheared region with a fully developed flow.
7. The results show that the mixture velocity profile is fairly insensitive to coarse particle segregation for fluids with yield stresses, even when there are significant concentration gradients near the bottom of the flume. In fact, the simulated mixture velocity profile does not differ significantly from that of a homogeneous carrier fluid. Therefore, for a wide range of mixtures of coarse particles in Bingham carrier fluids, homogeneous models can still be employed to provide an accurate prediction of the frictional effects. However, this is not likely to be true for conditions where there is a high degree of coarse particle segregation.
8. One of the limitations of the model is associated with the use of a mixture viscosity. As a result the model cannot distinguish between coarse particles and carrier fluid when solving the momentum equations. This limitation is particularly evident in the region of a packed bed where the mixture velocity becomes zero. The model is not capable of predicting the condition of a sliding bed moving en-bloc.
9. The experimental and numerical results of this study verify that resuspension mechanisms do exist in laminar flows as was demonstrated earlier in the work of Phillips et al. (1992). Non-Newtonian carrier fluids enhanced the coarse particle resuspension flux compared to Newtonian fluids. However, for the laminar flow test conditions examined in this study, the sedimentation flux is much larger than the resuspension forces. The model developed in this study indicated that resuspension of the coarse particles is possible if the density difference between the fluid and coarse particle phase is reduced.
10. The Phillips model is only appropriate in laminar flow. The non-equilibrium simulation results compared very closely to the viscous, low Reynolds number Thickened Tailings experiments performed in the flume. However, poor agreement was observed when

simulation results were compared to the experimental Consolidated Tailings (CT) experimental results. The CT slurries were less viscous and were conducted at higher Reynolds numbers which were near the transition to turbulent flow in the flume. This may explain the discrepancy.

8. RECOMMENDATIONS

1. In the experimental program, tests were performed using a single flume of circular cross-section. It is recommended that tests be performed using more flume geometries of various sizes.
2. Additional experiments and numerical modeling should be performed to determine the flume length required to obtain established flow.
3. The coarse solids fractions considered in this study were not high enough to generate a significant Coulombic friction component. Future investigations should extend experimental conditions to study the significance of Coulombic friction effects including higher coarse particle concentrations and lower volumetric flow rates. Coulombic friction effects should also be incorporated into the numerical model.
4. Further investigation of the model developed in this study is required. This should include modeling of the axial development of the flow and transient simulations in three dimensions.
5. Further experimental work should be performed in a viscometer (concentric cylinder and/or vane) to determine the effect coarse particle concentration has on the Bingham rheological parameters.
6. A more detailed analysis should be performed on sedimentation in Bingham fluids. In particular, tests on the settling in sheared regions needs to be performed to determine the parameters which govern the sedimentation process.
7. The effect of hindered settling on the sedimentation flux term needs to be better understood. As the concentration of coarse solids approaches the maximum packing concentration the flux does not approach zero. A possible solution to this problem is the inclusion of the linear concentration term (λ) in the hindrance function.
8. Alternate models, which treat the carrier fluid and coarse particles individually, should be investigated to account for phase lags (i.e. particle slip), particle structures, sliding beds and particle-level phenomena which are not observed by treating the slurry as a mixture.
9. The effect of low Reynolds numbers on Pitot tube measurements in non-Newtonian fluids should be investigated. In addition, specifically for slurry flows, the effect of a constant purge flow from the Pitot tube opening on Pitot tube velocity measurements needs to studied in more depth.

9. REFERENCES

Acrivos, A., Mauri, R., Fan, X., "Shear-Induced Resuspension in a Couette Device", Int. J. Multiphase Flow, v.19, (1993), 797-802

Acrivos, A., "Shear-Induced Particle Diffusion and its Effect on the Rheology of Concentrated Suspensions", 25th National and 1st International Conference on Fluid Mechanics and Fluid Power, (1998), 1-12

Addie, G.R., Pagalthivarthi, K.V., Kadambi, J.R., "PIV and finite element comparisons of particles inside a slurry pump casing", Hydrotransport 16, Santiago, Chile, v.2, (2004), 546-761

Albertson, M.L., Barton, J.R., Simons, D.B., *Fluid Mechanics for Engineers*, Prentice-Hall, Englewood Cliffs, NJ, (1960)

Altobelli, S.A., Givler, R.C., Fukushima, E., "Velocity and concentration measurements of suspensions by nuclear magnetic resonance imaging", J. Rheol., v.35 (5), (1991), 721-734

Ames, W.F., Numerical *Methods for Partial Differential Equations*, 2nd Ed., Academic Press, New York, (1977)

Annamalai, P., Cole, R., "Particle Migration in Rotating Liquids", Phys. Fluids, v.29 (3), (1986), 647-649

Astarita, G., Marrucci, G., Palumbo, G., "Non-Newtonian Gravity Flow Along Inclined Plane Surfaces", Ind. Engng. Chem. Fundls, v.3 (4), (1964), 333-339

Atapattu, D.D., Chhabra, R.P., Uhlherr, P.H.T., "Particle Drag and Equilibrium in Viscoplastic Fluids", Proc. Intl. Symp. Trans. Coal and Other Minerals, Indian Institute of Metals, Bhubaneswar, India, (1988), 253-260

Backer, G.P., Private Communication, (2004)

Bagnold, R.A., "Experiments on a Gravity-Free Dispersion of Large Solid Spheres in a Newtonian Fluid Under Shear", Proc. Roy. Soc., A, 225, (1954), 40-60

Balachandar, R., Blakely, D., Tachie, M.F., Putz, G., "Turbulent Boundary Layers in Open Channel Flows", Proc. ASME FEDSM', Fluids Engng. Div. Boston, MA, (2000), 1-8

Barker, M., "On the Use of Very Small Pitot-Tubes for Measuring Wind Velocity", Proc. Royal Society of London, A v.101, Issue 712, (1922), 435-445

Bartosik, A.S., Hill, K.B., Shook, C.A., "Numerical Modeling of Turbulent Bingham Flow", 9th Int. Conf. on Transport & Sedimentation of Solid Particles, Cracow, Poland, (1997), 69-81

Beal, S.K., "Deposition of Particles in Turbulent Flow on Channel or Pipe Walls", Nuclear Science and Engineering, v.40, (1970), 1-11

Bennett, C.O., Myers, J.E., *Momentum, Heat and Mass Transfer*, 3rd Ed., McGraw-Hill, USA, (1982)

Beverly, C.R, Tanner, R.I., "Numerical analysis of extrudate swell in viscoelastic materials with yield stress", J. Rheol., v.33 (6), (1989), 989-1009

Beverly, C.R., Tanner, R.I., "Numerical analysis of three-dimensional Bingham plastic flow", J. Non-Newtonian Fluid Mech., v.42, (1992), 85-115

Biemfohr, S., Looby, T., Biemfohr, Sh., Leighton, D.T., "Measurements of the Shear-Induced Coefficient of Self-Diffusion in Dilute Suspensions", Proc. Joint DOE/NSF Workshop on Flow of Particulates and Fluids, Ithaca, NY, (1993), 207-232

Bird, R.B., Stewart, W.E., Lightfoot, E.N., *Transport Phenomena*, Wiley, New York, (1960)

Blench, T., Galay, V.J., Peterson, A.W., "Steady Fluid-Solid Flow in Flumes", Hydrotransport 7, Sendai, Japan, (1980), 89-100

Brackebusch, F.W., "Basics of Paste Backfill Systems", Technical Papers, Mining Engineering, (1994)

Buffham, B.A., "Laminar Flow in Open Circular Channels and Symmetrical Lenticular Tubes", Trans. Instn. Chem Engrs, v.46, (1968), T152-157

Buyevich, Yu.A., "Particle Distribution in Suspension Shear Flow", Chem. Eng. Sci., v.51 (4), (1996), 635-647

Caffery, G.A., Analysis of Transport Phenomena in a Combusting Sulfide Particle Cloud: With Implications to the Flash Smelting of High-Grade Copper Concentrates, Ph.D. Thesis, University of British Columbia, Canada, (2002)

Casson, N., "A Flow Equation for Pigment-Oil Suspensions of the Printing Ink Type", Rheology of Disperse Systems, Proc. Conf. British Society of Rheology, Edited by C.C. Mill, Symposium Publications Div., Pergamon Press, (1959), 85-104

Chambre, P.L., "The Theory of the Impact Tube in a Viscous Compressible Gas", Univ. of Calif., Berkeley, Inst. of Engrg. Res., Rep. HE-150-50, (1948), 6+5p.

Chanson, H., *The Hydraulics of Open Channel Flow: An Introduction*, J. Wiley & Sons, New York, (1999)

Chapman, B.K., Leighton, D.T., "Dynamic Viscous Resuspension", Int. J. Multiphase Flow, v.17 (4), (1991), 469-483

Chaudhury, T.K., "On the Steady Flow of Viscous Liquid under Constant Pressure Gradient in a Cylinder of Lenticular Cross-Section", Translated from Rev. Roum. Sci. Techn., Mec. Appl., v.9 (4), (1964), 759-766

Chaudry, M.H., *Open-Channel Flow*, Prentice-Hall, New York, (1993)

Chebbi, B., Tavoularis, S., "Pitot-Static tube response at very low Reynolds numbers", Phys. Fluids A, v.3 (3), (1991), 481-483

Chhabra, R.P., “Sedimentation of particles in non-Newtonian media”, Hydrotransport 15, Banff, AB, v.1, (2002), 135-148

Chow, A.W., Sinton, S.W., Iwamiya, J.H., Stephens, T.S., “Shear-induced particle migration in Couette and parallel plate viscometers: NMR imaging and stress measurements”, Phys. Fluids, v.6 (8), (1994), 2561-2576

Churchill, S.W., “Friction Factor Spans All Fluid Regimes”, Chem. Eng., v.84 (24), (1977), 91-92

Coleman, N.L., “A new examination of sediment suspension”, J. Hydraulic Research, v.7 (1), (1969), 67-82

Cooke, R., “Laminar flow settling: the potential for unexpected problems”, Hydrotransport 15, Banff, AB, v.1, (2002), 121-133

Coussot, P., “Steady, laminar, flow of concentrated mud suspensions in open channel”, J. Hydraulic Research, v.32 (4), (1994), 535-559

Coussot, P., Proust, S., "Slow, Unconfined Spreading of a Mudflow", J. Geophys. Res., v.101, (1996), 25,217 – 25,229

Daniel, S.M., Flow of Suspensions in a Rectangular Channel, Ph.D. Thesis, University of Saskatchewan, Canada, (1965)

Davis, R.H., Acrivos, A., “Sedimentation of noncolloidal particles at low Reynolds numbers”, Ann. Rev. Fluid Mech., v.17, (1985), 91-118

Dedegil, M.Y., “Drag Coefficient and Settling Velocity of Particles in Non-Newtonian Suspensions”, ASME FED-38, Intl. Symp. Slurry Flows, (1986), 9-15

de Nevers, N., *Fluid Mechanics for Chemical Engineers*, 3rd Ed., McGraw Hill, Chemical Engineering Series, New York, (2005)

Dominguez, B., Souyris, R., Nazer, A., “Deposit Velocity of Slurry Flows in Open Channels”, Hydrotransport 13, Johannesburg, South Africa, (1996), 297-308

Eckstein, E.C., Bailey, D.G., Shapiro, A.H., “Self-diffusion of particles in shear flow of a suspension”, J. Fluid Mech., v.79, pt.1, (1977), 191-208

Elliot, D.E., Gliddon, B.J., “Hydraulic Transport of coal at high concentrations”, Hydrotransport 1, Cranfield, UK, (1970), G2

El-Nahhas, K., El-Hak, N.Gad., Rayan, M.A., Vlasak, P., El-Sawaf, I.A., “The laminar/turbulent transitional condition of non-Newtonian slurries in pipes”, Hydrotransport 16, Santiago, Chile, v.1, (2004), 47-60

Faddick, R.R., “Slurry Flume Design”, Hydrotransport 10, Innsbruck, Austria, (1986), 143-147

Fan, X., Masliyah, J., “Laboratory Investigations of Beach Profiles in Tailings Disposal”, J. Hydraulic Engineering, v.116 (7), (1990), 1357-1373

Federico, V.D., “Free-surface flow of hyperconcentrations”, Fluid Dynamics Research, v.24, (1999), 23-36

Ferraris, C.F., de Larrard, F., “Modified Slump Test to Measure Rheological Parameters of Fresh Concrete”, Cement, Concrete and Aggregates, CCAGDP, v.20 (2), (1998), 241-247

Fine Tailings Fundamentals Consortium (FTFC), *Advances in Oil Sands Tailings Research*, Alberta Department of Energy, Oil Sands and Research Division, Edmonton, AB, (1995)

Folsom, R.G., “Review of the Pitot Tube”, Trans ASME, v.78, pt.2, (1956), 1447-1460

Frankel, N.A., Acrivos, A., “On the viscosity of a concentrated suspension of solid spheres”, Chem. Eng. Sci., v.22, (1967), 847-853

Frankiewicz, T., Pangracs, G., Shook, C.A., Gillies, R.G., Small, M., “Pipeloop and pipeline flow tests on coal-oil (transCOM) and coal-condensate slurries”, Proc. of the 16th Intl. Conf. on Coal and Slurry Technologies, Coal and Slurry Technology Association, (1991), 205-216

Gadala-Maria, F., Acrivos, A., “Shear-induced structure in a concentrated suspension of solid spheres”, J. Rheology, v.24, (1980), 799-814

Ghosh, T., Pipeline Flow of Coarse Particles in a Non-Newtonian Carrier Fluid, M.Sc. Thesis, University of Saskatchewan, Canada, (1989)

Ghosh, T., Shook, C.A., “Transport of coarse particles in power law fluids”, Proc. 6th Int. Symp. on Freight Pipelines, Columbia, MO, (1989), 281-288

Gillies, R.G., Shook, C.A., Wilson, K.C., "An Improved Two-Layer Model for Horizontal Slurry Pipeline Flow", Can. J. Chem. Eng., v.69, (1991), 173-178

Gillies, R.G., Pipeline Flow of Coarse Particle Slurries, Ph.D. Thesis, University of Saskatchewan, Canada, (1993)

Gillies, R.G., Shook, C.A., “Concentration Distributions of Sand Slurries in Horizontal Pipe Flow”, Particulate Science and Technology, v.12, (1994), 45-69

Gillies, R.G., Hill, K.B., McKibben, M.J., Shook, C.A., “Solids transport by laminar Newtonian flows”, Powder Technology, v.104, (1999), 269-277

Gillies, R.G., Shook, C.A., “Modelling High Concentration Settling Slurry Flows”, Can. J. Chem. Eng., v.78, (2000), 709-716

Gillies, R.G., Schaan, J., Sumner, R.J., McKibben, M.J., Shook, C.A., "Deposition Velocities for Newtonian Slurries in Turbulent Flow", Can. J. Chem. Eng., v.78, (2000), 704-708

Gillies, R.G., Shook, C.A., Xu, J., “Modelling Heterogeneous Slurry Flows at High Velocities”, Can. J. Chem. Eng., v.82, (2004a), 1060-1065

Gillies, R.G., Sun, R., Shook, C.A., "Segregation in Pipeline Flow of Slurries with Broad Particle Size Distributions", Proc. 12th Int. Conf. on Transportation & Sedimentation of Solid Particles, Prague, Czech Republic, (2004b)

Gillies, R.G., Private Communication, (2006)

Gouesbet, G, Berlemont, A., "Eulerian and Lagrangian approaches for prediciting the behaviour of discrete particles in turbulent flows", Progress in Energy and Combustion Science, v.25, (1999), 133-159

Graham, L., Hamilton, R. Rudman, M., Strode, P., Pullum, L., "Coarse solids concentration profiles in laminar pipe flows", Hydrotransport 15, Banff, AB, v.1, (2002), 149-158

Haldenwang, R., Chhabra, R.P., Slatter, P.T., "Open channel flow of non-Newtonian fluids", 10th International Conference Transport & Sedimentation of Solid Particles, Wroclaw, Poland, (2000), 269-80

Haldenwang, R., Slatter, P.T., Chhabra, R.P., "Laminar and Transitional flow in open channels for non-Newtonian fluids", Hydrotransport 15, Banff, AB, v.2, (2002), 755-768

Haldenwang, R., Flow on Non-Newtonian Fluids in Open-Channels, Doctor Technologiae Thesis, Dept. of Civil Engineering, Cape Technikon, South Africa, (2003)

Haldenwang, R., Slatter, P.T., Vanyaza, S., Chhabra, R.P., "The effect of shape on laminar flow in open channel for non-Newtonian fluids", Hydrotransport 16, Santiago, Chile, v.1, (2004), 311-324

Hampton, R.E., Mammoli, A.A., Graham, A.L., Tetlow, N., "Migration of particles undergoing pressure-driven flow in a circular conduit", J. Rheol., v.41 (3), (1997), 621-640

Hao, Z., R. Zhenghai, "Discussion on law of resistance of hyperconcentration flow in open channels", Scientia Sinica, A, v.25 (12), (1982)

Henderson, F.M., *Open Channel Flow*, MacMillan, New York, (1966)

Heywood, N.I., Alderman, N.J., "Fundamentals of rheological classification and measurement of high solids concentration slurries and pastes", Hydrotransport 16, Santiago, Chile, v.2, (2004), 675-699

Hill, K.B., Pipeline Flow of Particles in Fluids with Yield Stresses, Ph.D. Thesis, University of Saskatchewan, Canada, (1996)

Hill, K.B., Ghosh, T., Shook, C.A., "Laminar flow of settling slurries", J. Hydrol. Hydromech., v.45 (5), (1997), 313-327

Hill, K.B., Shook, C.A., "Pipeline transport of coarse particles by water and by fluids with yield stresses", Particulate Science and Technology, v.16, (1998), 163-183

Hirt, C.W., Nichols, B.D., "Volume of Fluid (VOF) Method for the Dynamics of Free Boundaries", J. Comp. Physics, v.39, (1981), 201-225

Homann, F., "The Effect of High Viscosity on the Flow around a Cylinder and Around a Sphere", Univ. of Calif., Berkeley, Inst. of Engrg. Res., Rep. HE-150-88, (1931), 16+7p.

Hunt, J.N., "The turbulent transport of suspended sediment in open channels", Proc. Roy. Soc., A, v.224, (1954), 322-335

Hurd, C.W., Chesky, K.P., Shapiro, A.H., "Influence of Viscous Effects on Impact Tubes", Trans ASME, J. Applied Mechanics, v.75, (1953), 253-256

Incropera, F.P., DeWitt, D.P., *Fundamentals of Heat and Mass Transfer*, 3rd Ed, J. Wiley & Sons, (1981)

Jeffrey, G.B., "The motion of ellipsoidal particles immersed in a viscous fluid", Proc. Roy. Soc., A, v.102, (1922), 161

Jeffrey, D.J., Acrivos, A., "The Rheological Properties of Suspensions of Rigid Particles", A.I.Ch.E., v.22 (3), (1976), 417-432

Jobson, H.E., Sayre, W.W., "Predicting Concentration Profiles in Open Channels", J. Hydraul. Div., ASCE, v.96 (HY10), (1970), 1983-1996

Kawase, Y., Ulbrecht, J.J., "Sedimentation of particles in non-Newtonian fluids", Chem. Eng. Commun., v.13, (1981), 55-64

Kozicki, W., Chou, C.H., Tiu, C., "Non-Newtonian flow in ducts of arbitrary cross-sectional shape", Chem. Eng. Sci., v.21, (1966), 665-679

Kozicki, W., Tiu, C., "Non-Newtonian flow through open channels", Can. J. Chem. Eng., v. 45, (1967), 127-134

Kozicki, W., Tiu, C., "Improved Parametric Characterization of Flow Geometries", Can. J. Chem. Eng., v.49, (1971), 562-569

Kozicki, W, Tiu, C., Encyclopedia *of Fluid Mechanics, Rheology and Non-Newtonian Flows*, Gulf Publ. Co., v.7, ch.8, (1988), 199-252

Krieger, I.M., "Rheology of Monodisperse Latices" Adv. Colloid Interface Sci., v.3, (1972), 111-136

Krishnan, G.P., Leighton, D.T., "Dynamic Viscous Resuspension of Bidisperse Suspensions – I. Effective Diffusivity", Int. J. Multiphase Flow, v.21 (5), (1995), 721-732

Kuhn, M., "Hydraulic Transport of Solids in Flumes in the Mining Industry", Hydrotransport 7, Sendai, Japan, (1980), 111-122

Lalli, F., Mascio, A.D., "A Numerical Model for Fluid-Particle Flows", Int. J. Offshore and Polar Eng., v.7 (2), (1997), 89-93

Lalli, F., Esposito, P.G., Piscopia, R., Verzicco, R., "Fluid-particle flow simulation by averaged continuous model", Computers & Fluids, v.34, (2005), 1040-1061

Lalli, F., Esposito, P.G., Verzicco, R., "A Constitutive Equation for Fluid-Particle Flow Simulation", Int. J. Offshore and Polar Eng., v.16 (1), (2006), 18-24

Lam, Y.C., Chen, X., Tan, K.W., Chai, J.C., Yu, S.C.M., "Numerical investigation of particle migration in Poiseuille flow of composite system", Comp. Sci. Tech., v.64, (2004), 1001-1010

Leighton, D., Acrivos, A., "Measurement of shear-induced self-diffusion in concentrated suspensions of spheres", J. Fluid Mech., v.177, (1987a), 109-131

Leighton, D., Acrivos, A., "The shear-induced migration of particles in concentrated suspensions", J. Fluid Mech., v.181, (1987b), 415-439

Litzenberger, C.G., Rheological Study of Kaolin Clay Slurries, M.Sc. Thesis, University of Saskatchewan, Canada, (2003)

Litzenberger, C.G., Sumner, R.J., "Flow behaviour of kaolin clay slurries", Hydrotransport 16, Santiago, Chile, v.1, (2004), 77-91

Liu, KO.F., Mei, C.C., "Slow spreading of a sheet of Bingham fluid on an inclined plane", J. Fluid Mech., v.207, (1989), 505-529

Lytle, M.B., Reed, A.J., "Conveyance of Run-of-Mine Coal by Open Channel Flow", Hydrotransport 9, Rome, Italy, (1984), 129-148

Maciejewski, W., Oxenford, J., Shook, C.A., "Transport of coarse rock with sand and cay slurries", Hydrotransport 12, Cranfield, UK, (1993), 705-724

MacMillan, F.A., "Viscous Effects on Pitot Tubes at Low Speeds", J. Royal Aeronautical Society, v.58, (1954a), 570-572

MacMillan, F.A., "Viscous Effects on Flattened Pitot Tubes at Low Speeds", J. Royal Aeronautical Society, v.58, (1954b), 837-839

Matousek, V., "Flow Mechanism of Sand-Water Mixtures in Pipelines", Ph.D. Thesis, Delft University, The Netherlands, (1997)

Matousek, V., "Medium-sand flow over a plane stationary bed in 150-mm pipe", Hydrotransport 16, Santiago, Chile, v.2, (2004), 561-569

Matsuhisa, S., Bird, R.B., "Analytical and Numerical Solutions for Laminar Flow of the Non-Newtonian Ellis Fluid", Amer. Inst. Chem. Eng. J., v.11 (4), (1965), 588-595

Metzner, A.B., Reed, J.C., "Flow of Non-Newtonian Fluids – Correlation of the Laminar, Transition and Turbulent-flow Regions", American Inst. Chem. Eng. J., v.1, (1955), 434-440

Mikhailova, N.P., Repik, E.U., "Effect of the Viscosity on the Readings of Total-Head Tubes with Small Velocities of the Flow", Translated from Izvestiya Akademii Nauk SSSR, Mekhanika Zhidkosti i Gaza, No.1, (1976), 136-139

Mikhailova, N.P., Repik, E.U., "Influence of Viscosity on the Readings of Very Small Flattened Pitot Tubes at Low Flow Velocities", Translated from Izvestiya Akademii Nauk SSSR, Mekhanika Zhidkosti i Gaza, No.6, (1979), 148-152

Milthorpe, J.F., Tanner, R.I., "Numerical simulation of the flow of fluids with yield stresses", 3rd Int. Conf. on Numerical Methods in Laminar and Turbulent Flow, University of Washington, Seattle, WA, (1983), 680-690

Morris, J.F., Boulay, F., "Curvilinear flows of noncolloidal suspensions: The role of normal stress", J. Rheol., v.43 (5), (1999), 1213-1237

Nadim, A., "The measurement of shear-induced diffusion in concentrated suspensions with a Couette device", Phys. Fluids, v.31 (10), (1988), 2781-2785

Nguyen, Q.D., Boger, D.V., "Yield Stress Measurements for Concentrated Suspensions", J. Rheology, v.27 (4), (1983), 321-349

Nguyen, Q.D., Boger, D.V., "Direct Yield Stress Measurement with the Vane Method", J. Rheology, v.29 (3), (1985), 335-347

Nguyen, Q.D., Boger, D.V., "Characterization of yield stress with concentric cylinder viscometers", Rheol. Acta, v.26, (1987), 508-515

Nichols, B.D., Hirt, C.W., "Improved Free Surface Boundary Conditions for Numerical Incompressible-Flow Calculations", J. Comp. Physics, v.8, (1971), 434-448

Nir, A., Acrivos, A., "Experiments on the effective viscosity of concentrated suspensions of solid spheres", Int. J. Multiphase Flow, v.1, (1974), 373-381

Novak, P., Nalluri, C., "Correlations of Sediment Incipient Motion and Deposition in Pipes and Open Channels with Fixed Smooth Beds", Hydrotransport 3, Golden, CO, (1974), 4-45 to 4-56

Nnadi, F.N., "Bed-Load Transport at High Shear Stress: with Application to Friction in Rivers and Sand Waves", Ph.D. Thesis, Queen's University, Canada, (1992)

O'Donovan, E.J., Tanner, R.I., "Numerical study of the Bingham squeeze film problem", J. Non-Newtonian Fluid Mech., v.15 (1), (1984), 75-83

Pai, Shih-I, *Viscous Flow Theory*, D. Van Nostrand Company Inc., (1956)

Papanastasiou, T.C., "Flows of Materials With Yield", J. Rheol., v.31 (5), (1987), 385-404

Pashias, N., Boger, D.V., Summers, J., Glenister, D.J., "A fifty cent rheometer for yield stress measurement", J. Rheol., v.40 (6), (1996), 1179-1189

Patankar, S.V., *Numerical Heat Transfer and Fluid Flow*, McGraw-Hill, Toronto, (1980)

Paterson, A.J.C., Williamson, J.R.G., Salas, U.O.,"Hydraulic transport considerations for high density thickened copper tailings at Southern Peru Copper Corporation", Hydrotransport 16, Santiago, Chile, v.1, (2004), 13-24

Perry, R.H., Green, D.W., *Perry's Chemical Engineers' Handbook*, 7th Ed., McGraw-Hill, New York, (1997)

Phillips, R.J., Armstrong, R.C., Brown, R.A., Graham, A.L., Abbott, J.R., "A constitutive equation for concentrated suspensions that accounts for shear-induced particle migration", Phys. Fluids., A v.4 (1), (1992), 30-40

Press, W.H., Flannery, B.P., Teukolsky, S.A., Vetterling, W.T., *Numerical Recipes in C: The Art of Scientific Computing*, 2nd Ed., Cambridge University Press, (1992)

Pullum, L., Graham, L., Hamilton, R., Rudman, M., "Predicting fine particle suspension performance – the case for pipe tests", Hydrotransport 15, Banff, AB, v.1, (2002), 109-120

Pullum, L., Graham, L.W.J., Slatter, P.T., "A non-Newtonian two-layer model and its application to high density hydrotransport", Hydrotransport 16, Santiago, Chile, v. 2, (2004), 579-592

Rao, S.S., *Applied Numerical Methods for Engineers and Scientists*, Prentice hall, New Jersey, (2002)

Rao, R.R., Mondy, L.A., Baer, T.A., Altobelli, S.A., Stephens, T.S., "NMR Measurements and Simulations of Particle Migration in Non-Newtonian Fluids", Chem. Eng. Comm., v.189 (1), (2002), 1-22

Reddy, J.N., *An Introduction to the Finite Element Method*, McGraw Hill, New York, (1984)

Reynolds, O., "On the dilatancy of media composed of rigid particles in contact", Phil. Mag., v.20, (1885)

Richardson, J.F., Zaki, W.N., "Sedimentation and Fluidization: Part I", Trans. Inst. Chem. Eng., v.32, (1954), 35-53

Roco, M.C., Shook, C.A., "Modelling of slurry flow: The effect of particle size", Can. J. Chem. Eng., v.61, (1983), 494-503

Saffman, P.G., "The lift on a small sphere in a slow shear flow", J. Fluid Mech., v.22, pt.2, (1965), 385-400

Sanders, R.S., Ferre, A.L., Maciejewski, W.B., Gillies, R.G., Shook, C.A., "Bitumen Effects on Pipeline Hydraulics During Oil Sand Hydrotransport", Can. J. Chem. Eng., v.78, (2000), 731-742

Sanders, R.S., Schaan, J., Gillies, R.G., McKibben, M.J., Sun, R., Shook, C.A., "Solids transport in laminar open-channel flow of non-Newtonian slurries", Hydrotransport 15, Banff, AB, v.2, (2002), 597-612.

Sanders, R.S., Sun, R., Gillies, R.G., McKibben, M.J., Litzenberger, C., Shook, C.A., "Deposition velocities for particles of intermediate size in turbulent flow", Hydrotransport 16, Santiago, Chile, v.2, (2004), 561-569

Schaan, J, Sumner, R.J., Gillies, R.G., Shook, C.A., "The Effect of Particle Shape on Pipeline Friction for Newtonian Slurries of Fine Particles", Can. J. Chem. Eng., v.78, (2000), 717-725

Schaan, J. Sanders, R.S., Gillies, R.G., McKibben, M.J., Litzenberger, C., Sun, R-J., Shook, C.A., "Effects of shear history on the flow properties of flocculant dosed thickened tailings slurries", Hydrotransport 16, Santiago, Chile, v. 2, (2004), 403-414

Schaflinger, U., Acrivos, A., Zhang, K., "Viscous Resuspension of a Sediment Within a Laminar and Stratified Flow", Int. J. Multiphase Flow, v.16 (4), (1990), 567-578

Schaflinger, U., Acrivos, A., Stibi, H., "An Experimental Study of Viscous Resuspension in a Pressure Driven Channel Flow", Int. J. Multiphase. Flow, v.21 (4), (1995), 693-704

Schlichting, H., *Boundary Layer Theory*, 7th Ed., McGraw-Hill, New York, (1978)

Schowalter, W.R., Christensen, G., "Toward a rationalization of the slump test for fresh concrete: Comparisons of calculations and experiments", J. Rheol., v.42 (4), (1998), 865-870

Segerlind, L.J., *Applied Finite Element Analysis*, 2nd Ed, John Wiley & Sons, New York, (1984)

Sego, D., Lord, T., Hamza, H.,Sheeran, D.E., Goulden, W., "Centre for Mine Restoration Research Status Report: Phase 1 Oil Sands Tailings Research Facility, Devon, Alberta, April 2002",Geotechnical News, v. 20 (2), (2002), 30-35

Seifu, B., Nir, A., Semiat, R., "Viscous dissipation rate in concentrated suspensions", Phys. Fluids, v.6 (9), (1994), 3189-3191

Sestak, J., "Flow of non-Newtonian fluids in open circular channels", Can. J. Chem. Eng., v.52, (1974), 670-672

Shercliff, J.A., *The Theory of Electromagnetic Flow-Measurement*, Cambridge University Press, Cambridge, (1962)

Shook, C.A., Haas, D.B., Small, M.H., Gillies, R., Husband, W.H.W., "Investigation of the hydraulic transport of tar sand tailings in pipelines up to 20 inches in diameter", SRC Publication No. E 79-13, (1979)

Shook, C.A., "Suspension Mechanism Effects for Slurries in Streamline and Turbulent Flow", Symposium on Interaction of Solids and Fluids, Instn. Chem. Engrs., London, UK, (1980), 83-87

Shook, C.A., Geller, L., Gillies, R.G., Husband, W.H.W., Small, M., "Experiments With Coarse Particles in a 250mm Pipeline", Hydrotransport 10, Innsbruck, Austria, (1986), 219-226

Shook, C.A., McKibben, M., Small, M, "Experimental Investigation of Some Hydrodynamic Factors Affecting Slurry Pipeline Wall Erosion", Can. J. Chem. Eng., v.68, (1990), 17-23

Shook, C.A., M.C. Roco, *Slurry Flow: Principles and Practice*, Butterworth-Heinemann, Boston, (1991)

Shook, C.A., Sumner, R.J., "Deposition Velocities for Slurry Flows", Handbook of Conveying of Particulate Solids, (2001), 445-457

Shook, C.A., Gillies, R.G., Sanders, R.S., *Pipeline Hydrotransport with Applications in the Oil Sand Industry*, SRC Publication No. 11508-1E02, Saskatoon, SK, (2002)

Slatter, P.T., Wasp, E.J., "Yield stress, viscosity and non-Newtonian turbulent pipe flow", Hydrotransport 16, Santiago,Chile, v.1, (2004), 219-230

Song, T., Chiew, Y-M, "Settling Characteristics of Sediments in Moving Bingham Fluid", J. Hydraulic Engineering, v. 123 (9), (1997), 812-815

Spelay, R., Sumner, R.J., Sanders, R.S., Gillies, R.G., "Laminar Open Channel Flow of Kaolin Clay Slurries Containing Sand", 13th International Conference on Transport & Sedimentation of Solid Particles, Tbilisi, Georgia, (2006)

Spelay, R., Sumner, R.J., "Study of the Effect of Low Reynolds Number Flows on Pitot Tube Measurements", Publication in Progress, (2007)

Spiegel, M.R., *Mathematical Handbook of Formulas and Tables*, Schaum's Outline Series in Mathematics, McGraw-Hill, USA, (1968)

Stasa, F.L., *Applied Finite Element Analysis for Engineers*, HRW Series in Mech. Engineering, Holt, Rinehart, & Winston, CBS Publishing Co., New York, (1985)

Straub, L.G., Silberman, E, Nelson, H, "Open-Channel Flow at Small Reynolds Numbers", Trans ASCE, v.123, (1958), 685-714

Sumner, R.S., Munkler, J.J., Carriere, S.M., Shook, C.A., "Rheology of Kaolin Slurries Containing Large Silica Particles", J. Hydrology and Hydromechanics, v.48 (2), (2000), 110-124

Sun, R., McKibben, M.J., Gillies, R.G., "Pipeline Flow of Paste Backfill Mixtures: An SRC Multiclient Study: Final Report – Year 1", Saskatchewan Research Council Publication No. 11206-2C01, Saskatoon, SK, (2001)

Tadros, Th. F., "Rheology of Clays and Oxides", Applied Industrial Rheology, Somerset, NJ, (1988), 1-16

Tetlow, N., Graham, A.L., Ingber, M.S., Subia, S.R., Mondy, L.A., Altobelli, S.A., "Particle migration in a Couette apparatus: Experiment and modeling", J. Rheol., v.42 (2), (1998), 307-327

Thomas, D.G., "Transport characteristics of suspensions VII", A.I.Ch.E. J., v.9, (1963), 310- 316

Thomas, D.G., "Transport Characteristics of Suspensions VIII, A Note on the Viscosity of Newtonian Suspensions of Uniform Spherical Particles", J. Colloid Sci., v.20, (1965), 267-277

Thomas, A.D., "Coarse Particles in a Heavy Medium – Turbulent Pressure Drop Reduction and Deposition under Laminar Flow", Hydrotransport 5, Hanover, Germany, (1978)

Thomas, A.D., "Pipelining of Coarse Coal as a Stabilized Slurry – Another Viewpoint", Proc Intl Conf of Slurry Transportation, (1979), 196-205

Thomas, A. D., Wilson, K. C., "New Analysis of Non-Newtonian Turbulent Flow - Yield-Power-Law Fluids", Can. J. Chem. Eng., v. 65 (2), (1987), 335-338

Thomas, A.D., Pullum, L., Wilson, K.C., "Stabilised laminar slurry flow: review, trends and prognosis", Hydrotransport 16, Santiago, Chile, v. 2, (2004), 701-716

Tirumkudulu, M., Tripathi, A., Acrivos, A., "Particle segregation in monodisperse sheared suspensions", Phys. Fluids, v.11 (3), (1999), 507-509

Tiu, C., Kozicki, W., Phung, T.Q., "Geometric parameters for some flow channels", Can. J. Chem. Eng., v.46, (1968), 389-393

Tiu, C., Kozicki, W., "Geometric parameters for open circular channels", Can. J. Chem. Eng., v.47, (1969), 438-439

Tremblay, B., Sedgwick, G., Forshner, K., "Modelling of Sand Production From Wells on Primary Recovery", J. Can. Petroleum Tech., v.37 (3), (1998), 41-50

Van Olphen, H., *An Introduction to Clay Colloid Chemistry*, 2nd Ed., Wiley, New York, (1977)

Van Rhee, C., "The Influence of the Bed Shear Stress on the Sedimentation of Sand", 11th Int. Conf. Transport & Sedimentation of Solid Particle, Ghent, Belgium, (2002), 223-230

Van Rhee, C., "Numerical modeling of the flow and settling in a Trailing Suction Hopper Dredge", Hydrotransport 15, Banff, AB, v.2, (2002), 547-561

Van Rhee, C., "Sediment settling and pick-up at a flow velocity below the deposition limit", Hydrotransport 16, Santiago, Chile, v.1, (2004), 417-428

Wallis, G.B., *One-Dimensional Two-Phase Flow*, McGraw-Hill, USA, (1969)

Wan, Z., Wang, Z., *Hyperconcentrated Flow*, IAHR (International Association for Hydraulic Research), Monograph Series, Balkema, Rotterdam, Netherlands, Brookfield, VT, (1994)

Wasp, E.J., "Instability of Laminar Flow in Long Distance Pipelines", Proc. Rheology in the Mineral Industry II, Kakuka, Hawaii, USA, (1999)

Whitlock, L., Wilson, K.C., Sellgren A., "Effect of near-wall lift on frictional characteristics of sand slurries", Hydrotransport 16, Santiago, Chile, v.2, (2004), 443-454

Wilkinson, W.L., *Non-Newtonian Fluids: Fluid Mechanics*, Mixing and Heat Transfer, Pergamon Press, (1960)

Wilson, K.C., "A Unified Physically Based Analysis of Solid-Liquid Pipeline Flow", Hydrotransport 4, Cranfield, UK, (1976), 1-16

Wilson, K.C., "Analysis of Slurry Flows with a Free Surface", Hydrotransport 7, Sendai, Japan, (1980), 123-132

Wilson, K.C., Thomas, A.D., "A New Analysis of the Turbulent Flow of Non-Newtonian Fluids", Can. J. Chem. Eng., v. 63, (1985), 539-546

Wilson, K.C., Sellgren, A., "Near-wall particle lift and deposition in slurry pipelines", Hydrotransport 15, Banff, AB, v.2, (2002), 789-800

Wilson, K.C., Horsley, R.R., "Calculating fall velocities in non-Newtonian (and Newtonian) fluids: a new view", Hydrotransport 16, Santiago, Chile, v.1, (2004), 37-46

Wood, P.A., "Optimization of Flume Geometry for Open Channel Transport", Hydrotransport 7, Sendai, Japan, (1980), 101-110

Xu, J., Gillies, R., Small, M., Shook, C.A., "Laminar and Turbulent Flow of Kaolin Slurries", Hydrotransport 12, Cranfield, UK, (1993), 595-613

Yalin, M.S., *Mechanics of Sediment Transport*, 2nd Ed., Pergamon Press, (1977)

Yilmazer, U., Kalyon, D.M., "Slip Effects in Capillary and Parallel Disk Torsional Flows of Highly Filled Suspensions", J. Rheol., v.33 (8), (1989), 1197-1212

Zarraga, I.E., Leighton, D.T., "Shear Induced Diffusivity in a Dilute Bidisperse Suspension of Hard Spheres", J. Colloid and Interface Science, v.243, (2001a), 503-514

Zarraga, I.E., Leighton, D.T., "Normal stress and diffusion in a dilute suspension of hard spheres undergoing simple shear", Physics of Fluids, v.13, (2001b), 565-577

Zarraga, I.E., Leighton, D.T., "Measurement of an unexpectedly large shear-induced self-diffusivity in a dilute suspension of spheres", Physics of Fluids, v.14 (7), (2002), 2194-2201

APPPENDIX A:
COMPUTER CODE

The following code, written in Microsoft Visual Basic 6.3 for Applications in conjunction with Microsoft Excel (© 1987–2001 Microsoft Corp.) applies to the simulations performed for the transport of negatively buoyant particles in Bingham carrier fluids (model tailings slurries) in a flume (inclined plane of infinite width).

```
Option Explicit
'ensures that all variables must be declared

'Ryan Spelay
'Bingham Carrier Fluid - apparent viscosity of fluid varies over the domain with the shearrate
'Phillips 1D open channel solver
'w/ or w/o sedimentation flux
'Transient solution
'Time is used to relax solution
'No Flux BC at channel wall (Neumann)
'No Flux BC at free surface (Dirichlet)
'Concentration effects only scale viscP
'Shear effects scale tauY

'declaration of constants
Const N = 50
Const beta_diff_u = 1
Const beta_diff_phi = 1
Const beta_diff_gamma = 1
Const gravity = 9.81
Const pi = 3.14159265358979
Const u_relax = 1
Const conc_relax = 1
Const u_relax_temp = 1
Const conc_relax_temp = 1
Const iterations_max_u = 1000
Const iterations_max_conc = 1000
Const iterations_max = 100000
Const tolerance_u = 0.00000001
Const tolerance_conc = 0.00000001
Const tolerance = 0.00000001
Const rowstart = 10
Const colstart = 6
Const min = 0.000001
Const max = 0.9999
Const dt_min = 0.00001
Const dt_max = 100000
Const dt_scalar = 1
Const Kc = 0.4
Const Kn = 0.6
Const output_every = 1
Const scheme = "geometric"      'interpolation scheme can be either "linear" or "geometric"
'geometric interpolations are much more stable
Const override = "true"         'override the concentrations in the plug to reduce overshoot from the
singularity "true" or "false"
Const mesh = "uniform"              'can be either "uniform" or "non-uniform or cluster"
Const singularity = "true"          'can be either true or false, true if you want to correct for the singularity,
false if not
'singularity occurs at the unsheared/sheared interface
```

```
'internal discontinuity in the coefficients of the partial differential equations
'viscosity on north face goes to infinity ~ A*visP while that on the south face remains low

'declaration of variables
Dim restart As String          'can be "new" (from flat initial conditions) or "previous" (from values on the spreadsheet/restart)

Dim u(N + 1) As Double
Dim conc(N + 1) As Double
Dim u_temp(N + 1) As Double
Dim conc_temp(N + 1) As Double
Dim u_old(N + 1) As Double
Dim conc_old(N + 1) As Double
Dim shearrate_grad(N + 1) As Double     'north face of cell
Dim y(N + 1) As Double
Dim y_face(N + 1) As Double         'north face of cell

Dim aPu(N + 1) As Double
Dim aNu(N + 1) As Double
Dim aSu(N + 1) As Double
Dim bu(N + 1) As Double

Dim aPphi(N + 1) As Double
Dim aNphi(N + 1) As Double
Dim aSphi(N + 1) As Double
Dim bphi(N + 1) As Double

'viscosity effects due to shearrate on the yield stress
'viscosity effects due to concentration on the plastic viscosity
Dim tauY As Double          'Bingham yield stress of carrier fluid
Dim viscP As Double         'Bingham plastic viscosity of carrier fluid
Dim Amult As Double          'biviscosity model constant multiplier
Dim interface As Double     'y/h interface where the unsheared region meets the sheared region
Dim interface_high As Double     'y/h interface where the unsheared region meets the sheared region
Dim interface_low As Double     'y/h interface where the unsheared region meets the sheared region

Dim K As Double
Dim dt As Double

Dim dens_f As Double
Dim dens_s As Double
Dim conc_total As Double
Dim conc_max As Double
Dim d As Double
Dim a As Double
Dim h As Double
Dim theta As Double
Dim gy As Double
Dim gz As Double
Dim Ks As Double           'a constant only a function of the density difference since viscosity is lumped in with the hindrance function in the scaling of viscP approach
Dim iterate As Boolean
Dim iterate_conc As Boolean
Dim iterate_u As Boolean

Dim residual_u As Double
```

```
Dim residual_conc As Double
Dim residual_total As Double
Dim residual_u_old As Double
Dim residual_conc_old As Double
Dim residual_total_old As Double

Dim count As Long
Dim count_u As Long
Dim count_conc As Long

Dim start_time As Double
Dim sim_time As Double
Dim real_time As Double
Dim real_time_previous As Double


Sub Mainline()
Dim count_output As Integer

Range("status").Value = "Calculating"

Call Get_Input
Call Grid
Call Initial_conditions_u
Call Initial_conditions_conc
If restart = "new" Then
   Call Clear
   real_time_previous = 0
   count = 0
End If
Range("a1").Select
Range("sim_time").Value = sim_time
'transient solution time
start_time = current_time
'gets the present “clock” time in seconds
Call Output_Grid
Call Output_u
Call Output_conc

count_output = 1
iterate = True

While iterate
   count_u = 0
   iterate_u = True
   While iterate_u
      Call Boundary_Conditions_u_w
      Call Boundary_Conditions_u_fs
      Call Coefficients_u
      Call Solve_u
      Call Limits_u
      Call Error_u_calc
      Call Update_u
      Call Limits_u
      'Call Output_u
      count_u = count_u + 1
```

```
    Range("count_u").Value = count_u
Wend
Call Update_shearrate       'for the concentration solver
Call Find_Interface
count_conc = 0
iterate_conc = True
While iterate_conc
    Call Boundary_Conditions_phi_w
    Call Boundary_Conditions_phi_fs
    Call Coefficients_conc
    Call Solve_conc
    If override = "true" Then
        Call Override_Conc
    End If
    Call Limits_conc
    Call Error_conc_calc
    Call Update_conc
    Call Limits_conc
    'Call Scale_conc
    'Call Limits_conc
    'Call Output_conc
    count_conc = count_conc + 1
    Range("count_conc").Value = count_conc
Wend
Call Residual_u_calc
Call Residual_conc_calc
Call Convergence_check
'If residual_total < residual_total_old Then
    Call Update_forward
    'Call Increase_timestep
    real_time = real_time_previous + current_time - start_time
    'time elapsed in seconds
    Range("real_time").Value = real_time
    sim_time = sim_time + dt
    Range("sim_time").Value = sim_time
    'transient solution time
    Range("current_dt").Value = dt
    'current time step
    count = count + 1
    Range("count").Value = count
'Else
    'Call Update_backward
    'Call Decrease_timestep
    'real_time = current_time - start_time
    'time elapsed in seconds
    'Range("real_time").Value = real_time
'End If
If count_output = output_every Then
    Call Average_Calcs
    Call Output_u
    Call Output_conc
    Call Fluxes
    count_output = 1
Else
    count_output = count_output + 1
End If
```

```
Wend

Call Output_u
Call Output_conc
Range("status").Value = "Finished"

End Sub


Sub Restart_calc()

Range("status").Value = "Restart"
restart = "previous"
sim_time = Range("sim_time").Value
real_time_previous = Range("real_time").Value
count = Range("count").Value

Call Mainline

End Sub


Sub Solve_calc()

restart = "new"
Call Mainline

End Sub


Sub Stop_calc()

End
'Ends the calculation

End Sub


Sub Output_u()
Dim i As Integer

For i = 0 To N + 1
   Cells(rowstart + i, colstart + 2).Value = u(i)
Next i
End Sub


Sub Output_conc()
Dim i As Integer

For i = 0 To N + 1
   Cells(rowstart + i, colstart + 3).Value = conc(i)
Next i
End Sub
```

```
Sub Average_Calcs()
'Calculation of the in-situ and delivered concentrations
Dim u_avg As Double
Dim conc_avg As Double
Dim conc_avg_delivered As Double

Dim dy As Double
Dim i As Integer

u_avg = 0
conc_avg = 0
conc_avg_delivered = 0
For i = 1 To N
   'only consider value inside the flow domain
   dy = y_face(i) - y_face(i - 1)
   u_avg = u_avg + dy * u(i)
   conc_avg = conc_avg + dy * conc(i)
   conc_avg_delivered = conc_avg_delivered + dy * conc(i) * u(i)
Next i
u_avg = u_avg / h
conc_avg = conc_avg / h
conc_avg_delivered = conc_avg_delivered / (h * u_avg)
Cells(rowstart + N + 2, colstart + 2).Value = u_avg
Cells(rowstart + N + 2, colstart + 3).Value = conc_avg
Cells(rowstart + N + 3, colstart + 3).Value = conc_avg_delivered
'weighted averages for use with non-uniform grids

End Sub


Sub Get_Input()

dens_f = Range("dens_f").Value
conc_total = Range("conc_total").Value
conc_max = Range("conc_max").Value
d = (Range("d").Value) / 1000
a = d / 2
'particle size determines the stability and length of the transient solution (large particles - small
establishment time
'if larger particles are used a smaller dt must be used for stability
dens_s = Range("dens_s").Value
tauY = Range("tauY").Value
viscP = Range("viscP").Value
Amult = Range("Amult").Value
h = Range("h").Value
theta = Range("theta").Value
dt = Range("dt").Value
gy = -gravity * Cos(theta * pi / 180)
gz = gravity * Sin(theta * pi / 180)
Ks = 2 * (dens_s - dens_f) / 9

End Sub


Sub Grid()
Dim i As Integer
```

```
Dim dy As Double
Dim dy_plug As Double
Dim dy_shear As Double
Dim tauW As Double  '1st order wall shear stress approximation
Dim dens As Double  'dens of bulk homogeneous slurry
Dim interface_y_over_h As Double     'approximate y/h interface where the unsheared region meets the
sheared region
Const safety_factor = 0.1  'y/h safety factor for overlap at interface
Const plug_nodes = 10       '# of nodes in unsheared plug
Dim shear_nodes As Integer
Dim interface_y As Double
Const cluster = 1.1
Dim clustersum As Double
Dim bottom_shear_nodes As Integer   'nodes nearer the wall

If mesh = "uniform" Then
   dy = h / N
   'uniform grid, cell centered
   For i = 0 To N + 1
      y(i) = i * dy - dy / 2
      'north face of cell i
      y_face(i) = y(i) + dy / 2
   Next i
Else
   dens = conc_total * dens_s + (1 - conc_total) * dens_f
   tauW = dens * gz * h
   interface_y_over_h = 1 - tauY / tauW
   interface_y_over_h = interface_y_over_h * (1 + safety_factor)
   dy_plug = h * (1 - interface_y_over_h) / plug_nodes
   shear_nodes = N - plug_nodes

   If mesh = "non-uniform" Then
      dy_shear = h * interface_y_over_h / shear_nodes
      Dim check As Double
      'uniform grid in each domain, cell centered
      'multiblock approach
      For i = 0 To shear_nodes
         'north face of cell i
         y_face(i) = i * dy_shear
         y(i) = y_face(i) - dy_shear / 2
      Next i
      interface_y = y_face(shear_nodes)
      For i = (shear_nodes + 1) To N + 1
         y_face(i) = interface_y + (i - shear_nodes) * dy_plug
         y(i) = y_face(i) - dy_plug / 2
      Next i
   Else
      If mesh = "cluster" Then
         'nodes are clustered near the interface and the bottom of the pipe
         'split bottom sheared geometry in half
         'plug
         y(N + 1) = h + dy_plug / 2
         For i = N To (shear_nodes + 1) Step -1
            y_face(i) = h - (N - i) * dy_plug
            y(i) = y_face(i) - dy_plug / 2
         Next i
```

```
        'bottom of sheared region
        bottom_shear_nodes = shear_nodes / 2
        clustersum = 0
        For i = 1 To bottom_shear_nodes
           clustersum = clustersum + cluster ^ (i - 1)
        Next i
        'Calculating the wall dy & interface dy
        dy_shear = h * interface_y_over_h / 2 / clustersum
        y_face(0) = 0
        y(0) = -dy_shear / 2
        For i = 1 To bottom_shear_nodes
           y_face(i) = y_face(i - 1) + dy_shear * cluster ^ (i - 1)
           y(i) = y_face(i - 1) + (y_face(i) - y_face(i - 1)) / 2
        Next i

        'top of sheared
        For i = shear_nodes To (bottom_shear_nodes + 1) Step -1
           If i = shear_nodes Then
              y_face(i) = interface_y_over_h * h
           Else
              y_face(i) = y_face(i + 1) - dy_shear * cluster ^ (shear_nodes - i)
           End If
           y(i) = y_face(i) - (dy_shear * cluster ^ (shear_nodes - i)) / 2
        Next i
     End If
  End If
End If

End Sub


Sub Output_Grid()
Dim i As Integer

For i = 0 To N + 1
  Cells(rowstart + i, colstart).Value = i
  Cells(rowstart + i, colstart + 1).Value = y(i) / h
Next i

Cells(rowstart + N + 2, colstart + 1).Value = "AVG ="
End Sub


Sub Boundary_Conditions_u_w()
'mom'n, wall, y=0, no slip
aPu(0) = 1
aNu(0) = y(0) / y(1)
aSu(0) = 0
bu(0) = 0

End Sub


Sub Boundary_Conditions_u_fs()
'mom'n, free-surface, y=h, zero gradient
```

```
aPu(N + 1) = 1
aNu(N + 1) = 0
aSu(N + 1) = 1
bu(N + 1) = 0

End Sub


Sub Boundary_Conditions_phi_w()

Dim conc_w As Double
Dim shearrate_w As Double
Dim visc_w As Double
Dim f_w As Double
Dim dvisc_by_dconc_w As Double
Dim shearrate_min As Double

shearrate_min = tauY / (Amult * viscP)

'WALL
shearrate_w = shearrate(u(0), u(1), y(0), y(1))     'using the most recent values for the velocity to get an
accurate bc
conc_w = Interpolation(conc(0), conc(1), y(0), y(1), y_face(0))
'conc_w = Interpolation(conc_old(0), conc_old(1), y(0), y(1), y_face(0))     'use old values in BC
If conc_w < min Then
   'conc_w = min * conc_max
   conc_w = min
End If
If conc_w >= conc_max Then
   conc_w = max * conc_max
End If
visc_w = visc_shear(shearrate_w) + viscP * visc_rel(conc_w)
f_w = f_hindrance(conc_w, shearrate_w)
dvisc_by_dconc_w = viscP * dvisc_rel_by_dconc(conc_w)

Dim slope As Double
slope = (Ks * conc_w * f_w * gy - Kc * conc_w ^ 2 * shearrate_grad(0)) / (shearrate_w * conc_w * (Kc +
Kn * conc_w * dvisc_by_dconc_w / visc_w))

If (shearrate_w < shearrate_min) Then
   slope = 0   'slope = 0 constitutes a symmetry boundary condition
End If

'conc, wall, y=0, no flux
'explicit as solution is based on previous iterations conc(0) and conc(1) values
aPphi(0) = 1
aNphi(0) = 1
aSphi(0) = 0
bphi(0) = -(y(1) - y(0)) * slope

End Sub


Sub Boundary_Conditions_phi_fs()
'New and corrected boundary condition at the free surface
Dim i As Integer
```

```
Dim conc_fs As Double
Dim conc_fs_old As Double
Dim shearrate_fs As Double
Dim iterate_NR As Boolean
Const tolerance_NR = 0.000001
Dim f_of_phi As Double
Dim f_prime_of_phi As Double
Const omega = 1
Const iterations_max_NR = 1000
Dim count_NR As Integer
Dim Error_NR As Double

shearrate_fs = shearrate(u(N), u(N + 1), y(N), y(N + 1))
conc_fs = Interpolation(conc(N), conc(N + 1), y(N), y(N + 1), y_face(N))
'conc_fs = Interpolation(conc_old(N), conc_old(N + 1), y(N), y(N + 1), y_face(N))
If conc_fs < min Then
   'conc_fs = min * conc_max
   conc_fs = min
End If
If conc_fs >= conc_max Then
   conc_fs = max * conc_max
End If
conc_fs_old = conc_fs
count_NR = 0
iterate_NR = True

While iterate_NR
   'calculating Newton-Raphson functional relationships
   f_of_phi = Ks * gy * conc_fs * f_hindrance(conc_fs, shearrate_fs) - Kc * shearrate_grad(N) * conc_fs ^
2
   f_prime_of_phi = Ks * gy * (f_hindrance(conc_fs, shearrate_fs) + conc_fs * df_by_dconc(conc_fs,
shearrate_fs)) - 2 * Kc * shearrate_grad(N) * conc_fs

   'Newton-Raphson evaluation of conc_fs
   conc_fs = conc_fs_old - f_of_phi / f_prime_of_phi

   If conc_fs < min Then
      'conc_fs = min * conc_max
      conc_fs = min
   End If
   If conc_fs >= conc_max Then
      conc_fs = max * conc_max
   End If

   Error_NR = Abs(f_of_phi)
   If (Error_NR > tolerance_NR) And (count_NR < iterations_max_NR) Then
      iterate_NR = True
   Else
     iterate_NR = False
   End If
   count_NR = count_NR + 1
   conc_fs = conc_fs_old + omega * (conc_fs - conc_fs_old)
   conc_fs_old = conc_fs
Wend

conc_fs = 1
```

```
'FREE-SURFACE
'conc, wall, y=h, no flux
aPphi(N + 1) = y_face(N) - y(N)
aNphi(N + 1) = 0
aSphi(N + 1) = y_face(N) - y(N) - (y(N + 1) - y(N))
bphi(N + 1) = (y(N + 1) - y(N)) * conc_fs

End Sub


Sub Update_shearrate()
Dim i As Integer
Dim u_n As Double
Dim u_s As Double
Dim shearrate_cell(N + 1) As Double

'interpolate velocities to faces
For i = 1 To N
   u_n = Interpolation(u(i), u(i + 1), y(i), y(i + 1), y_face(i))
   'if statement allows for the use of geometric interpolation
   'can't geometrically interpolate at a no-slip conditions
   If ((i = 1) And (scheme = "geometric")) Then
      u_s = 0
   Else
      u_s = Interpolation(u(i - 1), u(i), y(i - 1), y(i), y_face(i - 1))
   End If
   'shearrate at cell center
   shearrate_cell(i) = shearrate(u_s, u_n, y_face(i - 1), y_face(i))
Next i
shearrate_cell(0) = shearrate(u(0), u(1), y(0), y(1))
shearrate_cell(N + 1) = shearrate(u(N), u(N + 1), y(N), y(N + 1))

'shearrate_grad is wanted at the cell faces
For i = 0 To N
   'north face of cell
   shearrate_grad(i) = beta_diff_gamma * (shearrate_cell(i + 1) - shearrate_cell(i)) / (y(i + 1) - y(i))
Next i

End Sub


Sub Coefficients_u()
Dim i As Integer
Dim conc_n As Double
Dim conc_s As Double
Dim visc_n As Double
Dim visc_s As Double
Dim shearrate_n As Double
Dim shearrate_s As Double
Dim dens As Double
Dim dy As Double
Dim aPunot As Double
Dim Source As Double

'mom'n
```

```
For i = 1 To N
   dy = y_face(i) - y_face(i - 1)
   dens = conc(i) * dens_s + (1 - conc(i)) * dens_f
   K = dens * gz
   conc_n = Interpolation(conc(i), conc(i + 1), y(i), y(i + 1), y_face(i))
   conc_s = Interpolation(conc(i - 1), conc(i), y(i - 1), y(i), y_face(i - 1))
   shearrate_n = shearrate(u(i), u(i + 1), y(i), y(i + 1))
   shearrate_s = shearrate(u(i - 1), u(i), y(i - 1), y(i))
   visc_n = visc_shear(shearrate_n) + viscP * visc_rel(conc_n)
   visc_s = visc_shear(shearrate_s) + viscP * visc_rel(conc_s)
   'solver coefficients
   aPunot = dens * dy / dt
   Source = K
   aNu(i) = beta_diff_u * visc_n / (y(i + 1) - y(i))
   aSu(i) = beta_diff_u * visc_s / (y(i) - y(i - 1))
   'bu(i) = aPunot * u(i) + Source * dy
   bu(i) = aPunot * u_old(i) + Source * dy     'use old value of u to get true transient behaviour
   aPu(i) = aPunot + aNu(i) + aSu(i)
Next i

End Sub


Sub Coefficients_conc()
Dim i As Integer
Dim conc_n As Double
Dim conc_s As Double
Dim conc_n_old As Double
Dim conc_s_old As Double
Dim visc_n As Double
Dim visc_s As Double
Dim dvisc_by_dconc_n As Double
Dim dvisc_by_dconc_s As Double
Dim shearrate_n As Double
Dim shearrate_s As Double
Dim Source_not As Double
Dim dSource_by_dconc_not As Double
Dim Sp As Double
Dim Sc As Double
Dim dy As Double
Dim aPphinot As Double

'conc
For i = 1 To N
   dy = y_face(i) - y_face(i - 1)
   conc_n = Interpolation(conc(i), conc(i + 1), y(i), y(i + 1), y_face(i))
   conc_s = Interpolation(conc(i - 1), conc(i), y(i - 1), y(i), y_face(i - 1))
   conc_n_old = Interpolation(conc_old(i), conc_old(i + 1), y(i), y(i + 1), y_face(i))
   conc_s_old = Interpolation(conc_old(i - 1), conc_old(i), y(i - 1), y(i), y_face(i - 1))
   shearrate_n = shearrate(u(i), u(i + 1), y(i), y(i + 1))
   shearrate_s = shearrate(u(i - 1), u(i), y(i - 1), y(i))
   visc_n = visc_shear(shearrate_n) + viscP * visc_rel(conc_n)
   visc_s = visc_shear(shearrate_s) + viscP * visc_rel(conc_s)
   'interface internal singularity correction
   If singularity = "true" Then
      visc_n = visc_discontinuity_correction(shearrate_n, shearrate_s, visc_n, visc_s)
```

```
        'shearrate_n = shearrate_discontinuity_correction(shearrate_n, shearrate_s)
    End If

    dvisc_by_dconc_n = viscP * dvisc_rel_by_dconc(conc_n)
    dvisc_by_dconc_s = viscP * dvisc_rel_by_dconc(conc_s)
    'Source term linearization (constant over cell)
    Source_not = Kc * (a ^ 2) * ((conc_n_old ^ 2) * shearrate_grad(i) - (conc_s_old ^ 2) * shearrate_grad(i -
1)) / dy - (a ^ 2) * gy * Ks * (conc_n_old * f_hindrance(conc_n_old, shearrate_n) - conc_s_old *
f_hindrance(conc_s_old, shearrate_s)) / dy
    dSource_by_dconc_not = Kc * (a ^ 2) * (2 * conc_n_old * shearrate_grad(i) - 2 * conc_s_old *
shearrate_grad(i - 1)) / dy - (a ^ 2) * gy * Ks * ((f_hindrance(conc_n_old, shearrate_n) + conc_n_old *
df_by_dconc(conc_n_old, shearrate_n)) - (f_hindrance(conc_s_old, shearrate_s) + conc_s_old *
df_by_dconc(conc_s_old, shearrate_s))) / dy
    'solver coefficients
    If dSource_by_dconc_not < 0 Then
        Sp = dSource_by_dconc_not
    Else
        Sp = 0        'set to zero if no source term linearization is desired
    End If
    'Sc = Source_not - Sp * conc(i)
    Sc = Source_not - Sp * conc_old(i)
    aPphinot = dy / dt
    aNphi(i) = beta_diff_phi * (a ^ 2) * conc_n * shearrate_n * (Kc + Kn * conc_n * dvisc_by_dconc_n /
visc_n) / (y(i + 1) - y(i))
    aSphi(i) = beta_diff_phi * (a ^ 2) * conc_s * shearrate_s * (Kc + Kn * conc_s * dvisc_by_dconc_s /
visc_s) / (y(i) - y(i - 1))
    'bphi(i) = aPphinot * conc(i) + dy * Sc
    bphi(i) = aPphinot * conc_old(i) + dy * Sc
    aPphi(i) = aPphinot + aNphi(i) + aSphi(i) - dy * Sp
Next i

End Sub


Function visc_discontinuity_correction(shearrate_n As Double, shearrate_s As Double, visc_n As Double,
visc_s As Double) As Double
Dim shearrate_min As Double

shearrate_min = tauY / (Amult * viscP)

'correcting the north face discontinuity
If ((shearrate_n <= shearrate_min) And (shearrate_s > shearrate_min)) Then
    If scheme = "geometric" Then
        visc_discontinuity_correction = (visc_s * visc_n) ^ 0.5
        'visc_discontinuity_correction = 2 * (visc_s * visc_n) / (visc_s + visc_n)
    Else
        If scheme = "linear" Then
            visc_discontinuity_correction = (visc_s + visc_n) / 2
        End If
    End If
Else
    visc_discontinuity_correction = visc_n
End If

End Function
```

```
Function shearrate_discontinuity_correction(shearrate_n As Double, shearrate_s As Double) As Double
Dim shearrate_min As Double

shearrate_min = tauY / (Amult * viscP)

'correcting the north face discontinuity
If ((shearrate_n <= shearrate_min) And (shearrate_s > shearrate_min)) Then
   If scheme = "geometric" Then
      shearrate_discontinuity_correction = (shearrate_s * shearrate_n) ^ 0.5
      'shearrate_discontinuity_correction = 2 * (shearrate_s * shearrate_n) / (shearrate_s + shearrate_n)
   Else
      If scheme = "linear" Then
         shearrate_discontinuity_correction = (shearrate_s + shearrate_n) / 2
      End If
   End If
Else
   shearrate_discontinuity_correction = shearrate_n
End If

End Function


Sub Solve_u()
Dim i As Integer
Dim iback As Integer
Dim alpha(N + 1) As Double
Dim beta(N + 1) As Double

'mon'n solver
alpha(0) = aNu(0) / aPu(0)
beta(0) = bu(0) / aPu(0)
'load alpha/beta
For i = 1 To N + 1
   alpha(i) = aNu(i) / (aPu(i) - aSu(i) * alpha(i - 1))
   beta(i) = (aSu(i) * beta(i - 1) + bu(i)) / (aPu(i) - aSu(i) * alpha(i - 1))
Next i

u(N + 1) = beta(N + 1)
For i = 0 To N
   iback = N - i
   u(iback) = alpha(iback) * u(iback + 1) + beta(iback)
Next i

End Sub


Sub Solve_conc()
Dim i As Integer
Dim iback As Integer
Dim alpha(N + 1) As Double
Dim beta(N + 1) As Double

'conc solver
alpha(0) = aNphi(0) / aPphi(0)
beta(0) = bphi(0) / aPphi(0)
```

```
'load alpha/beta
For i = 1 To N + 1
   alpha(i) = aNphi(i) / (aPphi(i) - aSphi(i) * alpha(i - 1))
   beta(i) = (aSphi(i) * beta(i - 1) + bphi(i)) / (aPphi(i) - aSphi(i) * alpha(i - 1))
Next i

conc(N + 1) = beta(N + 1)
For i = 0 To N
   iback = N - i
   conc(iback) = alpha(iback) * conc(iback + 1) + beta(iback)
Next i

End Sub


Sub Override_Conc()
Dim i As Integer
Dim shearrate_min As Double
Dim y_over_h As Double
Dim conc_n As Double
Dim conc_s As Double
Dim shearrate_n As Double
Dim shearrate_s As Double
Const overshoot = 0.05    'maximum allowable overshoot % of conc_total
'Override the concentration in the plug
'This is used to damp out the overshoots and oscillations due to the viscosity and velocity singularities

shearrate_min = tauY / (Amult * viscP)

For i = (N - 1) To 2 Step -1
   'don't perform any manipulation to point nearest the free surface or the point nearest the wall
   conc_n = Interpolation(conc(i), conc(i + 1), y(i), y(i + 1), y_face(i))
   conc_s = Interpolation(conc(i - 1), conc(i), y(i - 1), y(i), y_face(i - 1))
   shearrate_n = shearrate(u(i), u(i + 1), y(i), y(i + 1))
   shearrate_s = shearrate(u(i - 1), u(i), y(i - 1), y(i))
   y_over_h = y(i) / h

   If (y_over_h > interface_low) And (y_over_h < interface_high) Then
      'ensures that only points near the plug are considered
      If (shearrate_n <= shearrate_min) Or (shearrate_s <= shearrate_min) Then
         'if either face is in the plug region, allows for correction of node at plug transition
         If conc(i) > (1 + overshoot) * conc_total Then
            'if the concentration is indeed an overshoot
            'conc_total is the desired and theoretical concentration in the plug
            If scheme = "geometric" Then
               conc(i) = (conc_s * conc_n) ^ 0.5
               'conc(i) = 2 * (conc_s * conc_n) / (conc_s + conc_n)
            Else
               If scheme = "linear" Then
                  conc(i) = (conc_s + conc_n) / 2
               End If
            End If
         End If
      End If
   End If
Next i
```

```
End Sub


Sub Find_Interface()
Dim i As Integer
Dim shearrate_min As Double
Dim shearrate_n As Double
Dim shearrate_s As Double
Const safety_factor = 0.1  'y/h safety factor for overlap at interface

shearrate_min = tauY / (Amult * viscP)

For i = N To 1 Step -1
   shearrate_n = shearrate(u(i), u(i + 1), y(i), y(i + 1))
   shearrate_s = shearrate(u(i - 1), u(i), y(i - 1), y(i))
   If (shearrate_n <= shearrate_min) And (shearrate_s > shearrate_min) Then
      'location of interface occurs where shearrate splits over a cell volume, north side unsheared, south side
sheared
      interface = y(i) / h
   End If
Next i

Range("interface").Value = interface    'output true interface
interface_low = interface * (1 - safety_factor)     'safety factored interface low
interface_high = interface * (1 + safety_factor)     'safety factored interface low
'location of plug interface, includes safety factor to make sure overlap is considered

End Sub


Sub Limits_conc()
Dim i As Integer

For i = 1 To N
   If conc(i) < min Then
      'conc(i) = min * conc_max
      conc(i) = min
   End If
   If conc(i) >= conc_max Then
      conc(i) = max * conc_max
   End If
Next i

End Sub


Sub Limits_u()
Dim i As Integer

For i = 1 To N + 1
   'u(0) is allowed to be naegative as this ensures a positive wall shear stress and positive profile
   'only consider real nodes within the domain
   'since a symmetry condition exists at the free surface ensure that u(N+1) is also realistic
   'ensures conc BC at fs is realistic
   If u(i) < 0 Then
```

```
      u(i) = min
   End If
Next i

End Sub


Sub Error_u_calc()
Dim i As Integer
Dim Error_u As Double
Dim N_non_zero As Integer

Error_u = 0
N_non_zero = N
For i = 1 To N
   If u(i) <= 0 Then
      'do nothing
      N_non_zero = N_non_zero - 1
   Else
      Error_u = Error_u + Abs((u(i) - u_temp(i)) / u(i))
   End If
Next i
Error_u = Error_u / N_non_zero
Range("Error_u").Value = Error_u

If (Error_u < tolerance_u) Then
   'converged
   iterate_u = False
Else
   'not converged
   If iterations_max_u > count_u Then
      iterate_u = True
   Else
      iterate_u = False
   End If
End If

End Sub


Sub Error_conc_calc()
Dim i As Integer
Dim Error_conc As Double
Dim N_non_zero As Integer

Error_conc = 0
N_non_zero = N
For i = 1 To N
   If conc(i) <= 0 Then
      'do nothing
      N_non_zero = N_non_zero - 1
   Else
      Error_conc = Error_conc + Abs((conc(i) - conc_temp(i)) / conc(i))
   End If
Next i
Error_conc = Error_conc / N_non_zero
```

```
Range("error_conc").Value = Error_conc

If (Error_conc < tolerance_conc) Then
   'converged
   iterate_conc = False
Else
   'not converged
   If iterations_max_conc > count_conc Then
      iterate_conc = True
   Else
      iterate_conc = False
   End If
End If

End Sub


Sub Initial_conditions_u()

Dim i As Integer
Dim u_bulk As Double
Dim dens As Double
Dim visc As Double
Dim Rh As Double
Dim Dh As Double
Dim tw As Double
Dim tauY_slurry As Double
Dim viscP_slurry As Double
Dim ReZhang As Double
Dim lambda As Double

If restart = "new" Then
   'Rh = dx * h / (2 * h + dx)
   Rh = h      'approaches h
   Dh = 4 * Rh
   dens = conc_total * dens_s + (1 - conc_total) * dens_f
   tw = dens * gz * Rh
   lambda = 1 / ((conc_max / conc_total) ^ (1 / 3) - 1)
   'use Shook & Gillies scaling laws for tauY and viscP (1+const*lambda^power)
   tauY_slurry = tauY * (1 + 0.016 * lambda ^ 2.5)
   viscP_slurry = viscP * (1 + 0.21 * lambda ^ 2)
   'u_bulk = (tw / 2 - tauY_slurry) * Dh / (8 * viscP_slurry)
   Dim xi As Double
   Const a = 0.5
   Const b = 1
   'for an inclined plane of infinite width K & T and Sestak showed that a = 1/2, b = 1
   xi = tauY_slurry / tw
   u_bulk = (1 / (a + b) - xi / b + a * xi ^ (b / a + 1) / (b * (a + b))) * Dh * tw / (8 * viscP_slurry)

   For i = 1 To N
      u(i) = u_bulk
      u_old(i) = u(i)
      u_temp(i) = u(i)
   Next i

   u(0) = y(0) / y(1) * u(1)
```

```
   u_old(0) = u(0)
   u_temp(0) = u(0)

   u(N + 1) = u(N)
   u_old(N + 1) = u(N + 1)
   u_temp(N + 1) = u(N + 1)
Else
   For i = 0 To N + 1
      u(i) = Cells(rowstart + i, colstart + 2).Value
      u_old(i) = u(i)
      u_temp(i) = u(i)
   Next i
End If

End Sub


Sub Initial_conditions_conc()
Dim i As Integer
Dim j As Integer

If restart = "new" Then
   For i = 1 To N
      'for a flat initial concentration profile
      conc(i) = conc_total
      conc_old(i) = conc(i)
      conc_temp(i) = conc(i)
   Next i

   conc(0) = conc(1)
   conc_old(0) = conc(0)
   conc_temp(0) = conc(0)

   conc(N + 1) = conc(N)
   conc_old(N + 1) = conc(N + 1)
   conc_temp(N + 1) = conc(N + 1)
Else
   For i = 0 To N + 1
      conc(i) = Cells(rowstart + i, colstart + 3).Value
      conc_old(i) = conc(i)
      conc_temp(i) = conc(i)
   Next i
End If

End Sub


Sub Update_u()
Dim i As Integer
Dim diff_u As Double

For i = 0 To N + 1
   diff_u = u(i) - u_temp(i)
   u(i) = u_temp(i) + u_relax_temp * (u(i) - u_temp(i))
   u_temp(i) = u(i)
Next i
```

```
End Sub

Sub Update_conc()
Dim i As Integer
Dim diff_conc As Double

For i = 0 To N + 1
   diff_conc = conc(i) - conc_temp(i)
   conc(i) = conc_temp(i) + conc_relax_temp * diff_conc
   conc_temp(i) = conc(i)
Next i

End Sub


Sub Scale_conc()
Dim conc_avg As Double
Dim dy As Double
Dim i As Integer
Dim scale_mult As Double

'calculating the average conc value in the domain
conc_avg = 0
For i = 1 To N
   dy = y_face(i) - y_face(i - 1)
   conc_avg = conc_avg + dy * conc(i)
Next i
conc_avg = conc_avg / h

'scaling the concentration to ensure conservation of particles in the domain
'the zero gradient bc's for conc at wall don't necessarily conserve particle mass
scale_mult = conc_total / conc_avg
For i = 0 To N + 1
   conc(i) = scale_mult * conc(i)
Next i

End Sub


Sub Update_forward()
Dim i As Integer
Dim diff_u As Double
Dim diff_conc As Double

For i = 0 To N + 1
   diff_u = u(i) - u_old(i)
   u(i) = u_old(i) + u_relax * diff_u
   u_old(i) = u(i)
   u_temp(i) = u(i)
   diff_conc = conc(i) - conc_old(i)
   conc(i) = conc_old(i) + conc_relax * diff_conc
   conc_old(i) = conc(i)
   conc_temp(i) = conc(i)
Next i
residual_u_old = residual_u
```

```
residual_conc_old = residual_conc
residual_total_old = residual_total
End Sub


Sub Update_backward()
Dim i As Integer
Dim diff_u As Double
Dim diff_conc As Double

For i = 0 To N + 1
   u(i) = u_old(i)
   u_old(i) = u(i)
   u_temp(i) = u(i)
   conc(i) = conc_old(i)
   conc_old(i) = conc(i)
   conc_temp(i) = conc(i)
Next i
residual_u = residual_u_old
residual_conc = residual_conc_old
residual_total = residual_total_old

End Sub


Sub Residual_u_calc()
Dim i As Integer
Dim temp As Double

residual_u = 0
For i = 1 To N
   temp = Abs(aPu(i) * u_old(i) - (aNu(i) * u(i + 1) + aSu(i) * u(i - 1) + bu(i)))
   residual_u = residual_u + temp
Next i
residual_u = residual_u / N
Range("residual_u").Value = residual_u

End Sub


Sub Residual_conc_calc()
Dim i As Integer
Dim temp As Double

residual_conc = 0
For i = 1 To N
   temp = Abs(aPphi(i) * conc_old(i) - (aNphi(i) * conc(i + 1) + aSphi(i) * conc(i - 1) + bphi(i)))
   residual_conc = residual_conc + temp
Next i
residual_conc = residual_conc / N
Range("residual_conc").Value = residual_conc

End Sub


Sub Convergence_check()
```

```
residual_total = residual_u + residual_conc
Range("residual_total").Value = residual_total

If (residual_total < tolerance) Then
   'converged
   iterate = False
Else
   'not converged
   If iterations_max > count Then
      iterate = True
   Else
      iterate = False
   End If
End If

End Sub


Sub Fluxes()
Dim i As Integer
Dim Nc, Nn, Ns As Double
Dim shearrate_gradient_cell As Double
Dim shearrate_cell As Double
Dim conc_gradient_cell As Double
Dim visc As Double

For i = 1 To N
   shearrate_cell = shearrate(u(i - 1), u(i + 1), y(i - 1), y(i + 1))
   visc = visc_shear(shearrate_cell) + viscP * visc_rel(conc(i))
   shearrate_gradient_cell = shearrate_grad_cell(u(i + 1), u(i), u(i - 1), y(i + 1), y(i), y(i - 1), y_face(i),
y_face(i - 1))
   conc_gradient_cell = (conc(i + 1) - conc(i - 1)) / (y(i + 1) - y(i - 1))
   Nc = -Kc * (a ^ 2) * ((conc(i) ^ 2) * shearrate_gradient_cell + conc(i) * shearrate_cell *
conc_gradient_cell)
   Nn = -Kn * (a ^ 2) * shearrate_cell * (conc(i) ^ 2) * viscP * dvisc_rel_by_dconc(conc(i)) *
conc_gradient_cell / visc
   Ns = Ks * (a ^ 2) * conc(i) * f_hindrance(conc(i), shearrate_cell) * gy
   Cells(rowstart + i, colstart + 9).Value = Nc
   Cells(rowstart + i, colstart + 10).Value = Nn
   Cells(rowstart + i, colstart + 11).Value = Ns
   Cells(rowstart + i, colstart + 12).Value = Nc + Nn + Ns
   Cells(rowstart + i, colstart + 14).Value = visc
Next i

End Sub


Function shearrate_grad_cell(velN As Double, velP As Double, velS As Double, yN As Double, yP As
Double, yS As Double, y_n As Double, y_s As Double) As Double
Dim shearrate_n As Double
Dim shearrate_s As Double

shearrate_n = shearrate(velP, velN, yP, yN)
shearrate_s = shearrate(velS, velP, yS, yP)
```

```
shearrate_grad_cell = (shearrate_n - shearrate_s) / (y_n - y_s)

End Function


Sub Increase_timestep()

dt = dt * dt_scalar     'double time step

'Maximum/Minimum time step considerations
If dt > dt_max Then
   dt = dt_max
End If
If dt < dt_min Then
   dt = dt_min
End If

Range("current_dt").Value = dt

End Sub


Sub Decrease_timestep()

dt = dt / dt_scalar

'Maximum/Minimum time step considerations
If dt > dt_max Then
   dt = dt_max
End If
If dt < dt_min Then
   dt = dt_min
End If

Range("current_dt").Value = dt

End Sub


Sub Clear()
Dim i As Integer

Range("status").Value = "Clearing"
Range("count").Value = 0
Range("count_u").Value = 0
Range("count_conc").Value = 0
Range("error_u").Value = 0
Range("error_conc").Value = 0
Range("residual_u").Value = 0
Range("residual_conc").Value = 0
Range("residual_total").Value = 0
Range("real_time").Value = 0
Range("sim_time").Value = 0
Range("current_dt").Value = 0

For i = 0 To N + 1
```

```
    Cells(rowstart + i, colstart + 0).Select
    Selection.ClearContents
    Cells(rowstart + i, colstart + 1).Select
    Selection.ClearContents
    Cells(rowstart + i, colstart + 2).Select
    Selection.ClearContents
    Cells(rowstart + i, colstart + 3).Select
    Selection.ClearContents
    Cells(rowstart + i, colstart + 9).Select
    Selection.ClearContents
    Cells(rowstart + i, colstart + 10).Select
    Selection.ClearContents
    Cells(rowstart + i, colstart + 11).Select
    Selection.ClearContents
    Cells(rowstart + i, colstart + 12).Select
    Selection.ClearContents
Next i

Cells(rowstart + N + 2, colstart + 2).Select
Selection.ClearContents
Cells(rowstart + N + 2, colstart + 3).Select
Selection.ClearContents
Cells(rowstart + N + 3, colstart + 2).Select
Selection.ClearContents
Range("status").Value = "Ready"
Range("a1").Select

End Sub


Function Interpolation(phi1 As Double, phi2 As Double, y1 As Double, y2 As Double, yf As Double) As
Double
'function to interpolate values to cell faces
Dim delta2 As Double
Dim delta1 As Double
Dim r2 As Double
Dim r1 As Double

If scheme = "linear" Then
    Interpolation = phi1 + (phi2 - phi1) * (yf - y1) / (y2 - y1)
Else
    If scheme = "geometric" Then
        delta2 = y2 - yf
        delta1 = yf - y1
        r2 = delta2 / (delta2 + delta1)
        r1 = delta1 / (delta2 + delta1)
        Interpolation = phi1 * phi2 / (r2 * phi1 + r1 * phi2)
    End If
End If

End Function


Function visc_rel(phi As Double) As Double
Dim lambda As Double
```

```
If phi <= 0 Then
   visc_rel = 1
Else
   lambda = 1 / ((conc_max / phi) ^ (1 / 3) - 1)
   visc_rel = 1 + 2.5 * phi + 0.16 * (lambda ^ 2)
End If

End Function


Function dvisc_rel_by_dconc(phi As Double) As Double
Dim lambda As Double
Dim dlambda_by_dconc As Double

If phi <= 0 Then
   dvisc_rel_by_dconc = 300
   'order of magnitude analysis from Schaan visc formula
   'at conc ~ 1e-10, dvisc_rel_by_dconc ~ 300
Else
   lambda = 1 / ((conc_max / phi) ^ (1 / 3) - 1)
   dlambda_by_dconc = (lambda ^ 2) * ((conc_max / phi) ^ (1 / 3)) / (3 * phi)
   dvisc_rel_by_dconc = 2.5 + 2 * 0.16 * lambda * dlambda_by_dconc
End If

End Function


Function shearrate(vel1 As Double, vel2 As Double, y1 As Double, y2 As Double) As Double

shearrate = Abs((vel2 - vel1) / (y2 - y1))

End Function


Function f_hindrance(phi As Double, shearrate As Double) As Double
Dim visc As Double

visc = visc_shear(shearrate) + viscP * visc_rel(phi)
f_hindrance = (1 - phi) / visc

End Function


Function df_by_dconc(phi As Double, shearrate As Double) As Double
Dim visc As Double

visc = visc_shear(shearrate) + viscP * visc_rel(phi)
df_by_dconc = -(1 + f_hindrance(phi, shearrate) * viscP * dvisc_rel_by_dconc(phi)) / visc

End Function


Function visc_shear(shearrate_face As Double) As Double
Dim shearrate_min As Double
Dim visc_max As Double
'Const mexp = 100
```

```
shearrate_min = tauY / (Amult * viscP)
'shearrate_min = 0.0000000001
visc_max = Amult * viscP
'visc_max = tauY / shearrate_min

'the shear viscosity effect on tauY can be calculated at the face of each cell
If (shearrate_face < shearrate_min) Then
   'low shear/plug region
   visc_shear = visc_max
Else
   'high shear region
   visc_shear = tauY / shearrate_face
   'visc_shear = tauY / shearrate_face * (1 - Exp(-mexp * shearrate_face ^ 0.5))
End If

End Function


Function current_time() As Double

current_time = Year(Time) * 365 * 24 * 3600 + Day(Time) * 24 * 3600 + Hour(Time) * 3600 +
Minute(Time) * 60 + Second(Time)
'current time in seconds

End Function
```

The following additional subroutines apply to the boundary condition requirements for the simulation of neutrally buoyant particles in a Newtonian carrier fluid for the flow in a symmetrical duct of infinite width.

```
Sub Boundary_Conditions_u_w()
'mom'n, wall, y=0, no slip
aPu(0) = 1
aNu(0) = y(0) / y(1)
aSu(0) = 0
bu(0) = 0

End Sub


Sub Boundary_Conditions_u_fs()
'mom'n, free-surface, y=h, zero gradient
aPu(N + 1) = 1
aNu(N + 1) = 0
aSu(N + 1) = 1
bu(N + 1) = 0

End Sub


Sub Boundary_Conditions_phi_w()

Dim conc_w As Double
Dim shearrate_w As Double
Dim visc_w As Double
Dim f_w As Double
Dim dvisc_by_dconc_w As Double

'WALL
'possible iterate for conc_w
shearrate_w = shearrate(u(0), u(1), y(0), y(1))
conc_w = Interpolation(conc(0), conc(1), y(0), y(1), y_face(0))
If conc_w < min Then
   'conc_w = min * conc_max
   conc_w = min
End If
If conc_w >= conc_max Then
   conc_w = max * conc_max
End If
visc_w = visc_f * visc_rel(conc_w)
f_w = f_hindrance(conc_w)
dvisc_by_dconc_w = visc_f * dvisc_rel_by_dconc(conc_w)

'conc, wall, y=0, no flux
'explicit as solution is based on previous iterations conc(0) and conc(1) values
aPphi(0) = 1
aNphi(0) = 1
aSphi(0) = 0
bphi(0) = -(y(1) - y(0)) * (Ks * conc_w * f_w * gy - Kc * conc_w ^ 2 * shearrate_grad(0)) / (shearrate_w *
conc_w * (Kc + Kn * conc_w * dvisc_by_dconc_w / visc_w))
```

```
'Dim slope As Double
'slope = -bphi(0) / (y(1) - y(0))
End Sub


Sub Boundary_Conditions_phi_fs()
'conc, free-surface, y=h, zero gradient
aPphi(N + 1) = 1
aNphi(N + 1) = 0
aSphi(N + 1) = 1
bphi(N + 1) = 0

End Sub
```

The following additional subroutines apply to the boundary condition requirements for the simulation of negatively buoyant particles for the flow in a closed conduit duct of infinite width.

```
Sub Boundary_Conditions_u()

'mom'n, wall, y=0, no slip
aPu(0) = 1
aNu(0) = y(0) / y(1)
aSu(0) = 0
bu(0) = 0
'mom'n, wall, y=h, no slip
aPu(N + 1) = 1
aNu(N + 1) = 0
aSu(N + 1) = (h - y(N + 1)) / (h - y(N))   'for pipeflow
bu(N + 1) = 0

End Sub


Sub Boundary_Conditions_phi()
Dim conc_w As Double
Dim shearrate_w As Double
Dim visc_w As Double
Dim f_w As Double
Dim dvisc_by_dconc_w As Double

'WALL bottom
'possible iterate for conc_w
shearrate_w = shearrate(u(0), u(1), y(0), y(1))
conc_w = Interpolation(conc(0), conc(1), y(0), y(1), y_face(0))
If conc_w < min Then
   'conc_w = min * conc_max
   conc_w = min
End If
If conc_w >= conc_max Then
   conc_w = max * conc_max
End If
visc_w = visc_f * visc_rel(conc_w)
f_w = f_hindrance(conc_w)
dvisc_by_dconc_w = visc_f * dvisc_rel_by_dconc(conc_w)

'conc, wall, y=0, no flux
'explicit as solution is based on previous iterations conc(0) and conc(1) values
aPphi(0) = 1
aNphi(0) = 1
aSphi(0) = 0
bphi(0) = -(y(1) - y(0)) * (Ks * conc_w * f_w * gy - Kc * conc_w ^ 2 * shearrate_grad(0)) / (shearrate_w *
conc_w * (Kc + Kn * conc_w * dvisc_by_dconc_w / visc_w))

'WALL top
'possible iterate for conc_w
shearrate_w = shearrate(u(N), u(N + 1), y(N), y(N + 1))
conc_w = Interpolation(conc(N), conc(N + 1), y(N), y(N + 1), y_face(N))
If conc_w <= 0 Then
```

```
    'conc_w = min * conc_max
    conc_w = min
End If
If conc_w >= conc_max Then
    conc_w = max * conc_max
End If
visc_w = visc_f * visc_rel(conc_w)
f_w = f_hindrance(conc_w)
dvisc_by_dconc_w = visc_f * dvisc_rel_by_dconc(conc_w)

'conc, wall, y=h, no flux
'explicit as solution is based on previous iterations conc(N) and conc(N+1) values
aPphi(N + 1) = 1
aNphi(N + 1) = 0
aSphi(N + 1) = 1
bphi(N + 1) = (y(N + 1) - y(N)) * (Ks * conc_w * f_w * gy - Kc * conc_w ^ 2 * shearrate_grad(N)) /
(shearrate_w * conc_w * (Kc + Kn * conc_w * dvisc_by_dconc_w / visc_w))

End Sub


Sub Update_shearrate()
Dim i As Integer
Dim u_n As Double
Dim u_s As Double
Dim shearrate_cell(N + 1) As Double

'interpolate velocities to faces
For i = 1 To N
    'if statement allows for the use of geometric interpolation
    'can't geometric interpolate at a no-slip conditions
    'If ((i = N) And (scheme = "geometric")) Then
    '    u_n = 0
    'Else
    '    u_n = Interpolation(u(i), u(i + 1), y(i), y(i + 1), y_face(i))
    'End If
    '
    'If ((i = 1) And (scheme = "geometric")) Then
    '    u_s = 0
    'Else
    '    u_s = Interpolation(u(i - 1), u(i), y(i - 1), y(i), y_face(i - 1))
    'End If
    'shearrate at cell center
    'shearrate_cell(i) = shearrate(u_s, u_n, y_face(i - 1), y_face(i))
Next i
shearrate_cell(0) = shearrate(u(0), u(1), y(0), y(1))
shearrate_cell(N + 1) = shearrate(u(N), u(N + 1), y(N), y(N + 1))
'shearrate_grad is wanted at the cell faces
For i = 0 To N
    'north face of cell
    shearrate_grad(i) = beta_diff_gamma * (shearrate_cell(i + 1) - shearrate_cell(i)) / (y(i + 1) - y(i))
Next i

End Sub
```

APPPENDIX B:
MATERIALS

The following materials were employed during the experimental testing of the model tailings slurries with the SRC flume apparatus in 2002.

Sand

UNIMIN Corporation Round Grain Silica Sand
Granusil 5010
Industrial Quartz
d_{50} = 188μm
Le Sueur, MN, USA, 56058

Clay

Pioneer Kaolin Clay
DBK – Dry Branch Kaolin Clay
Dry Branch, GA, USA, 31020

Water

Saskatoon Tap Water
Saskatoon, SK Canada

Chemicals
Dispersant – TSPP
Tetrasodium Pyrophosphate
$Na_4P_2O_7$
Sigma Chemical Company
St. Louis, MO, USA, 63178

Coagulant – Ca^{2+}
Calcium Chloride Dihydrate
$CaCl_2 \cdot 2H_2O$
BHD Inc
Toronto, ON, CAN, M8Z 1K5

The following materials were employed during the experimental testing of the homogeneous kaolin clay-water slurries with the SRC flume apparatus in 2006.

Clay

KT Kaolin Clay
Kentucky-Tennessee Clay Company
Mayfield, KY, USA, 42066

Water

Saskatoon Tap Water
Saskatoon, SK Canada

Polishing Sand

Torpedo Sand
Sand with a fine aggregate
Washed and Screened (-3/8")
Inland Aggregates Limited
Saskatoon, SK, S7N 3A5

Chemicals
Dispersant – TSPP
Tetrasodium Pyrophosphate
$Na_4P_2O_7$
Sigma-Aldrich Company
St. Louis, MO, USA, 63178

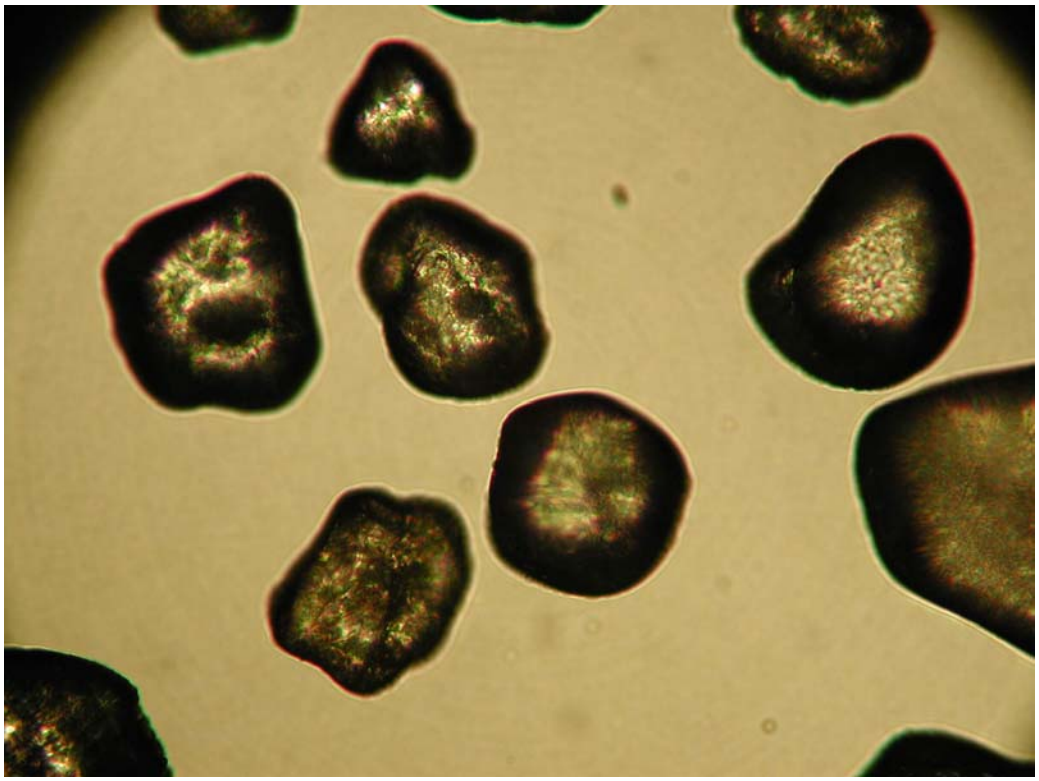

Figure B.1: Photomicrograph of the Unimin round grain sand used in the experimental tests (Granusil 5010, d_{50} = 188 μm)

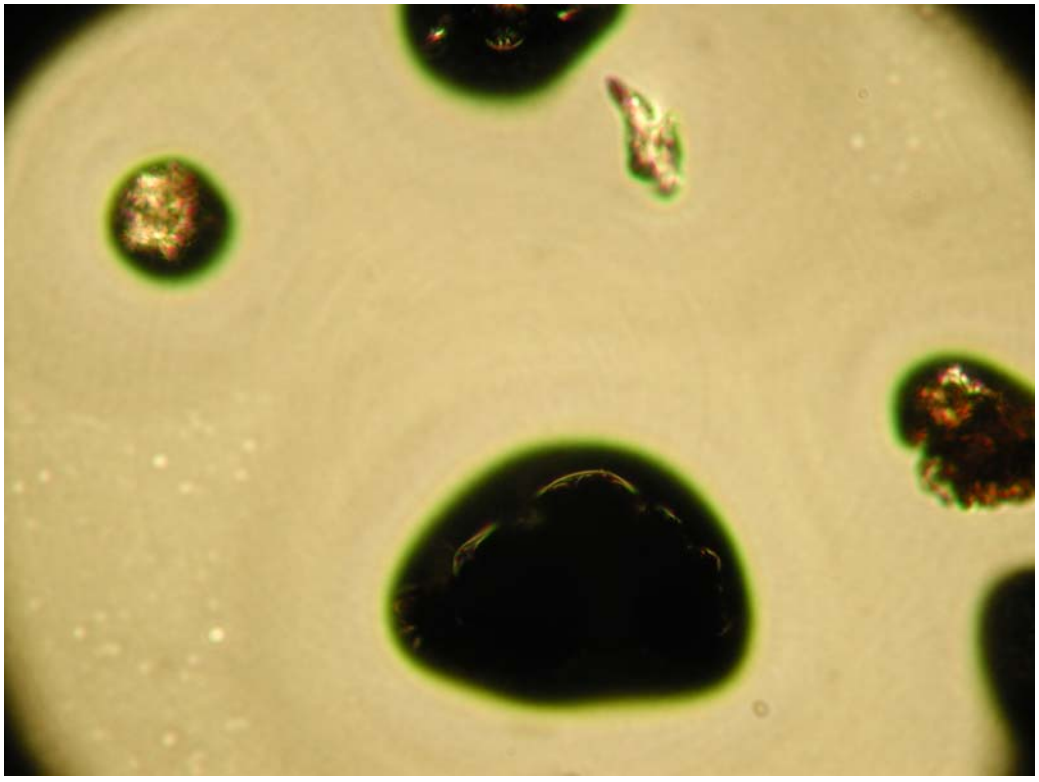

Figure B.2: Photomicrograph of the sand from Syncrude oil sand washed tailings

APPPENDIX C:
CALIBRATIONS

Magnetic Flowmeter Calibration

Instrument Description:	2" Magnetic Flux Flowmeter
Instrument Location:	Flume - 53 mm feed test section
Instrument Details:	The Foxboro Co. Ltd.
	La Salle, QC
Calibration Date:	July 4, 2002
Calibration Method:	Bucket & Stopwatch with Water
Calibrated By:	Ryan, Dan, Chad, Paul

Data Point	Elapsed Time (s)	Accumulated Weight (kg)	Water Density (kg/m^3)	Voltage Reading (volts)	Volumetric Flowrate (L/s)
1	61.2	0.0	998.0	0.966	0.000
2	108.2	134.7	997.1	1.472	1.249
3	53.9	128.3	999.0	1.919	2.383
4	35.5	137.5	997.8	2.547	3.884
5	29.5	151.9	997.6	3.072	5.167
6	19.0	135.8	998.1	3.905	7.156

Linear Calibration Curve

Slope (L/s/volt)	2.4349
Zero (volts)	0.9554
Corr. Coef. (R^2)	0.99995
Zeroing Instrument:	No

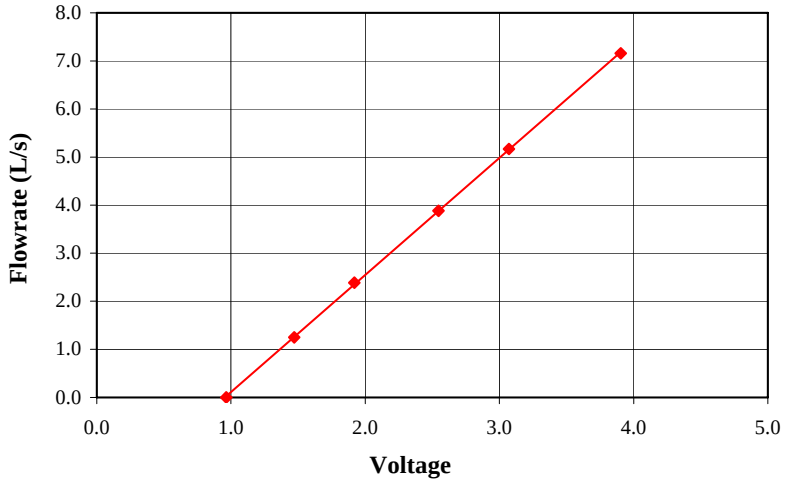

Temperature Sensor Calibration

Instrument Description:	Temperature Sensor (RTD #71)
Instrument Location:	Flume - 53mm feed test section
Instrument Details:	Aircom
	Edmonton, AB
Calibration Date:	July 5, 2002
Calibration Method:	Liquid (Mercury) in Glass Thermometer in Water
Calibrated By:	Ryan, Chad

Data Point	Voltage Reading (volts)	Water Temperature (^{o}C)
1	1.640	11.0
2	4.218	56.8
3	2.211	21.0
4	3.195	38.7

Linear Calibration Curve

Slope (^{o}C/volt)	17.7960
Zero (volts)	1.0249
Corr. Coef. (R^2)	0.99999
Zeroing Instrument:	No

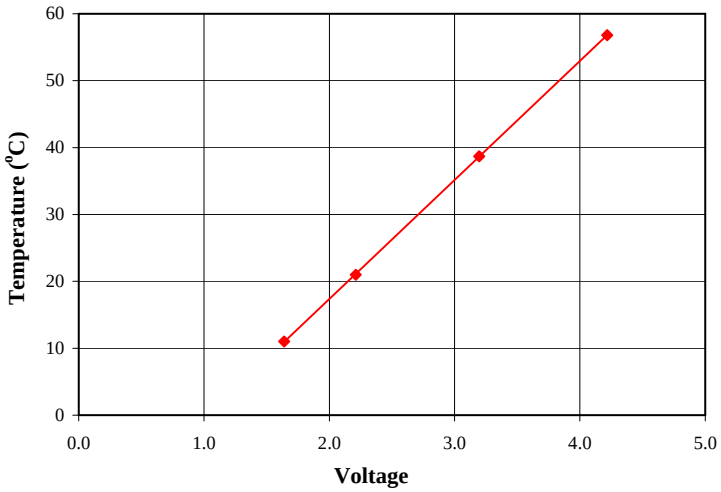

Densitometer Preliminary Calibration

Instrument Description:	Ronan Densitometer (Source #4)
Instrument Location:	Flume - 53mm feed test section
Instrument Details:	Ronan Engineering Ltd.
	Toronto, ON
	CS 137
Calibration Date:	July 5, 2002
Calibration Method:	Shutter Open and Shutter Closed
Calibrated By:	Ryan, Chad, Paul

Data Point	Voltage Reading (volts)	Observed Density (kg/m^3)
1	4.950	2000
2	0.979	500

Linear Calibration Curve

Slope (kg/m^3/volt)	377.7576
Zero (volts)	-0.3446
Corr. Coef. (R^2)	1.00000
Zeroing Instrument:	No

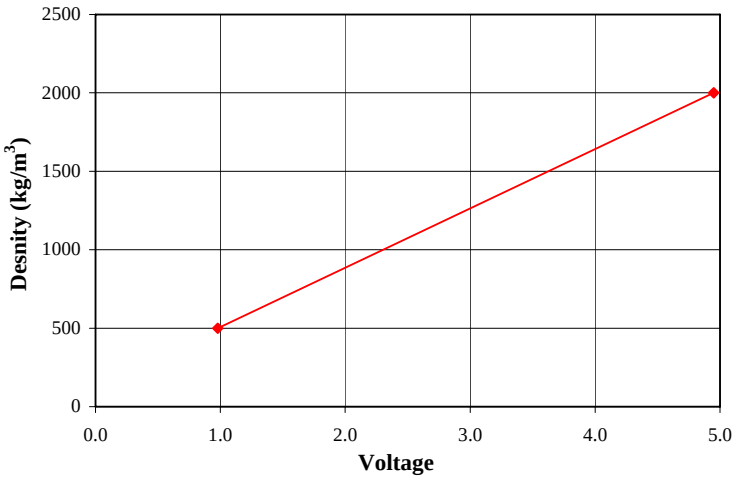

Pressure Transducer Calibration

Instrument Description:	Pressure Transducer (#15, 50 psi)
Instrument Location:	Flume - 53mm feed test section
Instrument Details:	Validyne Engineering
	Northridge, CA
Calibration Date:	July 8, 2002
Calibration Method:	Dead Weight Tester
	Double Area Gage Tester
	The Ashton Valve Co.
	Boston, MA
Calibrated By:	Ryan, Chad, Paul

Data Point	Voltage Reading (volts)	Dead Weight Pressure (psi)
1	0.010	0.0
2	1.008	10.0
3	2.019	20.0
4	3.028	30.0
5	4.017	40.0
6	4.496	45.0

Linear Calibration Curve

Slope (psi/volt)	10.0052
Zero (volts)	0.0143
Corr. Coef. (R^2)	0.99998
Zeroing Instrument:	Yes
Test Section Length (m)	4.877
Conversion (kPa/psi)	6.895

Adjusted Parameters (Pressure Gradient)

Slope (kPa/m/volt)	14.1450

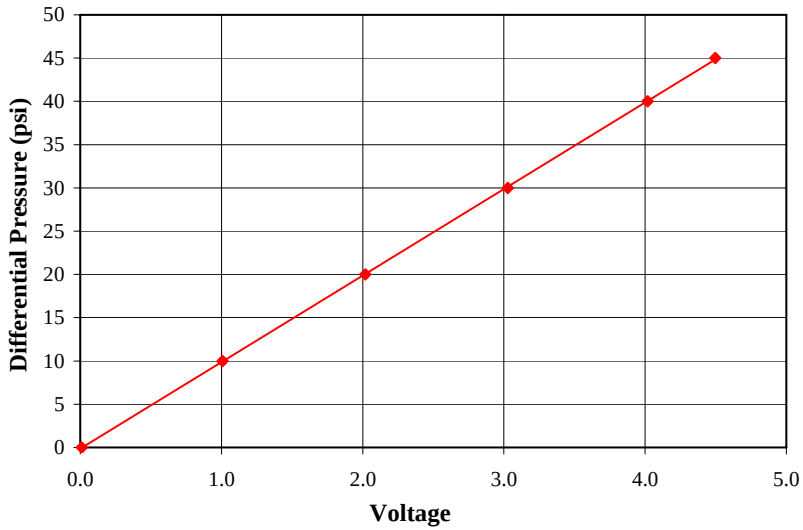

Pressure Transducer Calibration

Instrument Description:	Pressure Transducer (#17, 5 psi)
Instrument Location:	Flume - Pitot Tube
Instrument Details:	Validyne Engineering
	Northridge, CA
Calibration Date:	July 8, 2002
Calibration Method:	Merium Fluid (S = 1.75) Manometer
Calibrated By:	Ryan, Paul

Data Point	High Side (cm)	Low Side (cm)	Voltage Reading (volts)	Differential Pressure (kPa)
1	169.6	57.9	4.276	32.292
2	160.4	67.4	3.572	26.886
3	150.1	77.5	2.794	20.989
4	139.9	87.6	2.020	15.120
5	130.0	97.4	1.268	9.425
6	119.4	107.8	0.450	3.354
7	113.0	113.0	0.0	0.000

Linear Calibration Curve

Slope (kPa/volt)	7.5573
Zero (volts)	0.0121
Corr. Coef. (R^2)	0.99999
Zeroing Instrument:	Yes

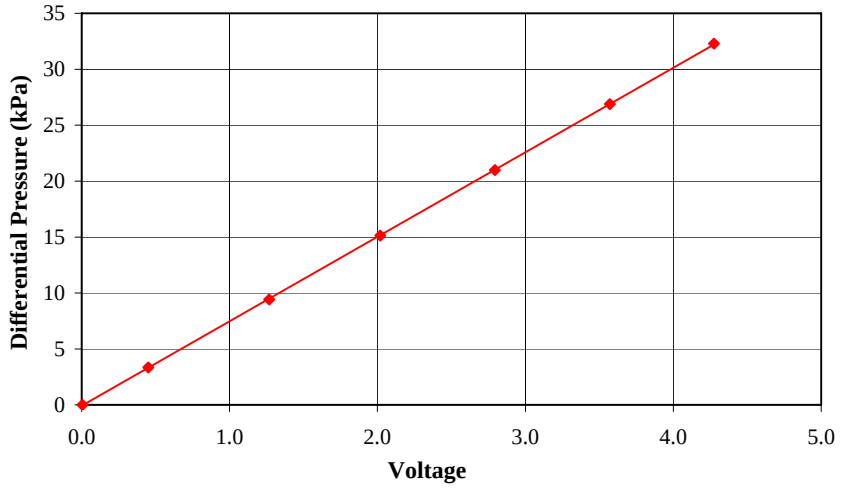

Depth of Flow Measurement Calibration

Instrument Description:	Depth of Flow Measurement Instruments
Instrument Location:	Flume Test Section
Instrument Details:	Zero Positions at Planes 1 & 2
	Separated by 5.84 m
Calibration Date:	July 16, 2002
Calibration Method:	Digital Vernier Calipers
	Mitutoyo Corporation
	Tokyo, Japan
Calibrated By:	Ryan

Data Point	Position 1 (mm)	Position 2 (mm)
1	48.57	52.42
2	48.56	52.47
3	48.59	52.46
4	48.58	52.36
5	48.55	52.48
6	48.55	52.45
7	48.56	52.45
8	48.57	52.39
AVG	*48.57*	*52.44*
STD DEV	*0.014*	*0.042*

Pitot Tube ID Calibration

Instrument Description:	Pitot Static Tube Opening Diameter
Instrument Location:	Flume - Pitot Tube
Instrument Details:	United Sensor Corporation Amherst, NH
Calibration Date:	September 17, 2002
Calibration Method:	detailed below
OD Measurement:	Digital Vernier Calipers Mitutoyo Corporation Tokyo, Japan
Software:	Adobe Photoshop 7.0 San Jose, CA
Camera:	Nikon Coolpix 990 Mississauga, ON
Calibrated By:	Ryan

Figure C.1: Sample digital photograph of the flume Pitot-static tube tip (2002)

OD (mm) 4.71

Picture	OD (pixels)		ID (pixels)		ID (mm)		Average Diameter (mm)	β (d/D)
	Horizontal	Vertical	Horizontal	Vertical	Horizontal	Vertical		
1	268	270	101	104	1.78	1.81	1.79	0.381
2	411	415	158	162	1.81	1.84	1.82	0.387
3	414	416	161	168	1.83	1.90	1.87	0.396
						AVG	*1.83*	*0.388*
						STD DEV	*0.04*	*0.0077*

Traversing Gamma Steel Plate Absorption Calibration

Instrument Description:	Ronan Traversing Gamma Ray Densitometer
Instrument Location:	Flume
Instrument Details:	Ronan Engineering Ltd.
	Toronto, ON
	Cs 137
Calibration Date:	July 3, 2002
Calibration Method:	Steel Plate Calibration
Calibrated By:	Ryan
Corrected for:	Background radiation (120 s duration counts)
Calibrated Against:	Unattenuated air counts (60 s duration)

Background:	
Counts/s	0.588
Unattenuated Air:	
Counts/s	11456.3
Corrected Counts/s	11455.7

Linear Calibration $\mu(cm^{-1}) = 6.9676x10^{-5}\rho(kg/m^3) + 1.5457x10^{-2}$

Steel Density (kg/m^3)	8020	
Steel Absorption (cm^{-1})	0.5743	correlation
Slope (cm^{-1})	0.5736	predicted
Intercept	-0.0574	
Corr. Coef. (R^2)	0.99997	
Difference (%)	-0.115	

Material	Density (kg/m^3)	Absorption (cm^{-1})
Water	1000	0.0851
Sand	2650	0.2001
Clay	2696	0.2033

Data Point	Thickness (cm)	Corrected (Counts/s)	-ln(N/N$_0$)
1	7.003	214.5	3.978
2	2.540	2857.1	1.389
3	5.083	660.0	2.854
4	4.460	950.4	2.489
5	9.543	51.6	5.402
6	1.920	4031.0	1.044
7	7.623	149.4	4.340
8	1.278	5802.2	0.680
9	0.643	8225.0	0.331
10	6.360	316.0	3.591
11	3.183	1980.3	1.755
12	8.265	105.3	4.689
13	8.900	73.9	5.043
14	3.818	1376.1	2.119
15	5.725	455.9	3.224

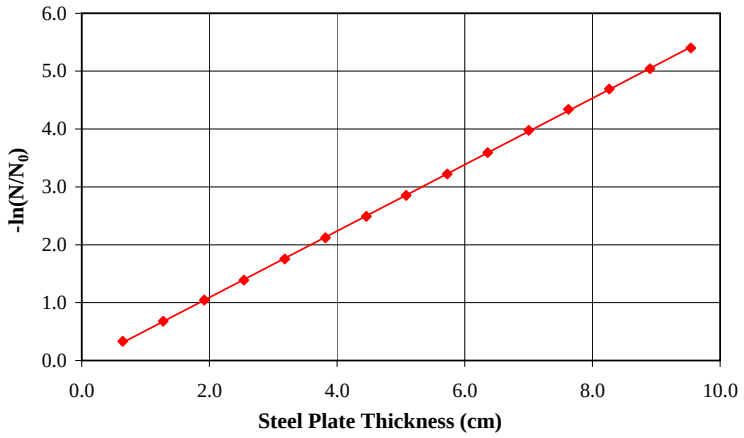

Traversing Gamma Path Length Calibration

Instrument Description:	Ronan Traversing Gamma Ray Densitometer	Pipe ID (mm)	156.7
Instrument Location:	Flume	Pipe OD (mm)	169.6
Instrument Details:	Ronan Engineering Ltd.	Top Wall Thickness (mm)	6.5
	Toronto, ON	Bottom Wall Thickness (mm)	6.4
	Cs 137	Outside Pipe Center (mm)	224.7 micrometer position
Calibration Date:	July 6, 2002	Inside Pipe Center (mm)	224.6 micrometer position
Calibration Method:	detailed below		
Measurement Positions:	Scans in Air		
Wall Thickness:	Scans in Water		
Path Length:	Scans in Water		
Calibrated By:	Ryan		
Corrected for:	Background radiation (120 s duration counts)		
Calibrated Against:	Unattenuated air counts (60 s duration)		

y/D		Micrometer Position (mm)	Wall Thickness (mm)	Path Length (mm)
top outside wall		309.5	n/a	n/a
1.00		303.0	5.78	1.67
0.95		295.1	2.70	6.15
0.90		287.3	2.04	8.99
0.85		279.5	1.72	10.84
0.80		271.6	1.56	12.11
0.75		263.8	1.45	13.06
0.70		256.0	1.38	13.80
0.65		248.1	1.33	14.39
0.60		240.3	1.30	14.81
0.55		232.5	1.27	15.06
0.50		224.6	1.27	15.11
0.45		216.8	1.28	14.98
0.40		208.9	1.30	14.67
0.35		201.1	1.34	14.22
0.30		193.3	1.43	13.63
0.25		185.4	1.48	12.91
0.20		177.6	1.59	12.00
0.15		169.8	1.76	10.75
0.10		161.9	2.08	8.86
0.05		154.1	2.75	5.85
0.00		146.2	5.69	0.97
bottom outside wall		139.9	n/a	n/a

Magnetic Flowmeter Calibration

Instrument Description:	2" Magnetic Flux Flowmeter
Instrument Location:	Flume - 53 mm feed test section
Instrument Details:	Brooks Mag 3570 Series
	Brooks Instrument Div.
	Emerson Electric Co.
	Statesboro, GA
Calibration Date:	February 16, 2006
Calibration Method:	Bucket & Stopwatch with Water
Calibrated By:	Ryan, Curtis, Paul

Data Point	Elapsed Time (s)	Accumulated Weight (kg)	Water Density (kg/m^3)	Voltage Reading (volts)	Volumetric Flowrate (L/s)
1	64.5	0.0	998.0	0.990	0.000
2	97.7	105.5	999.6	1.366	1.080
3	85.0	143.8	999.8	1.576	1.692
4	55.7	176.9	999.9	2.091	3.176
5	25.1	183.7	999.9	3.504	7.306
6	27.4	181.9	1000.0	3.272	6.650

Linear Calibration Curve

Slope (L/s/volt)	2.9139
Zero (volts)	0.9946
Corr. Coef. (R^2)	0.99999
Zeroing Instrument:	No

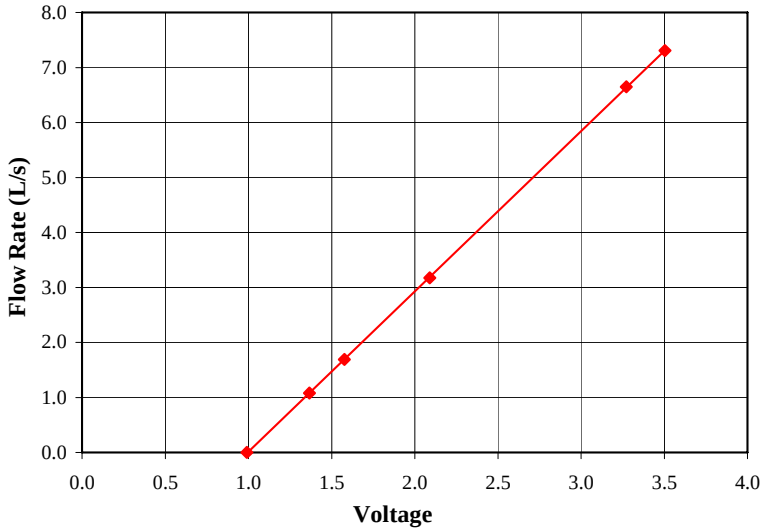

Temperature Sensor Calibration

Instrument Description:	Temperature Sensor (RTD #71)
Instrument Location:	Flume - 53 mm feed test section
Instrument Details:	Aircom
	Edmonton, AB
Calibration Date:	March 27, 2006
Calibration Method:	Liquid (Mercury) in Glass Thermometer in Water
Calibrated By:	Ryan

Linear Calibration Curve

Slope (^{o}C/volt)	17.4957
Zero (volts)	0.9959
Corr. Coef. (R^2)	0.99998
Zeroing Instrument:	No

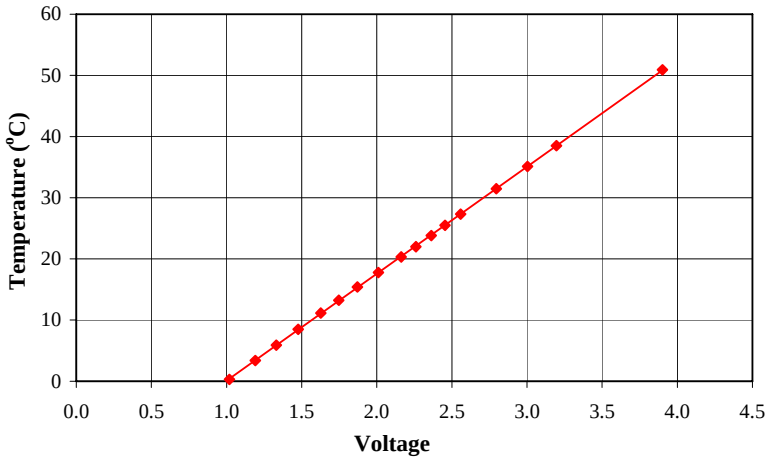

Data Point	Voltage Reading (volts)	Water Temperature (^{o}C)
1	3.901	50.9
2	3.196	38.5
3	3.003	35.1
4	2.795	31.5
5	2.558	27.3
6	2.454	25.5
7	2.362	23.8
8	2.260	22.0
9	2.162	20.3
10	2.010	17.8
11	1.871	15.4
12	1.746	13.3
13	1.627	11.2
14	1.477	8.5
15	1.331	5.9
16	1.192	3.4
17	1.020	0.3

Pressure Transducer Calibration

Instrument Description:	Pressure Transducer (#22, 20 psi)
Instrument Location:	Flume - 53 mm feed test section
Instrument Details:	Validyne Engineering
	Northridge, CA
Calibration Date:	February 10, 2006
Calibration Method:	Merium Fluid (S = 2.95) Manometer
Calibrated By:	Ryan, Paul, Curtis

Data Point	High Side (cm)	Low Side (cm)	Voltage Reading (volts)	Differential Pressure (kPa)
1	186.5	34.0	3.493	44.088
2	171.3	49.8	2.781	35.126
3	155.4	65.9	2.053	25.874
4	140.0	81.0	1.358	17.057
5	125.3	95.4	0.690	8.644
6	110.1	110.1	0.006	0.000

Linear Calibration Curve

Slope (kPa/volt)	12.6520
Zero (volts)	0.0071
Corr. Coef. (R^2)	1.00000
Zeroing Instrument:	Yes
Test Section Length (m)	4.877

Adjusted Parameters (Pressure Gradient)

Slope (kPa/m/volt)	2.5943

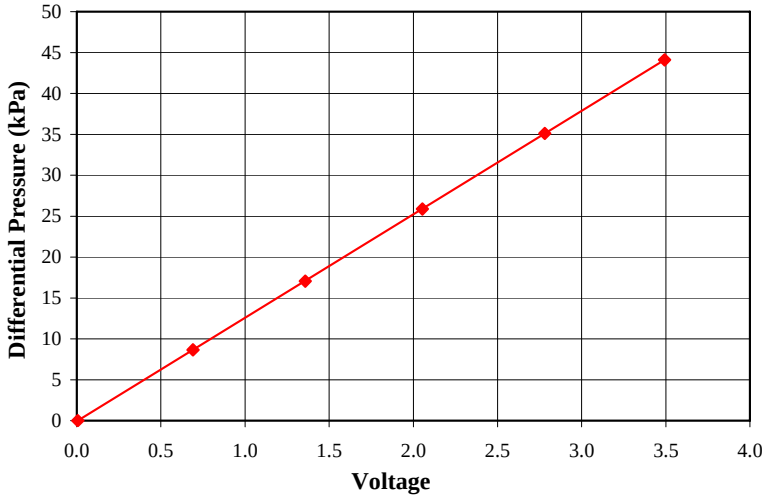

Pressure Transducer Calibration

Instrument Description:	Pressure Transducer (#4, 5 psi)
Instrument Location:	Flume - Pitot Tube
Instrument Details:	Validyne Engineering
	Northridge, CA
Calibration Date:	February 10, 2006
Calibration Method:	Merium Fluid (S = 2.95) Manometer
Calibrated By:	Ryan, Paul, Curtis

Data Point	High Side (cm)	Low Side (cm)	Voltage Reading (volts)	Differential Pressure (kPa)
1	163.3	57.7	4.439	30.529
2	150.5	70.6	3.365	23.099
3	139.9	81.2	2.478	16.970
4	129.7	91.3	1.623	11.101
5	120.1	100.9	0.813	5.551
6	110.3	110.3	0.004	0.000

Linear Calibration Curve

Slope (kPa/volt)	6.8820
Zero (volts)	0.0072
Corr. Coef. (R^2)	1.00000
Zeroing Instrument:	Yes

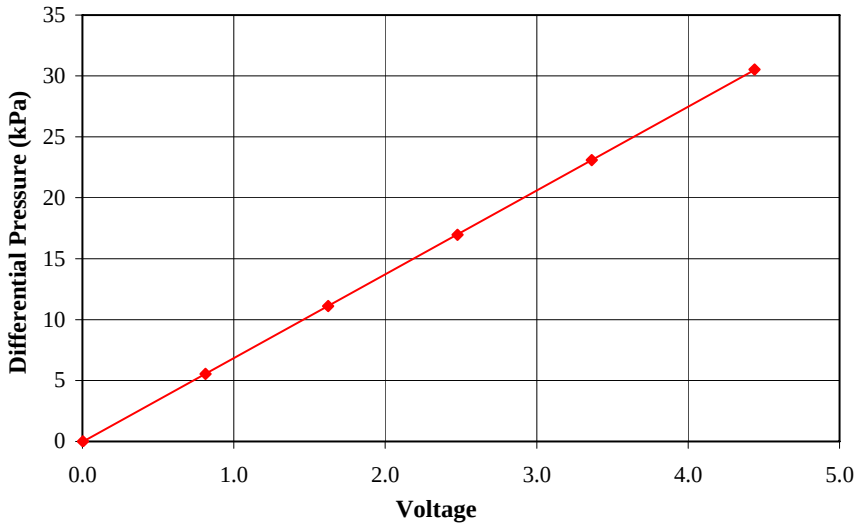

HPLC Pump Flowrate Calibration

Instrument Description:	HPLC Pump, Model No. 510
Instrument Location:	Flume - Pitot Tube
Instrument Details:	Waters Corporation
	Milford, MA
Calibration Date:	April 24, 2006
Calibration Method:	Bucket & Stopwatch with Water
Calibrated By:	Ryan

Linear Calibration Curve

Slope (n/a)	0.8536
Zero (n/a)	0.0000
Corr. Coef. (R^2)	0.99676
Zeroing Instrument:	No

Data Point	Elapsed Time (min)	Accumulated Weight (g)	Water Density (kg/m^3)	Specified Flowrate (mL/min)	Delivered Flowrate (mL/min)
1	5.00	0.00	997.8	0.0	0.00
2	5.01	33.28	997.7	8.0	6.66
3	5.01	29.19	997.7	7.0	5.84
4	5.01	26.00	997.6	6.0	5.20
5	5.01	21.60	997.6	5.0	4.33
6	5.01	18.03	997.6	4.0	3.61
7	5.01	13.57	997.6	3.0	2.72
8	5.01	9.10	997.6	2.0	1.82
9	5.01	4.50	997.6	1.0	0.90

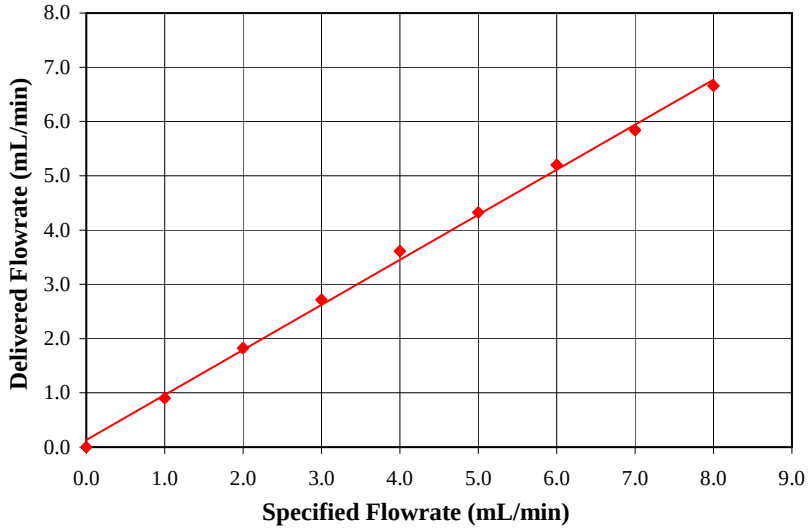

Depth of Flow Measurement Calibration

Instrument Description:	Depth of Flow Measurement Instruments
Instrument Location:	Flume Test Section
Instrument Details:	Zero Positions at Planes 1 & 2
	Separated by 5.84 m
Calibration Date:	March 31, 2006
Calibration Method:	Digital Vernier Calipers
	Mitutoyo Corporation
	Tokyo, Japan
Calibrated By:	Ryan

Data Point	Position 1 (mm)	Position 2 (mm)
1	48.56	52.44
2	48.54	52.44
3	48.55	52.42
4	48.53	52.43
5	48.54	52.42
6	48.55	52.44
7	48.53	52.45
8	48.55	52.44
9	48.56	52.43
10	48.55	52.46
AVG	*48.55*	*52.44*
STD DEV	*0.011*	*0.013*

Pitot Tube ID Calibration

Instrument Description:	Pitot Static Tube Opening Diameter
Instrument Location:	Flume - Pitot Tube
Instrument Details:	United Sensor Corporation
	Amherst, NH
Calibration Date:	April 2, 2006
Calibration Method:	detailed below
OD Measurement:	Digital Vernier Calipers
	Mitutoyo Corporation
	Tokyo, Japan
Software:	Adobe Photoshop 7.0
	San Jose, CA
Camera:	Fujifilm Finepix S3000Z
	Mississauga, ON
Calibrated By:	Ryan

Data Point	OD (mm)
1	4.73
2	4.73
3	4.72
4	4.73
5	4.72
6	4.75
7	4.76
8	4.73
9	4.73
10	4.73
AVG	*4.73*
STD DEV	*0.013*

Figure C.2: Sample digital photograph of the flume Pitot-static tube tip (2006)

Picture	OD (pixels)		ID (pixels)		ID (mm)		Average Diameter (mm)	β (d/D)
	Horizontal	Vertical	Horizontal	Vertical	Horizontal	Vertical		
1	162	162	63	62	1.84	1.81	1.83	0.386
2	149	150	58	57	1.84	1.80	1.82	0.385
3	170	171	65	64	1.81	1.77	1.79	0.378
4	193	195	72	74	1.77	1.80	1.78	0.376
5	173	174	65	69	1.78	1.88	1.83	0.386
6	171	171	66	68	1.83	1.88	1.85	0.392
7	174	173	66	68	1.80	1.86	1.83	0.386
8	175	176	67	70	1.81	1.88	1.85	0.390
						AVG	*1.82*	*0.385*
						STD DEV	*0.025*	*0.0053*

Magnetic Flowmeter Calibration (Water)

Instrument Description:	1" Magnetic Flow Transmitter
Instrument Location:	25 mm Vertical Pipe Loop
Instrument Details:	The Foxboro Co. Ltd.
	La Salle, QC
Calibration Date:	August 18, 2003
Calibration Method:	Bucket & Stopwatch with Water
Calibrated By:	Ryan, Andrew, Sun

Data Point	Elapsed Time (s)	Accumulated Weight (kg)	Water Density (kg/m^3)	Voltage Reading (volts)	Volumetric Flowrate (L/s)
1	11.2	0.0	998.0	0.732	0.000
2	50.8	29.0	990.4	1.335	0.576
3	34.4	32.0	988.5	1.712	0.940
4	26.9	34.0	988.0	2.056	1.279
5	23.6	39.8	987.1	2.475	1.704

Linear Calibration Curve

Slope (L/s/volt)	0.9763
Zero (volts)	0.7405
Corr. Coef. (R^2)	0.99991
Zeroing Instrument:	No

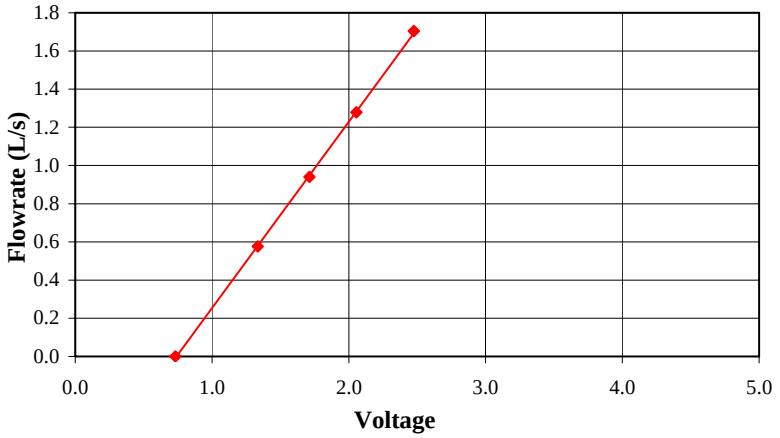

Magnetic Flowmeter Calibration (Glycol)

Instrument Description:	1" Magnetic Flow Transmitter
Instrument Location:	25 mm Vertical Pipe Loop
Instrument Details:	The Foxboro Co. Ltd.
	La Salle, QC
Calibration Date:	August 29, 2003
Calibration Method:	Bucket & Stopwatch with Glycol
Calibrated By:	Ryan, Chad

Data Point	Elapsed Time (s)	Accumulated Weight (kg)	Glycol Density (kg/m^3)	Voltage Reading (volts)	Volumetric Flowrate (L/s)
1	0.0	0.0	1123.8	0.693	0.000
2	50.7	15.2	1123.7	0.963	0.267
3	38.2	16.2	1123.7	1.080	0.378
4	33.6	22.5	1123.6	1.288	0.598
5	25.1	20.9	1123.4	1.426	0.741
6	0.0	0.0	1123.4	0.695	0.000

Linear Calibration Curve

Slope (L/s/volt)	1.0091
Zero (volts)	0.6967
Corr. Coef. (R^2)	0.99985
Zeroing Instrument:	No

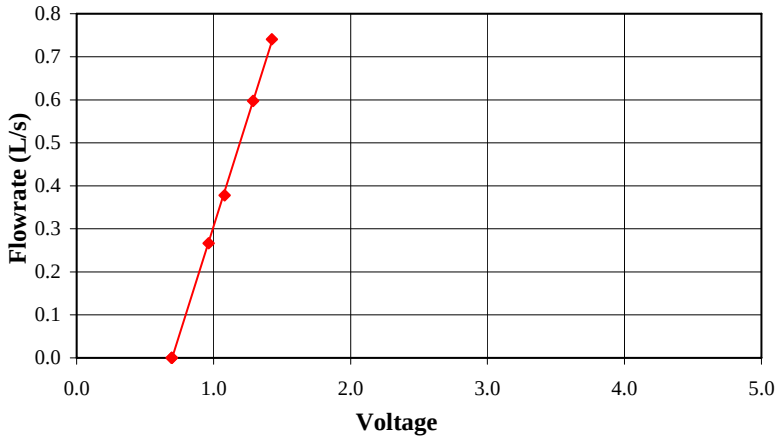

Magnetic Disc Counter (RPM) Calibration

Instrument Description:	Magentic Disc Counter (RPM)
Instrument Location:	Pump Speed - 25 mm Vertical Pipe Loop
Instrument Details:	Pulser Disc, Model No. 255
	Electro-Sensors
	Minnetonka, MN
Calibration Date:	August 29, 2003
Calibration Method:	Digital Photo Tachometer
	Extech Instruments, Model No. 461893
	Waltham, MA
Calibrated By:	Ryan, Chad

Data Point	Voltage Reading (volts)	Pump Speed (RPM)
1	0.990	0.0
2	1.338	87.4
3	1.477	123.1
4	1.760	194.4
5	1.946	241.6
6	0.990	0.0

Linear Calibration Curve

Slope (RPM/volt)	252.6045
Zero (volts)	0.9904
Corr. Coef. (R^2)	1.00000
Zeroing Instrument:	No

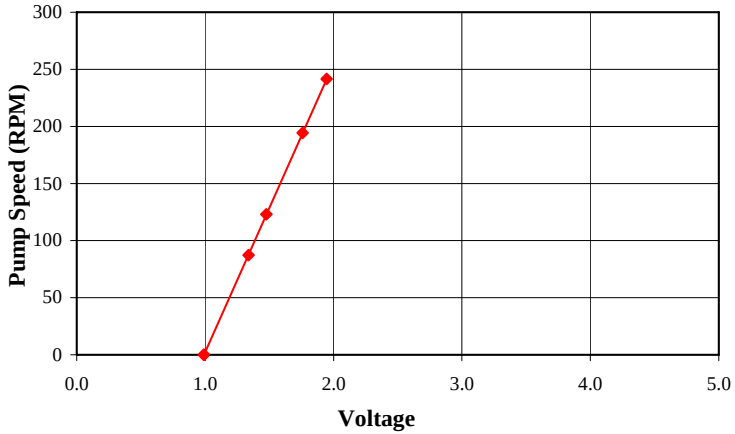

Moyno Pump Calibration (Glycol)

Instrument Description:	1" Moyno Progressive Cavity Pump
Instrument Location:	25 mm Vertical Pipe Loop
Instrument Details:	Model No: 316L CDQ
	Moyno Progressive Cavity Pumps
	Springfield, OH
Calibration Date:	August 29, 2003
Calibration Method:	Bucket & Stopwatch of Glycol vs Pump Speed
Calibrated By:	Ryan, Chad

Data Point	Elapsed Time (s)	Accumulated Weight (kg)	Glycol Density (kg/m^3)	Pump Speed (RPM)	Volumetric Flowrate (L/s)
1	0.0	0.0	1123.8	0.0	0.000
2	50.7	15.2	1123.7	87.4	0.267
3	38.2	16.2	1123.7	123.1	0.378
4	33.6	22.5	1123.6	194.4	0.598
5	25.1	20.9	1123.4	241.6	0.741
6	0.0	0.0	1123.4	0.0	0.000

Linear Calibration Curve

Slope (L/s/RPM)	0.003070
Intercept (L/s)	-0.000256
Corr. Coef. (R^2)	1.00000
Zeroing Instrument:	No

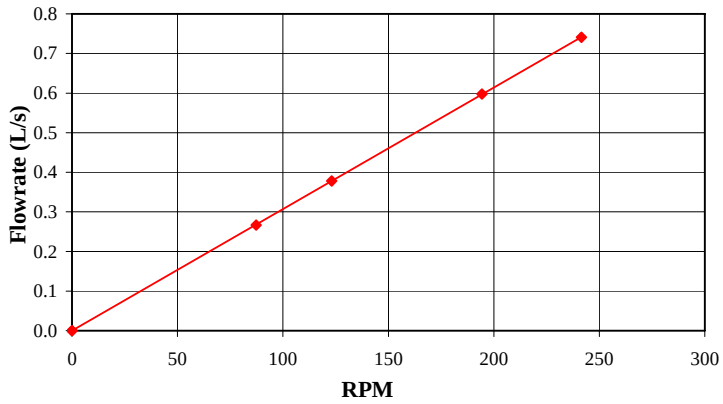

Temperature Sensor Calibration

Instrument Description:	Temperature Sesnor (RTD #73)
Instrument Location:	25 mm Vertical Pipe Loop
Instrument Details:	Aircom
	Edmonton, AB
Calibration Date:	August 19, 2003
Calibration Method:	Liquid (Mercury) in Glass Thermometer in Water
Calibrated By:	Ryan, Andrew

Linear Calibration Curve

Slope (^{o}C/volt)	17.4947
Zero (volts)	1.0098
Corr. Coef. (R^2)	0.99999
Zeroing Instrument:	No

Data Point	Voltage Reading (volts)	Water Temperature (^{o}C)
1	2.396	24.3
2	1.104	1.6
3	1.499	8.6
4	1.867	15.0
5	2.249	21.7
6	2.812	31.7
7	3.084	36.3
8	3.2791	39.8
9	3.7089	47.2
10	4.0346	52.8

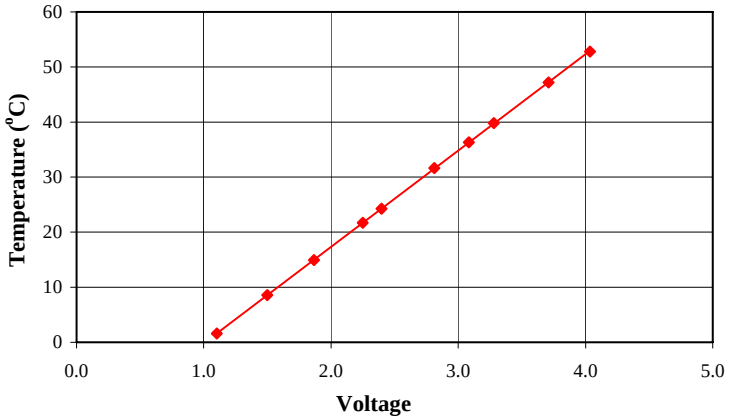

Pressure Transducer Calibration

Instrument Description:	Pressure Transducer (#14, 20 psi)
Instrument Location:	25 mm Vertical Pipe Loop - Up Test Section
Instrument Details:	Validyne Engineering
	Northridge, CA
Calibration Date:	August 14, 2003
Calibration Method:	Merium Fluid (S = 2.95) Manometer
Calibrated By:	Ryan, Sun

Linear Calibration Curve

Slope (kPa/volt)	28.9770
Zero (volts)	0.0144
Corr. Coef. (R^2)	1.00000
Zeroing Instrument:	Yes
Test Section Length (m)	1.830

Adjusted Parameters (Pressure Gradient)

Slope (kPa/m/volt)	15.8344

Data Point	High Side (cm)	Low Side (cm)	Voltage Reading (volts)	Differential Pressure (kPa)
1	171.9	12.2	1.608	46.169
2	160.8	23.4	1.385	39.722
3	149.8	34.3	1.166	33.391
4	140.0	44.1	0.971	27.725
5	130.5	53.5	0.783	22.261
6	119.7	64.3	0.568	16.016
7	110.5	73.5	0.384	10.697
8	101.0	82.9	0.195	5.233
9	91.9	91.9	0.014	0.000

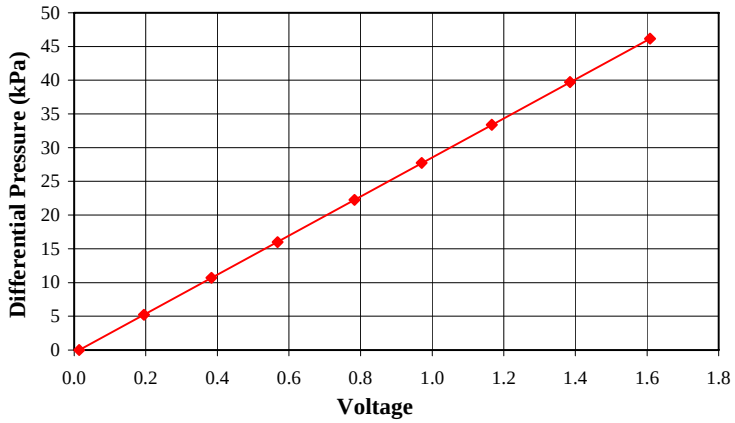

Pressure Transducer Calibration

Instrument Description:	Pressure Transducer (#16, 5 psi)
Instrument Location:	25 mm Vertical Pipe Loop - Pitot-Static
Instrument Details:	Validyne Engineering
	Northridge, CA
Calibration Date:	August 14, 2003
Calibration Method:	Merium Fluid (S = 2.95) Manometer
Calibrated By:	Ryan, Sun

Data Point	High Side (cm)	Low Side (cm)	Voltage Reading (volts)	Differential Pressure (kPa)
1	144.3	39.3	4.034	30.356
2	134.6	49.3	3.284	24.660
3	124.4	59.6	2.508	18.734
4	113.5	70.4	1.682	12.460
5	103.4	80.5	0.916	6.620
6	91.9	91.9	0.049	0.000

Linear Calibration Curve

Slope (kPa/volt)	7.6182
Zero (volts)	0.0479
Corr. Coef. (R^2)	1.00000
Zeroing Instrument:	Yes

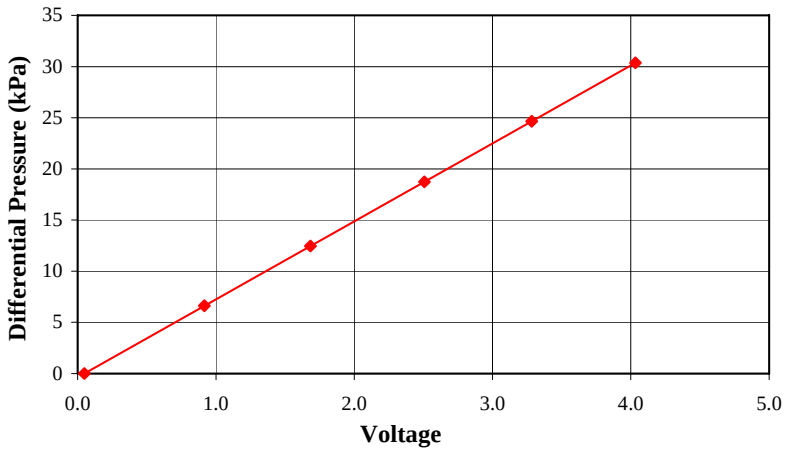

Pressure Transducer Calibration

Instrument Description:	Pressure Transducer (#15, 5 psi)
Instrument Location:	25 mm Vertical Pipe Loop - Pitot Wall
Instrument Details:	Validyne Engineering
	Northridge, CA
Calibration Date:	August 14, 2003
Calibration Method:	Merium Fluid (S = 2.95) Manometer
Calibrated By:	Ryan, Sun

Data Point	High Side (cm)	Low Side (cm)	Voltage Reading (volts)	Differential Pressure (kPa)
1	140.5	43.1	4.044	28.158
2	131.4	52.4	3.282	22.839
3	121.1	62.7	2.428	16.883
4	110.8	73.1	1.577	10.899
5	102.5	81.3	0.888	6.129
6	91.9	91.9	0.012	0.000

Linear Calibration Curve

Slope (kPa/volt)	6.9847
Zero (volts)	0.0124
Corr. Coef. (R^2)	1.00000
Zeroing Instrument:	Yes

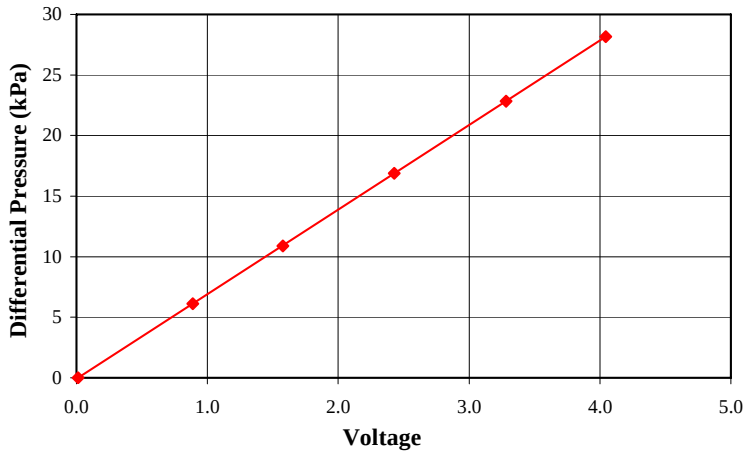

Pipe Diameter Calibration

Instrument Description:	Pipe ID - Downward Pitot Test Section (1" Pipe)
Instrument Location:	25 mm Vertical Pipe Loop - Pitot Wall
Calibration Date:	August 22, 2003
Calibration Method:	Volume determination by water addition deaired reverse osmosis water
Calibrated By:	Ryan, Andrew, Del

Water Addition:

Length of Pipe (cm)	152.45	5 feet
Beaker Full of Water (g)	1401.85	pipe empty
Water Remaining in Beaker (g)	487.74	pipe full
Water Temperature (^{o}C)	23.9	
Water Density (kg/m^{3})	997.4	
Water Mass Added (g)	914.11	
Volume Water Added (L)	0.91653	
Cross-sectional Area of Pipe (m^{2})	0.0006012	
ID of Pipe (m)	*0.02767*	

Micrometer Measurements:

Low (in)	1.075
High (in)	1.085
Average (in)	1.080
Average (m)	*0.02743*
Difference (%)	0.85

Pitot Tube ID Calibration

Instrument Description:	PSL - Pitot Static Tube Opening Diameter
Instrument Location:	25 mm Vertical Loop - Pitot Tube
Instrument Details:	United Sensor Corporation
	Instrument No: PCC-8-KL UEC 9117
	Amherst, NH
Calibration Date:	July 15, 2003
Calibration Method:	detailed below
OD Measurement:	Digital Vernier Calipers
	Mitutoyo Corporation
	Tokyo, Japan
Software:	Adobe Photoshop 7.0
	San Jose, CA
Camera:	Nikon Coolpix 990
	Mississauga, ON
Calibrated By:	Ryan

Data Point	OD (mm)
1	3.05
2	3.07
3	3.07
4	3.06
5	3.05
AVG	*3.06*
STD DEV	*0.010*

Figure C.3: Sample digital photograph of the PSL Pitot-static tube tip

Picture		OD (pixels)		ID (pixels)		ID (mm)		Average Diameter (mm)	β (d/D)
		Horizontal	Vertical	Horizontal	Vertical	Horizontal	Vertical		
1		185	186	65	74	1.08	1.22	1.15	0.375
2		171	180	59	69	1.06	1.17	1.11	0.364
3		170	183	62	70	1.12	1.17	1.14	0.374
4		173	185	59	70	1.04	1.16	1.10	0.360
							AVG	*1.13*	*0.368*
							STD DEV	*0.022*	*0.0073*

Pitot Tube ID Calibration

ıstrument Description:	PSS - Pitot Static Tube Opening Diameter
Instrument Location:	25 mm Vertical Loop - Pitot Tube
Instrument Details:	United Sensor Corporation
	Instrument No: PDA-8-F-6-KL
	Amherst, NH
Calibration Date:	July 15, 2003
Calibration Method:	detailed below
OD Measurement:	Digital Vernier Calipers
	Mitutoyo Corporation
	Tokyo, Japan
Software:	Adobe Photoshop 7.0
	San Jose, CA
Camera:	Nikon Coolpix 990
	Mississauga, ON
Calibrated By:	Ryan

Data Point	OD (mm)
1	1.62
2	1.63
3	1.63
4	1.62
5	1.62
AVG	*1.62*
STD DEV	*0.005*

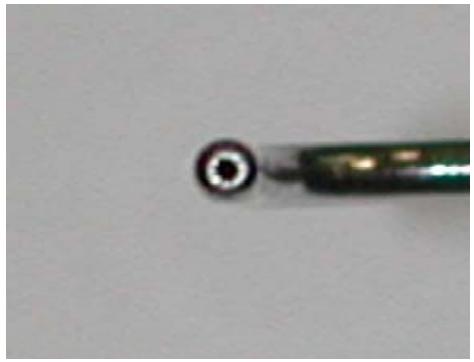

Figure C.4: Sample digital photograph of the PSS Pitot-static tube tip

Picture		OD (pixels)		ID (pixels)		ID (mm)		Average Diameter (mm)	β (d/D)
		Horizontal	Vertical	Horizontal	Vertical	Horizontal	Vertical		
1		83	91	29	31	0.57	0.55	0.56	0.345
2		81	89	24	27	0.48	0.49	0.49	0.300
3		86	89	27	31	0.51	0.57	0.54	0.331
4		83	87	25	27	0.49	0.50	0.50	0.306
							AVG	*0.52*	*0.320*
							STD DEV	*0.035*	*0.0213*

Ethylene Glycol Density Calibration

Instrument Description:	Glycol Density Determination
Instrument Location:	25 mm Vertical Pipe Loop
Calibration Date:	August 21, 2003
Calibration Method:	Liquid Pycnometry
	pycnometer volume determined with deaired re
	gravimetric analysis
Calibrated By:	Ryan

Data Point	Temperature (^oC)	Pyc Volume (mL)	Density (kg/m^3)
1	5.0	50.60	1133.4
2	10.0	50.60	1130.4
3	15.0	50.60	1126.7
4	20.0	50.60	1123.4
5	25.0	50.61	1119.7
6	30.0	50.61	1116.2
7	35.0	50.61	1112.8
8	40.0	50.62	1109.2
9	45.0	50.62	1105.7
10	50.0	50.62	1102.1

Linear Calibration Curve

Slope ($kg/m^3/^oC$)	-0.6997
Intercept (kg/m^3)	1137.2
Corr. Coef. (R^2)	0.99992

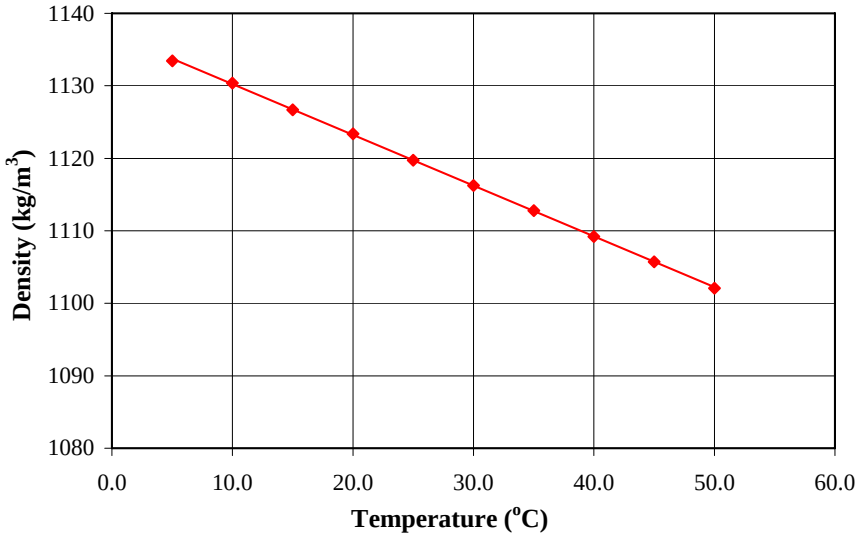

Ethylene Glycol Viscosity Calibration

Instrument Description:	Glycol Viscosity Determination
Instrument Location:	25 mm Vertical Pipe Loop
Calibration Date:	August 24, 2003
Calibration Method:	Concentric Cylinder Viscometry
	Haake Rheowin RS150
	Thermo Fisher Scientific, Inc.
	Waltham, MA
R_1 (m)	0.02071
R_2 (m)	0.021667
L (m)	0.055
Calibrated By:	Ryan

Data Point	Temperature (^oC)	Viscosity (mPa-s)	Inverse Temperature (K^{-1})	ln (Viscosity) [mPa-s]
1	5.2	45.1	0.00359	3.810
2	10.1	34.3	0.00353	3.534
3	15.0	27.3	0.00347	3.307
4	20.0	21.5	0.00341	3.070
5	25.0	17.5	0.00335	2.861
6	30.0	14.4	0.00330	2.668
7	35.0	12.0	0.00325	2.485
8	40.0	10.1	0.00319	2.315
9	45.0	8.6	0.00314	2.153
10	49.9	7.4	0.00310	2.000

Linear Calibration Curve

Slope (K)	3607.5
Intercept (n/a)	-9.206
Corr. Coef. (R^2)	0.99875

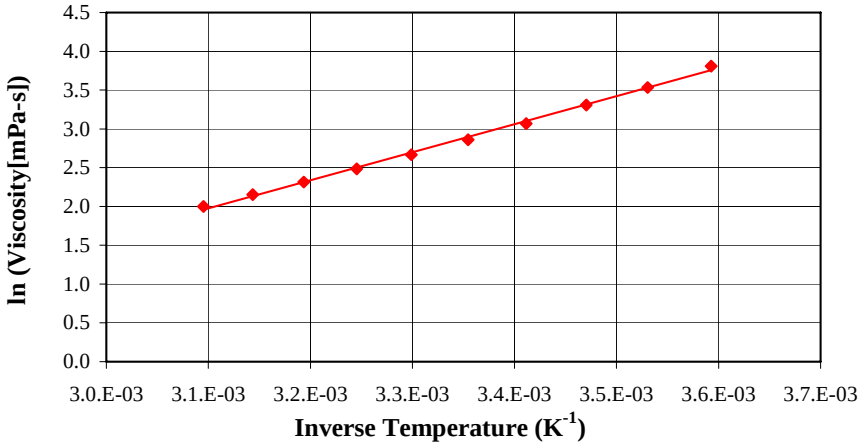

APPPENDIX D:
EXPERIMENTAL DATA

Table D.1: Pressure gradient versus velocity data for Saskatoon tap water to determine the roughness of the 53 mm pipe feed test section during the testing of the model tailings slurries

Saskatoon Tap Water							
Water001		Water002		Water004		Water006	
Velocity (m/s)	-dP/dz (kPa/m)	Velocity (m/s)	-dP/dz (kPa/m)	Velocity (m/s)	-dP/dz (kPa/m)	Velocity (m/s)	-dP/dz (kPa/m)
0.48	0.061	0.46	0.033	0.51	0.071	0.45	0.039
0.49	0.061	1.01	0.187	1.10	0.257	0.68	0.097
0.99	0.206	1.34	0.332	1.10	0.258	0.91	0.175
1.51	0.443	1.66	0.502	1.44	0.414	1.14	0.278
2.01	0.755	2.02	0.739	2.03	0.791	1.35	0.389
2.50	1.140	2.40	1.024	2.51	1.175	1.58	0.529
2.98	1.579	2.65	1.246	2.51	1.171	1.82	0.702
3.98	2.729	3.00	1.577	2.97	1.615	2.04	0.880
--	--	3.31	1.906	3.59	2.305	2.29	1.107
--	--	3.69	2.353	3.99	2.813	2.48	1.289
--	--	4.03	2.776	--	--	2.72	1.509
--	--	4.39	3.272	--	--	2.97	1.788
--	--	--	--	--	--	3.17	2.026
--	--	--	--	--	--	3.40	2.304
--	--	--	--	--	--	3.65	2.615
--	--	--	--	--	--	3.85	2.821
--	--	--	--	--	--	4.09	3.150
--	--	--	--	--	--	4.31	3.468
ε (μm)	23.4	ε (μm)	22.4	ε (μm)	28.2	ε (μm)	46.7
T (^{o}C)	24.2	T (^{o}C)	25.5	T (^{o}C)	23.4	T (^{o}C)	24.6

Table D.2: Pressure gradient versus velocity data for a 25% v/v sand-water slurry in the 53 mm pipe feed test section

25% v/v Sand-Water											
SandWater001		SandWater004		SandWater005		SandWater006		SandWater007		SandWater008	
Velocity (m/s)	-dP/dz (kPa/m)	Velocity (m/s)	-dP/dz (kPa/m)	Velocity (m/s)	-dP/dz (kPa/m)	Velocity (m/s)	-dP/dz (kPa/m)	Velocity (m/s)	-dP/dz (kPa/m)	Velocity (m/s)	-dP/dz (kPa/m)
1.84	1.154	2.26	1.559	2.70	1.987	2.71	1.977	2.25	1.532	2.94	2.291
1.62	1.104	2.03	1.370	2.70	1.992	2.70	1.980	2.25	1.537	2.93	2.285
1.24	1.191	1.82	1.202	2.48	1.784	2.47	1.728	2.24	1.531	2.93	2.292
1.54	1.054	1.71	1.146	2.26	1.568	2.26	1.533	2.24	1.535	2.93	2.292
1.56	1.035	1.69	1.129	2.03	1.370	2.04	1.342	2.24	1.530	2.93	2.294
1.55	1.021	--	--	1.81	1.206	1.79	1.167	2.24	1.530	--	--
--	--	--	--	2.72	2.047	1.57	1.038	2.03	1.367	--	--
--	--	--	--	2.49	1.793	2.70	1.976	2.03	1.369	--	--
--	--	--	--	2.27	1.576	2.48	1.735	2.03	1.366	--	--
--	--	--	--	2.04	1.386	2.26	1.533	1.75	1.190	--	--
--	--	--	--	1.82	1.221	2.04	1.343	1.75	1.200	--	--
--	--	--	--	1.72	1.162	1.80	1.167	1.76	1.182	--	--
--	--	--	--	2.68	1.996	1.60	1.046	2.71	2.003	--	--
--	--	--	--	2.50	1.795	2.70	1.999	2.72	2.004	--	--
--	--	--	--	2.27	1.579	2.47	1.754	2.72	2.000	--	--
--	--	--	--	2.16	1.478	2.30	1.591	2.47	1.750	--	--
--	--	--	--	--	--	2.05	1.368	2.47	1.745	--	--
--	--	--	--	--	--	1.83	1.201	2.53	1.817	--	--
--	--	--	--	--	--	1.57	1.066	2.53	1.817	--	--
--	--	--	--	--	--	2.72	2.009	2.53	1.820	--	--
--	--	--	--	--	--	2.48	1.745	--	--	--	--
--	--	--	--	--	--	2.24	1.511	--	--	--	--
--	--	--	--	--	--	2.04	1.345	--	--	--	--
--	--	--	--	--	--	1.79	1.160	--	--	--	--
--	--	--	--	--	--	1.54	1.009	--	--	--	--
--	--	--	--	--	--	2.70	1.965	--	--	--	--
--	--	--	--	--	--	2.48	1.726	--	--	--	--
--	--	--	--	--	--	2.44	1.686	--	--	--	--
--	--	--	--	--	--	2.39	1.640	--	--	--	--
--	--	--	--	--	--	2.35	1.596	--	--	--	--
--	--	--	--	--	--	2.69	1.963	--	--	--	--
--	--	--	--	--	--	2.49	1.754	--	--	--	--
--	--	--	--	--	--	2.49	1.754	--	--	--	--
--	--	--	--	--	--	2.35	1.625	--	--	--	--
--	--	--	--	--	--	2.26	1.541	--	--	--	--
--	--	--	--	--	--	2.03	1.352	--	--	--	--
--	--	--	--	--	--	1.81	1.195	--	--	--	--
--	--	--	--	--	--	1.76	1.147	--	--	--	--
T (^{o}C)	27.0	**T (^{o}C)**	24.8	**T (^{o}C)**	26.0	**T (^{o}C)**	24.5	**T (^{o}C)**	23.0	**T (^{o}C)**	22.8

Table D.3: Pressure gradient versus velocity data for a CT 'no gypsum' model tailings slurry in the 53 mm pipe feed test section

CT 'No Gypsum'					
0.00% TSPP		0.05% TSPP		0.10% TSPP	
Velocity (m/s)	-dP/dz (kPa/m)	Velocity (m/s)	-dP/dz (kPa/m)	Velocity (m/s)	-dP/dz (kPa/m)
0.95	*2.132*	*1.12*	*1.610*	1.39	0.966
1.44	*2.341*	*1.29*	*1.660*	1.16	0.720
1.73	*2.437*	*1.51*	*1.736*	1.61	1.214
2.07	*2.540*	*1.76*	*1.745*	1.73	1.380
2.33	*2.629*	1.96	1.885	1.96	1.669
2.63	2.845	2.17	2.11	2.18	1.984
2.98	3.350	2.40	2.54	2.44	2.358
3.29	4.070	2.63	2.96	2.63	2.669
3.53	4.575	2.94	3.57	2.87	3.070
3.77	5.104	3.18	4.04	3.07	3.424
4.01	5.605	3.39	4.47	3.39	4.005
4.20	6.057	3.64	5.03	3.63	4.470
--	--	3.85	5.48	3.86	4.949
T (^{o}C)	27.2	T (^{o}C)	25.8	T (^{o}C)	25.4

laminar data points in *italics*

Table D.4: Pressure gradient versus velocity data for a CT 'gypsum' model tailings slurry in the 53 mm pipe feed test section

CT 'Gypsum'							
0.005% Ca^{2+}		0.0125% TSPP		Gypsum01		Gypsum02	
Velocity (m/s)	-dP/dz (kPa/m)	Velocity (m/s)	-dP/dz (kPa/m)	Velocity (m/s)	-dP/dz (kPa/m)	Velocity (m/s)	-dP/dz (kPa/m)
1.16	*1.717*	*1.17*	*1.135*	*1.16*	*1.211*	*1.11*	*1.446*
1.39	*1.767*	*1.41*	*1.168*	*1.28*	*1.123*	*1.19*	*1.438*
1.61	*1.759*	1.61	1.497	1.38	1.158	*1.27*	*1.450*
1.84	*1.860*	1.82	1.879	1.46	1.240	*1.37*	*1.473*
2.04	2.187	2.04	2.275	1.59	1.442	*1.44*	*1.451*
2.28	2.692	2.27	2.73	1.70	1.624	1.51	1.445
2.49	3.124	2.51	3.20	1.85	1.906	1.63	1.514
2.75	3.696	2.73	3.64	2.05	2.287	1.72	1.633
2.96	4.154	2.95	4.10	2.28	2.726	1.82	1.819
3.19	4.683	3.16	4.56	2.49	3.165	2.01	2.192
3.39	5.158	3.40	5.09	2.71	3.628	2.25	2.694
3.64	5.757	3.62	5.57	2.95	4.129	2.46	3.135
--	--	3.28	4.78	3.17	4.622	2.73	3.708
--	--	3.06	4.31	--	--	--	--
T (^{o}C)	20.5	T (^{o}C)	18.1	T (^{o}C)	20.3	T (^{o}C)	24.6

laminar data points in *italics*

Table D.5: Pressure gradient versus velocity data for a model Thickened Tailings slurry in the 53 mm pipe feed test section

Thickened Tailings							
TT01		TT02		TT03		TT04	
Velocity (m/s)	-dP/dz (kPa/m)	Velocity (m/s)	-dP/dz (kPa/m)	Velocity (m/s)	-dP/dz (kPa/m)	Velocity (m/s)	-dP/dz (kPa/m)
0.53	*3.342*	*0.75*	*4.577*	*0.93*	*4.793*	*0.86*	*5.213*
0.71	*3.485*	*0.92*	*4.701*	*1.11*	*4.924*	*1.01*	*5.381*
0.81	*3.597*	*1.12*	*4.837*	*1.40*	*5.126*	*0.93*	*5.247*
0.94	*3.690*	*1.43*	*5.051*	*1.60*	*5.254*	*1.18*	*5.447*
1.18	*3.850*	*1.62*	*5.175*	*1.79*	*5.362*	*1.32*	*5.554*
1.30	*3.917*	*1.83*	*5.29*	*2.04*	*5.500*	*1.61*	*5.747*
1.40	*3.987*	*1.98*	*5.37*	*2.29*	*5.621*	*1.82*	*5.885*
1.52	*4.067*	*2.14*	*5.47*	*2.51*	*5.739*	*2.07*	*6.032*
1.71	*4.171*	*2.30*	*5.54*	*2.74*	*5.855*	*2.28*	*6.150*
1.85	*4.254*	*2.50*	*5.65*	*2.94*	*5.953*	*2.50*	*6.260*
2.04	*4.351*	*2.71*	*5.76*	*3.17*	*6.056*	*2.74*	*6.382*
2.21	*4.437*	*2.89*	*5.85*	*3.44*	*6.153*	*2.96*	*6.501*
2.47	*4.559*	*3.05*	*5.93*	*3.64*	*6.251*	*3.19*	*6.611*
2.36	*4.527*	*3.18*	*5.99*	*3.89*	*6.379*	*3.41*	*6.717*
2.69	*4.669*	--	--	4.09	6.550	*3.63*	*6.823*
2.80	*4.722*	--	--	4.18	6.687	*3.85*	*6.924*
2.99	*4.826*	--	--	4.29	6.845	*4.08*	*7.031*
3.21	*4.934*	--	--	--	--	*4.31*	*7.172*
3.61	*5.166*	--	--	--	--	--	--
3.81	5.428	--	--	--	--	--	--
4.12	6.263	--	--	--	--	--	--
T (^{o}C)	19.6	T (^{o}C)	23.2	T (^{o}C)	23.8	T (^{o}C)	24.7

laminar data points in *italics*

Table D.6: Pressure gradient versus velocity data for Saskatoon tap water to determine the roughness of the 53 mm pipe feed test section during the testing of the kaolin clay-water slurries before polishing

S'toon Tap Water	
Before Polishing	
Water001	
Velocity (m/s)	-dP/dz (kPa/m)
0.89	0.207
1.19	0.353
1.57	0.597
1.80	0.773
2.06	1.001
2.22	1.160
2.38	1.321
2.63	1.602
3.03	2.104
3.26	2.418
3.57	2.899
4.43	4.397
ε (μm)	95.7
T (^{o}C)	14.4

Table D.7: Pressure gradient versus velocity data for Saskatoon tap water to determine the roughness of the 53 mm pipe feed test section during the testing of the kaolin clay-water slurries after polishing but before testing

Saskatoon Tap Water											
After Polishing, Before Testing											
Water002		Water003		Water004		Water005		Water006		Water007	
Velocity (m/s)	-dP/dz (kPa/m)	Velocity (m/s)	-dP/dz (kPa/m)	Velocity (m/s)	-dP/dz (kPa/m)	Velocity (m/s)	-dP/dz (kPa/m)	Velocity (m/s)	-dP/dz (kPa/m)	Velocity (m/s)	-dP/dz (kPa/m)
0.80	0.149	0.339	0.037	2.35	1.133	2.74	1.571	3.54	2.568	3.64	2.743
1.27	0.352	0.708	0.127	2.34	1.133	2.74	1.571	3.54	2.569	3.65	2.744
1.70	0.611	1.146	0.305	2.34	1.132	2.74	1.573	3.54	2.569	3.15	2.065
2.10	0.911	1.579	0.552	2.34	1.131	2.74	1.571	3.54	2.569	3.15	2.063
2.48	1.255	2.020	0.878	2.34	1.131	2.74	1.572	3.54	2.568	2.71	1.548
2.91	1.704	2.469	1.285	2.34	1.130	2.74	1.568	3.54	2.567	2.71	1.548
3.38	2.275	2.928	1.780	2.34	1.129	2.30	1.116	3.54	2.569	2.25	1.080
3.80	2.852	3.443	2.431	1.34	0.395	1.78	0.690	3.53	2.566	2.25	1.081
4.39	3.779	3.976	3.190	0.88	0.183	1.39	0.431	3.16	2.055	1.83	0.734
4.43	3.850	4.397	3.866	1.85	0.731	0.94	0.208	2.71	1.526	1.83	0.732
4.11	3.329	4.119	3.404	2.78	1.597	0.71	0.124	2.19	1.013	1.38	0.428
3.59	2.563	3.618	2.646	2.78	1.598	0.54	0.074	1.81	0.695	1.38	0.427
3.17	2.008	3.144	2.018	2.63	1.433	0.38	0.040	1.37	0.408	0.91	0.200
2.70	1.479	2.674	1.481	2.23	1.046	0.22	0.014	0.92	0.187	0.91	0.199
2.26	1.053	2.241	1.055	1.80	0.697	0.14	0.005	0.70	0.108	0.66	0.111
1.84	0.710	1.819	0.712	1.31	0.382	3.23	2.167	0.45	0.042	0.66	0.111
1.44	0.448	1.376	0.422	0.88	0.181	3.24	2.170	0.32	0.036	0.45	0.056
1.02	0.237	0.957	0.218	0.49	0.063	3.24	2.170	0.22	0.021	0.45	0.056
0.55	0.079	0.529	0.077	0.44	0.053	3.24	2.171	0.10	0.009	0.33	0.034
0.27	0.025	0.242	0.023	0.24	0.018	3.24	2.172	3.66	2.756	0.33	0.034
0.12	0.009	--	--	0.22	0.016	2.74	1.572	3.19	2.110	0.23	0.019
--	--	--	--	2.72	1.535	2.28	1.101	2.73	1.547	0.23	0.019
--	--	--	--	2.72	1.536	1.79	0.689	2.26	1.071	0.10	0.006
--	--	--	--	2.25	1.061	1.35	0.401	1.81	0.724	0.10	0.006
--	--	--	--	1.83	0.717	0.88	0.175	1.37	0.431	--	--
--	--	--	--	1.37	0.413	0.68	0.106	0.88	0.194	--	--
--	--	--	--	0.92	0.198	0.45	0.047	0.88	0.194	--	--
--	--	--	--	0.45	0.055	0.35	0.027	0.89	0.194	--	--
--	--	--	--	0.24	0.019	0.26	0.012	0.88	0.194	--	--
--	--	--	--	2.74	1.561	2.76	1.596	0.88	0.194	--	--
--	--	--	--	2.28	1.096	2.76	1.597	0.88	0.194	--	--
--	--	--	--	1.78	0.685	2.76	1.596	0.88	0.193	--	--
--	--	--	--	1.37	0.415	2.76	1.597	0.88	0.195	--	--
--	--	--	--	0.89	0.188	2.76	1.597	0.66	0.118	--	--
--	--	--	--	0.47	0.060	2.76	1.596	0.46	0.066	--	--
--	--	--	--	0.26	0.022	2.76	1.598	0.37	0.047	--	--
--	--	--	--	2.70	1.510	2.76	1.597	0.22	0.024	--	--
--	--	--	--	2.27	1.075	2.22	1.042	0.10	0.012	--	--
--	--	--	--	1.80	0.695	1.84	0.720	--	--	--	--
--	--	--	--	1.37	0.412	1.84	0.721	--	--	--	--
--	--	--	--	0.92	0.195	1.35	0.408	--	--	--	--
--	--	--	--	0.46	0.054	1.35	0.408	--	--	--	--
--	--	--	--	0.25	0.016	0.89	0.186	--	--	--	--
--	--	--	--	--	--	0.89	0.187	--	--	--	--
--	--	--	--	--	--	0.68	0.116	--	--	--	--
--	--	--	--	--	--	0.68	0.115	--	--	--	--
--	--	--	--	--	--	0.42	0.048	--	--	--	--
--	--	--	--	--	--	0.42	0.048	--	--	--	--
--	--	--	--	--	--	0.33	0.031	--	--	--	--
--	--	--	--	--	--	0.33	0.031	--	--	--	--
--	--	--	--	--	--	0.23	0.015	--	--	--	--
--	--	--	--	--	--	0.22	0.015	--	--	--	--
--	--	--	--	--	--	0.10	0.003	--	--	--	--
--	--	--	--	--	--	0.10	0.002	--	--	--	--
ε (μm)	56.6	ε (μm)	58.3	ε (μm)	60.6	ε (μm)	62.8	ε (μm)	62.0	ε (μm)	64.1
T (^{o}C)	32.9	T (^{o}C)	21.3	T (^{o}C)	25.0	T (^{o}C)	21.1	T (^{o}C)	21.5	T (^{o}C)	20.7

Table D.8: Pressure gradient versus velocity data for Saskatoon tap water to determine the roughness of the 53 mm pipe feed test section during the testing of the kaolin clay-water slurries after testing

Saskatoon Tap Water					
After Testing					
Water008		Water009		Water010	
Velocity (m/s)	-dP/dz (kPa/m)	Velocity (m/s)	-dP/dz (kPa/m)	Velocity (m/s)	-dP/dz (kPa/m)
0.49	0.067	4.50	4.089	0.49	0.067
0.91	0.205	4.65	4.343	0.93	0.213
1.37	0.431	4.31	3.757	1.38	0.434
1.82	0.729	3.83	2.983	1.82	0.728
2.30	1.127	3.36	2.319	2.26	1.096
2.75	1.586	2.93	1.792	2.73	1.566
3.21	2.125	2.50	1.325	3.20	2.120
3.65	2.719	2.06	0.922	3.63	2.704
4.11	3.426	1.58	0.563	4.07	3.354
4.53	4.138	1.14	0.309	4.50	4.081
4.29	3.706	0.72	0.136	4.65	4.337
3.82	2.972	0.25	0.020	4.30	3.725
3.36	2.317	0.49	0.067	3.82	2.968
2.91	1.762	0.93	0.213	3.37	2.346
2.50	1.318	1.38	0.434	2.95	1.819
2.09	0.943	1.82	0.728	2.51	1.340
1.62	0.588	2.26	1.096	2.06	0.924
1.15	0.315	2.73	1.566	1.61	0.584
0.71	0.130	3.20	2.120	1.14	0.307
0.24	0.022	3.63	2.704	0.67	0.116
0.51	0.074	4.07	3.354	0.26	0.022
0.89	0.197	--	--	--	--
1.33	0.413	--	--	--	--
1.80	0.720	--	--	--	--
2.26	1.097	--	--	--	--
2.73	1.567	--	--	--	--
3.21	2.144	--	--	--	--
3.66	2.752	--	--	--	--
4.13	3.463	--	--	--	--
ε (μm)	60.5	ε (μm)	60.3	ε (μm)	59.8
T (^{o}C)	21.2	T (^{o}C)	19.8	T (^{o}C)	20.0

Table D.9: Pressure gradient versus velocity data for a 22.2% v/v kaolin clay-water slurry in the 53mm test section; ρ=1375 kg/m^3

22.2% v/v Kaolin Clay-Water															
ClayWater001		ClayWater002		ClayWater003		ClayWater004		ClayWater005		ClayWater006		ClayWater007		ClayWater008	
Velocity (m/s)	-dP/dz (kPa/m)	Velocity (m/s)	-dP/dz (kPa/m)	Velocity (m/s)	-dP/dz (kPa/m)	Velocity (m/s)	-dP/dz (kPa/m)	Velocity (m/s)	-dP/dz (kPa/m)	Velocity (m/s)	-dP/dz (kPa/m)	Velocity (m/s)	-dP/dz (kPa/m)	Velocity (m/s)	-dP/dz (kPa/m)
0.52	*3.286*	*2.74*	*4.126*	*2.76*	*4.132*	*2.71*	*4.109*	*1.59*	*3.697*	*0.32*	*2.876*	*2.72*	*4.111*	*2.69*	*4.150*
0.55	*3.307*	*2.78*	*4.149*	*2.27*	*3.971*	*2.30*	*3.985*	*1.32*	*3.580*	*0.31*	*2.878*	*2.29*	*3.980*	*2.25*	*4.011*
1.08	*3.644*	*2.24*	*3.958*	*1.78*	*3.789*	*1.84*	*3.813*	*1.14*	*3.497*	*0.32*	*2.882*	*1.87*	*3.828*	*1.86*	*3.864*
1.03	*3.624*	*2.21*	*3.950*	*1.41*	*3.624*	*1.38*	*3.616*	*0.90*	*3.364*	*0.32*	*2.885*	*1.33*	*3.596*	*1.37*	*3.651*
1.49	*3.837*	*1.81*	*3.794*	*1.39*	*3.621*	*1.39*	*3.617*	*0.68*	*3.213*	*0.32*	*2.889*	*1.33*	*3.595*	*1.37*	*3.648*
1.51	*3.841*	*1.81*	*3.795*	*1.18*	*3.519*	*1.05*	*3.449*	*0.43*	*3.014*	*0.32*	*2.892*	*1.33*	*3.595*	*1.38*	*3.656*
1.84	*3.975*	*1.38*	*3.615*	*1.11*	*3.477*	*1.03*	*3.440*	*0.42*	*3.007*	*0.33*	*2.899*	*1.33*	*3.595*	*1.38*	*3.657*
1.84	*3.976*	*1.41*	*3.629*	*0.94*	*3.389*	*1.03*	*3.436*	*0.43*	*3.012*	*0.33*	*2.904*	*1.33*	*3.594*	*1.38*	*3.659*
2.37	*4.165*	*1.16*	*3.504*	*0.66*	*3.210*	*1.03*	*3.436*	*0.44*	*3.022*	*0.32*	*2.895*	*1.33*	*3.595*	*1.38*	*3.658*
2.37	*4.166*	*0.91*	*3.372*	*0.67*	*3.215*	*0.92*	*3.374*	*0.45*	*3.031*	*0.31*	*2.887*	*1.33*	*3.596*	*1.38*	*3.658*
2.58	*4.228*	*0.58*	*3.147*	*0.43*	*3.019*	*0.66*	*3.202*	*0.46*	*3.042*	*0.31*	*2.885*	*1.33*	*3.596*	*1.37*	*3.657*
2.63	*4.227*	*0.46*	*3.042*	*0.43*	*3.013*	*0.43*	*3.013*	*0.47*	*3.051*	*0.32*	*2.893*	*1.33*	*3.595*	*1.38*	*3.658*
2.88	*4.312*	*0.46*	*3.040*	*0.42*	*3.007*	*0.32*	*2.896*	*0.48*	*3.060*	*0.32*	*2.894*	*1.33*	*3.595*	*0.81*	*3.347*
2.87	*4.311*	*0.47*	*3.049*	*0.44*	*3.027*	*0.22*	*2.761*	*0.49*	*3.066*	*0.32*	*2.896*	*1.33*	*3.594*	*0.57*	*3.171*
2.09	*4.034*	*0.47*	*3.056*	*0.45*	*3.032*	*0.11*	*2.550*	*0.49*	*3.071*	*0.32*	*2.900*	*0.90*	*3.367*	*0.42*	*3.035*
2.07	*4.031*	*0.48*	*3.065*	*0.45*	*3.035*	--	--	*0.47*	*3.054*	*0.33*	*2.907*	*0.61*	*3.170*	*0.31*	*2.918*
1.66	*3.867*	*0.46*	*3.047*	*0.46*	*3.048*	--	--	*0.48*	*3.059*	*0.33*	*2.907*	*0.45*	*3.033*	*0.22*	*2.791*
1.65	*3.865*	*0.50*	*3.068*	*0.46*	*3.049*	--	--	*0.33*	*2.906*	*0.33*	*2.906*	*0.34*	*2.922*	*0.11*	*2.593*
1.25	*3.676*	*0.49*	*3.068*	*0.46*	*3.043*	--	--	*0.33*	*2.906*	*0.33*	*2.903*	*0.24*	*2.797*	--	--
1.22	*3.667*	*0.48*	*3.063*	*0.46*	*3.051*	--	--	*0.23*	*2.772*	*0.33*	*2.905*	*0.12*	*2.574*	--	--
0.77	*3.413*	*0.48*	*3.066*	*0.34*	*2.930*	--	--	*0.13*	*2.599*	*0.33*	*2.901*	--	--	--	--
0.77	*3.418*	*0.48*	*3.063*	*0.22*	*2.765*	--	--	--	--	*0.32*	*2.900*	--	--	--	--
0.28	*2.989*	*0.34*	*2.919*	*0.12*	*2.577*	--	--	--	--	*0.32*	*2.903*	--	--	--	--
0.27	*2.969*	*0.23*	*2.781*	--	--	--	--	--	--	*0.33*	*2.902*	--	--	--	--
0.15	*2.787*	*0.11*	*2.560*	--	--	--	--	--	--	*0.33*	*2.907*	--	--	--	--
0.15	*2.784*	*0.11*	*2.566*	--	--	--	--	--	--	*0.33*	*2.904*	--	--	--	--
--	--	--	--	--	--	--	--	--	--	*0.33*	*2.91*	--	--	--	--
--	--	--	--	--	--	--	--	--	--	*0.33*	*2.91*	--	--	--	--
--	--	--	--	--	--	--	--	--	--	*0.33*	*2.91*	--	--	--	--
--	--	--	--	--	--	--	--	--	--	*0.32*	*2.90*	--	--	--	--
--	--	--	--	--	--	--	--	--	--	*0.33*	*2.91*	--	--	--	--
--	--	--	--	--	--	--	--	--	--	*0.32*	*2.91*	--	--	--	--
--	--	--	--	--	--	--	--	--	--	*0.33*	*2.91*	--	--	--	--
--	--	--	--	--	--	--	--	--	--	*0.33*	*2.91*	--	--	--	--
--	--	--	--	--	--	--	--	--	--	*0.33*	*2.91*	--	--	--	--
--	--	--	--	--	--	--	--	--	--	*0.24*	*2.79*	--	--	--	--
--	--	--	--	--	--	--	--	--	--	*0.13*	*2.59*	--	--	--	--
θ (^{o})	5.54	θ (^{o})	6.00	θ (^{o})	5.00	θ (^{o})	4.00	θ (^{o})	3.00	θ (^{o})	2.50	θ (^{o})	3.50	θ (^{o})	4.50
T (^{o}C)	24.6	T (^{o}C)	21.5	T (^{o}C)	21.2	T (^{o}C)	20.3	T (^{o}C)	20.0	T (^{o}C)	20.3	T (^{o}C)	20.5	T (^{o}C)	19.8

laminar data points in *italics*

Table D.10: Pressure gradient versus velocity data for a 22.6% v/v kaolin clay-water slurry with 0.03% TSPP in the 53mm test section; ρ=1384 kg/m^3

22.6% v/v Kaolin Clay-Water with 0.03% TSPP												
ClayWater009		ClayWater010		ClayWater011		ClayWater012		ClayWater013		ClayWater014	
Velocity (m/s)	-dP/dz (kPa/m)	Velocity (m/s)	-dP/dz (kPa/m)	Velocity (m/s)	-dP/dz (kPa/m)	Velocity (m/s)	-dP/dz (kPa/m)	Velocity (m/s)	-dP/dz (kPa/m)	Velocity (m/s)	-dP/dz (kPa/m)
1.72	1.184	2.21	1.806	2.22	1.821	2.27	1.895	2.27	1.862	2.05	1.561
1.72	1.179	1.82	1.281	1.85	1.338	2.02	1.509	1.86	1.320	1.82	1.292
1.72	1.174	1.59	1.015	1.62	1.058	1.81	1.281	1.58	0.997	1.57	0.999
1.72	1.176	*1.39*	*0.843*	*1.36*	*0.842*	1.58	0.994	*1.37*	*0.886*	*1.36*	*0.868*
1.42	*0.888*	*1.38*	*0.839*	*1.13*	*0.791*	*1.32*	*0.829*	*1.10*	*0.835*	*1.36*	*0.865*
1.15	*0.818*	*1.39*	*0.838*	*1.13*	*0.788*	*1.12*	*0.787*	*1.10*	*0.832*	*1.36*	*0.866*
0.90	*0.772*	*1.39*	*0.842*	*1.13*	*0.787*	*0.90*	*0.744*	*1.11*	*0.831*	*1.36*	*0.867*
0.65	*0.722*	*1.38*	*0.841*	*1.13*	*0.789*	*0.90*	*0.741*	*1.11*	*0.830*	*1.35*	*0.863*
0.45	*0.682*	*1.17*	*0.785*	*1.13*	*0.789*	*0.90*	*0.740*	*1.11*	*0.829*	*1.35*	*0.865*
0.33	*0.655*	*0.93*	*0.736*	*0.93*	*0.751*	*0.89*	*0.739*	*1.11*	*0.828*	*1.13*	*0.815*
0.22	*0.632*	*0.68*	*0.686*	*0.70*	*0.706*	*0.89*	*0.740*	*1.11*	*0.827*	*0.91*	*0.776*
0.14	*0.614*	*0.42*	*0.627*	*0.47*	*0.659*	*0.89*	*0.738*	*1.12*	*0.826*	*0.92*	*0.777*
--	--	*0.33*	*0.608*	*0.35*	*0.631*	*0.70*	*0.702*	*1.12*	*0.825*	*0.92*	*0.775*
--	--	*0.24*	*0.587*	*0.26*	*0.610*	*0.46*	*0.650*	*1.12*	*0.825*	*0.92*	*0.776*
--	--	*0.11*	*0.553*	*0.13*	*0.578*	*0.46*	*0.649*	*1.12*	*0.825*	*0.92*	*0.777*
--	--	--	--	--	--	*0.46*	*0.65*	*1.12*	*0.826*	*0.74*	*0.743*
--	--	--	--	--	--	*0.46*	*0.65*	*1.12*	*0.825*	*0.45*	*0.683*
--	--	--	--	--	--	*0.46*	*0.65*	*1.12*	*0.823*	*0.43*	*0.678*
--	--	--	--	--	--	*0.46*	*0.65*	*1.12*	*0.823*	*0.43*	*0.680*
--	--	--	--	--	--	*0.34*	*0.62*	*1.12*	*0.824*	*0.43*	*0.679*
--	--	--	--	--	--	*0.23*	*0.59*	*1.12*	*0.823*	*0.43*	*0.682*
--	--	--	--	--	--	*0.11*	*0.56*	*1.12*	*0.82*	*0.43*	*0.681*
--	--	--	--	--	--	--	--	*1.12*	*0.82*	*0.36*	*0.665*
--	--	--	--	--	--	--	--	*0.91*	*0.79*	*0.21*	*0.631*
--	--	--	--	--	--	--	--	*0.65*	*0.73*	*0.13*	*0.608*
--	--	--	--	--	--	--	--	*0.49*	*0.70*	--	--
--	--	--	--	--	--	--	--	*0.31*	*0.66*	--	--
--	--	--	--	--	--	--	--	*0.23*	*0.64*	--	--
--	--	--	--	--	--	--	--	*0.11*	*0.60*	--	--
θ (^{o})	5.00	θ (^{o})	4.00	θ (^{o})	3.00	θ (^{o})	2.00	θ (^{o})	1.00	θ (^{o})	6.00
T (^{o}C)	20.8	T (^{o}C)	19.4	T (^{o}C)	19.3	T (^{o}C)	19.7	T (^{o}C)	21.0	T (^{o}C)	20.3

laminar data points in *italics*

Table D.11: Pressure gradient versus velocity data for a 22.8% v/v kaolin clay-water slurry with 0.10% TSPP in the 53mm test section; ρ=1386 kg/m^3

22.8% v/v Kaolin Clay-Water with 0.10% TSPP												
ClayWater015		ClayWater016		ClayWater017		ClayWater018		ClayWater019		ClayWater020	
Velocity (m/s)	-dP/dz (kPa/m)	Velocity (m/s)	-dP/dz (kPa/m)	Velocity (m/s)	-dP/dz (kPa/m)	Velocity (m/s)	-dP/dz (kPa/m)	Velocity (m/s)	-dP/dz (kPa/m)	Velocity (m/s)	-dP/dz (kPa/m)
2.22	1.792	2.25	1.836	2.31	1.883	2.71	2.508	2.75	2.575	2.78	2.631
1.86	1.278	1.84	1.269	1.82	1.222	2.24	1.813	2.22	1.736	2.37	1.977
1.45	0.825	1.45	0.835	1.42	0.785	1.83	1.234	1.85	1.250	1.95	1.387
1.12	0.522	1.11	0.520	1.14	0.533	1.48	0.843	1.47	0.841	1.74	1.134
1.12	0.528	1.11	0.521	1.13	0.532	1.11	0.508	1.12	0.519	1.46	0.834
1.13	0.530	1.12	0.521	1.14	0.532	1.10	0.508	1.13	0.520	1.14	0.544
1.13	0.529	1.11	0.520	1.14	0.533	1.12	0.508	1.12	0.519	1.15	0.544
1.13	0.530	1.12	0.520	1.15	0.533	1.09	0.508	1.13	0.520	1.14	0.542
1.14	0.530	1.12	0.521	1.14	0.532	1.11	0.508	1.13	0.520	1.14	0.542
0.92	0.363	1.12	0.520	0.92	0.360	1.11	0.509	1.13	0.520	1.15	0.541
0.70	0.224	0.89	0.362	0.67	0.205	1.10	0.509	1.12	0.520	1.15	0.542
0.47	0.109	0.68	0.220	0.45	0.102	1.11	0.508	0.91	0.356	1.15	0.542
0.47	0.109	0.47	0.112	0.45	0.103	1.10	0.508	0.67	0.213	1.15	0.540
0.47	0.110	0.47	0.113	0.46	0.103	0.89	0.345	0.46	0.103	1.15	0.541
0.48	0.111	0.47	0.114	0.46	0.104	0.67	0.212	0.45	0.103	0.88	0.333
0.47	0.108	0.47	0.113	0.45	0.103	0.45	0.10	0.46	0.103	0.68	0.210
0.25	0.029	0.46	0.110	0.46	0.105	0.45	0.10	0.46	0.103	0.46	0.103
--	--	0.47	0.113	0.45	0.102	0.44	0.10	0.46	0.103	0.46	0.103
--	--	0.21	0.017	0.22	0.017	0.45	0.10	0.45	0.103	0.46	0.103
--	--	--	--	--	--	0.45	0.10	0.45	0.103	0.45	0.103
--	--	--	--	--	--	0.45	0.10	0.20	0.014	0.46	0.103
--	--	--	--	--	--	0.23	0.02	--	--	0.46	0.104
--	--	--	--	--	--	--	--	--	--	0.46	0.103
--	--	--	--	--	--	--	--	--	--	0.46	0.103
--	--	--	--	--	--	--	--	--	--	0.24	0.025
--	--	--	--	--	--	--	--	--	--	0.14	0.009
--	--	--	--	--	--	--	--	--	--	0.14	0.009
--	--	--	--	--	--	--	--	--	--	0.14	0.009
--	--	--	--	--	--	--	--	--	--	0.14	0.010
--	--	--	--	--	--	--	--	--	--	0.14	0.010
--	--	--	--	--	--	--	--	--	--	0.14	0.010
θ (^{o})	6.00	θ (^{o})	5.00	θ (^{o})	4.00	θ (^{o})	3.00	θ (^{o})	2.00	θ (^{o})	1.00
T (^{o}C)	19.2	T (^{o}C)	18.9	T (^{o}C)	19.6	T (^{o}C)	19.7	T (^{o}C)	19.9	T (^{o}C)	19.7

Table D.12a: Frictional loss measurements for Saskatoon tap water in the 156.7 mm flume

Water004								
Q (L/s)	T (^oC)	θ (^{o})	h_1 (m)	h_2 (m)	V (m/s)	τ_w (Pa)	Re	f
5.198	30.0	5.00	0.0288	0.0280	2.18	14.5	187784	0.0061
5.192	29.5	5.00	0.0288	0.0280	2.18	14.5	185395	0.0061
5.188	29.3	5.00	0.0288	0.0280	2.18	14.5	184549	0.0061
5.182	29.1	5.00	0.0288	0.0280	2.18	14.5	183746	0.0061
5.186	29.0	5.00	0.0288	0.0280	2.18	14.5	183420	0.0061
5.180	28.9	5.00	0.0288	0.0280	2.18	14.5	182635	0.0062
5.181	28.7	5.00	0.0288	0.0280	2.18	14.5	182144	0.0062
2.962	26.7	5.00	0.0226	0.0219	1.77	11.8	113300	0.0075
1.956	26.4	5.00	0.0184	0.0176	1.60	9.7	83206	0.0076
4.088	26.2	5.00	0.0259	0.0255	1.98	13.4	143401	0.0068
6.148	26.1	5.00	0.0339	0.0315	2.11	16.2	189641	0.0073
6.159	26.0	5.00	0.0339	0.0315	2.12	16.2	189740	0.0073
5.831	25.8	4.00	0.0336	0.0327	1.96	13.4	176982	0.0070
4.949	25.7	4.00	0.0313	0.0292	1.90	12.1	157790	0.0067
3.996	25.5	4.00	0.0274	0.0264	1.82	11.1	134881	0.0067
2.911	25.4	4.00	0.0227	0.0225	1.70	9.6	107269	0.0067
1.949	25.2	4.00	0.0182	0.0175	1.61	7.6	81174	0.0059
1.074	25.1	4.00	0.0139	0.0136	1.29	6.0	50935	0.0072
0.972	24.9	5.00	0.0123	0.0125	1.37	6.7	48493	0.0072
0.520	24.8	5.00	0.0095	0.0092	1.11	5.2	29876	0.0086
0.488	24.7	4.00	0.0099	0.0095	0.99	4.4	27510	0.0089
6.028	24.5	3.00	0.0369	0.0345	1.83	10.4	170958	0.0063
6.033	24.4	3.00	0.0369	0.0345	1.83	10.4	170849	0.0062
4.982	24.3	3.00	0.0334	0.0305	1.78	9.4	149931	0.0060
4.052	24.1	3.00	0.0304	0.0271	1.68	8.5	128697	0.0061
3.024	24.0	3.00	0.0252	0.0241	1.56	7.7	103376	0.0064
2.036	23.9	3.00	0.0203	0.0195	1.43	6.4	77561	0.0063
0.994	23.7	3.00	0.0145	0.0139	1.15	4.7	45062	0.0071
0.530	23.6	3.00	0.0107	0.0107	0.93	3.5	27721	0.0082
6.073	23.5	2.00	0.0406	0.0376	1.62	7.4	160230	0.0057
5.050	23.3	2.00	0.0366	0.0339	1.56	6.8	140613	0.0056
3.951	23.2	2.00	0.0327	0.0301	1.44	6.3	116825	0.0061
3.026	23.1	2.00	0.0283	0.0270	1.32	5.7	95356	0.0065
1.972	23.0	2.00	0.0229	0.0219	1.17	4.8	69288	0.0070
1.041	22.9	2.00	0.0165	0.0159	0.99	3.5	43201	0.0073
0.567	22.9	2.00	0.0125	0.0124	0.79	2.7	26924	0.0087
5.977	22.7	1.00	0.0488	0.0452	1.23	4.5	139674	0.0059
5.027	22.6	1.00	0.0452	0.0413	1.17	4.2	123090	0.0062
3.979	22.5	1.00	0.0398	0.0363	1.10	3.8	104304	0.0062
3.025	22.4	1.00	0.0340	0.0316	1.04	3.4	85741	0.0063
2.035	22.3	1.00	0.0273	0.0258	0.94	2.8	64309	0.0063
1.027	22.2	1.00	0.0196	0.0200	0.73	2.1	37769	0.0080
0.543	22.2	1.00	0.0148	0.0143	0.60	1.6	23438	0.0089

Table D.12b: Frictional loss measurements for Saskatoon tap water in the 156.7 mm flume

Water005								
Q (L/s)	T (^oC)	θ (^{o})	h_1 (m)	h_2 (m)	V (m/s)	τ_w (Pa)	Re	f
6.056	21.7	0.50	0.0586	0.0536	0.98	2.8	125229	0.0058
6.061	21.7	0.50	0.0586	0.0536	0.98	2.8	125318	0.0058
6.071	21.7	0.50	0.0586	0.0536	0.98	2.8	125504	0.0058
6.070	21.7	0.50	0.0586	0.0536	0.98	2.8	125458	0.0058
6.072	21.7	0.50	0.0586	0.0536	0.98	2.8	125491	0.0058
6.069	21.7	0.50	0.0586	0.0536	0.98	2.8	125431	0.0058
5.082	21.7	0.50	0.0536	0.0491	0.93	2.6	110501	0.0061
3.947	21.6	0.50	0.0471	0.0440	0.85	2.3	91454	0.0065
3.081	21.5	0.50	0.0417	0.0379	0.80	2.1	77096	0.0066
2.085	21.5	0.50	0.0332	0.0316	0.72	1.7	58074	0.0066
1.576	21.4	0.50	0.0285	0.0277	0.67	1.5	47309	0.0066
1.192	21.4	0.50	0.0251	0.0243	0.61	1.3	38296	0.0071
0.844	21.3	0.50	0.0213	0.0207	0.55	1.1	29530	0.0076
0.494	21.3	0.50	0.0169	0.0164	0.45	0.9	19488	0.0090
0.318	21.3	0.50	0.0134	0.0134	0.40	0.7	14004	0.0093
7.161	21.3	1.50	0.0437	0.0443	1.61	6.6	167587	0.0051
7.164	21.3	1.50	0.0437	0.0443	1.61	6.6	167687	0.0051
7.172	21.3	1.50	0.0437	0.0443	1.61	6.6	167944	0.0051
7.175	21.3	1.50	0.0437	0.0443	1.62	6.6	168027	0.0051
7.181	21.3	1.50	0.0437	0.0443	1.62	6.6	168198	0.0051
6.073	21.3	1.50	0.0440	0.0407	1.45	6.0	145802	0.0057
5.049	21.3	1.50	0.0405	0.0376	1.35	5.7	126649	0.0063
3.965	21.2	1.50	0.0344	0.0334	1.29	5.1	107167	0.0062
2.997	21.2	1.50	0.0295	0.0289	1.21	4.5	87601	0.0062
1.949	21.1	1.50	0.0236	0.0234	1.08	3.7	63875	0.0065
1.501	21.1	1.50	0.0208	0.0208	0.99	3.3	52417	0.0068
1.007	21.1	1.50	0.0173	0.0173	0.87	2.8	38704	0.0074
0.766	21.0	1.50	0.0152	0.0152	0.80	2.5	31410	0.0078
0.572	21.0	1.50	0.0135	0.0135	0.71	2.2	24944	0.0088
6.107	20.9	2.22	0.0392	0.0383	1.64	8.5	152036	0.0063
6.113	20.9	2.22	0.0392	0.0383	1.65	8.5	152161	0.0063
6.112	20.9	2.22	0.0392	0.0383	1.65	8.5	152134	0.0063
6.111	20.9	2.22	0.0392	0.0383	1.64	8.5	152105	0.0063
6.112	20.9	2.22	0.0392	0.0383	1.65	8.5	152128	0.0063
6.112	20.9	2.22	0.0392	0.0383	1.65	8.5	152140	0.0063
6.116	20.9	2.22	0.0392	0.0383	1.65	8.5	152217	0.0063
6.118	20.9	2.22	0.0392	0.0383	1.65	8.5	152277	0.0063
4.912	20.9	2.22	0.0352	0.0329	1.59	7.4	131509	0.0059
4.065	20.9	2.22	0.0314	0.0294	1.55	6.8	115623	0.0056
4.066	20.8	2.22	0.0314	0.0294	1.55	6.8	115613	0.0056
2.990	20.8	2.22	0.0270	0.0264	1.37	6.2	90877	0.0066
2.985	20.8	2.22	0.0270	0.0264	1.37	6.2	90711	0.0066
1.967	20.8	2.22	0.0215	0.0215	1.23	5.1	66939	0.0067
1.968	20.8	2.22	0.0215	0.0215	1.24	5.1	66973	0.0067
1.516	20.7	2.22	0.0189	0.0188	1.15	4.5	55251	0.0068
1.515	20.7	2.22	0.0189	0.0188	1.15	4.5	55204	0.0068
0.937	20.7	2.22	0.0149	0.0148	1.01	3.6	38585	0.0071
0.934	20.7	2.22	0.0149	0.0148	1.00	3.6	38448	0.0072
0.741	20.7	2.22	0.0134	0.0136	0.92	3.3	32072	0.0077
0.735	20.7	2.22	0.0134	0.0136	0.91	3.3	31813	0.0079
0.499	20.7	2.22	0.0114	0.0114	0.80	2.8	23571	0.0087
0.497	20.7	2.22	0.0114	0.0114	0.79	2.8	23478	0.0088
0.224	20.7	2.22	0.0082	0.0083	0.58	2.0	12480	0.0122
0.225	20.7	2.22	0.0082	0.0083	0.58	2.0	12508	0.0122

Table D.12c: Frictional loss measurements for Saskatoon tap water in the 156.7 mm flume

Water006								
Q (L/s)	T (^oC)	θ (^{o})	h_1 (m)	h_2 (m)	V (m/s)	τ_w (Pa)	Re	f
7.834	22.0	2.50	0.0412	0.0406	1.95	10.0	194143	0.0053
7.836	22.0	2.50	0.0412	0.0406	1.95	10.0	194138	0.0053
7.837	22.0	2.50	0.0412	0.0406	1.96	10.0	194171	0.0052
7.835	22.0	2.50	0.0412	0.0406	1.95	10.0	194147	0.0053
7.830	22.0	2.50	0.0412	0.0406	1.95	10.0	194018	0.0053
7.831	22.0	2.50	0.0412	0.0406	1.95	10.0	194048	0.0053
7.834	22.0	2.50	0.0412	0.0406	1.95	10.0	194151	0.0053
7.826	22.0	2.50	0.0412	0.0406	1.95	10.0	193973	0.0053
6.989	22.0	2.50	0.0397	0.0384	1.86	9.5	177720	0.0055
5.996	21.9	2.50	0.0380	0.0352	1.76	8.8	158326	0.0057
4.857	21.9	2.50	0.0335	0.0321	1.66	8.2	135586	0.0060
3.997	21.8	2.50	0.0301	0.0290	1.58	7.5	117906	0.0060
3.039	21.8	2.50	0.0265	0.0258	1.43	6.8	95501	0.0066
2.044	21.7	2.50	0.0217	0.0211	1.29	5.7	71411	0.0068
1.543	21.7	2.50	0.0184	0.0185	1.21	5.0	58155	0.0068
0.991	21.7	2.50	0.0152	0.0148	1.05	4.1	41536	0.0074
0.703	21.6	2.50	0.0129	0.0128	0.94	3.5	31940	0.0080
0.487	21.6	2.50	0.0109	0.0109	0.83	3.0	24038	0.0087
0.213	21.6	2.50	0.0077	0.0079	0.60	2.1	12504	0.0120
8.101	21.5	3.50	0.0415	0.0382	2.11	13.0	201942	0.0059
7.073	21.5	3.50	0.0357	0.0357	2.14	12.7	186706	0.0055
6.035	21.4	3.50	0.0339	0.0340	1.96	12.2	163514	0.0064
5.000	21.4	3.50	0.0319	0.0305	1.83	11.0	141850	0.0066
4.013	21.3	3.50	0.0289	0.0268	1.73	9.9	120918	0.0066
3.042	21.2	3.50	0.0244	0.0235	1.64	8.8	99038	0.0066
1.957	21.2	3.50	0.0199	0.0194	1.40	7.4	70605	0.0075
1.957	21.2	3.50	0.0199	0.0194	1.40	7.4	70543	0.0075
1.960	21.1	3.50	0.0199	0.0194	1.40	7.4	70600	0.0075
1.955	21.1	3.50	0.0199	0.0194	1.40	7.4	70338	0.0075
1.957	21.1	3.50	0.0199	0.0194	1.40	7.4	70392	0.0075
1.956	21.1	3.50	0.0199	0.0194	1.40	7.4	70335	0.0075
1.951	21.0	3.50	0.0199	0.0194	1.40	7.4	70098	0.0076
1.958	21.0	3.50	0.0199	0.0194	1.40	7.4	70331	0.0075
1.462	20.9	3.50	0.0175	0.0165	1.30	6.5	56614	0.0077
1.023	20.9	3.50	0.0144	0.0140	1.18	5.4	43383	0.0078
0.812	20.9	3.50	0.0123	0.0125	1.15	4.7	36925	0.0072
0.488	20.8	3.50	0.0103	0.0103	0.90	4.0	24341	0.0097
0.217	20.8	3.50	0.0073	0.0070	0.69	2.8	13065	0.0119

Table D.12d: Frictional loss measurements for Saskatoon tap water in the 156.7 mm flume

Water007								
Q (L/s)	T (^oC)	θ (^{o})	h_1 (m)	h_2 (m)	V (m/s)	τ_w (Pa)	Re	f
8.071	20.8	4.50	0.0362	0.0380	2.31	17.5	205378	0.0065
8.072	20.8	4.50	0.0362	0.0380	2.31	17.5	205555	0.0065
6.970	20.8	4.50	0.0366	0.0345	2.12	15.7	181860	0.0070
6.967	20.8	4.50	0.0366	0.0345	2.12	15.7	181807	0.0070
6.002	20.8	4.50	0.0335	0.0315	2.08	14.5	164487	0.0067
6.005	20.8	4.50	0.0335	0.0315	2.08	14.5	164579	0.0067
4.975	20.8	4.50	0.0300	0.0288	1.99	13.5	143658	0.0069
4.975	20.8	4.50	0.0300	0.0288	1.99	13.5	143617	0.0069
4.058	20.8	4.50	0.0268	0.0263	1.88	12.4	123612	0.0071
4.055	20.8	4.50	0.0268	0.0263	1.88	12.4	123499	0.0071
3.053	20.7	4.50	0.0232	0.0220	1.78	10.7	101278	0.0067
3.052	20.7	4.50	0.0232	0.0220	1.78	10.7	101225	0.0067
2.023	20.7	4.50	0.0190	0.0186	1.55	9.1	73809	0.0076
2.022	20.7	4.50	0.0190	0.0186	1.54	9.1	73742	0.0076
1.460	20.7	4.50	0.0157	0.0157	1.45	7.7	58442	0.0073
1.464	20.7	4.50	0.0157	0.0157	1.46	7.7	58615	0.0072
0.985	20.7	4.50	0.0131	0.0134	1.26	6.5	43027	0.0082
0.989	20.6	4.50	0.0131	0.0134	1.26	6.5	43162	0.0082
0.740	20.6	4.50	0.0112	0.0116	1.19	5.6	34958	0.0079
0.741	20.6	4.50	0.0112	0.0116	1.19	5.6	35031	0.0079
0.507	20.6	4.50	0.0098	0.0098	1.00	4.9	25779	0.0097
0.510	20.6	4.50	0.0098	0.0098	1.01	4.9	25912	0.0096
0.230	20.6	4.50	0.0069	0.0071	0.75	3.5	13895	0.0123
0.232	20.6	4.50	0.0069	0.0071	0.76	3.5	13980	0.0121

Table D.13: Old Inlet frictional loss measurements for a 25% v/v, sand-water slurry in the 156.7 mm flume; ρ=1410 kg/m^3

25% v/v Sand-Water								
Q (m^3/s)	T (^oC)	θ (^{o})	h_1 (m)	h_2 (m)	V (m/s)	τ_w (Pa)	Re	f
0.00407	26.5	6.99	0.0268	0.0254	1.93	27.0	201944	0.0103
0.00358	26.7	6.99	0.0224	0.0231	2.07	22.2	191735	0.0074
0.00341	27.2	6.99	0.0227	0.0231	1.95	22.3	183881	0.0083
0.00501	24.6	5.99	0.0292	0.0288	2.04	26.9	224762	0.0092
0.00450	24.8	5.99	0.0272	0.0285	1.94	25.5	207571	0.0096
0.00402	24.8	5.99	0.0261	0.0254	1.94	22.6	193402	0.0085
0.00374	24.9	5.99	0.0244	0.0249	1.92	21.4	184381	0.0082
0.00598	25.1	5.99	0.0321	0.0315	2.13	30.6	258137	0.0095
0.00549	25.6	5.99	0.0298	0.0306	2.11	28.7	247109	0.0091
0.00500	25.7	5.99	0.0289	0.0287	2.06	26.6	231170	0.0089
0.00449	25.7	5.99	0.0269	0.0270	2.03	24.2	214870	0.0083
0.00400	25.8	5.99	0.0257	0.0259	1.93	22.8	196265	0.0087
0.00602	26.0	4.99	0.0346	0.0336	1.95	28.1	255625	0.0105
0.00552	26.0	4.99	0.0303	0.0326	2.00	25.8	245595	0.0091
0.00502	26.0	4.99	0.0292	0.0314	1.92	24.2	227930	0.0093
0.00452	26.1	4.99	0.0285	0.0305	1.80	23.1	208282	0.0101
0.00404	26.2	4.99	0.0271	0.0280	1.77	20.9	192897	0.0095
0.00593	26.5	4.03	0.0359	0.0356	1.79	24.4	248104	0.0108
0.00554	26.6	4.03	0.0354	0.0343	1.73	23.5	235731	0.0111
0.00504	26.7	4.03	0.0347	0.0321	1.68	22.1	220035	0.0111
0.00478	26.7	4.03	0.0327	0.0315	1.68	20.9	213247	0.0104

Table D.14: New Inlet frictional loss measurements for a 25% v/v, sand-water slurry in the 156.7 mm flume; ρ=1410 kg/m^3

25% v/v Sand-Water								
Q (m^3/s)	T (^oC)	θ (^{o})	h_1 (m)	h_2 (m)	V (m/s)	τ_w (Pa)	Re	f
0.00598	23.7	7.01	0.0290	0.0294	2.41	30.1	261792	0.0074
0.00546	23.8	7.01	0.0261	0.0271	2.52	26.7	252102	0.0060
0.00501	23.9	7.01	0.0259	0.0256	2.42	24.8	235810	0.0060
0.00451	23.9	7.01	0.0236	0.0254	2.35	23.8	218750	0.0061
0.00397	23.9	7.01	0.0222	0.0232	2.30	21.1	199741	0.0057
0.00348	23.9	7.01	0.0211	0.0207	2.27	18.4	182822	0.0050
0.00598	24.0	6.00	0.0293	0.0314	2.28	27.9	258894	0.0076
0.00548	24.1	6.00	0.0283	0.0287	2.29	24.9	245534	0.0067
0.00501	24.1	6.00	0.0270	0.0285	2.18	24.2	228163	0.0073
0.00451	24.2	6.00	0.0263	0.0256	2.16	21.5	212865	0.0065
0.00398	24.2	6.00	0.0243	0.0248	2.06	20.0	193612	0.0067
0.00354	24.2	6.00	0.0228	0.0211	2.16	16.5	183136	0.0050
0.00598	24.3	5.00	0.0311	0.0325	2.14	24.6	254145	0.0076
0.00547	24.4	5.00	0.0287	0.0314	2.12	23.1	240756	0.0073
0.00509	24.5	5.00	0.0279	0.0286	2.15	20.6	230811	0.0063
0.00454	24.5	5.00	0.0271	0.0291	1.94	20.5	207256	0.0078
0.00406	24.5	5.00	0.0258	0.0279	1.85	19.1	190180	0.0079
0.00348	24.5	5.00	0.0249	0.0258	1.72	17.4	167714	0.0083
0.00602	24.5	3.99	0.0333	0.0348	1.95	21.7	247365	0.0081
0.00548	24.6	3.99	0.0307	0.0342	1.91	20.7	232937	0.0081
0.00497	24.6	3.99	0.0303	0.0330	1.79	19.6	213591	0.0087
0.00453	24.7	3.99	0.0291	0.0313	1.74	18.2	199652	0.0085
0.00397	24.7	3.99	0.0278	0.0294	1.65	16.6	180122	0.0086
0.00341	24.7	3.99	0.0264	0.0277	1.54	15.3	159516	0.0092
0.00599	24.8	3.00	0.0356	0.0392	1.70	18.9	236253	0.0092
0.00549	24.8	3.00	0.0344	0.0391	1.60	18.4	219881	0.0101
0.00541	24.7	3.00	0.0358	0.0381	1.56	18.1	213637	0.0106
0.00530	24.7	3.00	0.0341	0.0369	1.62	17.3	214628	0.0093
0.00519	24.9	3.00	0.0366	0.0373	1.49	18.0	205760	0.0114
0.00595	24.8	3.51	0.0340	0.0368	1.83	20.4	241654	0.0087
0.00551	24.9	3.51	0.0332	0.0348	1.79	19.0	228683	0.0084
0.00501	24.9	3.51	0.0333	0.0354	1.60	19.1	207109	0.0105
0.00450	25.0	3.51	0.0312	0.0339	1.56	17.6	192237	0.0103
0.00400	25.0	3.51	0.0307	0.0328	1.43	16.8	172891	0.0116
0.00390	25.0	3.51	0.0301	0.0323	1.43	16.4	170338	0.0114
0.00496	22.9	3.51	0.0326	0.0364	1.59	19.2	196557	0.0108
0.00449	23.2	3.51	0.0311	0.0337	1.57	17.5	184738	0.0101
0.00389	23.0	3.51	0.0303	0.0322	1.43	16.4	161857	0.0115
0.00601	23.2	3.00	0.0362	0.0399	1.67	19.3	226769	0.0098
0.00560	23.5	3.00	0.0363	0.0398	1.55	19.0	212542	0.0111
0.00650	22.9	3.00	0.0368	0.0418	1.73	20.6	239603	0.0098

Table D.15: Frictional loss measurements for a CT 'no gypsum' model tailings slurry in the 156.7 mm flume; ρ=1598 kg/m^3

CT 'No Gypsum'								
Q (m˘/s)	T (˘C)	θ (˘)	h_1 (m)	h_2 (m)	V (m/s)	τ_w (Pa)	Re	f
0.00497	25.4	3.00	0.0370	0.0367	1.44	17.8	27029	0.0108
0.00504	25.4	2.00	0.0423	0.0411	1.23	14.2	25614	0.0118
0.00499	25.4	1.50	0.0445	0.0447	1.11	11.7	24415	0.0120
0.00259	25.4	3.00	0.0335	0.0378	0.79	15.6	14435	0.0313

Table D.16: Frictional loss measurements for a CT 'gypsum' model tailings slurry in the 156.7 mm flume; ρ=1598 kg/m^3

CT 'Gypsum'								
Q (m^3/s)	T (^{o}C)	θ (^{o})	h_1 (m)	h_2 (m)	V (m/s)	τ_w (Pa)	Re_{Zhang}	f
0.00497	16.7	3.00	0.0378	0.0369	1.41	18.1	2207	0.0114
0.00504	21.8	1.92	0.0425	0.0419	1.20	13.8	1649	0.0119
0.00498	24.3	2.47	0.0395	0.0388	1.32	15.5	1432	0.0111
0.00255	21.2	3.00	0.0364	0.0427	0.67	16.7	387	0.0458

Table D.17: Frictional loss measurements for a model Thickened Tailings slurry in the 156.7 mm flume; ρ=1510 kg/m^3

Thickened Tailings								
Q (m^3/s)	T (^{o}C)	θ (^{o})	h_1 (m)	h_2 (m)	V (m/s)	τ_w (Pa)	Re_{Zhang}	f
0.00497	21.6	4.00	0.0909	0.0993	0.41	41.0	55	0.3275
0.00498	22.4	4.50	0.0849	0.0931	0.44	44.7	48	0.3027
0.00510	26.6	5.41	0.0805	0.0834	0.50	54.6	59	0.2892
0.00253	25.0	4.50	0.0998	0.1054	0.19	49.7	8	1.8379

Table D.18a: Frictional loss measurements for a 22.2% v/v kaolin clay-water slurry in the 156.7 mm flume; ρ=1375 kg/m^3

22.2% v/v Kaolin Clay-Water								
ClayWater001								
Q (L/s)	T (^{o}C)	θ (^{o})	h_1 (m)	h_2 (m)	V (m/s)	τ_w (Pa)	Re_{Zhang}	f
1.145	23.9	5.54	0.0508	0.0509	0.21	37.0	13.3	1.212
1.210	23.9	5.54	0.0508	0.0509	0.22	37.0	14.8	1.086
2.402	23.9	5.54	0.0550	0.0542	0.40	39.8	47.7	0.359
2.289	23.9	5.54	0.0550	0.0542	0.38	39.8	43.3	0.395
3.310	23.9	5.54	0.0570	0.0564	0.53	40.8	81.3	0.215
3.334	23.9	5.54	0.0570	0.0564	0.53	40.8	82.5	0.212
4.071	24.0	5.54	0.0592	0.0586	0.61	42.0	110.5	0.162
4.074	24.0	5.54	0.0592	0.0586	0.61	42.0	110.6	0.162
5.249	24.1	5.54	0.0601	0.0588	0.78	42.7	178.1	0.101
5.244	24.1	5.54	0.0601	0.0588	0.78	42.7	177.8	0.102
5.707	24.3	5.54	0.0601	0.0603	0.84	42.3	202.6	0.088
5.821	24.4	5.54	0.0601	0.0603	0.85	42.3	210.6	0.085
6.375	24.6	5.54	0.0617	0.0611	0.91	43.3	239.4	0.076
6.350	24.7	5.54	0.0617	0.0611	0.91	43.3	237.6	0.077
4.630	24.8	5.54	0.0586	0.0586	0.70	41.6	144.2	0.122
4.584	24.8	5.54	0.0586	0.0586	0.70	41.6	141.4	0.125
3.675	24.9	5.54	0.0568	0.0563	0.59	40.6	100.6	0.172
3.660	24.9	5.54	0.0568	0.0563	0.58	40.6	99.8	0.174
2.758	25.0	5.54	0.0552	0.0532	0.47	40.3	63.9	0.271
2.696	25.0	5.54	0.0552	0.0532	0.46	40.3	61.1	0.283
1.701	25.1	5.54	0.0520	0.0514	0.31	38.0	27.9	0.589
1.700	25.1	5.54	0.0520	0.0514	0.31	38.0	27.9	0.590
0.628	25.3	5.54	0.0471	0.0471	0.13	34.9	5.0	3.063
0.593	25.3	5.54	0.0471	0.0471	0.12	34.9	4.4	3.441
0.335	25.4	5.54	0.0448	0.0447	0.07	33.6	1.6	9.017
0.332	25.4	5.54	0.0448	0.0447	0.07	33.6	1.6	9.189

Table D.18b: Frictional loss measurements for a 22.2% v/v kaolin clay-water slurry in the 156.7 mm flume; ρ=1375 kg/m^3

ClayWater002								
Q (L/s)	T (^{o}C)	θ (^{o})	h_1 (m)	h_2 (m)	V (m/s)	τ_w (Pa)	Re_{Zhang}	f
4.957	21.7	6.00	0.0529	0.0518	0.88	41.8	239.0	0.079
4.891	21.7	6.00	0.0529	0.0518	0.87	41.8	232.8	0.081
4.013	21.8	6.00	0.0510	0.0486	0.76	41.0	181.4	0.103
3.999	21.8	6.00	0.0510	0.0486	0.76	41.0	180.2	0.103
3.065	21.8	6.00	0.0493	0.0486	0.60	39.4	111.8	0.162
3.131	21.9	6.00	0.0493	0.0486	0.61	39.4	116.6	0.155
2.562	22.0	6.00	0.0482	0.0473	0.52	38.7	84.2	0.212
2.019	21.9	6.00	0.0467	0.0461	0.42	37.7	56.7	0.309
1.284	21.8	6.00	0.0443	0.0440	0.29	36.0	26.7	0.631
1.016	21.7	6.00	0.0430	0.0434	0.23	34.9	17.8	0.921
1.011	21.4	6.00	0.0430	0.0434	0.23	34.9	17.6	0.930
1.034	21.4	6.00	0.0430	0.0434	0.24	34.9	18.4	0.888
1.046	21.3	6.00	0.0430	0.0434	0.24	34.9	18.9	0.868
1.066	21.2	6.00	0.0430	0.0434	0.25	34.9	19.6	0.836
1.025	21.1	6.00	0.0430	0.0434	0.24	34.9	18.1	0.905
1.101	21.1	6.00	0.0430	0.0434	0.25	34.9	20.9	0.784
1.076	21.1	6.00	0.0430	0.0434	0.25	34.9	19.9	0.821
1.070	21.0	6.00	0.0430	0.0434	0.25	34.9	19.7	0.830
1.071	21.0	6.00	0.0430	0.0434	0.25	34.9	19.8	0.828
1.064	21.0	6.00	0.0430	0.0434	0.25	34.9	19.5	0.839
0.745	21.1	6.00	0.0418	0.0416	0.18	34.2	10.6	1.521
0.513	21.2	6.00	0.0406	0.0400	0.13	33.5	5.6	2.853
0.243	21.4	6.00	0.0377	0.0378	0.07	31.3	1.5	9.887
0.247	21.4	6.00	0.0377	0.0378	0.07	31.3	1.6	9.561

Table D.18c: Frictional loss measurements for a 22.2% v/v kaolin clay-water slurry in the 156.7 mm flume; ρ=1375 kg/m^3

ClayWater003								
Q (L/s)	T (^{o}C)	θ (^{o})	h_1 (m)	h_2 (m)	V (m/s)	τ_w (Pa)	Re_{Zhang}	f
6.104	21.7	5.00	0.0641	0.0627	0.83	40.4	218.5	0.084
5.032	21.8	5.00	0.0624	0.0619	0.71	39.4	157.5	0.115
3.947	21.9	5.00	0.0607	0.0608	0.57	38.4	103.8	0.171
3.117	21.8	5.00	0.0582	0.0593	0.47	36.9	71.2	0.241
3.089	21.7	5.00	0.0562	0.0568	0.49	36.0	77.5	0.216
2.617	21.4	5.00	0.0569	0.0573	0.41	36.4	54.4	0.313
2.450	21.3	5.00	0.0569	0.0573	0.39	36.4	47.7	0.357
2.082	21.1	5.00	0.0555	0.0561	0.34	35.7	36.8	0.456
1.467	21.0	5.00	0.0534	0.0535	0.25	34.8	20.7	0.793
1.478	21.0	5.00	0.0534	0.0535	0.25	34.8	21.0	0.782
0.963	21.0	5.00	0.0510	0.0509	0.18	33.6	10.2	1.562
0.947	21.0	5.00	0.0510	0.0509	0.17	33.6	9.9	1.615
0.933	21.0	5.00	0.0510	0.0509	0.17	33.6	9.6	1.666
0.971	21.0	5.00	0.0510	0.0509	0.18	33.6	10.4	1.536
0.990	21.0	5.00	0.0510	0.0509	0.18	33.6	10.8	1.478
0.992	21.0	5.00	0.0510	0.0509	0.18	33.6	10.8	1.471
1.016	21.0	5.00	0.0510	0.0509	0.19	33.6	11.3	1.403
1.025	21.0	5.00	0.0510	0.0509	0.19	33.6	11.5	1.378
1.010	21.0	5.00	0.0512	0.0520	0.18	33.5	10.8	1.461
1.029	21.0	5.00	0.0512	0.0520	0.19	33.5	11.2	1.408
0.763	21.0	5.00	0.0497	0.0500	0.14	32.8	6.8	2.288
0.486	21.1	5.00	0.0479	0.0485	0.10	31.7	3.0	4.963
0.262	21.3	5.00	0.0456	0.0454	0.06	30.7	1.0	14.145

Table D.18d: Frictional loss measurements for a 22.2% v/v kaolin clay-water slurry in the 156.7 mm flume; ρ=1375 kg/m^3

ClayWater004								
Q (L/s)	T (^{o}C)	θ (^{o})	h_1 (m)	h_2 (m)	V (m/s)	τ_w (Pa)	Re_{Zhang}	f
6.002	20.4	4.00	0.0818	0.0848	0.58	36.9	104.6	0.162
5.093	20.4	4.00	0.0787	0.0814	0.51	36.1	83.4	0.199
4.069	20.4	4.00	0.0764	0.0786	0.43	35.6	57.9	0.283
3.061	20.5	4.00	0.0734	0.0747	0.34	34.9	37.1	0.435
3.070	20.5	4.00	0.0734	0.0747	0.34	34.9	37.3	0.433
2.333	20.4	4.00	0.0702	0.0719	0.27	33.7	24.0	0.651
2.278	20.3	4.00	0.0702	0.0719	0.27	33.7	22.9	0.683
2.275	20.3	4.00	0.0702	0.0719	0.27	33.7	22.8	0.685
2.273	20.2	4.00	0.0702	0.0719	0.27	33.7	22.8	0.686
2.035	20.0	4.00	0.0693	0.0709	0.24	33.4	19.0	0.818
1.451	20.0	4.00	0.0664	0.0685	0.18	32.3	10.7	1.406
0.955	20.0	4.00	0.0636	0.0650	0.13	31.5	5.3	2.788
0.712	20.1	4.00	0.0617	0.0628	0.10	30.9	3.2	4.516
0.494	20.1	4.00	0.0594	0.0605	0.07	30.0	1.7	8.244
0.239	20.2	4.00	0.0559	0.0572	0.04	28.6	0.5	28.617

Table D.18e: Frictional loss measurements for a 22.2% v/v kaolin clay-water slurry in the 156.7 mm flume; ρ=1375 kg/m^3

ClayWater005								
Q (L/s)	T (^{o}C)	θ (^{o})	h_1 (m)	h_2 (m)	V (m/s)	τ_w (Pa)	Re_{Zhang}	f
3.525	20.0	3.00	0.1118	0.1111	0.24	33.2	19.4	0.835
2.913	19.8	3.00	0.1070	0.1063	0.21	32.7	14.6	1.096
2.522	19.7	3.00	0.1039	0.1039	0.19	32.1	11.6	1.350
1.997	19.7	3.00	0.0989	0.0989	0.16	31.4	8.2	1.883
1.498	19.7	3.00	0.0951	0.0957	0.12	30.7	5.0	3.003
0.957	19.8	3.00	0.0892	0.0898	0.08	29.7	2.4	6.108
0.940	19.9	3.00	0.0892	0.0898	0.08	29.7	2.3	6.330
0.949	19.9	3.00	0.0892	0.0898	0.08	29.7	2.4	6.205
0.972	19.9	3.00	0.0892	0.0898	0.09	29.7	2.5	5.917
0.991	20.0	3.00	0.0892	0.0898	0.09	29.7	2.6	5.696
1.019	20.0	3.00	0.0892	0.0898	0.09	29.7	2.7	5.389
1.035	20.0	3.00	0.0892	0.0898	0.09	29.7	2.8	5.226
1.059	20.1	3.00	0.0892	0.0898	0.09	29.7	2.9	4.989
1.077	20.1	3.00	0.0892	0.0898	0.09	29.7	3.0	4.825
1.094	20.1	3.00	0.0892	0.0898	0.10	29.7	3.1	4.676
1.046	20.1	3.00	0.0892	0.0898	0.09	29.7	2.9	5.114
1.056	20.2	3.00	0.0892	0.0898	0.09	29.7	2.9	5.016
0.731	20.3	3.00	0.0868	0.0863	0.07	29.5	1.5	9.611
0.729	20.3	3.00	0.0868	0.0863	0.07	29.5	1.5	9.660
0.505	20.4	3.00	0.0828	0.0836	0.05	28.3	0.8	17.469
0.287	20.5	3.00	0.0783	0.0795	0.03	27.2	0.3	45.539

Table D.18f: Frictional loss measurements for a 22.2% v/v kaolin clay-water slurry in the 156.7 mm flume; ρ=1375 kg/m^3

ClayWater006								
Q (L/s)	T (^{o}C)	θ (^{o})	h_1 (m)	h_2 (m)	V (m/s)	τ_w (Pa)	Re_{Zhang}	f
0.698	20.6	2.50	0.1158	0.1087	0.05	30.0	0.8	19.506
0.692	20.5	2.50	0.1158	0.1087	0.05	30.0	0.8	19.836
0.702	20.5	2.50	0.1158	0.1087	0.05	30.0	0.9	19.257
0.710	20.5	2.50	0.1158	0.1087	0.05	30.0	0.9	18.813
0.710	20.4	2.50	0.1158	0.1087	0.05	30.0	0.9	18.842
0.716	20.4	2.50	0.1158	0.1087	0.05	30.0	0.9	18.524
0.725	20.4	2.50	0.1158	0.1087	0.05	30.0	0.9	18.056
0.734	20.4	2.50	0.1158	0.1087	0.05	30.0	0.9	17.611
0.718	20.3	2.50	0.1158	0.1087	0.05	30.0	0.9	18.399
0.695	20.3	2.50	0.1158	0.1087	0.05	30.0	0.8	19.652
0.697	20.3	2.50	0.1158	0.1087	0.05	30.0	0.8	19.553
0.708	20.3	2.50	0.1158	0.1087	0.05	30.0	0.9	18.922
0.710	20.3	2.50	0.1158	0.1087	0.05	30.0	0.9	18.832
0.712	20.3	2.50	0.1158	0.1087	0.05	30.0	0.9	18.711
0.720	20.3	2.50	0.1158	0.1087	0.05	30.0	0.9	18.331
0.730	20.3	2.50	0.1158	0.1087	0.05	30.0	0.9	17.824
0.730	20.3	2.50	0.1158	0.1087	0.05	30.0	0.9	17.832
0.729	20.3	2.50	0.1158	0.1087	0.05	30.0	0.9	17.867
0.726	20.3	2.50	0.1158	0.1087	0.05	30.0	0.9	18.018
0.726	20.2	2.50	0.1158	0.1087	0.05	30.0	0.9	17.988
0.721	20.2	2.50	0.1158	0.1087	0.05	30.0	0.9	18.264
0.716	20.2	2.50	0.1158	0.1087	0.05	30.0	0.9	18.531
0.718	20.2	2.50	0.1158	0.1087	0.05	30.0	0.9	18.422
0.720	20.2	2.50	0.1158	0.1087	0.05	30.0	0.9	18.322
0.726	20.3	2.50	0.1158	0.1087	0.05	30.0	0.9	18.026
0.723	20.3	2.50	0.1158	0.1087	0.05	30.0	0.9	18.174
0.725	20.3	2.50	0.1158	0.1087	0.05	30.0	0.9	18.038
0.731	20.3	2.50	0.1158	0.1095	0.05	29.7	0.9	17.776
0.723	20.3	2.50	0.1158	0.1095	0.05	29.7	0.9	18.134
0.719	20.3	2.50	0.1158	0.1095	0.05	29.7	0.9	18.380
0.728	20.3	2.50	0.1158	0.1095	0.05	29.7	0.9	17.923
0.718	20.3	2.50	0.1158	0.1095	0.05	29.7	0.9	18.418
0.731	20.3	2.50	0.1158	0.1095	0.05	29.7	0.9	17.742
0.729	20.3	2.50	0.1158	0.1095	0.05	29.7	0.9	17.870
0.731	20.3	2.50	0.1158	0.1095	0.05	29.7	0.9	17.752
0.734	20.3	2.50	0.1158	0.1095	0.05	29.7	0.9	17.622
0.523	20.4	2.50	0.1102	0.1047	0.04	29.1	0.5	30.714
0.284	20.6	2.50	0.1015	0.0975	0.02	27.8	0.2	83.620

Table D.18g: Frictional loss measurements for a 22.2% v/v kaolin clay-water slurry in the 156.7 mm flume; ρ=1375 kg/m^3

ClayWater007								
Q (L/s)	T (^{o}C)	θ (^{o})	h_1 (m)	h_2 (m)	V (m/s)	τ_w (Pa)	Re_{Zhang}	f
6.018	20.5	3.50	0.0967	0.1006	0.47	35.1	70.0	0.230
5.069	20.6	3.50	0.0930	0.0964	0.42	34.5	54.8	0.290
4.139	20.7	3.50	0.0894	0.0927	0.36	33.8	40.2	0.388
2.945	20.7	3.50	0.0848	0.0871	0.27	33.1	23.5	0.651
2.947	20.7	3.50	0.0848	0.0871	0.27	33.1	23.5	0.650
2.939	20.7	3.50	0.0848	0.0871	0.27	33.1	23.4	0.654
2.944	20.6	3.50	0.0848	0.0871	0.27	33.1	23.5	0.652
2.936	20.6	3.50	0.0848	0.0871	0.27	33.1	23.4	0.655
2.936	20.5	3.50	0.0848	0.0871	0.27	33.1	23.4	0.655
2.936	20.5	3.50	0.0848	0.0871	0.27	33.1	23.4	0.655
2.944	20.5	3.50	0.0848	0.0871	0.27	33.1	23.5	0.652
2.935	20.4	3.50	0.0848	0.0871	0.27	33.1	23.4	0.656
2.938	20.4	3.50	0.0848	0.0871	0.27	33.1	23.4	0.655
2.941	20.3	3.50	0.0848	0.0871	0.27	33.1	23.5	0.653
1.998	20.3	3.50	0.0800	0.0813	0.20	32.3	12.7	1.175
1.361	20.3	3.50	0.0771	0.0784	0.14	31.5	6.5	2.256
1.003	20.3	3.50	0.0740	0.0753	0.11	30.7	3.9	3.647
0.761	20.4	3.50	0.0716	0.0730	0.09	29.9	2.5	5.690
0.542	20.4	3.50	0.0691	0.0705	0.07	29.2	1.4	9.973
0.265	20.5	3.50	0.0647	0.0662	0.03	27.8	0.4	33.391

Table D.18h: Frictional loss measurements for a 22.2% v/v kaolin clay-water slurry in the 156.7 mm flume; ρ=1375 kg/m^3

ClayWater008								
Q (L/s)	T (^{o}C)	θ (^{o})	h_1 (m)	h_2 (m)	V (m/s)	τ_w (Pa)	Re_{Zhang}	f
5.956	19.8	4.50	0.0709	0.0700	0.71	39.1	155.8	0.113
4.977	19.9	4.50	0.0694	0.0690	0.61	38.4	114.2	0.152
4.112	20.0	4.50	0.0678	0.0681	0.51	37.6	82.2	0.208
3.028	20.0	4.50	0.0647	0.0655	0.40	36.1	50.2	0.329
3.026	20.0	4.50	0.0647	0.0655	0.40	36.1	50.2	0.329
3.052	20.0	4.50	0.0647	0.0655	0.40	36.1	51.0	0.323
3.055	19.9	4.50	0.0647	0.0655	0.40	36.1	51.2	0.323
3.055	19.8	4.50	0.0647	0.0655	0.40	36.1	51.1	0.323
3.060	19.8	4.50	0.0647	0.0655	0.40	36.1	51.3	0.322
3.052	19.7	4.50	0.0647	0.0655	0.40	36.1	51.0	0.323
3.042	19.7	4.50	0.0647	0.0655	0.40	36.1	50.7	0.325
3.045	19.7	4.50	0.0647	0.0655	0.40	36.1	50.8	0.325
1.792	19.6	4.50	0.0607	0.0613	0.26	34.6	21.1	0.754
1.268	19.6	4.50	0.0586	0.0592	0.19	33.6	11.7	1.331
0.931	19.7	4.50	0.0566	0.0573	0.15	32.7	6.9	2.193
0.697	19.7	4.50	0.0548	0.0556	0.11	31.9	4.2	3.520
0.487	19.8	4.50	0.0527	0.0539	0.08	30.8	2.3	6.319
0.249	19.9	4.50	0.0500	0.0508	0.05	29.6	0.7	19.814

Table D.19a: Frictional loss measurements for a 22.6% v/v kaolin clay-water slurry with 0.03% TSPP in the 156.7 mm flume; ρ=1384 kg/m^3

ClayWater009								
Q (L/s)	T (^{o}C)	θ (^{o})	h_1 (m)	h_2 (m)	V (m/s)	τ_w (Pa)	Re_{Zhang}	f
3.815	20.6	5.00	0.0309	0.0238	1.74	19.9	3523	0.009
3.804	20.6	5.00	0.0309	0.0238	1.74	19.9	3505	0.010
3.815	20.6	5.00	0.0309	0.0238	1.74	19.9	3522	0.009
3.819	20.6	5.00	0.0309	0.0238	1.75	19.9	3529	0.009
3.149	20.7	5.00	0.0274	0.0218	1.67	18.3	3169	0.010
2.544	20.8	5.00	0.0246	0.0200	1.54	17.0	2702	0.010
1.998	20.8	5.00	0.0221	0.0186	1.38	15.9	2173	0.012
1.433	20.9	5.00	0.0189	0.0173	1.16	14.0	1568	0.015
0.993	20.9	5.00	0.0172	0.0160	0.91	13.0	1008	0.023
0.729	21.0	5.00	0.0159	0.0149	0.75	12.1	694	0.031
0.495	21.0	5.00	0.0147	0.0138	0.57	11.2	419	0.050
0.303	21.1	5.00	0.0135	0.0108	0.45	10.8	266	0.077

Table D.19b: Frictional loss measurements for a 22.6% v/v kaolin clay-water slurry with 0.03% TSPP in the 156.7 mm flume; ρ=1384 kg/m^3

ClayWater010								
Q (L/s)	T (^{o}C)	θ (^{o})	h_1 (m)	h_2 (m)	V (m/s)	τ_w (Pa)	Re_{Zhang}	f
4.899	20.5	4.00	0.0357	0.0283	1.77	17.5	4138	0.008
4.029	20.2	4.00	0.0325	0.0259	1.66	16.6	3617	0.009
3.522	19.6	4.00	0.0305	0.0244	1.58	16.0	3286	0.009
3.080	19.4	4.00	0.0285	0.0233	1.50	15.4	2948	0.010
3.064	19.3	4.00	0.0285	0.0233	1.49	15.4	2922	0.010
3.070	19.3	4.00	0.0285	0.0233	1.50	15.4	2932	0.010
3.073	19.3	4.00	0.0285	0.0233	1.50	15.4	2936	0.010
3.059	19.2	4.00	0.0285	0.0233	1.49	15.4	2914	0.010
2.598	19.1	4.00	0.0265	0.0219	1.40	14.7	2559	0.011
2.056	19.1	4.00	0.0247	0.0206	1.21	14.2	1970	0.014
1.499	19.1	4.00	0.0217	0.0192	1.02	12.8	1419	0.018
0.922	19.1	4.00	0.0188	0.0174	0.75	11.3	797	0.029
0.732	19.2	4.00	0.0179	0.0167	0.63	10.9	587	0.039
0.531	19.2	4.00	0.0165	0.0156	0.51	10.0	394	0.055
0.254	19.3	4.00	0.0152	0.0133	0.29	9.5	137	0.161

Table D.19c: Frictional loss measurements for a 22.6% v/v kaolin clay-water slurry with 0.03% TSPP in the 156.7 mm flume; ρ=1384 kg/m^3

ClayWater011								
Q (L/s)	T (^{o}C)	θ (^{o})	h_1 (m)	h_2 (m)	V (m/s)	τ_w (Pa)	Re_{Zhang}	f
4.918	19.1	3.00	0.0371	0.0309	1.62	13.8	3342	0.008
4.101	19.0	3.00	0.0346	0.0287	1.49	13.4	2861	0.009
3.584	19.0	3.00	0.0338	0.0279	1.36	13.5	2409	0.011
3.005	19.0	3.00	0.0322	0.0264	1.23	13.3	1984	0.013
2.503	19.1	3.00	0.0307	0.0255	1.08	13.1	1582	0.016
2.501	19.1	3.00	0.0307	0.0255	1.08	13.1	1580	0.016
2.498	19.2	3.00	0.0307	0.0255	1.08	13.1	1577	0.016
2.497	19.2	3.00	0.0307	0.0255	1.08	13.1	1575	0.016
2.505	19.2	3.00	0.0307	0.0255	1.09	13.1	1585	0.016
2.070	19.3	3.00	0.0286	0.0241	0.98	12.4	1304	0.019
1.540	19.4	3.00	0.0257	0.0226	0.82	11.4	935	0.024
1.047	19.4	3.00	0.0236	0.0213	0.62	10.6	550	0.040
0.777	19.5	3.00	0.0222	0.0204	0.50	10.1	360	0.059
0.571	19.6	3.00	0.0214	0.0193	0.39	9.8	230	0.092
0.282	19.7	3.00	0.0194	0.0177	0.22	9.0	76	0.267

Table D.19d: Frictional loss measurements for a 22.6% v/v kaolin clay-water slurry with 0.03% TSPP in the 156.7 mm flume; ρ=1384 kg/m^3

ClayWater012								
Q (L/s)	T (^{o}C)	θ (^{o})	h_1 (m)	h_2 (m)	V (m/s)	τ_w (Pa)	Re_{Zhang}	f
5.036	19.8	2.00	0.0428	0.0368	1.32	11.0	2415	0.009
4.479	19.9	2.00	0.0418	0.0357	1.22	11.0	2087	0.011
3.997	19.9	2.00	0.0412	0.0350	1.12	11.1	1768	0.013
3.493	19.9	2.00	0.0399	0.0339	1.02	11.1	1494	0.015
2.932	19.9	2.00	0.0391	0.0327	0.89	11.2	1167	0.020
2.480	20.0	2.00	0.0380	0.0319	0.78	11.1	916	0.026
1.999	19.9	2.00	0.0364	0.0310	0.66	10.8	669	0.035
1.993	19.8	2.00	0.0364	0.0310	0.66	10.8	666	0.036
1.985	19.8	2.00	0.0364	0.0310	0.66	10.8	661	0.036
1.980	19.7	2.00	0.0364	0.0310	0.66	10.8	657	0.036
1.980	19.7	2.00	0.0364	0.0310	0.66	10.8	658	0.036
1.981	19.7	2.00	0.0364	0.0310	0.66	10.8	658	0.036
1.555	19.6	2.00	0.0347	0.0297	0.55	10.4	468	0.050
1.025	19.6	2.00	0.0329	0.0287	0.39	10.0	237	0.097
1.017	19.6	2.00	0.0329	0.0287	0.38	10.0	233	0.099
1.020	19.6	2.00	0.0329	0.0287	0.38	10.0	234	0.098
1.018	19.6	2.00	0.0329	0.0287	0.38	10.0	234	0.098
1.023	19.6	2.00	0.0329	0.0287	0.38	10.0	236	0.098
1.017	19.6	2.00	0.0329	0.0287	0.38	10.0	233	0.099
0.756	19.6	2.00	0.0315	0.0286	0.29	9.5	140	0.158
0.509	19.6	2.00	0.0289	0.0276	0.22	8.6	76	0.267
0.240	19.7	2.00	0.0276	0.0265	0.11	8.2	20	1.004

Table D.19e: Frictional loss measurements for a 22.6% v/v kaolin clay-water slurry with 0.03% TSPP in the 156.7 mm flume; ρ=1384 kg/m^3

ClayWater013								
Q (L/s)	T (^{o}C)	θ (^{o})	h_1 (m)	h_2 (m)	V (m/s)	τ_w (Pa)	Re_{Zhang}	f
5.029	21.0	1.00	0.0649	0.0669	0.65	7.9	640	0.027
4.125	21.4	1.00	0.0671	0.0751	0.49	6.8	364	0.042
3.499	21.6	1.00	0.0694	0.0753	0.40	7.3	252	0.065
3.041	21.7	1.00	0.0680	0.0743	0.36	7.1	200	0.080
2.444	21.7	1.00	0.0673	0.0722	0.30	7.3	136	0.122
2.446	21.7	1.00	0.0673	0.0722	0.30	7.3	137	0.121
2.452	21.6	1.00	0.0673	0.0722	0.30	7.3	137	0.121
2.458	21.5	1.00	0.0673	0.0722	0.30	7.3	138	0.120
2.459	21.5	1.00	0.0673	0.0722	0.30	7.3	138	0.120
2.459	21.4	1.00	0.0665	0.0723	0.30	7.1	140	0.114
2.463	21.3	1.00	0.0665	0.0723	0.30	7.1	140	0.114
2.470	21.2	1.00	0.0665	0.0723	0.30	7.1	141	0.114
2.470	21.1	1.00	0.0665	0.0723	0.30	7.1	141	0.113
2.473	21.0	1.00	0.0665	0.0723	0.30	7.1	142	0.113
2.471	20.8	1.00	0.0665	0.0723	0.30	7.1	141	0.113
2.472	20.8	1.00	0.0655	0.0714	0.31	7.0	147	0.107
2.472	20.7	1.00	0.0655	0.0714	0.31	7.0	147	0.107
2.470	20.7	1.00	0.0655	0.0714	0.31	7.0	146	0.107
2.474	20.6	1.00	0.0655	0.0714	0.31	7.0	147	0.107
2.475	20.6	1.00	0.0655	0.0714	0.31	7.0	147	0.107
2.474	20.6	1.00	0.0655	0.0714	0.31	7.0	147	0.107
2.472	20.6	1.00	0.0655	0.0714	0.31	7.0	147	0.107
2.480	20.5	1.00	0.0655	0.0714	0.31	7.0	148	0.107
2.023	20.5	1.00	0.0652	0.0684	0.26	7.5	105	0.163
1.450	20.5	1.00	0.0647	0.0676	0.19	7.5	56	0.309
1.074	20.5	1.00	0.0629	0.0656	0.14	7.4	33	0.512
0.683	20.5	1.00	0.0618	0.0643	0.09	7.4	14	1.200
0.508	20.5	1.00	0.0616	0.0615	0.07	7.9	8	2.194
0.255	20.6	1.00	0.0607	0.0610	0.04	7.7	2	8.252

Table D.19f: Frictional loss measurements for a 22.6% v/v kaolin clay-water slurry with 0.03% TSPP in the 156.7 mm flume; ρ=1384 kg/m^3

ClayWater014								
Q (L/s)	T (^{o}C)	θ (^{o})	h_1 (m)	h_2 (m)	V (m/s)	τ_w (Pa)	Re_{Zhang}	f
4.532	20.8	6.00	0.0263	0.0233	2.33	20.4	5441	0.005
4.025	20.6	6.00	0.0250	0.0220	2.23	19.7	4993	0.006
3.484	20.5	6.00	0.0234	0.0207	2.12	18.9	4481	0.006
3.001	20.4	6.00	0.0220	0.0196	1.99	18.2	3951	0.007
3.016	20.4	6.00	0.0220	0.0196	2.00	18.1	3984	0.007
3.011	20.3	6.00	0.0220	0.0196	1.99	18.2	3973	0.007
3.005	20.3	6.00	0.0220	0.0196	1.99	18.2	3960	0.007
2.995	20.3	6.00	0.0220	0.0196	1.98	18.2	3940	0.007
2.996	20.2	6.00	0.0220	0.0196	1.98	18.2	3942	0.007
2.495	20.2	6.00	0.0202	0.0183	1.84	17.2	3410	0.007
2.023	20.2	6.00	0.0186	0.0172	1.66	16.2	2797	0.009
2.045	20.2	6.00	0.0186	0.0172	1.68	16.2	2848	0.008
2.040	20.1	6.00	0.0186	0.0172	1.67	16.2	2835	0.008
2.039	20.1	6.00	0.0186	0.0172	1.67	16.2	2833	0.008
2.033	20.1	6.00	0.0186	0.0172	1.67	16.2	2819	0.008
1.648	20.2	6.00	0.0170	0.0161	1.51	15.1	2343	0.010
0.986	20.2	6.00	0.0147	0.0141	1.12	13.3	1355	0.015
0.949	20.2	6.00	0.0147	0.0141	1.08	13.3	1271	0.017
0.953	20.2	6.00	0.0147	0.0141	1.08	13.3	1280	0.016
0.946	20.2	6.00	0.0147	0.0141	1.07	13.3	1264	0.017
0.961	20.3	6.00	0.0147	0.0141	1.09	13.3	1297	0.016
0.960	20.3	6.00	0.0147	0.0141	1.09	13.3	1295	0.016
0.795	20.3	6.00	0.0138	0.0133	0.98	12.6	1072	0.019
0.464	20.4	6.00	0.0123	0.0117	0.69	11.3	559	0.035
0.278	20.5	6.00	0.0113	0.0098	0.50	10.7	314	0.062

Table D.20a: Frictional loss measurements for a 22.8% v/v kaolin clay-water slurry with 0.10% TSPP in the 156.7 mm flume; ρ=1386 kg/m^3

ClayWater015								
Q (L/s)	T (^{o}C)	θ (^{o})	h_1 (m)	h_2 (m)	V (m/s)	τ_w (Pa)	Re	f
4.923	19.1	6.00	0.0282	0.0273	2.14	23.9	28367	0.008
4.114	19.2	6.00	0.0261	0.0257	1.97	22.6	24583	0.008
3.215	19.2	6.00	0.0234	0.0228	1.82	20.4	20412	0.009
2.487	19.2	6.00	0.0205	0.0205	1.67	18.2	16808	0.009
2.482	19.2	6.00	0.0205	0.0205	1.67	18.2	16777	0.009
2.508	19.2	6.00	0.0205	0.0205	1.69	18.2	16951	0.009
2.499	19.2	6.00	0.0205	0.0205	1.68	18.2	16888	0.009
2.500	19.2	6.00	0.0205	0.0205	1.68	18.2	16896	0.009
2.514	19.2	6.00	0.0205	0.0205	1.69	18.2	16991	0.009
2.031	19.2	6.00	0.0185	0.0186	1.58	16.6	14465	0.010
1.543	19.3	6.00	0.0161	0.0166	1.45	14.6	11750	0.010
1.042	19.3	6.00	0.0138	0.0142	1.23	12.6	8594	0.012
1.040	19.3	6.00	0.0138	0.0142	1.22	12.6	8574	0.012
1.039	19.3	6.00	0.0138	0.0142	1.22	12.6	8566	0.012
1.060	19.3	6.00	0.0138	0.0142	1.25	12.6	8744	0.012
1.033	19.3	6.00	0.0138	0.0142	1.22	12.6	8517	0.012
0.557	19.3	6.00	0.0103	0.0106	1.01	9.4	5335	0.013

Table D.20b: Frictional loss measurements for a 22.8% v/v kaolin clay-water slurry with 0.10% TSPP in the 156.7 mm flume; ρ=1386 kg/m^3

ClayWater016								
Q (L/s)	T (^{o}C)	θ (^{o})	h_1 (m)	h_2 (m)	V (m/s)	τ_w (Pa)	Re	f
4.985	19.1	5.00	0.0299	0.0296	1.96	21.3	27241	0.008
4.073	19.0	5.00	0.0272	0.0263	1.86	19.3	23558	0.008
3.220	19.0	5.00	0.0244	0.0242	1.69	17.8	19587	0.009
2.448	19.0	5.00	0.0214	0.0214	1.55	15.8	15927	0.010
2.462	19.1	5.00	0.0214	0.0214	1.56	15.8	16022	0.009
2.470	19.1	5.00	0.0214	0.0214	1.56	15.8	16075	0.009
2.461	19.1	5.00	0.0214	0.0214	1.56	15.8	16016	0.009
2.479	19.1	5.00	0.0214	0.0214	1.57	15.8	16131	0.009
2.491	19.1	5.00	0.0214	0.0214	1.58	15.8	16208	0.009
2.481	19.1	5.00	0.0214	0.0214	1.57	15.8	16145	0.009
1.978	19.0	5.00	0.0194	0.0193	1.45	14.4	13565	0.010
1.510	18.8	5.00	0.0167	0.0160	1.41	12.4	11313	0.009
1.031	18.8	5.00	0.0143	0.0141	1.19	10.8	8303	0.011
1.030	18.7	5.00	0.0143	0.0141	1.19	10.8	8298	0.011
1.037	18.7	5.00	0.0143	0.0141	1.20	10.8	8353	0.011
1.046	18.7	5.00	0.0143	0.0141	1.21	10.8	8428	0.011
1.017	18.7	5.00	0.0143	0.0141	1.17	10.8	8192	0.011
1.043	18.7	5.00	0.0143	0.0141	1.20	10.8	8401	0.011
0.463	18.8	5.00	0.0099	0.0098	0.91	7.6	4494	0.013

Table D.20c: Frictional loss measurements for a 22.8% v/v kaolin clay-water slurry with 0.10% TSPP in the 156.7 mm flume; ρ=1386 kg/m^3

ClayWater017								
Q (L/s)	T (^{o}C)	θ (^{o})	h_1 (m)	h_2 (m)	V (m/s)	τ_w (Pa)	Re	f
5.107	19.7	4.00	0.0313	0.0305	1.90	17.5	29523	0.007
4.035	19.8	4.00	0.0283	0.0275	1.74	16.1	24627	0.008
3.138	19.9	4.00	0.0249	0.0248	1.60	14.5	20376	0.008
2.517	19.9	4.00	0.0224	0.0226	1.48	13.2	17220	0.009
2.512	19.9	4.00	0.0224	0.0226	1.48	13.2	17186	0.009
2.516	19.9	4.00	0.0224	0.0226	1.48	13.2	17209	0.009
2.532	19.9	4.00	0.0224	0.0226	1.49	13.2	17320	0.009
2.536	19.8	4.00	0.0224	0.0226	1.49	13.2	17348	0.009
2.522	19.8	4.00	0.0224	0.0226	1.48	13.2	17253	0.009
2.031	19.7	4.00	0.0201	0.0202	1.40	11.9	14727	0.009
1.477	19.5	4.00	0.0176	0.0174	1.25	10.5	11522	0.010
1.002	19.4	4.00	0.0146	0.0147	1.10	8.8	8573	0.010
1.007	19.3	4.00	0.0146	0.0147	1.11	8.8	8615	0.010
1.012	19.2	4.00	0.0146	0.0147	1.12	8.8	8663	0.010
1.017	19.2	4.00	0.0146	0.0147	1.12	8.8	8703	0.010
0.999	19.2	4.00	0.0146	0.0147	1.10	8.8	8549	0.011
1.019	19.2	4.00	0.0146	0.0147	1.12	8.8	8718	0.010
1.005	19.2	4.00	0.0146	0.0147	1.11	8.8	8600	0.010
0.498	19.3	4.00	0.0105	0.0103	0.91	6.4	5085	0.011

Table D.20d: Frictional loss measurements for a 22.8% v/v kaolin clay-water slurry with 0.10% TSPP in the 156.7 mm flume; ρ=1386 kg/m^3

ClayWater018								
Q (L/s)	T (^{o}C)	θ (^{o})	h_1 (m)	h_2 (m)	V (m/s)	τ_w (Pa)	Re	f
5.999	19.6	3.00	0.0390	0.0361	1.69	15.3	31169	0.008
4.968	19.7	3.00	0.0336	0.0331	1.66	14.1	27458	0.007
4.053	19.7	3.00	0.0300	0.0297	1.58	12.8	23772	0.007
3.270	19.7	3.00	0.0275	0.0269	1.46	11.8	20154	0.008
2.448	19.6	3.00	0.0240	0.0238	1.32	10.5	16173	0.009
2.427	19.6	3.00	0.0240	0.0238	1.31	10.5	16034	0.009
2.473	19.6	3.00	0.0240	0.0238	1.33	10.5	16339	0.009
2.419	19.6	3.00	0.0240	0.0238	1.30	10.5	15981	0.009
2.455	19.6	3.00	0.0240	0.0238	1.32	10.5	16219	0.009
2.455	19.6	3.00	0.0240	0.0238	1.32	10.5	16216	0.009
2.434	19.6	3.00	0.0240	0.0238	1.31	10.5	16078	0.009
2.469	19.7	3.00	0.0240	0.0238	1.33	10.5	16309	0.009
2.438	19.7	3.00	0.0240	0.0238	1.31	10.5	16107	0.009
1.971	19.7	3.00	0.0213	0.0211	1.26	9.4	13858	0.009
1.478	19.7	3.00	0.0191	0.0186	1.13	8.5	11061	0.010
0.993	19.7	3.00	0.0155	0.0154	1.01	7.0	8239	0.010
0.991	19.8	3.00	0.0155	0.0154	1.01	7.0	8215	0.010
0.977	19.8	3.00	0.0155	0.0154	0.99	7.0	8102	0.010
0.986	19.8	3.00	0.0155	0.0154	1.00	7.0	8173	0.010
1.006	19.9	3.00	0.0155	0.0154	1.02	7.0	8345	0.010
0.987	19.9	3.00	0.0155	0.0154	1.00	7.0	8184	0.010
0.504	19.9	3.00	0.0117	0.0110	0.81	5.3	4910	0.012

Table D.20e: Frictional loss measurements for a 22.8% v/v kaolin clay-water slurry with 0.10% TSPP in the 156.7 mm flume; ρ=1386 kg/m^3

ClayWater019								
Q (L/s)	T (^{o}C)	θ (^{o})	h_1 (m)	h_2 (m)	V (m/s)	τ_w (Pa)	Re	f
6.079	20.1	2.00	0.0425	0.0398	1.51	11.1	31011	0.007
4.905	20.1	2.00	0.0372	0.0362	1.43	10.2	26602	0.007
4.087	20.0	2.00	0.0345	0.0328	1.35	9.5	23264	0.008
3.258	19.9	2.00	0.0305	0.0291	1.28	8.5	19796	0.008
2.490	19.9	2.00	0.0272	0.0261	1.14	7.8	16046	0.009
2.493	19.8	2.00	0.0272	0.0261	1.15	7.8	16065	0.009
2.486	19.8	2.00	0.0272	0.0261	1.14	7.8	16017	0.009
2.491	19.8	2.00	0.0272	0.0261	1.14	7.8	16054	0.009
2.508	19.8	2.00	0.0272	0.0261	1.15	7.8	16164	0.008
2.493	19.8	2.00	0.0272	0.0261	1.15	7.8	16066	0.009
2.489	19.8	2.00	0.0272	0.0261	1.14	7.8	16039	0.009
2.009	19.8	2.00	0.0244	0.0237	1.07	7.1	13684	0.009
1.488	19.8	2.00	0.0207	0.0204	1.00	6.1	10994	0.009
1.008	19.8	2.00	0.0170	0.0171	0.89	5.1	8212	0.009
1.006	19.8	2.00	0.0170	0.0171	0.88	5.1	8193	0.009
1.016	19.8	2.00	0.0170	0.0171	0.89	5.1	8273	0.009
1.009	19.8	2.00	0.0170	0.0171	0.89	5.1	8215	0.009
1.012	19.8	2.00	0.0170	0.0171	0.89	5.1	8240	0.009
1.005	19.8	2.00	0.0170	0.0171	0.88	5.1	8188	0.009
0.996	19.8	2.00	0.0170	0.0171	0.88	5.1	8114	0.010
0.454	19.8	2.00	0.0124	0.0123	0.64	3.8	4369	0.013

Table D.20f: Frictional loss measurements for a 22.8% v/v kaolin clay-water slurry with 0.10% TSPP in the 156.7 mm flume; ρ=1386 kg/m^3

ClayWater020								
Q (L/s)	T (^{o}C)	θ (^{o})	h_1 (m)	h_2 (m)	V (m/s)	τ_w (Pa)	Re	f
6.162	19.8	1.00	0.0507	0.0488	1.17	6.7	27844	0.007
5.259	19.8	1.00	0.0484	0.0455	1.08	6.4	24575	0.008
4.313	19.8	1.00	0.0423	0.0401	1.07	5.7	21679	0.007
3.845	19.8	1.00	0.0409	0.0382	1.01	5.6	19774	0.008
3.231	19.8	1.00	0.0375	0.0350	0.96	5.2	17434	0.008
2.530	19.7	1.00	0.0329	0.0313	0.89	4.7	14577	0.008
2.549	19.7	1.00	0.0329	0.0313	0.90	4.7	14683	0.008
2.534	19.7	1.00	0.0329	0.0313	0.89	4.7	14596	0.008
2.516	19.7	1.00	0.0329	0.0313	0.89	4.7	14494	0.009
2.537	19.7	1.00	0.0329	0.0313	0.89	4.7	14615	0.008
2.536	19.7	1.00	0.0329	0.0313	0.89	4.7	14608	0.008
2.539	19.7	1.00	0.0329	0.0313	0.89	4.7	14625	0.008
2.538	19.7	1.00	0.0329	0.0313	0.89	4.7	14624	0.008
2.547	19.7	1.00	0.0329	0.0313	0.90	4.7	14676	0.008
1.941	19.7	1.00	0.0287	0.0276	0.83	4.2	11999	0.009
1.498	19.7	1.00	0.0253	0.0244	0.76	3.7	9892	0.009
1.010	19.7	1.00	0.0209	0.0200	0.68	3.1	7394	0.010
1.016	19.7	1.00	0.0209	0.0200	0.69	3.1	7436	0.010
1.008	19.7	1.00	0.0209	0.0200	0.68	3.1	7380	0.010
1.005	19.7	1.00	0.0209	0.0200	0.68	3.1	7360	0.010
1.022	19.7	1.00	0.0209	0.0200	0.69	3.1	7481	0.009
1.012	19.7	1.00	0.0209	0.0200	0.68	3.1	7412	0.010
1.013	19.6	1.00	0.0209	0.0200	0.68	3.1	7413	0.010
1.018	19.7	1.00	0.0209	0.0200	0.69	3.1	7453	0.009
0.536	19.7	1.00	0.0151	0.0152	0.56	2.3	4578	0.010
0.316	19.7	1.00	0.0110	0.0104	0.55	1.7	3239	0.008
0.314	19.7	1.00	0.0110	0.0104	0.55	1.7	3220	0.008
0.312	19.7	1.00	0.0110	0.0104	0.55	1.7	3197	0.008
0.315	19.7	1.00	0.0110	0.0104	0.55	1.7	3227	0.008
0.311	19.7	1.00	0.0110	0.0104	0.55	1.7	3186	0.008
0.309	19.7	1.00	0.0110	0.0104	0.54	1.7	3164	0.008

Table D.21: Solids (sand) concentration profile measurements for a 25% v/v sand-water slurry in the 156.7 mm flume; ρ=1410 kg/m^3

y/D	Old Inlet $C_{solids} = C_{sand}$ (v/v)			New Inlet $C_{solids} = C_{sand}$ (v/v)			New Inlet $C_{solids} = C_{sand}$ (v/v)		
0.95	--	--	--	--	--	--	--	--	--
0.90	--	--	--	--	--	--	--	--	--
0.85	--	--	--	--	--	--	--	--	--
0.80	--	--	--	--	--	--	--	--	--
0.75	--	--	--	--	--	--	--	--	--
0.70	--	--	--	--	--	--	--	--	--
0.65	--	--	--	--	--	--	--	--	--
0.60	--	--	--	--	--	--	--	--	--
0.55	--	--	--	--	--	--	--	--	--
0.50	--	--	--	--	--	--	--	--	--
0.45	--	--	--	--	--	--	--	--	--
0.40	--	--	--	--	--	--	--	--	--
0.35	--	--	--	--	--	--	--	--	--
0.30	--	--	--	--	--	--	--	--	--
0.25	--	--	--	--	--	--	--	--	--
0.20	--	--	--	--	--	--	0.157	0.111	0.086
0.15	--	0.152	0.051	0.170	0.179	0.144	0.274	0.219	0.235
0.10	0.072	0.228	0.227	0.270	0.271	0.260	0.346	0.290	0.290
0.05	0.135	0.270	0.299	0.322	0.326	0.335	0.418	0.334	0.345
h (m)	0.0232	0.0313	0.0282	0.0363	0.0349	0.0326	0.0418	0.0410	0.0406
θ (^{o})	7	6	5	3.5	3.5	3.5	3	3	3
Q (L/s)	3.5	6	4	5	4.5	3.9	6.5	6	5.6

Table D.22: Solids and sand concentration profile measurements for a CT 'no gypsum' model tailings slurry in the 156.7 mm flume; ρ=1598 kg/m^3

y/D	C_{solids} (v/v)				C_{sand} (v/v)			
0.95	--	--	--	--	--	--	--	--
0.90	--	--	--	--	--	--	--	--
0.85	--	--	--	--	--	--	--	--
0.80	--	--	--	--	--	--	--	--
0.75	--	--	--	--	--	--	--	--
0.70	--	--	--	--	--	--	--	--
0.65	--	--	--	--	--	--	--	--
0.60	--	--	--	--	--	--	--	--
0.55	--	--	--	--	--	--	--	--
0.50	--	--	--	--	--	--	--	--
0.45	--	--	--	--	--	--	--	--
0.40	--	--	--	--	--	--	--	--
0.35	--	--	--	--	--	--	--	--
0.30	--	--	--	--	--	--	--	--
0.25	--	0.284	0.335	0.116	--	0.195	0.252	0.006
0.20	0.307	0.323	0.339	0.371	0.220	0.238	0.256	0.292
0.15	0.323	0.324	0.337	0.428	0.239	0.239	0.255	0.357
0.10	0.329	0.337	0.340	0.544	0.245	0.254	0.258	0.487
0.05	0.340	0.305	0.350	0.593	0.258	0.218	0.269	0.542
h (m)	0.0367	0.0410	0.0449	0.0396	0.0367	0.0410	0.0449	0.0396
θ (^{o})	3	2	1.5	3	3	2	1.5	3
Q (L/s)	5	5	5	2.5	5	5	5	2.5

Table D.23: Solids and sand concentration profile measurements for a CT 'gypsum' model tailings slurry in the 156.7 mm flume; ρ=1598 kg/m^3

y/D	C_{solids} (v/v)				C_{sand} (v/v)			
0.95	--	--	--	--	--	--	--	--
0.90	--	--	--	--	--	--	--	--
0.85	--	--	--	--	--	--	--	--
0.80	--	--	--	--	--	--	--	--
0.75	--	--	--	--	--	--	--	--
0.70	--	--	--	--	--	--	--	--
0.65	--	--	--	--	--	--	--	--
0.60	--	--	--	--	--	--	--	--
0.55	--	--	--	--	--	--	--	--
0.50	--	--	--	--	--	--	--	--
0.45	--	--	--	--	--	--	--	--
0.40	--	--	--	--	--	--	--	--
0.35	--	--	--	--	--	--	--	--
0.30	--	--	--	0.342	--	--	--	0.260
0.25	--	--	0.336	0.392	--	--	0.253	0.316
0.20	0.253	0.308	0.326	0.461	0.160	0.221	0.241	0.394
0.15	0.324	0.301	0.347	0.531	0.240	0.214	0.265	0.472
0.10	0.325	0.315	0.373	0.574	0.240	0.230	0.294	0.520
0.05	0.324	0.346	0.480	0.589	0.239	0.264	0.415	0.537
h (m)	0.0356	0.0394	0.0445	0.0499	0.0356	0.0394	0.0445	0.0499
θ (^{o})	3	2.5	2	3	3	2.5	2	3
Q (L/s)	5	5	5	2.5	5	5	5	2.5

Table D.24: Solids and sand concentration profile measurements for a model Thickened Tailings slurry in the 156.7 mm flume; ρ=1510 kg/m^3

y/D	C_{solids} (v/v)				C_{sand} (v/v)			
0.95	--	--	--	--	--	--	--	--
0.90	--	--	--	--	--	--	--	--
0.85	--	--	--	--	--	--	--	--
0.80	--	--	--	--	--	--	--	--
0.75	--	--	--	--	--	--	--	--
0.70	--	--	--	--	--	--	--	--
0.65	--	--	--	0.247	--	--	--	0.083
0.60	--	--	0.277	0.263	--	--	0.120	0.104
0.55	--	0.272	0.280	0.262	--	0.114	0.124	0.101
0.50	0.272	0.270	0.280	0.261	0.114	0.112	0.124	0.101
0.45	0.275	0.267	0.287	0.253	0.117	0.108	0.132	0.091
0.40	0.276	0.273	0.287	0.252	0.119	0.115	0.132	0.089
0.35	0.273	0.276	0.285	0.256	0.115	0.118	0.129	0.094
0.30	0.270	0.263	0.281	0.250	0.111	0.103	0.125	0.087
0.25	0.272	0.267	0.281	0.253	0.114	0.108	0.125	0.091
0.20	0.258	0.252	0.271	0.252	0.097	0.089	0.112	0.090
0.15	0.256	0.255	0.267	0.255	0.095	0.093	0.108	0.093
0.10	0.277	0.296	0.316	0.284	0.120	0.143	0.168	0.129
0.05	0.332	0.360	0.400	0.333	0.187	0.221	0.270	0.189
h (m)	0.0861	0.0968	0.1039	0.1077	0.0861	0.0968	0.1039	0.1077
θ (^{o})	5.4	4.5	4	4.5	5.4	4.5	4	4.5
Q (L/s)	5	5	5	2.5	5	5	5	2.5

Table D.25: Centerline mixture velocity profile measurements for Saskatoon tap water in the 156.7 mm flume

Water005		Water006		Water006	
y/h	**v/V**	**y/h**	**v/V**	**y/h**	**v/V**
0.90	1.35	0.86	1.36	0.85	1.42
0.73	1.37	0.80	1.36	0.74	1.40
0.50	1.34	0.68	1.35	0.64	1.36
0.28	1.22	0.55	1.32	0.48	1.31
0.17	1.14	0.43	1.28	0.33	1.24
--	--	0.30	1.21	0.23	1.17
--	--	0.18	1.11	0.18	1.12
--	--	0.06	0.95	0.13	1.08
Q (L/s)	7.17	Q (L/s)	7.83	Q (L/s)	1.96
θ (^{o})	1.50	θ (^{o})	2.50	θ (^{o})	3.50
h (m)	0.0443	h (m)	0.0406	h (m)	0.0194
V (m/s)	1.60	V (m/s)	1.97	V (m/s)	1.43
HPLC	off	HPLC	on	HPLC	on

Table D.26: Centerline mixture velocity profile measurements for a 22.6% v/v kaolin clay-water slurry with 0.03% TSPP in the 156.7 mm flume; ρ=1384 kg/m^3

ClayWater009		ClayWater010		ClayWater011		ClayWater014		ClayWater014	
y/h	**v/V**	**y/h**	**v/V**	**y/h**	**v/V**	**y/h**	**v/V**	**y/h**	**v/V**
0.74	1.68	0.92	1.60	0.84	1.58	0.86	1.65	0.86	1.68
0.49	1.69	0.76	1.61	0.68	1.59	0.73	1.66	0.66	1.70
0.31	1.49	0.53	1.60	0.49	1.57	0.59	1.66	0.49	1.68
0.14	0.95	0.32	1.45	0.29	1.36	0.43	1.62	0.32	1.52
--	--	0.14	0.91	0.13	0.75	0.28	1.46	0.20	1.27
--	--	--	--	--	--	0.18	1.02	--	--
Q (L/s)	3.81	Q (L/s)	3.07	Q (L/s)	2.50	Q (L/s)	3.00	Q (L/s)	2.04
θ (^{o})	5.00	θ (^{o})	4.00	θ (^{o})	3.00	θ (^{o})	6.00	θ (^{o})	6.00
h (m)	0.0238	h (m)	0.0233	h (m)	0.0255	h (m)	0.0196	h (m)	0.0172
V (m/s)	2.07	V (m/s)	1.71	V (m/s)	1.23	V (m/s)	2.15	V (m/s)	1.77
HPLC	on	HPLC	on	HPLC	on	HPLC	on	HPLC	on

Table D.27a: Centerline mixture velocity profile measurements for a 22.8% v/v kaolin clay-water slurry with 0.10% TSPP in the 156.7 mm flume; ρ=1386 kg/m^3

ClayWater015		ClayWater016		ClayWater016		ClayWater017		ClayWater017	
y/h	**v/V**	**y/h**	**v/V**	**y/h**	**v/V**	**y/h**	**v/V**	**y/h**	**v/V**
0.75	1.45	0.77	1.45	0.74	1.48	0.78	1.41	0.78	1.46
0.64	1.41	0.65	1.42	0.60	1.43	0.64	1.37	0.67	1.42
0.47	1.34	0.54	1.37	0.46	1.37	0.51	1.32	0.57	1.39
0.32	1.26	0.42	1.31	0.38	1.34	0.38	1.25	0.47	1.35
0.22	1.19	0.30	1.25	0.31	1.31	0.24	1.19	0.37	1.30
0.16	1.15	0.21	1.18	0.24	1.26	0.15	1.10	0.30	1.27
--	--	0.16	1.14	--	--	--	--	0.23	1.22
--	--	--	--	--	--	--	--	--	--
Q (L/s)	2.50	Q (L/s)	2.47	Q (L/s)	1.03	Q (L/s)	2.52	Q (L/s)	1.01
θ (^{o})	6.00	θ (^{o})	5.00	θ (^{o})	5.00	θ (^{o})	4.00	θ (^{o})	4.00
h (m)	0.0205	h (m)	0.0214	h (m)	0.0141	h (m)	0.0224	h (m)	0.0146
V (m/s)	1.68	V (m/s)	1.56	V (m/s)	1.20	V (m/s)	1.47	V (m/s)	1.11
HPLC	on	HPLC	on	HPLC	on	HPLC	on	HPLC	on

Table D.27b: Centerline mixture velocity profile measurements for a 22.8% v/v kaolin clay-water slurry with 0.10% TSPP in the 156.7 mm flume

ClayWater018		ClayWater018		ClayWater019		ClayWater020	
y/h	**v/V**	**y/h**	**v/V**	**y/h**	**v/V**	**y/h**	**v/V**
0.82	1.39	0.80	1.43	0.84	1.43	0.93	1.37
0.20	1.11	0.68	1.39	0.72	1.40	0.77	1.35
0.14	1.06	0.55	1.35	0.61	1.37	0.62	1.32
0.57	1.30	0.41	1.30	0.49	1.34	0.48	1.27
0.69	1.35	0.28	1.24	0.37	1.33	0.32	1.21
--	--	0.22	1.20	0.26	1.24	0.22	1.15
--	--	--	--	0.20	1.20	0.17	1.11
--	--	--	--	--	--	0.13	1.05
Q (L/s)	2.45	Q (L/s)	0.99	Q (L/s)	1.01	Q (L/s)	1.01
θ (^{o})	3.00	θ (^{o})	3.00	θ (^{o})	2.00	θ (^{o})	1.00
h (m)	0.0238	h (m)	0.0154	h (m)	0.0171	h (m)	0.0200
V (m/s)	1.33	V (m/s)	1.01	V (m/s)	0.88	V (m/s)	0.71
HPLC	on	HPLC	on	HPLC	on	HPLC	on

Table D.28: Flume two-dimensional mixture velocity profile measurement positions in the 156.7 mm flume (see Figure D.1)

Point	**Micrometer**	
	x (mm)	**y (mm)**
1	8.8	69.6
2	9.6	42.5
3	26.3	52.1
4	35.9	68.7
5	8.3	14.9
6	24.5	19.3
7	38.9	27.6
8	50.7	39.4
9	59.1	53.9
10	63.4	70.0
11	8.8	87.1
12	9.6	114.3
13	26.3	104.6
14	35.9	88.0
15	8.3	141.8
16	24.5	137.5
17	38.9	129.1
18	50.7	117.3
19	59.1	102.8
20	63.4	86.7

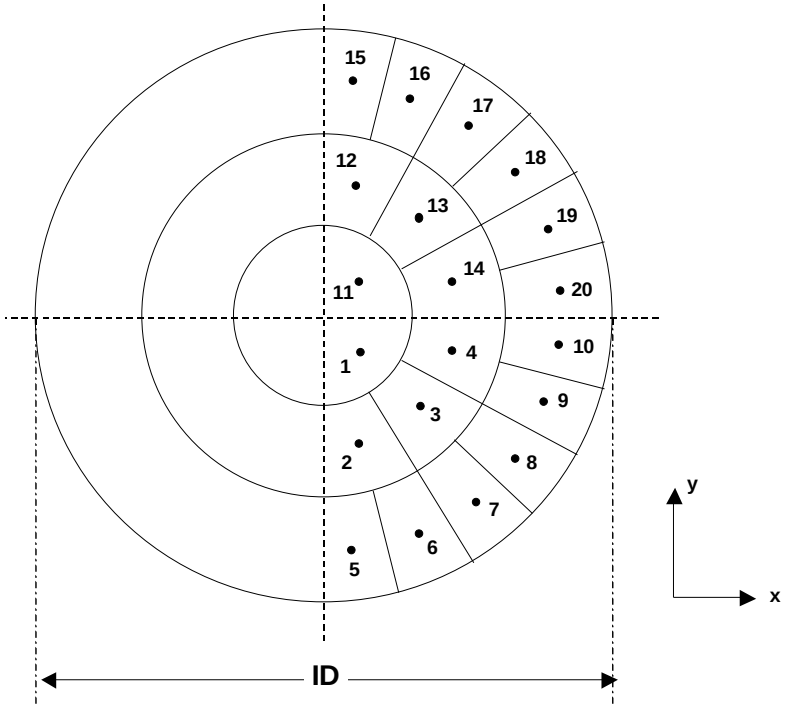

Figure D.1: Flume two-dimensional mixture velocity profile measurement positions in the 156.7 mm flume (see Table D.28)

Table D.29: Mixture velocity profile measurements for a 25% v/v sand-water slurry in the 156.7 mm flume; ρ=1410 kg/m^3

25% v/v Sand-Water								
Point	**x/R**	**y/R**	**v/V**	**v/V**	**v/V**	**v/V**	**v/V**	**v/V**
5	0.11	0.19	1.17	1.20	1.16	0.98	0.90	1.07
6	0.31	0.25	1.24	1.30	1.30	0.99	1.16	1.15
7	0.50	0.35	1.34	1.40	1.41	1.17	1.31	1.32
		Q (L/s)	5	4.5	3.9	6.5	6	5.6
		θ (^{o})	3.5	3.5	3.5	3	3	3
		h (m)	0.0350	0.0351	0.0323	0.0401	0.0406	0.0401
		V (m/s)	1.55	1.39	1.35	1.67	1.51	1.44

Table D.30: Mixture velocity profile measurements for a CT ‘no gypsum’ model tailings slurry in the 156.7 mm flume; ρ=1598 kg/m^3

CT 'No Gypsum'						
Point	**x/R**	**y/R**	**v/V**	**v/V**	**v/V**	**v/V**
2	0.12	0.54	--	--	1.39	--
3	--	--	--	--	--	--
4	--	--	--	--	--	--
5	0.11	0.19	1.21	1.07	1.12	0.57
6	0.31	0.25	1.23	1.17	1.15	0.69
7	0.50	0.35	1.26	1.27	1.15	1.46
8	0.65	0.50	--	1.14	1.18	1.68
		Q (L/s)	5	5	5	2.5
		θ (^{o})	3	2	1.5	3
		h (m)	0.0369	0.0414	0.0450	0.0396
		V (m/s)	1.44	1.24	1.09	0.68

Table D.31: Mixture velocity profile measurements for a CT ‘gypsum’ model tailings slurry in the 156.7 mm flume; ρ=1598 kg/m^3

CT 'Gypsum'						
Point	**x/R**	**y/R**	**v/V**	**v/V**	**v/V**	**v/V**
2	0.12	0.54	--	1.88	--	3.10
3	0.37	0.63	--	--	--	2.95
4	--	--	--	--	--	--
5	0.11	0.19	1.21	0.96	1.25	0.69
6	0.31	0.25	1.25	1.14	1.35	0.79
7	0.50	0.35	1.20	1.39	1.40	1.03
8	0.65	0.50	--	1.25	--	1.60
9	0.75	0.65	--	--	--	1.68
		Q (L/s)	5	5	5	2.5
		θ (^{o})	3	2	2.5	3
		h (m)	0.0349	0.0467	0.0401	0.0536
		V (m/s)	1.55	1.04	1.28	0.44

Table D.32: Mixture velocity profile measurements for a model Thickened Tailings slurry in the 156.7 mm flume; ρ=1510 kg/m^3

Thickened Tailings						
Point	**x/R**	**y/R**	**v/V**	**v/V**	**v/V**	**v/V**
1	0.11	0.89	1.75	2.37	2.37	2.41
2	0.12	0.54	1.80	2.29	2.24	2.94
3	0.34	0.66	1.71	2.35	2.19	2.45
4	0.46	0.88	1.72	2.41	2.27	2.96
5	0.11	0.19	0.82	1.70	1.40	1.96
6	0.31	0.25	0.89	1.76	1.53	2.27
7	0.50	0.35	1.00	1.71	1.67	2.04
8	0.65	0.50	0.98	1.84	1.77	1.51
9	0.75	0.69	1.17	1.78	1.80	0.59
10	0.81	0.89	1.11	1.87	1.85	1.21
11	0.11	1.11	--	2.33	2.38	2.95
12	--	--	--	--	--	--
13	0.34	1.34	--	--	--	2.11
14	0.46	1.12	--	2.30	2.37	3.09
15	--	--	--	--	--	--
16	--	--	--	--	--	--
17	--	--	--	--	--	--
18	--	--	--	--	--	--
19	0.75	1.31	--	--	1.87	1.54
20	0.81	1.11	--	2.02	1.92	2.39
		Q (L/s)	5	5	5	2.5
		θ (^{o})	5.4	4.5	4	4.5
		h (m)	0.0873	0.0970	0.1048	0.1077
		V (m/s)	0.46	0.40	0.36	0.18

Table D.33: Pressure gradient versus velocity data for Saskatoon tap water to determine the roughness of the 25 mm up test section for the low Reynolds number Pitot tube experiments

Saskatoon Tap Water													
Water001		Water003		Water004		Water005		Water006		Water007		Water008	
Velocity (m/s)	-dP/dz (kPa/m)	Velocity (m/s)	-dP/dz (kPa/m)	Velocity (m/s)	-dP/dz (kPa/m)	Velocity (m/s)	-dP/dz (kPa/m)	Velocity (m/s)	-dP/dz (kPa/m)	Velocity (m/s)	-dP/dz (kPa/m)	Velocity (m/s)	-dP/dz (kPa/m)
3.00	3.328	3.31	4.099	3.249	3.994	3.25	3.853	0.24	0.056	0.25	0.056	3.25	3.907
2.51	2.430	2.98	3.411	3.003	3.482	3.00	3.346	0.50	0.161	0.49	0.168	3.00	3.411
2.01	1.664	2.71	2.897	2.755	3.002	2.76	2.886	0.74	0.316	0.74	0.333	2.74	2.910
1.76	1.324	2.47	2.459	2.499	2.531	0.24	0.044	1.00	0.521	1.00	0.534	2.50	2.465
1.51	1.021	2.25	2.096	2.249	2.098	0.51	0.157	1.25	0.764	1.25	0.779	2.25	2.063
1.25	0.731	1.98	1.690	2.490	2.521	0.75	0.311	1.50	1.043	1.49	1.045	2.00	1.679
0.99	0.496	1.69	1.276	2.250	2.109	1.01	0.502	1.75	1.356	1.75	1.379	1.75	1.337
0.75	0.314	1.26	0.778	1.984	1.695	1.25	0.731	2.01	1.723	1.99	1.715	1.49	1.015
0.50	0.157	1.53	1.075	1.760	1.377	1.50	1.007	2.25	2.097	2.25	2.114	1.25	0.744
0.25	0.051	0.98	0.509	1.478	1.023	1.75	1.301	2.51	2.544	2.51	2.557	1.01	0.522
--	--	0.76	0.336	1.236	0.751	2.00	1.649	2.75	2.979	2.74	3.020	0.75	0.314
--	--	0.50	0.170	1.002	0.523	2.25	2.012	3.01	3.478	3.00	3.491	0.50	0.166
--	--	0.26	0.064	0.749	0.283	2.50	2.429	3.25	3.989	3.24	4.008	0.24	0.052
--	--	--	--	0.504	0.157	2.75	2.860	--	--	--	--	--	--
--	--	--	--	0.251	0.049	3.00	3.345	--	--	--	--	--	--
--	--	--	--	--	--	3.25	3.864	--	--	--	--	--	--
ε (μm)	3.4	ε (μm)	5.9	ε (μm)	6.0	ε (μm)	4.5	ε (μm)	6.4	ε (μm)	7.6	ε (μm)	6.3
T (^{o}C)	22.2	T (^{o}C)	20.4	T (^{o}C)	18.8	T (^{o}C)	25.4	T (^{o}C)	20.7	T (^{o}C)	20.4	T (^{o}C)	25.3

Table D.34a: Low Reynolds number Pitot tube data with ethylene glycol using the PSL in the 25 mm vertical pipe circuit

PSL01										
Bulk Velocity (m/s)	Temp (^oC)	Viscosity (mPa-s)	Density (kg/m^3)	Pitot Velocity (m/s)	Pitot ΔP (kPa)		Re	Red	Cp	
					Wall	Pitot-Static	Pipe	Pitot	Wall	Pitot-Static
0.749	6.5	37.5	1133	1.498	1.245	1.244	626	51.0	0.98	0.98
0.879	6.5	37.3	1133	1.758	1.724	1.721	738	60.1	0.98	0.98
1.010	6.6	36.8	1133	2.020	2.278	2.278	860	70.0	0.99	0.99
1.166	7.0	36.0	1132	2.332	3.028	3.033	1015	82.6	0.98	0.98
1.296	7.5	35.1	1132	2.593	3.754	3.758	1155	94.1	0.99	0.99
1.422	7.4	36.3	1132	2.844	4.604	4.623	1227	99.9	1.01	1.01
1.660	6.9	37.6	1132	3.319	6.390	6.421	1382	112.5	1.02	1.03

Table D.34b: Low Reynolds number Pitot tube data with ethylene glycol using the PSL in the 25 mm vertical pipe circuit

PSL03										
Bulk Velocity (m/s)	Temp (^oC)	Viscosity (mPa-s)	Density (kg/m^3)	Pitot Velocity (m/s)	Pitot ΔP (kPa)		Re	Red	Cp	
					Wall	Pitot-Static	Pipe	Pitot	Wall	Pitot-Static
0.269	10.1	35.0	1130	0.538	0.182	0.196	240	19.6	1.11	1.20
0.325	9.8	34.8	1130	0.651	0.253	0.268	292	23.8	1.06	1.12
0.380	9.9	34.7	1130	0.759	0.342	0.357	342	27.9	1.05	1.09
0.435	9.7	33.8	1130	0.871	0.442	0.457	402	32.7	1.03	1.07
0.479	9.8	33.3	1130	0.958	0.528	0.542	449	36.6	1.02	1.05
0.525	9.9	32.6	1130	1.050	0.631	0.643	504	41.1	1.01	1.03
0.575	10.1	31.8	1130	1.151	0.743	0.754	566	46.1	0.99	1.01
0.644	10.1	30.9	1130	1.289	0.906	0.920	652	53.0	0.97	0.98
0.725	10.5	30.3	1130	1.450	1.139	1.150	748	60.9	0.96	0.97
0.783	10.3	31.8	1130	1.566	1.399	1.413	769	62.6	1.01	1.02
0.845	10.0	31.7	1130	1.690	1.569	1.586	834	67.9	0.97	0.98
0.890	10.0	31.8	1130	1.779	1.829	1.842	874	71.2	1.02	1.03
0.952	10.3	31.2	1130	1.904	2.085	2.098	953	77.6	1.02	1.02
1.007	10.4	31.0	1130	2.015	2.337	2.346	1015	82.6	1.02	1.02
1.067	10.2	31.2	1130	2.135	2.594	2.604	1069	87.0	1.01	1.01
1.122	10.2	31.2	1130	2.243	2.843	2.851	1126	91.6	1.00	1.00
1.371	10.3	30.9	1130	2.743	4.221	4.241	1390	113.1	0.99	1.00

Table D.34c: Low Reynolds number Pitot tube data with ethylene glycol using the PSL in the 25 mm vertical pipe circuit

PSL04										
Bulk Velocity (m/s)	Temp (^oC)	Viscosity (mPa-s)	Density (kg/m^3)	Pitot Velocity (m/s)	Pitot ΔP (kPa)		Re	Red	Cp	
					Wall	Pitot-Static	Pipe	Pitot	Wall	Pitot-Static
0.275	15.1	25.1	1127	0.551	0.169	0.168	342	27.8	0.99	0.98
0.331	14.9	25.8	1127	0.663	0.253	0.249	400	32.5	1.02	1.01
0.402	14.7	25.7	1127	0.803	0.367	0.359	488	39.7	1.01	0.99
0.475	14.5	25.6	1127	0.949	0.496	0.489	578	47.1	0.98	0.96
0.537	14.5	25.4	1127	1.075	0.655	0.647	659	53.7	1.01	0.99
0.590	14.5	25.3	1127	1.180	0.764	0.754	727	59.2	0.97	0.96
0.750	14.8	24.8	1127	1.500	1.274	1.258	944	76.9	1.00	0.99
0.795	14.9	24.7	1127	1.590	1.428	1.412	1004	81.7	1.00	0.99
0.840	15.1	24.6	1127	1.680	1.589	1.574	1066	86.8	1.00	0.99
1.104	15.2	24.8	1127	2.208	2.726	2.719	1387	112.9	0.99	0.99

Table D.34d: Low Reynolds number Pitot tube data with ethylene glycol using the PSL in the 25 mm vertical pipe circuit

PSL06										
Bulk Velocity (m/s)	Temp (^oC)	Viscosity (mPa-s)	Density (kg/m^3)	Pitot Velocity (m/s)	Pitot ΔP (kPa)		Re	Red	Cp	
					Wall	Pitot-Static	Pipe	Pitot	Wall	Pitot-Static
0.258	5.3	43.9	1133	0.515	0.212	0.209	184	15.0	1.41	1.39
0.299	5.3	43.5	1133	0.599	0.254	0.251	216	17.6	1.25	1.23
0.347	5.6	42.8	1133	0.694	0.318	0.318	254	20.7	1.16	1.17
0.401	5.5	42.6	1133	0.802	0.405	0.406	295	24.1	1.11	1.11
0.455	5.5	42.8	1133	0.910	0.507	0.510	333	27.1	1.08	1.09
0.510	5.4	42.6	1133	1.020	0.625	0.627	375	30.5	1.06	1.06
0.602	5.4	42.2	1133	1.204	0.848	0.851	447	36.4	1.03	1.04
0.749	5.4	41.5	1133	1.498	1.269	1.281	566	46.1	1.00	1.01
1.005	5.0	41.6	1134	2.010	2.307	2.327	758	61.7	1.01	1.02
1.262	5.1	41.1	1134	2.523	3.628	3.652	964	78.5	1.01	1.01
1.508	5.3	40.9	1134	3.016	5.207	5.241	1157	94.2	1.01	1.02
0.502	5.5	41.8	1133	1.004	0.644	0.641	377	30.7	1.13	1.12
0.376	5.8	42.6	1133	0.752	0.371	0.368	277	22.5	1.16	1.15
0.282	5.4	43.8	1133	0.565	0.226	0.225	202	16.4	1.25	1.24

Table D.34e: Low Reynolds number Pitot tube data with ethylene glycol using the PSL in the 25 mm vertical pipe circuit

PSL08										
Bulk Velocity (m/s)	Temp (^oC)	Viscosity (mPa-s)	Density (kg/m^3)	Pitot Velocity (m/s)	Pitot ΔP (kPa)		Re	Red	Cp	
					Wall	Pitot-Static	Pipe	Pitot	Wall	Pitot-Static
0.174	8.3	39.1	1131	0.347	0.103	0.090	139	11.3	1.51	1.33
0.265	8.1	38.3	1132	0.531	0.185	0.189	217	17.6	1.16	1.19
0.316	8.5	38.1	1131	0.632	0.246	0.253	259	21.1	1.09	1.12
0.371	8.0	38.1	1132	0.742	0.328	0.332	305	24.8	1.05	1.07
0.424	8.2	37.7	1131	0.847	0.421	0.428	351	28.6	1.04	1.05
0.468	7.8	37.7	1132	0.937	0.510	0.517	389	31.6	1.03	1.04
0.505	7.8	37.1	1132	1.010	0.593	0.599	426	34.7	1.03	1.04
0.742	8.1	36.3	1132	1.483	1.260	1.275	639	52.0	1.01	1.02
1.024	7.9	35.7	1132	2.047	2.388	2.407	899	73.1	1.01	1.01
1.276	8.1	35.4	1132	2.551	3.696	3.721	1128	91.8	1.00	1.01
1.483	8.0	35.7	1132	2.965	5.059	5.084	1300	105.9	1.02	1.02
0.533	8.4	35.7	1131	1.066	0.695	0.691	467	38.0	1.08	1.08
0.452	8.3	36.1	1131	0.904	0.498	0.499	392	31.9	1.08	1.08
0.398	8.4	36.3	1131	0.795	0.392	0.392	343	27.9	1.10	1.10
0.353	8.4	36.3	1131	0.707	0.310	0.311	304	24.8	1.10	1.10
0.296	8.5	36.6	1131	0.591	0.221	0.222	253	20.6	1.12	1.13
0.249	8.5	37.0	1131	0.497	0.163	0.164	210	17.1	1.17	1.17
0.200	8.6	37.3	1131	0.401	0.116	0.122	168	13.7	1.27	1.35

Table D.34f: Low Reynolds number Pitot tube data with ethylene glycol using the PSL in the 25 mm vertical pipe circuit

PSL10										
Bulk Velocity (m/s)	Temp (^oC)	Viscosity (mPa-s)	Density (kg/m^3)	Pitot Velocity (m/s)	Pitot ΔP (kPa)		Re	Red	Cp	
					Wall	Pitot-Static	Pipe	Pitot	Wall	Pitot-Static
0.179	6.6	42.3	1133	0.359	0.136	0.110	133	10.8	1.87	1.51
0.256	6.4	42.6	1133	0.511	0.182	0.174	188	15.3	1.23	1.17
0.350	6.7	43.0	1133	0.701	0.309	0.303	256	20.8	1.11	1.09
0.458	6.1	42.4	1133	0.917	0.510	0.508	339	27.6	1.07	1.07
0.532	5.9	41.9	1133	1.063	0.659	0.662	398	32.4	1.03	1.03
0.781	5.7	40.6	1133	1.561	1.344	1.357	603	49.1	0.97	0.98
1.047	5.6	40.3	1133	2.094	2.496	2.517	815	66.3	1.00	1.01
1.501	5.9	39.9	1133	3.001	5.169	5.207	1179	96.0	1.01	1.02
1.745	5.7	40.6	1133	3.491	7.117	7.151	1348	109.7	1.03	1.04
1.249	5.6	40.4	1133	2.498	3.635	3.659	969	78.8	1.03	1.03
0.488	5.9	41.1	1133	0.976	0.593	0.593	372	30.3	1.10	1.10
0.397	5.9	41.6	1133	0.793	0.404	0.404	299	24.3	1.13	1.13
0.286	5.9	42.0	1133	0.572	0.228	0.223	213	17.4	1.23	1.20
0.209	6.0	42.4	1133	0.418	0.135	0.135	155	12.6	1.37	1.36
0.161	6.2	42.3	1133	0.321	0.087	0.073	119	9.7	1.49	1.25

Table D.34g: Low Reynolds number Pitot tube data with ethylene glycol using the PSL in the 25 mm vertical pipe circuit

PSL11										
Bulk Velocity (m/s)	Temp (^oC)	Viscosity (mPa-s)	Density (kg/m^3)	Pitot Velocity (m/s)	Pitot ΔP (kPa)		Re	Red	Cp	
					Wall	Pitot-Static	Pipe	Pitot	Wall	Pitot-Static
0.207	10.6	33.5	1130	0.414	0.128	0.076	193	15.7	1.33	
0.312	10.6	33.0	1130	0.625	0.242	0.253	296	24.1	1.10	1.15
0.422	10.5	33.0	1130	0.844	0.422	0.427	400	32.6	1.05	1.06
0.503	10.3	32.8	1130	1.006	0.588	0.597	479	39.0	1.03	1.04
0.750	10.1	32.4	1130	1.501	1.293	1.305	725	59.0	1.02	1.03
1.011	10.1	31.9	1130	2.022	2.342	2.360	991	80.6	1.01	1.02
1.491	10.4	31.7	1130	2.981	5.135	5.169	1468	119.5	1.02	1.03
0.551	10.5	31.5	1130	1.102	0.753	0.745	546	44.5	1.10	1.09
0.451	10.6	32.1	1130	0.902	0.505	0.504	439	35.7	1.10	1.10
0.351	10.6	32.8	1130	0.702	0.314	0.316	335	27.3	1.13	1.14
0.249	10.5	33.2	1130	0.497	0.168	0.139	234	19.1	1.20	
0.160	10.5	34.3	1130	0.320	0.084	0.059	145	11.8	1.46	

Table D.34h: Low Reynolds number Pitot tube data with ethylene glycol using the PSL in the 25 mm vertical pipe circuit

PSL16										
Bulk Velocity (m/s)	Temp (^oC)	Viscosity (mPa-s)	Density (kg/m^3)	Pitot Velocity (m/s)	Pitot ΔP (kPa)		Re	Red	Cp	
					Wall	Pitot-Static	Pipe	Pitot	Wall	Pitot-Static
0.549	15.1	24.8	1127	1.098	0.654	0.679	689	56.1	0.96	1.00
0.762	15.4	24.7	1126	1.523	1.299	1.324	959	78.1	0.99	1.01
1.000	15.8	24.2	1126	1.999	2.251	2.276	1285	104.6	1.00	1.01
0.495	15.8	24.5	1126	0.990	0.601	0.597	628	51.2	1.09	1.08

Table D.35a: Low Reynolds number Pitot tube data with ethylene glycol using the PSS in the 25 mm vertical pipe circuit

PSS07										
Bulk Velocity (m/s)	Temp (oC)	Viscosity (mPa-s)	Density (kg/m^3)	Pitot Velocity (m/s)	Pitot ΔP (kPa)		Re	Red	Cp	
					Wall	Pitot-Static	Pipe	Pitot	Wall	Pitot-Static
1.001	18.2	20.9	1124	2.001	2.149	2.159	1489	56.0	0.95	0.96
0.901	18.4	20.7	1124	1.803	1.768	1.766	1353	50.9	0.97	0.97
0.791	18.4	20.7	1124	1.582	1.403	1.407	1189	44.7	1.00	1.00
0.699	18.4	20.9	1124	1.398	1.108	1.118	1041	39.2	1.01	1.02
0.699	18.4	20.8	1124	1.398	1.094	1.101	1044	39.3	1.00	1.00
0.603	18.4	20.6	1124	1.206	0.836	0.862	909	34.2	1.02	1.06
0.488	18.4	20.5	1124	0.976	0.557	0.580	739	27.8	1.04	1.08
0.447	18.4	20.6	1124	0.893	0.464	0.482	675	25.4	1.03	1.08
0.404	18.4	20.7	1124	0.809	0.395	0.419	606	22.8	1.07	1.14
0.347	18.5	21.0	1124	0.694	0.348	0.361	514	19.3	1.28	1.33
0.348	18.5	21.0	1124	0.695	0.338	0.349	515	19.4	1.24	1.28
0.348	18.4	21.1	1124	0.697	0.327	0.343	514	19.3	1.20	1.26
0.348	18.4	21.1	1124	0.697	0.323	0.341	514	19.3	1.18	1.25
0.303	18.4	21.1	1124	0.605	0.229	0.249	447	16.8	1.11	1.21
0.489	18.4	20.9	1124	0.977	0.577	0.590	727	27.4	1.08	1.10
0.189	18.3	21.8	1124	0.378	0.116	0.121	270	10.2	1.45	1.50
0.294	18.3	21.2	1124	0.587	0.223	0.232	430	16.2	1.15	1.20
0.246	18.3	21.4	1124	0.492	0.168	0.175	358	13.5	1.23	1.28
0.999	18.4	20.9	1124	1.998	2.181	2.198	1490	56.1	0.97	0.98

Table D.35b: Low Reynolds number Pitot tube data with ethylene glycol using the PSS in the 25 mm vertical pipe circuit

PSS13										
Bulk Velocity (m/s)	Temp (oC)	Viscosity (mPa-s)	Density (kg/m^3)	Pitot Velocity (m/s)	Pitot ΔP (kPa)		Re	Red	Cp	
					Wall	Pitot-Static	Pipe	Pitot	Wall	Pitot-Static
0.482	15.3	25.7	1126	0.964	0.619	0.615	585	22.0	1.18	1.17
0.481	15.0	25.8	1127	0.962	0.601	0.594	580	21.8	1.15	1.14
0.480	14.9	25.9	1127	0.960	0.579	0.578	578	21.8	1.11	1.11
0.480	14.7	25.9	1127	0.960	0.590	0.582	578	21.7	1.14	1.12
0.429	14.8	25.7	1127	0.859	0.487	0.478	521	19.6	1.17	1.15
0.429	14.8	25.6	1127	0.858	0.476	0.468	522	19.7	1.15	1.13
0.396	15.0	25.4	1127	0.792	0.413	0.408	486	18.3	1.17	1.15
0.396	15.0	25.4	1127	0.792	0.411	0.406	486	18.3	1.16	1.15
0.341	15.1	25.4	1127	0.681	0.329	0.322	418	15.7	1.26	1.23
0.339	15.7	25.6	1126	0.678	0.347	0.354	413	15.5	1.34	1.37
0.340	15.6	25.7	1126	0.679	0.359	0.365	412	15.5	1.38	1.41
0.340	15.3	25.2	1126	0.679	0.306	0.306	421	15.8	1.18	1.18
0.939	15.3	23.8	1126	1.878	1.991	2.000	1227	46.2	1.00	1.01
0.753	15.3	24.1	1126	1.507	1.329	1.336	976	36.7	1.04	1.05
0.606	15.2	24.4	1127	1.212	0.857	0.857	774	29.1	1.04	1.04
0.503	15.2	24.5	1127	1.005	0.644	0.643	639	24.1	1.13	1.13
0.406	15.3	24.6	1127	0.813	0.455	0.449	516	19.4	1.22	1.21
0.350	15.4	24.8	1126	0.700	0.353	0.347	441	16.6	1.28	1.26
0.304	15.4	25.1	1126	0.607	0.283	0.277	377	14.2	1.36	1.34
0.503	15.2	24.5	1127	1.007	0.612	0.622	641	24.1	1.07	1.09
0.502	15.2	24.5	1127	1.005	0.629	0.630	638	24.0	1.11	1.11
0.503	15.2	24.5	1127	1.005	0.619	0.622	639	24.0	1.09	1.09
0.304	15.3	25.1	1127	0.608	0.273	0.268	378	14.2	1.31	1.29
0.510	15.3	24.4	1127	1.021	0.618	0.621	651	24.5	1.05	1.06
0.295	15.4	25.2	1126	0.590	0.252	0.245	366	13.8	1.28	1.25
0.248	15.4	25.6	1126	0.496	0.188	0.182	302	11.4	1.36	1.31
0.249	15.4	25.5	1126	0.498	0.181	0.176	304	11.4	1.29	1.26
0.200	15.5	26.4	1126	0.399	0.129	0.122	235	8.9	1.44	1.36
0.220	15.4	26.1	1126	0.440	0.136	0.135	262	9.9	1.25	1.24
0.220	15.3	26.2	1126	0.439	0.146	0.142	261	9.8	1.34	1.31
0.173	15.3	27.0	1127	0.345	0.102	0.096	199	7.5	1.52	1.43
0.171	15.3	27.2	1127	0.343	0.101	0.094	196	7.4	1.52	1.42
0.987	15.2	23.9	1127	1.973	2.102	2.110	1288	48.4	0.96	0.96
0.500	15.3	24.4	1126	1.001	0.660	0.646	638	24.0	1.17	1.14

Table D.35c: Low Reynolds number Pitot tube data with ethylene glycol using the PSS in the 25 mm vertical pipe circuit

PSS14										
Bulk Velocity (m/s)	Temp (oC)	Viscosity (mPa-s)	Density (kg/m^3)	Pitot Velocity (m/s)	Pitot ΔP (kPa)		Re	Red	Cp	
					Wall	Pitot-Static	Pipe	Pitot	Wall	Pitot-Static
0.748	9.9	31.7	1130	1.496	1.330	1.368	738	27.8	1.05	1.08
0.747	9.9	31.6	1130	1.495	1.351	1.377	739	27.8	1.07	1.09
0.747	9.9	31.5	1130	1.494	1.361	1.382	741	27.9	1.08	1.10
0.875	10.1	30.5	1130	1.749	1.695	1.724	897	33.8	0.98	1.00
0.870	10.1	30.4	1130	1.740	1.751	1.767	893	33.6	1.02	1.03
0.872	10.2	30.2	1130	1.744	1.739	1.750	902	33.9	1.01	1.02
0.873	10.4	30.0	1130	1.745	1.725	1.736	908	34.2	1.00	1.01
1.004	10.3	30.3	1130	2.009	2.269	2.293	1037	39.0	1.00	1.01
1.004	10.3	30.3	1130	2.008	2.316	2.345	1037	39.0	1.02	1.03
1.003	10.3	30.3	1130	2.006	2.334	2.351	1036	39.0	1.03	1.03
1.004	10.3	30.2	1130	2.008	2.322	2.337	1040	39.1	1.02	1.03
0.693	10.4	30.6	1130	1.386	1.105	1.121	708	26.6	1.02	1.03
0.693	10.4	30.7	1130	1.385	1.121	1.132	705	26.5	1.03	1.04
0.693	10.4	30.7	1130	1.385	1.127	1.141	704	26.5	1.04	1.05
0.693	10.3	30.8	1130	1.385	1.134	1.148	704	26.5	1.05	1.06
0.708	10.1	31.0	1130	1.415	1.159	1.187	715	26.9	1.02	1.05
0.713	10.0	30.7	1130	1.425	1.145	1.163	726	27.3	1.00	1.01
0.715	10.0	30.5	1130	1.430	1.160	1.178	734	27.6	1.00	1.02
0.650	10.1	30.6	1130	1.301	1.019	1.023	665	25.0	1.07	1.07
0.645	10.3	30.5	1130	1.290	1.017	1.020	661	24.9	1.08	1.08
0.648	10.3	30.2	1130	1.295	1.010	1.017	670	25.2	1.07	1.07
0.655	10.3	30.1	1130	1.310	1.001	1.009	680	25.6	1.03	1.04
0.594	10.3	30.7	1130	1.189	0.904	0.897	605	22.8	1.13	1.12
0.593	10.4	30.6	1130	1.185	0.879	0.885	604	22.7	1.11	1.12
1.003	10.0	30.4	1130	2.006	2.261	2.293	1030	38.8	0.99	1.01
0.599	10.2	31.4	1130	1.198	0.977	0.966	597	22.5	1.21	1.19
0.599	10.2	31.2	1130	1.198	0.926	0.928	599	22.6	1.14	1.14
0.546	10.4	31.1	1130	1.093	0.814	0.811	549	20.7	1.21	1.20
0.547	10.4	30.9	1130	1.093	0.797	0.785	552	20.8	1.18	1.16

Table D.35d: Low Reynolds number Pitot tube data with ethylene glycol using the PSS in the 25 mm vertical pipe circuit

PSS15										
Bulk Velocity (m/s)	Temp (oC)	Viscosity (mPa-s)	Density (kg/m^3)	Pitot Velocity (m/s)	Pitot ΔP (kPa)		Re	Red	Cp	
					Wall	Pitot-Static	Pipe	Pitot	Wall	Pitot-Static
0.982	10.1	31.4	1130	1.964	2.187	2.214	979	36.8	1.00	1.02
0.981	10.1	31.3	1130	1.962	2.150	2.170	981	36.9	0.99	1.00
0.981	10.2	31.1	1130	1.963	2.129	2.147	985	37.1	0.98	0.99
0.500	10.6	31.8	1130	1.000	0.694	0.697	491	18.5	1.23	1.23
0.500	10.5	32.1	1130	1.000	0.687	0.700	488	18.3	1.22	1.24
0.597	10.3	31.9	1130	1.194	0.900	0.914	585	22.0	1.12	1.14
0.597	10.2	31.9	1130	1.194	0.905	0.918	585	22.0	1.12	1.14
0.553	10.3	31.9	1130	1.105	0.808	0.814	542	20.4	1.17	1.18
0.552	10.3	31.7	1130	1.105	0.783	0.801	544	20.5	1.14	1.16
0.455	10.5	32.0	1130	0.910	0.572	0.578	444	16.7	1.22	1.24
0.455	10.6	32.1	1130	0.909	0.579	0.584	443	16.7	1.24	1.25
0.402	10.6	32.6	1130	0.805	0.482	0.482	385	14.5	1.32	1.32
0.402	10.6	32.7	1130	0.805	0.465	0.473	385	14.5	1.27	1.29
0.752	10.3	31.1	1130	1.504	1.359	1.376	756	28.4	1.06	1.08
0.752	10.3	31.0	1130	1.504	1.367	1.380	758	28.5	1.07	1.08
0.752	10.4	31.0	1130	1.504	1.328	1.351	759	28.6	1.04	1.06
0.402	10.6	32.5	1130	0.804	0.497	0.478	387	14.5	1.36	1.31
0.346	10.7	33.5	1130	0.692	0.436	0.421	322	12.1	1.61	1.56
0.765	11.2	29.8	1129	1.530	1.282	1.321	802	30.2	0.97	1.00
0.764	10.8	30.4	1130	1.528	1.307	1.339	785	29.5	0.99	1.02
0.349	10.8	33.0	1130	0.698	0.407	0.389	331	12.5	1.48	1.41
0.349	10.8	33.1	1130	0.698	0.377	0.370	330	12.4	1.37	1.34
0.302	10.3	33.6	1130	0.604	0.305	0.292	281	10.6	1.48	1.42
0.302	10.2	33.5	1130	0.605	0.288	0.281	282	10.6	1.40	1.36
0.302	10.2	33.4	1130	0.604	0.271	0.266	283	10.6	1.31	1.29
0.510	10.3	31.5	1130	1.020	0.652	0.652	506	19.0	1.11	1.11
0.246	10.5	32.8	1130	0.493	0.258	0.237	235	8.8	1.88	1.72
0.247	10.6	32.6	1130	0.494	0.240	0.214	236	8.9	1.74	1.56
0.151	10.6	34.8	1130	0.302	0.124	0.110	136	5.1	2.41	2.14
0.151	10.7	35.0	1130	0.301	0.131	0.114	134	5.1	2.56	2.23
0.151	10.7	35.0	1130	0.302	0.104	0.101	135	5.1	2.02	1.96
0.200	10.6	33.9	1130	0.400	0.125	0.127	184	6.9	1.39	1.40
0.199	10.6	34.2	1130	0.398	0.151	0.141	182	6.9	1.69	1.58
0.199	10.6	34.5	1130	0.397	0.140	0.139	180	6.8	1.57	1.56

Table D.35e: Low Reynolds number Pitot tube data with ethylene glycol using the PSS in the 25 mm vertical pipe circuit

PSS16										
Bulk Velocity (m/s)	Temp (oC)	Viscosity (mPa-s)	Density (kg/m^3)	Pitot Velocity (m/s)	Pitot ΔP (kPa)		Re	Red	Cp	
					Wall	Pitot-Static	Pipe	Pitot	Wall	Pitot-Static
0.514	7.1	40.5	1132	1.029	0.683	0.711	398	15.0	1.14	1.19
0.515	6.7	41.1	1133	1.030	0.718	0.734	393	14.8	1.20	1.22
0.515	6.5	41.6	1133	1.030	0.717	0.735	388	14.6	1.19	1.22
1.001	4.7	41.6	1134	2.002	2.363	2.396	756	28.4	1.04	1.05
0.999	4.6	41.6	1134	1.999	2.364	2.383	753	28.3	1.04	1.05
0.998	4.6	41.6	1134	1.997	2.344	2.366	753	28.3	1.04	1.05
0.998	4.6	41.5	1134	1.996	2.364	2.381	755	28.4	1.05	1.05
1.507	4.8	40.0	1134	3.014	5.023	5.065	1180	44.4	0.98	0.98
1.506	4.7	40.1	1134	3.012	5.045	5.062	1177	44.3	0.98	0.98
1.504	4.7	40.2	1134	3.009	5.049	5.068	1174	44.2	0.98	0.99
1.253	4.7	40.6	1134	2.507	3.677	3.670	969	36.5	1.03	1.03
1.253	4.7	40.5	1134	2.505	3.659	3.668	970	36.5	1.03	1.03
1.252	4.7	40.5	1134	2.505	3.661	3.657	970	36.5	1.03	1.03
1.104	4.6	41.0	1134	2.207	2.868	2.854	845	31.8	1.04	1.03
1.104	4.6	41.0	1134	2.207	2.857	2.869	845	31.8	1.03	1.04
0.895	4.4	42.3	1134	1.790	1.951	1.972	665	25.0	1.07	1.08
0.895	4.4	41.9	1134	1.790	1.954	1.965	670	25.2	1.08	1.08
0.895	4.5	41.6	1134	1.789	1.955	1.963	675	25.4	1.08	1.08
0.842	4.8	41.5	1134	1.684	1.757	1.772	637	24.0	1.09	1.10
0.842	4.7	41.6	1134	1.685	1.732	1.748	635	23.9	1.08	1.09
0.791	4.7	42.2	1134	1.583	1.579	1.581	589	22.1	1.11	1.11
0.792	4.6	42.2	1134	1.583	1.568	1.579	588	22.1	1.10	1.11
0.740	4.6	42.4	1134	1.480	1.411	1.416	548	20.6	1.14	1.14
0.740	4.6	42.3	1134	1.481	1.415	1.414	549	20.7	1.14	1.14
0.741	4.6	42.2	1134	1.481	1.370	1.382	551	20.7	1.10	1.11
0.697	4.7	42.2	1134	1.394	1.247	1.235	518	19.5	1.13	1.12
0.698	4.7	42.2	1134	1.396	1.181	1.181	519	19.5	1.07	1.07
0.698	5.0	42.2	1134	1.397	1.292	1.340	519	19.5	1.17	1.21
0.699	4.8	42.5	1134	1.397	1.296	1.329	515	19.4	1.17	1.20
0.698	4.7	42.7	1134	1.397	1.295	1.326	513	19.3	1.17	1.20
0.646	4.7	43.0	1134	1.292	1.141	1.137	472	17.7	1.21	1.20
0.646	4.7	42.9	1134	1.292	1.107	1.119	473	17.8	1.17	1.18
0.646	4.7	42.8	1134	1.291	1.109	1.105	474	17.8	1.17	1.17
0.646	4.7	42.7	1134	1.292	1.082	1.094	475	17.9	1.14	1.16
0.594	4.9	42.8	1134	1.187	0.934	0.938	435	16.4	1.17	1.17
0.594	4.9	42.8	1134	1.187	0.950	0.957	435	16.4	1.19	1.20
0.594	4.9	42.8	1134	1.188	0.919	0.932	435	16.4	1.15	1.16
0.552	5.1	43.3	1134	1.104	0.783	0.797	400	15.1	1.13	1.15
0.552	5.1	43.2	1134	1.105	0.815	0.826	401	15.1	1.18	1.19
0.552	5.1	43.3	1134	1.103	0.806	0.813	399	15.0	1.17	1.18
0.498	4.9	43.3	1134	0.996	0.666	0.675	361	13.6	1.18	1.20
0.498	4.9	43.3	1134	0.996	0.694	0.689	361	13.6	1.23	1.23
0.498	4.9	43.2	1134	0.997	0.657	0.665	362	13.6	1.17	1.18
0.445	5.2	43.7	1134	0.890	0.580	0.573	319	12.0	1.29	1.28
0.445	5.2	43.7	1134	0.890	0.543	0.550	320	12.0	1.21	1.22
0.446	5.2	43.7	1134	0.891	0.546	0.553	320	12.0	1.21	1.23
0.400	4.9	44.1	1134	0.801	0.470	0.473	284	10.7	1.29	1.30
0.401	4.9	44.0	1134	0.802	0.456	0.469	286	10.7	1.25	1.29
0.400	4.9	44.2	1134	0.800	0.446	0.448	284	10.7	1.23	1.24
0.400	4.9	44.2	1134	0.800	0.450	0.451	284	10.7	1.24	1.24

Table D.35e: Low Reynolds number Pitot tube data with ethylene glycol using the PSS in the 25 mm vertical pipe circuit

PSS16										
Bulk Velocity (m/s)	Temp (oC)	Viscosity (mPa-s)	Density (kg/m^3)	Pitot Velocity (m/s)	Pitot ΔP (kPa)		Re	Red	Cp	
					Wall	Pitot-Static	Pipe	Pitot	Wall	Pitot-Static
0.993	4.5	41.9	1134	1.986	2.266	2.349	743	28.0	1.01	1.05
0.498	4.8	43.3	1134	0.997	0.764	0.754	361	13.6	1.36	1.34
0.401	4.8	44.2	1134	0.802	0.527	0.518	284	10.7	1.45	1.42
0.348	5.2	44.8	1134	0.696	0.414	0.412	244	9.2	1.51	1.50
0.348	5.2	44.9	1134	0.696	0.399	0.396	243	9.1	1.45	1.44
0.348	5.2	45.0	1134	0.696	0.387	0.395	243	9.1	1.41	1.44
0.292	4.8	45.8	1134	0.583	0.301	0.301	200	7.5	1.56	1.56
0.291	4.9	46.0	1134	0.581	0.319	0.309	198	7.5	1.66	1.61
0.291	4.9	45.9	1134	0.582	0.288	0.290	199	7.5	1.50	1.51
0.151	4.9	50.9	1134	0.303	0.155	0.144	93	3.5	2.99	2.76
0.152	4.9	50.5	1134	0.304	0.150	0.143	94	3.5	2.86	2.74
0.153	5.0	50.0	1134	0.305	0.146	0.133	96	3.6	2.76	2.52
0.198	5.3	47.6	1134	0.396	0.177	0.174	131	4.9	1.99	1.96
0.199	5.3	47.4	1134	0.398	0.161	0.170	132	5.0	1.79	1.89
0.199	5.3	47.8	1134	0.398	0.171	0.172	131	4.9	1.90	1.91
0.247	5.1	46.8	1134	0.494	0.210	0.212	165	6.2	1.52	1.54
0.250	5.1	46.8	1134	0.500	0.191	0.208	167	6.3	1.35	1.47
0.247	5.1	46.5	1134	0.495	0.213	0.219	167	6.3	1.53	1.58

Table D.35f: Low Reynolds number Pitot tube data with ethylene glycol using the PSS in the 25 mm vertical pipe circuit

PSS17										
Bulk Velocity (m/s)	Temp (oC)	Viscosity (mPa-s)	Density (kg/m^3)	Pitot Velocity (m/s)	Pitot ΔP (kPa)		Re	Red	Cp	
					Wall	Pitot-Static	Pipe	Pitot	Wall	Pitot-Static
0.802	7.4	35.8	1132	1.603	1.600	1.616	702	26.4	1.10	1.11
0.801	7.3	35.9	1132	1.603	1.585	1.601	699	26.3	1.09	1.10
0.801	7.3	36.0	1132	1.603	1.596	1.605	698	26.2	1.10	1.10
0.993	7.6	34.8	1132	1.986	2.299	2.316	894	33.6	1.03	1.04
1.501	8.5	32.6	1131	3.001	5.018	5.034	1439	54.2	0.99	0.99
1.497	8.6	32.6	1131	2.994	5.007	5.033	1435	54.0	0.99	0.99
0.498	6.8	40.1	1132	0.995	0.780	0.785	389	14.6	1.39	1.40
0.498	6.7	39.9	1133	0.997	0.775	0.778	391	14.7	1.38	1.38
0.498	6.6	39.8	1133	0.995	0.741	0.750	392	14.7	1.32	1.34
0.498	6.5	39.6	1133	0.995	0.718	0.714	394	14.8	1.28	1.27
0.497	6.5	39.4	1133	0.993	0.770	0.763	395	14.8	1.38	1.37
0.399	7.0	38.6	1132	0.799	0.556	0.536	324	12.2	1.54	1.48
0.399	7.0	38.4	1132	0.798	0.531	0.519	325	12.2	1.47	1.44
0.399	7.3	37.4	1132	0.799	0.511	0.502	334	12.6	1.41	1.39
0.299	7.5	40.7	1132	0.599	0.310	0.305	230	8.7	1.53	1.50
0.299	7.4	40.8	1132	0.599	0.309	0.309	230	8.7	1.52	1.52
0.300	7.2	40.5	1132	0.600	0.313	0.302	232	8.7	1.53	1.48
0.205	7.2	40.6	1132	0.411	0.207	0.190	158	6.0	2.17	1.99
0.205	7.3	40.3	1132	0.411	0.238	0.224	160	6.0	2.50	2.34
0.206	7.4	40.4	1132	0.411	0.192	0.189	159	6.0	2.01	1.97
0.148	7.4	43.5	1132	0.295	0.147	0.146	106	4.0	2.98	2.95
0.148	7.4	43.6	1132	0.296	0.144	0.133	106	4.0	2.92	2.69
0.149	7.4	43.8	1132	0.298	0.144	0.136	106	4.0	2.87	2.70

Table D.35g: Low Reynolds number Pitot tube data with ethylene glycol using the PSS in the 25 mm vertical pipe circuit

PSS18										
Bulk Velocity (m/s)	Temp (oC)	Viscosity (mPa-s)	Density (kg/m^3)	Pitot Velocity (m/s)	Pitot ΔP (kPa)		Re	Red	Cp	
					Wall	Pitot-Static	Pipe	Pitot	Wall	Pitot-Static
0.994	6.5	36.9	1133	1.988	2.234	2.272	845	31.8	1.00	1.01
0.993	6.6	36.6	1133	1.987	2.299	2.313	851	32.0	1.03	1.03
0.993	6.8	36.1	1132	1.985	2.255	2.261	861	32.4	1.01	1.01
0.500	7.4	38.6	1132	1.000	0.728	0.751	405	15.3	1.29	1.33
0.500	7.2	38.6	1132	1.000	0.723	0.735	406	15.3	1.28	1.30
0.499	7.0	38.5	1132	0.999	0.733	0.727	406	15.3	1.30	1.29
0.446	6.8	38.4	1132	0.892	0.629	0.611	364	13.7	1.40	1.36
0.445	6.9	38.0	1132	0.891	0.580	0.571	367	13.8	1.29	1.27
0.453	7.1	37.3	1132	0.907	0.578	0.580	381	14.3	1.24	1.25
0.394	7.4	37.4	1132	0.789	0.458	0.456	331	12.4	1.30	1.29
0.395	7.5	37.6	1132	0.789	0.459	0.453	329	12.4	1.30	1.29
0.412	7.2	38.7	1132	0.824	0.489	0.500	333	12.5	1.27	1.30
0.348	6.9	39.3	1132	0.696	0.407	0.400	277	10.4	1.48	1.46
0.348	6.8	39.2	1132	0.695	0.399	0.391	278	10.4	1.46	1.43
0.292	7.1	39.3	1132	0.583	0.345	0.322	233	8.7	1.79	1.67
0.291	7.2	39.0	1132	0.583	0.319	0.301	234	8.8	1.66	1.57
0.292	7.3	38.7	1132	0.584	0.306	0.299	236	8.9	1.58	1.55
0.247	7.2	39.2	1132	0.493	0.239	0.228	197	7.4	1.73	1.66
0.247	7.2	39.4	1132	0.494	0.242	0.240	197	7.4	1.75	1.73
0.247	7.2	39.9	1132	0.494	0.241	0.234	194	7.3	1.74	1.69
0.199	7.2	41.7	1132	0.399	0.192	0.185	150	5.6	2.14	2.06
0.199	7.1	41.8	1132	0.399	0.195	0.187	149	5.6	2.17	2.08
0.199	7.1	41.7	1132	0.399	0.177	0.170	150	5.6	1.97	1.89
0.149	7.2	43.0	1132	0.298	0.125	0.120	109	4.1	2.49	2.39
0.149	7.2	42.9	1132	0.298	0.124	0.110	109	4.1	2.47	2.19
0.149	7.3	42.6	1132	0.298	0.124	0.113	109	4.1	2.48	2.26
0.545	7.1	38.1	1132	1.090	0.718	0.743	448	16.8	1.07	1.10
0.999	6.7	36.6	1133	1.999	2.268	2.292	856	32.2	1.00	1.01
0.998	6.9	36.0	1132	1.997	2.277	2.297	868	32.6	1.01	1.02
0.999	7.0	35.8	1132	1.997	2.294	2.303	873	32.9	1.02	1.02
0.888	6.9	36.6	1132	1.777	1.902	1.910	761	28.6	1.06	1.07
0.889	6.8	36.6	1132	1.778	1.832	1.844	761	28.6	1.02	1.03
0.888	6.8	36.5	1132	1.777	1.903	1.911	763	28.7	1.06	1.07
0.888	6.9	36.3	1132	1.776	1.898	1.911	767	28.8	1.06	1.07
0.778	6.9	36.7	1132	1.555	1.489	1.499	663	24.9	1.09	1.10
0.778	6.8	36.9	1132	1.555	1.488	1.497	660	24.8	1.09	1.09
0.779	6.8	36.8	1132	1.557	1.488	1.495	664	25.0	1.08	1.09
0.744	7.0	36.2	1132	1.487	1.372	1.373	643	24.2	1.10	1.10
0.743	7.0	36.3	1132	1.487	1.338	1.357	642	24.1	1.07	1.08
0.744	7.0	36.4	1132	1.488	1.367	1.372	640	24.1	1.09	1.09
0.693	6.9	37.0	1132	1.385	1.198	1.214	586	22.0	1.10	1.12
0.692	6.9	37.1	1132	1.385	1.207	1.209	585	22.0	1.11	1.11
0.692	6.8	37.1	1132	1.385	1.218	1.215	586	22.0	1.12	1.12
0.641	6.9	36.7	1132	1.283	1.066	1.055	547	20.6	1.14	1.13
0.642	6.9	36.6	1132	1.283	1.045	1.050	550	20.7	1.12	1.13
0.641	7.0	36.5	1132	1.282	1.059	1.049	550	20.7	1.14	1.13
0.598	7.0	37.0	1132	1.196	0.898	0.912	506	19.0	1.11	1.13
0.598	7.0	37.1	1132	1.197	0.907	0.919	505	19.0	1.12	1.13
0.598	6.9	37.3	1132	1.195	0.925	0.933	502	18.9	1.14	1.15
0.547	7.1	37.3	1132	1.094	0.789	0.787	459	17.3	1.16	1.16
0.547	7.1	37.1	1132	1.093	0.784	0.788	461	17.3	1.16	1.16

Table D.35g: Low Reynolds number Pitot tube data with ethylene glycol using the PSS in the 25 mm vertical pipe circuit

PSS18										
Bulk Velocity (m/s)	Temp (oC)	Viscosity (mPa-s)	Density (kg/m^3)	Pitot Velocity (m/s)	Pitot ΔP (kPa)		Re	Red	Cp	
					Wall	Pitot-Static	Pipe	Pitot	Wall	Pitot-Static
0.547	7.1	37.1	1132	1.093	0.787	0.782	462	17.4	1.16	1.15
0.502	7.2	37.3	1132	1.004	0.674	0.676	422	15.9	1.18	1.18
0.503	7.2	37.4	1132	1.005	0.662	0.668	421	15.8	1.16	1.17
0.502	7.2	37.6	1132	1.004	0.669	0.676	418	15.7	1.17	1.19
0.397	7.2	38.3	1132	0.794	0.472	0.457	325	12.2	1.32	1.28
0.295	7.3	38.7	1132	0.590	0.336	0.314	239	9.0	1.70	1.59
0.203	7.1	39.7	1132	0.407	0.211	0.189	160	6.0	2.25	2.02

APPPENDIX E:
SIMULATION DATA

Table E.1: Steady state Phillips model verification simulation results for neutrally buoyant spheres in a rectangular duct of infinite width

Simulation Input	
h =	0.05 m
ρ_f =	870 kg/m^3
ρ_s =	870 kg/m^3
μ_f =	0.20 Pa-s
ϕ_{total} =	0.40 v/v
ϕ_{max} =	0.58 v/v
θ =	5.0 deg
dt =	100 s

Simulation Output		d (mm)	0.475	d (mm)	0.188	Phillips et al. (1992)	
i	y/h	u (m/s)	ϕ (v/v)	u (m/s)	ϕ (v/v)	γ	ϕ (v/v)
0	-0.01	-0.02	0.278	-0.02	0.278	49.25	n/a
1	0.01	0.02	0.280	0.02	0.279	48.45	0.281
2	0.03	0.07	0.282	0.07	0.282	46.72	0.284
3	0.05	0.12	0.285	0.12	0.284	44.86	0.287
4	0.07	0.16	0.288	0.16	0.287	43.00	0.290
5	0.09	0.20	0.291	0.20	0.291	41.17	0.293
6	0.11	0.24	0.295	0.24	0.294	39.36	0.296
7	0.13	0.28	0.298	0.28	0.297	37.59	0.300
8	0.15	0.32	0.301	0.32	0.300	35.84	0.303
9	0.17	0.35	0.304	0.35	0.304	34.13	0.306
10	0.19	0.39	0.308	0.39	0.307	32.45	0.310
11	0.21	0.42	0.311	0.42	0.311	30.81	0.313
12	0.23	0.45	0.315	0.45	0.314	29.20	0.317
13	0.25	0.48	0.319	0.48	0.318	27.62	0.321
14	0.27	0.50	0.323	0.50	0.322	26.08	0.325
15	0.29	0.53	0.326	0.53	0.326	24.58	0.329
16	0.31	0.55	0.330	0.55	0.330	23.12	0.333
17	0.33	0.57	0.334	0.58	0.334	21.69	0.337
18	0.35	0.59	0.339	0.60	0.338	20.31	0.341
19	0.37	0.61	0.343	0.62	0.342	18.96	0.345
20	0.39	0.63	0.347	0.64	0.347	17.66	0.350
21	0.41	0.65	0.352	0.65	0.351	16.39	0.354
22	0.43	0.66	0.356	0.67	0.356	15.17	0.359
23	0.45	0.68	0.361	0.68	0.360	14.00	0.364
24	0.47	0.69	0.366	0.70	0.365	12.87	0.368
25	0.49	0.70	0.371	0.71	0.370	11.78	0.373
26	0.51	0.72	0.376	0.72	0.375	10.74	0.379
27	0.53	0.73	0.381	0.73	0.380	9.75	0.384
28	0.55	0.73	0.386	0.74	0.386	8.80	0.389
29	0.57	0.74	0.392	0.75	0.391	7.91	0.395
30	0.59	0.75	0.398	0.75	0.397	7.06	0.401
31	0.61	0.76	0.403	0.76	0.403	6.26	0.407
32	0.63	0.76	0.409	0.77	0.409	5.51	0.413
33	0.65	0.77	0.416	0.77	0.415	4.81	0.419
34	0.67	0.77	0.422	0.78	0.422	4.16	0.426
35	0.69	0.78	0.429	0.78	0.428	3.56	0.433
36	0.71	0.78	0.436	0.78	0.435	3.02	0.440
37	0.73	0.78	0.443	0.79	0.442	2.52	0.447
38	0.75	0.78	0.450	0.79	0.450	2.07	0.454
39	0.77	0.79	0.458	0.79	0.457	1.67	0.462
40	0.79	0.79	0.466	0.79	0.465	1.32	0.470
41	0.81	0.79	0.474	0.79	0.474	1.02	0.478
42	0.83	0.79	0.483	0.79	0.482	0.76	0.487
43	0.85	0.79	0.492	0.80	0.491	0.54	0.496
44	0.87	0.79	0.501	0.80	0.501	0.37	0.504
45	0.89	0.79	0.511	0.80	0.511	0.24	0.513
46	0.91	0.79	0.522	0.80	0.522	0.14	0.520
47	0.93	0.79	0.533	0.80	0.533	0.07	0.522
48	0.95	0.79	0.546	0.80	0.545	0.03	0.510
49	0.97	0.79	0.559	0.80	0.559	0.01	n/a
50	0.99	0.79	0.580	0.80	0.580	0.00	n/a
51	1.01	0.79	0.580	0.80	0.580	0.00	n/a
	In-Situ =	**0.60**	**0.390**	**0.61**	**0.389**		
	Delivered =	--	**0.414**	--	**0.414**		
	iterations =	**181**	--	**1003**	--		
	real time (s) =	**28**	--	**157**	--		
	sim time (s) =	**18100**	--	**100300**	--		

Table E.2: Model simulation results at t = 9.5 s for a Thickened Tailings test (5 L/s, 4 ^{o})

Simulation Input	
h =	0.0455 m
d =	0.188 mm
ρ_f =	1303 kg/m^3
ρ_s =	2650 kg/m^3
μ_P =	0.0245 Pa-s
τ_y =	33.6 Pa
A_{mult} =	1.0E+05
ϕ_{total} =	0.000 v/v
ϕ_{max} =	0.582 v/v
θ =	4.0 deg
dt =	0.5 s

Simulation Output			
i	**y/h**	**u (m/s)**	**ϕ (v/v)**
0	-0.01	-0.06	0.294
1	0.01	0.06	0.264
2	0.03	0.25	0.132
3	0.05	0.48	0.117
4	0.07	0.69	0.119
5	0.09	0.87	0.119
6	0.11	1.04	0.117
7	0.13	1.19	0.117
8	0.15	1.31	0.116
9	0.17	1.42	0.116
10	0.19	1.50	0.115
11	0.21	1.57	0.116
12	0.23	1.61	0.117
13	0.25	1.63	0.125
14	0.27	1.63	0.135
15	0.29	1.63	0.131
16	0.31	1.63	0.131
17	0.33	1.63	0.131
18	0.35	1.63	0.131
19	0.37	1.63	0.131
20	0.39	1.63	0.131
21	0.41	1.63	0.131
22	0.43	1.63	0.131
23	0.45	1.63	0.131
24	0.47	1.63	0.131
25	0.49	1.63	0.131
26	0.51	1.63	0.131
27	0.53	1.63	0.131
28	0.55	1.63	0.131
29	0.57	1.63	0.131
30	0.59	1.63	0.131
31	0.61	1.63	0.131
32	0.63	1.63	0.131
33	0.65	1.63	0.131
34	0.67	1.63	0.131
35	0.69	1.63	0.131
36	0.71	1.63	0.131
37	0.73	1.63	0.131
38	0.75	1.63	0.131
39	0.77	1.63	0.131
40	0.79	1.63	0.131
41	0.81	1.63	0.131
42	0.83	1.63	0.131
43	0.85	1.63	0.131
44	0.87	1.63	0.131
45	0.89	1.63	0.131
46	0.91	1.63	0.131
47	0.93	1.63	0.131
48	0.95	1.63	0.131
49	0.97	1.63	0.131
50	0.99	1.63	0.131
51	1.01	1.63	1.869
In-Situ =		**1.48**	**0.131**
Delivered =		**--**	**0.128**
iterations =		**19**	**--**
real time (s) =		**17**	**--**
sim time (s) =		**9.5**	**--**

Table E.3: Transient model simulation results for a Thickened Tailings test (5 L/s, 4 ^{o})

Simulation Output															
i	**y/h**	**u (m/s)**	**ϕ (v/v)**	**u (m/s)**	**ϕ (v/v)**	**u (m/s)**	**ϕ (v/v)**	**u (m/s)**	**ϕ (v/v)**	**u (m/s)**	**ϕ (v/v)**	**u (m/s)**	**ϕ (v/v)**	**u (m/s)**	**ϕ (v/v)**
0	-0.01	-0.21	0.180	-0.08	0.257	-0.06	0.302	-0.04	0.340	0.00	0.544	0.00	0.582	0.00	0.582
1	0.01	0.21	0.142	0.08	0.218	0.06	0.275	0.04	0.321	0.00	0.541	0.00	0.582	0.00	0.582
2	0.03	0.55	0.126	0.29	0.120	0.25	0.136	0.21	0.156	0.05	0.308	0.00	0.532	0.00	0.582
3	0.05	0.80	0.130	0.51	0.121	0.47	0.117	0.43	0.118	0.20	0.151	0.07	0.232	0.05	0.260
4	0.07	1.01	0.130	0.71	0.124	0.68	0.118	0.65	0.112	0.42	0.098	0.27	0.085	0.26	0.063
5	0.09	1.16	0.130	0.89	0.123	0.87	0.117	0.84	0.111	0.64	0.076	0.51	0.030	0.54	0.002
6	0.11	1.28	0.130	1.05	0.123	1.04	0.116	1.02	0.110	0.84	0.068	0.75	0.023	0.79	0.004
7	0.13	1.37	0.130	1.18	0.123	1.19	0.115	1.18	0.108	1.03	0.065	0.96	0.024	1.01	0.003
8	0.15	1.43	0.130	1.30	0.122	1.31	0.115	1.31	0.107	1.19	0.063	1.14	0.022	1.20	0.004
9	0.17	1.47	0.130	1.40	0.122	1.42	0.114	1.42	0.107	1.34	0.061	1.29	0.022	1.37	0.003
10	0.19	1.49	0.130	1.47	0.122	1.51	0.114	1.52	0.106	1.45	0.059	1.42	0.022	1.50	0.004
11	0.21	1.49	0.131	1.53	0.123	1.57	0.114	1.59	0.106	1.54	0.058	1.52	0.022	1.60	0.004
12	0.23	1.49	0.131	1.57	0.124	1.61	0.115	1.64	0.107	1.61	0.059	1.59	0.023	1.67	0.004
13	0.25	1.49	0.131	1.58	0.129	1.64	0.123	1.66	0.115	1.65	0.065	1.63	0.027	1.72	0.007
14	0.27	1.49	0.131	1.58	0.132	1.64	0.136	1.67	0.132	1.67	0.105	1.64	0.063	1.73	0.029
15	0.29	1.49	0.131	1.58	0.131	1.64	0.131	1.67	0.131	1.67	0.135	1.64	0.111	1.73	0.123
16	0.31	1.49	0.131	1.58	0.131	1.64	0.131	1.67	0.131	1.67	0.131	1.64	0.131	1.73	0.131
17	0.33	1.49	0.131	1.58	0.131	1.64	0.131	1.67	0.131	1.67	0.131	1.64	0.131	1.73	0.131
18	0.35	1.49	0.131	1.58	0.131	1.64	0.131	1.67	0.131	1.67	0.131	1.64	0.131	1.73	0.131
19	0.37	1.49	0.131	1.58	0.131	1.64	0.131	1.67	0.131	1.67	0.131	1.64	0.131	1.73	0.131
20	0.39	1.49	0.131	1.58	0.131	1.64	0.131	1.67	0.131	1.67	0.131	1.64	0.131	1.73	0.131
21	0.41	1.49	0.131	1.58	0.131	1.64	0.131	1.67	0.131	1.67	0.131	1.64	0.131	1.73	0.131
22	0.43	1.49	0.131	1.58	0.131	1.64	0.131	1.67	0.131	1.67	0.131	1.64	0.131	1.73	0.131
23	0.45	1.49	0.131	1.58	0.131	1.64	0.131	1.67	0.131	1.67	0.131	1.64	0.131	1.73	0.131
24	0.47	1.49	0.131	1.58	0.131	1.64	0.131	1.67	0.131	1.67	0.131	1.64	0.131	1.73	0.131
25	0.49	1.49	0.131	1.58	0.131	1.64	0.131	1.67	0.131	1.67	0.131	1.64	0.131	1.73	0.131
26	0.51	1.49	0.131	1.58	0.131	1.64	0.131	1.67	0.131	1.67	0.131	1.64	0.131	1.73	0.131
27	0.53	1.49	0.131	1.58	0.131	1.64	0.131	1.67	0.131	1.67	0.131	1.64	0.131	1.73	0.131
28	0.55	1.49	0.131	1.58	0.131	1.64	0.131	1.67	0.131	1.67	0.131	1.64	0.131	1.73	0.131
29	0.57	1.49	0.131	1.58	0.131	1.64	0.131	1.67	0.131	1.67	0.131	1.64	0.131	1.73	0.131
30	0.59	1.49	0.131	1.58	0.131	1.64	0.131	1.67	0.131	1.67	0.131	1.64	0.131	1.73	0.131
31	0.61	1.49	0.131	1.58	0.131	1.64	0.131	1.67	0.131	1.67	0.131	1.64	0.131	1.73	0.131
32	0.63	1.49	0.131	1.58	0.131	1.64	0.131	1.67	0.131	1.67	0.131	1.64	0.131	1.73	0.131
33	0.65	1.49	0.131	1.58	0.131	1.64	0.131	1.67	0.131	1.67	0.131	1.64	0.131	1.73	0.131
34	0.67	1.49	0.131	1.58	0.131	1.64	0.131	1.67	0.131	1.67	0.131	1.64	0.131	1.73	0.131
35	0.69	1.49	0.131	1.58	0.131	1.64	0.131	1.67	0.131	1.67	0.131	1.64	0.131	1.73	0.131
36	0.71	1.49	0.131	1.58	0.131	1.64	0.131	1.67	0.131	1.67	0.131	1.64	0.131	1.73	0.131
37	0.73	1.49	0.131	1.58	0.131	1.64	0.131	1.67	0.131	1.67	0.131	1.64	0.131	1.73	0.131
38	0.75	1.49	0.131	1.58	0.131	1.64	0.131	1.67	0.131	1.67	0.131	1.64	0.131	1.73	0.131
39	0.77	1.49	0.131	1.58	0.131	1.64	0.131	1.67	0.131	1.67	0.131	1.64	0.131	1.73	0.131
40	0.79	1.49	0.131	1.58	0.131	1.64	0.131	1.67	0.131	1.67	0.131	1.64	0.131	1.73	0.131
41	0.81	1.49	0.131	1.58	0.131	1.64	0.131	1.67	0.131	1.67	0.131	1.64	0.131	1.73	0.131
42	0.83	1.49	0.131	1.58	0.131	1.64	0.131	1.67	0.131	1.67	0.131	1.64	0.131	1.73	0.131
43	0.85	1.49	0.131	1.58	0.131	1.64	0.131	1.67	0.131	1.67	0.131	1.64	0.131	1.73	0.131
44	0.87	1.49	0.131	1.58	0.131	1.64	0.131	1.67	0.131	1.67	0.131	1.64	0.131	1.73	0.131
45	0.89	1.49	0.131	1.58	0.131	1.64	0.131	1.67	0.131	1.67	0.131	1.64	0.131	1.73	0.131
46	0.91	1.49	0.131	1.58	0.131	1.64	0.131	1.67	0.131	1.67	0.131	1.64	0.131	1.73	0.131
47	0.93	1.49	0.131	1.58	0.131	1.64	0.131	1.67	0.131	1.67	0.131	1.64	0.131	1.73	0.131
48	0.95	1.49	0.131	1.58	0.131	1.64	0.131	1.67	0.131	1.67	0.131	1.64	0.131	1.73	0.131
49	0.97	1.49	0.131	1.58	0.131	1.64	0.131	1.67	0.131	1.67	0.131	1.64	0.131	1.73	0.131
50	0.99	1.49	0.131	1.58	0.131	1.64	0.131	1.67	0.131	1.67	0.131	1.64	0.131	1.73	0.131
51	1.01	1.49	1.869	1.58	1.869	1.64	1.869	1.67	1.869	1.67	1.869	1.64	1.869	1.73	1.869
In-Situ =		**1.41**	**0.131**	**1.44**	**0.131**	**1.48**	**0.131**	**1.51**	**0.130**	**1.47**	**0.130**	**1.44**	**0.128**	**1.51**	**0.125**
Delivered =		**--**	**0.130**	**--**	**0.129**	**--**	**0.128**	**--**	**0.127**	**--**	**0.120**	**--**	**0.112**	**--**	**0.109**
sim time (s) =		**0.5**	**--**	**5.0**	**--**	**10**	**--**	**15**	**--**	**50**	**--**	**100**	**--**	**200**	**--**

Table E.4: Model simulation results at t = 48.5 s for a Thickened Tailings test (5 L/s, 4.5 ^{o})

Simulation Input	
h =	0.0441 m
d =	0.188 mm
ρ_f =	1303 kg/m^3
ρ_s =	2650 kg/m^3
μ_P =	0.023259 Pa-s
τ_y =	45.4 Pa
A_{mult} =	1.0E+06
ϕ_{total} =	0.11 v/v
ϕ_{max} =	0.582 v/v
θ =	4.5 deg
dt =	0.5 s

Simulation Output			
i	**y/h**	**u (m/s)**	**ϕ (v/v)**
0	-0.01	-0.03	0.262
1	0.01	0.03	0.221
2	0.03	0.09	0.079
3	0.05	0.15	0.057
4	0.07	0.18	0.066
5	0.09	0.18	0.102
6	0.11	0.18	0.114
7	0.13	0.18	0.113
8	0.15	0.18	0.113
9	0.17	0.18	0.113
10	0.19	0.18	0.113
11	0.21	0.18	0.113
12	0.23	0.18	0.113
13	0.25	0.18	0.113
14	0.27	0.18	0.113
15	0.29	0.18	0.113
16	0.31	0.18	0.113
17	0.33	0.18	0.113
18	0.35	0.18	0.113
19	0.37	0.18	0.113
20	0.39	0.18	0.113
21	0.41	0.18	0.113
22	0.43	0.18	0.113
23	0.45	0.18	0.113
24	0.47	0.18	0.113
25	0.49	0.18	0.113
26	0.51	0.18	0.113
27	0.53	0.18	0.113
28	0.55	0.18	0.113
29	0.57	0.18	0.113
30	0.59	0.18	0.113
31	0.61	0.18	0.113
32	0.63	0.18	0.113
33	0.65	0.18	0.113
34	0.67	0.18	0.113
35	0.69	0.18	0.113
36	0.71	0.18	0.113
37	0.73	0.18	0.113
38	0.75	0.18	0.113
39	0.77	0.18	0.113
40	0.79	0.18	0.113
41	0.81	0.18	0.113
42	0.83	0.18	0.113
43	0.85	0.18	0.113
44	0.87	0.18	0.113
45	0.89	0.18	0.113
46	0.91	0.18	0.113
47	0.93	0.18	0.113
48	0.95	0.18	0.113
49	0.97	0.18	0.113
50	0.99	0.18	0.113
51	1.01	0.18	1.887
In-Situ =		**0.18**	**0.113**
Delivered =		**--**	**0.111**
iterations =		**97**	**--**
real time (s) =		**95**	**--**
sim time (s) =		**48.5**	**--**

Table E.5: Model simulation results at t = 8.5 s for a Thickened Tailings test (5 L/s, 5.4 ^{o})

Simulation Input	
h =	0.0415 m
d =	0.188 mm
ρ_f =	1303 kg/m^3
ρ_s =	2650 kg/m^3
μ_P =	0.021373 Pa-s
τ_y =	47.3 Pa
A_{mult} =	1.0E+06
ϕ_{total} =	0.11 v/v
ϕ_{max} =	0.582 v/v
θ =	5.4 deg
dt =	0.5 s

Simulation Output			
i	**y/h**	**u (m/s)**	**ϕ (v/v)**
0	-0.01	-0.06	0.224
1	0.01	0.06	0.192
2	0.03	0.22	0.097
3	0.05	0.37	0.098
4	0.07	0.49	0.101
5	0.09	0.58	0.100
6	0.11	0.64	0.100
7	0.13	0.67	0.108
8	0.15	0.67	0.118
9	0.17	0.67	0.115
10	0.19	0.67	0.115
11	0.21	0.67	0.115
12	0.23	0.67	0.115
13	0.25	0.67	0.115
14	0.27	0.67	0.115
15	0.29	0.67	0.115
16	0.31	0.67	0.115
17	0.33	0.67	0.115
18	0.35	0.67	0.115
19	0.37	0.67	0.115
20	0.39	0.67	0.115
21	0.41	0.67	0.115
22	0.43	0.67	0.115
23	0.45	0.67	0.115
24	0.47	0.67	0.115
25	0.49	0.67	0.115
26	0.51	0.67	0.115
27	0.53	0.67	0.115
28	0.55	0.67	0.115
29	0.57	0.67	0.115
30	0.59	0.67	0.115
31	0.61	0.67	0.115
32	0.63	0.67	0.115
33	0.65	0.67	0.115
34	0.67	0.67	0.115
35	0.69	0.67	0.115
36	0.71	0.67	0.115
37	0.73	0.67	0.115
38	0.75	0.67	0.115
39	0.77	0.67	0.115
40	0.79	0.67	0.115
41	0.81	0.67	0.115
42	0.83	0.67	0.115
43	0.85	0.67	0.115
44	0.87	0.67	0.115
45	0.89	0.67	0.115
46	0.91	0.67	0.115
47	0.93	0.67	0.115
48	0.95	0.67	0.115
49	0.97	0.67	0.115
50	0.99	0.67	0.115
51	1.01	0.67	1.885
In-Situ =		**0.64**	**0.115**
Delivered =		**--**	**0.114**
iterations =		**17**	**--**
real time (s) =		**15**	**--**
sim time (s) =		**8.5**	**--**

Table E.6: Model simulation results at t = 500 s for a Thickened Tailings test with a reduced immersed weight (4 ^{o})

Simulation Input	
h =	0.0500 m
d =	0.188 mm
ρ_f =	1600 kg/m^3
ρ_s =	2000 kg/m^3
μ_p =	0.05 Pa-s
τ_y =	50.0 Pa
A_{mult} =	1.0E+06
ϕ_{total} =	0.15 v/v
ϕ_{max} =	0.58 v/v
θ =	4.0 deg
dt =	1 s

Simulation Output			
i	**y/h**	**u (m/s)**	**ϕ (v/v)**
0	-0.01	-0.03	0.176
1	0.01	0.03	0.188
2	0.03	0.09	0.110
3	0.05	0.15	0.096
4	0.07	0.20	0.085
5	0.09	0.23	0.077
6	0.11	0.25	0.087
7	0.13	0.25	0.150
8	0.15	0.25	0.150
9	0.17	0.25	0.150
10	0.19	0.25	0.150
11	0.21	0.25	0.150
12	0.23	0.25	0.150
13	0.25	0.25	0.150
14	0.27	0.25	0.150
15	0.29	0.25	0.150
16	0.31	0.25	0.150
17	0.33	0.25	0.150
18	0.35	0.25	0.150
19	0.37	0.25	0.150
20	0.39	0.25	0.150
21	0.41	0.25	0.150
22	0.43	0.25	0.150
23	0.45	0.25	0.150
24	0.47	0.25	0.150
25	0.49	0.25	0.150
26	0.51	0.25	0.150
27	0.53	0.25	0.150
28	0.55	0.25	0.150
29	0.57	0.25	0.150
30	0.59	0.25	0.150
31	0.61	0.25	0.150
32	0.63	0.25	0.150
33	0.65	0.25	0.150
34	0.67	0.25	0.150
35	0.69	0.25	0.150
36	0.71	0.25	0.150
37	0.73	0.25	0.150
38	0.75	0.25	0.150
39	0.77	0.25	0.150
40	0.79	0.25	0.150
41	0.81	0.25	0.150
42	0.83	0.25	0.150
43	0.85	0.25	0.150
44	0.87	0.25	0.150
45	0.89	0.25	0.150
46	0.91	0.25	0.150
47	0.93	0.25	0.150
48	0.95	0.25	0.150
49	0.97	0.25	0.150
50	0.99	0.25	0.150
51	1.01	0.25	1.850
In-Situ =		**0.24**	**0.145**
Delivered =		**--**	**0.145**
iterations =		**500**	**--**
real time (s) =		**232**	**--**
sim time (s) =		**500**	**--**

Table E.7: Model simulation results at t = 0.65 s for a CT 'gypsum' test (5 L/s, 2 ^{o})

Simulation Input	
h =	0.0256 m
d =	0.188 mm
ρ_f =	1188 kg/m^3
ρ_s =	2650 kg/m^3
μ_P =	0.0028 Pa-s
τ_y =	7.3 Pa
A_{mult} =	1.0E+06
ϕ_{total} =	0.275 v/v
ϕ_{max} =	0.582 v/v
θ =	2.0 deg
dt =	0.05 s

Simulation Output			
i	**y/h**	**u (m/s)**	**ϕ (v/v)**
0	-0.01	-0.03	0.446
1	0.01	0.03	0.428
2	0.03	0.19	0.297
3	0.05	0.44	0.242
4	0.07	0.67	0.240
5	0.09	0.86	0.247
6	0.11	1.02	0.247
7	0.13	1.13	0.250
8	0.15	1.22	0.255
9	0.17	1.27	0.261
10	0.19	1.31	0.265
11	0.21	1.33	0.270
12	0.23	1.34	0.275
13	0.25	1.34	0.276
14	0.27	1.34	0.275
15	0.29	1.34	0.275
16	0.31	1.34	0.275
17	0.33	1.34	0.275
18	0.35	1.34	0.275
19	0.37	1.34	0.275
20	0.39	1.34	0.275
21	0.41	1.34	0.275
22	0.43	1.34	0.275
23	0.45	1.34	0.275
24	0.47	1.34	0.275
25	0.49	1.34	0.275
26	0.51	1.34	0.275
27	0.53	1.34	0.275
28	0.55	1.34	0.275
29	0.57	1.34	0.275
30	0.59	1.34	0.275
31	0.61	1.34	0.275
32	0.63	1.34	0.275
33	0.65	1.34	0.275
34	0.67	1.34	0.275
35	0.69	1.34	0.275
36	0.71	1.34	0.275
37	0.73	1.34	0.275
38	0.75	1.34	0.275
39	0.77	1.34	0.275
40	0.79	1.34	0.275
41	0.81	1.34	0.275
42	0.83	1.34	0.275
43	0.85	1.34	0.275
44	0.87	1.34	0.275
45	0.89	1.34	0.275
46	0.91	1.34	0.275
47	0.93	1.34	0.275
48	0.95	1.34	0.275
49	0.97	1.34	0.275
50	0.99	1.34	0.275
51	1.01	1.34	1.725
	In-Situ =	**1.24**	**0.274**
	Delivered =	--	**0.272**
	iterations =	**13**	--
	real time (s) =	**11**	--
	sim time (s) =	**0.65**	--

Table E.8: Transient model simulation results for a CT 'gypsum' test (5 L/s, 2 ^{o})

Simulation Output															
i	**y/h**	**u (m/s)**	**ϕ (v/v)**	**u (m/s)**	**ϕ (v/v)**	**u (m/s)**	**ϕ (v/v)**	**u (m/s)**	**ϕ (v/v)**	**u (m/s)**	**ϕ (v/v)**	**u (m/s)**	**ϕ (v/v)**	**u (m/s)**	**ϕ (v/v)**
0	-0.01	-0.53	0.275	-0.05	0.420	-0.01	0.492	0.00	0.562	0.00	0.573	0.00	0.577	0.00	0.581
1	0.01	0.53	0.273	0.05	0.398	0.01	0.479	0.00	0.560	0.00	0.572	0.00	0.577	0.00	0.580
2	0.03	0.97	0.273	0.25	0.275	0.09	0.353	0.00	0.526	0.00	0.565	0.00	0.568	0.00	0.579
3	0.05	1.15	0.280	0.53	0.243	0.29	0.256	0.03	0.437	0.00	0.561	0.00	0.560	0.00	0.576
4	0.07	1.23	0.275	0.76	0.251	0.52	0.227	0.14	0.296	0.00	0.551	0.00	0.570	0.00	0.565
5	0.09	1.26	0.274	0.94	0.255	0.73	0.228	0.34	0.207	0.01	0.478	0.00	0.582	0.00	0.542
6	0.11	1.27	0.274	1.07	0.254	0.91	0.232	0.58	0.178	0.12	0.260	0.00	0.580	0.00	0.552
7	0.13	1.27	0.275	1.17	0.257	1.05	0.235	0.80	0.175	0.37	0.128	0.00	0.547	0.00	0.576
8	0.15	1.27	0.275	1.24	0.262	1.16	0.240	0.98	0.180	0.65	0.102	0.13	0.201	0.00	0.582
9	0.17	1.27	0.275	1.29	0.266	1.24	0.246	1.13	0.186	0.91	0.105	0.47	0.036	0.15	0.160
10	0.19	1.27	0.275	1.32	0.270	1.30	0.252	1.25	0.194	1.12	0.111	0.80	0.040	0.56	0.005
11	0.21	1.27	0.275	1.33	0.274	1.34	0.259	1.35	0.203	1.30	0.118	1.08	0.037	0.93	0.008
12	0.23	1.27	0.275	1.33	0.276	1.37	0.266	1.42	0.213	1.44	0.126	1.33	0.044	1.27	0.004
13	0.25	1.27	0.275	1.33	0.275	1.38	0.274	1.47	0.224	1.54	0.135	1.54	0.047	1.57	0.008
14	0.27	1.27	0.275	1.33	0.275	1.38	0.277	1.50	0.241	1.62	0.148	1.71	0.053	1.84	0.006
15	0.29	1.27	0.275	1.33	0.275	1.38	0.275	1.51	0.267	1.68	0.171	1.84	0.061	2.07	0.012
16	0.31	1.27	0.275	1.33	0.275	1.38	0.275	1.51	0.283	1.70	0.225	1.94	0.076	2.26	0.009
17	0.33	1.27	0.275	1.33	0.275	1.38	0.275	1.51	0.275	1.71	0.282	2.00	0.103	2.42	0.017
18	0.35	1.27	0.275	1.33	0.275	1.38	0.275	1.51	0.275	1.71	0.278	2.03	0.174	2.54	0.013
19	0.37	1.27	0.275	1.33	0.275	1.38	0.275	1.51	0.275	1.71	0.275	2.04	0.272	2.63	0.018
20	0.39	1.27	0.275	1.33	0.275	1.38	0.275	1.51	0.275	1.71	0.275	2.04	0.276	2.69	0.015
21	0.41	1.27	0.275	1.33	0.275	1.38	0.275	1.51	0.275	1.71	0.275	2.04	0.275	2.71	0.119
22	0.43	1.27	0.275	1.33	0.275	1.38	0.275	1.51	0.275	1.71	0.275	2.04	0.275	2.71	0.255
23	0.45	1.27	0.275	1.33	0.275	1.38	0.275	1.51	0.275	1.71	0.275	2.04	0.275	2.71	0.275
24	0.47	1.27	0.275	1.33	0.275	1.38	0.275	1.51	0.275	1.71	0.275	2.04	0.275	2.71	0.275
25	0.49	1.27	0.275	1.33	0.275	1.38	0.275	1.51	0.275	1.71	0.275	2.04	0.275	2.71	0.275
26	0.51	1.27	0.275	1.33	0.275	1.38	0.275	1.51	0.275	1.71	0.275	2.04	0.275	2.71	0.275
27	0.53	1.27	0.275	1.33	0.275	1.38	0.275	1.51	0.275	1.71	0.275	2.04	0.275	2.71	0.275
28	0.55	1.27	0.275	1.33	0.275	1.38	0.275	1.51	0.275	1.71	0.275	2.04	0.275	2.71	0.275
29	0.57	1.27	0.275	1.33	0.275	1.38	0.275	1.51	0.275	1.71	0.275	2.04	0.275	2.71	0.275
30	0.59	1.27	0.275	1.33	0.275	1.38	0.275	1.51	0.275	1.71	0.275	2.04	0.275	2.71	0.275
31	0.61	1.27	0.275	1.33	0.275	1.38	0.275	1.51	0.275	1.71	0.275	2.04	0.275	2.71	0.275
32	0.63	1.27	0.275	1.33	0.275	1.38	0.275	1.51	0.275	1.71	0.275	2.04	0.275	2.71	0.275
33	0.65	1.27	0.275	1.33	0.275	1.38	0.275	1.51	0.275	1.71	0.275	2.04	0.275	2.71	0.275
34	0.67	1.27	0.275	1.33	0.275	1.38	0.275	1.51	0.275	1.71	0.275	2.04	0.275	2.71	0.275
35	0.69	1.27	0.275	1.33	0.275	1.38	0.275	1.51	0.275	1.71	0.275	2.04	0.275	2.71	0.275
36	0.71	1.27	0.275	1.33	0.275	1.38	0.275	1.51	0.275	1.71	0.275	2.04	0.275	2.71	0.275
37	0.73	1.27	0.275	1.33	0.275	1.38	0.275	1.51	0.275	1.71	0.275	2.04	0.275	2.71	0.275
38	0.75	1.27	0.275	1.33	0.275	1.38	0.275	1.51	0.275	1.71	0.275	2.04	0.275	2.71	0.275
39	0.77	1.27	0.275	1.33	0.275	1.38	0.275	1.51	0.275	1.71	0.275	2.04	0.275	2.71	0.275
40	0.79	1.27	0.275	1.33	0.275	1.38	0.275	1.51	0.275	1.71	0.275	2.04	0.275	2.71	0.275
41	0.81	1.27	0.275	1.33	0.275	1.38	0.275	1.51	0.275	1.71	0.275	2.04	0.275	2.71	0.275
42	0.83	1.27	0.275	1.33	0.275	1.38	0.275	1.51	0.275	1.71	0.275	2.04	0.275	2.71	0.275
43	0.85	1.27	0.275	1.33	0.275	1.38	0.275	1.51	0.275	1.71	0.275	2.04	0.275	2.71	0.275
44	0.87	1.27	0.275	1.33	0.275	1.38	0.275	1.51	0.275	1.71	0.275	2.04	0.275	2.71	0.275
45	0.89	1.27	0.275	1.33	0.275	1.38	0.275	1.51	0.275	1.71	0.275	2.04	0.275	2.71	0.275
46	0.91	1.27	0.275	1.33	0.275	1.38	0.275	1.51	0.275	1.71	0.275	2.04	0.275	2.71	0.275
47	0.93	1.27	0.275	1.33	0.275	1.38	0.275	1.51	0.275	1.71	0.275	2.04	0.275	2.71	0.275
48	0.95	1.27	0.275	1.33	0.275	1.38	0.275	1.51	0.275	1.71	0.275	2.04	0.275	2.71	0.275
49	0.97	1.27	0.275	1.33	0.275	1.38	0.275	1.51	0.275	1.71	0.275	2.04	0.275	2.71	0.275
50	0.99	1.27	0.275	1.33	0.275	1.38	0.275	1.51	0.275	1.71	0.275	2.04	0.275	2.71	0.275
51	1.01	1.27	1.725	1.33	1.725	1.38	1.725	1.51	1.725	1.71	1.725	2.04	1.725	2.71	1.725
In-Situ =		**1.25**	**0.275**	**1.23**	**0.274**	**1.25**	**0.274**	**1.31**	**0.274**	**1.41**	**0.274**	**1.60**	**0.273**	**2.04**	**0.258**
Delivered =			**0.275**		**0.273**		**0.270**		**0.263**		**0.252**		**0.238**		**0.216**
sim time (s) =		**0.05**		**0.5**		**1.0**		**2.5**		**5.0**		**10**		**25**	

Table E.9: Model simulation results at t = 0.20 s for a CT 'gypsum' test (5 L/s, 2.5 ^{o})

Simulation Input	
h =	0.0231 m
d =	0.188 mm
ρ_f =	1188 kg/m^3
ρ_s =	2650 kg/m^3
μ_P =	0.0028 Pa-s
τ_y =	10.3 Pa
A_{mult} =	1.0E+06
ϕ_{total} =	0.227 v/v
ϕ_{max} =	0.582 v/v
θ =	2.5 deg
dt =	0.05 s

Simulation Output			
i	**y/h**	**u (m/s)**	**ϕ (v/v)**
0	-0.01	-0.10	0.321
1	0.01	0.10	0.273
2	0.03	0.34	0.197
3	0.05	0.52	0.218
4	0.07	0.64	0.222
5	0.09	0.71	0.222
6	0.11	0.75	0.225
7	0.13	0.76	0.227
8	0.15	0.76	0.228
9	0.17	0.76	0.227
10	0.19	0.76	0.227
11	0.21	0.76	0.227
12	0.23	0.76	0.227
13	0.25	0.76	0.227
14	0.27	0.76	0.227
15	0.29	0.76	0.227
16	0.31	0.76	0.227
17	0.33	0.76	0.227
18	0.35	0.76	0.227
19	0.37	0.76	0.227
20	0.39	0.76	0.227
21	0.41	0.76	0.227
22	0.43	0.76	0.227
23	0.45	0.76	0.227
24	0.47	0.76	0.227
25	0.49	0.76	0.227
26	0.51	0.76	0.227
27	0.53	0.76	0.227
28	0.55	0.76	0.227
29	0.57	0.76	0.227
30	0.59	0.76	0.227
31	0.61	0.76	0.227
32	0.63	0.76	0.227
33	0.65	0.76	0.227
34	0.67	0.76	0.227
35	0.69	0.76	0.227
36	0.71	0.76	0.227
37	0.73	0.76	0.227
38	0.75	0.76	0.227
39	0.77	0.76	0.227
40	0.79	0.76	0.227
41	0.81	0.76	0.227
42	0.83	0.76	0.227
43	0.85	0.76	0.227
44	0.87	0.76	0.227
45	0.89	0.76	0.227
46	0.91	0.76	0.227
47	0.93	0.76	0.227
48	0.95	0.76	0.227
49	0.97	0.76	0.227
50	0.99	0.76	0.227
51	1.01	0.76	1.773
In-Situ =		**0.73**	**0.227**
Delivered =		--	**0.226**
iterations =		**4**	--
real time (s) =		**5**	--
sim time (s) =		**0.20**	--

Table E.10: Model simulation results at t = 3.3 s for a CT 'gypsum' test (2.5 L/s, 3 ^{o})

Simulation Input	
h =	0.0281 m
d =	0.188 mm
ρ_f =	1188 kg/m^3
ρ_s =	2650 kg/m^3
μ_P =	0.0028 Pa-s
τ_y =	10.3 Pa
A_{mult} =	1.0E+06
ϕ_{total} =	0.280 v/v
ϕ_{max} =	0.582 v/v
θ =	3.0 deg
dt =	0.05 s

Simulation Output			
i	**y/h**	**u (m/s)**	**ϕ (v/v)**
0	-0.01	0.00	0.541
1	0.01	0.00	0.541
2	0.03	0.02	0.505
3	0.05	0.08	0.457
4	0.07	0.22	0.400
5	0.09	0.47	0.340
6	0.11	0.84	0.286
7	0.13	1.30	0.240
8	0.15	1.82	0.204
9	0.17	2.33	0.181
10	0.19	2.81	0.169
11	0.21	3.21	0.168
12	0.23	3.55	0.174
13	0.25	3.81	0.184
14	0.27	4.01	0.196
15	0.29	4.16	0.209
16	0.31	4.27	0.224
17	0.33	4.33	0.243
18	0.35	4.37	0.269
19	0.37	4.38	0.291
20	0.39	4.38	0.282
21	0.41	4.38	0.280
22	0.43	4.38	0.280
23	0.45	4.38	0.280
24	0.47	4.38	0.280
25	0.49	4.38	0.280
26	0.51	4.38	0.280
27	0.53	4.38	0.280
28	0.55	4.38	0.280
29	0.57	4.38	0.280
30	0.59	4.38	0.280
31	0.61	4.38	0.280
32	0.63	4.37	0.280
33	0.65	4.37	0.280
34	0.67	4.37	0.280
35	0.69	4.37	0.280
36	0.71	4.37	0.280
37	0.73	4.37	0.280
38	0.75	4.37	0.280
39	0.77	4.37	0.280
40	0.79	4.37	0.280
41	0.81	4.37	0.280
42	0.83	4.37	0.280
43	0.85	4.37	0.280
44	0.87	4.37	0.280
45	0.89	4.37	0.280
46	0.91	4.37	0.280
47	0.93	4.37	0.280
48	0.95	4.37	0.280
49	0.97	4.37	0.280
50	0.99	4.37	0.280
51	1.01	4.37	1.720
	In-Situ =	**3.64**	**0.279**
	Delivered =	**--**	**0.264**
	iterations =	**66**	**--**
	real time (s) =	**48**	**--**
	sim time (s) =	**3.3**	**--**

Table E.11: Model concentration gradient comparison for the transport of a sand in glycol slurry in laminar pipe flow (Gillies et al., 1999)

Simulation Input	
h =	0.0525 m
d =	0.43 mm
ρ_f =	1132 kg/m^3
ρ_s =	2650 kg/m^3
μ =	0.0460 Pa-s
ϕ_{total} =	0.200 v/v
ϕ_{max} =	0.64 v/v
θ =	0.0 deg
-dp/dz =	2.05 kPa/m
dt =	0.1

Simulation Output				Concentration Gradient Comparison	
i	y/h	u (m/s)	ϕ (v/v)	Present Model $-d\phi/dy$	Gillies et al. (1999) $-d\phi/dy$
0	-0.01	0.00	0.591	n/a	n/a
1	0.01	0.00	0.593	2.94	2.44
2	0.03	0.01	0.583	4.46	3.59
3	0.05	0.02	0.579	3.77	3.77
4	0.07	0.03	0.576	3.32	4.01
5	0.09	0.05	0.572	3.62	4.33
6	0.11	0.06	0.568	4.11	4.70
7	0.13	0.07	0.564	4.69	5.13
8	0.15	0.09	0.558	5.36	5.62
9	0.17	0.11	0.552	6.15	6.19
10	0.19	0.13	0.546	7.12	6.84
11	0.21	0.15	0.537	8.34	7.60
12	0.23	0.18	0.528	9.90	8.50
13	0.25	0.21	0.517	11.99	9.56
14	0.27	0.24	0.503	14.94	10.81
15	0.29	0.29	0.485	19.56	12.32
16	0.31	0.34	0.461	28.10	14.10
17	0.33	0.42	0.426	47.58	16.08
18	0.35	0.54	0.362	98.33	17.82
19	0.37	0.77	0.227	91.21	17.02
20	0.39	1.50	0.000	0.00	0.00
21	0.41	2.17	0.000	0.00	0.00
22	0.43	2.80	0.000	0.00	0.00
23	0.45	3.38	0.000	0.00	0.00
24	0.47	3.91	0.000	0.00	0.00
25	0.49	4.39	0.000	0.00	0.00
26	0.51	4.82	0.000	0.00	0.00
27	0.53	5.20	0.000	0.00	0.00
28	0.55	5.53	0.000	0.00	0.00
29	0.57	5.81	0.000	0.00	0.00
30	0.59	6.05	0.000	0.00	0.00
31	0.61	6.23	0.000	0.00	0.00
32	0.63	6.37	0.000	0.00	0.00
33	0.65	6.45	0.000	0.00	0.00
34	0.67	6.49	0.000	0.00	0.00
35	0.69	6.48	0.000	0.00	0.00
36	0.71	6.42	0.000	0.00	0.00
37	0.73	6.30	0.000	0.00	0.00
38	0.75	6.15	0.000	0.00	0.00
39	0.77	5.94	0.000	0.00	0.00
40	0.79	5.68	0.000	0.00	0.00
41	0.81	5.37	0.000	0.00	0.00
42	0.83	5.02	0.000	0.00	0.00
43	0.85	4.61	0.000	0.00	0.00
44	0.87	4.16	0.000	0.00	0.00
45	0.89	3.65	0.000	0.00	0.00
46	0.91	3.10	0.000	0.00	0.00
47	0.93	2.50	0.000	0.00	0.00
48	0.95	1.85	0.000	0.00	0.00
49	0.97	1.15	0.000	0.00	0.00
50	0.99	0.40	0.000	0.00	0.00
51	1.01	-0.40	-0.248	n/a	n/a
	In-Situ =	**2.87**	**0.195**		
	Delivered =	**--**	**0.011**		
	iterations =	**20600**	**--**		
	real time (s) =	**3388**	**--**		
	sim time (s) =	**2060**	**--**		

Table E.12: Model concentration gradient comparison for the transport of a sand in oil slurry in laminar pipe flow (Gillies et al., 1999)

Simulation Input	
h =	0.1047 m
d =	0.43 mm
ρ_f =	870 kg/m^3
ρ_s =	2650 kg/m^3
μ =	0.7140 Pa-s
ϕ_{total} =	0.200 v/v
ϕ_{max} =	0.64 v/v
θ =	0.0 deg
-dp/dz =	1.65 kPa/m
dt =	1

Simulation Output				Concentration Gradient Comparison	
i	y/h	u (m/s)	ϕ (v/v)	Present Model $-d\phi/dy$	Gillies et al. (1999) $-d\phi/dy$
0	-0.01	0.00	0.615	n/a	n/a
1	0.01	0.00	0.616	1.00	0.96
2	0.03	0.00	0.610	1.58	1.46
3	0.05	0.00	0.607	1.48	1.60
4	0.07	0.00	0.604	1.45	1.76
5	0.09	0.00	0.601	1.63	1.95
6	0.11	0.00	0.598	1.89	2.19
7	0.13	0.00	0.593	2.20	2.47
8	0.15	0.01	0.588	2.59	2.80
9	0.17	0.01	0.583	3.08	3.19
10	0.19	0.01	0.576	3.70	3.66
11	0.21	0.01	0.567	4.53	4.23
12	0.23	0.01	0.557	5.66	4.92
13	0.25	0.02	0.543	7.32	5.76
14	0.27	0.02	0.526	10.03	6.80
15	0.29	0.03	0.502	15.19	8.06
16	0.31	0.04	0.463	27.18	9.50
17	0.33	0.06	0.393	54.78	10.83
18	0.35	0.10	0.239	53.37	11.43
19	0.37	0.26	0.000	0.00	0.00
20	0.39	0.41	0.000	0.00	0.00
21	0.41	0.54	0.000	0.00	0.00
22	0.43	0.67	0.000	0.00	0.00
23	0.45	0.78	0.000	0.00	0.00
24	0.47	0.89	0.000	0.00	0.00
25	0.49	0.99	0.000	0.00	0.00
26	0.51	1.07	0.000	0.00	0.00
27	0.53	1.15	0.000	0.00	0.00
28	0.55	1.21	0.000	0.00	0.00
29	0.57	1.27	0.000	0.00	0.00
30	0.59	1.31	0.000	0.00	0.00
31	0.61	1.35	0.000	0.00	0.00
32	0.63	1.37	0.000	0.00	0.00
33	0.65	1.39	0.000	0.00	0.00
34	0.67	1.39	0.000	0.00	-0.01
35	0.69	1.38	0.000	0.00	0.00
36	0.71	1.37	0.000	0.00	0.00
37	0.73	1.34	0.000	0.00	0.00
38	0.75	1.31	0.000	0.00	0.00
39	0.77	1.26	0.000	0.00	0.00
40	0.79	1.20	0.000	0.00	0.00
41	0.81	1.14	0.000	0.00	0.00
42	0.83	1.06	0.000	0.00	0.00
43	0.85	0.97	0.000	0.00	0.00
44	0.87	0.88	0.000	0.00	0.00
45	0.89	0.77	0.000	0.00	0.00
46	0.91	0.65	0.000	0.00	0.00
47	0.93	0.53	0.000	0.00	0.00
48	0.95	0.39	0.000	0.00	0.00
49	0.97	0.24	0.000	0.00	0.00
50	0.99	0.08	0.000	0.00	0.00
51	1.01	-0.08	-0.355	n/a	n/a
In-Situ =		**0.62**	**0.195**		
Delivered =			**0.004**		
iterations =		**10437**	--		
real time (s) =		**1772**	--		
sim time (s) =		**7750**	--		

APPPENDIX F:
PHOTOGRAPHS

Figure F.1: Rippled free surface of a turbulent water flow in the 156.7 mm flume test section

Figure F.2: Deposit in the old 156.7 mm flume inlet with the 25% v/v sand-water tests

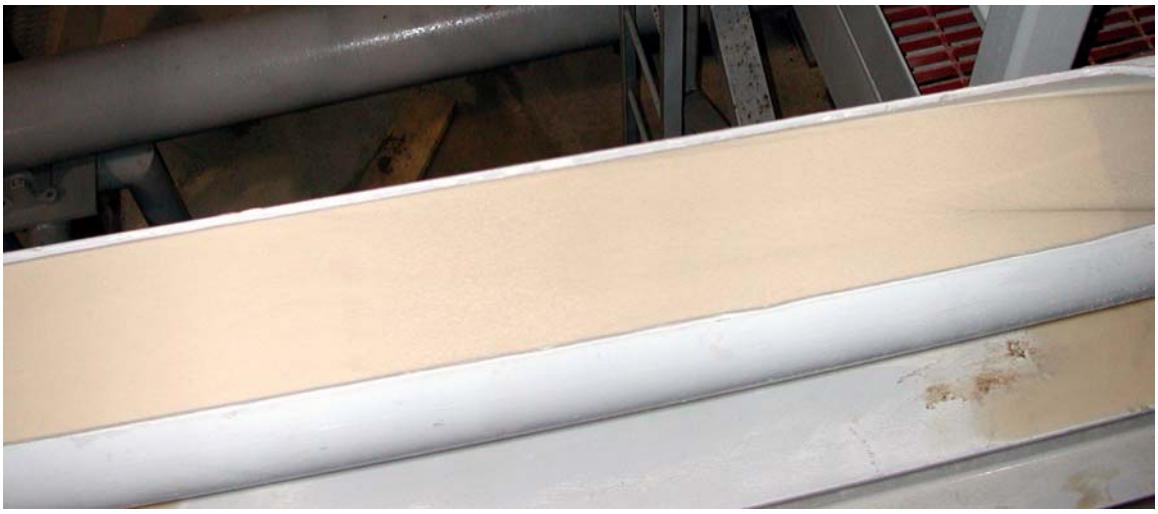

Figure F.3: Deposit in the 156.7 mm flume test section with the 25% v/v sand-water tests

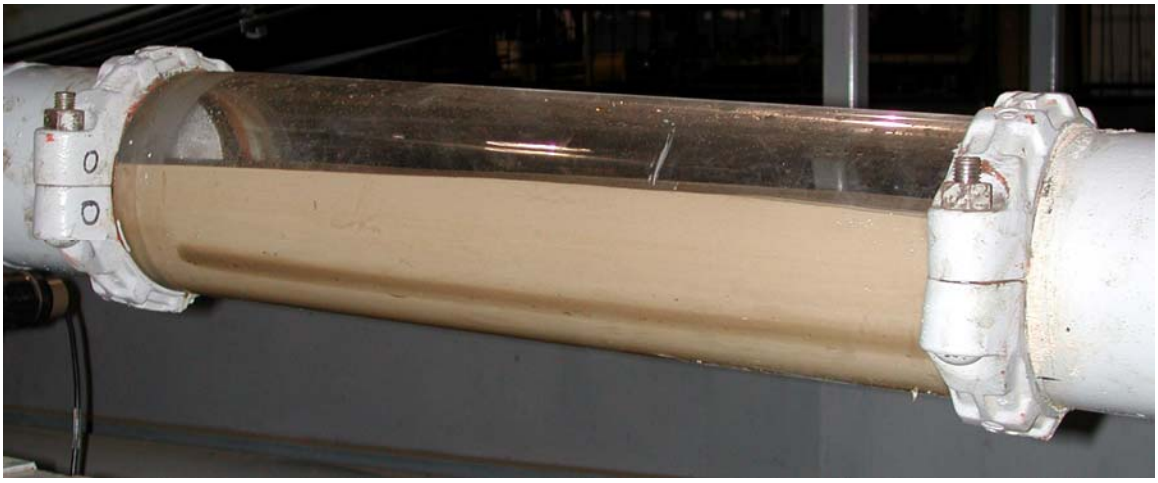

Figure F.4: Deposit in the 156.7 mm flume viewing section with the 25% v/v sand-water tests

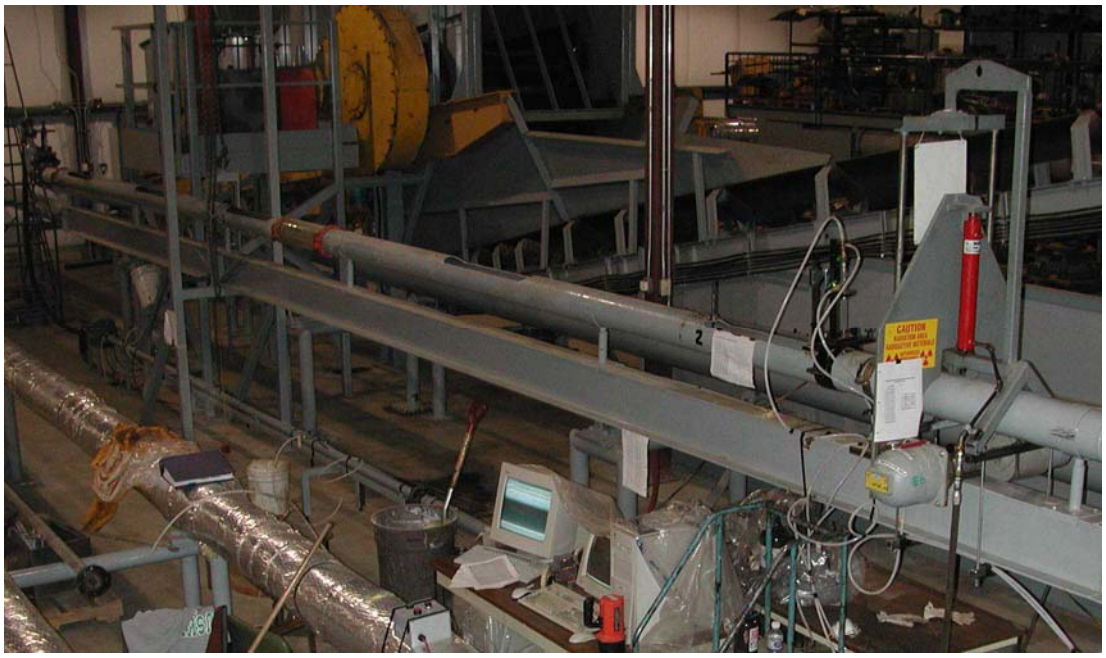

Figure F.5: View of the 156.7 mm flume circuit from the stand tank catwalk

Figure F.6: View of the 156.7 mm flume circuit from inlet to outlet (left to right)

Figure F.7: View of the 156.7 mm flume circuit winch and hoisting apparatus

Figure F.8: Landscape view of the 156.7 mm flume development length and test section (left to right)

Figure F.9: Data acquisition computer workstations used in the 156.7 mm flume experiments

Figure F.10: Data acquisition server computer used in the 156.7 mm flume experiments

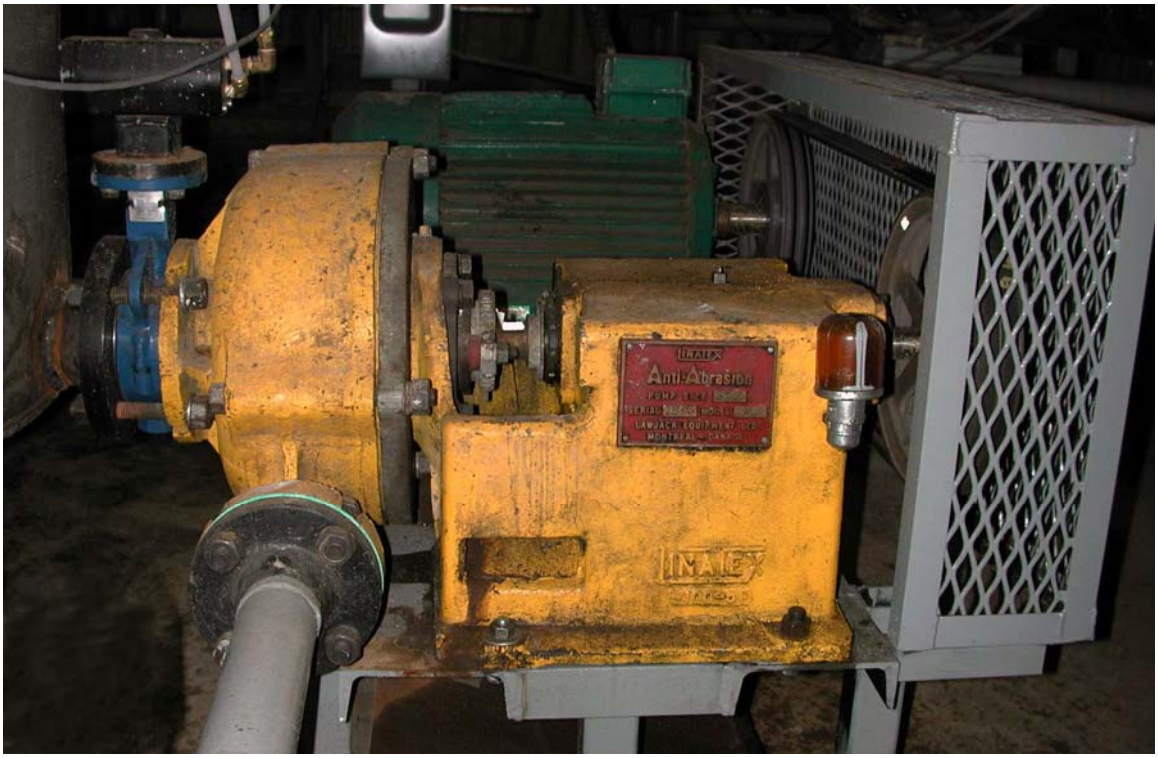

Figure F.11: Linatex 3x2 centrifugal pump on the 53 mm feed pipe used in the 156.7 mm flume experiments

Figure F.12: Ronan densitometer on the 53 mm feed pipe used in the 156.7 mm flume experiments

Figure F.13: Aircom temperature sensor on the 53 mm feed pipe used in the 156.7 mm flume experiments

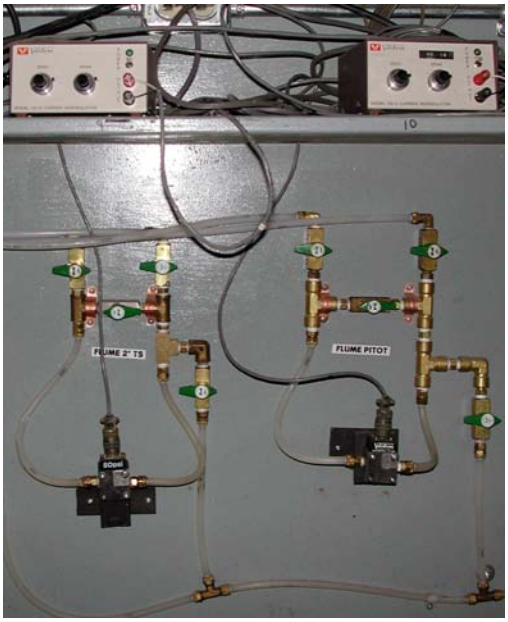

Figure F.14: Validyne pressure transducer bodies and demodulators used in the 156.7 mm flume experiments

Figure F.15: Pump motor variable frequency drive (VFD) pot used in the 156.7 mm flume experiments

Figure F.16: Proportional controller for the system temperature on the 53 mm feed pipe used in the 156.7 mm flume experiments

Figure F.17: Belimo control valve on the glycol-water fluid heat exchanger line used to control the system temperature in the 53 mm feed pipe used in the 156.7 mm flume experiments

Figure F.18: 2 inch Foxboro magnetic flowmeter on the 53 mm feed pipe used in the 156.7 mm flume experiments

Figure F.19: New 156.7 mm flume inlet conditions

Figure F.20: Depth of flow measurement gauge on the 156.7 mm flume test section

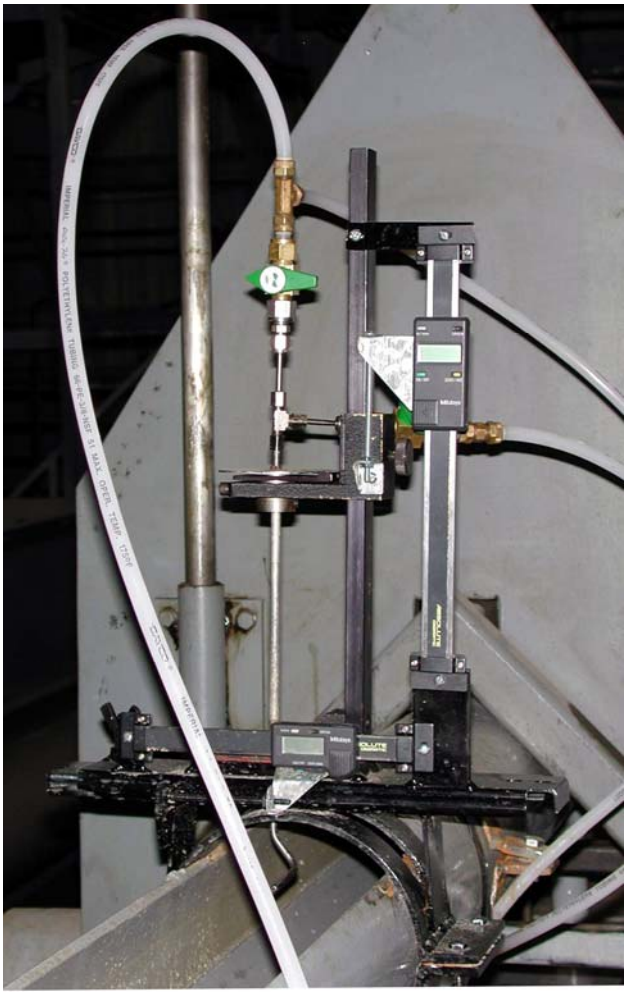

Figure F.21: Traversing Pitot-static tube apparatus on the 156.7 mm flume

Figure F.22: HPLC purge pump for the Pitot-static tube measurements during the 156.7 mm flume experiments

Figure F.23: Ronan traversing gamma ray densitometer on the 156.7 mm flume

Figure F.24: Hand pump apparatus used to traverse the Ronan gamma ray densitometer on the 156.7 mm flume

Figure F.25: Stand tank for the 156.7 mm flume circuit

Figure F.26: Baldor mixer in the 156.7 mm flume circuit stand tank